CRYSTAL STRUCTURE AND PHASE TRANSFORMATIONS IN 1D NANOSTRUCTURES

Martin Košiček

Doctoral Dissertation
Jožef Stefan International Postgraduate School
Ljubljana, Slovenia

Supervisor: Prof. Dr. Uroš Cvelbar, Jožef Stefan International Postgraduate School and Department of Gaseous Electronics, Jožef Stefan Institute, Ljubljana, Slovenia
Co-Supervisors: Asst. Prof. Dr. Janez Zavašnik, Jožef Stefan International Postgraduate School and Jožef Stefan Institute, Ljubljana, Slovenia
Asst. Prof. Dr. Uroš Puc, Jožef Stefan International Postgraduate School, Ljubljana, Slovenia, and Zurich University of Applied Sciences, Winterthur, Switzerland

Evaluation Board:
Asst. Prof. Dr. Kristina Žagar Soderžnik, Chair, Jožef Stefan International Postgraduate School and Jožef Stefan Institute, Ljubljana, Slovenia
Assoc. Prof. Dr. Alexandre Nominé, Member, University of Lorraine, Nancy, France
Prof. Dr. Johannes Berndt, Member, GREMI CNRS-University of Orleans, Orleans, France

MEDNARODNA PODIPLOMSKA ŠOLA JOŽEFA STEFANA
JOŽEF STEFAN INTERNATIONAL POSTGRADUATE SCHOOL

Martin Košiček

CRYSTAL STRUCTURE AND PHASE TRANSFORMATIONS IN 1D NANOSTRUCTURES

Doctoral Dissertation

KRISTALNA STRUKTURA IN FAZNE TRANSFORMACIJE V 1D NANOSTRUKTURAH

Doktorska disertacija

Supervisor: Prof. Dr. Uroš Cvelbar

Co-Supervisors: Asst. Prof. Dr. Janez Zavašnik, Asst. Prof. Dr. Uroš Puc

Ljubljana, Slovenia, September 2023

To my dear Tamara, my parents, brothers and grandparents

Acknowledgments

I would like sincerely to thank to my supervisor Uroš Cvelbar for his guidance, suggestions, and discussions. By showing me the key elements necessary to succeed in science, he helped me move my research skills to the next level. Many thanks also to my co-supervisor, Janez Zavašnik, for helping me with discussions, suggestions, and introducing me to the field of electron microscopy. I would also like to thank my co-supervisor Uroš Puc.
I am extremely grateful to our colleague from Kharkiv, Oleg Baranov, who helped me with his theoretical modeling skills and greatly contributed to the research results in this thesis. Special thanks to our secretary Urška Kisovec, who took care of every administrative obstacle and made my work much easier.

Thanks to all my other colleagues from the F6 department: Neel, Vasya, Andrea, Ardita, Jaka, Juš, Nataša, Martina, Vinko, Marko, Aswathy, and Gregor for all the discussions, suggestions, support, and feedback.
Special thanks also to our technician, Damjan Vengust. When laboratory instruments did not want to obey me, I could always rely on his help.

Many thanks to the Slovenian research agency, which provided funding for my work. Thank you also to the Jožef Stefan Institute and the Jožef Stefan International Postgraduate School.
I am grateful to my closest friends and colleagues from the faculty of chemistry, Matjaž, Jure, Zupi, Jan, and Blaž, for their company during my time in Ljubljana.

I am immensely thankful to my brothers Matjaž and Miha for being the best bros and my friend Sebastjan for being the best company during weekend trips or hikes.

I would also like to thank my parents and grandparents, who never stopped believing in me, for their encouragement and support throughout my life. Without their support, I would not be where I am now. Many thanks also to my uncles, aunts and cousins.

Last but not least, I would like to thank my dear Tamara for her love, support, understanding, all our shared moments, and for being the perfect person for me in every aspect. Many thanks also to her family for accepting me.

Abstract

Metal oxide and sulfide nanostructures are a versatile family of materials with wide-ranging applications, and their development remains ongoing. In nanoscience, attention is being directed towards their synthesis and further advancement, including the creating of new complex structures and morphologies. In this regard, ion-exchange reactions have emerged as a cutting-edge strategy for synthesizing novel ionic nanomaterials, allowing precise control over the phase and the morphology. This field continuously evolves, with discoveries of new mechanisms and phenomena contributing to improved materials being synthesized.

This thesis was focused on the synthesis of metal oxide nanostructures, specifically CuO nanowires, and their use as a model material for investigating anion-exchange transformation as a potential mechanism for the synthesis of new materials. The selection of CuO nanowires as a model material is ideal due to their one-dimensional shape, simplifying the study of phase transformations. For that reason, ultra-thin nanowires are desired for exploring the transformation processes. The synthesis of CuO nanowires was achieved through the thermal oxidation of copper in air. The method is straightforward; however, the nanowire-growth mechanism is complex and poorly understood. Hence, the research efforts in the first part of the thesis were dedicated to unraveling the mechanism behind the thermal growth of CuO nanowires. We found that the nanowires likely originated from twinned CuO grains, where oxidation preferentially occurred at the twin-boundary defect on the grain surface. During the oxidation, the NW roots become partially buried in the CuO layer growing below the nanowires. A theoretical model we developed supported the growth of nanowires and underlying oxide layers. To study the size-dependent effects on the phase transformations and to observe how nanowires behave close to the limit of quantum confinement, we also identified the optimum oxidation temperature for obtaining ultrathin CuO nanowires with the minimum diameters, serving as an ideal template material for this purpose. This limiting temperature corresponded to slightly below 200 °C, and the correlation between the nanowire's diameter and the temperature was explained through the modeling of nucleation processes.

Following the synthesis of CuO nanowires, we carried out thermally dependent sulfurization to induce an oxide-to-sulfide phase transformation. The resulting nanostructures are morphology and phase dependent on the availability of copper cations participating in the reaction. When sulfurized nanowires were isolated, with the amount of copper involved limited to that present in the nanowires, the resulting structures were voided CuS nanowires. However, if the nanowires were still attached to the underlying substrate during sulfurization, an unlimited supply of copper from the substrate led to continued growth of the nanowire, resulting in a bulky Cu_2S structure. We also developed a theoretical model to explain this intriguing observation.

The investigation into phase transformations in CuO nanowires was extended by utilizing plasma in the post-glow region of a microwave discharge as a sulfurization environment. The plasma-induced dimensionality changes by reshaping the nanowires into two-dimensional CuS structures. The proposed mechanism behind this transformation provided valuable insights into the unique processes occurring in a plasma environment and their potential in anion-exchange reactions.

The outcomes of this thesis shed light on the growth and phase transformations in copper oxide nanowires, offering valuable insights into nanoscale processes that are dependent on molecules or radicals interacting with surfaces. The understanding of the nanowire growth mechanism will aid in the development and application of copper oxide nanostructures. Additionally, the described phenomena and mechanisms of anion-exchange processes open up new possibilities for synthesizing materials through phase-transformation reactions, while also contributing to fundamental scientific knowledge.

Povzetek

Nanostrukture kovinskih oksidov in sulfidov predstavljajo skupino materialov, uporabnih v številnih aplikacijah, njihov razvoj pa še vedno poteka. Njihova sinteza, vključno s sintezo novih kompleksnih struktur in morfologij, je v nanoznanosti deležna velike pozornosti in zanimanja. Na tem področju so se reakcije ionske izmenjave izkazale kot obetavna strategija za sintezo novih ionskih nanomaterialov, ki omogoča natančen nadzor nad fazo in morfologijo. Področje ionske izmenjave v trdnem stanju se konstantno razvija, z nenehnimi odkritji novih mehanizmov in pojavov, ki prispevajo k izboljšanju lastnosti sintetiziranih materialov.

Poudarek te doktorske naloge je bil na sintezi nanostruktur kovinskih oksidov, natančneje CuO nanožic, kot modelnega materiala in njihovi uporabi za raziskave transformacije anionskih izmenjav kot potencialnega mehanizma za sintezo novih materialov. Izbira CuO nanožic kot modelnega materiala je idealna zaradi njihove enodimenzionalne oblike, ki poenostavlja preučevanje faznih transformacij. Zaradi tega so ultratanke nanožice zaželene za raziskovanje transformacijskih procesov. Sinteza CuO nanožic je bila dosežena s termično oksidacijo bakra. Metoda je zelo preprosta, vendar je mehanizem rasti nanožic precej zapleten in še ne dodobra raziskan. Prvi del naloge je bil tako namenjen preučevanju mehanizma termične rasti CuO nanožic. Ugotovljeno je bilo, da nanožice izvirajo iz dvojčičenih CuO zrn, saj oksidacija najhitreje poteka na dvojčični meji na površini zrn. Med samo oksidacijo se spodnji deli nanožic zakopljejo v CuO plast, ki se formira pod nanožicami. Rast nanožic in oksidnih plasti je bila podprta z razvitim teoretičnim modelom. Z nadaljnjimi raziskavami je bila ugotovljena tudi optimalna oksidacijska temperatura za pridobivanje CuO nanožic z minimalnimi premeri, ki je znašala malo pod 200 °C. Korelacija med premerom nanožic in temperaturo pa je bila razložena z modeliranjem procesov nukleacije.

Po sintezi CuO nanožic so bile te termično sulfurizirane v fazni transformaciji oksida v sulfid. Nastale sulfidne nanostrukture so morfološko in fazno odvisne od razpoložljivosti bakrovih kationov, ki sodelujejo v reakciji. Ko so nanožice izolirane, z omejeno količino bakra, ki lahko sodeluje v sulfurizaciji, nastanejo votle enodimenzionalne CuS strukture. Če pa so nanožice med sulfurizacijo še vedno pritrjene na substrat, s katerega so zrasle, neomejena dobava bakra iz substrata povzroči nadaljnjo rast nanožic v večje Cu_2S strukture. Ta zanimiv pojav je bil podprt tudi s teoretičnim modeliranjem.

Preiskava faznih transformacij v CuO nanožicah je bila razširjena z uporabo mikrovalovne plazme kot sulfurizacijskega medija. Uporaba plazme je omogočila spremembo dimenzionalnosti s preoblikovanjem nanožic v dvodimenzionalne CuS strukture. Predlagani mehanizem te transformacije je omogočil dragocen vpogled v edinstvene procese, ki se pojavljajo v plazemskem okolju, in njihov potencial v reakcijah anionske izmenjave.

Rezultati te doktorske naloge prinašajo nove odgovore o mehanizmih rasti in faznih transformacij v nanožicah bakrovega oksida ter ponujajo dragocen vpogled v procese na nanometrski skali. Razumevanje mehanizma rasti nanožic bo dodatno pripevalo k razvoju in uporabi nanostruktur bakrovega oksida. Poleg tega odpirajo opisani pojavi in mehanizmi procesov ionskih izmenjav nove načine za sintezo materialov preko reakcij faznih transformacij, hkrati pa predstavljajo velik doprinos k temeljnim znanstvenim spoznanjem.

Contents

Abbreviations

1D	. . . One Dimensional
2D	. . . Two Dimensional
3D	. . . Three Dimensional
$AgNO_3$	. . . Silver Nitrate
Ag_2Se	. . . Silver Selenide
BDS	. . . Broadband Dielectric Spectroscopy
Cd	. . . Cadmium
Cd^{2+}	. . . Cadmium Cation
CdNCN	. . . Cadmium Cyanamide
$Cd(NO_3)_2$	. . . Cadmium Nitrate
CdS	. . . Cadmium Sulfide
CdSe	. . . Cadmium Selenide
CoS	. . . Cobalt (Ii) Sulfide
Co_9S_8	. . . Cobalt Sulfide, Cobaltpentlandite
Cu^+	. . . Copper (1+) Cation
Cu^{2+}	. . . Copper (2+) Cation
CuO	. . . Copper (Ii) Oxide, Tenorite
Cu_2O	. . . Copper (I) Oxide, Cuprite
CuS_2	. . . Villamaninite
CuS	. . . Copper (Ii) Sulfide, Covellite
Cu1.12	. . . Yarrowite
Cu1.39	. . . Spionkopite
Cu1.6	. . . Geerite
Cu1.75	. . . Anilite
Cu1.8	. . . Digenite, Roxbyite
Cu1.96	. . . Djurleite
Cu_2S	. . . Copper (I) Sulfide, Chalcocite
$Cu_{2-x}S$	. . . Non-Stoichiometric Copper Sulfide
Cu_2Se	. . . Copper (I) Selenide
$Cu_{2-x}Se$	. . . Non-Stoichiometric Copper Selenide
Cu	. . . Copper
CVD	. . . Chemical Vapor Deposition
eV	. . . Electron Volt
Fe_2O_3	. . . Iron (Iii) Oxide, Hematite
Fe_3O_4	. . . Iron (II,III) Oxide, Magnetite
Fe_3S_4	. . . Iron (II,III) Sulfide), Greigite
H_2S	. . . Hydrogen Sulfide
MnS	. . . Manganese (II) Sulfide
NCN^{2-}	. . . Cyanamide Anion
Ni	. . . Nickel
Ni_3Se_4	. . . Nickel Selenide, Wilkmanite
NP	. . . Nanoparticle
NW	. . . Nanowire
O^{2-}	. . . Oxygen(2-) Anion
PbS	. . . Lead (Ii) Sulfide
Pb	. . . Lead
Pb^{2+}	. . . Lead(2+) Cation
PbSe	. . . Lead (Ii) Selenide
S^{2-}	. . . Sulfur(2-) Anion

Se	. . .	Selenium
SEM	. . .	Scanning Electron Microscopy
SLS	. . .	Solution-Liquid-Solid
TEM	. . .	Transmission Electron Microscopy
TiO_2	. . .	Titanium (Iv) Oxide
TMS_2O	. . .	Bis-(Trimethylsilyl) Oxide
TMS-ODA	. . .	(Z)-N-Trimethylsilyloctadec-9-En-1-Amine
UV	. . .	Ultraviolet
VLS	. . .	Vapor-Liquid-Solid
VSS	. . .	Vapor-Solid-Solid
$W_{18}O_{49}$	. . .	Tungsten Pentoxide, Mineral Blue
Zn^{2+}	. . .	Zinc(2+) Cation
ZnO	. . .	Zinc Oxide
$ZnO_xS_{(1-x)}$	. . .	Zinc (Oxide, Sulfide) Intermediate
ZnS	. . .	Zinc Sulfide

Chapter 1

Introduction

1.1 Nanowires

Nanowires (NWs) are 1D nanomaterials with nanoscale diameters, with a wide variety of applications in many fields, which sets them apart from bulk materials. Their diameters are typically smaller than 100 nm, and they can be engineered from various materials, including semiconductors like silicon and semiconducting metal oxides, metals like gold and silver, and even organic compounds [1], [2].

One of the most useful features of NWs is their high aspect ratio, with lengths often thousands of times greater than their diameters. In addition, a 1D structure with nanoscale diameters confines electrons in the radial direction, resulting in novel physical properties where quantum and surface effects dominate over bulk behavior. The electronic properties of NWs can vary depending on their size and composition, making them highly customizable for specific applications. They can exhibit tunable electrical conductivity, bandgaps, and charge-carrier mobility [3].

Recently, there has been a great deal of research into the application of nanowires (NWs) across various fields [1], [4]. The literature [5], [6], in particular, underscores the significance of semiconducting NWs, such as metal oxide NWs. Notably, NW properties exhibit marked deviations from those of bulk materials, particularly in aspects like electrical conductivity. NWs have garnered attention for their catalytic utility, attributed to their slower sintering rate compared to most nanoparticles (NPs), thereby offering greater specific surface areas [7]. Amid diverse materials, metal oxides frequently undergo testing in applications spanning gas sensing, photonics, catalysis, photovoltaics, and energy storage [1]. The pivotal attributes driving the application of metal oxide NWs in these fields include well-defined crystal structures, crystallinity, large specific surface areas, and distinct electrical properties. Copper oxide (CuO) NWs have similar areas of applications, for example, in photovoltaics due to their semiconducting properties, as well as in optoelectronics, as catalysts, photocatalysts, gas sensors and field-emission sources [4], [8]. Many other metal oxide NWs exhibit properties similar to those described above [1], [4], [7], [9]. Due to their wide variety of applications and facile synthesis, CuO NWs represent an ideal model material for the fundamental research of 1D materials, such as growth mechanisms and phase transformations.

However, despite their potential, challenges remain in the large-scale synthesis and assembly of NWs, as well as their integration into practical devices. In addition, mechanisms of NW growth are, to a large extent, still not understood, with fundamental questions, such as why the growth of NWs occurs predominantly in one dimension, still unanswered. As a result, the growth of NWs remains a hot topic for the nanoscience community. New studies continue to explore innovative fabrication methods and investigate the fundamental properties of NWs to unlock their full potential and pave the way for a new era of nanotechnology.

1.1.1 NWs as a Model Material to Study Phase Transformations in Nanomaterials

In ionic materials such as metal oxides, the common phase transformations include cation or anion exchange. These types of transformations are greatly facilitated by nanomaterials, compared to bulk materials [10], and, therefore, the materials of choice should be nanoscale.

Due to their shape, NWs serve as ideal model nanostructures for investigating processes within nanomaterials. When the size of NPs is decreased below their Bohr exciton radius, the electrons become confined, resulting in the quantification of their energy states. This quantification can occur in 1D (in 2D nanomaterials such as nanoplates), 2D (in 1D nanomaterials such as nanowires, nanotubes, etc.) or 3D (in 0D nanomaterials, i.e., quantum dots). In comparison to materials with higher dimensionalities, 1D materials exhibit a higher surface-to-volume ratio and their theoretical and practical treatment is much simpler. This stems from the simplified nature of observations, theoretical modeling, and calculations achievable in 1D systems. The 1D geometry reduces the complexity of the system compared to bulk materials or three-dimensional counterparts. By condensing the system into a single dimension, the study becomes more manageable and computationally less demanding. Furthermore, the diameter of the NWs can often be adjusted by modifying the synthesis parameters, facilitating the precise exploration of size-dependent properties. On the other hand, the presence of additional degrees of freedom in 2D and 3D structures introduces complications for both experimental and theoretical examinations of nanomaterial processes.

Moreover, the free movement of electrons and holes in an axial direction makes NWs a material where both bulk effects in an axial direction and quantum effects in a radial direction can be studied and compared, representing an ideal compromise between a bulk material and a nanomaterial.

1.1.2 Growth of NWs

NWs can be synthesized using various methods, which can be categorized into synthesis from the liquid phase and synthesis from the vapor phase. Liquid-phase techniques involve using precursors in solute form for NW synthesis. Examples of liquid-based methods include hydrothermal synthesis, electrodeposition, sol-gel, and sonochemical [1]. Achieving one-dimensional growth is accomplished by employing strategies such as template-assisted methods and catalyst utilization. In template-assisted methods, a porous substrate serves as the template for NW preparation. Various methods can utilize these templates. For instance, in template-assisted electrodeposition, a template with nanoscale pores, such as anodized aluminum oxide or a polycarbonate membrane, is employed. When this template is immersed in an ionic solution, and a potential is applied, ions from the solution are reduced within the substrate pores, forming one-dimensional structures that adopt the shape of the pore. Another approach to achieving one-dimensional growth from solutions involves using a catalyst for the so-called solution-liquid-solid (SLS) growth of NWs. Common catalysts are NPs of transition metals with low melting points, such as gallium, indium, tin, or bismuth, and even gold and silver NPs can be utilized. These catalysts can be dispersed in the solution or formed in situ. When molten catalysts come into contact with precursors for NW growth, they catalyze the transformation of these precursors into the material that will make up the NW. Upon supersaturation of the catalyst droplets, NW nucleation occurs and continues for as long as the precursor is supplied to the catalyst droplet. Crystal growth occurs at the interface between the forming NW and the molten catalyst droplet, leading to anisotropic crystal growth.

Conversely, catalyst-free NW growth is also reported in some methods. For instance, the hydrothermal growth of metal oxide NWs is often reported without the use of a specific strategy to achieve unidirectional crystal growth. Although catalyst-free NW synthesis is advantageous for production, explaining anisotropic crystal growth in such cases can be challenging, and the underlying mechanisms often remain unknown.

Vapor-phase methods for NW synthesis encompass techniques like chemical vapor deposition (CVD), physical vapor deposition, laser ablation, molecular beam epitaxy, plasma-based techniques, and others that utilize NW precursors in the vapor phase. Like liquid-phase techniques, templates or catalysts are common strategies for achieving anisotropic growth. Template-assisted CVD, for instance, has proven effective in obtaining silicon NWs [11]. Catalyst utilization is also widespread for synthesizing NWs from the vapor phase using the well-known vapor-liquid-solid (VLS) system. This process is analogous to the SLS mechanism described earlier, but the precursors essential for NW growth are introduced from the vapor phase rather than a solution. The catalysts employed are NPs of transition metals that melt during the process. The vapor-phase NW precursors can react with or dissolve into the catalyst NPs, causing them to become supersaturated. This leads to NW phase nucleation and growth at the interface between the catalyst nucleus

and the NW, resulting in a unidirectional product. A similar process using solid catalyst particles is referred to as the vapor-solid-solid (VSS) mechanism.

In present work, for the synthesis of CuO NWs, we employed the thermal oxidation of metallic copper, which is an example of catalyst-free NW growth. Apart from copper, other metals such as iron [12]–[14] or zinc [15], [16] can also be thermally oxidized to produce metal oxide nanowires.

1.1.3 Copper Oxide NWs: Properties and Synthesis

Copper (II) oxide (CuO) NWs represent an environmentally friendly, narrow-band-gap, semiconducting nanomaterial, with band-gap energies between 1.2 and 2 eV [17]–[24]. CuO NWs are promising materials for nanotechnological applications due to their facile synthesis and properties, making them an excellent candidate material for gas sensing [25]–[34], photocatalysis [35], [36], energy-storage applications [37]–[43], biomedical applications [44], opto-electronic devices [18], [45]–[47] etc. They can be synthesized using electrodeposition, sol-gel, hydrothermal, other wet-chemical methods, plasma-assisted methods, etc. [8] However, the simplest method for their fabrication is thermal oxidation. Here, CuO NWs can be synthesized by heating metallic copper in air or an oxygen-rich atmosphere. There have been numerous reports of thermal oxidation as a route to synthesizing CuO NWs, and the method is well-established for obtaining arrays of CuO NWs. However, the fundamental science behind the thermal growth of NWs is still lacking details of the mechanisms driving their growth, which is currently mostly based on assumptions. Determining the mechanism of CuO NW growth presents a challenge and a knowledge gap that must be bridged.

1.1.4 Mechanism of CuO NW Growth by the Thermal Oxidation Method

The mechanism behind the thermal growth of CuO NWs remains a controversial topic within the nanoscience community, prompting numerous studies to resolve it. When metallic copper undergoes oxidation at elevated temperatures, two oxide layers typically form before NW formation. A Cu_2O layer emerges directly atop the copper surface, followed by the CuO layer, which serves as the inception point for the CuO NW growth. The Cu_2O layer is thicker than the CuO layer and contains larger grains. Over time and with increasing temperature, both the CuO and Cu_2O layers become thickner according to the parabolic growth law [48]. The roots of CuO NWs are embedded in the CuO layer. A central twin boundary inside CuO NWs is commonly reported in most research. The dimensions of NWs, including their length and diameter, also exhibit correlations with temperature; higher temperatures result in thicker and longer NWs. Conversely, only the NW's length experiences growth over time, with the NW diameter remaining relatively unchanged. Presently, the precise mechanism governing CuO NW growth through copper thermal oxidation remains incompletely understood. Although discrepancies exist among various reports, there is a consensus that in the case of copper thermal oxidation, NW growth does not follow Vapor-Liquid-Solid (VLS) or Vapor-Solid-Solid (VSS) mechanisms, as the melting and boiling points of copper and its oxides are above the temperature range of 300 °C to 700 °C where CuO NW growth is commonly observed [49]. The most widely accepted theory links the growth of CuO NWs to the stress arising at the interfaces between metallic copper and copper oxide layers. According to the literature, stress triggers the rapid grain-boundary diffusion of copper species from the copper substrate to the surface. Given that grain-boundary diffusion predominates within the temperature range of NW growth, numerous studies associate NW growth with this stress-induced grain-boundary diffusion [48], [50]–[52]. However, the rationale behind how such diffusion leads to NW growth remains elusive, necessitating further research to establish a connection between grain-boundary diffusion and one-dimensional growth. Another mechanism proposed more recently revolves around NW central twin boundaries. The top of the NW, where the twin boundary emerges, acts as a catalytic site on the NW surface, facilitating the reaction between copper and oxygen and subsequently forming the CuO phase, which elongates the NW [53], [54]. Indeed, these studies have demonstrated that NWs grow on the tops where copper species need to be transported during oxidation. Surface diffusion and twin-boundary diffusion are the most likely pathways, with lattice diffusion being excluded due to its higher activation energy.

The third proposed CuO NW growth mechanism is tied to an oxygen gradient formed on the surface of copper during oxidation. This gradient results from the rapid consumption of oxygen during the oxidation reaction, leading to a lower oxygen concentration at the substrate surface. Consequently, the oxygen concentration is higher around elevated portions of the substrate, thereby facilitating oxidation at these regions and elongating the elevated parts into NWs [55]. Thus, the existing literature reveals numerous knowledge gaps concerning the mechanism of NW growth. These gaps include understanding the contributions of processes in the underlying Cu_2O and CuO layers to CuO NW growth, a topic that remains largely unexplored and overlooked. Additionally, it is unclear what are the exact conditions needed for the growth of NWs. In particular, the limiting temperature needed for their growth is unknown. Therefore, we had to explore the conditions for NW growth.

1.2 Phase Transformations in Nanomaterials

From a fundamental point of view, studying phase transformations represents a unique way to observe different phenomena and mechanisms in solid-state reactions. From the applicative point of view, phase transformations in nanomaterials represent a way to tune the properties of initial nanomaterials or a way to synthesize completely new materials. Phase transformations in nanomaterials can be induced by controlled tuning of external factors such as temperature, pressure, and chemical environment, resulting in an altered crystal structure and composition of the initial nanomaterial. Understanding the mechanism and controlling these phase transformations is crucial to tailoring the properties and functionalities of nanomaterials for specific applications.

Apart from the reaction conditions used to achieve the transformation, the transformation's outcome depends on the material type used. For example, phase transformations in metal-organic frameworks often result in the preservation of single crystallinity during the transformation due to their porous and flexible structure, enabling a facile rearrangement of the crystal's building blocks during transformations [56], [57]. On the other hand, preservation of single crystallinity is rarely reported in ionic crystals with compact structures, such as metal oxides or other inorganic crystals with densely packed crystal structures. Nevertheless, the phase transformations of binary ionic inorganic nanomaterials, such as metal oxides, represent a unique way to fabricate new materials, which would be hard or almost impossible to produce using conventional bottom-up techniques.

When chemically modifying the material, numerous strategies can be used to transform nanomaterials. In recent years, ion-exchange reactions have emerged as a new promising method for the synthesis of complex ionic nanomaterials [58], [59].

1.2.1 Ion-exchange Reactions in Nanomaterials

Ion-exchange reactions in the solid-state occur within ionic crystals, where cations or anions within the crystal lattice are either partially or fully replaced by ions that are introduced from external sources. While ion exchange is often conducted in solution, gaseous precursors can also be utilized. Ion-exchange reactions represent a powerful strategy for developing new nanomaterials with tailored properties and functionalities. By carefully selecting the precursor materials and controlling the ion-exchange process, it is possible to produce complex, functionally graded materials. Beyond the synthesis of new materials, ion-exchange reactions also find their applications in doping or the surface modifications of nanomaterials. Moreover, a partial ion-exchange transformation is a route to synthesize multiple-phase nanomaterials with different morphologies [58], representing a method that could facilitate the production of epitaxial nanostructures.

The advantages of ion-exchange reactions extend beyond those of conventional bottom-up methods for synthesizing nanomaterials. One key advantage lies in their ability to generate nanomaterials with metastable phases. This is a consequence of the topotactic reaction pathway frequently taken by ion-exchange reactions, aiming to maintain analogies between anion and cation sublattices. Consequently, emerging phases can be metastable under specific conditions [59]. Furthermore, the morphology of the initial nanomaterial also influences the phase of the transformed material [60].

Ion-exchange reactions in the solid state have predominantly been observed in nanoscale materials. This occurrence is attributed to the possible reduction in the activation energy within nanoscale crystals due to the presence of high-energy sites in the form of crystal defects, curved surfaces and low-coordination facets. This lowered activation energy not only facilitates the reaction, but also enables the formation of metastable phases. The diminished crystal size may also promote a more straightforward strain relief during the process. In nanomaterials such as NWs, the majority of atoms reside close to the surface and can easily compensate for a lattice distortion. When the ion exchange is performed in solution, the solvation of the exchanged cations also influences the reaction, with stronger solvation reducing the ion-exchange activation energy and promoting the reaction [10].

The two types of ion-exchange reactions are cation exchange and anion exchange.

In this thesis the central topic was anion exchange in metal oxide NWs, with copper oxide NWs serving as the model material. To explore the potential applicability of these reactions to other ionic materials, understand the underlying principles and phenomena, and gain insights into how the model material might respond to cation exchange instead of anion exchange, it is essential to conduct a brief literature review, which will encompass the existing research on both cation- and anion-exchange processes involving various materials. This was carried out in subsections 1.2.1.1 and 1.2.1.2.

1.2.1.1 Cation-Exchange Reactions in Nanomaterials

Cation-exchange reactions are more common and easier to achieve than anion-exchange reactions. The reason for that is the higher mobility of the smaller cations in the crystal lattice, enabling the faster exchange of cations without altering the anionic sublattice. Therefore, in most cation-exchange reactions, the anionic sublattice is retained, and its rigidity is the reason for the structural preservation of the solid material during the reaction [58], [59]. Ion-exchange reactions also strongly depend on the size of the material, as will be demonstrated in the examples below. The exact mechanism of ion-exchange reactions is not entirely understood. However, there are some studies that are shedding light on it. In reference [61] the authors used molecular dynamics simulations to simulate a PbS-to-CdS transformation. From the results, they concluded that a cation exchange is initiated by Cd interstitials, which "kick" the Pb cations out of the PbS core. The Pb^{2+} ions then migrate through the interstitial sites. In CdS domains, the jumping of the Pb cations between octahedral interstitial sites is greatly facilitated by the formation of Cd Frenkel defects by lowing the repulsive forces, which would occur between the Pb^{2+} and the Cd^{2+} ions if the latter were to occupy their original positions in the crystal structure.

One of the most important factors that determines whether the transformation would be complete and the morphology of the nanomaterial retained, is the preservation of the anion sublattice during the cation exchange. This was demonstrated by Jeong *et al.* [62], [63], who report on the transformation of orthorhombic Ag_2Se NWs to wurtzite-type CdSe NWs. In the process, the single crystallinity was preserved, which was attributed to the topotactical relationship between the Se sublattices, minimizing significant lattice alterations during the cation exchange, a crucial factor for preserving the morphology and single crystallinity [64], [65].

Similarly, Powell *et al.* [66] achieved a complete transformation of roxbyite $Cu_{1.8}S$ nanoplatelets to CoS and MnS NPs via cation exchange. In both cases the formation of metastable wurtzite polymorphs was favored over more stable polymorphs due to the preservation of the anion sublattice.

Li *et al.* [67] performed cation exchange on the CdSe nanocrystals. Here, Cd^{2+} cations were exchanged with Cu^{+} cations, followed by Cu^{+} exchange with Zn^{2+}. If the transformation was conducted on the cubic CdSe polymorph, the resulting copper and zinc selenides also exhibited a cubic structure. On the other hand, if the starting material used was the hexagonal CdSe polymorph, the resulting copper and zinc selenides were metastable hexagonal polymorphs, which were, in this case, favored over the more stable cubic polymorphs.

A similar example was reported by Kim *et al.* [68], who performed Cu cation exchange on the berzelianite $Cu_{2-x}Se$ nanocrystals with Ni cations. In the process, single crystalline, metastable, Ni_3Se_4 nanocrystals with spinel-type crystal structures were formed, and the anion face-centered-cubic sub-structure was retained.

Another example of how the crystal structure can dictate the course of the cation-exchange transformation was pointed out by Gariano *et al.* [69], who performed the cation

exchange of Cu^{2+} cations on cubic and metastable, hexagonal Cu_2Se nanocrystals with Pb^{2+} cations. Since PbSe only has one stable phase, i.e., cubic, the resulting nanocrystals always attained this form. However, the course of the reaction depended on the crystal structure of the initial crystal. When the cubic Cu_2Se polymorph was used as a starting material, the cation exchange proceeded via the random nucleation of the PbSe phase on the Cu_2Se nanocrystals. However, when the hexagonal polymorph of Cu_2Se was the starting material, the preferred Pb^{2+} diffusion through the a and b planes produced PbSe stripes in the Cu_2Se structure.
Another factor influencing the outcome of the ion-exchange transformations is the size as shown in reference [70]. Here, the authors achieved a reversible cation exchange of Cd^{2+} with Ag^{+} in CdSe NPs. This transformation only occurred in NPs, not micro-scale particles, indicating size-dependent reaction barriers. Furthermore, nanorods, tetrapods, and hollow nanospheres with diameters larger than 5 nm retained their shape, while nanorods with diameters smaller than 5 nm transformed into spheres due to a disruption of the anion sublattice. The Ag_2Se crystal structure also depended on the initial crystal size, with thicker nanorods becoming tetragonal Ag_2Se and thinner ones forming a cubic structure.

A factor which also influences the transformation is the shape of the treated crystals, as pointed out by Li *et al.* [71], who performed copper cation-exchange reactions on $Cu_{1.8}S$ (roxbyite) NPs of different shapes with cobalt cations. When nanoplates were used as the shape of the initial nanocrystal, the anion sublattice was preserved in the transformation, and metastable wurtzite-type CoS was the transformation product. On the other hand, when nanorods were used as the initial crystal shape, thermodynamically stable petlantide-type Co_9S_8 was formed; however, the arrangement of the anion sublattice was not preserved during the transformation. This shape-dependent crystal structure of the transformed NP was attributed to the larger surface area of the nanorods compared to nanoplates, which would expose faces of lower stability, if the transformed phase were wurtzite-type CoS. Consequently, the lower thermodynamic stability of the nanorods could result in a rearrangement of the anion lattice to a more stable form.

1.2.1.2 Anion-Exchange Reactions in Nanomaterials

In contrast to cation-exchange reactions, anion-exchange reactions are less commonly reported. This is because anions tend to have less mobility than cations, and it is the rigidness of the anion lattice that enables the preservation of the cation and anion sublattices during cation-exchange reactions. On the other hand, anion-exchange reactions are often accompanied by a complete breakdown and reorganization of the structure, forming voids, hollow structures, and core-shell structures [59].

One such example was demonstrated by Park *et al.* [72], who transformed ZnO NPs to ZnS NPs by exposing them to hexamethyldisilathiane at elevated temperatures. Initially, the formation of a ZnS shell, which grows epitaxially on ZnO NPs, was observed. Although ZnO and ZnS both possess wurtzite-type crystal structures, the lattice mismatch between them is high, and it manifests itself as stress on the boundary between the phases. Stress is released by diffusion of the ZnO core outwards. Oxygen was confirmed in the shell region in the intermediate phase $ZnO_xS_{(1-x)}$ before the anion exchange occurred. The final hollow ZnS NPs were of the same shape as the initial ZnO NPs, and they were single crystalline as well. Nevertheless, the morphology was not preserved as the final NPs were hollow.

Another research reporting the hollowing of the NPs during an anion-exchange reaction was conducted by Hong *et al.* [73], who performed a ZnO-to-ZnS transformation with the use of di-tert-butyl disulfide as a sulfurizing agent to form hollow sulfide NPs.

There are, however, ways to avoid the hollowing of the NPs in the process of an anion exchange. One such way is the use of an anion-extracting agent. For example, recently, Lim *et al.* [74] successfully transformed inverse spinel Fe_3O_4 nanocrystals to inverse spinel Fe_3S_4 with the use of the oxygen-extracting reagent (Z)-N-trimethylsilyloctadec-9-en-1-amine (TMS-ODA). H_2S gas was used as a sulfurizing agent. Oxygen extraction by TMS-ODA results in the formation of oxygen vacancies, which increase the anion diffusivity and decrease the activation energy for anion diffusion. The anion-extracting reagent thus increases the anion mobility and makes it comparable to cation mobility.

Another report, where the mobility of the anions was increased and the single crystallinity in the anion exchange was preserved, is described by Jia *et al.* [75]. Here, CdNCN NPs with a distorted NaCl crystal structure were reacted with Se nanopowder to produce CdSe NPs with a sphalerite-type crystal structure. The transformation started on the surface

of the CdNCN NPs with the formation of core-shell structures. The interesting fact here is that the single crystallinity of the intermediate core-shell structures was not altered; the NPs remained crystalline throughout the progress of the reaction. Another surprising outcome of the reaction is the formation of sphalerite-type, structured CdSe instead of the more thermodynamically stable wurtzite-type CdSe. This phenomenon is analogous to the one described in cation-exchange reactions, where metastable phases preferentially form in cation-exchange transformations if the substructure of the anion sublattice is preserved. This can be explained by taking into consideration the anisotropic arrangement of NCN^{2-} anions, which results in the formation of 2D channels. The diffusion of anions is greatly facilitated in this way, with little impact on the cation sublattice. As the transformation is slow, it also enables the controlled rearrangement of Cd^{2+} without the loss of the single crystallinity.

Thangala *et al.* [76] found that, similar to cation exchange, the anion-exchange size plays a major role when it comes to the retention of crystallinity in gas-solid-reaction-induced phase transformations. In their research, they nitride tungsten oxide $W_{18}O_{49}$ NWs by exposing them to ammonia at elevated temperatures. NWs with diameters of less than 10 nm retained the single crystallinity during transformations, whereas the nitriding of thicker tungsten oxide NWs resulted in polycrystalline nitride NWs with highly oriented grains along the longitudinal direction of the NW. Nucleation of the nitride phase was observed to be epitaxially related to the oxide phase. This can be explained in the following way. In thinner NWs, the nucleation occurs along the NW. With the size of the nuclei and diameter of the NWs having approximately the same value, this means that nuclei form in only one dimension. Because nuclei have a preferred orientation in the longitudinal direction of the NW, they can easily merge into one single crystal. On the other hand, in thicker NWs, when the nucleation starts, multiple nuclei form on the cross-section of the NW, which may not have the same orientation in the radial direction. Consequently, the fusion of those nuclei into one single crystal is more difficult.

When studying anion-exchange reactions, we can see that even though they are harder to achieve than cation-exchange reactions, and preservation of single crystallinity is much harder, similar principles apply for anion-exchange reactions as for cation-exchange reactions. In both cases the factors which should be considered are: (i) similarity between crystal structures of initial and transformed crystal, (ii) size of the treated crystal, (iii) use of the catalyst and (iv) shape and morphology of the initial crystal.

However, many factors have not yet been explored, even though their influence on the ion-exchange transformations could be significant. These include the access of treated NPs to additional material that could contribute to the reaction (for example if treated NPs are isolated or embedded in the bulk substrate, that could also contribute to the reaction). Furthermore, the influence of a non-equilibrium ion-exchange environment (such as plasma) as an ion-exchanging environment, has also not been researched. Therefore, the influence of these two factors on ion-exchange reactions was our main focus in this thesis.

1.3 Motivation and Thesis Objectives

Ion-exchange phase transformations have recently gained popularity, particularly as a method for the synthesis of advanced nanomaterials with unique morphologies and phase compositions [58], [59], which are difficult or practically impossible to achieve via conventional bottom-up methods. Further progress in the area related to the synthesis of new nanomaterials with the use of ion-exchange reactions will contribute to the development of new nanomaterials. However, the mechanisms of their transformations are still in the process of exploration. Furthermore, numerous factors influencing the outcome of the ion-exchange transformations and many new remarkable phenomena (examples are described in Sections 1.2.1.1 and 1.2.1.2) are constantly being discovered, signaling that there is still much more to discover before the general mechanism of ion-exchange transformations can be determined.

There are numerous factors influencing the course of ion-exchange reactions, including the phase and morphology of initial crystal, the use of an ion-extracting agent, etc. Hence, when it comes to the design of new materials with ion-exchange reactions, it is crucial that the research community is familiar with these factors. Many more factors could influence the course of ion-exchange phase transformations that have not been described in the literature yet. One such factor is whether the initially treated nanomaterial has access to a

limited or unlimited amount of ions, which could potentially participate in the ion-exchange transformation. For example, in our model system, copper oxide NWs grow from underlying copper/copper oxide substrates. Their roots are embedded in the underlying oxide layers. During their growth, the NWs have constant access to additional copper cations, which diffuse from the underlying substrates to the NW top, where they react with oxygen. Therefore, if the anion-exchange reaction is performed on such NWs, cations from the underlying substrate can also participate in the reaction. On the other hand, this is impossible if the NWs are detached from the substrate and, in this way, isolated prior to sulfurization. This phenomenon has never been emphasized in the literature. However, it may influence the outcome of the reaction and play a role in the design of new nanomaterials.

Another factor that influences the reaction's course is the reaction environment. For example, the mechanism of transformation could differ depending on whether ion exchange is performed in an equilibrium or non-equilibrium environment. This difference can be observed if anion exchange is performed in a gaseous environment (environment in thermodynamic equilibrium) or in a plasma environment (non-equilibrium environment). In the former case, excited metastable species participate in the reaction, altering the mechanism and outcome of the transformation.

Furthermore, the size of the nanomaterial used in the transformations is another potential factor influencing the outcome. The preservation of single crystallinity is very difficult in anion-exchange reactions due to migrations and rearrangements of the cation and anion sublattices during the transformation. However, if the rearrangements are minimal, this could potentially lead to the preservation of single crystallinity during anion-exchange transformation.

Therefore, the CuO NWs were selected as a model material to study anion-exchange phase transformations to explore the phenomena described above. The anion exchange will be achieved via sulfurization, using gaseous (H_2S) to achieve the exchange of oxygen anions with sulfur anions. To realize the described research, the thesis has the following objectives:

Objective 1: Understanding the mechanism driving the growth of metal oxide NWs formed during the oxidation of metal foil.

CuO NWs were selected as a model material to study the phase transformations due to their simple production and wide application range. For our purpose, the ideal model material should have low dimensionality; ideally, it should exhibit a 1D shape (NWs), as using 1D model material would simplify the observation and theoretical analysis of the studied processes during the transformation. For the synthesis of our model material, thermal oxidation was selected as a method to obtain the NWs because of its simplicity, low cost, and good control over the NW parameters. To achieve a complete phase transformation in the NWs, ultra-thin NWs are required. To obtain such NWs, we first have to optimize the reaction parameters needed for their growth. Moreover, the NW growth should be performed under a wide range of experimental conditions, which will, apart from optimization of the 1D growth, also provide us with information about the mechanism of the growth, which is necessary to understand the fundamental science and answer why the NW parameters change with the experimental conditions. As described in Section 1.1.5, the mechanism of metal oxide NW growth via thermal oxidation is still not completely understood, and further research is needed.

The development of metal oxide layers on the metal substrate serving as a NW base might play a major role in the NW growth. However, this was not yet explained in the literature. Thus, apart from NWs, metal oxide layers formed prior to the NWs should also be studied, and their role in the NW growth should be explained. The NW morphology and crystal structure should be examined with electron microscopy to find the triggers of 1D growth in metal oxide nanocrystals. Furthermore, the experimental results should be supported with theoretical modeling to confirm the validity of the assumptions for the NW growth processes. Finally, to generalize metal oxidation as a technique to produce NWs, the other variations of metal oxidation should be studied, such as plasma-assisted metal oxidation, and expanded to the oxidation of other metals apart from copper.

This objective is addressed in Chapter 2. The outcome of this objective is the production of CuO NWs as 1D model material, which will enable further studies of the phase transformations. Emphasis should be placed on understanding the mechanism of NW growth, which will enable the targeted synthesis of NWs with specific parameters desired for use as a model material in phase-transformation reactions.

Objective 2: Finding the conditions for the synthesis of ultra-thin NWs and determine the lower limit for the NW diameter that can be achieved with thermal oxidation

To achieve complete phase transformations in our model CuO NWs, they should be as thin as possible. Apart from complete transformation, this, in combination with transformations, also enables the observation of size effect in phase transformations. Therefore, to find the lower limit of NW thickness produced via thermal oxidation, limiting conditions for the NW growth should be found, and the smallest diameter obtained via thermal oxidation should be determined. From the literature, it is known that the NW diameter and length generally increase with increasing temperature. Therefore, it can be concluded that the thinnest NWs can be produced at the lowest temperature where NW growth is possible. However, the reports of the temperature range for the NW growth are conflicting. For example, the growth of CuO NWs is most commonly reported in the temperature range 400 °C to 700 °C [49], [77]–[80], while the growth of NWs was also reported at 250 °C [81], [82]. Furthermore, neither of the studies focused on determining the lower limiting temperature. Therefore, the minimum temperature for CuO NW growth is still unknown. NW growth should be studied around the limiting temperature to find the smallest NW diameter. Furthermore, correlations between NW diameter and reaction conditions should be performed under limiting conditions by supporting experimental observations with a theoretical model. Objective 2 addresses this missing gap in the growth of NWs under limiting conditions. The outcome of this objective is knowing the lowest temperature at which CuO NWs still grow and finding the smallest NW diameter that can be achieved via thermal oxidation. Ultra-thin NWs can then be used to study anion-exchange phase transformations as a model system.

Objective 3: Exploration of the anion-exchange phase-transformation mechanism and factors influencing the mechanism, using metal oxide–metal sulfide as a model system

This objective focuses on studying the anion-exchange phase transformations in thermally synthesized CuO NWs. In our case, oxygen-sulfur exchange was chosen as the ion exchange of interest as both metal oxides and sulfides have a wide range of applications and represent materials that will undoubtedly be subjected to further development. In particular, the focus of the research is placed on determining whether the mechanism and outcome of the reaction are altered if the CuO NWs have limited or unlimited access to metal cations. Furthermore, the influence of a non-equilibrium environment on the anion-exchange mechanism should be studied. By performing anion exchange on NWs of different thicknesses, it should also be possible to observe the NW size effect on the outcome of the transformation reactions and morphology of the transformed NWs.

To study the effect of cation (non-) limitation on the outcome of the oxygen-sulfur anion-exchange reaction, oxide NWs should be sulfurized in two regimes. First, the whole substrate with grown CuO NWs should be sulfurized by subjecting it to thermal treatment in an H_2S atmosphere. In this case, the cations from the bulk substrate can also diffuse inside the NW and participate in the reaction. Secondly, the sulfurization should be performed on isolated NWs. In this case, the amount of cations that could participate in the reactions is limited and only metal cations already present inside the NW can participate in the reaction. To explore how cation limitation affects the sulfurization reaction, the morphology and crystal structure of the treated NWs should be examined.

To study how the introduction of a non-equilibrium reaction environment affects the anion-exchange outcome, the NWs should be subjected to plasma-assisted sulfurization, using H_2S plasma as a sulfurizing agent. In this case the sulfurizing agents are excited sulfur species produced in plasma. The morphology and phase of the resulting metal sulfide NWs should be compared to the NWs that were sulfurized thermally, where H_2S molecules in thermal equilibrium are used as a sulfurizing agent. The difference in mechanisms and the advantages of the non-equilibrium environment for performing anion-exchange reactions can be inferred by examining the morphologies and structures of the transformed NWs.

Furthermore, sulfurization of CuO NWs with different thicknesses should provide us with the influence of the size effect on the transformation outcome and answer the question of whether the preservation of single crystallinity is possible in a copper oxide, copper sulfide 1D system by controlling the NW diameter.

Objective 3 is addressed in Chapter 3. The outcome of this objective is determining the anion-exchange mechanism in our model system and studying how a limited or unlimited cation supply affects the mechanism of the reaction, as well as determining how the

introduction of a non-equilibrium reaction environment in the form of plasma affects the course of the transformation.

Chapter 2

Growth of Ultra-Thin Copper Oxide Nanowires

Chapter 2 presents our results on the growth and optimization of the growth for copper oxide nanowires, which will serve as a model nanomaterial used to study phase transformations. For our purpose the ideal model material would have a one-dimensional shape as a 1D system simplifies the observation and theoretical treatment of the processes occurring during the transformation reactions as described in Subsection 1.1.1. Therefore, the main emphasis of Chapter 2 lies in exploring the growth mechanism of CuO NWs by thermal oxidation.

Section 2.1 explores the mechanism for the CuO NWs grown by thermal oxidation. The mechanism provides quantitative information on the influence of the experimental conditions on the NW parameters. Since the goal is to synthesize NWs that are as thin as possible, the knowledge of the NW growth mechanism is very important. The mechanism was determined by performing the growth of CuO NWs by thermally oxidizing metallic copper substrates under various experimental conditions (temperature, pressure, and time of oxidation). The dependence of the NW parameters on the experimental conditions was monitored by electron microscopy. Furthermore, the evolution of the underlying copper oxide layers serving as the NW base was also studied and their role in the growth of NWs was determined. Based on the results, the theoretical model was developed for a quantitative description of NW growth. Next, the limiting conditions for the growth of CuO NWs via thermal oxidation were explored and determined in order to obtain the thinnest NWs possible.

In Section 2.2. the growth of CuO NWs is expanded to plasma-assisted techniques and to the oxidation of different metals to show the versatility of metal oxidation as a route to the synthesis of metal oxide NWs. The growth of ZnO, CuO, and Fe_2O_3 nanostructures was studied. The mechanism for the growth of nanostructures was proposed and supported by theoretical modeling.

2.1 Synthesis of CuO NWs by Thermal Oxidation and Exploration of the Growth Mechanism

In Section 2.1, the mechanism of CuO NW growth is explored. This section is divided into two subsections: Subsection 2.2.1, focusing on experimental observations with detailed electron microscopy analysis of the CuO NWs and copper oxide layers serving as the NW base, and Subsection 2.2.2, focusing on developing the theoretical model for the NW growth.

2.1.1 Understanding the Growth of Copper Oxide Nanowires and Layers by Thermal Oxidation over a Broad Temperature Range at Atmospheric Pressure

In Subsection 2.1.1 the thermal CuO NW growth was studied. Apart from the NW parameters (length, diameter, density, etc.), the focus was on a detailed analysis of the NW crystal structure and microstructural analysis of the oxide layers forming below the NWs to gain a complete insight into the NW growth mechanism.

The parameters varied were time and temperature. Electron microscopy was used to analyze the formed NWs and copper oxide layers. Based on observations, the processes of the copper oxide layer's development and NW growth are described. Results suggest that NW growth starts in the CuO layer from twinned CuO grains. The defect in the structure represents a catalytic spot where the oxidation reaction most likely proceeds, elongating the crystal in one dimension. NWs and the CuO layer grow on top with the reaction between copper species and oxygen molecules, while the Cu_2O layer grows at the expense of the CuO layer at the Cu_2O/CuO interface. The position of the interface is determined by the oxygen concentration in the oxide layers. Deeper in the layer, where oxygen concentration is lower, the oxygen deficient Cu_2O layer forms preferentially.

This subsection addresses Objective 1. The results of this subsection were published in a peer-reviewed scientific article in the journal *Crystal Growth and Design*

Regarding my contribution, I synthesized the CuO NWs, performed SEM and part of TEM analysis, analyzed and interpreted the results and wrote the initial text of the manuscript.

CRYSTAL GROWTH & DESIGN

pubs.acs.org/crystal Article

Understanding the Growth of Copper Oxide Nanowires and Layers by Thermal Oxidation over a Broad Temperature Range at Atmospheric Pressure

Martin Košiček, Janez Zavašnik, Oleg Baranov, Barbara Šetina Batič, and Uroš Cvelbar*

Cite This: Cryst. Growth Des. 2022, 22, 6656–6666 Read Online

ACCESS | Metrics & More | Article Recommendations | Supporting Information

ABSTRACT: In this paper, we explore the development of copper oxide layers and their evolution into nanowires on thermally oxidized copper and underlying chemical processes governing the growth of unidirectional, one-dimensional copper oxide (CuO), especially focusing on the role of underlying oxide layers. Extensive experimental data sets of grown nanowires in an ambient atmosphere at different oxidation temperatures and times were collected, analysed, and correlated with theoretical modeling of growth processes. Detailed microstructural analysis revealed that upon annealing in air, the Cu_2O layer of randomly oriented columnar grains forms first, followed by preferentially oriented CuO grains, evolving into CuO nanowires. Our results highlight the importance of copper and oxygen diffusion and concentration in equilibrium between Cu_2O and CuO phases in the oxide film and indicate that CuO nanowires originate in twinned CuO grains, which elongate due to the twin boundary's instability. With broad experimental data sets on growth conditions, we obtain the complete picture of experimental and modeled growth of copper oxide nanowires, which will enable the tailored design of nanowires and their implementation in catalysis, sensing, and other applications.

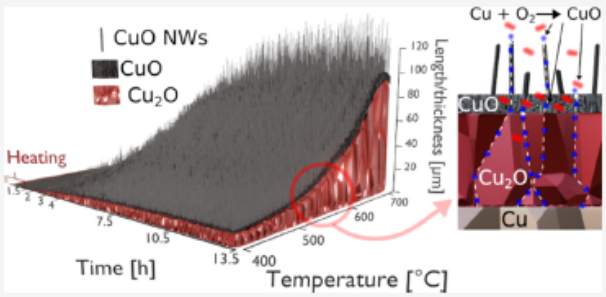

INTRODUCTION

Understanding the processes that govern the formation of nanowires (NWs) and their anisotropic growth is a fundamental scientific challenge. At the same time, resolving the mechanism of NW formation is important for facilitating NW synthesis in practical applications, where control over their physical, structural, and chemical properties is needed. Specifically, copper oxide (CuO) NWs are explored due to their potential use in hydrogen sulfide (H_2S),[1−4] ammonia (NH_3),[5,6] ethanol vapors,[7−10] and other gas sensing,[11,12] as well as various applications in photocatalysis,[13,14] field emitters,[15,16] batteries,[17−20] supercapacitors,[21−23] surface-enhanced Raman spectroscopy,[24] antibacterial agents,[25] and so forth. Up to now, the anisotropic growth of CuO NWs[26] was realized by solution-based methods, hydrothermal and electrochemical methods, plasma oxidation,[27,28] and so forth. However, the most common and simple technique is thermal oxidation, where a metallic copper substrate is heated in ambient air or an oxygen-rich atmosphere. Oxidation temperature and annealing time are key determinants of the resulting NW's physical properties. CuO NW growth is reported in the temperature range 400−700 °C;[29] however, growth at lower temperatures has also been reported.[30] In the literature, CuO NW length and diameter increase with the increase in oxidation temperature,[31−34] whereas increased heating rate reduces their number density.[35]

Despite extensive research, the mechanism of one-dimensional (1D) metal oxide NW formation upon thermal oxidation has yet to be unraveled. So far, several theories have been suggested, but without consensus and suffering from limited data for direct comparison. Among other factors, stress gradients[36] are believed to be the main driving force for NW growth; however, gas humidity and external electric field[37] should be taken into account. Nevertheless, there are common conclusions to all investigations: upon annealing, first a Cu_2O layer forms on top of the Cu substrate, followed by a CuO layer on which CuO NWs grow, forming a three-layered composite: $Cu/Cu_2O/CuO$.[29,38−41] During thermal oxidation, the Cu ions migrate from the Cu substrate by grain boundary diffusion to the top of the CuO layer[42] or toward the Cu_2O/CuO boundary by the Kirkendall effect.[43] Combined with lattice-mismatch-induced compressive stress on the Cu_2O/CuO boundary, this expedites Cu ion diffusion through oxide layers to the top of the CuO layer, facilitating growth. Such stress-driven grain boundary diffusion[40,43,44] and stress relaxation[45−47] are

Received: July 30, 2022
Revised: October 14, 2022
Published: October 24, 2022

https://doi.org/10.1021/acs.cgd.2c00863
Cryst. Growth Des. 2022, 22, 6656−6666

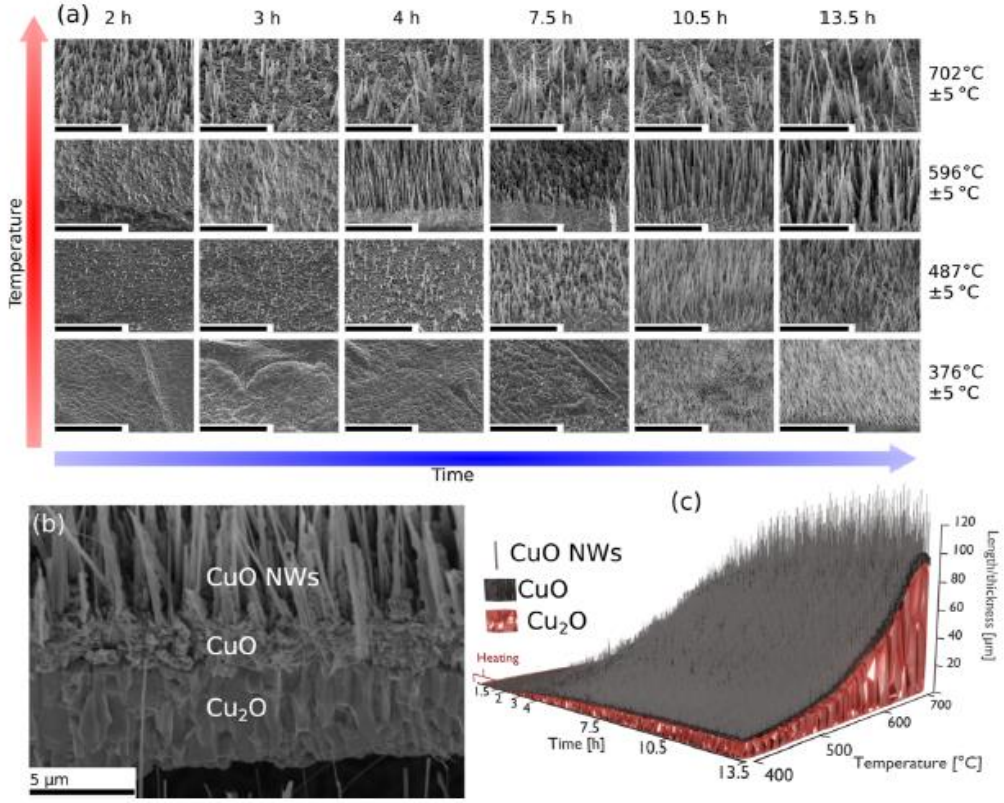

Figure 1. (a) SEM micrographs of CuO NWs prepared by thermal oxidation of copper at different times and temperatures. The scale bars correspond to 20 μm. (b) SEM micrograph of the fracture cross-section of the oxide layers, showing three distinct regions. The sample was oxidized at 487 ± 5 °C for 13.5 h. (c) Summary of time and temperature development of Cu_2O and CuO layers, as well as CuO NWs.

commonly listed as causes for CuO NW growth. Meanwhile, oxygen gradient-driven diffusion due to oxygen consumption on the CuO NW surface is the cause for CuO crystal elongation.[48] As the growth of CuO NWs has also been observed by Cu_2O thermal oxidation without a metallic Cu substrate,[49] Cu_2O or the Cu_2O/CuO phase interface may play a crucial role in CuO NW growth.

To solve these questions, in the present work, we systematically study copper oxidation, Cu_2O and CuO layer evolution, and CuO NW growth in the temperature range roughly determined between 400 and 700 °C at different oxidation times (2−13.5 h). We particularly focus on the investigation of the oxide layers, as it has been unclear up to now what their role is in the NW growth, where in the oxide layers NWs originate and what initiates and drives 1D growth of NWs. A thorough investigation of how oxidation conditions influence the NW parameters (length, diameter, and number density), the role of structural defects and the microstructure relationship between CuO and Cu_2O oxide layers enabled us to gain further insights into the growth mechanism of CuO NWs. To describe the NW growth, theoretical modeling was utilized.

■ EXPERIMENTAL SECTION

For the thermal oxidation synthesis of CuO NWs, copper foil (Alfa Aesar, purity 99.95%, thickness 0.25 mm, annealed and oxygen-free) was power-punched into 10 mm diameter discs, placed on alumina holders, inserted into a quartz tube, and heated in a tube furnace (OTF-1200X, MTI Corporation). Heating started at room temperature (20 °C), and the final temperature was reached after 90 min. Discs were oxidized at four different temperatures: Final temperatures were in the temperature furnace program set and indicated as 400, 500, 600, and 700 °C. However, the real sample temperature measurements with the thermocouple indicated some discrepancy between the set and the actual measured temperature. This can be expected as the quartz tube was held open on one side and additional oxygen flow was introduced on the other side, which could contribute to the cooling of the environment in the quartz tube. Final temperatures reached were thus measured as 376, 487, 596, and 702 °C, with an error estimated at about 5 °C. Oxidation was carried out at each temperature for six different durations (2, 3, 4, 7.5, 10.5, and 13.5 h; 90 min heating from room temperature included). All experiments were carried out at atmospheric pressure with an additional supply of oxygen flowing at 180 sccm to assure oxygen-rich conditions.

As-oxidized samples were analyzed by scanning electron microscopy (SEM, Prisma E, Thermo Fisher Scientific Inc.) to assess NW length and diameter and the thicknesses of oxide layers. Cross-sections of samples were metallographically prepared by epoxy resin mounting and polishing with 500−4000 grit size SiC sandpapers, followed by polishing with 3 μm diamond paste and 0.04 μm colloidal silica (OP-S). The microstructure was analyzed by electron backscatter diffraction (EBSD, EDAX Hikari Super) coupled with a focused ion beam (FIB-SEM; CrossBeam 550, Zeiss).

Microstructure and phase composition were further analyzed by transmission electron microscopy (TEM, JEM-2100, JEOL Inc.). Individual NWs were extracted by sonication in EtOH(abs) and transferred in the solution onto nickel (Ni)-supported amorphous carbon grids. The bulk cross-sectional samples were prepared by mechanical thinning and final argon (Ar) ion etching (further details are provided in the Supporting Information).

■ RESULTS

Copper was oxidized in the temperature range 376 ± 5−702 ± 5 °C as 400−700 °C is the most commonly reported temperature range where CuO NWs grow.[29] Upon oxidation, all copper

https://doi.org/10.1021/acs.cgd.2c00863
Cryst. Growth Des. 2022, 22, 6656−6666

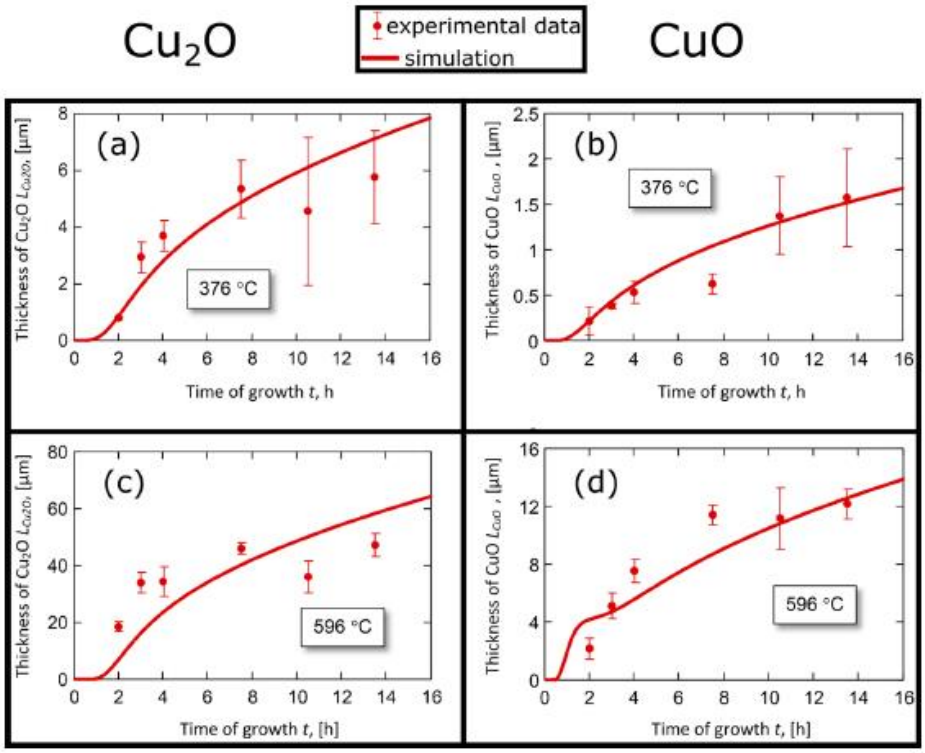

Figure 2. Time dependence of oxide layer thicknesses for the Cu_2O layer at temperatures 376 ± 5 (a) and 596 ± 5 °C (c) and for the CuO layer at temperatures 376 ± 5 (b) and 596 ± 5 °C (d). Red circles and error bars represent measured data. The curves reflect the square root law known from other experiments and theoretically described in the present model.

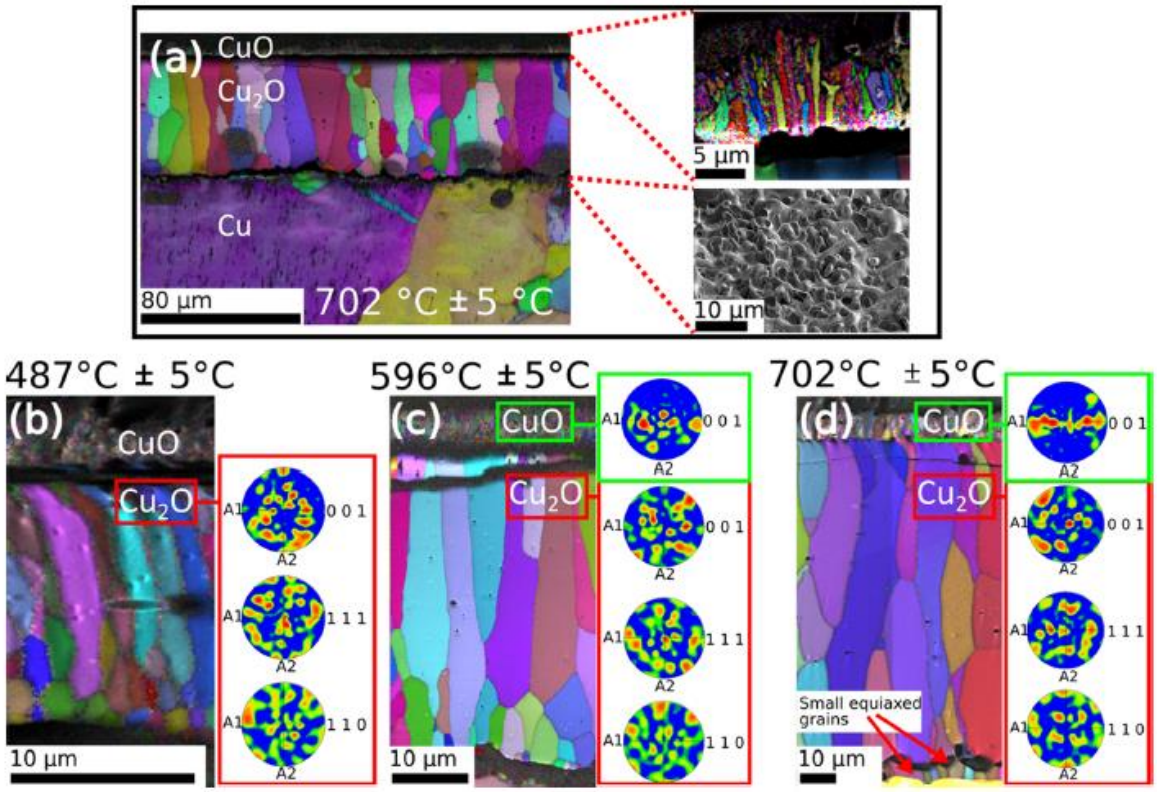

Figure 3. SEM−EBSD analysis of oxide layers produced at different temperatures, oxidized for 13.5 h. (a) Low-magnification EBSD map of the sample oxidized with visible Cu/Cu_2O/CuO layering. In the insets are a magnified EBSD map of the CuO layer and a SEM micrograph of equiaxed grains formed at the Cu/Cu_2O interface, where oxide layers peeled off the Cu substrate. (b−d) EBSD maps of oxide layers synthesized at the following: (b) 487 ± 5, (c) 596 ± 5, and (d) 702 ± 5 °C with corresponding EBSD pole figures showing Cu_2O and CuO texturing.

https://doi.org/10.1021/acs.cgd.2c00863
Cryst. Growth Des. 2022, 22, 6656−6666

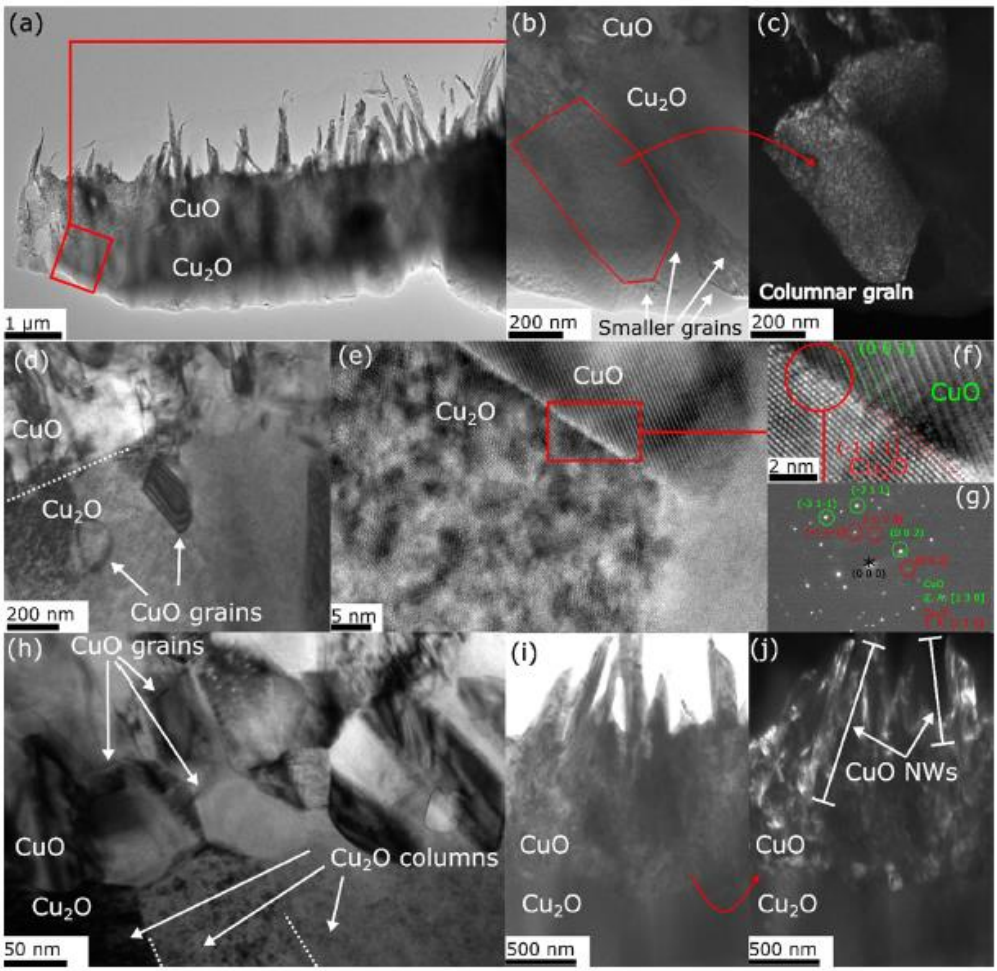

Figure 4. Overview TEM micrograph of the Cu oxide sample oxidized at 376 ± 5 °C for 10.5 h. (a) Cross section of oxide layers: Cu_2O, followed by the CuO layer, topped by CuO NWs. (b,c) Bright- and dark-field TEM micrograph pair on the Cu_2O/CuO interface outlining a single columnar Cu_2O grain. (d) Cu_2O/CuO interface with visible CuO grains intercalated between Cu_2O columnar grains. (e) Cu_2O/CuO interface with a well-defined incoherent phase boundary. (f) High-resolution TEM (HR-TEM) micrograph of the phase boundary with marked lattice planes and corresponding (g) selected area electron diffraction (SAED) recorded over the interface. (h) Cu_2O/CuO interface with visible equiaxed CuO grains at the interface. (i,j) Bright- and dark-field TEM micrograph pair of the CuO layer, outlining the protrusion of CuO NWs into the CuO layer.

plates turned black, which indicated the formation of CuO. SEM micrographs of all sample surfaces after oxidation are presented in Figure 1a

Except for the sample oxidized at 376 ± 5 °C for 2 h (90 min heating 20−376 ± 5 °C, and 30 min holding at 376 ± 5 °C), NW growth was observed in all samples. As expected, on top of the oxidized Cu substrate, a layered Cu_2O/CuO/CuO NW composite formed, as seen in Figure 1b. NW parameters and thicknesses of both layers under all conditions used are summarized in the schematic representation in Figure 1c.

In order to study the processes governing oxidation, we began the investigation on Cu_2O and CuO layers below the NWs. The thickness of Cu_2O and CuO oxide layers increased with time in the initial stages of oxidation, as seen in Figure 2a−d. Experimental measurements were fitted with the square root law from the developed theoretical model. The measurements and theoretical simulations were performed at 376 ± 5 and 596 ± 5 °C to see if the trend differed at different temperatures. The theoretical model used in the fittings was developed in our previous research;[50] calculations are included in the Supporting Information. The Cu_2O layer was thick and grew significantly faster than the CuO layer. The growth of both oxide layers drastically increased with temperature (Figure S3a−d). As can be seen, the theoretical model fit was satisfactory for the CuO layer, but deviated at high temperatures for Cu_2O. Such deviations at higher temperatures (596 ± 5 and 702 ± 5 °C) are caused by the formation of voids and cracks at the Cu/Cu_2O interface, interrupting Cu diffusion due to the loss of contact between the layers. The decrease or loss of contact between Cu and Cu_2O phases changes the energies of copper diffusion from the copper substrate and may even terminate copper delivery from the main copper layer, which was not taken into account in the simulation model.

The microstructure of Cu oxide layers was analyzed by EBSD. Representative samples were oxidized in the temperature range 487 ± 5−702 ± 5 °C for a total oxidation time of 13.5 h to assure sufficient layer thickness for the technique. The original Cu substrate consisted of large randomly oriented copper grains, exceeding 100 μm (Figure 3a). On top of the Cu substrate, mostly columnar Cu_2O grains were found (Figure 3b−d). The column's width depended on the temperature: at 487 ± 5 °C, columns were on average less than 2 μm thick and became progressively thicker with the increase in temperature, reaching more than 10 μm at 702 ± 5 °C. Apart from columnar grains,

https://doi.org/10.1021/acs.cgd.2c00863
Cryst. Growth Des. 2022, 22, 6656−6666

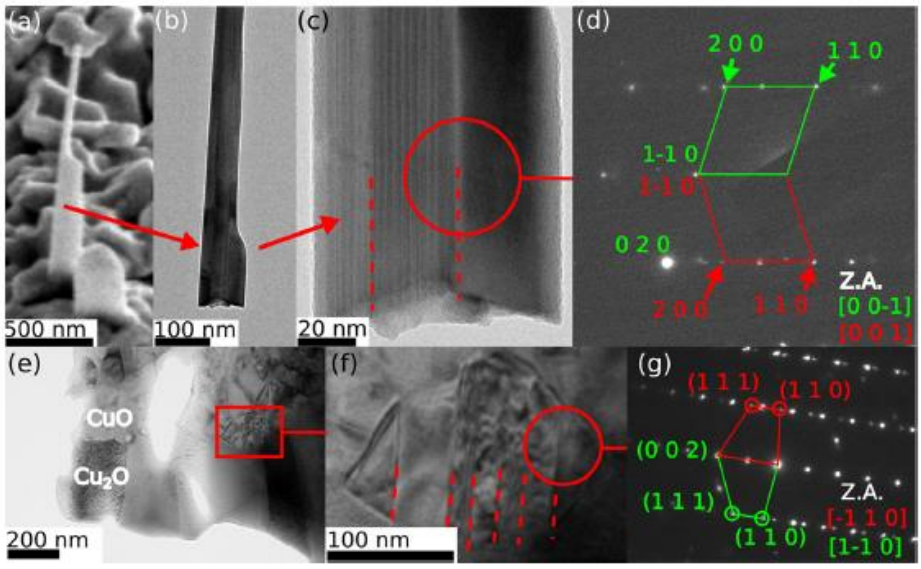

Figure 5. (a) SEM and (b) TEM micrographs of a CuO NW with diameter change as the NW grows; the bottom segment is noticeably wider, but quickly narrows and remains constant. (c) HR-TEM of the bottom NW segment with multiple planar defects and central twin boundary, marked with a red dashed line. (d) SAED pattern recorded over a central defect corresponding to a twin boundary with the (1−10) twinning plane. (e,f) TEM micrograph of the Cu_2O/CuO interface, with a CuO grain with multiple twins, and corresponding (g) SAED indicating the twin boundary with the (002) twinning plane.

smaller equiaxed 2−5 μm Cu_2O grains were observed at the Cu interface, as evident from Figure 3d. The close-up SEM image in Figure 3a shows an area where oxide layers peeled off the copper substrate after the samples were cooled down, allowing insights into the initial oxidation stages. After oxidation, an initially flat copper surface (Figure S4a in the Supporting Information) attained an indented structure. Dents formed where nucleation of Cu_2O took place, and Cu ions and electrons were extracted from the Cu substrate to Cu_2O nuclei, occupying the dents, as Cu_2O grew at the expense of the Cu phase and oxygen. Thus, these small Cu_2O crystallites actually served as an entry point for Cu atoms to diffuse from the copper substrate into the oxide layers. Slightly above the Cu/Cu_2O boundary, grains became bigger, although some still equiaxed, and eventually evolved into a columnar shape, indicating Cu_2O layer top growth by elongation of columns. Such hierarchical microstructure, starting from small grains at the Cu/Cu_2O interface, followed by elongation into columnar grains, was observed at all oxidation temperatures. Grains and pillars in the Cu_2O layer were randomly oriented and their orientation did not depend on the orientation of the underlying Cu grains (Figure 3b−d, individual grain poles can be seen in Figure S5 in the Supporting Information).

On top of the Cu_2O columns, smaller CuO grains formed. Due to limitations of the technique, only larger grains synthesized at 596 ± 5 and 702 ± 5 °C gave satisfactory EBSD signals. In contrast to Cu_2O grains, CuO grains showed strong texturing, that is, preferential growth in a certain crystallographic orientation. As indicated in the pole figures for CuO in Figure 3c,d, the [001] direction of most CuO grains at 596 ± 5 and 702 ± 5 °C was preferentially oriented perpendicularly to the growth direction of the oxide layers. The shape of the CuO grains can be clearly resolved at 702 ± 5 °C (see EBSD of the enlarged part in Figure 3a), where anisotropically shaped grains elongated parallel to the direction of oxide growth prevail. Some anisotropic grains extended above the CuO layer to form NWs, suggesting that elongated grains represent lower parts of NWs, buried in the CuO layer, and NWs originate deeper in the CuO layer.

The microstructures of the CuO layer produced at lower temperatures, and particularly the interface between oxide layers, were analyzed on an atomic scale by TEM. Because TEM examines a much smaller area and thus fewer grains, the statistical component of the analysis was lost. Nevertheless, it provided valuable information about the oxide layers and their relation on a much smaller scale than EBSD. TEM analysis was performed on the sample oxidized for 10.5 h at 376 ± 5 °C (Figure 4a). The reader should note that because TEM preparation of the sample included ion thinning, the oxide layers and NWs were partially etched, which reduced the thickness of Cu_2O and the length of CuO NWs of the analyzed sample in Figure 4a.

As expected, grains of both oxide phases produced at 376 ± 5 °C were the smallest of all analyzed temperatures, but the microstructure followed the same principles: in the lower part of the Cu_2O layer, smaller equiaxed grains were observed (Figure 4b), whereas in the upper part of the Cu_2O layer, thicker columnar grains could be observed (Figure 4c) (additional results on Cu_2O columns are included in Supporting Information, Figure S6). Grain boundaries between the Cu_2O columns close to the Cu_2O/CuO interface contained individual CuO grains, as seen in Figure 4d. The interface between oxides was well defined, the oxide phases were in contact across the whole interface, without visible voids or cracks on micro- (Figure 4b,d) or nanoscales (Figure 4e,f). There was no visible epitaxial relationship between the phases, as indicated by the SAED pattern in Figure 4g.

The microstructural composition of the CuO phase for the sample oxidized at 376 ± 5 °C differed from the one oxidized at 702 ± 5 °C. At 376 ± 5 °C, the CuO layer at the Cu_2O/CuO interface consisted mostly of faceted equiaxed CuO grains, measuring around 100 nm in diameter, separated by grain boundaries running along the facets (Figure 4h). Similarly to samples oxidized at higher temperatures, the CuO layer also

https://doi.org/10.1021/acs.cgd.2c00863
Cryst. Growth Des. 2022, 22, 6656−6666

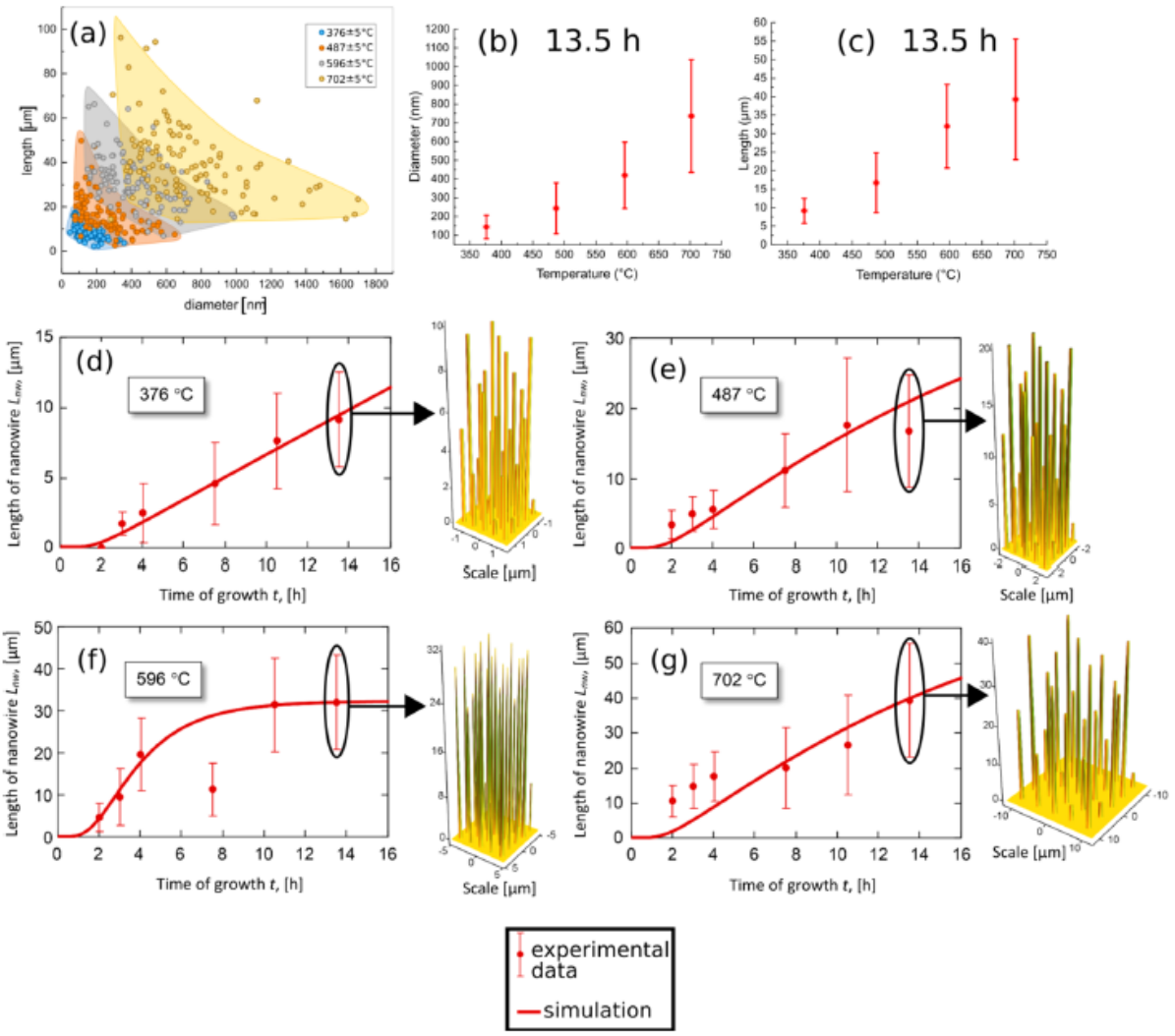

Figure 6. (a) Temperature influence on length and diameter for samples oxidized at 376 ± 5 °C (blue circles), 487 ± 5 °C (orange circles), 596 ± 5 °C (gray circles), and 702 ± 5 °C (yellow circles). Every circle represents one NW. The total time of oxidation was 13.5 h for all samples. (b) Temperature dependence of average NW diameter for samples oxidized for 13.5 h. (c) Temperature dependence of average NW length. (d–g) Time dependence of NW lengths at different temperatures: (d) 376 ± 5, (e) 487 ± 5, (f) 596 ± 5, and (g) 702 ± 5 °C. Red dots represent experimental measurements, and red lines are results of our theoretical simulations for the growth of copper oxides at thermal oxidation of Cu at 376, 487, 596, and 702 °C. Simulated NWs are shown for samples oxidized for 13.5 h at every temperature.

contained anisotropic grains, which elongated to form NWs growing above the CuO layer (Figure 4i). However, as seen in Figure 4j, at 376 ± 5 °C, NW roots were not buried as deep in the layer as for the sample oxidized at 702 ± 5 °C, where some NWs extended across the whole CuO layer (Figure 3a). It is also evident that the proportion of elongated grains was lower in samples oxidized at lower temperatures.

Elongated grains from which CuO NWs have formed exhibit central planar defects identified as twin boundaries. It is often the case that the lower part of a NW is thicker and contains more than one twin boundary; examples are shown in Figure 5a,b. As the NW elongates, the growth of some twinned crystals may cease, while others continued to grow, resulting in NWs with thicker parts closer to the root. The twin boundary ran along the (1−10) twinning plane for the NW in Figure 5b,c, as seen from SAED in Figure 5d. However, other twinning planes in CuO NWs have been reported in the literature,[51] indicating that there are multiple types of twin boundaries possible in CuO. Twin boundaries are not limited only to NWs, as they can be found in grains as well. One such example is shown in Figure 5e,f, where the analyzed grain contained polysynthetic twin boundaries, with (002) twining plane (Figure 5g), suggesting that all CuO grains are prone to the formation of twin boundaries, resulting in an anisotropic grain shape.

Statistical data about grown NWs were obtained by measuring the length and diameter of about 100 randomly chosen NWs for every sample. The temperature effect on length and diameter is visible in Figure 6a–c. Figure 6a shows the correlation between the diameter and length at all four temperatures used. Each point on a graph represents one NW. It is evident that the range of the diameters and lengths on each sample was large. We found short, long, thin, and thick NWs on every sample, with thicker NWs generally shorter, resulting in large standard deviations when we measured average lengths and diameters. This indicates that multiple types of NWs grew on the sample: thin NWs, which have the potential to significantly grow in length, and thicker ones, which elongate at a much slower pace. Both, the average diameter and length increased with temperature (Figure 6b,c,

https://doi.org/10.1021/acs.cgd.2c00863
Cryst. Growth Des. 2022, 22, 6656−6666

respectively) for NWs grown for 13.5 h, agreeing well with previous reports.[38,47]

All samples at all temperatures followed a similar length and diameter time dependence trend. The diameter did not seem to drastically change with time and was more or less constant (within the range of error) regardless of the oxidation duration (diameter dependence on time can be seen in Figure S7), which is in good agreement with previous reports[47] and the theoretical model. NW length increased with the increase in time, as seen in Figure 6d–g, which is also consistent with literature reports, where parabolic NW length–time dependence is commonly observed.[38] In our case, monotonic growth with saturation was observed in the samples, correlating well with the developed theoretical model.

DISCUSSION

Detailed microstructural analysis of oxide layers allows for the acquisition of important information about processes taking place during copper oxidation. Based on our results, the dynamics of events in the oxide phases can be deduced, and is summarized in Figure 7.

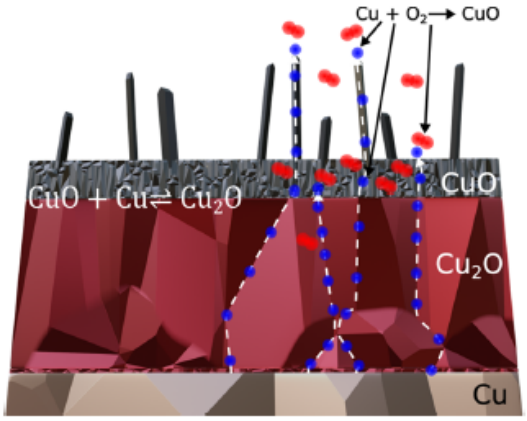

Figure 7. Mechanism summary of copper oxide growth after thermal oxidation of copper. Blue circles represent copper atoms, and red circles represent oxygen atoms.

Understanding the Formation and Role of the Cu_2O Layer. Copper oxidation starts with oxygen adsorption on the copper surface. There, each oxygen molecule accepts four electrons from four copper atoms in the Cu phase in a redox reaction

$$4Cu + O_2 \rightarrow 2Cu_2O \quad (1)$$

Here, copper atoms are extracted from the Cu phase and diffuse inside the emerging Cu_2O phase. Because at temperatures lower than 250 °C only the Cu_2O phase is usually observed,[52] we can safely assume that at the beginning of the oxidation, when the copper substrate is heating up, initially only Cu_2O forms directly on the surface of the Cu substrate, whereas CuO forms at higher temperatures. Cu_2O/Cu boundary formation takes place via random nucleation of Cu_2O nuclei. To compensate for the lattice mismatch between the metallic and oxide phases, nuclei size right at the Cu/Cu_2O boundary is limited, which assures a large number of grain boundaries and facilitates fast grain boundary diffusion of Cu atoms from the Cu substrate to Cu_2O. Above the initially formed Cu_2O crystallites, newly nucleated crystallites are not as limited in size due to stress and can grow significantly. However, as they do so, their neighboring grains start to hinder lateral grain growth, and a direction perpendicular to the copper substrate becomes the prevailing direction of growth, resulting in columnar grains.[53] As noted in the Results section, multiple Cu_2O grains form on a single, much larger Cu grain, indicating that as long as copper grains are sufficiently larger than Cu_2O grains right at the Cu/Cu_2O interface, the copper substrate merely plays the role of the copper atom source and its microstructure does not impact the microstructure of oxide grains growing above it. It is thus indicated that small crystallites at the Cu/Cu_2O interface play an important role in Cu microstructure shielding effects on the microstructure of oxide layers above them. The Cu_2O layer plays an important role in copper oxidation, as copper is transported through the layer to the Cu_2O/CuO boundary. In the temperature range of our experiments, grain boundary Cu ion diffusion is the prevailing type of diffusion,[29] and the polycrystalline nature of the layer is thus necessary to facilitate transport.

Role and Chemistry of the Cu_2O/CuO Interface. Based on the results, we propose the following mechanism of growth and reactions at the interface between oxide phases. At the interface, the oxide phases are in the following equilibrium

$$CuO + Cu \rightleftharpoons Cu_2O \quad (2)$$

Here, Cu atoms that diffuse from the Cu substrate to reach the interface between the oxides and jump between the oxide phases. Their transfer (jump) from the Cu_2O to the CuO phase results in reaction 2, which increases the size of the Cu_2O layer. However, reaction 2 is reversible, and in the next step, Cu_2O can transform back to Cu and CuO, releasing Cu atoms, which can then jump into another CuO unit to start a new "jump" cycle. This set of jumps ends when the Cu atom eventually meets and reacts with an oxygen molecule diffusing from the atmosphere inside the oxide layers to form CuO. This process is summarized in reaction 3 and Figure 8a

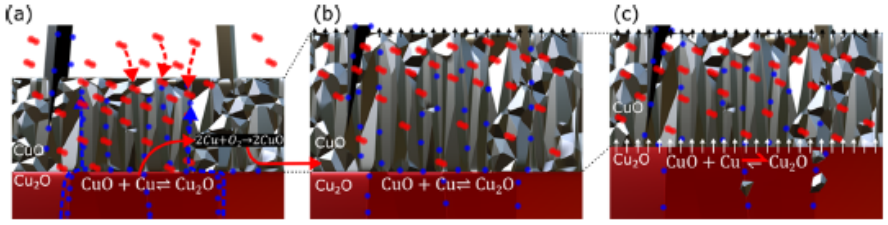

Figure 8. Mechanism and reactions involved in shifting the Cu_2O/CuO interface. (a) As oxide phases are in equilibrium at the interface, the CuO layer grows by the reaction between Cu atoms and O_2 molecules. (b) As the CuO layer thickens, the oxygen concentration at the interface decreases. (c) Decrease in oxygen concentration at the interface favors the formation of the Cu_2O layer. Blue circles represent copper atoms, and red circles represent oxygen atoms.

https://doi.org/10.1021/acs.cgd.2c00863
Cryst. Growth Des. 2022, 22, 6656–6666

Crystal Growth & Design pubs.acs.org/crystal Article

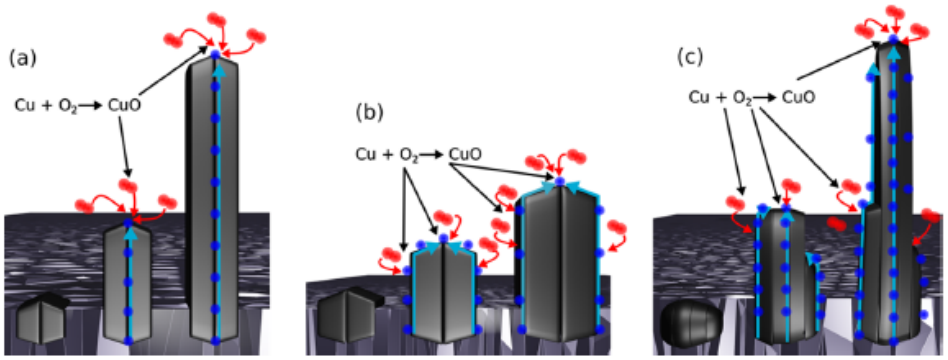

Figure 9. Different modes of copper diffusion toward the NW top. (a) Twin boundary Cu diffusion, followed by a reaction with oxygen on top, results in long and thin NWs. (b) Surface diffusion results in thick and short NWs. Here, a portion of diffusing Cu atoms is consumed in the reaction on the NW walls; hence, fewer Cu atoms reach the NW top. (c) Combination of both copper diffusion modes. Some twinned crystals grow via twin boundary diffusion of Cu and significantly elongate, other grains grow via surface diffusion and grow significantly slower. Blue circles represent copper atoms, and red circles represent oxygen atoms.

$$2Cu_2O + O_2 \rightarrow 4CuO \quad (3)$$

From the arrangement of oxide layers, it can be concluded that the concentration of oxygen molecules in the oxide layers determines the equilibrium nature of reaction 2. Above the Cu_2O/CuO interface, where oxygen concentration is relatively high, the oxygen-richer CuO phase is more stable. In contrast, underneath the interface, where oxygen concentration is lower, Cu_2O is more stable. The deeper below the Cu_2O/CuO interface we look, the lower the oxygen concentration gets, and equilibrium in reaction 2 is shifted further toward the formation of the more stable Cu_2O phase. On the other hand, above the Cu_2O/CuO interface, in the CuO layer, oxygen concentration increases as we approach the surface of the CuO layer, and equilibrium in reaction 2 is shifted toward CuO formation. A similar arrangement is seen in the oxidation of iron: at an oxidation temperature of 600 °C, three iron oxide phases (FeO, Fe_3O_4, and α-Fe_2O_3) coexist and are arranged in a layered fashion from the iron substrate to the atmosphere: $FeO/Fe_3O_4/Fe_2O_3$.[54] Hence, oxygen-richer phases are found closer to the atmosphere, and the oxygen concentration gradient in the oxide layers determines the order in which phases are arranged. In this way, the position of the Cu_2O/CuO interface is regulated by the oxygen concentration gradient, as schematically shown in Figure 8a–c. When the CuO layer thickens, the oxygen concentration at the Cu_2O/CuO interface simultaneously decreases as the oxygen diffusion path to this interface increases. Lower oxygen concentration shifts equilibrium in reaction 2 toward Cu_2O formation; hence, the CuO layer decomposes at the Cu_2O/CuO interface, and the Cu_2O layer grows at the expense of CuO. CuO grains found between Cu_2O columns (Figure 4d) are most likely remnants of the CuO phase and indicate that, at some point of oxidation, the phase interface was located there.

From the CuO Layer to CuO NWs. The lack of epitaxial relationship and much smaller grains in the CuO layers compared to Cu_2O indicate that the microstructure of CuO should be independent of the Cu_2O microstructure as long as Cu_2O grains are sufficiently large. Equiaxed faceted CuO grains, which along buried NWs comprise the CuO layers, are of a similar size to NW diameters; hence, an assumption can be made that some of those faceted grains act as seeds for the initiation of NW growth and elongate in one direction. The question that arises here is which properties a seed needs to possess for 1D growth.

The vapor–liquid–solid and vapor–solid–solid mechanisms commonly used for describing NW growth can be safely ruled out: the melting point of copper (1085 °C) and its oxides (CuO 1326 °C, and Cu_2O 1232 °C) are much higher than the temperature range of CuO NW growth. Instead, 1D growth could be ascribed to the formation of twin boundaries in CuO grains, resulting in CuO texturing. Apart from being preferentially oriented with the [001] crystallographic orientation perpendicular to the direction of oxide layer growth, CuO grains also preferentially elongate in that particular direction.

Twin boundaries from the NW in Figure 5c and grain in Figure 5f have different twinning planes. However, both (1 −1 0) and (0 0 2) twinning planes are parallel to the determined preferred orientation of CuO grain growth. Hence, it is surmised that twin boundaries dictate the direction of CuO grain elongation. Twin boundaries found in many CuO grains suggest that the CuO phase is very prone to forming 2D defects in its crystal structure, and the twin boundaries are observed in most CuO NWs. The twin boundary represents a catalytic spot where growth will continue.[55] On such catalytic spots, the Cu atoms, which are not consumed in the reaction at the Cu_2O/CuO interface, are more likely to react with oxygen,[55] and grains, thus, elongate in the direction parallel with the twinning plane. Therefore, to answer the question of which CuO grains elongate in one direction, grains which exhibit vertical twin boundaries are likely to elongate and become NWs. This is, of course, true only if there are no other grains to physically prevent growth, meaning that grains formed deep in the CuO layer or at the Cu_2O/CuO interface in equilibrium reactions described above are unlikely to become NWs even if they are twinned. Such an example is the grain in Figure 5f.

CuO NWs grow on the top; hence, for NWs to vertically elongate, copper has to be supplied through the NW on the very tip. This can be achieved via diffusion along the surface of the NWs,[40,43,51] or by diffusion through the twin boundary in bicrystalline NWs.[39] The twin boundaries present important pathways for the diffusion of Cu atoms, and the diffusion of Cu through the twin boundary may even be favorable over surface diffusion.[39]

In our theoretical model, we considered both copper supply routes to the NW top: surface diffusion and twin boundary diffusion. We observed that if one or the other is prevailing, the morphology of NWs is different, which could explain why the range of diameters and lengths of NWs on a single sample is so

https://doi.org/10.1021/acs.cgd.2c00863
Cryst. Growth Des. 2022, 22, 6656–6666

broad. Copper atoms delivered from a NW root via surface diffusion are involved in the reaction with oxygen adsorbed on the side surface of the NW.[50] In this case, thick NWs grow, and their length is limited by the maximal diffusion path. Adsorption of oxygen molecules is required for the reaction, and it is higher on a relatively defected NW surface caused by low temperature or a certain orientation of the crystalline planes. In contrast, long and thin NWs are formed when oxygen molecules do not adsorb in a large quantity on a relatively perfect crystalline NW structure, or the copper atoms diffuse from the root to the tip of the NW through the twin boundary and are protected by the NW walls from interacting with oxygen. In this case, the diffusion path is much longer; however, the initial diameter of the NW does not increase. Consideration of different diffusion modes resulted in a large variety of lengths and diameters in simulated NWs as well (Figure 6d−g). Diffusion modes are schematically shown in Figure 9a−c.

Different Cu atom diffusion modes may also explain why some NWs are thicker at the root (e.g., NWs in Figure 5a−c). Such NWs exhibit multiple central twin boundaries and in such cases, some of the twinned crystals grow predominantly by surface diffusion of Cu atoms, while others grow by twin boundary diffusion (Figure 9c). Crystals where twin boundary diffusion of Cu is dominant will result in longer NWs, while the opposite is true for twinned crystals growing via surface diffusion of Cu atoms.

CONCLUSIONS

In summary, we performed a systematic study of CuO NW growth via thermal oxidation at different times and temperatures. With the assistance of electron microscopy techniques and numerical simulations, we investigated the evolution of copper oxide phases on a copper surface and their transition to NWs. Microstructural analysis of the underlying layers combined with numerical simulations allowed us to acquire insights into the chemical processes governing the relationship between CuO and Cu_2O phases, as well as the formation of NWs.

The evolution of Cu_2O microstructure starts with the formation of small equiaxed nuclei on the copper surface, followed by columnar grains. CuO phase growing on top consists of equiaxed and vertically elongated grains, some of which grow above the surface of the CuO layer to become NWs. The relationship between Cu_2O and CuO phases is governed by the flux of copper from the Cu substrate and oxygen from the atmosphere. Copper atoms diffusing from the Cu substrate are, during their diffusion path, involved in various reactions. They participate in equilibrium between CuO and Cu_2O phases at their interface and are also consumed in the reaction with oxygen molecules diffusing into the oxide layers. In this way, the oxygen concentration gradient also indirectly affects the equilibrium between oxide phases and determines the position of the boundary between oxygen-rich CuO and oxygen-deficient Cu_2O phases.

CuO NWs most likely originate in twinned CuO grains. Twinned sites act as catalytic spots, where a reaction between copper and oxygen is most probable. Diffusion of copper toward the NW top can proceed via the twin boundary or NW side surface. Different diffusion modes result in different nanowire shapes.

ASSOCIATED CONTENT

Supporting Information

The Supporting Information is available free of charge at https://pubs.acs.org/doi/10.1021/acs.cgd.2c00863.

Description of the theoretical model used in numerical simulations of copper oxidation, images from TEM sample preparation, time dependencies of NW number density and diameters, additional SEM and TEM images of NWs and oxide layers, and pole figures from EBSD analysis (PDF)

AUTHOR INFORMATION

Corresponding Author

Uroš Cvelbar − *Jožef Stefan Institute, 1000 Ljubljana, Slovenia; Jožef Stefan International Postgraduate School, 1000 Ljubljana, Slovenia;* orcid.org/0000-0002-1957-0789; Email: uros.cvelbar@ijs.si

Authors

Martin Košiček − *Jožef Stefan Institute, 1000 Ljubljana, Slovenia; Jožef Stefan International Postgraduate School, 1000 Ljubljana, Slovenia*

Janez Zavašnik − *Jožef Stefan Institute, 1000 Ljubljana, Slovenia; Jožef Stefan International Postgraduate School, 1000 Ljubljana, Slovenia;* orcid.org/0000-0002-8822-4089

Oleg Baranov − *Jožef Stefan Institute, 1000 Ljubljana, Slovenia; Plasma Laboratory, National Aerospace University, 61070 Kharkiv, Ukraine*

Barbara Šetina Batič − *Institute of Metals and Technology, 1000 Ljubljana, Slovenia*

Complete contact information is available at: https://pubs.acs.org/10.1021/acs.cgd.2c00863

Author Contributions

The paper was written through contributions of all authors. M.K., J.Z., and U.C. conceptualized the research, M.K. synthesized NWs, conducted SEM/TEM, and wrote first draft, J.Z. and B.S.B. contributed to TEM and SEM−EBSD analyses, O.B. performed simulations, U.C. prepared the final version of the paper, and all authors contributed to writing and editing of this paper. All authors have given approval to the final version of the paper.

Notes

The authors declare no competing financial interest.

ACKNOWLEDGMENTS

Authors acknowledge financial support from the Slovenian Research Agency ARRS program P1-0417 and project N2-0107 and NATO project G5814 "NOOSE". O.B. acknowledges support from the project funded by National Research Foundation of Ukraine, under grant agreement no. 2020.02/0119.

ABBREVIATIONS

NW, nanowire; TEM, transmission electron microscopy; SEM, scanning electron microscopy; SAED, selected area electron diffraction; EBSD, electron backscatter diffraction

REFERENCES

(1) Chen, J.; Wang, K.; Hartman, L.; Zhou, W. H2S Detection by Vertically Aligned CuO Nanowire Array Sensors. *J. Phys. Chem. C* **2008**, *112*, 16017−16021.

https://doi.org/10.1021/acs.cgd.2c00863
Cryst. Growth Des. 2022, 22, 6656−6666

(2) Kim, J. Y.; Lee, J. H.; Kim, J. H.; Mirzaei, A.; Woo Kim, H.; Kim, S. S. Realization of H2S Sensing by Pd-Functionalized Networked CuO Nanowires in Self-Heating Mode. *Sens. Actuators, B* **2019**, *299*, 126965.
(3) Li, X.; Wang, Y.; Lei, Y.; Gu, Z. Highly Sensitive H2S Sensor Based on Template-Synthesized CuO Nanowires. *RSC Adv.* **2012**, *2*, 2302−2307.
(4) Steinhauer, S.; Brunet, E.; Maier, T.; Mutinati, G. C.; Köck, A. Suspended CuO Nanowires for Ppb Level H2S Sensing in Dry and Humid Atmosphere. *Sens. Actuators, B* **2013**, *186*, 550−556.
(5) Shao, F.; Hernández-Ramírez, F.; Prades, J. D.; Fàbrega, C.; Andreu, T.; Morante, J. R. Copper (II) Oxide Nanowires for p-Type Conductometric NH3 Sensing. *Appl. Surf. Sci.* **2014**, *311*, 177−181.
(6) Mashock, M.; Yu, K.; Cui, S.; Mao, S.; Lu, G.; Chen, J. Modulating Gas Sensing Properties of CuO Nanowires through Creation of Discrete Nanosized P-n Junctions on Their Surfaces. *ACS Appl. Mater. Interfaces* **2012**, *4*, 4192−4199.
(7) Lupan, O.; Postica, V.; Cretu, V.; Wolff, N.; Duppel, V.; Kienle, L.; Adelung, R. Single and Networked CuO Nanowires for Highly Sensitive P-Type Semiconductor Gas Sensor Applications. *Phys. Status Solidi RRL* **2016**, *10*, 260−266.
(8) Raksa, P.; Gardchareon, A.; Chairuangsri, T.; Mangkorntong, P.; Mangkorntong, N.; Choopun, S. Ethanol Sensing Properties of CuO Nanowires Prepared by an Oxidation Reaction. *Ceram. Int.* **2009**, *35*, 649−652.
(9) Li, D.; Hu, J.; Wu, R.; Lu, J. G. Conductometric Chemical Sensor Based on Individual CuO Nanowires. *Nanotechnology* **2010**, *21*, 485502.
(10) Zhong, M. L.; Zeng, D. C.; Liu, Z. W.; Yu, H. Y.; Zhong, X. C.; Qiu, W. Q. Synthesis, Growth Mechanism and Gas-Sensing Properties of Large-Scale CuO Nanowires. *Acta Mater.* **2010**, *58*, 5926−5932.
(11) Kim, J. H.; Katoch, A.; Choi, S. W.; Kim, S. S. Growth and Sensing Properties of Networked P-CuO Nanowires. *Sens. Actuators, B* **2015**, *212*, 190−195.
(12) Zhang, H.; Zhao, T.; Zhu, W.; Kong, L.; Huang, Y.; Liu, H. Enhanced Field Emission of CuO Nanowires by Aluminum Coating for Volatile Organic Compound Detection. *Sens. Actuators, B* **2022**, *353*, 131181.
(13) Scuderi, V.; Amiard, G.; Boninelli, S.; Scalese, S.; Miritello, M.; Sberna, P. M.; Impellizzeri, G.; Privitera, V. Photocatalytic Activity of CuO and Cu2O Nanowires. *Mater. Sci. Semicond. Process.* **2016**, *42*, 89−93.
(14) Zhang, Q.; Huang, L.; Kang, S.; Yin, C.; Ma, Z.; Cui, L.; Wang, Y. CuO/Cu2O nanowire arrays grafted by reduced graphene oxide: synthesis, characterization, and application in photocatalytic reduction of CO2. *RSC Adv.* **2017**, *7*, 43642−43647.
(15) Feng, L.; Yan, H.; Li, H.; Zhang, R.; Li, Z.; Chi, R.; Yang, S.; Ma, Y.; Fu, B.; Liu, J. Excellent Field Emission Properties of Vertically Oriented CuO Nanowire Films. *AIP Adv.* **2018**, *8*, 045109.
(16) Sung, W. Y.; Kim, W. J.; Lee, S. S. M.; Lee, H. Y.; Kim, Y. H.; Park, K. H.; Lee, S. S. M. Field Emission Characteristics of CuO Nanowires by Hydrogen Plasma Treatment. *Vacuum* **2007**, *81*, 851−856.
(17) Wang, Z.; Zhang, Y.; Xiong, H.; Qin, C.; Zhao, W.; Liu, X. Yucca Fern Shaped CuO Nanowires on Cu Foam for Remitting Capacity Fading of Li-Ion Battery Anodes. *Sci. Rep.* **2018**, *8*, 6530.
(18) Wang, L.; Zhang, K.; Hu, Z.; Duan, W.; Cheng, F.; Chen, J. Porous CuO Nanowires as the Anode of Rechargeable Na-Ion Batteries. *Nano Res.* **2014**, *7*, 199−208.
(19) Wang, F.; Tao, W.; Zhao, M.; Xu, M.; Yang, S.; Sun, Z.; Wang, L.; Song, X. Controlled Synthesis of Uniform Ultrafine CuO Nanowires as Anode Material for Lithium-Ion Batteries. *J. Alloys Compd.* **2011**, *509*, 9798−9803.
(20) Liu, Q.; Yang, T.; Du, C.; Tang, Y.; Sun, Y.; Jia, P.; Chen, J.; Ye, H.; Shen, T.; Peng, Q.; Zhang, L.; Huang, J. In Situ Imaging the Oxygen Reduction Reactions of Solid State Na-O2 Batteries with CuO Nanowires as the Air Cathode. *Nano Lett.* **2018**, *18*, 3723−3730.
(21) Luan, V. H.; Han, J. H.; Kang, H. W.; Lee, W. Highly Porous and Capacitive Copper Oxide Nanowire/Graphene Hybrid Carbon Nanostructure for High-Performance Supercapacitor Electrodes. *Composites, Part B* **2019**, *178*, 107464.
(22) Deka, B. K.; Hazarika, A.; Kim, J.; Park, Y. B.; Park, H. W. Multifunctional CuO nanowire embodied structural supercapacitor based on woven carbon fiber/ionic liquid-polyester resin. *Composites, Part A* **2016**, *87*, 256−262.
(23) Zhang, X.; Zhang, C.; Abas, A.; Zhang, A.; Mu, Y.; Zhou, X.; Su, J.; Lan, Q.; Xie, W.; Xie, E. Ag Nanoparticles Enhanced Vertically-Aligned CuO Nanowire Arrays Grown on Cu Foam for Stable Hybrid Supercapacitors with High Energy Density. *Electrochim. Acta* **2019**, *296*, 535−544.
(24) Shvalya, V.; Filipič, G.; Vengust, D.; Zavašnik, J.; Modic, M.; Abdulhalim, I.; Cvelbar, U. Reusable Au/Pd-Coated Chestnut-like Copper Oxide SERS Substrates with Ultra-Fast Self-Recovery. *Appl. Surf. Sci.* **2020**, *517*, 146205.
(25) Mahmoodi, A.; Solaymani, S.; Amini, M.; Nezafat, N. B.; Ghoranneviss, M. Structural, Morphological and Antibacterial Characterization of CuO Nanowires. *Silicon* **2017**, *10*, 1427−1431.
(26) Filipič, G.; Cvelbar, U.; Search, H.; Journals, C.; Contact, A.; Iopscience, M.; Address, I. P. Copper Oxide Nanowires: A Review of Growth. *Nanotechnology* **2012**, *23*, 194001.
(27) Filipič, G.; Baranov, O.; Mozetič, M.; Ostrikov, K.; Cvelbar, U. Uniform Surface Growth of Copper Oxide Nanowires in Radio-frequency Plasma Discharge and Limiting Factors. *Phys. Plasmas* **2014**, *21*, 113506.
(28) Filipič, G.; Baranov, O.; Mozetič, M.; Cvelbar, U. Growth Dynamics of Copper Oxide Nanowires in Plasma at Low Pressures. *J. Appl. Phys.* **2015**, *117*, 043304.
(29) Xiang, C.; Guo, X.; Wu, M.; Cai, L.; Zhou, N.; Zhang, J.; Wu, C.; Cai, M.; Zhou, X.; Zhang, N. A Brief Review on the Growth Mechanism of CuO Nanowires via Thermal Oxidation. *J. Mater. Res.* **2018**, *33*, 2264−2280.
(30) Moise, C. C.; Enache, L. B.; Anăstăsoaie, V.; Lazăr, O. A.; Mihai, G. V.; Bercu, M.; Enăchescu, M. On the Growth of Copper Oxide Nanowires by Thermal Oxidation near the Threshold Temperature at Atmospheric Pressure. *J. Alloys Compd.* **2021**, *886*, 161130.
(31) Tran, T. H.; Nguyen, M. H.; Nguyen, T. H. T.; Dao, V. P. T.; Nguyen, P. M.; Nguyen, V. T.; Pham, N. H.; Le, V. V.; Sai, C. D.; Nguyen, Q. H.; Nguyen, T. T.; Ho, K. H.; Doan, Q. K. Effect of Annealing Temperature on Morphology and Structure of CuO Nanowires Grown by Thermal Oxidation Method. *J. Cryst. Growth* **2019**, *505*, 33−37.
(32) Zúñiga, A.; Fonseca, L.; Souza, J. A.; Rivaldo-Gomez, C.; Pomar, C. D.; Criado, D. Anomalous Ferromagnetic Behavior and Size Effects in CuO Nanowires. *J. Magn. Magn. Mater.* **2019**, *471*, 77−81.
(33) Mohamed, S. H.; Al-Mokhtar, K. M. Characterization of Cu2O/CuO nanowire arrays synthesized by thermal method at various temperatures. *Appl. Phys. A* **2018**, *124*, 493.
(34) Jafari, A.; Terohid, S. A. A.; Kokabi, A.; Moradiani, A. Electrical, Structural, and Photocatalytic Properties of Copper Oxide Nanowire. *J. Chem. Res.* **2020**, *44*, 471−474.
(35) Nkhaili, L.; Narjis, A.; Agdad, A.; Tchenka, A.; El Kissani, A.; Outzourhit, A.; Oueriagli, A. A Simple Method to Control the Growth of Copper Oxide Nanowires for Solar Cells and Catalytic Applications. *Adv. Condens. Matter Phys.* **2020**, *2020*, 5470817.
(36) Jagtap, P.; Chason, E. A Unified Kinetic Model for Stress Relaxation and Recovery during and after Growth Interruptions in Polycrystalline Thin Films. *Acta Mater.* **2020**, *193*, 202−209.
(37) Sondors, R.; Kosmaca, J.; Kunakova, G.; Jasulaneca, L.; Ramma, M. M.; Meija, R.; Kauranens, E.; Antsov, M.; Erts, D. Size Distribution, Mechanical and Electrical Properties of CuO Nanowires Grown by Modified Thermal Oxidation Methods. *Nanomaterials* **2020**, *10*, 1051.
(38) Gonçalves, A. M. B.; Campos, L. C.; Ferlauto, A. S.; Lacerda, R. G. On the Growth and Electrical Characterization of CuO Nanowires by Thermal Oxidation. *J. Appl. Phys.* **2009**, *106*, 034303.
(39) Sun, X.; Zhu, W.; Wu, D.; Liu, Z.; Chen, X.; Yuan, L.; Wang, G.; Sharma, R.; Zhou, G. Atomic-Scale Mechanism of Unidirectional Oxide Growth. *Adv. Funct. Mater.* **2020**, *30*, 1906504.
(40) Yuan, L.; Wang, Y.; Mema, R.; Zhou, G. Driving Force and Growth Mechanism for Spontaneous Oxide Nanowire Formation

https://doi.org/10.1021/acs.cgd.2c00863
Cryst. Growth Des. 2022, 22, 6656−6666

during the Thermal Oxidation of Metals. *Acta Mater.* **2011**, *59*, 2491–2500.
(41) Mimura, K.; Lim, J.-W.; Isshiki, M.; Zhu, Y.; Jiang, Q. Brief review of oxidation kinetics of copper at 350 °C to 1050 °C. *Metall. Mater. Trans. A* **2006**, *37*, 1231–1237.
(42) Baranov, O.; Filipič, G.; Cvelbar, U. Towards a Highly-Controllable Synthesis of Copper Oxide Nanowires in Radio-Frequency Reactive Plasma: Fast Saturation at the Targeted Size. *Plasma Sources Sci. Technol.* **2018**, *28*, 084002.
(43) Shi, J.; Qiao, L.; Zhao, Y.; Sun, Z.; Feng, W.; Zhang, Z.; Wang, J.; Men, X. Synergistic Effects on Thermal Growth of CuO Nanowires. *J. Alloys Compd.* **2020**, *815*, 152355.
(44) Chen, M.; Yue, Y.; Ju, Y. Growth of Metal and Metal Oxide Nanowires Driven by the Stress-Induced Migration. *J. Appl. Phys.* **2012**, *111*, 104305.
(45) Mema, R.; Yuan, L.; Du, Q.; Wang, Y.; Zhou, G. Effect of Surface Stresses on CuO Nanowire Growth in the Thermal Oxidation of Copper. *Chem. Phys. Lett.* **2011**, *512*, 87–91.
(46) Kaur, M.; Muthe, K. P.; Despande, S. K.; Choudhury, S.; Singh, J. B.; Verma, N.; Gupta, S. K.; Yakhmi, J. V. Growth and Branching of CuO Nanowires by Thermal Oxidation of Copper. *J. Cryst. Growth* **2006**, *289*, 670–675.
(47) Kumar, A.; Srivastava, A. K.; Tiwari, P.; Nandedkar, R. V. The Effect of Growth Parameters on the Aspect Ratio and Number Density of CuO Nanorods. *J. Phys. Condens. Matter* **2004**, *16*, 8531–8543.
(48) Cao, F.; Jia, S.; Zheng, H.; Zhao, L. L.; Liu, H.; Li, L.; Zhao, L. L.; Hu, Y.; Gu, H.; Wang, J. Thermal-Induced Formation of Domain Structures in CuO Nanomaterials. *Phys. Rev. Mater.* **2017**, *1*, 053401.
(49) Li, A.; Song, H.; Zhou, J.; Chen, X.; Liu, S. CuO Nanowire Growth on Cu2O by in Situ Thermal Oxidation in Air. *CrystEngComm* **2013**, *15*, 8559–8564.
(50) Baranov, O.; Košiček, M.; Filipič, G.; Cvelbar, U. A Deterministic Approach to the Thermal Synthesis and Growth of 1D Metal Oxide Nanostructures. *Appl. Surf. Sci.* **2021**, *566*, 150619.
(51) Sheng, H.; Zheng, H.; Jia, S.; Li, L.; Cao, F.; Wu, S.; Han, W.; Liu, H.; Zhao, D.; Wang, J. Twin Structures in CuO Nanowires. *J. Appl. Crystallogr.* **2016**, *49*, 462–467.
(52) Guillén, C.; Herrero, J. Single-Phase Cu2O and CuO Thin Films Obtained by Low-Temperature Oxidation Processes. *J. Alloys Compd.* **2018**, *737*, 718–724.
(53) Zavašnik, J.; Peng, J.; Palm, M. TEM investigation of pre-oxidised Fe-Al with improved aqueous corrosion resistance. *Corros. Sci.* **2021**, *179*, 109170.
(54) Yuan, L.; Wang, Y.; Cai, R.; Jiang, Q.; Wang, J.; Li, B.; Sharma, A.; Zhou, G. The Origin of Hematite Nanowire Growth during the Thermal Oxidation of Iron. *Mater. Sci. Eng. B* **2012**, *177*, 327–336.
(55) Rackauskas, S.; Jiang, H.; Wagner, J. B.; Shandakov, S. D.; Hansen, T. W.; Kauppinen, E. I.; Nasibulin, A. G. In Situ Study of Noncatalytic Metal Oxide Nanowire Growth. *Nano Lett.* **2014**, *14*, 5810–5813.

https://doi.org/10.1021/acs.cgd.2c00863
Cryst. Growth Des. 2022, 22, 6656–6666

Supporting information file for manuscript:

Understanding the Growth of Copper Oxide Nanowires and Layers by Thermal Oxidation over a Broad Temperature Range at Atmospheric Pressure

Martin Košiček[a,b], Janez Zavašnik[a,b], Oleg Baranov[a,c], Barbara Šetina Batič[d], and Uroš Cvelbar[a,b,]*

[a] Jožef Stefan Institute, Jamova cesta 39, 1000 Ljubljana, Slovenia

[b] Jožef Stefan International Postgraduate School, Jamova cesta 39, 1000 Ljubljana, Slovenia

[c] Plasma laboratory, National Aerospace University, 61070 Kharkiv, Ukraine

[d] Institute of Metals and Technology, Lepi pot 11, 1000 Ljubljana, Slovenia

* corresponding author: uros.cvelbar@ijs.si

Content:

1. Theoretical model of copper oxide development on thermally oxidized copper

The model describes the growth of two oxide layers (Cu_2O) and CuO) on a surface of a copper sample treated at some temperature in oxygen-containing atmosphere. Thus, two reactions are considered to describe the shifting of the boundary between the oxides:

$$Cu_2O + O \rightarrow 2CuO, \qquad \text{(S1)}$$

$$CuO + Cu \rightarrow Cu_2O. \qquad \text{(S2)}$$

When describing the motion of a copper atom from the copper sample to the upper surface of Cu_2O oxide, two types of diffusion, namely short-circuit diffusion between Cu_2O grains and lattice diffusion through the volume of Cu_2O grain, are considered. When the copper atom reaches to upper surface of Cu_2O layer, it can jump into the layer of CuO oxide that is formed on the layer of Cu_2O. At that, one molecule of CuO is turned to Cu_2O molecule. Then the movement of a copper atom is described as a set of jumps to overcome a potential well, where a molecule of Cu_2O containing two copper atoms at the moment, is converted again into CuO molecule thus releasing one copper atom, and then a new Cu_2O molecule is created in the neighboring node of the lattice after the released copper atom jumps into this node. This transformation is described by the reactions:

$$Cu_2O \rightarrow CuO + Cu \rightarrow Cu_2O. \qquad \text{(S3)}$$

This set of jumps is finalized when Cu atom reaches an oxygen atom and the molecule of Cu_2O is converted into two molecules of CuO as described by reaction (1); the new CuO molecule is generated at that, and a thickness of CuO oxide layer increases.

Langmuir adsorption isotherms are used in the model to describe the densities n_{x0}, n_{x2s}, and n_{x2t} of oxygen molecules adsorbed on the surface of the substrate, on the side surface of a nanowire and on the nanowire tip[1]:

$$\frac{n_{x0}}{n_0} = \frac{P_{O2}}{P_{00}+P_{O2}}, \qquad \frac{n_{x2s}}{n_0} = \frac{P_{O2}}{P_{0s}+P_{O2}}, \qquad \frac{n_{x2t}}{n_0} = \frac{P_{O2}}{P_{0t}+P_{O2}}. \qquad \text{(S4)}$$

where n_0 is a density of adsorption nodes on a surface of CuO, P_{00}, P_{0s}, P_{ot} are the constants that do not depend on the pressure P_{O2}, but depend on the temperature:

$$P_{0i} = \left(\frac{M_{O2}}{2\pi\hbar^2}\right)^{3/2} (k_B T_s)^{5/2} exp\left[-\frac{e(\varepsilon_{aO2i}-\varepsilon_{i-O2i})}{k_B T_s}\right], \qquad \text{(S5)}$$

where M_{O2} is the mass of the oxygen molecule, kg; $\varepsilon_{aO2(i)}$ are the adsorption energies (eV) of oxygen molecules on the surface of the oxide layer ($i \rightarrow 0$), the side surface of NW ($i \rightarrow s$), and the top surface of NW ($i \rightarrow t$), respectively; $\varepsilon_{i\text{-}O2i}$ are the internal energies (eV) of oxygen molecules on the above-listed surfaces;

P_{O2} is the partial pressure of oxygen, Pa, and is dependent on the total pressure P in the chamber, Pa:

$$P_{O2} = \frac{\phi_{O2}}{\phi_{add}+\phi_{O2}} P, \qquad \text{(S6)}$$

where ϕ_{O2} is the oxygen flow, and ϕ_{add} is the sum of flows of the additional gases, sccm.

Two above mentioned fluxes of copper atoms through the thickness of Cu_2O oxide are described by the flows φ_{Cu1b} and φ_{Cu1l}, respectively, with the same equations of the diffusion through a layer with a thickness L_i at the absence of sources and sinks due to the reactions in the layer. Hence, the reactions on the inter-oxide boundary are responsible for the creation of the driving force of the diffusion. The total flux of copper atoms to the boundary between Cu_2O and CuO layers is a sum:

$$\varphi_{Cu1} = P_{Cu1b}\varphi_{Cu1b} + P_{Cu1l}\varphi_{Cu1l}, \quad \text{(S7)}$$

where P_{Cu1b} and P_{Cu1l} are the factors that describe the cross-sections of the inter-grain boundaries and grains with respect to the total cross-section. The factors are expressed as a ratio:

$$P_{Cu1b} = \frac{S_{Cu2Ogb}}{S_{Cu2Ogb}+S_{Cu2Olat}}, \qquad P_{Cu1l} = \frac{S_{Cu2Olat}}{S_{Cu2Ogb}+S_{Cu2Olat}}. \quad \text{(S8)}$$

where $S_{Cu2Og)}$ and $S_{Cu2Olat}$ are the surface area occupied by the grain boundaries and grains, respectively. By considering the columnar shape of Cu_2O grains that is approximated by cylinder shape, the above parameters are:

$$S_{Cu2Ogb} = \frac{\pi\left(d_{Cu2O}+\frac{b_{Cu2O}}{2}\right)^2}{4} - \frac{\pi d_{Cu2O}^2}{4} = \frac{\pi d_{Cu2O}^2}{4}\left(\left(1+\frac{b_{Cu2O}}{2d_{Cu2O}}\right)^2 - 1\right), \quad S_{Cu2Olat} = \frac{\pi d_{Cu2O}^2}{4}, \quad \text{(S9)}$$

$$P_{Cu1b} = \frac{\left(\left(1+\frac{b_{Cu2O}}{2d_{Cu2O}}\right)^2-1\right)}{\left(1+\frac{b_{Cu2O}}{2d_{Cu2O}}\right)^2}, \qquad P_{Cu1l} = \frac{1}{\left(1+\frac{b_{Cu2O}}{2d_{Cu2O}}\right)^2}. \quad \text{(S10)}$$

where d_{Cu2O} and b_{Cu2O} are the diameter of Cu_2O grain and thickness of the grain boundary, respectively.

The density $n_{cu}(z)$ of the copper atoms on the boundary between the oxides is calculated by the equations:

$$D_{Cu1i}\frac{d^2 n_{Cui}}{dz^2} = 0, \quad \text{(S11)}$$

$$n_{Cu} - n_{Cu0} = -\frac{\varphi_{Cu1i}}{D_{Cu1i}}a_0 L_{ox1}, \quad \text{(S12)}$$

where D_{Cu1i} is a diffusion coefficient, and indexes "b" or "l" should be substituted to distinguish the flows through the grain boundaries and lattice, respectively.

The flows of copper φ_{Cu1i} at the coordinate $z = L_{ox1}$ is:

$$\varphi_{Cu1i} = \frac{1}{2}n_{Cu}v_{c1} = \frac{1}{2}n_{Cu}v_0 exp\left[-\frac{e\varepsilon_{c1i}}{k_B T_s}\right], \quad \text{(S13)}$$

where the exponent expresses the probability to overcome the potential well ε_{c1i}; T_s is a temperature of the sample; k_B is Boltzmann constant.

The diffusion coefficient is[2]:

$$D_{Cu1i} = D_{0c1i} exp\left[-\frac{e\varepsilon_{c1i}}{k_B T_s}\right], \quad \text{(S14)}$$

where D_{0c1} is described as

$$D_{0c1i} = \alpha_{Dc1i}\frac{\nu_0 a_0^2}{2}, \qquad \text{(S15)}$$

α_{Dc1} is a numerical coefficient, and ν_0 is the frequency of the lattice vibration that depends on the temperature[3]:

$$\nu_0 = \frac{2k_B T_s}{h}, \qquad \text{(S16)}$$

h is the Plank's constant.

Then the flow φ_{Cu1} is:

$$\varphi_{Cu1i} = \frac{1}{1+\frac{a_0\nu_0}{2D_{0c1i}}L_{ox1}}\frac{n_{Cu0}\nu_0}{2}exp\left[-\frac{e\varepsilon_{c1i}}{k_B T_s}\right], \qquad \text{(S17)}$$

$$\varphi_{Cu1} = \left(\frac{1}{\left(1+\frac{d_{Cu20}}{2b_{Cu20}}\right)\left(1+\frac{a_0\nu_0}{2D_{0c1b}}L_{ox1}\right)}exp\left[-\frac{e\varepsilon_{c1b}}{k_B T_s}\right]+\frac{1}{\left(1+\frac{2b_{Cu20}}{d_{Cu20}}\right)\left(1+\frac{a_0\nu_0}{2D_{0c1l}}L_{ox1}\right)}exp\left[-\frac{e\varepsilon_{c1l}}{k_B T_s}\right]\right)\frac{n_{Cu0}\nu_0}{2}, \qquad \text{(S18)}$$

where a_0 is a lattice parameter; n_{cu0} is the surface density of atoms of the copper sample, m^{-2}; L_{ox1} is a current length of the cuprous oxide grain.

Similar evaluations are used to describe the delivery of oxygen molecules from the surface of CuO layer exposed to the gas phase, to the boundary between the CuO and Cu_2O layers. The flow φ_{x2} is found by use of the density n_{x2} of oxygen molecules on the inter-oxide boundary:

$$D_{x2}\frac{d^2 n_{x2}}{dz^2} = 0, \qquad \text{(S19)}$$

$$D_{x2} = D_{0x2}exp\left(-\frac{e\varepsilon_{x2}}{k_B T_s}\right), \qquad \text{(S20)}$$

$$n_{x2} - n_{x0} = -\frac{\varphi_{x2}a_0}{D_{0x2}}L_{ox2}, \qquad \text{(S21)}$$

where D_{0x2} is a constant; D_{x2} is a coefficient of oxygen diffusion, ε_{x2} is a potential well, eV; n_{x0} is the density of oxygen molecules adsorbed on the surface of CuO oxide, m^{-2}; L_{ox2} is a current thickness of CuO oxide.

Then one can write

$$\varphi_{x1} = n_{x1}\nu_{x-dec} = 2n_{x2}\nu_{x-dec} = 2n_{x2}\frac{\nu_0}{2}exp\left(-\frac{e\varepsilon_{x2}}{k_B T_s}\right)exp\left(-\frac{e\varepsilon_{x-dis}}{k_B T_s}\right) =$$

$$= n_{x2}\nu_0 exp\left(-\frac{e(\varepsilon_{x2}+\varepsilon_{x-dis})}{k_B T_s}\right), \qquad \text{(S22)}$$

where $n_{x1} = 2n_{x2}$ is a density of oxygen atoms after the dissociation of O_2 molecules on Cu_2O/CuO boundary; $\nu_0/2\,exp(-e(\varepsilon_{x2}+\varepsilon_{x-dis})/k_B T_s)$ is a frequency of the jumps of the oxygen molecule from CuO toward Cu_2O oxide followed by the molecule dissociation, $\varepsilon_{x\text{-}dis}$ is the energy of O_2 dissociation at the presence of Cu_2O.

After combining the equations (S21) and (S22), the flux of oxygen atoms to the boundary between Cu_2O and CuO layers is:

$$\varphi_{x1} = \frac{n_{x0}}{1+\frac{a_0\nu_0}{2D_{0x2}}L_{ox2}}\frac{\nu_0}{2}exp\left(-\frac{e(\varepsilon_{x2}+\varepsilon_{x-dis})}{k_B T_s}\right). \qquad \text{(S23)}$$

The same approach is used to deduce the flow of copper atoms from the boundary between the oxides to the upper surface of CuO oxide that is exposed to the action of the gas phase:

$$\varphi_{Cu2} = \frac{1}{2} n_{Cu2} \frac{n_{x0}}{n_0} \nu_{c2} = \frac{n_{x0}}{1+\frac{a_0 \nu_0}{2D_{0c2}} L_{ox2}} \frac{\nu_0}{2} exp\left(-\frac{e(\varepsilon_{c2}+\varepsilon_{x-dis})}{k_B T_s}\right), \quad \text{(S24)}$$

where n_{Cu2} is a density of Cu atoms on the surface of CuO oxide; n_{x0}/n_0 is a relative density of oxygen molecule adsorbed on the surface of CuO from the gas phase; ν_{c2} is a frequency of the jumps of Cu toward O_2 molecule from Cu_2O oxide followed by the dissociation of the oxide, ε_{c2} is the energy of dissociation in reaction (3); D_{0c2} is a constant.

When describing the growth of CuO nanowires, the loss of copper atoms on the surfaces of the nanowires that are exposed to the oxygen adsorption should be considered, while for the surfaces submerged into CuO layer – should not.

Thus, for the diffusion of copper along the NW surface that is located in the layer of CuO oxide, and thus no oxidation takes place here, the density n_{Cu20nw} of copper atoms at the root of the nanowire is:

$$n_{Cu20nw} = n_{Cu20} - \frac{\varphi_{Cu2nw}}{D_{Cu2}} a_0 L_{ox2} = n_0 - \frac{\varphi_{Cu2nw}}{D_{Cu2}} a_0 L_{ox2}, \quad \text{(S25)}$$

$$D_{Cu2} = D_{0c2} exp\left(-\frac{e\varepsilon_{c2}}{k_B T_s}\right) \quad \text{(S26)}$$

where the initial density n_{Cu20} of copper atoms is considered to be equal to n_0, since this is the density of Cu_2O in the Cu_2O/CuO boundary.

The density of the copper atoms along the nanowire surface exposed to oxygen atmosphere is:

$$D_{Cus} \frac{\partial^2 n_{cu}(z)}{\partial z^2} = -n_{Cu}(z) \frac{n_{x2s}}{n_0} \nu_0 exp\left(-\frac{e\varepsilon_{x-dis}}{k_B T_s}\right), \quad \text{(S27)}$$

$$D_{Cus} = D_{Cus0} exp\left(-\frac{e\varepsilon_{c2s}}{k_B T_s}\right), \quad \text{(S28)}$$

$$\frac{\partial^2 n_{cu}(z)}{\partial z^2} = n_{Cu}(z) \frac{n_{x2s}}{n_0} \frac{\nu_0}{D_{Cus0}} exp\left(-\frac{e(\varepsilon_{x-dis}-\varepsilon_{c2s})}{k_B T_s}\right), \quad \text{(S29)}$$

where n_{x2s} is the number density of oxygen molecules adsorbed on the side surface of the nanowire; ε_{c2s} is the energy of dissociation in the reaction (S3) for the nanowire side surface exposed to gaseous oxygen.

The solution of equation (S29) $n_{Cu}(0) = n_{Cu20nw}$ is

$$n_{Cu}(z) = n_{Cu20nw} cos\left[\left(\frac{n_{x2s}}{n_0} \frac{\nu_0}{D_{Cus0}} exp\left[-\frac{e(\varepsilon_{x-dis}-\varepsilon_{c2s})}{k_B T_s}\right]\right)^{1/2} z\right]. \quad \text{(S30)}$$

The rate of conversion of copper atoms from Cu_2O to CuO oxide by a side surface of one nanowire with the length L_{nw} is:

$$N_{Cus}(L_{nw}) = \int_0^{L_{nw}} n_{Cu}(z) \frac{n_{x2s}}{n_0} \nu_0 exp\left(-\frac{e\varepsilon_{x-dis}}{k_B T_s}\right) 2\pi R_{nw}(z) dz =$$

$$= n_{Cu20nw} \frac{n_{x2s}}{n_0} \nu_0 exp\left(-\frac{e\varepsilon_{x-dis}}{k_B T_s}\right) 2\pi \int_0^{L_{nw}} R_{nw}(z) cos\left[\left(\frac{n_{x2s}}{n_0} \frac{\nu_0}{D_{Cus0}} exp\left[-\frac{e(\varepsilon_{x-dis}-\varepsilon_{c2s})}{k_B T_s}\right]\right)^{1/2} z\right] dz. \quad \text{(S31)}$$

By assuming the constant radius of a nanowire along the nanowire length $R_{nw}(0) \approx R_{nw}(L_{nw})$, the last expression is simplified:

$$N_{Cus}(L_{nw}) = 2\pi R_{nw}(0)\frac{\frac{n_{x2s}}{n_0}\nu_0 exp\left(-\frac{e\varepsilon_{x-dis}}{k_B T_s}\right)}{\left(\frac{n_{x2s}}{n_0}\frac{\nu_0}{D_{Cus0}}exp\left[-\frac{e(\varepsilon_{x-dis}-\varepsilon_{c2s})}{k_B T_s}\right]\right)^{1/2}}\times$$

$$\times n_{Cu20nw} sin\left[\left(\frac{n_{x2s}}{n_0}\frac{\nu_0}{D_{Cus0}}exp\left[-\frac{e(\varepsilon_{x-dis}-\varepsilon_{c2s})}{k_B T_s}\right]\right)^{1/2} L_{nw}\right]. \quad \text{(S32)}$$

The rate of conversion of copper atoms on a tip of the nanowire with the length L_{nw} is:

$$N_{Cut}(L_{nw}) = n_{Cu}(L_{nw})\frac{n_{x2t}}{n_0}\nu_0 exp\left(-\frac{e\varepsilon_{x-dis}}{k_B T_s}\right)\pi R_{nw}^2(L_{nw}) =$$

$$= \pi R_{nw}^2(L_{nw})\frac{n_{x2t}}{n_0}\nu_0 exp\left(-\frac{e\varepsilon_{x-dis}}{k_B T_s}\right) n_{Cu20nw} cos\left[\left(\frac{n_{x2s}}{n_0}\frac{\nu_0}{D_{Cus0}}exp\left[-\frac{e(\varepsilon_{x-dis}-\varepsilon_{c2s})}{k_B T_s}\right]\right)^{1/2} L_{nw}\right], \quad \text{(S33)}$$

where n_{x2t} is the number density of oxygen molecules adsorbed on the top surface of a nanowire.

The flux of the copper atoms consumed by one nanowire is

$$\varphi_{Cu2nw}(L_{nw}) = \frac{1}{\pi R_{nw}^2(0)}[N_{Cus}(L_{nw}) + N_{Cut}(L_{nw})]. \quad \text{(S34)}$$

If the radius of the nanowire is the same along the nanowire length, the last expression is:

$$\varphi_{Cu2nw}(L_{nw}) = n_{Cu20nw}\frac{n_{x2s}}{n_0}\nu_0 exp\left(-\frac{e\varepsilon_{x-dis}}{k_B T_s}\right)F(L_{nw}), \quad \text{(S35)}$$

$$F(L_{nw}) = \left[\frac{2\left(\frac{n_{x2s}}{n_0}\frac{\nu_0}{D_{Cus0}}exp\left[-\frac{e(\varepsilon_{x-dis}-\varepsilon_{c2s})}{k_B T_s}\right]\right)^{-1/2}}{R_{nw}(0)} sin\left[\left(\frac{n_{x2s}}{n_0}\frac{\nu_0}{D_{Cus0}}exp\left[-\frac{e(\varepsilon_{x-dis}-\varepsilon_{c2s})}{k_B T_s}\right]\right)^{1/2} L_{nw}\right] + \right.$$
$$\left. + \frac{n_{x2t}}{n_{x2s}} cos\left[\left(\frac{n_{x2s}}{n_0}\frac{\nu_0}{D_{Cus0}}exp\left[-\frac{e(\varepsilon_{x-dis}-\varepsilon_{c2s})}{k_B T_s}\right]\right)^{1/2} L_{nw}\right]\right] \quad \text{(S36)}$$

After substitution (S35) into (S25), the flux is:

$$\varphi_{Cu2nw}(L_{nw}) = \frac{n_{x2s}\nu_0 exp\left(-\frac{e\varepsilon_{x-dis}}{k_B T_s}\right)F(L_{nw})}{1+\frac{a_0\nu_0}{D_{Oc2}}L_{ox2}\frac{n_{x2s}}{n_0}exp\left[-\frac{e(\varepsilon_{x-dis}-\varepsilon_{c2})}{k_B T_s}\right]F(L_{nw})}, \quad \text{(S37)}$$

and the density of the copper atoms at the nanowire root after substitution (S33) to (S25) is:

$$n_{Cu20nw}(L_{ox2}) = \frac{n_0}{1+2\frac{a_0\nu_0}{2D_{Oc2}}L_{ox2}\gamma_L F(L_{nw})}, \quad \text{(S38)}$$

The whole set of nanowires grown per unit of area at a time t consume the flux:

$$\varphi_{Cu2n}(t) = \int_0^{L_{nw-m}} \rho_D(L)\varphi_{Cu2nw}(L)dL =$$

$$= \int_0^{L_{nw-m}} \rho_D(L)\frac{n_{x2s}\nu_0 exp\left(-\frac{e\varepsilon_{x-dis}}{k_B T_s}\right)F(L)}{1+\frac{a_0\nu_0}{D_{Oc2}}L_{ox2}\frac{n_{x2s}}{n_0}exp\left[\frac{e(\varepsilon_{x-dis}-\varepsilon_{c2})}{k_B T_s}\right]F(L)}dL, \quad \text{(S39)}$$

where $\rho_D(L)$ is the density of distribution of the nanowires on length.

Then the rates of nanowire growth, and the rate of growth of the side surface are:

$$\frac{dL_{nw}}{dt}(L_{nw}) = N_{Cut}(L_{nw})\frac{a_0^3}{\pi R_{nw}^2(L_{nw})} =$$

$$= n_{Cu20nw}(L_{nw})cos\left[\left(\frac{n_{x2s}}{n_0}\frac{v_0}{D_{Cus0}}exp\left[-\frac{e(\varepsilon_{x-dis}-\varepsilon_{c2s})}{k_BT_s}\right]\right)^{1/2}L_{nw}\right]\frac{n_{x2t}}{n_0}v_0exp\left(-\frac{e\varepsilon_{x-dis}}{k_BT_s}\right)a_0^3. \quad (S40)$$

$$\frac{dR_{nw}}{dt}(z,t,L_{nw}) = n_{Cu}(z)\frac{n_{x2s}}{n_0}v_0exp\left(-\frac{e\varepsilon_{x-dis}}{k_BT_s}\right)a_0^3 =$$

$$= n_{Cu20nw}(L_{nw})\frac{n_{x2s}}{n_0}v_0exp\left(-\frac{e\varepsilon_{x-dis}}{k_BT_s}\right)a_0^3cos\left[\left(\frac{n_{x2s}}{n_0}\frac{v_0}{D_{Cus0}}exp\left[-\frac{e(\varepsilon_{x-dis}-\varepsilon_{c2s})}{k_BT_s}\right]\right)^{1/2}z\right]. \quad (S41)$$

After combining the above expressions, a system of the equations to describe the growth of oxide layers with thicknesses $L_{ox1}(t)$ and $L_{ox2}(t)$, as well as the length $L_{nw}(t)$ and radius $R_{nw}(t)$ of the nanowires can be written:

$$\frac{dL_{ox1}}{dt} = \begin{cases} \left(\frac{P_{b1}}{1+a_{b1}L_{ox1min}}+\frac{P_{l1}}{1+a_{l1}L_{ox1min}}\right)A_c, \\ (L_{ox1}(t) \le L_{ox1min}) \wedge (L_{ox2}(t) \le L_{ox2min}); \\ \left(\frac{P_{b1}}{1+a_{b1}L_{ox1}}+\frac{P_{l1}}{1+a_{l1}L_{ox1}}\right)A_c - \left(\frac{2B_c}{1+bL_{ox2min}}+\frac{2C_c}{1+cL_{ox2min}}\right) - D_{nw}\frac{a_{ox1}^3}{a_{ox2}^3}D_c(L_{ox2min}), \\ (L_{ox1}(t) > L_{ox1min}) \wedge (L_{ox2}(t) \le L_{ox2min}); \\ \left(\frac{P_{b1}}{1+a_{b1}L_{ox1}}+\frac{P_{l1}}{1+a_{l1}L_{ox1}}\right)2A_c - \left(\frac{2B_c}{1+bL_{ox2}}+\frac{2C_c}{1+cL_{ox2}}\right) - D_{nw}\frac{a_{ox1}^3}{a_{ox2}^3}D_c(L_{ox2}), \\ (L_{ox1}(t) > L_{ox1min}) \wedge (L_{ox2}(t) > L_{ox2min}); \\ \left(\frac{P_{b1}}{1+a_{b1}L_{ox1min}}+\frac{P_{l1}}{1+a_{l1}L_{ox1min}}\right)2A_c, \\ (L_{ox1}(t) \le L_{ox1min}) \wedge (L_{ox2}(t) > L_{ox2min}); \\ 0, \quad \text{otherwise} \end{cases} \quad (S42)$$

$$\frac{dL_{ox2}}{dt} = \begin{cases} \left(\frac{2B_c}{1+bL_{ox2min}}+\frac{2C_c}{1+cL_{ox2min}}\right), \\ (L_{ox1}(t) > L_{ox1min}) \wedge (L_{ox2}(t) \le L_{ox2min}); \\ -\left(\frac{P_{b1}}{1+a_{b1}L_{ox1}}+\frac{P_{l1}}{1+a_{l1}L_{ox1}}\right)A_c + \left(\frac{2B_c}{1+bL_{ox2}}+\frac{2C_c}{1+cL_{ox2}}\right), \\ (L_{ox1}(t) > L_{ox1min}) \wedge (L_{ox2}(t) > L_{ox2min}); \\ -\left(\frac{P_{b1}}{1+a_{b1}L_{ox1min}}+\frac{P_{l1}}{1+a_{l1}L_{ox1min}}\right)A_c, \\ (L_{ox1}(t) \le L_{ox1min}) \wedge (L_{ox2}(t) > L_{ox2min}); \\ 0, \quad \text{otherwise} \end{cases} \quad (S43)$$

$$\frac{dR_{nw}}{dt} = \begin{cases} \alpha_L(t)\frac{n_{x2s}(t)}{n_{x2t}(t)}n_{Cu20nw}(L_{ox2min}), \\ (L_{ox1}(t) > L_{ox1min}) \wedge (L_{ox2}(t) \le L_{ox2min}); \\ \alpha_L(t)\frac{n_{x2s}(t)}{n_{x2t}(t)}n_{Cu20nw}(L_{ox2}), \\ (L_{ox1}(t) > L_{ox1min}) \wedge (L_{ox2}(t) > L_{ox2min}); \\ 0, \quad \text{otherwise} \end{cases} \quad (S44)$$

$$\frac{dL_{nw}}{dt} = \begin{cases} \alpha_L(t) n_{Cu20nw}(L_{ox2min}) cos(\beta_L L_{nw}), \\ (L_{ox1}(t) > L_{ox1min}) \wedge (L_{ox2}(t) \le L_{ox2min}); \\ \alpha_L(t) n_{Cu20nw}(L_{ox2}) cos(\beta_L L_{nw}), \\ (L_{ox1}(t) > L_{ox1min}) \wedge (L_{ox2}(t) > L_{ox2min}); \\ 0, \quad \text{otherwise} \end{cases} \tag{S45}$$

$$\frac{dL_{ox}}{dt} = \begin{cases} \left(\frac{P_{b1}}{1+a_{b1}L_{ox1min}} + \frac{P_{l1}}{1+a_{l1}L_{ox1min}}\right) A_c, \\ (L_{ox1}(t) \le L_{ox1min}) \wedge (L_{ox2}(t) \le L_{ox2min}); \\ \left(\frac{P_{b1}}{1+a_{b1}L_{ox1}} + \frac{P_{l1}}{1+a_{l1}L_{ox1}}\right) A_c - D_{nw} \frac{a_{ox1}^3}{a_{ox2}^3} D_c(L_{ox2min}), \\ (L_{ox1}(t) > L_{ox1min}) \wedge (L_{ox2}(t) \le L_{ox2min}); \\ \left(\frac{P_{b1}}{1+a_{b1}L_{ox1}} + \frac{P_{l1}}{1+a_{l1}L_{ox1}}\right) A_c - D_{nw} \frac{a_{ox1}^3}{a_{ox2}^3} D_c(L_{ox2}), \\ (L_{ox1}(t) > L_{ox1min}) \wedge (L_{ox2}(t) > L_{ox2min}); \\ \left(\frac{P_{b1}}{1+a_{b1}L_{ox1min}} + \frac{P_{l1}}{1+a_{l1}L_{ox1min}}\right) A_c, \\ (L_{ox1}(t) \le L_{ox1min}) \wedge (L_{ox2}(t) > L_{ox2min}); \\ 0, \quad \text{otherwise} \end{cases} \tag{S46}$$

where the initial conditions are $L_{ox1}(0) = L_{10}$, $L_{ox2}(0) = L_{20}$, $L_{ox}(0) = L_{10} + L_{20}$, and the parameters are:

$$A_c = n_{CuO} a_0^3 \frac{\nu_0}{2}; \qquad B_c = 2n_{x0} a_0^3 \frac{\nu_0}{2} exp\left(-\frac{e(\varepsilon_{x2} + \varepsilon_{x-dec})}{k_B T_s}\right);$$

$$C_c = n_{x0} a_0^3 \frac{\nu_0}{2} exp\left(-\frac{e(\varepsilon_{c2} + \varepsilon_{x-dec})}{k_B T_s}\right);$$

$$D_c(L_i) = n_{Cu20nw}(L_i) \pi R_{nw}^2(L_{nw}) \alpha_L cos(\beta_L(t) L_{nw}) + 2\pi R_{nw}(0) \frac{n_{x2s}}{n_{x2t}} \frac{\alpha_L}{\beta_L} sin(\beta_L L_{nw});$$

$$a_{b1} = \frac{a_0 \nu_0}{2D_{oc1b}}; \qquad a_{l1} = \frac{a_0 \nu_0}{2D_{oc1l}}; \qquad b = \frac{a_0 \nu_0}{2D_{ox2}}; \qquad c = \frac{a_0 \nu_0}{2D_{oc2}};$$

$$\alpha_L = \frac{n_{x2t}}{n_0} a_{0s}^3 \nu_0 exp\left(-\frac{e\varepsilon_{x-dis}}{k_B T_s}\right); \qquad \beta_L = \left(\frac{n_{x2s}}{n_0} \frac{\nu_0}{D_{Cuso}} exp\left[-\frac{e(\varepsilon_{x-dis} - \varepsilon_{c2s})}{k_B T_s}\right]\right)^{1/2};$$

$$\gamma_L(t) = \frac{n_{x2s}(t)}{n_{os}} exp\left[-\frac{e(\varepsilon_{x-dis} - \varepsilon_{c2})}{k_B T_s}\right]; \qquad n_{Cu20nw}(L_i) = \frac{n_0}{1 + 2cL_i \gamma_L F(L_{nw})};$$

$$F(L_{nw}) = \frac{2}{\beta_L R_{nw}(0)} sin(\beta_L L_{nw}) + \frac{n_{x2t}}{n_{x2s}} cos(\beta_L L_{nw}).$$

The experimental dependence of the sample temperature is approximated for the calculations by the expression: $T_s(t) = (T_{max} - T_0)(1 - exp[-t/\tau]) + 293$ (K), where T_{max} is 376, 487, 596, or 702 °C; $T_0 = 20$°C, $\tau = 2500$ s. The value of the adsorption energy $\varepsilon_{aO2} = 1.15$ eV is selected from the calculated by Sun *et al.* for the adsorption of O_2 on the oxygen-deficient CuO surface[4]; $\varepsilon_{iO2s} = \varepsilon_{iO2t} = 1.29$ eV is the energy of atomization of oxygen molecule. The value of the dissociation energy of O_2 on the Cu_2O surface $\varepsilon_{x\text{-}dis} = 0.65$ eV is located within the range 0.13...0.85 eV calculated by Zhang *et al.*[5] for O_2 dissociation on the Cu_2O oxygen-deficient surface. The energies ε_{c1b} and ε_{c1l} of the copper atom diffusion through the Cu_2O layer were set to correspond to the data on the temperature dependence of the diffusion

mechanisms reported in the literature[6,7] and to fit the results on the measured values of the oxides. The energy $\varepsilon_{x2} = 0.8$ eV of oxygen diffusion was set to describe the kinetics of the CuO layer, and the value was validated in the reported paper while describing the results obtained by Zhu *et al.* and Yuan *et al.* in their experiments[8,9]. The energies ε_{c2} and $\varepsilon_{c2s} = 0.36$ eV of copper diffusion in the CuO layer and along the nanowire side surface were adjusted to fit the ratio of thicknesses of CuO and Cu_2O oxides to the data from the experiments. The internal energies $\varepsilon_{i\text{-}O2t}$ and $\varepsilon_{i\text{-}O2s}$ of oxygen molecules adsorbed on the side and top surfaces of a nanowire, which are shown in Table 1, are just the numerical parameters necessary to evaluate the real difference between the adsorption energies ε_{aO2nwt} and ε_{aO2nws} for the oxygen molecule on top and side surfaces of the nanowire.

Interesting conclusions can be made after analyzing the values listed in the table. The energies ε_{c1b} and ε_{c1l} that are responsible for the diffusion of copper atoms through Cu_2O layer by use of the inter-grain (short-circuit) and lattice mechanisms, respectively, are characterized with the similar values in the temperature range 487°C to 702 °C, and both of them are lower for approximately 0.2 eV for 376 °C.

Table 1 – Energies $\varepsilon_{i\text{-}O2s}$ and $\varepsilon_{i\text{-}O2t}$ used in the calculations

T, °C	Energies, eV				
	ε_{c1b}	ε_{c1l}	ε_{c2}	ε_{aO2nws}	ε_{aO2nwt}
376	1.02	1.56	0.68	0.72	1.19
487	1.224	1.754	0.81	0.74	1.14
596	1.26	1.78	0.6	0.67	1.15
702	1.26	1.78	0.67	0.58	1.09

This change in the energies can be explained by two possible reasons: the oxide layer is either too porous at the temperature of 376 °C, or too strained by the stress that affects the energies through the expression $\varepsilon_i = \varepsilon_{i0} + \alpha F_i/e$, where ε_i is the energy at the absence of the stress, α is a coefficient, e is the electron charge (to fit the summand to eV). Non-monotonic behavior with maximum of the energy ε_{c2} of copper diffusion through CuO layer (the difference between the maximal and minimal energy is 0.21 eV) can also be explained by the superposition of porosity and stress in this oxide layer. In contrast, the decrease in the energies ε_{aO2nws} and ε_{aO2nwt} can be explained by the formation of more perfect crystalline structure of the growing nanowire at the temperature increase.

2. TEM cross-section sample preparation procedure

Oxide cross-sections were analyzed with TEM on two samples: the one oxidized at 376±5 °C for 10.5 h and the one at 596±5 °C for 10.5 h. They were both prepared in the same way, following the classical TEM preparation procedure: Oxide layers, which peeled off the sample after the synthesis, when the sample was cooled to the room temperature, were placed in the brass tube (outer diameter 3 mm), fitted between two Si wafer slabs and fixated by epoxy resin. After thermal treatment to harden the epoxy resin, the brass tube with the samples was cut with a precision diamond saw into shorter pieces, which were the thinned first with mechanical polishing with silicon carbide sandpapers, followed by dimpling and ion milling to obtain electron transparent cross-section sample (images from the optical microscope of the prepared sample synthesized at 596±5 °C for total oxidation time 10.5 h are shown in figure S1).

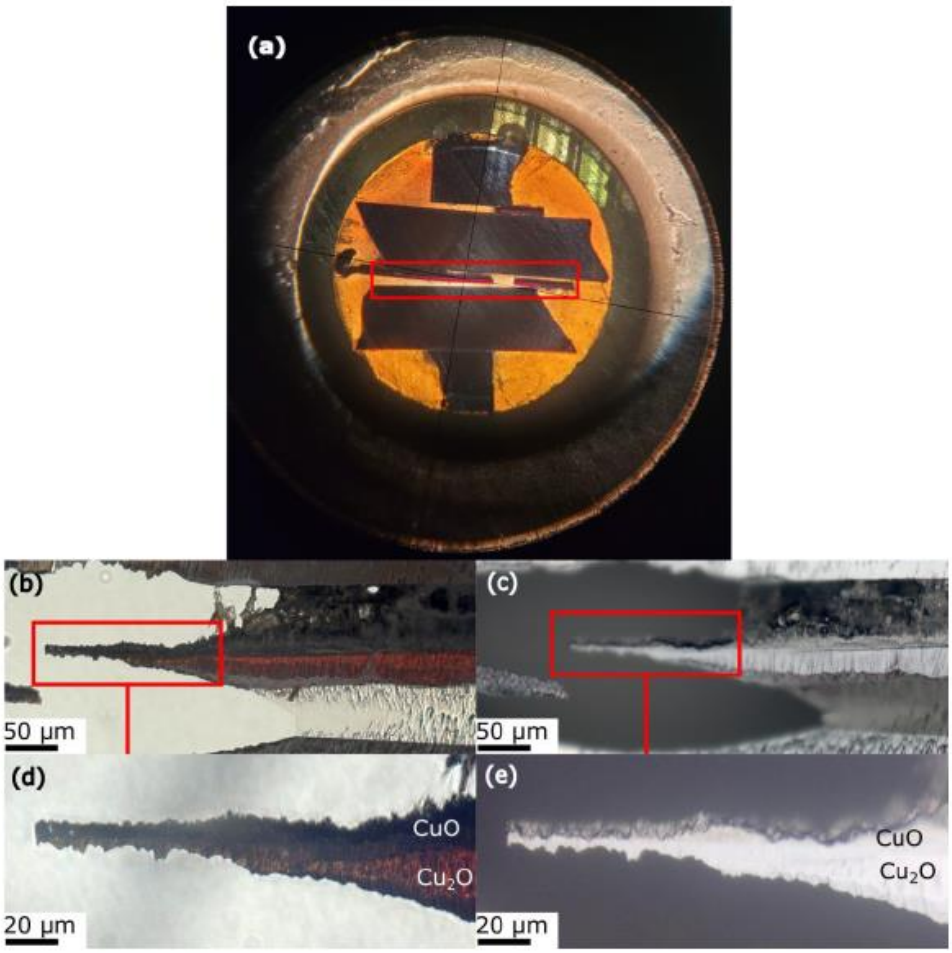

Figure S1. (a) Intermediate and (b-e) final step of conventional TEM cross-section sample preparation; sample oxidized at 596±5 °C for 10.5 h. (a) Transmission optical microscope micrographs of cross-section of Cu_2O-CuO sample embedded in epoxy resin, fixed between two Si slabs providing additional support. The sample was already mechanically thinned down to about 10 µm in the disc center; the Cu_2O is red transparent layer, marked with red rectangle. (b) – (e) TEM cross-section of Cu_2O-CuO sample after Ar^+ ion thinning process; (b), (d) transmission light mode; (c) and (e) reflected light mode.

3. Time and temperature dependence of number densities

Figure S2 shows the experimentally measured time dependence of number densities at the temperatures of 376±5 °C, 487±5 °C, 596±5 °C, and 702±5 °C, as well as the temperature dependence of number density at four different times of oxidation. The developed model does not predict these values and only uses the measured density to calculate the growth of the nanowires under assumption of the formation of the nanowire nuclei. We believe that the nucleation should be theoretically described by a separate model after considering the stress and strain problem for the oxide layers.

NW number density changes with time, (Figure S2). Density seems to reach a peak at some point. The saturation peak is shifted to lower annealing times as the temperature rises (Figure S2). The densest NW array obtained at 702±5 °C was observed only after 2 h of oxidation. At 596±5 °C, the peak was observed after 3 h of oxidation, whereas at 376±5 °C and 487±5 °C, the number density peak shifted to 10.5 h of oxidation.

The peak in density indicates that some NWs at one point most likely stopped growing and were overgrown by the CuO layer. Number density–time dependence analysis indicates that new NW formation slows at longer times, and a peak in number density is observed after which the density may drop. This peak is shifted to shorter times when temperature increases, due to faster kinetics of oxidation processes at higher temperatures.

At this point, we can only speculate why some NWs would stop growing. This could arise due to various dynamic processes in the CuO layer during oxidation. For example, nucleation and growth of new grains, as well as decomposition of smaller grains at the expense of larger ones are processes that are constantly shifting positions of grain boundaries in the CuO layer. Hence, the grain boundary diffusion path of Cu atoms through the layers is constantly changing. If the bottom of the twin boundary at some point loses contact with the main path of Cu diffusion, diffusion to the NW top may terminate.

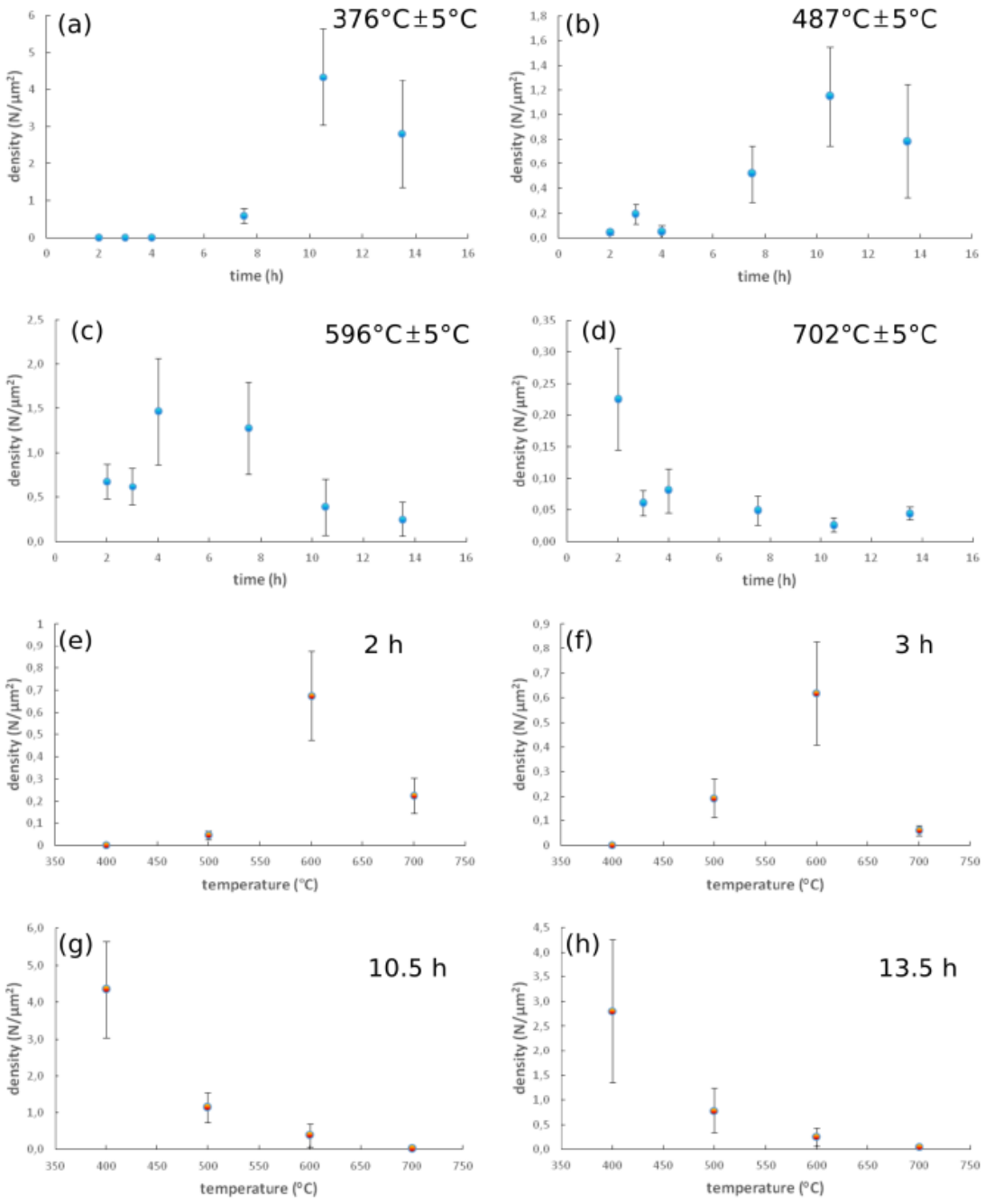

Figure S2. Time dependence of number densities at all temperatures: (a) 376±5 °C, (b) 487±5 °C, (c) 596±5 °C, (d) 702±5 °C and temperature dependence of number density at four different times of oxidation (e) 2 h, (f) 3 h, (g) 10.5 h, (h) 13.5 h.

4. SEM analysis of Cu2O and CuO layers

Thickness of both oxide layers Cu_2O and CuO increases with the temperature as evident from the SEM images of the oxide cross sections.

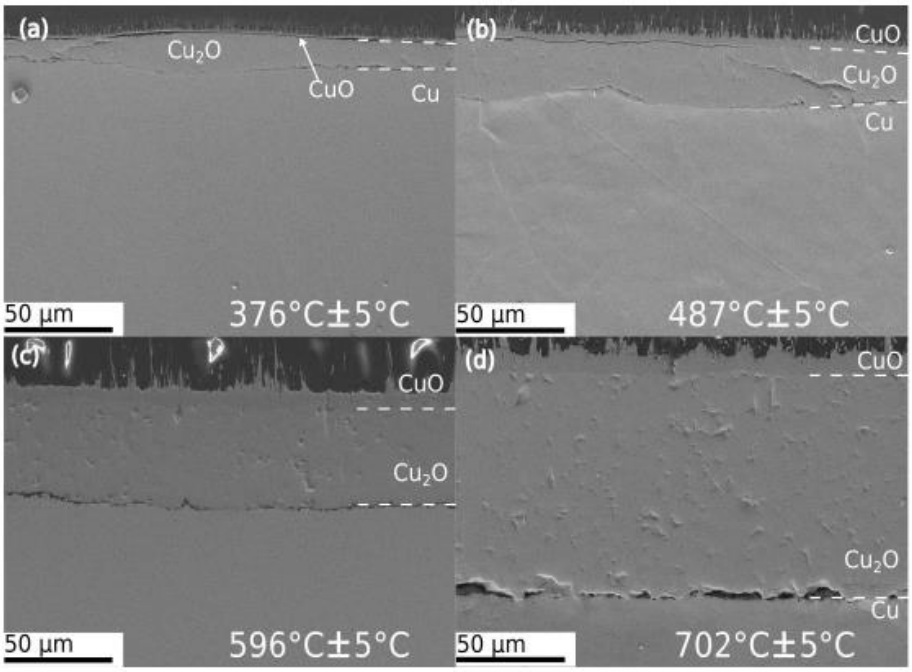

Figure S3. SEM micrographs of oxide layer cross-sections for samples oxidized for 13.5 h, at (a) 376±5 °C, (b) 487±5 °C, (c) 596±5 °C, (d) 702±5 °C

5. SEM and EDS analysis of Cu – Cu_2O interface

The surface of Cu metal under the oxide layers, after the oxide layers peeling.

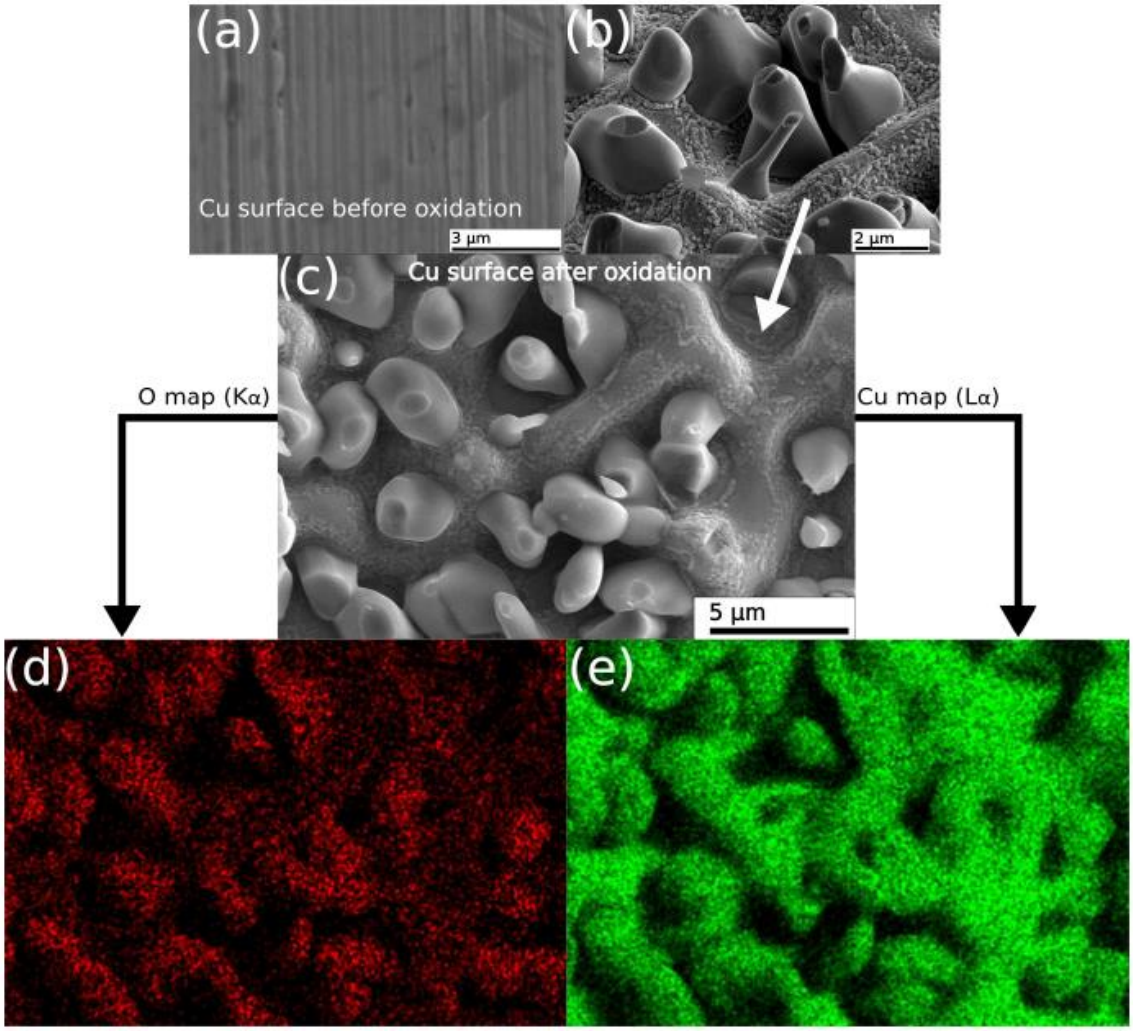

Figure S4. SEM analysis of the Cu sample oxidized at 702±5 °C for 7.5 h: (a) original Cu surface, (b), (c) the interface below the Cu_2O layer (peeled off). (d), (e) The EDS elemental map of spatial distribution of oxygen (O-Kα) and copper (Cu-Lα).

6. EBSD pole figures

Figure S5 shows orientation of individual grains in the Cu_2O and CuO layer. The grains in Cu_2O layer are randomly oriented, whereas grains in CuO layer show preferential orientation perpendicular to [001] direction. Texturing of the grains in the CuO layer depends on the temperature. As seen from pole figures for the CuO phase in Figures S5(a) and (b), at 702±5 °C, the CuO layer is strongly textured, whereas at 596±5 °C the preferred orientation is still perceivable, but the texturing is weaker.

Preferred growth orientation of CuO grains indicates that the growth rate is faster in that direction and that CuO grains are susceptible to formation of elongated grains. A portion of elongated grains in the CuO layer grows with an increase in oxidation temperature (as noted in the main text), which is also the case with texture strength, indicating that elongated grains have a preferred orientation, whereas equiaxed grains are randomly oriented and contribute to weaker textures at lower oxidation temperatures. Improper orientation of equiaxed grains stops them from elongating, as they cannot grow laterally due to the physical hindrance of neighboring grains. As the growth of equiaxed grains is restricted and elongated grains continue to elongate, elongated grains may even grow at the expense of the smaller equiaxed grains. The energy in this process is higher at higher temperatures, hence a portion of elongated grains increases with temperature (at 702±5 °C, the majority of grains in the CuO layer are elongated, as seen in the EBSD map of the CuO layer in Figure 3(a)) from the main text.

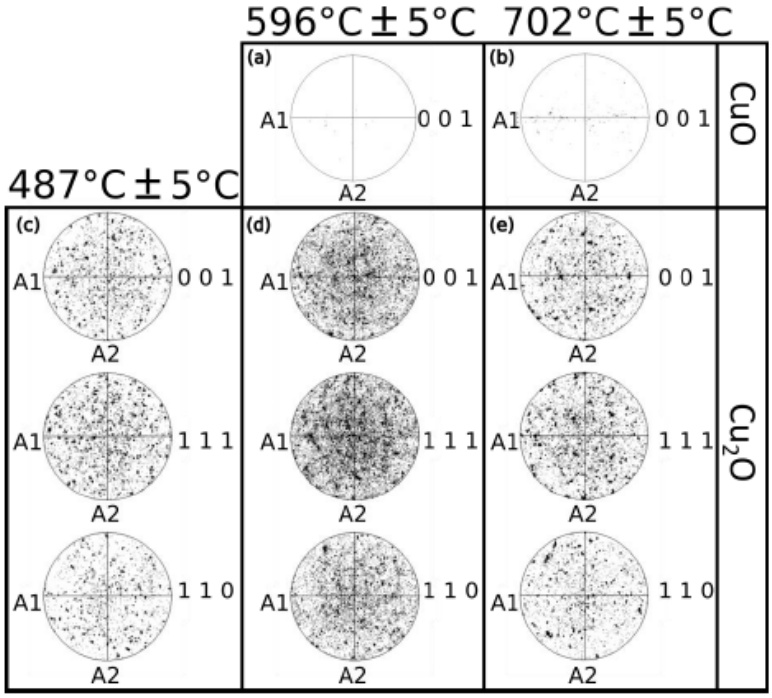

Figure S5. Pole figures showing orientations of individual copper oxide grains in different oxide phases and at different oxidation temperatures. Time of oxidation was 13.5 h in all samples. (a) CuO, oxidation temperature 596±5 °C, (b) CuO, oxidation temperature 702±5 °C, (c) Cu_2O, oxidation temperature 487±5 °C, (d) Cu_2O, oxidation temperature 596±5 °C, (e) Cu_2O, oxidation temperature 702±5 °C.

7. TEM analysis of Cu_2O/CuO interface

TEM images showing the Cu_2O/CuO interface with well-defined boundary between phases. Individual grains in both layers can also be resolved. Cu_2O layer consists mostly of columnar grains, while CuO consists predominantly of equiaxed grains at the interface.

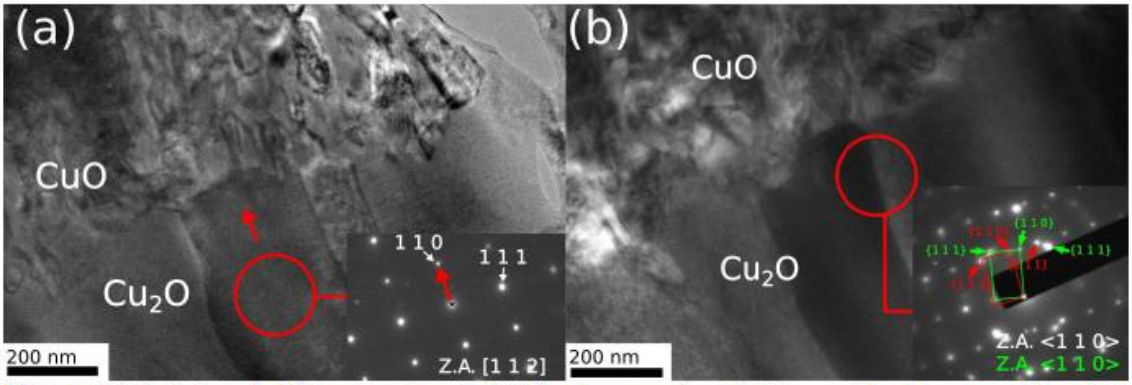

Figure S6.1. (a) and (b) conventional TEM micrographs of Cu - oxide layers, oxidized at 376±5 °C, with visible microstructure of both oxide layers: elongated Cu_2O and equiaxed CuO grains. Corresponding SAED patterns recorded over Cu_2O columns (marked red) are shown in inset.

Overview TEM micrograph of the sample oxidized at 596±5 °C for 10.5 h (Figure S6.2). The "root" of NW is visible, marked on the image with red dashed lines. At 596±5 °C NW, the "root" is in direct incoherent contact with the underlying Cu_2O layer. The interface between oxide layers is well defined, however as seen from SAEDs of CuO and Cu_2O (Figures S6.2 (b) and (c)) respectively), the phases are not in any epitaxial relationship, and their orientation is random.

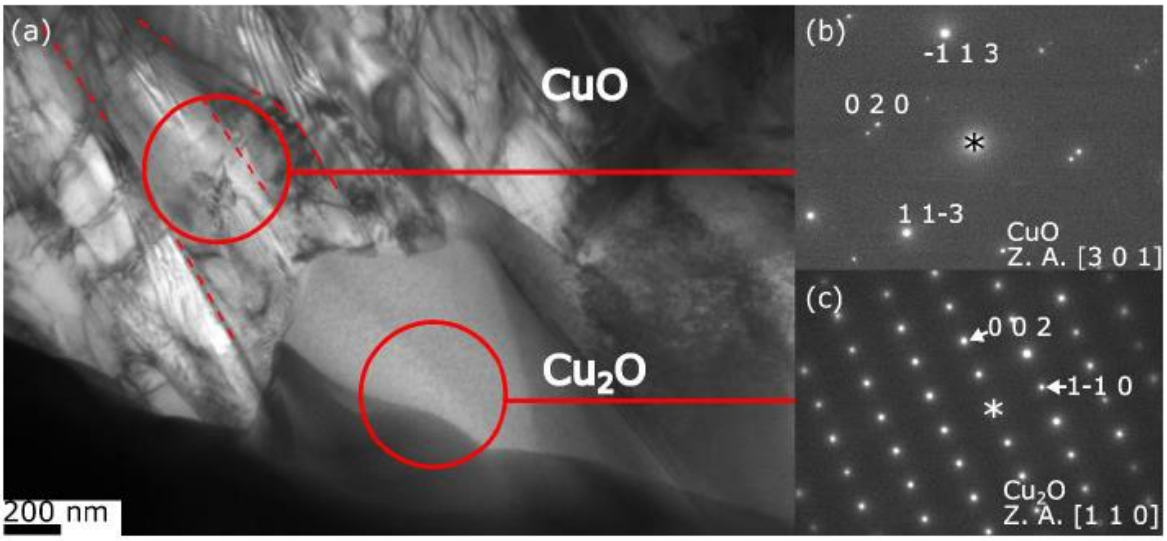

Figure S6.2. TEM analysis of the interface for the sample oxidized at 596±5 °C for 10.5 h. (a) TEM image of the Cu_2O/CuO interface with visible columnar grains on both sides. Elongated CuO grains are marked with red dashed lines. (b) SAED of the CuO layer in the area above the Cu_2O columnar grain; diffraction peaks are indexed as CuO. (c) SAED of the Cu_2O columnar grain, diffraction peaks are indexed as Cu_2O.

8. Time dependence of NW diameter

Figure S7 presents the experiments results (dots with error bars) and calculations (red continuous line) for the dependence of the nanowire diameters on time. One can see that this dependence is not so unambiguous as the dependence of the nanowire length on time (Ref. figure 6 (d) – (g)) that exhibits the monotonous growth and saturation. Here, the experimental data does not allow clearly stating whether the diameter does not change with time, has a minimal or maximal value. However, the simulation allows obtaining the dependencies that fit to the error bars.

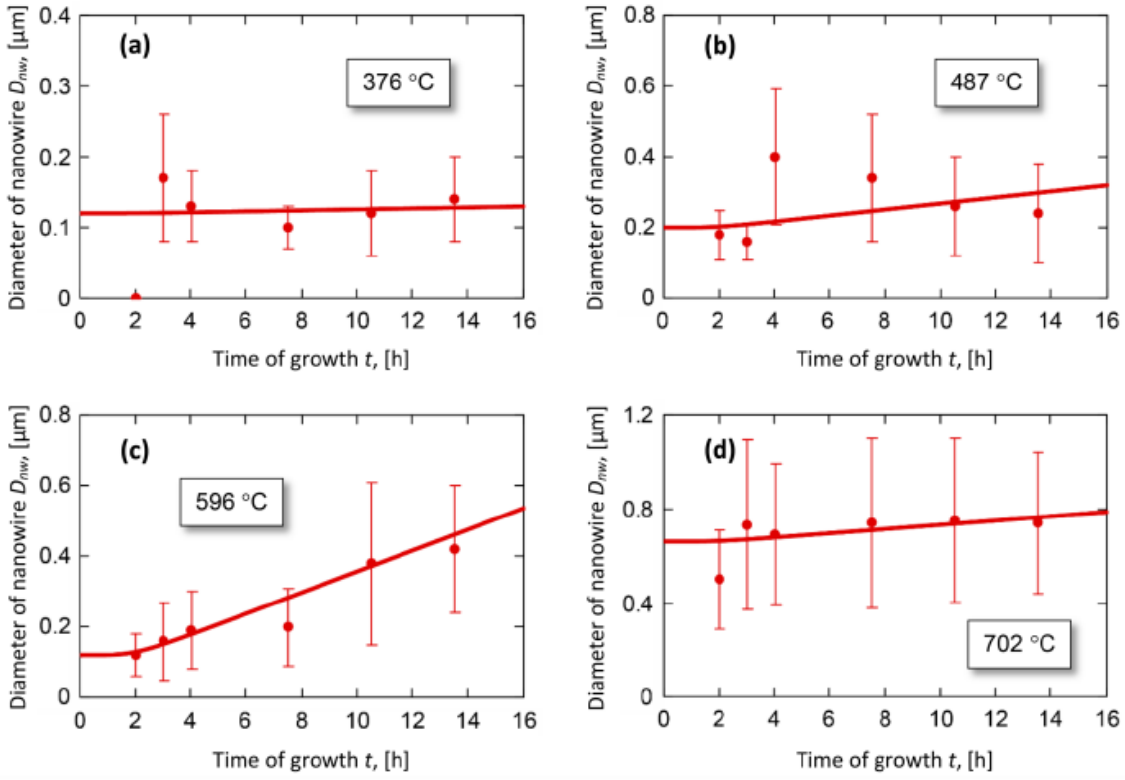

Figure S7. Time dependence of NW diameters at all temperatures (a) 376±5 °C, (b) 487±5 °C, (c) 596±5 °C, (d) 702±5 °C. Simulations were performed for temperatures (a) 376 °C, (b) 487 °C, (c) 596 °C and (d) 702 °C as marked on figures. Experimental data: dots with error bars, simulation data: red line.

9. TEM micrographs of detached NWs

On the TEM micrographs of the isolated nanowires, the central defect (twin boundary) present in each nanowire, is clearly visible. Several examples of such nanowires, which were detached from the Cu foil by sonication, can be seen in figure S8.

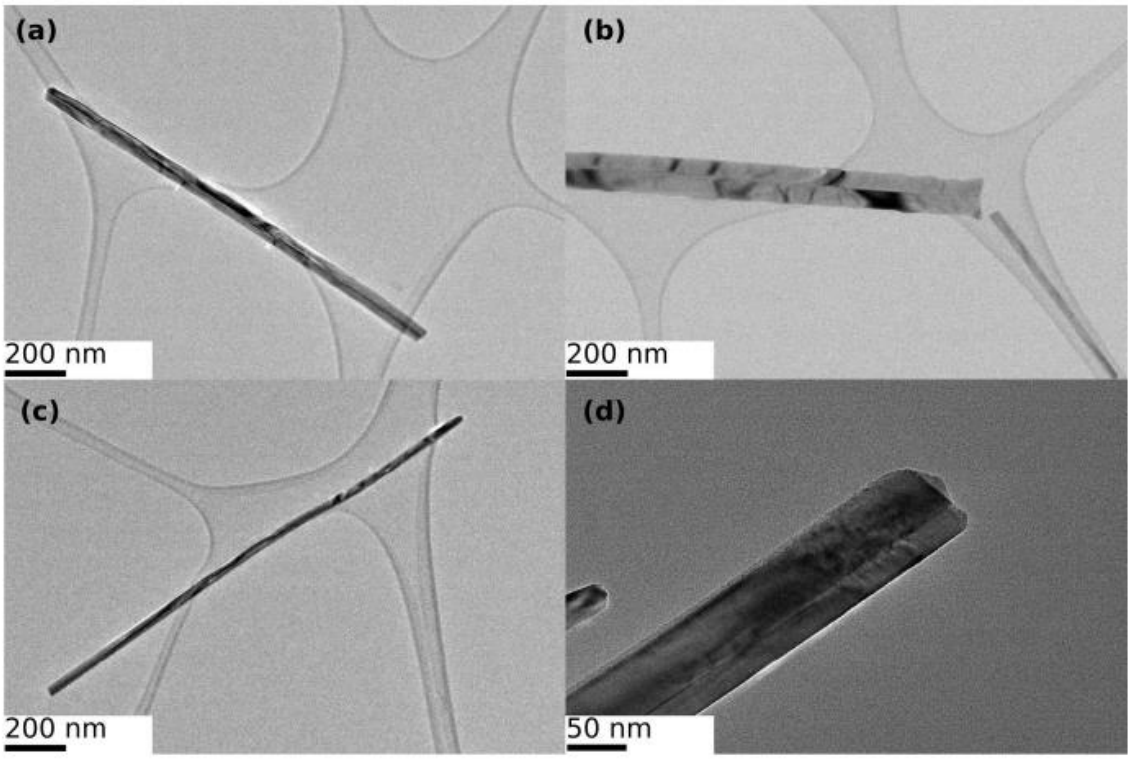

Figure S8. (a) – (d): CuO NWs detached from the substrate and deposited onto the amorphous carbon TEM support grids. The NWs exhibit central defect i.e. the twin boundary.

2.1.2 Development of a Theoretical Model to Describe CuO NW Growth by Thermal Oxidation

In Subsection 2.1.2 the CuO growth mechanism is further studied with an emphasis on the development of the theoretical model that would describe the thermal growth of CuO NWs. This was achieved by studying the thermal oxidation of copper under different experimental conditions (temperature, pressure, time, and oxygen flow). The dependencies of the experimental results, such as NW diameters, lengths, number densities, and thicknesses of the base copper oxide layers, on the experimental conditions, were used to develop a theoretical model describing the growth of the CuO NW.

The main conclusions from the model are:

- The diffusion of copper species from the underlying substrate to the NW tops proceeds via surface and twin-boundary diffusion. A different diffusion regime results in a different NW morphology, with twin-boundary diffusion resulting in longer and thinner NWs, while surface diffusion results in shorter but thicker NWs.
- In oxygen-rich conditions, at atmospheric pressure, oxygen flow does not play a large role in the growth of NWs.
- Oxygen pressure does not affect the growth of the Cu_2O layer, although it affects the growth of the CuO layer.
- The parameter that affects the growth of the nanowires the most is the temperature, as the processes involved in the growth (adsorption of oxygen molecules and diffusion of copper species) strongly depend on the temperature.
- The internal energy of the oxygen molecules is redistributed during the adsorption of an oxygen molecule. Part of this energy can be used to desorb the molecule. This process is more common on the NW side than on the top, as the energy for oxygen adsorption is higher on the NW top. Hence, the NW top represents the active site for the oxidation reaction. This is the main reason for NW's growth.

This subsection addresses Objective 1. The results of this subsection were published in a peer-reviewed scientific article in the journal *Applied Surface Science*.

Regarding my contribution, I performed part of the experimental work (synthesis of CuO NWs under different conditions and part of SEM analysis of the samples. Furthermore, I analyzed the results (measurements of NW diameters, length, density and thickness of copper oxide layers) and performed a statistical analysis of the measurements. Moreover, I contributed to the writing of the research paper with the other co-authors.

Applied Surface Science 566 (2021) 150619

Contents lists available at ScienceDirect

Applied Surface Science

journal homepage: www.elsevier.com/locate/apsusc

Full Length Article

A deterministic approach to the thermal synthesis and growth of 1D metal oxide nanostructures

Oleg Baranov [a,b,*], Martin Košiček [b,c], Gregor Filipič [b], Uroš Cvelbar [b,c,*]

[a] Plasma Laboratory, National Aerospace University, Kharkiv, Ukraine
[b] Jožef Stefan Institute, Ljubljana, Slovenia
[c] Jožef Stefan International Postgraduate School, Ljubljana, Slovenia

ARTICLE INFO

Keywords:
Copper oxide
Nanowires
Thermal growth

ABSTRACT

The 1D metal oxide nanostructures, including nanowires, are researched for at least two decades. However, the theoretical models on their synthesis and growth mechanisms are still controversial, even for the simplest growth method, namely thermal oxidation of a metallic surface. In this paper, the relevance analysis of the growth conditions reported in the literature is conducted, followed by the developed theoretical model, which was verified by our experiment on copper oxide nanowires. The model quantitatively describes the two most applied hypotheses concerning the single- and bi-crystalline growth of copper oxide nanowires. The numerical simulations reveal the conditions for both obtained mechanisms. It is also established that for the growth of the relatively thick nanowires associated with the single crystals, the internal energy of oxygen molecules determines the mechanism of oxygen adsorption. The energy can be re-distributed at the oxygen attachment, and the molecule can desorb at the account of this energy. Furthermore, the obtained result are also useful for developing the theory on nanowire seed generation, identifying the key control factors and basic mechanisms behind the growth modes, making a step toward a deterministic, highly predictable synthesis of dense 1D copper oxide nanostructures.

1. Introduction

Semiconducting metal oxide nanomaterials have gained high interest in the scientific community over the last two decades, mainly due to their size and morphology dependent properties. One of the most studied and prominent representatives of metal oxide nanomaterials are copper oxide (II) nanostructures (CuO NS). CuO NS can attain numerous shapes, among which 1D nanostructures, also known as nanowires (NWs), are of considerable interest. Their unique properties lay in a high surface to volume ratio and exposure of specific crystal faces. Copper oxide nanowires have been found to exhibit promising properties, which can be applied in many different fields, such as in gas sensing of ammonia [1], acetone, benzene, toluene, benzaldehyde, benzyl alcohol [2], ethanol [3], hydrogen [4], and hydrogen sulphide [5]; catalysis [6] and photocatalysis [7,8,9], batteries [10,11], optoelectronics [12], field emission [13], supercapacitor applications [14,15], broadband visible-light-driven recyclable SERS substrates [16] etc. One of the advantages of CuO NWs is their facile synthesis. There are many ways to synthesise CuO nanowires [17], with the thermal oxidation of copper film or foil in an oxygen atmosphere or plain air being the simplest method, with numerous results reported by different research groups. Other known methods like chemical [18,19] or plasma-enhanced [20,21] complicate the theoretical description by involving the presence of reagents or electric and magnetic fields [22,23]. Due to this fact, this method was chosen as the subject of our research conducted with the purpose to develop the theoretical model that describes the whole kinetics of the nanowire growth and considers the known experimental data.

Such model is necessary to perform the quantitative analysis of the experimental results to overcome the contradictions in various hypotheses and to perform the relevance analysis of the growth parameters. Up to now, despite numerous reports on thermally grown CuO NWs, the mechanism of their growth is still controversial and not fully explained, which, in turn, restrains the development and implementation of the technologies of synthesis of metal-oxide nanowires in industry. It is commonly observed that when copper is exposed to oxygen at elevated temperatures, both stable copper oxides (CuO and Cu_2O) form and they arrange in a layered fashion: on top of the copper

* Corresponding authors at: Jožef Stefan Institute, Ljubljana, Slovenia.
E-mail addresses: o.baranov@khai.edu (O. Baranov), uros.cvelbar@ijs.si (U. Cvelbar).

https://doi.org/10.1016/j.apsusc.2021.150619
Received 31 March 2021; Received in revised form 22 June 2021; Accepted 9 July 2021
Available online 16 July 2021

substrate layer of Cu_2O is formed, followed by a layer of CuO [24]. It is suggested that the processes of the formation of the oxides are strongly related with the metal oxide nanowire seeding and growth [25], and if the conditions (temperature and oxygen/air pressure) are 'right', the NWs are formed on top; thus, the *linking dynamics of the growth of the oxide layers and nanowires should be considered*. There are different reports on the temperature range in which NWs grow, but most commonly, NWs are grown between 400 °C and 700 °C [26]. The growth process is usually conducted at atmospheric pressure, yet the low-pressure growth is also reported [27,28]. The initial copper layer being oxidised needs to have sufficient thickness for NWs to grow – the limit is presumably around 400 nm for oxidation at 450 °C [29]. Thus, in the experiments of Chawla *et al.*, the temperature range for the generation of nanowires was found in a range of 400 to 500 °C. At that, for 6 h in the air, only small growth of nanowires with a diameter of 0.58 μm was observed, but not on the entire surface of the film at the temperature of 400 °C. When the temperature is increased to 450 °C, then the highly-dense nanowires with length and diameter of 1.57 μm and 0.86 μm are grown, respectively. However, only small nanowires with a length of 0.66 μm are found at low density on the surface after the temperature increase to 500 °C. Moreover, almost negligible growth is observed at the temperature of 550 °C, and no growth at the temperatures such as 600 °C and 700 °C. For the results of Jafari *et al.* [30], the fabrication of CuO nanowires by thermal oxidation on foil with a thickness of 0.15 mm in air *is shifted with respect to the reported above* – to temperatures of 500 °C to 700 °C. The nanowires become denser, and their diameter reaches 1–3 μm as the temperature increases to 700 °C. In addition, the sample grown at 700 °C showed the best photocatalytic performance and electrical conductivity attributed to various electron-scattering mechanisms; the authors concluded about the importance of compressive stress in the oxide layer on the length and density of nanowires. Growth of nanowires at the lower limit of 400 °C was investigated by Mahmoodi *et al.* [31], and very few nanowires with a length of ~1 μm were found after the annealing for 5 h. Then the length increased to 2–3 μm for the treatment time between 5 h and 7 h, and finally, become 2.5–3.5 μm for the time of 7 h to 9 h. *The diameters of the nanowires were not dependent on time* and ranged between 50 and 70 nm.

The experiments at the temperatures 400 °C, 450 °C and 500 °C under ambient conditions for 4 to 12 h were performed by Feng *et al.* [32]. In these experiments, *both the diameters and lengths of the nanowires increased with the temperature and the growth time*. The aspect ratio increased with the temperature under the same growth time; however, it had a different growth trend under the same temperature. A remarkable maximum was found at 8 h in each temperature group, which was explained by the *slower growth of the nanowires in length than in diameter as the growth time exceeds some value*.

The effect of the heating rate during 4 h process in the air at 550 °C was studied by Nkhaili *et al.* [33]. Samples of copper foil with a thickness of 0.3 mm were covered by nanowires with almost the same diameter of 200 nm when the heating rate was 1, 2, 5, and 10 °C/min, yet the density of the nanowires slightly decreases with increasing the heating rate. In the research carried out by Tran *et al.* [34], the lowest growth temperature was 400 °C where the nanowire length and width obtained was in the range of 3–5 μm, and 30–60 nm, respectively. As the temperature increased from 400 to 600 °C, the average diameter of nanowires was extended from 30 nm to 200 nm. *The diameter of the wire gradually decreased from the base to the top of the wire*. Simultaneously, the grain size of CuO layer was increased as the temperature raised from 400 to 600 °C. With the XRD, the authors also observed *the dependence of the sizes and density of nanowires on the grain sizes of a copper oxide layer*. The two effects resulted in the formation of densely packed nanowire arrays with small NW diameters. The result was obtained due to the efficient diffusion of Cu ions through the increased number of grain boundaries in the CuO layer and the rise of the diffusion rate with temperature. Namely, the wider wires with lower density preferred to grow at high temperature. Nanowires with 0.3 mm in diameter were synthesised by Zúñiga *et al.* [35] in the air at 400 and 500 °C within 2 h. For both temperatures, the diameter and length of nanowires increased with time, and *the nanowires were found to be bicrystals*. Furthermore, the formation of Cu_2O/CuO-mixed nanowires was conducted by Mohamed *et al.* [36] in thermal oxidation of copper foil of 0.508 mm at temperatures of 550, 600, and 650 °C, under a gas flow of Ar (100 sccm) and O_2 (50 sccm) mixture for 4 h. The NWs that grew at 550 °C had a low density and smaller diameters ranging from 95 to 250 nm, whereas the lengths extended to more than 9 μm. The nanowires obtained at 600 and 650 °C were even denser with lengths from 12 to 30 μm, and diameters from 105 to 295 nm or 100 to 543, respectively. However, it was noticed that some nanowires broke after reaching a certain length. It was also assumed that the interlayer of Cu/Cu_2O/CuO produces significant stresses because of the lattice mismatch between Cu_2O and Cu. It is believed that the release of these stresses is one of the driving forces during nanowire formation. A model proposed by Zhu *et al.* [37] explained the bi-crystalline growth. However, *the model still has to be improved to explain the mono-crystalline nanowire formation* [38]. In accordance, two mechanisms on copper diffusion to the nanowire top prevail in the literature [39]: the first is diffusion through the twin boundary layer, and the second is surface diffusion, where Cu ions diffuse along the NW surface.

In experiments, the oxygen flow is considered an important parameter for NW growth. As it was demonstrated by Hansen *et al.*, the diameters and lengths of the NWs depend on the oxygen flow/concentration [40]. Indeed, as a low-purity copper foil was put into a furnace, heated to 500 °C, and oxidised for 150 min with the oxygen gas flow at 0.5, 0.75, 1.0 and 5.0 ml/min, the diameters and lengths of the NWs were increased with increasing oxygen flow/concentration. This also holds for the O_2/Ar mixtures, and therefore *it is concluded that the oxygen concentration is the real control parameter*. Furthermore, Kumar *et al.* also studied the effect of the oxygen flow during oxidation of copper on the NW growth [41], where the optimal flow rate was found. This was also suggested in other studies where optimal values for oxygen flow at different temperatures were determined, under which NW density was maximised [42]. Furthermore, the influence of humidity was studied Xu *et al.* [43] within different oxidising atmospheres, including wet air and wet oxygen. In contrast to dry air, it was found that the wet air atmosphere oxidation results in denser and more uniform NWs distribution. The diameters and lengths of the NWs were about 80 nm and 3 μm, respectively. However, the wet oxygen oxidation resulted in a decrease in NW density coverage. The authors concluded that the water vapour affects the nucleation and growth rate of the NWs. Moreover, next to humidity, the external electric field affects nanowire growth as well [44].

Furthermore, for 400 °C, no NWs were formed at the 500 nm thick films, whereas at thickness 1 μm growth of NWs was observed [45]. The copper substrate's initial roughness is similarly considered a factor influencing nanowire density surface. The rougher surfaces are associated with smaller grains in the oxide layers, which is favourable for the grain boundary diffusion, and higher densities of nanowires are grown [46,47]. When NWs grow, copper needs to be supplied from underlying substrates, and there are a few ways through which this may occur. First of all, the copper could be delivered through the Cu_2O layer to Cu_2O/CuO oxide boundary, and both the lattice [48] and grain boundary [49] diffusion mechanisms are possible. Here, the grain boundary diffusion prevails at temperatures between 350 and 500 °C, while the lattice diffusion needs to be considered the main mechanism at temperatures above 800–900 °C [50]. Since the nanowire growth temperature lies between the ranges, *both the lattice and grain boundary diffusion mechanisms need to be considered* in the theoretical model. Furthermore, the presence of impurities or cracks can influence the activation energy of the diffusion processes, as was developed by Tang *et al.* [51] and can be explained by the Kirkendall effect [52]. The driving force for the diffusion is generally associated with stress gradient along the oxide layers, resulting from different molar volumes between the two oxides and the

metal phase [53]. Mema *et al.* reported successful implementation of controlled mechanical stress when the enhanced growth of nanowires was observed on a surface with the in-plane tensile stresses generated at the mechanical deformation of Cu foil [54]. However, it should be noted that the value of the macroscopic stresses generated at this might be a few orders of magnitude less than the structural stresses reported above. A qualitative description of the two-step process consisting of the formation of hillocks of copper to relieve the compressive stress, followed by the formation of the Cu_2O phase at the oxidation of the hillocks, was proposed by Park *et al.* [55].

An important question is: "What drives the one-dimensional growth of nanowires?". The temperatures in the range of 300 °C – 800 °C are too low to drive NW growth by the vapour-solid (VS) or vapour-liquid–solid (VLS) mechanisms, as copper and its oxides have considerably higher melting points [56]. Recent observations show that CuO nanowires grow on their tops [57,58]; thus, copper needs to be somehow supplied to the top of the nanowire to react with oxygen. Two beliefs on copper diffusion to the NW top prevail in the literature: the first is surface diffusion, where Cu ions diffuse along NW surface [58], and the second is through the twin boundary layer [27,28]. The counterargument for the first explanation is that majority of reports on uniformly thick NWs, whereas one would expect thicker NWs at the bottom if Cu ions would diffuse along the NW surface. On the other hand, the second explanation fails to explain the growth of NWs without twin boundary, which was also observed in the literature. Interesting results were obtained by J. Chen *et al.* with respect to the effect of the annealing time: a large number of long thing nanowires was grown at 500 °C and 8 h of exposition, and only CuO crystallites were developed at the same temperature for 24 h annealing [59]. These results are considered in favour of the reaction between copper and oxygen on the side surface of the nanowire (without making a conclusion about the source of the copper flow from the top or bottom of the nanowire) and, respectively, to the mechanism of the nanowire growth in diameter. A conclusion about the formation of oxide molecules on side surfaces of the nanowires through the surface diffusion of copper atoms along the external side surface of the growing nanowire was made by M. Chen *et al.* after obtaining the time dependencies of the nanowire diameter and length, which exhibit the non-monotonic increase [58]. The fact is that twin boundary represents the site, where nucleation of a new phase is favourable and such nucleation at the twin boundary site was observed by in-situ TEM studies above certain oxygen pressures [27,28,60], and numerous researches report about the bi-crystalline NW structure with twin boundary in the middle [61,62]. In this discussion, a suggestion about the synergistic effects on thermal growth of CuO nanowires proposed by Shi *et al.* looks reasonable to explain the variety of single-crystal, bi-crystal, and cone-shaped nanowires observed in the experiments [52]. Moreover, Tu *et al.* reported the thermal growth of the single-crystal nanowires at 400 °C, while bi-crystal nanowires were obtained at 500–600 °C [63]. This is why the *theoretical model should explain the NW formation by the copper diffusion along the outer surface of a nanowire as well as through the bi-crystalline route.*

As can be seen, many parameters influence CuO NW growth induced by thermal oxidation, and there are still many unanswered questions. In addition to the theoretical model, it is necessary to conduct the experiments where the growth of the nanowires is examined under different temperatures, oxygen pressures and flows to improve the understanding of the CuO nanowire growth mechanism.

In this work, we examined the growth of nanowires under the different oxygen flows, temperatures and pressures. The motivation for this research was to improve the understanding of the CuO NW growth mechanism. In the proposed deterministic model, which is based on the partial explanations in previously reported models of the nanowire growth [64,65] and formation of copper oxide layers [66], the linking dynamics of the processes at the growth of nanowires and oxide layers is considered. The deterministic model will provide i) information about the conditions for single- and bi-crystal NW growth; and ii) parameters for Langmuir isotherm, which will be used to upgrade the theoretical model of CuO NW growth.

2. Materials and methods

The CuO NWs were synthesised by heating copper samples (polycrystalline, oxygen-free high conductivity—OFHC copper, purity 99.98%, Advent Research Materials) in the oxygen atmosphere. Experiments were conducted inside the quartz tube, placed in the MTI Corporation Dual Zone Split Tube furnace OTF-1200X. Copper substrates were cut into round pieces, which were 14 mm in diameter. The controlled-environment thermal oxidation of copper samples was performed in the regulated pure oxygen atmosphere (down to 1 Pa). The residual water vapour was negligible. The chamber's partial oxygen pressure was controlled by pressure measurements and sustained by a constant oxygen inflow. The copper substrates were positioned on the ceramic combustion boats, and the experiments were conducted at temperatures of 550 °C, 600 °C, 650 °C, and 700 °C. Three different oxygen pressures were used: 70 Pa, 890 Pa and atmospheric. Oxygen inlet was positioned on one side of the quartz tube with oxygen flows of 97 sccm, 146 sccm, and 175 sccm set to 600 °C, while for other temperatures, the flow of 146 sccm was used. At the atmospheric pressure experiments, the oxygen exhaust was through the KF 16 port located on the opposite side of the quartz tube. In the experiments, the rectangular position of samples to the gas glow was intentionally avoided to prevent an increase in a local concentration of oxygen molecules when a surface is placed perpendicularly to the flow. According to the flow continuity equation $n_s = n_0 V_0 / V_s$, where $n_0 V_0$ is a flow without the obstacle (sample), and V_s is a flow velocity near the sample surface placed perpendicularly to the flow. When $V_s < V_0$, the concentration n_s of the molecules increases. This phenomenon may be wrongly treated as the changed flow, while it is just a manifestation of the local concentration increase in the gas molecules near the surface. However, this phenomenon plays an important role in the growth process of NWs, since concentrations of molecules are higher.

In experiments where the lower pressure was used, the exhaust KF port was connected to the rotary pump. After thermal oxidation, the samples were taken out of the quartz tube and cooled at ambient temperature. A schematic of the setup is shown in Fig. 1.

The surfaces of oxidised copper substrates were observed by field emission scanning electron microscopes (Jeol JSM-7600F and FEI Helios NanoLab 650). Images from microscopes were used to estimate the average length, diameter and number density of the grown CuO NWs as well as thicknesses of Cu_2O and CuO layers.

3. Experimental results

After the oxidation, all samples turned black. This indicated the presence of a CuO layer on the surface of the substrates. Surface examination with SEM showed clearly visible Cu_2O and CuO layers, on top of which the arrays of NWs were grown, and the densest array of NWs was found around 600 °C. Some SEM images are presented in Fig. 2(a, c, e). Furthermore, the measured time dependencies of NW length, diameter and thicknesses of layers at different conditions (temperature, pressure and oxygen flow) are displayed in Figs. 4–6. In all cases, thicknesses of oxide layers increased with time. This growth is done as

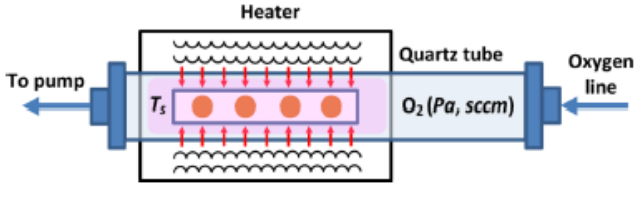

Fig. 1. Schematic of the experimental setup.

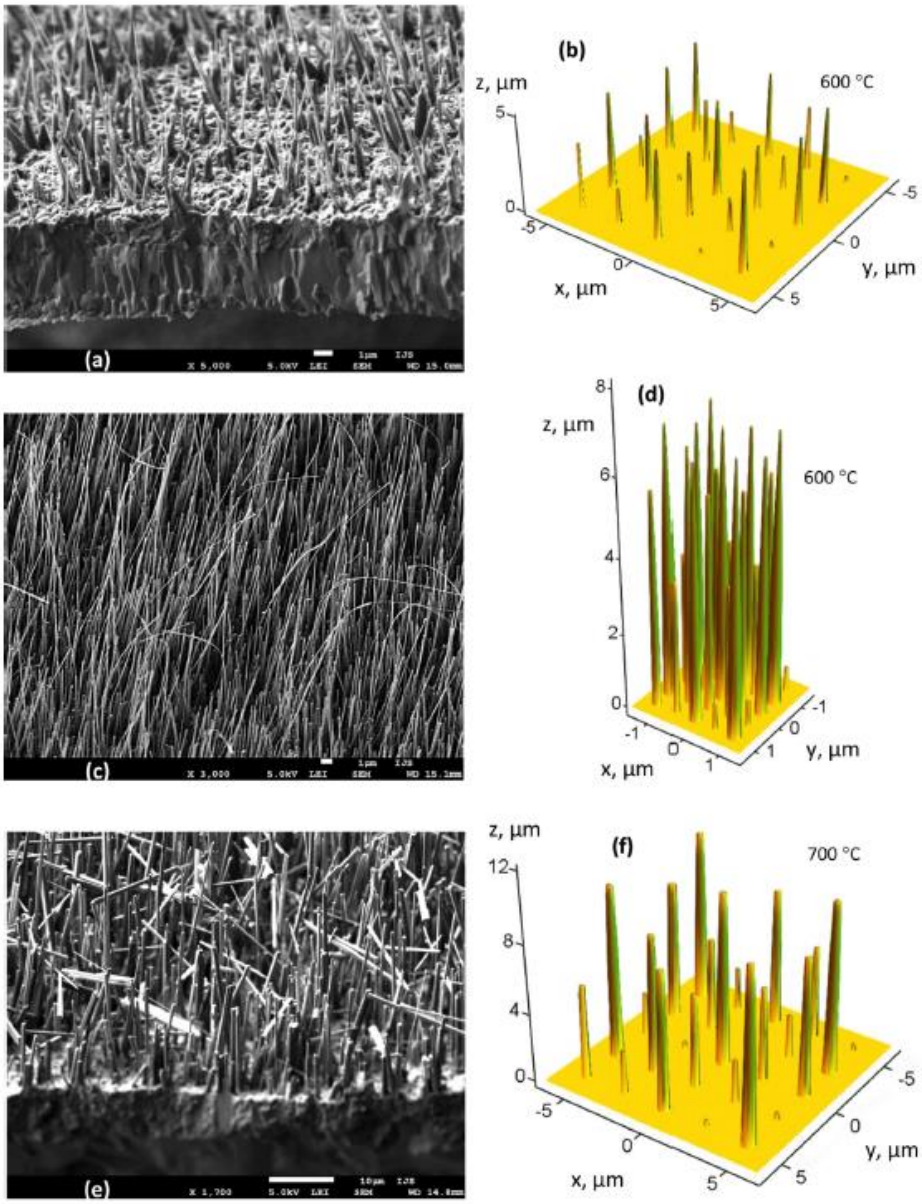

Fig. 2. SEM images (a, c, e) and simulation (b, d, f) of growth of CuO nanowires: a, b – at 890 Pa, 600 °C and 146 sccm of oxygen flow; c, d - at atmospheric pressure, 600 °C and 146 sccm of oxygen flow; e, f - at atmospheric pressure, 700 °C and 146 sccm of oxygen flow.

parabolic law, which is widely accepted in the literature and theoretically described elsewhere [50,67]. The NW length and diameters increased with time; however, the long thin nanowires with an almost constant distribution of the diameter along the length were also observed.

The influence of the oxygen flow was studied at the temperature of 600 °C and atmospheric pressure. Flow doesn't appear to have a large impact on oxide layer thicknesses. However, at a high oxidation time, the lower flow seems to result in slightly thicker layers. Therefore, it appears that oxygen consumption during oxidation was not affected by the flow, and for all three cases, oxygen supply for sufficient oxidation was not a limitation. The NW lengths and diameters were also not strongly affected. Thus, the small influence of oxygen flow in our experiments is probably a narrow range of oxygen flows used to study the effect.

The influence of pressure was studied at the temperatures of 600 °C and 700 °C by performing oxidations at three different pressures of 70 Pa (low-pressure regime), 890 Pa (intermediate pressure regime) and atmospheric pressure (high-pressure regime). At that, an increase in the density of nanowires on the sample surface with pressure was evident. At low pressure, only a small amount of NWs grew at 600 °C, while they were practically non-existent at 700 °C. When the pressure was increased to 890 Pa, NW density at 600 °C gradually increased. On the other hand, there were no NWs at 700 °C. When the pressure was at the atmosphere, NWs also grew at 700 °C; but their density was higher at 600 °C. NW parameters (length and diameter) were not strongly affected by the pressure in comparison to their density. Only a slight increase in NW length is observed as we move from low pressure to atmospheric. Contrarily, NW diameter even seemed to decrease with increasing pressure; however, a small number of nanowires observed in the low-pressure mode does not allow considering the results as reliable. Pressure also had a smaller influence on thicknesses of both oxide layers, with a slight increase in thicknesses at the intermediate pressure.

The influence of temperature is most noticeable in oxide layer thicknesses as considerable thickening is observed when the temperature rises from 550 °C to 700 °C. Gradual increase of the NW length with

temperature is observed, particularly at high oxidation time. It is also seen that NW growth slows down considerably faster at lower temperatures. NW diameter only slightly increased when the temperature was changed from 550 °C to 600 °C, while a larger increase is observed from 600 °C to 700 °C.

4. Theoretical model

To explain the obtained results and the experimental data described in the introduction, the following theoretical model was developed. The model does not consider the formation of a nanowire seed and proposes a nanowire growth mechanism under the condition of seed generation. A schematic of the processes is presented in Fig. 3. *The growth of the nanowire due to the diffusion of copper along the side surface of the nanowire is considered to develop a set of equations, hence it describes the single crystal growth; the way to reduce the equations with respect to describing the bi-crystal growth will be developed later in this paper.*

Both Cu_2O and CuO oxides are involved in the following reactions, which shifts the boundary between the oxides:

$$Cu_2O + O \rightarrow 2CuO; \quad (1)$$

$$CuO + Cu \rightarrow Cu_2O. \quad (2)$$

When considering the copper delivery along the CuO layer through the surface or lattice diffusion, the diffusion of Cu_2O oxide into CuO oxide is described. At that, the motion of a copper atom is associated with a set of 'jumps', when the atom is released at the dissociation of the cuprous oxide, it shifts to the neighbouring node occupied by CuO oxide that catches the atom:

$$Cu_2O \rightarrow CuO + Cu \rightarrow Cu_2O. \quad (3)$$

When reaching an oxygen atom, the 'molecule' of Cu_2O is a subject of reaction (1), when the new CuO 'molecule' is generated, and the CuO oxide layer grows.

4.1. Oxygen adsorption

The densities of oxygen molecules adsorbed on the surface (n_{x0}) of the substrate ($z = 0$), side (n_{x2s}), and top (n_{x2t}) surfaces of copper oxide nanowire are expressed in the form of Langmuir adsorption isotherm [68]:

$$\frac{n_{x0}}{n_0} = \frac{P_{O2}}{P_{00} + P_{O2}}; \quad \frac{n_{x2s}}{n_0} = \frac{P_{O2}}{P_{0s} + P_{O2}}; \quad \frac{n_{x2t}}{n_0} = \frac{P_{O2}}{P_{0t} + P_{O2}}, \quad (4)$$

where P_{O2} is the partial pressure of oxygen, Pa; P_{00}, P_{0s}, P_{ot} are the constants that do not depend on the pressure P_{O2}, but depend on the temperature; n_0 is a surface density of the CuO adsorption nodes. The value of the constants are expressed as

$$P_{0(i)} = \left(\frac{M_{O2}}{2\pi\hbar^2}\right)^{3/2} (k_B T_s)^{5/2} exp\left[-\frac{e\left(\varepsilon_{aO2(i)} - \varepsilon_{i-O2(i)}\right)}{k_B T_s}\right], \quad (5)$$

where M_{O2} is the mass of the oxygen molecule, kg; $\varepsilon_{aO2(i)}$ are the adsorption energies (eV) of oxygen molecules on the surface of the oxide layer ($(i) \rightarrow 0$), the side surface of NW ($(i) \rightarrow s$), and the top surface of NW ($(i) \rightarrow t$), respectively; $\varepsilon_{i\text{-}O2(i)}$ are the internal energies (eV) of oxygen molecules on the above-listed surfaces.

The oxygen pressure is described by the known expression

$$P_{O2} = \frac{\phi_{O2}}{\phi_{add} + \phi_{O2}} P, \quad (6)$$

where P is the total pressure in the chamber, Pa; ϕ_{O2} is the oxygen flow, and ϕ_{add} is the sum of flows of the additional gases (this sum equals to zero in our experiment, so $P_{O2} = P$), sccm.

In the model, two paths of copper atom diffusion towards the inter-oxide boundary are considered, namely grain and lattice diffusion described by the flows φ_{Cu1b} and φ_{Cu1l}, respectively (Ref. Fig. 3). Each of the routes is described with the same type of equations that describes the diffusion along a layer with a thickness L_i at the absence of the diffusion species loss due to the reactions in the layer volume. The reactions on the inter-oxide boundary are the driving force of the diffusion.

Thus, the total flux of copper atoms to the inter-oxide Cu_2O/CuO boundary is a sum of two fluxes with a probability of realisation of either of two diffusion routs:

$$\varphi_{Cu1} = P_{Cu1b}\varphi_{Cu1b} + P_{Cu1l}\varphi_{Cu1l}, \quad (7)$$

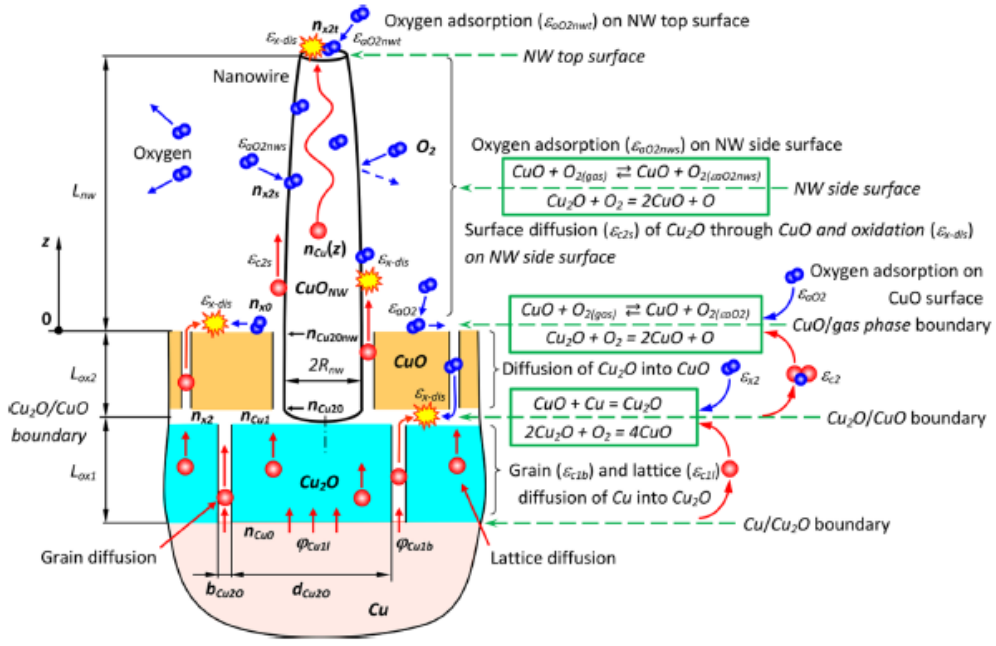

Fig. 3. Schematic of the nanowire thermal growth for the single-crystal; the processes on the side surface of the nanowire should be neglected for the bi-crystal growth.

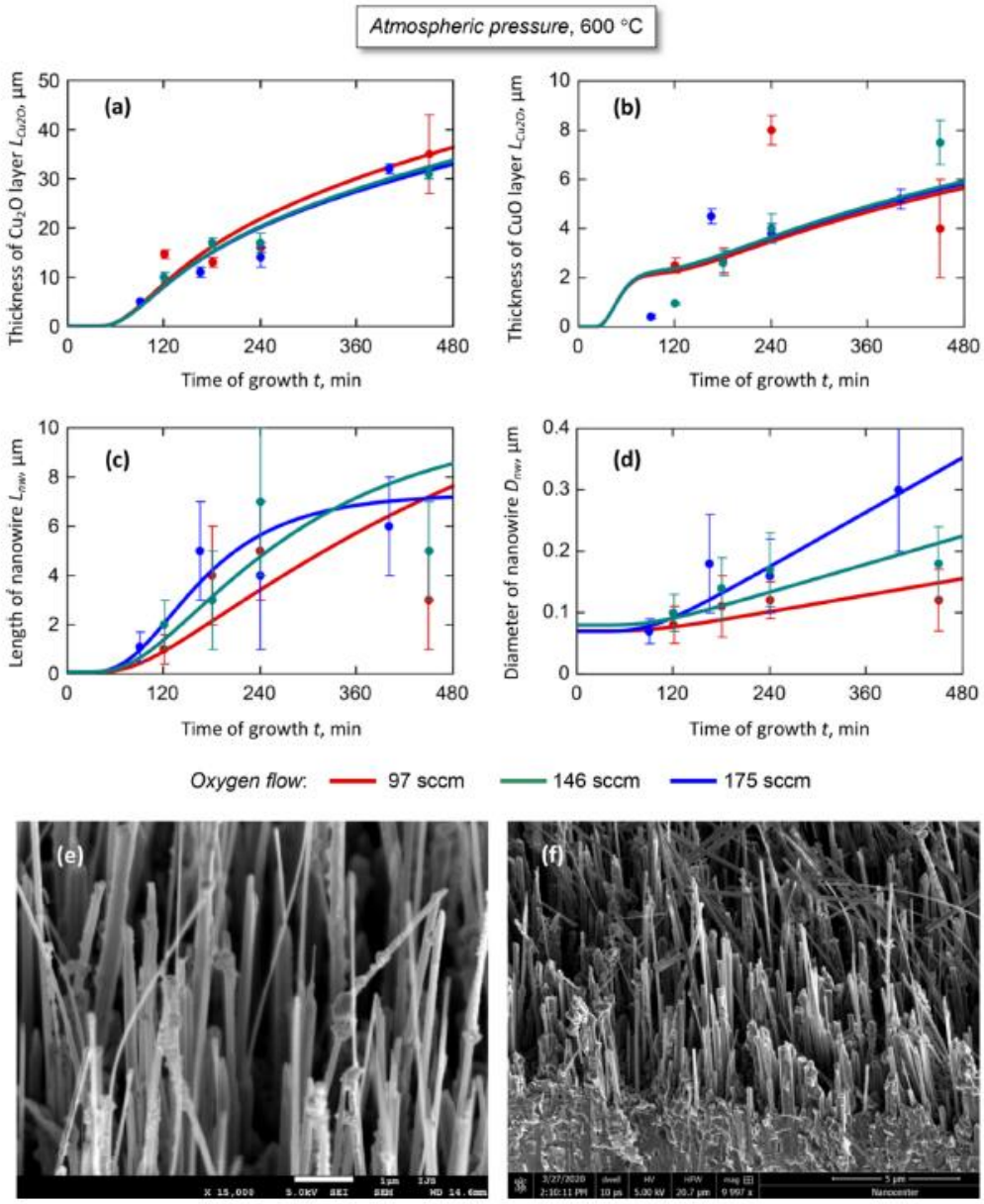

Fig. 4. Results of the experiments and calculations of the nanostructure growth for different oxygen flows at 600 °C and atmospheric pressure: a, b – thickness of Cu_2O and CuO layers, respectively; c, d – length and diameter of CuO nanowires; e, f – SEM images of nanostructures after 7.5 h of growth under oxygen flows of 97 sccm and 175 sccm, respectively. The results do not allow considering the oxygen flow as one of the control parameters at the atmospheric pressure.

where P_{CuIb} and P_{CuII} are the probabilities of the diffusion through the grain boundaries and volume, respectively.

The probabilities are expressed as a ratio of the surface occupied by the inter-grain boundaries to the total surface of Cu_2O oxide at the cross-section of the oxide:

$$P_{CuIb} = \frac{S_{Cu2Ob}}{S_{Cu2Ob} + S_{Cu2OI}}; \quad P_{CuII} = \frac{S_{Cu2OI}}{S_{Cu2Ob} + S_{Cu2OI}}, \tag{8}$$

where S_{Cu2Ob} and S_{Cu2OI} are the surface area occupied by the grain boundaries and grains, respectively.

By considering the columnar shape of Cu_2O grains, which is approximated by cylinder shape, we express the above parameters:

$$S_{Cu2Ob} = \frac{\pi\left(d_{Cu2O} + \frac{b_{Cu2O}}{2}\right)^2}{4} - \frac{\pi d_{Cu2O}^2}{4} = \frac{\pi d_{Cu2O}^2}{4}\left(\left(1 + \frac{b_{Cu2O}}{2d_{Cu2O}}\right)^2 - 1\right); \quad S_{Cu2OI} = \frac{\pi d_{Cu2O}^2}{4}; \tag{9}$$

$$P_{CuIb} = \frac{\left(\left(1 + \frac{b_{Cu2O}}{2d_{Cu2O}}\right)^2 - 1\right)}{\left(1 + \frac{b_{Cu2O}}{2d_{Cu2O}}\right)^2}; \quad P_{CuII} = \frac{1}{\left(1 + \frac{b_{Cu2O}}{2d_{Cu2O}}\right)^2}, \tag{10}$$

where d_{Cu2O} and b_{Cu2O} are the diameter of Cu_2O grain and thickness of the grain boundary, respectively. In the last expression, the space between two neighbouring grains, related to the grain boundary, is divided equally between the grains.

In the model, the assumption of even distribution of copper atoms

along the inter-oxide boundary is used, i.e. the rate of the diffusion on the inter-oxide boundary is considered as greatly exceeding the rates of the above-mentioned lattice and boundary diffusion.

Under the last assumption, a density $n_{cu}(z)$ of the copper atoms in the inter-oxide Cu/Cu_2O boundary can be calculated for the stationary diffusion by the equation where the reactions in the oxide volume are neglected:

$$D_{Culi}\frac{d^2 n_{Cui}}{dz^2} = 0; \tag{11}$$

$$n_{Cu} - n_{Cu0} = -\frac{\varphi_{Culi}}{D_{Culi}} a_0 L_{ox1}, \tag{12}$$

where D_{Culi} is a diffusion coefficient, and indexes "b" or "l" should be substituted to distinguish the flows through the grain boundaries and lattice, respectively.

The flows of copper φ_{Culi} at the coordinate $z = L_{ox1}$ is:

$$\varphi_{Culi} = \frac{1}{2} n_{Cu} \nu_{c1} = \frac{1}{2} n_{Cu} \nu_0 exp\left[-\frac{e\varepsilon_{c1i}}{k_B T_s}\right], \tag{13}$$

where the numerical coefficient describes that only a half of the copper atoms move toward the positive direction of z coordinate in Fig. 3; the exponent expresses the probability of the jump, T_s is the temperature of the sample, k_B is Boltzmann constant.

It should be emphasised that all the energies used to describe the diffusion of species through the oxide layers or along a nanowire are influenced by the stresses (tensile or compressive), electric fields etc. Formally, this action is described by substitution $\varepsilon_i \rightarrow \varepsilon_{i0} + \alpha F_i/e$, *where* ε_i *is the energy at the absence of the discussed perturbing factor (stress of field),* α *is a coefficient, e is the electron charge (to fit the summand to eV).* Later the way of considering the stress is shown in the text. However, since the data on the action of such factors to the discussed growth processes are missing or are not sufficient in the literature, the energies of the activation of the thermal processes in the paper are considered as taking into account the action of various perturbing factors.

A depth of the potential well ε_{c1i} is also used to express the diffusion coefficient in a form [69]:

$$D_{Culi} = D_{0c1i} exp\left[-\frac{e\varepsilon_{c1i}}{k_B T_s}\right], \tag{14}$$

where D_{0c1i} is a coefficient described as

$$D_{0c1i} = \alpha_{Dc1i}\frac{\nu_0 a_0^2}{2}, \tag{15}$$

α_{Dc1i} is a coefficient, and ν_0 is the frequency of the lattice vibration, which should depend on the temperature [70]:

$$\nu_0 = \frac{2k_B T_s}{h}, \tag{16}$$

h is the Planck's constant.

After combining Eqs. (12) and (13), the flow φ_{Cul} is expressed:

$$\varphi_{Culi} = \frac{1}{1 + \frac{a_0 \nu_0}{2D_{0c1i}} L_{ox1}} \frac{n_{Cu0}\nu_0}{2} exp\left[-\frac{e\varepsilon_{c1i}}{k_B T_s}\right] \tag{17}$$

After substitution into Eqn. (7), the following expression is obtained:

$$\varphi_{Cu1} = \left(\frac{1}{\left(1 + \frac{d_{Cu20}}{2b_{Cu20}}\right)\left(1 + \frac{a_0 \nu_0}{2D_{0c1b}} L_{ox1}\right)} exp\left[-\frac{e\varepsilon_{c1b}}{k_B T_s}\right] + \frac{1}{\left(1 + \frac{2b_{Cu20}}{d_{Cu20}}\right)\left(1 + \frac{a_0 \nu_0}{2D_{0c1l}} L_{ox1}\right)} exp\left[-\frac{e\varepsilon_{c1l}}{k_B T_s}\right] \right) \frac{n_{Cu0}\nu_0}{2}, \tag{18}$$

where a_0 is a lattice parameter of the grain; n_{cu0} is the surface density of atoms of the copper sample, m^{-2}; L_{ox1} is a current length of the cuprous oxide grain.

4.2. Diffusion of oxygen to the CuO/Cu_2O boundary

The oxygen molecules are delivered to the boundary between the CuO and Cu_2O oxides by a flow φ_{x2} from the surface where they are adsorbed from the gas phase; the expression for the flow is found like for the copper flows of copper atoms. First, the density n_{x2} of oxygen molecules on the inter-oxide boundary is evaluated:

$$D_{x2}\frac{d^2 n_{x2}}{dz^2} = 0; \tag{19}$$

$$D_{x2} = D_{0x2} exp\left(-\frac{e\varepsilon_{x2}}{k_B T_s}\right); \tag{20}$$

$$n_{x2} - n_{x0} = -\frac{\varphi_{x2} a_0}{D_{0x2}} L_{ox2}, \tag{21}$$

where D_{0x2} is a constant; D_{x2} is a coefficient of oxygen diffusion, ε_{x2} is a potential barrier, eV; n_{x0} is the density of oxygen molecules adsorbed on the surface of CuO oxide, which is exposed to the action of the gas phase, m^{-2}; L_{ox2} is a current thickness of CuO oxide.

Second, the oxygen flux to the Cu_2O/CuO boundary is described by the expression:

$$\begin{aligned}\varphi_{x1} &= n_{x1}\nu_{x-dec} = 2n_{x2}\nu_{x-dec} = 2n_{x2}\frac{\nu_0}{2} exp\left(-\frac{e\varepsilon_{x2}}{k_B T_s}\right) exp\left(-\frac{e\varepsilon_{x-dis}}{k_B T_s}\right) \\ &= n_{x2}\nu_0 exp\left(-\frac{e(\varepsilon_{x2} + \varepsilon_{x-dis})}{k_B T_s}\right),\end{aligned} \tag{22}$$

where $n_{x1} = 2n_{x2}$ is a density of oxygen atoms after the dissociation of O_2 molecules on Cu_2O/CuO boundary; $\nu_0/2exp(-e(\varepsilon_{x2} + \varepsilon_{x-dis})/k_B T_s)$ is a frequency of the jumps of the oxygen molecule from CuO toward Cu_2O oxide followed by the molecule dissociation, $\varepsilon_{x\text{-}dis}$ is the energy of O_2 dissociation at the presence of Cu_2O.

And finally, the flux of oxygen atoms to the inter-oxide boundary is deduced by combining Eqs. (21) and (22):

$$\varphi_{x1} = \frac{n_{x0}}{1 + \frac{a_0 \nu_0}{2D_{0x2}} L_{ox2}} \frac{\nu_0}{2} exp\left(-\frac{e(\varepsilon_{x2} + \varepsilon_{x-dis})}{k_B T_s}\right) \tag{23}$$

4.3. Grain boundary diffusion of Cu_2O into CuO layer

The flow of Cu from the Cu_2O/CuO boundary to the surface of CuO oxide exposed to the oxygen atmosphere is

$$\varphi_{Cu2} = \frac{1}{2} n_{Cu2} \frac{n_{x0}}{n_0} \nu_{c2} = \frac{n_{x0}}{1 + \frac{a_0 \nu_0}{2D_{0c2}} L_{ox2}} \frac{\nu_0}{2} exp\left(-\frac{e(\varepsilon_{c2} + \varepsilon_{x-dis})}{k_B T_s}\right), \tag{24}$$

where n_{Cu2} is a density of Cu atoms on the surface of CuO oxide; n_{x0}/n_0 is a relative density of oxygen molecule adsorbed on the surface of CuO from the gas phase; ν_{c2} is a frequency of the jumps of Cu toward O_2 molecule from Cu_2O oxide followed by the dissociation of the oxide, ε_{c2} is the energy of dissociation in reaction (3); D_{0c2} is a constant.

4.4. Growth of nanowires as diffusion of Cu_2O into CuO layer

For the nanowire growth, the transport of copper Cu_2O into CuO is determined by the oxidation process on the whole surface of the NW, including the side and top surfaces, unlike the growth of CuO and Cu_2O layers.

The first equation describes the diffusion of Cu_2O along the part of the NW surface that is located in the layer of CuO oxide layer, and thus no oxidation takes place here:

$$n_{Cu20nw} = n_{Cu20} - \frac{\varphi_{Cu2nw}}{D_{Cu2}} a_0 L_{ox2} = n_0 - \frac{\varphi_{Cu2nw}}{D_{Cu2}} a_0 L_{ox2}; \quad (25)$$

The number of copper atoms converted per one second from Cu_2O to CuO oxide by a side surface of one nanowire with the length L_{nw} is:

$$N_{Cus}(L_{nw}) = \int_0^{L_{nw}} n_{Cu}(z) \frac{n_{x2s}}{n_0} \nu_0 exp\left(-\frac{e\varepsilon_{x-dis}}{k_B T_s}\right) 2\pi R_{nw}(z) dz$$
$$= n_{Cu20nw} \frac{n_{x2s}}{n_0} \nu_0 exp\left(-\frac{e\varepsilon_{x-dis}}{k_B T_s}\right) 2\pi \int_0^{L_{nw}} R_{nw}(z) cos\left[\left(\frac{n_{x2s}}{n_0}\frac{\nu_0}{D_{Cus0}} exp\left[-\frac{e(\varepsilon_{x-dis}-\varepsilon_{c2s})}{k_B T_s}\right]\right)^{1/2} z\right] dz. \quad (31)$$

$$D_{Cu2} = D_{0c2} exp\left(-\frac{e\varepsilon_{c2}}{k_B T_s}\right), \quad (26)$$

where n_{Cu20nw} is the density of copper atoms at the bottom of the NW (NW 'root'), and the initial density n_{Cu20} of copper atoms is considered to be equal to n_0, since this is the density of Cu_2O in the Cu_2O/CuO boundary.

Under the condition of oxidation reaction on the side surface of a nanowire, the distribution of the copper atoms along the NW surface is determined by the equation:

$$D_{Cus}\frac{\partial^2 n_{cu}(z)}{\partial z^2} = -n_{Cu}(z)\frac{n_{x2s}}{n_0}\nu_0 exp\left(-\frac{e\varepsilon_{x-dis}}{k_B T_s}\right), \quad (27)$$

By assuming that the radius of a NW is weakly changing from the NW root to the top, and $R_{nw}(0) \approx R_{nw}(L_{nw})$, we may simplify the above expression:

$$N_{Cus}(L_{nw}) = 2\pi R_{nw}(0) \frac{\frac{n_{x2s}}{n_0}\nu_0 exp\left(-\frac{e\varepsilon_{x-dis}}{k_B T_s}\right)}{\left(\frac{n_{x2s}}{n_0}\frac{\nu_0}{D_{Cus0}} exp\left[-\frac{e(\varepsilon_{x-dis}-\varepsilon_{c2s})}{k_B T_s}\right]\right)^{1/2}} \times n_{Cu20nw} sin\left[\left(\frac{n_{x2s}}{n_0}\frac{\nu_0}{D_{Cus0}} exp\left[-\frac{e(\varepsilon_{x-dis}-\varepsilon_{c2s})}{k_B T_s}\right]\right)^{1/2} L_{nw}\right] \quad (32)$$

The number of copper atoms converted per one second from Cu_2O to CuO oxide by a top surface of the nanowire with the length L_{nw} is:

$$N_{Cut}(L_{nw}) = n_{Cu}(L_{nw})\frac{n_{x2t}}{n_0}\nu_0 exp\left(-\frac{e\varepsilon_{x-dis}}{k_B T_s}\right)\pi R_{nw}^2(L_{nw})$$
$$= \pi R_{nw}^2(L_{nw})\frac{n_{x2t}}{n_0}\nu_0 exp\left(-\frac{e\varepsilon_{x-dis}}{k_B T_s}\right) n_{Cu20nw} cos\left[\left(\frac{n_{x2s}}{n_0}\frac{\nu_0}{D_{Cus0}} exp\left[-\frac{e(\varepsilon_{x-dis}-\varepsilon_{c2s})}{k_B T_s}\right]\right)^{1/2} L_{nw}\right], \quad (33)$$

where n_{x2s} is the number density of oxygen molecules adsorbed on the side surface of a NW.

The diffusion coefficient D_{Cus} is expressed as

$$D_{Cus} = D_{Cus0} exp\left(-\frac{e\varepsilon_{c2s}}{k_B T_s}\right); \quad (28)$$

$$\frac{\partial^2 n_{cu}(z)}{\partial z^2} = n_{Cu}(z)\frac{n_{x2s}}{n_0}\frac{\nu_0}{D_{Cus0}} exp\left(-\frac{e(\varepsilon_{x-dis}-\varepsilon_{c2s})}{k_B T_s}\right), \quad (29)$$

where ε_{c2s} is the energy of dissociation at the reaction (3) that occurs on the nanowire side surface exposed to gaseous oxygen.

The solution of the above equation is known, and for $n_{Cu}(0) = n_{Cu20nw}$

$$F(L_{nw}) = \left[\frac{2\left(\frac{n_{x2s}}{n_0}\frac{\nu_0}{D_{Cus0}} exp\left[-\frac{e(\varepsilon_{x-dis}-\varepsilon_{c2s})}{k_B T_s}\right]\right)^{-1/2}}{R_{nw}(0)} sin\left[\left(\frac{n_{x2s}}{n_0}\frac{\nu_0}{D_{Cus0}} exp\left[-\frac{e(\varepsilon_{x-dis}-\varepsilon_{c2s})}{k_B T_s}\right]\right)^{1/2} L_{nw}\right] + \frac{n_{x2t}}{n_{x2s}} cos\left[\left(\frac{n_{x2s}}{n_0}\frac{\nu_0}{D_{Cus0}} exp\left[-\frac{e(\varepsilon_{x-dis}-\varepsilon_{c2s})}{k_B T_s}\right]\right)^{1/2} L_{nw}\right]\right] \quad (36)$$

is

$$n_{Cu}(z) = n_{Cu20nw} cos\left[\left(\frac{n_{x2s}}{n_0}\frac{\nu_0}{D_{Cus0}} exp\left[-\frac{e(\varepsilon_{x-dis}-\varepsilon_{c2s})}{k_B T_s}\right]\right)^{1/2} z\right] \quad (30)$$

where n_{x2t} is the number density of oxygen molecules adsorbed on the top surface of a NW.

Hence the flux of the copper atoms consumed by one nanowire is

$$\varphi_{Cu2nw}(L_{nw}) = \frac{1}{\pi R_{nw}^2(0)}\left[N_{Cus}(L_{nw}) + N_{Cut}(L_{nw})\right] \quad (34)$$

By assuming that the radius of a NW is weakly changing from the NW bottom to the top, and $R_{nw}(0) \approx R_{nw}(L_{nw})$, we may simplify the above expression:

$$\varphi_{Cu2nw}(L_{nw}) = n_{Cu20nw}\frac{n_{x2s}}{n_0}\nu_0 exp\left(-\frac{e\varepsilon_{x-dis}}{k_B T_s}\right) F(L_{nw}); \quad (35)$$

After substitution (35) into (25), we obtain:

$$\varphi_{Cu2nw}(L_{nw}) = \frac{n_{x2s}\nu_0 exp\left(-\frac{e\varepsilon_{x-dix}}{k_B T_s}\right) F(L_{nw})}{1 + \frac{a_0\nu_0}{D_{0x2}} L_{ox2} \frac{n_{x2s}}{n_0} exp\left[-\frac{e(\varepsilon_{x-dix}-\varepsilon_{c2})}{k_B T_s}\right] F(L_{nw})}. \quad (37)$$

Thus, we can find the density of the copper atoms at the NW root after substitution (33)–(25):

$$n_{Cu20nw}(L_{ox2}) = \frac{n_0}{1 + 2\frac{a_0\nu_0}{2D_{0x2}} L_{ox2}\gamma_L F(L_{nw})}. \quad (38)$$

At a time t the nanowires grown per unit of area consume the flux:

$$\varphi_{Cu2n}(t) = \int_0^{L_{nw-m}} \rho_D(L)\varphi_{Cu2nw}(L)dL = \int_0^{L_{nw-m}} \rho_D(L) \frac{n_{x2s}\nu_0 exp\left(-\frac{e\varepsilon_{x-dix}}{k_B T_s}\right) F(L)}{1 + \frac{a_0\nu_0}{D_{0x2}} L_{ox2} \frac{n_{x2s}}{n_0} exp\left[-\frac{e(\varepsilon_{x-dix}-\varepsilon_{c2})}{k_B T_s}\right] F(L)} dL, \quad (39)$$

where $\rho_D(L)$ is the density of distribution of the nanowires on length. It should be noted that the length of the oxide layer L_{ox2} is the same in the integral.

The rate of nanowire growth is

$$\frac{dL_{ox2}}{dt} = \begin{cases} \left(\frac{2B_c}{1+bL_{ox2min}} + \frac{2C_c}{1+cL_{ox2min}}\right), \\ (L_{ox1}(t) > L_{ox1min}) \wedge (L_{ox2}(t) \le L_{ox2min}); \\ -\left(\frac{P_{b1}}{1+a_{b1}L_{ox1}} + \frac{P_{l1}}{1+a_{l1}L_{ox1}}\right)A_c + \left(\frac{2B_c}{1+bL_{ox2}} + \frac{2C_c}{1+cL_{ox2}}\right), \\ (L_{ox1}(t) > L_{ox1min}) \wedge (L_{ox2}(t) > L_{ox2min}); \\ -\left(\frac{P_{b1}}{1+a_{b1}L_{ox1min}} + \frac{P_{l1}}{1+a_{l1}L_{ox1min}}\right)A_c, \\ (L_{ox1}(t) \le L_{ox1min}) \wedge (L_{ox2}(t) > L_{ox2min}); \\ 0, \quad \text{otherwise} \end{cases} \quad (43)$$

The rate of growth of the side surface is:

$$\frac{dR_{nw}}{dt} = \begin{cases} \alpha_L(t)\frac{n_{x2s}(t)}{n_{x2t}(t)} n_{Cu20nw}(L_{ox2min}), \\ (L_{ox1}(t) > L_{ox1min}) \wedge (L_{ox2}(t) \le L_{ox2min}); \\ \alpha_L(t)\frac{n_{x2s}(t)}{n_{x2t}(t)} n_{Cu20nw}(L_{ox2}), \\ (L_{ox1}(t) > L_{ox1min}) \wedge (L_{ox2}(t) > L_{ox2min}); \\ 0, \quad \text{otherwise} \end{cases} \quad (44)$$

$$\frac{dL_{nw}}{dt}(L_{nw}) = N_{Cu}(L_{nw})\frac{a_0^3}{\pi R_{nw}^2(L_{nw})} = n_{Cu20nw}(L_{nw})cos\left[\left(\frac{n_{x2s}}{n_0}\frac{\nu_0}{D_{Cu0}} exp\left[-\frac{e(\varepsilon_{x-dix}-\varepsilon_{c2s})}{k_B T_s}\right]\right)^{1/2} L_{nw}\right] \frac{n_{x2t}}{n_0}\nu_0 exp\left(-\frac{e\varepsilon_{x-dix}}{k_B T_s}\right) a_0^3. \quad (40)$$

$$\frac{dR_{nw}}{dt}(z,t,L_{nw}) = n_{Cu}(z)\frac{n_{x2s}}{n_0}\nu_0 exp\left(-\frac{e\varepsilon_{x-dix}}{k_B T_s}\right) a_0^3 = n_{Cu20nw}(L_{nw})\frac{n_{x2s}}{n_0}\nu_0 exp\left(-\frac{e\varepsilon_{x-dix}}{k_B T_s}\right) a_0^3 cos\left[\left(\frac{n_{x2s}}{n_0}\frac{\nu_0}{D_{Cu0}} exp\left[-\frac{e(\varepsilon_{x-dix}-\varepsilon_{c2s})}{k_B T_s}\right]\right)^{1/2} z\right] \quad (41)$$

4.5. Linking dynamics of the base and oxide layers with nanowires

By knowing the flows of copper and oxygen, we can obtain the equations of the thickness dependencies on time for the oxide layer with thicknesses $L_{ox1}(t)$ and $L_{ox2}(t)$, as well as for the length $L_{nw}(t)$ and radius $R_{nw}(t)$ of the nanowires.

After combining the above expressions, a system of the equations to describe the growth dynamics of the oxide layer can be written:

$$\frac{dL_{nw}}{dt} = \begin{cases} \alpha_L(t) n_{Cu20nw}(L_{ox2min}) cos(\beta_L L_{nw}), \\ (L_{ox1}(t) > L_{ox1min}) \wedge (L_{ox2}(t) \le L_{ox2min}); \\ \alpha_L(t) n_{Cu20nw}(L_{ox2}) cos(\beta_L L_{nw}), \\ (L_{ox1}(t) > L_{ox1min}) \wedge (L_{ox2}(t) > L_{ox2min}); \\ 0, \quad \text{otherwise} \end{cases} \quad (45)$$

$$\frac{dL_{ox1}}{dt}=\begin{cases}\left(\frac{P_{b1}}{1+a_{b1}L_{ox1min}}+\frac{P_{l1}}{1+a_{l1}L_{ox1min}}\right)A_c,\\ (L_{ox1}(t)\le L_{ox1min})\wedge(L_{ox2}(t)\le L_{ox2min});\\ \left(\frac{P_{b1}}{1+a_{b1}L_{ox1}}+\frac{P_{l1}}{1+a_{l1}L_{ox1}}\right)A_c-\left(\frac{2B_c}{1+bL_{ox2min}}+\frac{2C_c}{1+cL_{ox2min}}\right)-D_{nw}\frac{a_{ox1}^3}{a_{ox2}^3}D_c(L_{ox2min}),\\ (L_{ox1}(t)>L_{ox1min})\wedge(L_{ox2}(t)\le L_{ox2min});\\ \left(\frac{P_{b1}}{1+a_{b1}L_{ox1}}+\frac{P_{l1}}{1+a_{l1}L_{ox1}}\right)2A_c-\left(\frac{2B_c}{1+bL_{ox2}}+\frac{2C_c}{1+cL_{ox2}}\right)-D_{nw}\frac{a_{ox1}^3}{a_{ox2}^3}D_c(L_{ox2}),\\ (L_{ox1}(t)>L_{ox1min})\wedge(L_{ox2}(t)>L_{ox2min});\\ \left(\frac{P_{b1}}{1+a_{b1}L_{ox1min}}+\frac{P_{l1}}{1+a_{l1}L_{ox1min}}\right)2A_c,\\ (L_{ox1}(t)\le L_{ox1min})\wedge(L_{ox2}(t)>L_{ox2min});\\ 0,\quad \text{otherwise}\end{cases}\tag{42}$$

$$\frac{dL_{ox}}{dt}=\begin{cases}\left(\frac{P_{b1}}{1+a_{b1}L_{ox1min}}+\frac{P_{l1}}{1+a_{l1}L_{ox1min}}\right)A_c,\\ (L_{ox1}(t)\le L_{ox1min})\wedge(L_{ox2}(t)\le L_{ox2min});\\ \left(\frac{P_{b1}}{1+a_{b1}L_{ox1}}+\frac{P_{l1}}{1+a_{l1}L_{ox1}}\right)A_c-D_{nw}\frac{a_{ox1}^3}{a_{ox2}^3}D_c(L_{ox2min}),\\ (L_{ox1}(t)>L_{ox1min})\wedge(L_{ox2}(t)\le L_{ox2min});\\ \left(\frac{P_{b1}}{1+a_{b1}L_{ox1}}+\frac{P_{l1}}{1+a_{l1}L_{ox1}}\right)A_c-D_{nw}\frac{a_{ox1}^3}{a_{ox2}^3}D_c(L_{ox2}),\\ (L_{ox1}(t)>L_{ox1min})\wedge(L_{ox2}(t)>L_{ox2min});\\ \left(\frac{P_{b1}}{1+a_{b1}L_{ox1min}}+\frac{P_{l1}}{1+a_{l1}L_{ox1min}}\right)A_c,\\ (L_{ox1}(t)\le L_{ox1min})\wedge(L_{ox2}(t)>L_{ox2min});\\ 0,\quad \text{otherwise}\end{cases}\tag{46}$$

where the initial conditions are determined as $L_{ox1}(0)=L_{10}$, $L_{ox2}(0)=L_{20}$, $L_{ox}(0)=L_{10}+L_{20}$, and the parameters are:

$$A_c=n_{CuO}a_0^3\frac{\nu_0}{2};\quad B_c=2n_{s0}a_0^3\frac{\nu_0}{2}exp\left(-\frac{e(\varepsilon_{x2}+\varepsilon_{x-dec})}{k_BT_s}\right);\quad C_c=n_{s0}a_0^3\frac{\nu_0}{2}exp\left(-\frac{e(\varepsilon_{c2}+\varepsilon_{x-dec})}{k_BT_s}\right);$$

$$D_c(L_i)=n_{Cu20nw}(L_i)\pi R_{nw}^2(L_{nw})\alpha_L cos(\beta_L(t)L_{nw})+2\pi R_{nw}(0)\frac{n_{x2s}}{n_{x2t}}\frac{\alpha_L}{\beta_L}sin(\beta_L L_{nw});$$

$$P_{b1}=\frac{1}{\left(1+\frac{d_{Cu20}}{2b_{Cu20}}\right)}exp\left[-\frac{e\varepsilon_{c1b}}{k_BT_s}\right];\quad P_{l1}=\frac{1}{\left(1+\frac{2b_{Cu20}}{d_{Cu20}}\right)}exp\left[-\frac{e\varepsilon_{c1l}}{k_BT_s}\right];$$

$$a_{b1}=\frac{a_0\nu_0}{2D_{0c1b}};\quad a_{l1}=\frac{a_0\nu_0}{2D_{0c1l}};\quad b=\frac{a_0\nu_0}{2D_{0x2}};\quad c=\frac{a_0\nu_0}{2D_{0c2}};$$

$$\alpha_L=\frac{n_{x2t}}{n_0}a_{03}^3\nu_0exp\left(-\frac{e\varepsilon_{x-dis}}{k_BT_s}\right);\quad \beta_L=\left(\frac{n_{x2s}}{n_0}\frac{\nu_0}{D_{Cu0}}exp\left[-\frac{e(\varepsilon_{x-dis}-\varepsilon_{c2s})}{k_BT_s}\right]\right)^{1/2};$$

$$\gamma_L(t)=\frac{n_{x2s}(t)}{n_{0s}}exp\left[-\frac{e(\varepsilon_{x-dis}-\varepsilon_{c2})}{k_BT_s}\right];\quad n_{Cu20nw}(L_i)=\frac{n_0}{1+2cL_i\gamma_L F(L_{nw})};$$

$$F(L_{nw})=\frac{2}{\beta_L R_{nw}(0)}sin(\beta_L L_{nw})+\frac{n_{x2t}}{n_{x2s}}cos(\beta_L L_{nw})$$

5. Results and discussion

The developed model simulates the nanowire growth under the different growth conditions with oxygen pressure and substrate temperature as the main growth parameters. In the model, many energies are introduced, but their values can't be precisely defined, neither by use of the literature nor by direct experiments.

The experimental dependence of the sample temperature is approximated for the calculations by the expression: $T_s(t)=(T_{max}-T_0)(1-exp[-t/\tau])+293$ (K), where T_{max} is 550, 600, 650, or 700 °C; T_0 = 20 °C, τ = 2000 s. This dependence was used in couple with a system of Eqs. (42)–(46) to calculate the thickness of the cuprous oxide (Cu_2O) layer $L_{ox1}(t)$, cupric oxide (CuO) layer $L_{ox2}(t)$, and then to calculate the dependence $L_{ox}(t)$ of the total oxide thickness, as well as the nanowire length $L_{nw}(t)$ and diameter $2R_{nw}(t)$ on time t.

The value of the adsorption energy ε_{aO2} = 1.15 eV is selected from the calculated by Sun *et al.* for the adsorption of O_2 on the oxygen-deficient CuO surface; ε_{aO2nws} = 0.27 eV corresponds to the energy calculated by Hu *et al.* and is close to the lowest energy calculated by Sun *et al.* for the adsorption of O_2 on the perfect CuO surface; ε_{aO2nwt} = 0.5 eV is close to the highest energy calculated by Sun *et al.* for the adsorption of O_2 on the perfect CuO surface. The value of the dissociation energy of O_2 on the Cu_2O surface $\varepsilon_{x\text{-}dis}$ = 0.65 eV is located within the range 0.13… 0.85 eV calculated by Zhang *et al.* for O_2 dissociation on the Cu_2O oxygen-deficient surface. The energies ε_{c1b} and ε_{c1l} of the copper atom diffusion through the Cu_2O layer were set to correspond to the data on the temperature dependence of the diffusion mechanisms reported in the literature [29,31] and to fit the results on the measured values of the oxides. The energy ε_{x2} of oxygen diffusion was set to describe the kinetics of the CuO layer, and the value was validated in the reported paper while describing the results obtained by Zhu *et al.* and Yuan *et al.* in their experiments [34,71]. The energies ε_{c2} and ε_{c2s} of copper diffusion in the CuO layer and along the NW surface were adjusted to fit the ratio of thicknesses of CuO and Cu_2O oxides to the data from the experiments. The internal energies $\varepsilon_{i\text{-}O2t}$ and $\varepsilon_{i\text{-}O2s}$ of oxygen molecules adsorbed on the side and top surfaces of a nanowire, which are given in Table 1, are just the numerical parameters necessary in the model not

Table 1
Energies used in the calculations.

$T_{,(flow)}$ °C$_{(sccm)}$	Energies, eV											P, Pa
	ε_{c1b}	ε_{c1l}	ε_{c2}	ε_{c2s}	ε_{aO2}	ε_{aO2nws}	$\varepsilon_{l\text{-}O2s}$	ε_{aO2nwt}	$\varepsilon_{l\text{-}O2t}$	ε_{x2}	$\varepsilon_{x\text{-}ds}$	
$550_{(146)}$	1.275	1.815	1.0	0.53	1.15	0.27	0.9	0.5	0.75	0.8	0.65	10^5
$600_{(146)}$	1.3	1.85	0.3	0.2	1.15	0.27	0.23	0.5	0.25	0.8	0.65	70
$600_{(146)}$	1.3	1.84	0.36	0.36	1.15	0.27	0.48	0.5	0.38	0.8	0.65	890
$600_{(97)}$	1.27	1.81	0.67	0.36	1.15	0.27	0.95	0.5	0.78	0.8	0.65	10^5
$600_{(146)}$	1.28	1.82	0.67	0.36	1.15	0.27	0.86	0.5	0.72	0.8	0.65	10^5
$600_{(175)}$	1.28	1.82	0.67	0.36	1.15	0.27	0.91	0.5	0.75	0.8	0.65	10^5
$650_{(146)}$	1.28	1.82	0.57	0.3	1.15	0.27	0.89	0.5	0.8	0.8	0.65	10^5
$700_{(146)}$	1.4	1.96	0.28	0.2	1.15	0.27	0.88	0.5	0.8	0.8	0.65	70
$700_{(146)}$	1.344	1.911	0.27	0.2	1.15	0.27	0.88	0.5	0.8	0.8	0.65	890
$700_{(146)}$	1.325	1.884	0.55	0.2	1.15	0.27	0.9	0.5	0.8	0.8	0.65	10^5

only to fit the calculations to the experiment but also to evaluate the *real difference* between the adsorption energies ε_{aO2nwt} and ε_{aO2nws} for the oxygen molecule on top and side surfaces of the nanowire. The detailed list of the energies used in the calculations is presented in Table 1.

A large number of energies are conditioned by the number of linked processes described in the model. Indeed, the necessity to describe the experimentally observed two kinds of copper diffusion (boundary and lattice) through a layer of Cu_2O oxide urges to introduce the energies ε_{c1b} and ε_{c1b} while the diffusion of Cu_2O through CuO layer is described by energy ε_{c2} that is different from energy ε_{c2s} because the latter describes the diffusion along CuO surface. In accordance, the energies of the oxygen molecule interaction with CuO are different in the cases of oxygen adsorption on a surface of CuO layer (ε_{x2}), on the top and side surfaces of a nanowire (ε_{aO2nwt} and ε_{aO2nws}, respectively). Unfortunately, their precise values cannot be found due to the non-ideality of the surface and the large number of factors like the presence of defects, stresses, complicated morphology etc., which all affect the energies. This uncertainty restricts the calculation accuracy and allows only fitting the integral results of simulations to the experimental data. An alternative to this approach is the use of simplified models, where the linked growth

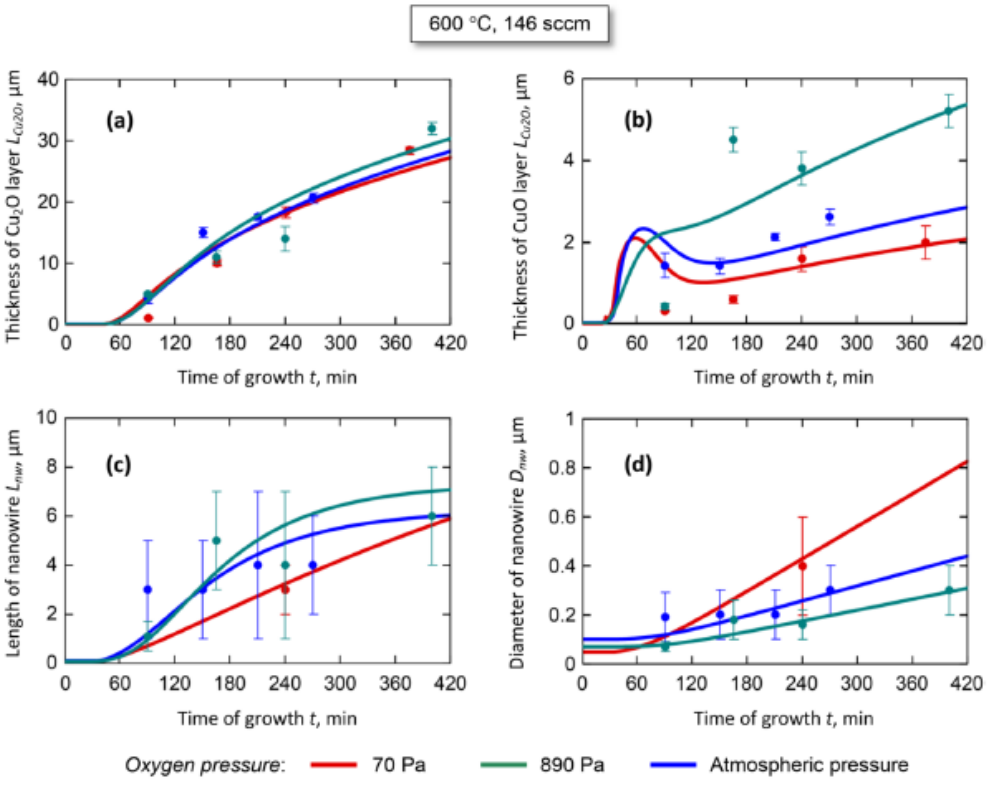

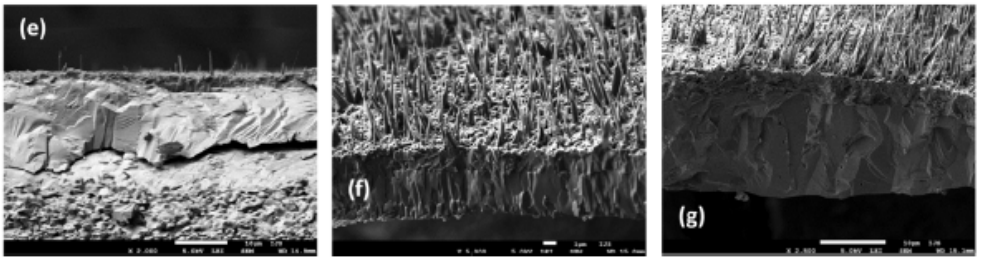

Fig. 5. Results of the experiments and calculations of the nanostructure growth at the different oxygen pressures at 600 °C and oxygen flow of 146 sccm: a, b – thickness of Cu_2O and CuO layers; c, d – length and diameter of CuO nanowires; e, f, g – SEM images of the nanostructures grown at 70, 890, and 10^5 Pa, respectively. The oxygen pressure definitely affects the thickness of the CuO layer due to the dependence of the oxidation rate on the density of oxygen molecules adsorbed on the surface exposed to the gas phase.

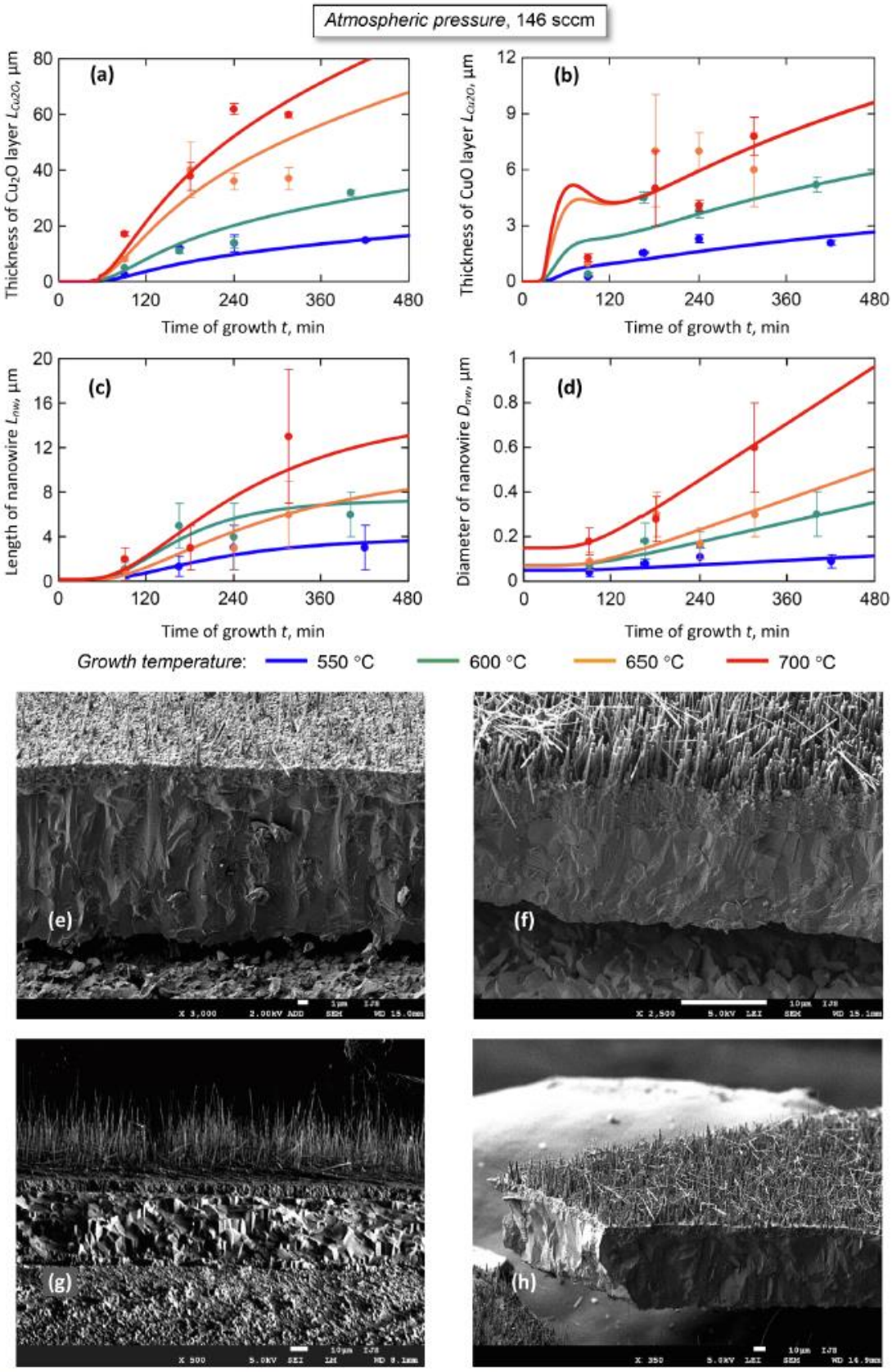

Fig. 6. Results of the experiments and calculations of the nanostructure growth at the different temperatures at atmospheric pressure and oxygen flow of 146 sccm: a, b – thickness of Cu_2O and CuO layers; c, d – length and diameter of CuO nanowires; e, f, g, h – SEM images of nanostructures grown at 550 °C, 600 °C, 650 °C, 700 °C, respectively. The growth temperature strongly affects the whole set of the growth structures due to the dependence of the diffusion, which is the basic mechanism of the growth, on the temperature.

dynamics of two oxide layers and an array of nanowires are essentially described by one diffusion equation. However, in our opinion, this approach is not the best since it is difficult to explain why the motion of species is mixed when moving through a layer under constrained conditions with moving along the free surface with various defects etc. In addition, a more thorough description of the processes facilitates the integration of a model into more general growth models that took into account the mechanisms of the seed formation, e.g. In the proposed model, the taking into account stresses is reduced by adding a corresponding value to the diffusion energy without changing the already introduced equations. In addition, a correlation between our measurements and the results reported in the literature can serve as an additional yet indirect indicator of the efficiency of the proposed model.

The experiments and calculation for the growth dynamics, where the oxygen flow is considered the variable, are presented in Fig. 4. The experiment was conducted at the atmospheric pressure, and the substrate temperature was 600 °C. As it could be seen, the dependencies of the thickness of Cu_2O and CuO layers and the length of the nanowires can be considered as not depending strongly on the oxygen flow. On the other hand, the diameter of the nanowires exhibits such dependence with respect to the averaged values. Yet, the large spread in the data does not allow a conclusion about the necessity of introducing the flow as the vital parameter to control the nanowire growth.

- *Oxygen flow under conditions of parallel (non-rectangular) arrangement of the treated surface with respect to oxygen flow does not affect greatly the parameters of the nanostructures grown at the atmospheric pressure.*

This result is consistent with the developed model since only the local oxygen concentration near the growth location should affect the nanowire growth. The concentration can be increased either by increasing the oxygen partial pressure (according to expression (4) and experimental data [40]), or by slowing down the oxygen flux by a surface position rectangularly. In addition, the oxygen concentration associated with the oxygen pressure greatly affects the rate of growth of CuO oxide, as is exhibited below, thus making a big impact on the process of nanowire seed formation. The latter process should be treated using a separate model by solving the stress-and-strain problem and is not a subject of the present research. However, the influence of the local oxygen concentration on the rate of oxide growth can explain the observed results of the optimal flow rate [41] after considering the dependence of the thin film stress on growth rate, temperature, and microstructure reported by Chason *et al.* [72,73].

Many broken nanowires are observed after the growth time of 7.5 h, which explains the difference between the calculated and measured lengths. At that, the bulky outgrowths along the nanowire stem are found in abundance for the large annealing times exceeding 6–6.5 h. This effect can be explained by the action of the secondary nucleation centres on the NWs after the damages caused at the NW breakage. It can be speculated that the stresses generated when the nanowire reaches some critical length are followed by the generation of nanocracks alone the NW surface, which serve as the absorption sites for oxygen. Cu_2O molecules diffuse along the external surface or through the channel in the body of the nanowire and interact with the oxygen, thus forming bubble-shaped outgrowths.

The influence of the oxygen pressure on the growth of the nanostructures is illustrated in Fig. 5. In this case, the dependence of CuO layer thickness on that parameter can be clearly stated. At the same time, the thickness of Cu_2O does not depend on the oxygen pressure, and the theoretical model explains. In the stationary mode, when both oxides are present on a copper sample, the growth rate of Cu_2O oxide depends mostly on the density of CuO molecules on the top of the Cu_2O layer. Since that density is much greater than the density of oxygen molecules diffused from the top of the CuO layer to the Cu_2O/CuO boundary, the growth of the Cu_2O layer is almost insensitive to the pressure-dependent density of O_2 adsorbed on the CuO layer. The growth rate of CuO oxide is dependent on the oxygen pressure at the high pressures, when the ratio of the adsorption nodes on CuO top, covered by O_2 molecules, can reach the values of unity, thus competing with the density of Cu_2O nodes at the bottom of CuO oxide. At the pressure of 70 Pa, only one sample exhibited the presence of nanowires, and the result cannot be considered reliable, while for the two other pressures (890 and 10^5 Pa), the results are similar.

- *Oxygen pressure does not affect the growth of the Cu_2O layer while strongly affects to the growth of CuO, which is explained by the fact that the density of CuO molecules on the top of the Cu_2O layer is much larger*

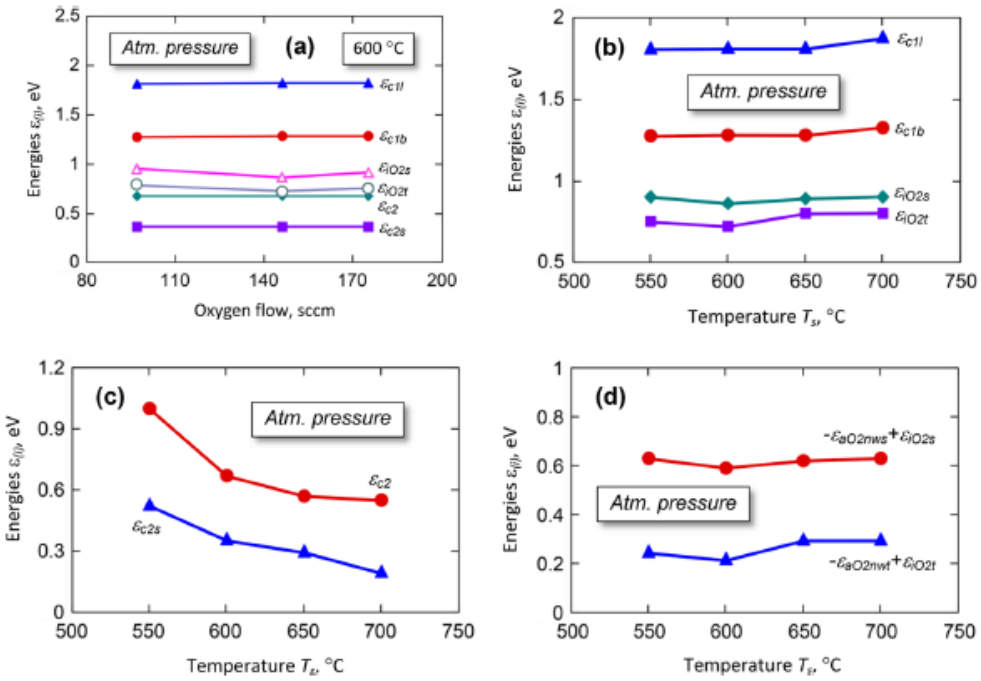

Fig. 7. Results of simulation.

than the density of oxygen molecules diffused from the top of CuO layer to the Cu_2O/CuO boundary.

In the experiments, an increase in the density of nanowires on the sample surface with pressure was evident. However, this fact is not explained directly in the frame of the proposed model. The growth of a nanowire was considered under the assumption that the seeds for their growth are already formed. Their initial length L_{nw0} and diameter D_{nw0} are the parameters substituted into the systems of the differential Eqs. (42)–(46) in our model. It is assumed that the seeds' formation should be considered a process that greatly depends on the stress and strain conditions of the oxide layers and thus should be treated in a separate model to provide the initial distribution of the seeds and their dimensions. In addition, such a model can theoretically calculate the change in the energies of the diffusion of Cu_2O molecule through the layer of CuO oxide and along the surface of CuO nanowire, which are used in our model.

Opposite to the oxygen flow and pressure, the substrate temperature during the nanowire growth is the parameter that affects all the measured characteristics of the nanostructures, as presented in Fig. 6. The most prominent results are obtained for the thickness of the Cu_2O layer and the diameter of the nanowires. The results are explained by the dependencies of all the described diffusion processes on the temperature: the higher is the temperature, the higher is the diffusion rates; oxygen adsorption is also temperature-dependent. At that, the top surface of the CuO layer exposed to the oxygen atmosphere shows non-monotonic dependence on the temperature since the thickness of that layer is almost the same for the temperatures of 650 and 700 °C. This effect is explained by the compensation caused by the decreased adsorption to the increased diffusion of the species at high temperatures. The increased adsorption at the low temperatures also explains the presence of the maximums in Figs. 4–6 (b) for the time of growth less than 120 min. For that time interval, the temperature in the chamber did not reach the specified temperatures of 600, 650, or 700 °C and the density of the oxygen molecules adsorbed on the top of the CuO layer was increased with respect to the values in the stationary temperature mode, which results in a higher rate of CuO generation.

- *The substrate temperature is the most influential parameter that strongly affects the growth of all copper oxide structures because diffusion and adsorption are two processes, which establish the 'building' routine. They, in turn, are strongly dependent on the temperature.*

One more important conclusion can be made after considering the initial values of the nanostructures, which should be used to get the best fit of the calculation with the experiments. In our experiments, the diameters of the seeds were dependent on the growth parameters; however, to fit the simulation to the experimental results, the initial diameter of the nanowire (seed) should be of the same order of magnitude as the diameter at the end of growth. Any attempt to substitute the initial diameters of a nanometer size to obtain the final diameter of about hundreds of nanometers failed. Thus, it was hard to consider such small objects like screw dislocations [74] as the seeds. At the same time, our observation showed that the nanowire's final diameter was close to the size of CuO oxide grains, which follows the trend about the dependence of the sizes and density of nanowires on the grain sizes of the copper oxide layer [34]. Moreover, the analysis of SEM images of $Cu_2O/CuO/CuO$ NWs cross-sections has shown that the roots of the nanowires are organic parts of CuO layer and can be treated as grains of CuO oxide that started to develop in one direction. As for this preferential growth, the stresses and strains generated due to conditions of growth of oxide layers can be assumed as the main factors, and this problem is considered the next stage of our research. Following the analysis of the literature [75], it can be concluded about the importance of stress gradients [76]; the stress is dependent on the rate of the oxide layer growth [77] and its thickness [78] yet the dependence can be non-monotonic [79] and can be tailored by ion bombardment [80]. Thus, the following conclusion can be made:

- *Seeds of nanowires are rather large objects which correspond to the size of CuO grains.*

The energies used in the calculations are shown in Fig. 7. As can be seen, the experiments with the varied oxygen flow are described using the energies that are not dependent on the flows (Fig. 7(a)). Almost the same values can be used for the energies of copper boundary (ε_{c1b}) or lattice (ε_{c1l}) diffusion through the layer of Cu_2O towards the Cu_2O/CuO boundary, when the dependence on the substrate energy is considered (Fig. 7(b)). However, the energies of the diffusion of Cu_2O "molecule" through the layer of CuO oxide (ε_{c2}) and along the surface of CuO nanowire decrease with the temperature increase (Fig. 7(c)). The decrease can be attributed to the development of the surface stress in the CuO layer, so ε_{c2} should be replaced by the dependence like: $\varepsilon_{c2}(T_s) = \varepsilon_{c2}(T_0) - \mu a_0^3 \sigma_{CuO}(T_s)/e$, where a_0 is the lattice constant, $\sigma_{CuO}(T_s)$ is the temperature-dependent stress, e is the electron charge, and μ is a constant. Another possible explanation is based on a suggestion of the less defected surface of CuO grains and nanowires, which are healed at the temperature rise.

However, *the most interesting result with respect to the energies is related to the dependencies of the sums* $-\varepsilon_{aO2nws} + \varepsilon_{iO2s}$ and $-\varepsilon_{aO2nwt} + \varepsilon_{iO2t}$. The first term in both sums presents the adsorption energies of oxygen molecules on the side (s) or top (t) surface of NW, respectively, while the second term is the internal energy of oxygen molecules on the surfaces. The exponential factors, which contain the sums, describe the possibility

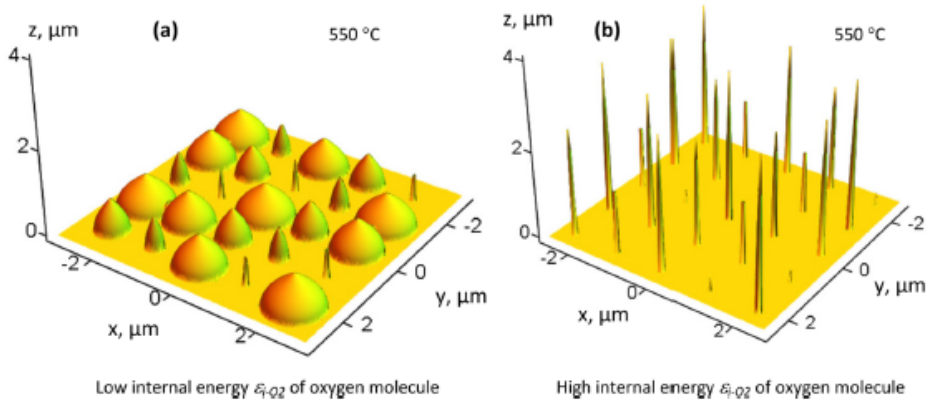

Fig. 8. Simulation results show the importance of the internal energy of oxygen molecules, which can provide them with additional energy necessary to desorb them from the side surface of the growing nanowires and ensure 1D growth of the nanowires. *MW treatment can be the way to control the internal energy of the molecules.*

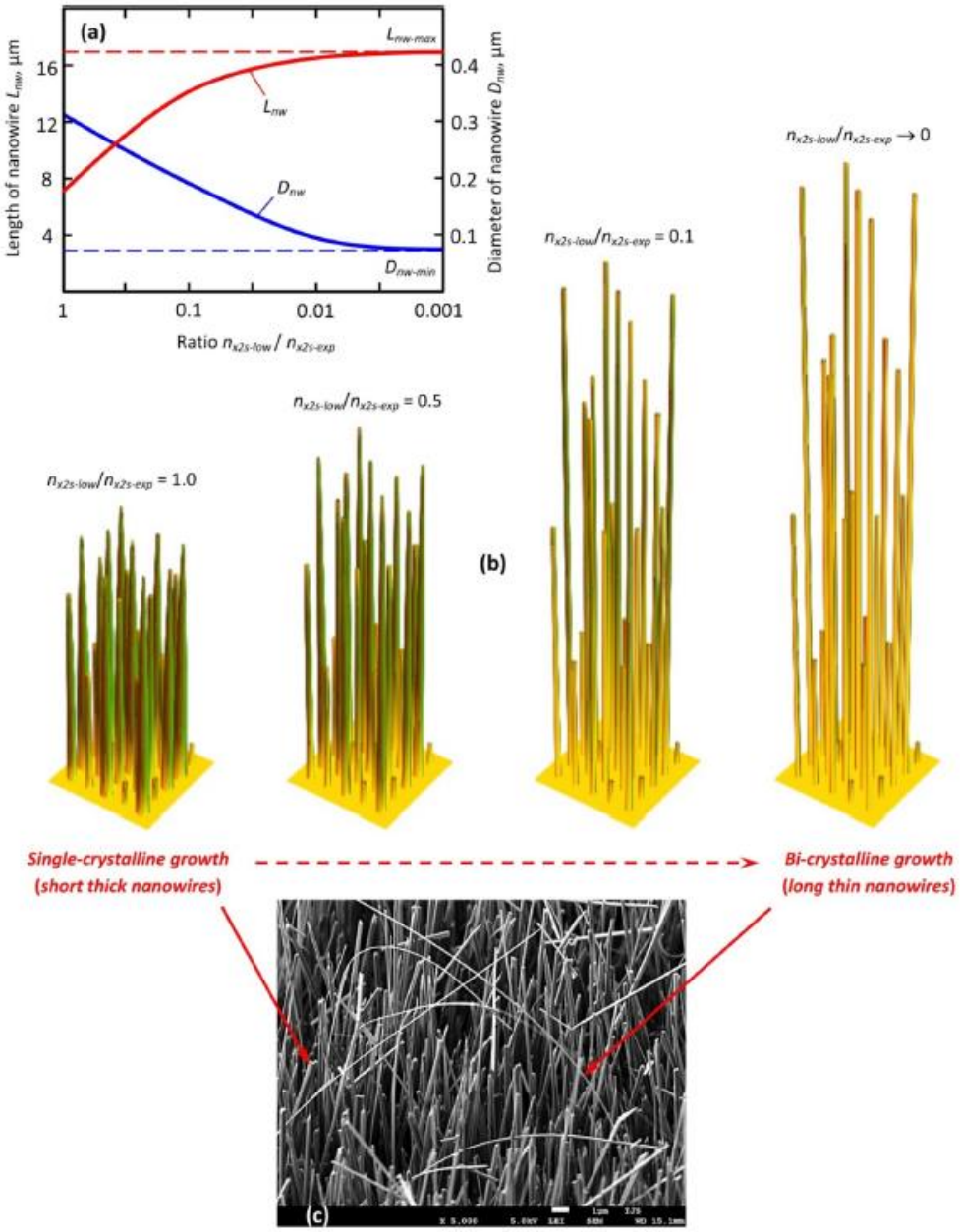

Fig. 9. Results of simulation and SEM images which confirm the simultaneous growth of nanowires with the possibly different growth mechanisms: calculation of the passage to the limit $n_{x2s} \rightarrow 0$ for the NW length and diameter (a), and 3D simulation (b); SEM image of the nanowires associated with the single- and bi-crystalline growth mechanisms (c).

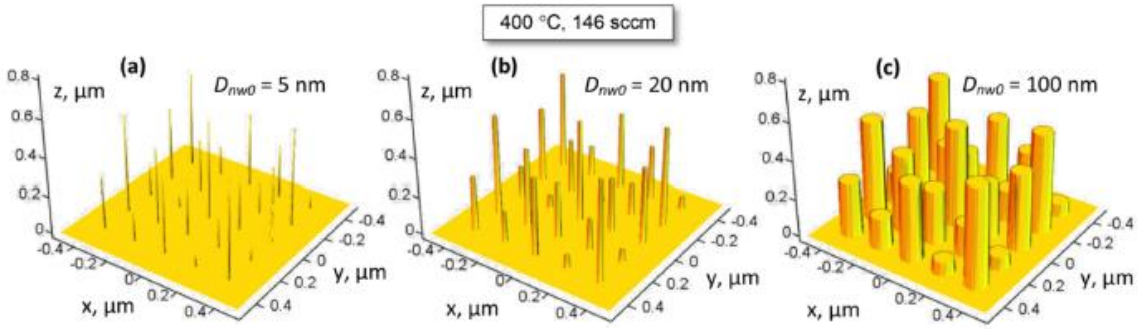

Fig. 10. Growth of nanowires at 400 °C at the dependence on the size of the nanowire seed D_{nw0}: 5 nm (a); 20 nm (b); 200 nm (c). The density of the nanowires is set to $3.2 \cdot 10^{13}$ m^{-2} to enhance the visualisation. It can be seen that the length of the nanowires is small; coupled with the dependence of the nanowire diameter on the seed diameter, the formation of the columnar structures fit to describe CuO oxide layer appearance can be obtained. The time of growth is 6 h.

of desorption for the molecule that is adsorbed a nanowire's side or top surface. The *molecule has some internal energy* at that. As follows from Fig. 7(b), almost constant values should be used in the calculations to fit the sums to the experiments, and the sums are positive. It means that *the internal energies exceed the adsorption energies. The introduction of just the adsorption energies cannot explain the low density of the oxygen adsorbed on the nanowires*. To grow the nanostructures long and thin like nanowires, it is necessary to use the assumption about the molecules with the additional energy spared in the molecules. At the interaction with a nanowire surface, the internal energy can be released and transformed to the translational displacement of the molecules with respect to the surface. This process reminds the interaction of a swelled balloon with a wall when the balloon bursts while touching the wall and moves away from it.

- *Gas molecules involved in the nanowire growth process, re-distribute the energy between the states at the adsorption, and part of the internal energy of the molecule can be used to desorb the molecule.*

Under the assumption that the internal energy of the molecules adsorbed on the side and top surfaces of a nanowire should be the same, i.e. $\varepsilon_{iO2s} = \varepsilon_{iO2t}$, the difference $[(-\varepsilon_{aO2nws} + \varepsilon_{iO2s}) - (-\varepsilon_{aO2nwt} + \varepsilon_{iO2t})]$ allows calculating from Fig. 7(d) the real difference between the energies $[(-\varepsilon_{aO2nws}) - (-\varepsilon_{aO2nwt})] = [\varepsilon_{aO2nwt} - \varepsilon_{aO2nws}] \approx 0.4$ eV of the adsorption on the side and top surfaces (it should be reminded to the reader that the values shown in Table 1 are just an estimation from the literature data with rather large spread).

- *The energy of adsorption of oxygen molecule on the top surface of CuO nanowire is approximately 0.4 eV higher than the energy of adsorption on the side surface, which should be attributed to a large number of the lattice imperfections on the nanowire top; thus, the NW top indeed is the 'active site'.*

The action of the nanowire top as the 'active site' was confirmed by direct observations, and interaction of the delivered copper atoms with various defects of the crystalline structure is considered [39]. These defects can affect the optical and magnetic properties of CuO nanowires [81], photoluminescence properties [82], electrical transport mechanisms [83], field emission [84], and that is why their concentration definitely should be controlled. However, to develop the ways of control, the number of the defects and their diversity, a mechanism of generation of the nanowire seeds, including the transition from the single- to bi-crystalline growth modes, should be developed. Such a model, complemented by a model of growth like the presented one, can serve as a theoretical basis to solve the controlled concentration of the defects for a specific application of nanowires.

In a case when the internal energy of oxygen molecules is low, the adsorption of oxygen of the side surface of the nanowires is high, which prevents the effective delivery of copper atoms to the top of the nanowire, as they will be involved in the reaction of CuO formation on the side but not the top of the nanowire; as a result, the bulky 3D nanostructures will be grown instead of 1D structure with a high aspect ratio. To illustrate the idea, two cases were calculated. The structures shown in Fig. 8(a) are obtained using 'cold gas', when the internal energy of oxygen molecule is 0.23 eV less than for the nanowires shown in Fig. 8(b), while the other growth parameters are the same. Hence, the internal energy of oxygen molecule plays a vital role in the growth of 1D structures in the case of copper diffusion along the external surface of nanowires.

Now we consider how the developed model can describe the single-crystal as bi-crystal growth mechanisms. As it can be seen from the equations, the main difference occurs in the description of the diffusion flow of copper delivered from the NW bottom ('seed') to the NW top ('tip'), since for the single-crystal growth, the flow is partially lost along the length of the nanowire due to the reaction with oxygen adsorbed on the side surface. In contrast, for the bi-crystal growth, the copper flow is untouched along the NW length. This fact can be considered by a formal substitution $n_{x2s} \rightarrow 0$ of the density of oxygen adsorbed on the side surface of the nanowire. The analysis of the equations shows that the length of the nanowires will grow at the passage to the limit and reaches some maximum value $L_{nw\text{-}max}$, while the diameter of the nanowire reaches the minimum value that is equal to the initial diameter of the nanowire seed $D_{nw\text{-}min} = D_{nw0}$.

Another moment is associated with the cross-section of the diffusion flow through the bi-crystal boundary, which also needs to be fitted to replace the value of $2\pi R_{nw}a_0$ used for the single-crystal diffusion, to the specified value of the bi-crystal boundary cross-section, as well as to adjust the value of diffusion activation energy ε_{c2s}. To illustrate the idea in our simulation, we calculated the limiting process under the assumption of changing just the density n_{x2s} of oxygen, while other parameters stayed the same; the results of the calculations are shown in Fig. 9. It can be seen how the nanowire length and diameter reach their limiting values. The values indeed correspond to the long and thin nanowires with the same diameter along the NW length (the length is increased from about 7 to 17 μm, while the diameter is decreased from about 300 nm to 75 nm; thus, the aspect ratio grows from 23 to 270), Ref. Fig. 9(a,b). The fact of the simultaneous growth of the nanowires with such a big difference in their geometrical parameters was mentioned while describing the experimental results; SEM image of the nanowires is shown in Fig. 9(c). Thus, the developed model allows describing different nanowire growth mechanisms, yet the mechanism of generation of the single- and bi-crystals is out of the model's scope.

According to the reports, interesting results are obtained when applying the model to calculate the growth of the nanostructures for the lower temperatures where the nanowires still grow, according to the reports [29,31,32,35]. The growth was calculated for 400 °C, while other parameters were fixed at the values used for 500 °C. At that, short nanostructures can be obtained, yet their appearance depends greatly on the initial conditions, namely the diameter of the seeds. Fig. 10 illustrates the results. When the seed diameter was 5 nm, thin nanowires are grown with a height of 600 nm and diameter of about 7 nm as shown in Fig. 10, a. When changing the seed diameter to 20 nm, more bulky nanowires with a length of 600 nm and a diameter of 22 nm were simulated, Fig. 10, b. After applying the initial diameter of 200 nm (Fig. 10, c), the formation of the columnar nanostructures with a diameter of 210 nm were obtained. The results can be explained as follows; Seeds of the nanostructures are formed due to the action of stress in the layers of copper oxide, but the origins of the seeds are not fully understood. So they can be active borders or transformational-catalytic oxide grains [85]. Suppose the origin of the seed is represented by a 0D or 1D objects like an atomic cluster of a screw dislocation. In that case, the nanowires can be obtained at temperatures of 400 °C, according to our calculations. However, in a case when the oxide grain starts its transformation under stress in the layer, thus being the origin of the seed, a porous columnar structure can be obtained, and it can be hardly distinguished from the regular structure of CuO layer observed in the numerous experiments. In our experiments, the stable results of the formation of CuO nanowires were not obtained, which can be explained by the different stress conditions. At the same time, our observations confirm that the root of a nanowire looks like a structure developed from a regular grain of CuO oxide [65]. As stated in the theoretical section of the paper, the model does not consider the formation of a nanowire seed and proposes a nanowire growth mechanism under seed generation. The stress and strain problems are out of the scope of this paper, where the growth of the nanowires are considered under the condition that the seeds are already formed, yet the reasons for the formation are not discussed. The explanation of the stress generation and transformation of the oxide layer structure due to the stress is included in our group's future research.

6. Conclusions

The developed deterministic theoretical model describes, for the first time, the controversial mechanisms of single- and bi-crystal nanowire growth within a frame of the diffusion model, where the copper atoms are delivered from the nanowire bottom either along the side surface of the nanowire or through the bi-crystal boundary. In the former case, the copper flow is consumed by the oxidation reactions on its path toward the nanowire top, while in the latter case – it is not. This difference results in changing the appearance of the nanowires since the single crystal nanowires are relatively thick with a low aspect ratio, while the bi-crystal nanowires are relatively long and thin. In both cases, the difference between the copper atom concentrations on the NW surfaces exposed to the oxidation and on the Cu_2O/CuO boundary is the driving force of the diffusion. In the experiments conducted under the condition of parallel arrangement of the sample surface to the flow, the dependence of the growth process on the oxygen flow was not confirmed, implying the necessity to expand the flow range used in the experiment. However, the obtained results and literature analysis imply the importance of a local concentration of oxygen near nanostructure formation rather than flow that is a product of the concentration and velocity. At that, oxygen flow can affect the growth by changing the oxygen partial pressure in gas mixtures. It was also observed that the oxygen pressure does not affect the growth of the Cu_2O layer, while it strongly affects the growth of CuO. This result is described by use of the developed model: the rate of growth of Cu_2O oxide depends mostly on the density of CuO molecules on the top of the Cu_2O layer; since that density is much greater than the density of oxygen molecules diffused from the top of CuO layer to the Cu_2O/CuO boundary, the growth of Cu_2O layer is almost insensitive to the pressure-dependent density of O_2 adsorbed on CuO layer. Unlike the nanowire growth, the nanowire seeding was not described in the paper. At the same time, the conducted analysis of the results and their comparison with the reported data allowed formulating the main approach to the seed formation model that should be founded on solving the stress and strain problem. The model describes the linking dynamics of the growth of two oxide layers and an array of nanowires in the presence of seeds. While the study of the nanowire seed formation is out of the scope of the present research, an important result is evaluated: sizes of the seeds of the nanowires correspond to the sizes of CuO grains and are rather large objects, unlike screw dislocations, atomic clusters etc. For the nanowire growth, another important result is obtained with respect to the internal energy of oxygen molecules involved in the reactions on the NW surface: the energy is re-distributed at the molecule attachment and can be used to break the bond of the molecule with the surface. This process is vital for the formation of a 1D nanostructure. If this process is not conducted, the adsorption of oxygen on the side surface of the nanowires is *always* high at any adsorption energy equal or lesser than zero, which prevents the effective delivery of copper atoms to the top of the nanowire for the single-crystalline growth; as a result, the bulky 3D nanostructures will be grown instead of 1D single-crystalline nanowires. Bi-crystalline growth is not affected by this process of energy re-distribution. The energy of oxygen adsorption on a nanowire top is approximately 0.4 eV higher than for the adsorption on the nanowire side surface, as evaluated from the comparison of the experiment with the simulation.

CRediT authorship contribution statement

Oleg Baranov: Conceptualization, Methodology, Writing - original draft, Validation. **Martin Košiček:** Formal analysis. **Gregor Filipič:** Formal analysis, Writing - review & editing. **Uroš Cvelbar:** Conceptualization, Methodology, Supervision, Validation, Resources, Writing - review & editing.

Declaration of Competing Interest

The authors declare that they have no known competing financial interests or personal relationships that could have appeared to influence the work reported in this paper.

Acknowledgements

The research was in part sponsored by the NATO Science for Peace and Security Programme under grant id. G5814 project NOOSE. O.B. acknowledges the support from the project funded National Research Foundation of Ukraine, under grant agreement No. 2020.02/0119, whereas U.C., G.F. and M. K. acknowledge the support from Slovenian Research Agency grant N2-0107.

References

[1] F. Shao, F. Hernández-Ramírez, J.D. Prades, C. Fàbrega, T. Andreu, J.R. Morante, Copper (II) oxide nanowires for p-type conductometric NH_3 sensing, Appl. Surf. Sci. 311 (2014) 177–181, https://doi.org/10.1016/j.apsusc.2014.05.038.
[2] F. Yang, J. Guo, M. Liu, S. Yu, N. Yan, J. Li, Z. Guo, Design and understanding of a high-performance gas sensing material based on copper oxide nanowires exfoliated from a copper mesh substrate, J. Mater. Chem. A. 3 (41) (2015) 20477–20481, https://doi.org/10.1039/C5TA06806A.
[3] M.L. Zhong, D.C. Zeng, Z.W. Liu, H.Y. Yu, X.C. Zhong, W.Q. Qiu, Synthesis, growth mechanism and gas-sensing properties of large-scale CuO nanowires, Acta Mater. 58 (18) (2010) 5926–5932, https://doi.org/10.1016/j.actamat.2010.07.008.
[4] L.D. Duc, D.T.T. Le, N. Van Duy, N.D. Hoa, N. Van Hieu, Single crystal cupric oxide nanowires: Length- and density-controlled growth and gas-sensing characteristics, Phys. E Low-Dimensional Syst. Nanostructures. 58 (2014) 16–23, https://doi.org/10.1016/j.physe.2013.11.013.
[5] S. Steinhauer, E. Brunet, T. Maier, G.C. Mutinati, A. Köck, O. Freudenberg, C. Gspan, W. Grogger, A. Neuhold, R. Resel, Gas sensing properties of novel CuO nanowire devices, Sensors Actuators, B Chem. 187 (2013) 50–57, https://doi.org/10.1016/j.snb.2012.09.034.
[6] Y. Feng, X. Zheng, Plasma-enhanced catalytic CuO nanowires for CO oxidation, Nano Lett. 10 (11) (2010) 4762–4766, https://doi.org/10.1021/nl1034545.
[7] V. Scuderi, G. Amiard, S. Boninelli, S. Scalese, M. Miritello, P.M. Sberna, G. Impellizzeri, V. Privitera, Photocatalytic activity of CuO and Cu_2O nanowires, Mater. Sci. Semicond. Process. 42 (2016) 89–93, https://doi.org/10.1016/j.mssp.2015.08.008.
[8] W. Wang, L. Wang, H. Shi, Y. Liang, A room temperature chemical route for large scale synthesis of sub-15 nm ultralong CuO nanowires with strong size effect and enhanced photocatalytic activity, CrystEngComm. 14 (2012) 5914–5922, https://doi.org/10.1039/c2ce25666e.
[9] W.-N. Wang, F. Wu, Y. Myung, D.M. Niedzwiedzki, H.S. Im, J. Park, P. Banerjee, P. Biswas, Surface Engineered CuO Nanowires with ZnO Islands for CO_2 Photoreduction, ACS Appl. Mater. Interfaces. 7 (10) (2015) 5685–5692, https://doi.org/10.1021/am508590j.
[10] L. Wang, K. Zhang, Z. Hu, W. Duan, F. Cheng, J. Chen, Porous CuO nanowires as the anode of rechargeable Na-ion batteries, Nano Res. 7 (2) (2014) 199–208, https://doi.org/10.1007/s12274-013-0387-6.
[11] Y. Su, T. Liu, P. Zhang, P. Zheng, CuO nanowire arrays synthesized at room temperature as a high-performance anode material for Li/Na-ion batteries, Thin Solid Films 690 (2019) 137522, https://doi.org/10.1016/j.tsf.2019.137522.
[12] B.J. Hansen, N. Kouklin, G. Lu, I.-K. Lin, J. Chen, X. Zhang, Transport, analyte detection, and opto-electronic response of p-type CuO nanowires, J. Phys. Chem. C. 114 (6) (2010) 2440–2447, https://doi.org/10.1021/jp908850j.
[13] C. Tang, X. Liao, W. Zhong, H. Yu, Z. Liu, Electric field assisted growth and field emission properties of thermally oxidized CuO nanowires, RSC Adv. 7 (11) (2017) 6439–6446, https://doi.org/10.1039/C6RA27426A.
[14] D. Majumdar, S. Ghosh, Recent advancements of copper oxide based nanomaterials for supercapacitor applications, J. Energy Storage 34 (2021) 101995, https://doi.org/10.1016/j.est.2020.101995.
[15] C.S. Lee, J. Bae, Room-temperature growth ("farming") and high-performance supercapacitor applications of highly crystalline CuO nanowires/graphene nanoplatelet nanopowders, J. Mater. Sci. - Mater. El. 29 (17) (2018) 15097–15105, https://doi.org/10.1007/s10854-018-9650-7.
[16] K. Xu, H. Yan, C.F. Tan, Y. Lu, Y. Li, G.W. Ho, R. Ji, M. Hong, Hedgehog Inspired CuO Nanowires/Cu2 O Composites for Broadband Visible-Light-Driven Recyclable Surface Enhanced Raman Scattering, Adv. Opt. Mater. 6 (7) (2018) 1701167, https://doi.org/10.1002/adom.201701167.
[17] G. Filipič, U. Cvelbar, Copper oxide nanowires: A review of growth, Nanotechnology. 23 (19) (2012) 194001, https://doi.org/10.1088/0957-4484/23/19/194001.
[18] S. Sundar, G. Venkatachalam, S.J. Kwon, Biosynthesis of Copper Oxide (CuO) Nanowires and Their Use for the Electrochemical Sensing of Dopamine, Nanomaterials. 8 (10) (2018) 823, https://doi.org/10.3390/nano8100823.
[19] M.J. Kim, S. Alvarez, T. Yan, V. Tadepalli, K.A. Fichthorn, B.J. Wiley, Modulating the Growth Rate, Aspect Ratio, and Yield of Copper Nanowires with Alkylamines,

Chem. Mater. 30 (8) (2018) 2809–2818, https://doi.org/10.1021/acs.chemmater.8b00760.
[20] B. Guo, M. Košiček, J. Fu, Y. Qu, G. Lin, O. Baranov, J. Zavašnik, Q. Cheng, K. Ostrikov, U. Cvelbar, Single-Crystalline Metal Oxide Nanostructures Synthesized by Plasma-Enhanced Thermal Oxidation, Nanomaterials 9 (10) (2019) 1405, https://doi.org/10.3390/nano9101405.
[21] A. Altaweel, G. Filipič, T. Gries, T. Belmonte, Controlled growth of copper oxide nanostructures by atmospheric pressure micro-afterglow, J. Cryst. Growth 407 (2014) 17–24, https://doi.org/10.1016/j.jcrysgro.2014.08.029.
[22] O. Baranov, M. Romanov, M. Wolter, S. Kumar, X. Zhong, K. Ostrikov, Low-pressure planar magnetron discharge for surface deposition and nanofabrication, Phys. Plasmas 17 (5) (2010) 053509, https://doi.org/10.1063/1.3431098.
[23] I. Levchenko, M. Romanov, O. Baranov, M. Keidar, Ion deposition in a crossed E×B field system with vacuum arc plasma sources, Vacuum 72 (3) (2003) 335–344, https://doi.org/10.1016/j.vacuum.2003.09.002.
[24] JianBo Liang, N. Kishi, T. Soga, T. Jimbo, Cross-sectional characterization of cupric oxide nanowires grown by thermal oxidation of copper foils, Appl. Surf. Sci. 257 (1) (2010) 62–66, https://doi.org/10.1016/j.apsusc.2010.06.034.
[25] K. Ostrikov, I. Levchenko, U. Cvelbar, M. Sunkarad, M. Mozetic, From nucleation to nanowires: a single-step process in reactive plasmas, Nanoscale 2 (2010) 2012–2027, https://doi.org/10.1039/C0NR00366B.
[26] L. Xiang, J. Guo, C. Wu, M. Cai, X. Zhou, N. Zhang, A brief review on the growth mechanism of CuO nanowires via thermal oxidation, J. Mater. Res. 33 (16) (2018) 2264–2280, https://doi.org/10.1557/jmr.2018.215.
[27] S. Rackauskas, H. Jiang, J.B. Wagner, S.D. Shandakov, T.W. Hansen, E. I. Kauppinen, A.G. Nasibulin, In situ study of noncatalytic metal oxide nanowire growth, Nano Lett. 14 (10) (2014) 5810–5813, https://doi.org/10.1021/nl502687s.
[28] X. Sun, W. Zhu, D. Wu, Z. Liu, X. Chen, L.u. Yuan, G. Wang, R. Sharma, G. Zhou, Atomic-Scale Mechanism of Unidirectional Oxide Growth, Adv. Funct. Mater. 30 (4) (2020) 1906504, https://doi.org/10.1002/adfm.v30.410.1002/adfm.201906504.
[29] V. Chawla, N. Sardana, H. Kaur, A. Kumar, R. Chandra, S. Mishra, Effect of annealing parameters and activation top layer on the growth of copper oxide nanowires, Appl. Surf. Sci. 504 (2020) 144369, https://doi.org/10.1016/j.apsusc.2019.144369.
[30] A. Jafari, S. Terohid, A. Kokabi, A. Moradiani, Electrical, structural, and photocatalytic properties of copper oxide nanowire, J. Chem. Res. 44 (7–8) (2020) 471–474, https://doi.org/10.1177/1747519819899068.
[31] A. Mahmoodi, S. Solaymani, M. Amini, N.B. Nezafat, M. Ghoranneviss, Structural, Morphological and Antibacterial Characterization of CuO Nanowires, Silicon 10 (4) (2017) 1427–1431, https://doi.org/10.1007/s12633-017-9621-2.
[32] L. Feng, H. Yan, H. Li, R. Zhang, Z. Li, R. Chi, S. Yang, Y. Ma, B. Fu, J. Liu, Excellent field emission properties of vertically oriented CuO nanowire films, AIP Adv. 8 (4) (2018) 045109, https://doi.org/10.1063/1.5022320.
[33] L. Nkhaili, A. Narjis, A. Agdad, A. Tchenka, A. El Kissani, A. Outzourhit, A. Oueriagli, A Simple Method to Control the Growth of Copper Oxide Nanowires for Solar Cells and Catalytic Applications, Adv. Cond. Matter. Phys. 2020 (2020) 1–8, https://doi.org/10.1155/2020/5470817.
[34] T.H. Tran, M.H. Nguyen, T.H.T. Nguyen, V.P.T. Dao, P.M. Nguyen, V.T. Nguyen, N. H. Pham, V.V. Le, C.D. Sai, Q.H. Nguyen, T.T. Nguyen, K.H. Ho, Q.K. Doan, Effect of annealing temperature on morphology and structure of CuO nanowires grown by thermal oxidation method, J. Cryst. Growth 505 (2019) 33–37, https://doi.org/10.1016/j.jcrysgro.2018.10.010.
[35] A. Zúñiga, L. Fonseca, J.A. Souza, C. Rivaldo-Gomez, C.D. Pomar, D. Criado, Anomalous ferromagnetic behavior and size effects in CuO nanowires, J. Magn. Magn. Mater. 471 (2019) 77–81, https://doi.org/10.1016/j.jmmm.2018.09.048.
[36] S.H. Mohamed, K.M. Al-Mokhtar, Characterization of Cu_2O/CuO nanowire arrays synthesized by thermal method at various temperatures, Appl. Phys. A 124 (7) (2018) 493, https://doi.org/10.1007/s00339-018-1914-9.
[37] Y. Zhu, K. Mimura, M. Isshiki, Influence of oxide grain morphology on formation of the CuO scale during oxidation of copper at 600–1000°C, Corros. Sci. 47 (2) (2005) 537–544, https://doi.org/10.1016/j.corsci.2004.06.020.
[38] Q. Zhang, K. Zhang, D. Xu, G. Yang, H. Huang, F. Nie, C. Liu, S. Yang, CuO nanostructures: Synthesis, characterization, growth mechanisms, fundamental properties, and applications, Prog. Mater. Sci. 60 (2014) 208–337, https://doi.org/10.1016/j.pmatsci.2013.09.003.
[39] S. Rackauskas, A.G. Nasibulin, Nanowire Growth without Catalysts: Applications and Mechanisms at the Atomic Scale, ACS Appl. Nano Mater. 3 (8) (2020) 7314–7324, https://doi.org/10.1021/acsanm.0c01179.
[40] B.J. Hansen, G. Lu, J. Chen, Direct Oxidation Growth of CuO Nanowires from Copper-Containing Substrates, J. Nanomater. 2008 (2008) 1–7, https://doi.org/10.1155/2008/830474.
[41] A. Kumar, A.K. Srivastava, P. Tiwari, R.V. Nandedkar, The effect of growth parameters on the aspect ratio and number density of CuO nanorods, J. Phys. Condens. Matter. 16 (47) (2004) 8531–8543, https://doi.org/10.1088/0953-8984/16/47/007.
[42] F. Cao, S. Jia, H. Zheng, L. Zhao, H. Liu, L. Li, L. Zhao, Y. Hu, H. Gu, J. Wang, Thermal-induced formation of domain structures in CuO nanomaterials, Phys. Rev. Mater. 1 (2017), 053401, https://doi.org/10.1103/PhysRevMaterials.1.053401.
[43] C.H. Xu, C.H. Woo, S.Q. Shi, The effects of oxidative environments on the synthesis of CuO nanowires on Cu substrates, Superlattices Microstruct. 36 (1-3) (2004) 31–38, https://doi.org/10.1016/j.spmi.2004.08.021.
[44] R. Sondors, J. Kosmaca, G. Kunakova, L. Jasulaneca, M.M. Ramma, R. Meija, E. Kauranens, M. Antsov, D. Erts, Size Distribution, Mechanical and Electrical Properties of CuO Nanowires Grown by Modified Thermal Oxidation Methods, Nanomaterials 10 (6) (2020) 1051, https://doi.org/10.3390/nano10061051.
[45] Y. Wang, R. Shen, X. Jin, P. Zhu, Y. Ye, Y. Hu, Formation of CuO nanowires by thermal annealing copper film deposited on Ti/Si substrate, Appl. Surf. Sci. 258 (1) (2011) 201–206, https://doi.org/10.1016/j.apsusc.2011.08.031.
[46] G. Fritz-Popovski, F. Sosada-ludwikowska, A. Köck, J. Keckes, G.A. Maier, Study of CuO Nanowire Growth on Different Copper Surfaces, Sci. Rep. 9 (2019) 1–13, https://doi.org/10.1038/s41598-018-37172-8.
[47] L.u. Yuan, G. Zhou, Enhanced CuO Nanowire Formation by Thermal Oxidation of Roughened Copper, J. Electrochem. Soc. 159 (4) (2012) C205–C209, https://doi.org/10.1149/2.102204jes.
[48] N.L. Peterson, C.L. Wiley, Diffusion and Point Defects in Cu_2O, J. Phys. Chem. Solids 45 (3) (1984) 281–294.
[49] A.M.B. Gonçalves, L.C. Campos, A.S. Ferlauto, R.G. Lacerda, On the growth and electrical characterization of CuO nanowires by thermal oxidation, J. Appl. Phys. 106 (3) (2009) 034303, https://doi.org/10.1063/1.3187833.
[50] K. Mimura, J.-W. Lim, M. Isshiki, Y. Zhu, Q. Jiang, Brief Review of Oxidation Kinetics of Copper at 350 °C to 1050 °C, Metall. and Mat. Trans. A 37 (4) (2006) 1231–1237.
[51] C.M. Tang, Y.B. Wang, R.H. Yao, H.L. Ning, W.Q. Qiu, Z.W. Liu, Enhanced adhesion and field emission of CuO nanowires synthesized by simply modified thermal oxidation technique, Nanotechnology 27 (39) (2016) 395605, https://doi.org/10.1088/0957-4484/27/39/395605.
[52] J. Shi, L. Qiao, Y.i. Zhao, Z. Sun, W. Feng, Z. Zhang, J. Wang, X. Men, Synergistic effects on thermal growth of CuO nanowires, J. Alloys Compd. 815 (2020) 152355, https://doi.org/10.1016/j.jallcom.2019.152355.
[53] L.u. Yuan, Y. Wang, R. Mema, G. Zhou, Driving force and growth mechanism for spontaneous oxide nanowire formation during the thermal oxidation of metals, Acta Mater. 59 (6) (2011) 2491–2500, https://doi.org/10.1016/j.actamat.2010.12.052.
[54] R. Mema, L.u. Yuan, Q. Du, Y. Wang, G. Zhou, Effect of surface stresses on CuO nanowire growth in the thermal oxidation of copper, Chem. Phys. Lett. 512 (1-3) (2011) 87–91, https://doi.org/10.1016/j.cplett.2011.07.012.
[55] Y.-W. Park, N.-J. Seong, H.-J. Jung, A. Chanda, S.-G. Yoon, Growth Mechanism of the Copper Oxide Nanowires from Copper Thin Films Deposited on CuO-Buffered Silicon Substrate, J. Electrochem. Soc. 157 (6) (2010) K119–K124.
[56] M. Kaur, K.P. Muthe, S.K. Despande, S. Choudhury, J.B. Singh, N. Verma, S. K. Gupta, J.V. Yakhmi, Growth and branching of CuO nanowires by thermal oxidation of copper, Journal of Crystal Growth 289 (2) (2006) 670–675, https://doi.org/10.1016/j.jcrysgro.2005.11.111.
[57] M. Komatsu, H. Mori, In situ HVEM study on copper oxidation using an improved environmental cell, J. Electron Microsc. (Tokyo) 54 (2005) 99–107, https://doi.org/10.1093/jmicro/dfi032.
[58] M. Chen, Y. Yue, Y. Ju, Growth of metal and metal oxide nanowires driven by the stress-induced migration, in, J. Appl. Phys., American Institute of Physics AIP 111 (10) (2012) 104305, https://doi.org/10.1063/1.4718436.
[59] J.T. Chen, F. Zhang, J. Wang, G.A. Zhang, B.B. Miao, X.Y. Fan, D. Yan, P.X. Yan, CuO nanowires synthesized by thermal oxidation route, J. Alloys Compd. 454 (1-2) (2008) 268–273, https://doi.org/10.1016/j.jallcom.2006.12.032.
[60] S. Rackauskas, S.D. Shandakov, H. Jiang, J.B. Wagner, A.G. Nasibulin, Direct observation of nanowire growth and decomposition, Sci. Rep. 7 (2017) 1–6, https://doi.org/10.1038/s41598-017-12381-9.
[61] H. Sheng, H.e. Zheng, S. Jia, L. Li, F. Cao, S. Wu, W. Han, H. Liu, D. Zhao, J. Wang, Twin structures in CuO nanowires, J. Appl. Crystallogr. 49 (2) (2016) 462–467, https://doi.org/10.1107/S1600576716001461/nb5166sup1.pdf.
[62] X. Jiang, T. Herricks, Y. Xia, CuO Nanowires Can Be Synthesized by Heating Copper Substrates in Air, Nano Lett. 2 (12) (2002) 1333–1338, https://doi.org/10.1021/nl0257519.
[63] C.-H. Tu, C.-C. Chang, C.-H. Wang, H.-C. Fang, M.R.S. Huang, Y.-C. Li, H.-J. Chang, C.H. Lu, Y.-C. Chen, R.-C. Wang, Y. Tzeng, C.-P. Liu, Resistive Memory Devices with High Switching Endurance through Single Filaments in Bi-crystal CuO Nanowires, Journal of Alloys and Compounds 615 (5) (2014) 754–760, https://doi.org/10.1016/j.jallcom.2014.05.145.
[64] G. Filipič, O. Baranov, M. Mozetič, K. Ostrikov, U. Cvelbar, Uniform surface growth of copper oxide nanowires in radiofrequency plasma discharge and limiting factors, Phys. Plasmas. 21 (11) (2014) 113506, https://doi.org/10.1063/1.4901813.
[65] G. Filipič, O. Baranov, M. Mozetič, U. Cvelbar, Growth dynamics of copper oxide nanowires in plasma at low pressures, J. Appl. Phys. 117 (4) (2015) 043304, https://doi.org/10.1063/1.4906501.
[66] O. Baranov, G. Filipič, U. Cvelbar, Towards a highly-controllable synthesis of copper oxide nanowires in radio-frequency reactive plasma: fast saturation at the targeted size, Plasma Sources Sci. Technol. 28 (8) (2019) 084002, https://doi.org/10.1088/1361-6595/aae12e.
[67] A. Atkinson, Transport Processes during the Growth of Oxide Films at Elevated Temperature, Rev. Mod. Phys. 57 (2) (1985) 637–1470.
[68] C. Kittel, H. Kroemer, Thermal Physics, W. H. Freeman and Co, New York, 1980.
[69] C.-L. Cheng, Y.-R. Ma, M.H. Chou, C.Y. Huang, V. Yeh, S.Y. Wu, Direct Observation of Short-Circuit Diffusion During the Formation of a Single Cupric Oxide Nanowire, Nanotechnology 18 (24) (2007) 245604, https://doi.org/10.1088/0957-4484/18/24/245604.
[70] I. Levchenko, U. Cvelbar, M. Keidar, Graphene Flakes in Arc Plasma: Conditions for the Fast Single-Layer Growth, Graphene 05 (02) (2016) 81–89.
[71] Y. Zhu, K. Mimura, M. Isshiki, Oxidation Mechanism of Copper at 623–1073 K, Mater. Trans., JIM 43 (9) (2002) 2173–2176.

[72] E. Chason, J.W. Shin, S.J. Hearne, L.B. Freund, Kinetic model for dependence of thin film stress on growth rate, temperature, and microstructure, J. Appl. Phys. 111 (8) (2012) 083520, https://doi.org/10.1063/1.4704683.
[73] E. Chason, A.M. Engwall, Z. Rao, T. Nishimura, Kinetic model for thin film stress including the effect of grain growth, J. Appl. Phys. 123 (2018), 185305. http://aip.scitation.org/toc/jap/123/18.
[74] F. Meng, S.A. Morin, S. Jin, in Springer Handbook of Nanomaterials, edited by R, Springer, Vajtai, Berlin, 2013.
[75] P. Jagtap, E. Chason, A unified kinetic model for stress relaxation and recovery during and after growth interruptions in polycrystalline thin films, Acta Mater. 193 (2020) 202–209, https://doi.org/10.1016/j.actamat.2020.04.013.
[76] A. Altaweel, T. Gries, S. Migot, P. Boulet, A. Mézin, T. Belmonte, Localised growth of CuO nanowires by micro-afterglow oxidation at atmospheric pressure: Investigation of the role of stress, Surf. Coat. Tech. 305 (2016) 254–263, https://doi.org/10.1016/j.surfcoat.2016.08.001.
[77] E. Chason, A.F. Bower, Kinetic Monte Carlo simulations of stress and morphology evolution in polycrystalline thin films, J. Appl. Phys. 125 (11) (2019) 115304, https://doi.org/10.1063/1.5085313.
[78] L. Filipovic, S. Selberherr, Performance and Stress Analysis of Metal Oxide Films for CMOS-Integrated Gas Sensors, Sensors 15 (2015) 7206–7227, https://doi.org/10.3390/s150407206.
[79] H.Z. Yu, C.V. Thompson, Grain growth and complex stress evolution during Volmer-Weber growth of polycrystalline thin films, Acta Mater. 67 (2014) 189–198, https://doi.org/10.1016/j.actamat.2013.12.031.
[80] F. Cemin, G. Abadias, T. Minea, C. Furgeaud, F. Brisset, D. Solas, D. Lundin, Benefits of energetic ion bombardment for tailoring stress and microstructural evolution during growth of Cu thin films, Acta Mater. 141 (2017) 120–130, https://doi.org/10.1016/j.actamat.2017.09.007.
[81] M. Vila, C. Diaz-Guerra, J. Piqueras, Optical and magnetic properties of CuO nanowires grown by thermal oxidation, J. Phys. D: Appl. Phys. 43 (13) (2010) 135403, https://doi.org/10.1088/0022-3727/43/13/135403.
[82] X. Zhao, P. Wang, Z. Yan, N. Ren, Room temperature photoluminescence properties of CuO nanowire arrays, Opt. Mater. 42 (2015) 544–547, https://doi.org/10.1016/j.optmat.2014.12.032.
[83] Z. Lin, R. Zhan, L. Li, H. Liu, S. Jia, H. Chen, S. Tang, J. She, S. Deng, N. Xu, J. Chen, Defect-concentration dependence of electrical transport mechanisms in CuO nanowires, RSC Adv. 8 (4) (2018) 2188–2195, https://doi.org/10.1039/C7RA11862G.
[84] Z. Lin, W. Chen, R. Zhan, Y. Chen, Z. Zhang, X. Song, J. She, S. Deng, N. Xu, J. Chen, Thermal-enhanced field emission from CuO nanowires due to defect-induced localized states, AIP Adv. 5 (10) (2015) 107229, https://doi.org/10.1063/1.4935046.
[85] E. Vasco, C. Polop, Intrinsic Compressive Stress in Polycrystalline Films is Localized at Edges of the Grain Boundaries, Phys. Rev. Lett. 119 (2017), 256102, https://doi.org/10.1103/physrevlett.119.256102.

2.2 In Search of the Limits of CuO Thermal Oxidation Nanowire Growth by Combining Experiment and Theory

In Section 2.2, the limiting conditions for the growth of CuO NWs by thermal oxidation are explored. The results describing the precise control of the physical properties of CuO NWs resolve the contradictory reports in the literature. They are needed to establish the experimental platform for the future research of anion-exchange phase-transformation experiments. In NWs, the radial diffusion can be limited by using NWs that are as thin as possible. In the research described in the previous section, it was shown that the NW diameter increases with temperature. Therefore, the temperature used for the synthesis of thin model NWs should be just above the limiting temperature needed for NW growth.

The lower limits were researched by oxidizing copper at temperatures below 300 °C. The temperature was gradually decreased until no more NWs were observed. The results were again supported by modeling the NW nucleation process.

This Section addresses Objective 2. The results of this subsection were published in a peer-reviewed scientific article in the journal *Applied Physics Letters*.

Regarding my contribution, I performed the experimental work (synthesis and electron microscopy of NWs), analyzed the experimental results and wrote the initial manuscript.

Applied Physics Letters ARTICLE pubs.aip.org/aip/apl

In search of the limits of CuO thermal oxidation nanowire growth by combining experiment and theory

Cite as: Appl. Phys. Lett. **123**, 041601 (2023); doi: 10.1063/5.0151293
Submitted: 20 March 2023 · Accepted: 12 July 2023 ·
Published Online: 25 July 2023

Martin Košiček,[1,2] Oleg Baranov,[1,3] Janez Zavašnik,[1,2] and Uroš Cvelbar[1,2,a)]

AFFILIATIONS

[1]Jožef Stefan Institute, Jamova Cesta 39, 1000 Ljubljana, Slovenia
[2]Jožef Stefan Postgraduate School, Jamova Cesta 39, 1000 Ljubljana, Slovenia
[3]Plasma Laboratory, National Aerospace University, Kharkiv 61070, Ukraine

[a)]Author to whom correspondence should be addressed: uros.cvelbar@ijs.si

ABSTRACT

In the present study, we report on the temperature limiting conditions for the growth of copper oxide nanowires via thermal oxidation of copper, which have been puzzling scientists for decades and were up until now unknown. We explore the lowest temperature limits for nanowire synthesis and find the lowest nanowire diameter that can be achieved via thermal oxidation. This was achieved by gradually lowering the temperature of the oxidation and observing when the nanowire growth will cease with the use of electron microscopy techniques. The lowest temperature, where the growth of nanowires was observed, corresponded to 187 ± 5 °C, and the lowest nanowire diameter which can be achieved was found to be between 3 and 4 nm. Experimental results are supported by theoretical modeling of the nanowire nucleation processes, providing deterministic aspects. The nanowire limiting diameter is governed by the temperature dependence of the critical nucleus size.

Semiconductor nanowires (NWs) have been envisioned for applications in next-generation devices.[1–4] For metal oxide NWs, thermal[5–26] and plasma oxidation[27–38] are common processes for the fabrication of single crystalline NWs. In the thermal oxidation method, anisotropic one-dimensional NW growth is achieved by metal annealing in oxidative atmosphere. The diameter and length of produced NWs correlate with the oxidation temperature; generally, lower oxidation temperature results in thinner and shorter NWs.[5,9,10,20,39] However, there is a lower temperature limit, below which the growth of NWs is not observed; hence, this limiting temperature determines the smallest NW diameters that can be grown by this method.

In the case of copper(II) oxide (CuO), conflicting low-temperature thermal oxidation limits of NW growth are reported: dogmatically, CuO NW growth cannot be achieved below 400 °C,[5,17,20,40,41] but CuO NW growth was observed even at 250 °C.[42,43]

The smallest NW diameter that can be achieved by thermal oxidation is yet unknown. Furthermore, it is unknown why such a limit exists, i.e., why further lowering of the oxidation temperature does not produce NWs with smaller diameters but instead terminates growth.

In this communication, we report on the temperature limiting conditions of CuO NWs grown via thermal oxidation, correlate the limiting conditions with the physical properties of CuO NWs, and discuss the growth restricting mechanisms.

CuO NWs were synthesized by heating metallic copper in a tube furnace, starting at room temperature (20 °C) with a heat ramp of 30 min and oxidation holding time of 720 min. We wanted to achieve as dense NW arrays as possible to be able to observe NW formation even at limiting conditions, and as NW densities generally increase with time,[5] a longer oxidation time was used. We explored NW growth at limiting conditions below 300 °C. Hence, the first oxidation temperature chosen was set as 300 °C. For subsequent experiments, lower temperatures were used until we found the temperature where NW growth ceased. However, it has to be mentioned that we found large discrepancies between temperatures set on the furnace temperature program and actual temperatures in the reaction chamber, measured by a thermocouple. This is understandable as the quartz tube was partially opened to the atmosphere, and oxygen flow was continuously introduced inside the quartz tube. The flow was set to 180 sccm. In Ref. 9, we observed a negligible impact of the oxygen flow on the

Applied Physics Letters ARTICLE pubs.aip.org/aip/apl

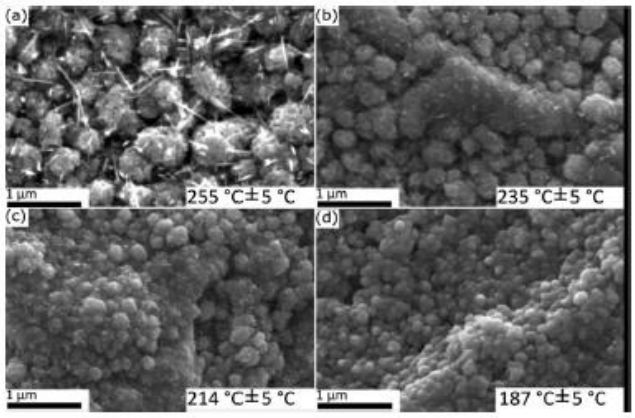

FIG. 1. SEM micrographs of the CuO samples synthesized via thermal oxidation at (a) 255 ± 5 °C, (b) 235 ± 5 °C, (c) 214 ± 5 °C, and (d) 187 ± 5 °C. In all figures, grainy CuO structures are visible. Thermal oxidation of copper starts with the formation of copper oxide layers on top of the copper substrate.

NW parameters in the narrow oxygen flow range (97–175 sccm). On the other hand, authors in Ref. 44 found that the oxygen flow of 150 sccm resulted in the highest NW number density and aspect ratio. Therefore, we chose the oxygen flow of a similar value, 180 sccm. We selected oxygen rich atmosphere, as previous research shows that NW density is increased when oxidation is done in pure oxygen rather than in ambient air.[45] On the other hand, in Ref. 44, suppression of NW growth was observed when oxygen flow was increased over 500 sccm. Therefore, the optimal conditions regarding oxygen supply are still unclear. Copper substrate does not considerably affect NW growth,[5] as long as copper supply is sufficient—in Ref. 46, the growth of NWs on copper thin films ceased when the thickness was decreased below 300 nm. Therefore, the experimental parameters were set to give the maximum NW density at a fixed temperature. (See further experimental details in the supplementary material.)

Layers of stable oxides, Cu_2O and CuO, are formed and arranged in the following order: On top of metallic copper substrate, the Cu_2O layer is formed, and the topmost layer from which NWs grow is the CuO layer.[5] The thickness of both layers increases with temperature. The Cu_2O layer is composed of columnar, randomly oriented grains, while grains in the CuO layer exhibit preferential orientation of growth.[10] As evident from Figs. 1(a)–1(d), NWs begin as grainy CuO nanostructures. In the literature, the highest NW density at fixed oxidation times is commonly observed at oxidation temperatures around 400 °C.[20,44] The decrease or increase in the oxidation temperature from this value leads to thinner and more diffuse NWs. In the temperature range, where we are close to the lower temperature limit for the growth of NWs, their diameters and number density decrease to such an extent that their observation via scanning electron microscopy (SEM) becomes difficult. For that reason, transmission electron microscopy (TEM) was used as the technique to evaluate the presence of NWs, their morphology, and crystal structure and to measure their diameters. To prepare the NWs for TEM analysis, oxidized copper samples were placed in the beaker and immersed in absolute ethanol. The beaker was then placed on the ultrasonic bath to detach the NWs from the copper surface and disperse them in the ethanol. After that, couple drops of ethanol containing NWs were dropped on the Nickel supported amorphous carbon TEM grid. We found that the lowest temperature at which NW growth occurred was 187 ± 5 °C. When the temperature was decreased further, by another 10 °C, no NWs were found in the TEM. Examples of NWs synthesized at 187 ± 5, 207 ± 5, and 255 ± 5 °C are shown in Figs. 2(a)–2(c), respectively. More examples of NWs synthesized at different temperatures can be found in the supplementary material (Figs. S2–S6).

From the TEM micrographs [Figs. 2(a)–2(c)], we can conclude that NWs have a single-crystal structure and grow in the ⟨110⟩ direction. Histograms of NW diameter measurements for all temperatures, where NWs were analyzed with TEM, are plotted in Figs. 3(a)–3(e). As seen from Fig. 3(f), NW diameters gradually increase with temperature. However, NW diameters never fall below 3 nm. At 214 °C, very

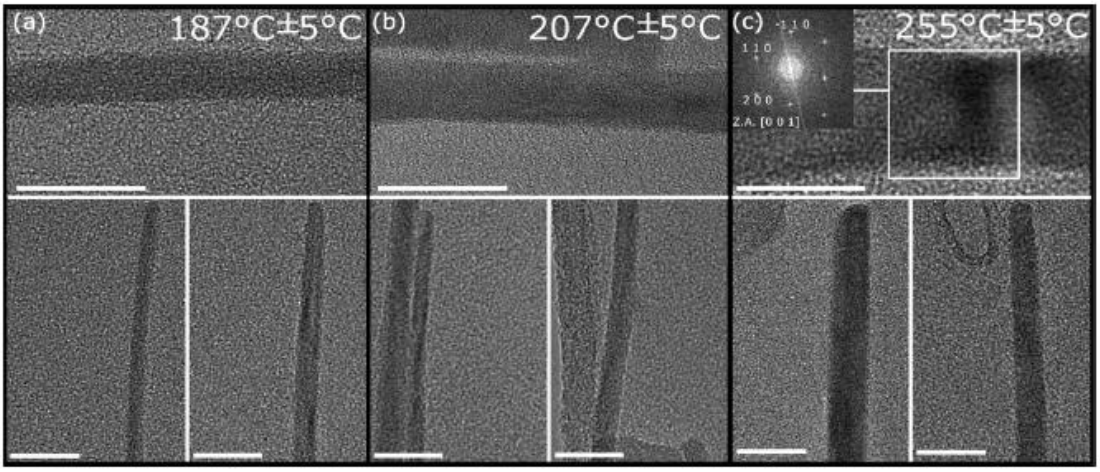

FIG. 2. TEM micrographs of the CuO NWs synthesized at oxidation temperatures (a) 187 ± 5 °C, (b) 207 ± 5 °C, and (c) 255 ± 5 °C. Inset in (c) shows FFT of the area marked with a white square, indexed for the CuO phase, from which crystallographic orientation of the NW can be deduced. NWs grow along the ⟨110⟩ direction. All scale bars in the figure correspond to 20 nm.

Applied Physics Letters ARTICLE pubs.aip.org/aip/apl

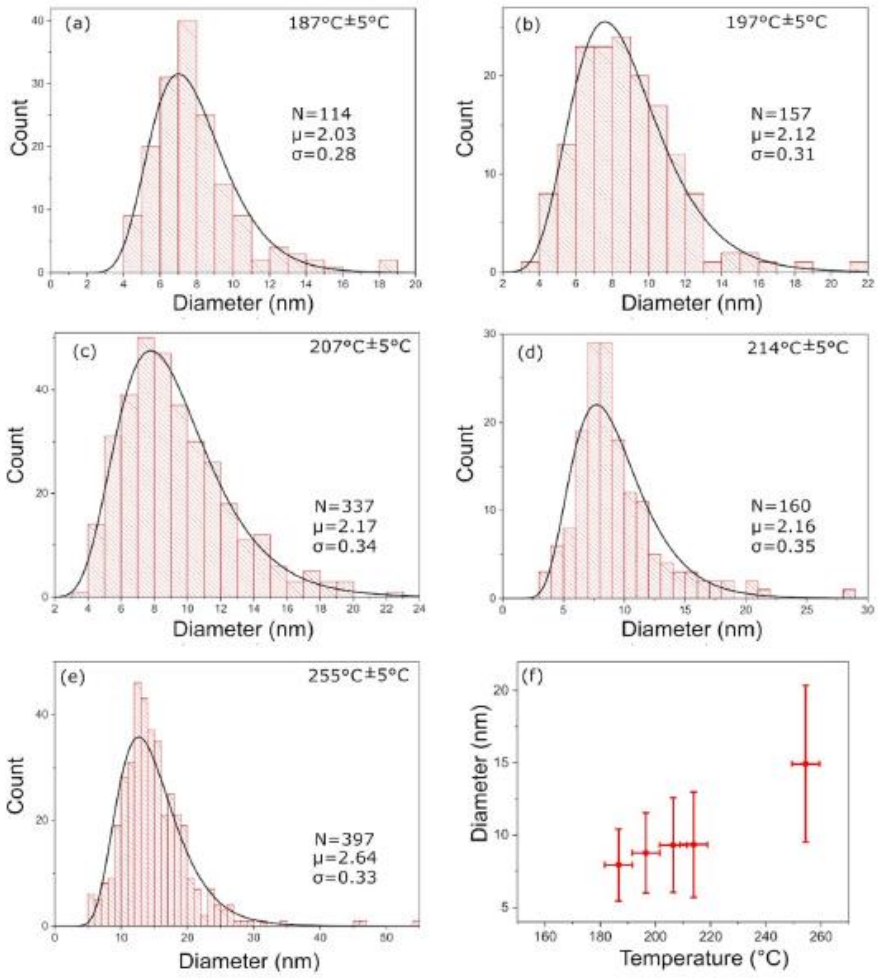

FIG. 3. Diameter histograms from NWs synthesized at oxidation temperatures: (a) 187 ± 5 °C, (b) 197 ± 5 °C, (c) 207 ± 5 °C, (d) 214 ± 5 °C, and (e) 255 ± 5 °C. Black line represents log-normal distribution fitted to data in histogram, with parameters μ the mean, σ the standard deviation, and (f) the temperature dependence of the average NW diameter.

few NWs were found, with diameters ranging between 3 and 4 nm. When decreasing the temperature, the shortest NW diameters never fell below the 3–4 nm range [Figs. 3(a)–3(e)]. Hence, our estimation is that the lowest NW diameter that can be obtained at 214 ± 5 °C is 3 nm, which would correspond to the size of the critical nucleus formed at this temperature.

The value of a limiting diameter can be explained by simple theoretical modeling of a NW nucleation process and finding the diameter of a critical NW nucleus. The common mechanisms describing NW nucleation and growth are the vapor–liquid–solid (VLS) mechanism and vapor–solid–solid (VSS). However, since copper and its oxides exhibit much higher melting points than the temperatures used in our experiments, neither of the two mechanisms is valid for describing the NW nucleation and the growth process. Instead, the NW nucleus is formed in the reaction between the oxygen and copper ions diffusing from the copper substrate through the Cu_2O layer toward the surface.[9,10,12,20,47] The nucleation process takes place in the CuO layer as NWs are buried in the layer.[10] After its formation, the nucleus can serve as the seed for the NW growth. Since not all NWs exhibit the same diameter, we can infer that NWs grow from nuclei of different sizes. As NWs grow, their diameters do not change with oxidation time;[20,44] hence, after NW starts elongating, it grows in only one dimension. Therefore, the size of the seed from which an NW grows determines the size of the NW diameter. The value of approximately 3 nm is, thus, the value of the smallest seed, i.e., a critical nucleus diameter for nucleation of CuO at 214 °C. Thicker NWs grow from larger seeds. As NWs exhibit large standard deviation when it comes to their lengths and diameters, while their density generally increases with time,[10] it can be concluded that nucleation of new NWs occurs throughout the duration of the oxidation.

During the formation of a spherical nucleus, the formation of a new surface and volume is accompanied by a change in free energy. It was assumed that the formation of NW nuclei is a process where CuO grains acquire certain types of defects, which serve as starting points for further development of CuO NWs. It was also assumed, for the first approximation, that only a part α of CuO spherical grain surface and volume undergoes the transformation. As for the type of defect, it was assumed on a base of recent investigation, that twin boundaries can be considered as a suitable candidate.[10] If there are no fields and

Applied Physics Letters ARTICLE pubs.aip.org/aip/apl

charges present, the change in the free energy (ΔG_i) can be described as in following equation:

$$\Delta G_i = 4\pi r^2 \alpha \frac{\partial G_i}{\partial S} + \frac{4}{3}\pi r^3 \alpha \frac{\partial G_i}{\partial V} = 4\pi r^2 \alpha \sigma_S - \frac{4}{3}\pi r^3 \alpha \Delta G_V, \quad (1)$$

where r is the radius of a spherical nucleus, S is the formed surface area, V is the formed volume, α is a part of CuO spherical grain surface and volume, which undergoes the transformation of CuO grain into CuO NW nuclei and contains the defect, and σ_S and ΔG_V are energies per surface and volume unit, respectively. The critical radius can be obtained by considering $\partial \Delta G_i / \partial r = 0$. After introducing the temperature dependencies of σ_S and ΔG_V, we get the expression for the critical radius r_{cr} at given temperature T_s [Eq. (2) (further details are in the supplementary material)],

$$r_{cr} = 2a_0 \frac{e\varepsilon_{c2s0} - k_B T_s}{e\varepsilon_{V0} - k_B T_s}, \quad (2)$$

where ε_{c2s0} and ε_{V0} are minimal values of the energies ε_{c2s} and ε_V, respectively, which represent energies needed for the formation of a surface a_0^2 and volume a_0^3, respectively; a_0 is a lattice constant. By taking into account the estimation r_{cr} of 1.5 nm at 214 °C and estimating r_{cr} at 700 °C as 25 nm (Ref. 9) (details can be found in the supplementary material), we obtain the values $\varepsilon_{c2s0} = 0.15$ eV and $\varepsilon_{V0} = 0.086$ eV. These energies allow us to fit the critical radius dependence with temperature [Fig. 4(a)]. As can be seen from the predicted values of r_{cr}, the proposed model allows the growth of nanoscale structures up to temperatures above 700 °C. To account for the error in the estimation of r_{cr} at 700 °C in calculation of ε_{c2s0} and ε_{V0}, fittings were also performed for multipliers of r_{cr} at 700 °C by $n = 0.5$, 1, 2, 3, and 4. It was found that as long as the critical radius was underestimated ($n = 2$, 3, and 4), the error in r_{cr} at different temperatures is small. On the other hand, if we overestimate r_{cr} at 700 °C ($n = 0.5$) (i.e., actual r_{cr} is lower than our estimation), the errors may be high [see Fig. S7(a) in the supplementary material].

From the calculated ε_{V0}, it is possible to obtain the highest temperature at which NW nucleation still takes place. This was determined to be the following equation:

$$T_{smax} = \frac{e\varepsilon_{V0}}{k_B} - 273\,^\circ\mathrm{C} = 719\,^\circ\mathrm{C}. \quad (3)$$

The determined temperature is in good agreement with the temperature 700 °C, which is most commonly listed in the literature as the upper limiting temperature at which CuO NWs grow[5] and no NWs are observed if the oxidation temperature is increased to 800 °C.[48]

For the obtained values of ε_{c2s0} and ε_{V0}, ΔG_i was calculated as a function of nucleus radius at different temperatures [Fig. 4(b)], which resulted in "classical" graphs with maxima at $T_s < T_{smax}$. The maxima correspond to the radii of the critical nuclei and are absent for $T_s > T_{smax}$, indicating that NW nucleation is not favorable above T_{smax}. Below T_{smax}, our model predicts the critical nucleus radius at different temperatures as r_{cr} (214 °C) = 1.5 nm, r_{cr} (250 °C) = 1.6 nm, r_{cr} (500 °C) = 2.7 nm, r_{cr} (600 °C) = 4.4 nm, and r_{cr} (650 °C) = 7.2 nm. Experimentally determined values[9] are slightly higher than theoretically predicted ones [Fig. 4(a)]. However, they show a similar trend: both gradually increase with temperature, and the increase becomes more pronounced as the temperature approaches T_{smax}. The difference between the experimental and calculated values may be explained by

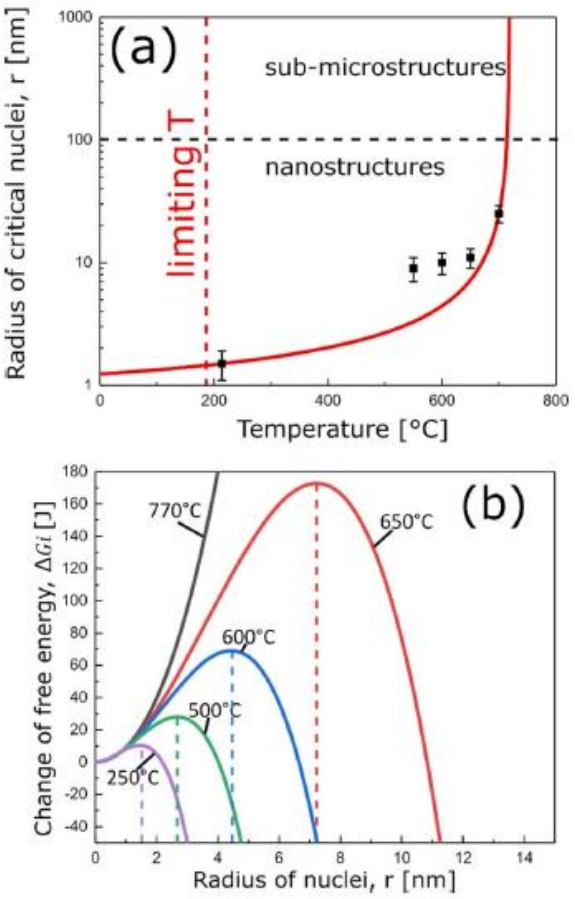

FIG. 4. Calculation results of growth parameters. (a) Temperature dependence of the critical nucleus radius: red line represents results calculated from the theoretical model, and black squares are experimentally determined values with estimated errors. (b) Free energy dependence on the nucleus radius at different temperatures.

the thickening of the nucleus before it starts growing unidirectionally to form an NW. In such a case, NW diameters would exceed the diameters of the initial nuclei.

The change in r_{cr} also becomes less sensitive to temperature at lower temperatures. For example, calculated r_{cr} values for the temperatures 207, 197, and 187 °C all give 1.5 nm; a change is noticeable only to the second decimal place. This explains why almost no difference is observed in the diameters of the thinnest NWs at different temperatures in limiting conditions. Therefore, it can be concluded that changes in the free energy, which arise due to nucleus surface and volume formation, play a significant role in the process of nucleus formation, as experimental data fit well with the model.

While the smallest CuO NW diameter as well as upper limiting temperature for NW growth can be explained by considering the size of a critical nucleus and thermodynamics of NW nucleus formation, the lower limiting temperature of 187 ± 5 °C requires further discussion.

One reason for the absence of NWs below 187 ± 5 °C could be decreased formation of the CuO phase at lower temperatures.

Applied Physics Letters ARTICLE pubs.aip.org/aip/apl

As observed in Ref. 49, copper oxidation at 100 °C results in predominantly Cu_2O phase, and CuO phase is found only after days of oxidation. Furthermore, in Ref. 50, where 3 h oxidation of copper thin films was carried out, the presence of CuO phase was observed only above 330 °C. Therefore, as the temperature decreases, CuO phase formation is hindered, which could decrease and terminate the formation of NWs at some temperature limit.

Another reason for the absence of NWs could be connected to the NW growth mechanism. The processes that are involved in the growth of CuO NWs and could determine the rate of NW growth are nucleation and reaction between copper and oxygen, resulting in crystal growth. Since CuO NWs grow from the peak of the sample,[51] copper needs to be supplied from the copper substrate to the NW top. Hence, copper diffusion from the copper substrate might also be a rate-determining step in the NW growth. The literature suggests that the NW growth mechanism is associated with the fast grain boundary diffusion of copper from the copper substrate to the surface of the oxide layers,[20,52,53] induced by stress gradients due to lattice mismatch in the copper oxide layers, as NWs grow in the temperature range at which grain boundary diffusion is the main diffusion type. If the stress in the oxide layers decreases to a certain extent, the diffusion of Cu to the top may not be sufficient, particularly when coupled with lower temperatures. Even though the thickness of oxide layers decreases with temperature,[10] which should result in higher stress gradients, the lowering of stress may be the result of smaller crystal grains in the oxide layers at lower temperature.[10] In the absence of grain boundary diffusion or if other types of diffusion prevail (such as lattice diffusion or even surface diffusion), NW growth will cease. Furthermore, as oxidation temperature decreases, shrinking NW length and diameter results in NWs with a higher surface-to-volume ratio, becoming progressively less stable structures. Hence, the combination of reduced NW stability at lower temperatures with insufficient copper grain boundary diffusion could explain the absence of CuO NWs at oxidation temperatures below 187 ± 5 °C. However, even though grain boundary diffusion from the copper substrate seems to be associated with the growth of CuO NWs, a clear explanation of how stress gradients present in the oxide layers initiate NW growth is still lacking, and further theoretical studies are needed to explain the role of grain boundary diffusion in NW growth.

In summary, we have determined that the lowest temperature at which NWs grow via thermal oxidation at atmospheric pressure and oxygen rich conditions is 187 ± 5 °C. The diameters of the thinnest NWs at this temperature were measured to be between 3 and 4 nm. As NW diameters correlate with oxidation temperature, it was concluded that this value is the smallest diameter that thermal oxidation can achieve. Our experimental conditions, time and oxygen flow, were fixed and optimized according to the literature to result in the highest NW number densities. The processes were explained by a simple theoretical model invoking temperature dependence of the critical nucleus size from which NWs emerge. Possible reasons why NWs are not obtainable below 187 ± 5 °C are the absence or decreased rate of CuO phase formation at lower temperatures and insufficient grain boundary diffusion with reduced NW stability at lower temperatures.

For future research on this topic, the effects of other numerous conditions which could influence the NW formation are still unexplored, such as the composition of the oxidative atmosphere, humidity, thickness, composition, and microstructure of the metallic copper substrate, etc. should be studied in limiting conditions of CuO NW growth.

See the supplementary material for experimental details, additional SEM and TEM images of synthesized CuO NWs at different temperatures, and a theoretical model for description of their nucleation.

This work was supported by the Slovenian Research Agency ARRS, Program No. P1-0417, Project No. N2-0107, and NATO project G5814 "NOOSE." O. Baranov acknowledges the support from the project funded by the National Research Foundation of Ukraine, under Grant Agreement No. 2020.02/0119.

AUTHOR DECLARATIONS

Conflict of Interest

The authors have no conflicts to disclose.

Author Contributions

Martin Košiček: Data curation (lead); Formal analysis (equal); Investigation (lead); Writing – original draft (equal). **Oleg Baranov:** Methodology (equal); Validation (equal); Writing – original draft (equal). **Janez Zavasnik:** Conceptualization (equal); Validation (equal); Writing – review & editing (equal). **Uroš Cvelbar:** Conceptualization (lead); Funding acquisition (equal); Methodology (equal); Project administration (equal); Supervision (equal); Validation (equal); Visualization (equal); Writing – review & editing (equal).

DATA AVAILABILITY

The data that support the findings of this study are available from the corresponding author upon reasonable request.

REFERENCES

[1]M. Tonezzer, D. Thi Thanh Le, L. van Duy, N. D. Hoa, F. Gasperi, N. van Duy, and F. Biasioli, Nanotechnol. Rev. **11**, 897 (2022).
[2]M. Nehra, N. Dilbaghi, G. Marrazza, A. Kaushik, R. Abolhassani, Y. K. Mishra, K. H. Kim, and S. Kumar, Nano Energy **76**, 104991 (2020).
[3]N. P. Dasgupta, J. Sun, C. Liu, S. Brittman, S. C. Andrews, J. Lim, H. Gao, R. Yan, and P. Yang, Adv. Mater. **26**, 2137 (2014).
[4]C. M. Hung, D. T. T. Le, and N. van Hieu, J. Sci. Adv. Mater. Devices **2**, 263 (2017).
[5]L. Xiang, J. Guo, C. Wu, M. Cai, X. Zhou, and N. Zhang, J. Mater. Res. **33**, 2264 (2018).
[6]J. T. Chen, F. Zhang, J. Wang, G. A. Zhang, B. B. Miao, X. Y. Fan, D. Yan, and P. X. Yan, J. Alloys Compd. **454**, 268 (2008).
[7]M. M. Arafat, S. Rozali, A. S. M. A. Haseeb, and S. Ibrahim, Nanotechnology **31**, 175603 (2020).
[8]C. X. Zhao, Y. F. Li, J. Zhou, L. Y. Li, S. Z. Deng, N. S. Xu, and J. Chen, Cryst. Growth Des. **13**, 2897 (2013).
[9]O. Baranov, M. Košiček, G. Filipič, and U. Cvelbar, Appl. Surf. Sci. **566**, 150619 (2021).
[10]M. Košiček, J. Zavašnik, O. Baranov, B. Šetina Batič, and U. Cvelbar, Cryst. Growth Des. **22**, 6656 (2022).
[11]G. Filipič and U. Cvelbar, Nanotechnology **23**, 194001 (2012).
[12]J. Shi, L. Qiao, Y. Zhao, Z. Sun, W. Feng, Z. Zhang, J. Wang, and X. Men, J. Alloys Compd. **815**, 152355 (2020).
[13]L. Nkhaili, A. Narjis, A. Agdad, A. Tchenka, A. E. Kissani, A. Outzourhit, and A. Oueriagli, Adv. Condens. Matter Phys. **2020**, 5470817.
[14]S. Rackauskas and A. G. Nasibulin, ACS Appl. Nano Mater. **3**, 7314 (2020).

Applied Physics Letters ARTICLE pubs.aip.org/aip/apl

[15]S. Rackauskas, A. G. Nasibulin, H. Jiang, Y. Tian, G. Statkute, S. D. Shandakov, H. Lipsanen, and E. I. Kauppinen, Appl. Phys. Lett. **95**, 183114 (2009).
[16]S. Rackauskas, S. D. Shandakov, H. Jiang, J. B. Wagner, and A. G. Nasibulin, Sci. Rep. **7**, 12310 (2017).
[17]X. Jiang, T. Herricks, and Y. Xia, Nano Lett. **2**, 1333 (2002).
[18]D. Zappa, E. Comini, R. Zamani, J. Arbiol, J. R. Morante, and G. Sberveglieri, Procedia Eng. **25**, 753 (2011).
[19]A. G. Nasibulin, S. Rackauskas, H. Jiang, Y. Tian, P. R. Mudimela, S. D. Shandakov, L. I. Nasibulina, S. Jani, and E. I. Kauppinen, Nano Res. **2**, 373 (2009).
[20]A. M. B. Goŋalves, L. C. Campos, A. S. Ferlauto, and R. G. Lacerda, J. Appl. Phys. **106**, 034303 (2009).
[21]L. Yuan, Y. Wang, R. Mema, and G. Zhou, Acta Mater. **59**, 2491 (2011).
[22]R. S. Devan, R. A. Patil, J. H. Lin, and Y. R. Ma, Adv. Funct. Mater. **22**, 3326 (2012).
[23]S. Grigorescu, C. Y. Lee, K. Lee, S. Albu, I. Paramasivam, I. Demetrescu, and P. Schmuki, Electrochem. Commun. **23**, 59 (2012).
[24]T. Dlugosch, A. Chnani, P. Muralidhar, A. Schirmer, J. Biskupek, and S. Strehle, Semicond. Sci. Technol. **32**, 084001 (2017).
[25]M. R. Khanlary, V. Vahedi, and A. Reyhani, Molecules **17**, 5021 (2012).
[26]C. Florica, N. Preda, A. Costas, I. Zgura, and I. Enculescu, Mater. Lett. **170**, 156 (2016).
[27]U. Cvelbar, Z. Chen, M. K. Sunkara, and M. Mozetič, Small **4**, 1610 (2008).
[28]M. Mozetič, U. Cvelbar, M. K. Sunkara, and S. Vaddiraju, Adv. Mater. **17**, 2138 (2005).
[29]S. Sunkara, V. K. Vendra, J. H. Kim, T. Druffel, and M. K. Sunkara, Catal. Today **199**, 27 (2013).
[30]U. Cvelbar, J. Phys. D: Appl. Phys. **44**, 174014 (2011).
[31]O. Baranov, G. Filipič, and U. Cvelbar, Plasma Sources Sci. Technol. **28**, 084002 (2019).
[32]A. Altaweel, G. Filipič, T. Gries, and T. Belmonte, J. Cryst. Growth **407**, 17 (2014).
[33]K. Ostrikov, I. Levchenko, U. Cvelbar, M. Sunkara, and M. Mozetic, Nanoscale **2**, 2012 (2010).
[34]B. Guo, M. Košiček, J. Fu, Y. Qu, G. Lin, O. Baranov, J. Zavašnik, Q. Cheng, K. K. Ostrikov, and U. Cvelbar, Nanomaterials **9**, 1405 (2019).
[35]U. Cvelbar, Z. Chen, I. Levchenko, R. M. Sheetz, J. B. Jasinski, M. Menon, M. K. Sunkara, and K. Ostrikov, Chem. Commun. **48**, 11070 (2012).
[36]Q. Cheng, W. Yan, L. Randeniya, F. Zhang, and K. Ostrikov, J. Appl. Phys. **115**, 124310 (2014).
[37]Y. Kumar, J. H. Kim, C. Pendyala, B. Chernomordik, and M. K. Sunkara, J. Phys. Chem. C **112**, 17750 (2008).
[38]A. Altaweel, A. Imam, J. Ghanbaja, D. Mangin, P. Miska, T. Gries, and T. Belmonte, Nanotechnology **28**, 085602 (2017).
[39]M. L. Zhong, D. C. Zeng, Z. W. Liu, H. Y. Yu, X. C. Zhong, and W. Q. Qiu, Acta Mater. **58**, 5926 (2010).
[40]C. H. Xu, C. H. Woo, and S. Q. Shi, Chem. Phys. Lett. **399**, 62 (2004).
[41]K. Zhang, C. Rossi, C. Tenailleau, P. Alphonse, and J.-Y. Chane-Ching, Nanotechnology **18**, 275607 (2007).
[42]C. C. Moise, L. B. Enache, V. Anăstăsoaie, O. A. Lazăr, G. V. Mihai, M. Bercu, and M. Enăchescu, J. Alloys Compd. **886**, 161130 (2021).
[43]J. Hilman, A. J. Yost, J. Tang, B. Leonard, and T. Y. Chien, Nano-Struct. Nano-Objects **11**, 124 (2017).
[44]A. Kumar, A. K. Srivastava, P. Tiwari, and R. V. Nandedkar, J. Phys.: Condens. Matter **16**, 8531 (2004).
[45]C. H. Xu, C. H. Woo, and S. Q. Shi, Superlattices Microstruct. **36**, 31 (2004).
[46]A. A. El Mel, M. Buffière, N. Bouts, E. Gautron, P. Y. Tessier, K. Henzler, P. Guttmann, S. Konstantinidis, C. Bittencourt, and R. Snyders, Nanotechnology **24**, 265603 (2013).
[47]D. Zhu, L. Wang, W. Yu, and H. Xie, Sci. Rep. **8**, 5282 (2018).
[48]J. Liang, N. Kishi, T. Soga, and T. Jimbo, Appl. Surf. Sci. **257**, 62 (2010).
[49]J. Aromaa, M. Kekkonen, M. Mousapour, A. Jokilaakso, and M. Lundström, Corros. Mater. Degrad. **2**, 625–640 (2021).
[50]S. Choudhary, J. V. N. Sarma, and S. Gangopadhyay, AIP Conf. Proc. **1724**, 020116 (2016).
[51]S. Rackauskas, H. Jiang, J. B. Wagner, S. D. Shandakov, T. W. Hansen, E. I. Kauppinen, and A. G. Nasibulin, Nano Lett. **14**, 5810 (2014).
[52]G. Fritz-popovski, F. Sosada-Ludwikowska, A. Köck, J. Keckes, and G. A. Maier, Sci. Rep. **9**, 807 (2019).
[53]L. Yuan and G. Zhou, J. Electrochem. Soc. **159**, C205 (2012).

Supplementary material for manuscript

In Search of the Limits of CuO Thermal Oxidation Nanowire Growth by Combining Experiment and Theory

Martin Košiček, [a,b] Janez Zavašnik [a,b], Oleg Baranov [a,c] and Uroš Cvelbar *[a,b]

[a] Jožef Stefan Institute, Jamova cesta 39, 1000 Ljubljana, Slovenia

[b] Jožef Stefan International Postgraduate School, Jamova cesta 39, 1000 Ljubljana, Slovenia

[c] Plasma laboratory, National Aerospace University, 61070 Kharkiv, Ukraine

* corresponding author: uros.cvelbar@ijs.si

Contents

Experimental details

Synthesis of CuO nanowires

Square copper plates (1 cm x 1 cm) (Alfa Aesar, purity 99.95%, thickness 0.25 mm, annealed) were placed on alumina holders and inserted inside a quartz tube in a tube furnace (OTF-1200X, MTI Corporation), where they underwent thermal oxidation. During oxidation, oxygen flowing at 180 sccm was continuously supplied inside the quartz tube. An oxygen inlet was located on one side of the quartz tube while the other was held open to ambient air through the KF16 orifice. The furnace temperature program was set in the following way. Heating from room temperature (20 °C) to the final temperature took 30 min. The final temperature was then maintained for an additional 12 h. The final temperatures were set as: 300 °C, 290 °C, 270 °C, 260 °C, 250 °C, 240 °C, 230 °C, 220 °C, 210 °C and 200 °C. However, we also measured actual temperatures that were achieved during oxidation by using a thermocouple placed inside the tube furnace in the alumina holder. The discrepancies between set and actual temperatures were quite high (this is many times the major problem of reported results) – oxidations were actually carried out at 167±5 °C, 177±5 °C, 187±5 °C, 197±5 °C, 207±5 °C, 214±5 °C, 224±5 °C, 235±5 °C, 255±5 °C and 265±5 °C. The measurement error was determined by several measurements of the temperature in the furnace with the thermocouple positioned on the same spot where copper plates were during oxidation. Temperature measurements were conducted in two regimes. First, the desired temperature was reached by heating the furnace from room to set temperature and noting the constant signal from the thermocouple. In the second regime, the temperature was increased to at least 100 °C above the desired temperature, followed by cooling down to the desired temperature. After the signal was constant, the value from the thermocouple was noted. The differences of temperatures between different temperature program regimes were higher than the differences within the same temperature regime (heating or cooling). However, the differences were never higher than 5 °C. Hence this was our estimated error in the measurement.

Electron microscopy analysis

Oxidized samples were analysed with scanning electron microscopy (SEM, Prisma E, Thermo Fischer Scientific Inc.) to see the morphology of the oxidised samples (Figure 1 in main text and Figure S1). NWs can be easily observed for samples oxidised at 255±5 °C (Figure 1(a) in the main text) and 265±5 °C (Figure S1(a)). At lower temperatures, NW number density seems to decrease and NWs become shorter and thinner. Their detection and diameter measurements become very difficult with the use of SEM, particularly at temperatures below 224±5 °C. Therefore, NW diameters were measured with a transmission electron microscope (TEM, JEM-2100, JEOL Inc.). NWs were prepared for observations in TEM in the following way. Oxidised samples were placed inside a beaker and immersed in absolute ethanol. Since the number density in samples oxidised at lower temperatures was low, 9–10 oxidised copper plates were placed inside the beaker for preparation of samples oxidised at temperatures 207±5°C or lower to assure that enough NWs were available for analysis. For higher temperatures, one copper plate was used. The beaker was then placed in an ultrasonic bath for approximately 5 min to detach the NWs from the sample

surface and disperse them in the ethanol. Couple drops of ethanol with detached NWs were then dropped onto the Ni-supported amorphous carbon TEM grid.

With the use of SEM and TEM methods, we found NWs on samples oxidized at 265±5 °C (Figure S1(a)), 255±5 (Figure S2) °C, 235±5 °C (Main text, Figure 1(b)), 224±5 °C (Figure S1(b)), 214±5 °C (Figure S3), 207±5 °C (Figure S4), 197±5 °C (Figure S5) and 187±5 °C (Figure S6). Therefore the lowest oxidation temperature at which NWs were still found on the TEM grid was 187±5 °C. For lower temperatures (167±5 °C and 177±5 °C), no NWs were found.

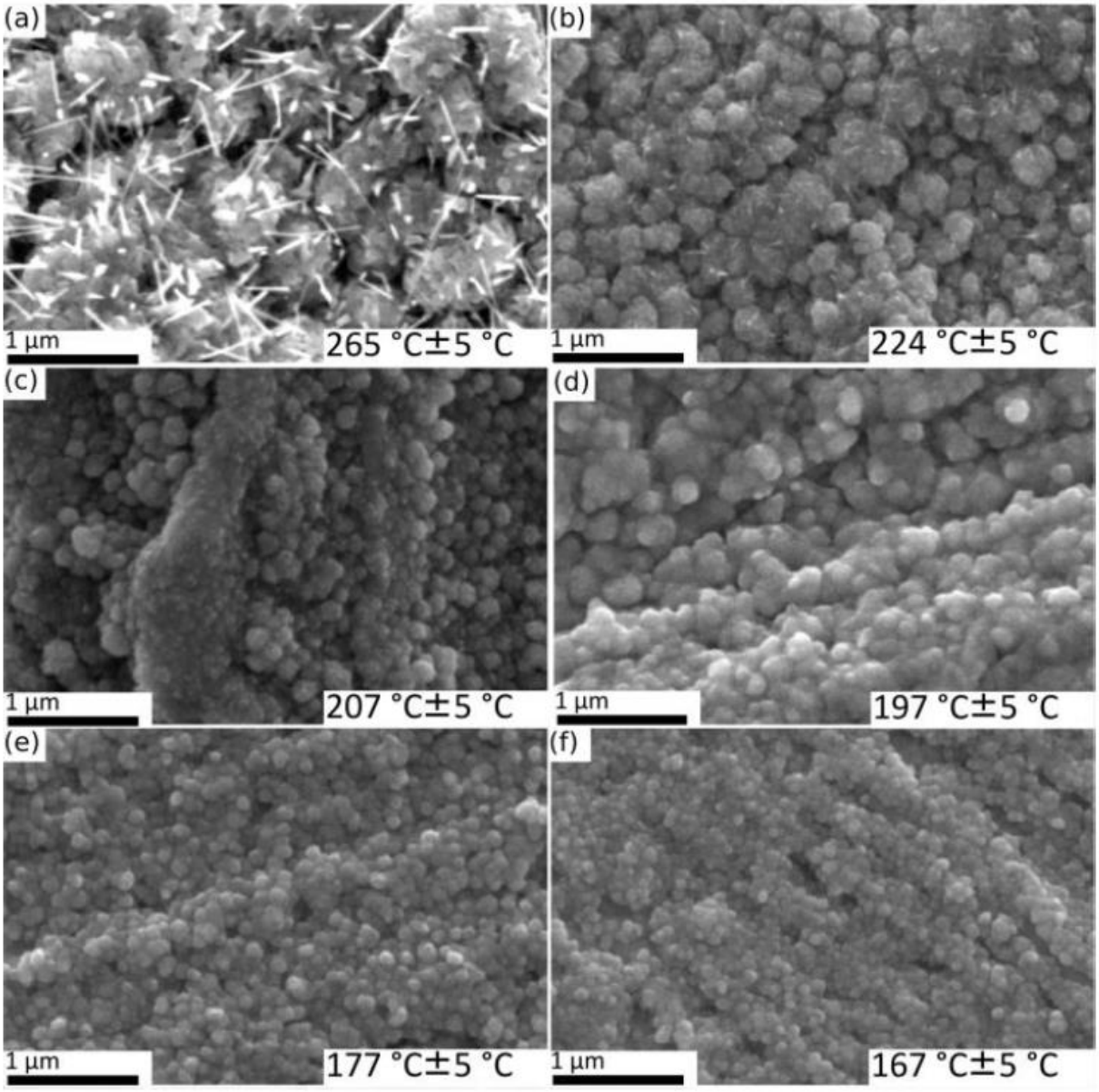

FIG. S1. SEM secondary electron (SE) micrographs of the oxidised copper samples. Samples were oxidised at 265±5 °C, 224±5 °C, 207±5 °C, 197±5 °C, 177±5 °C, 167±5 °C.

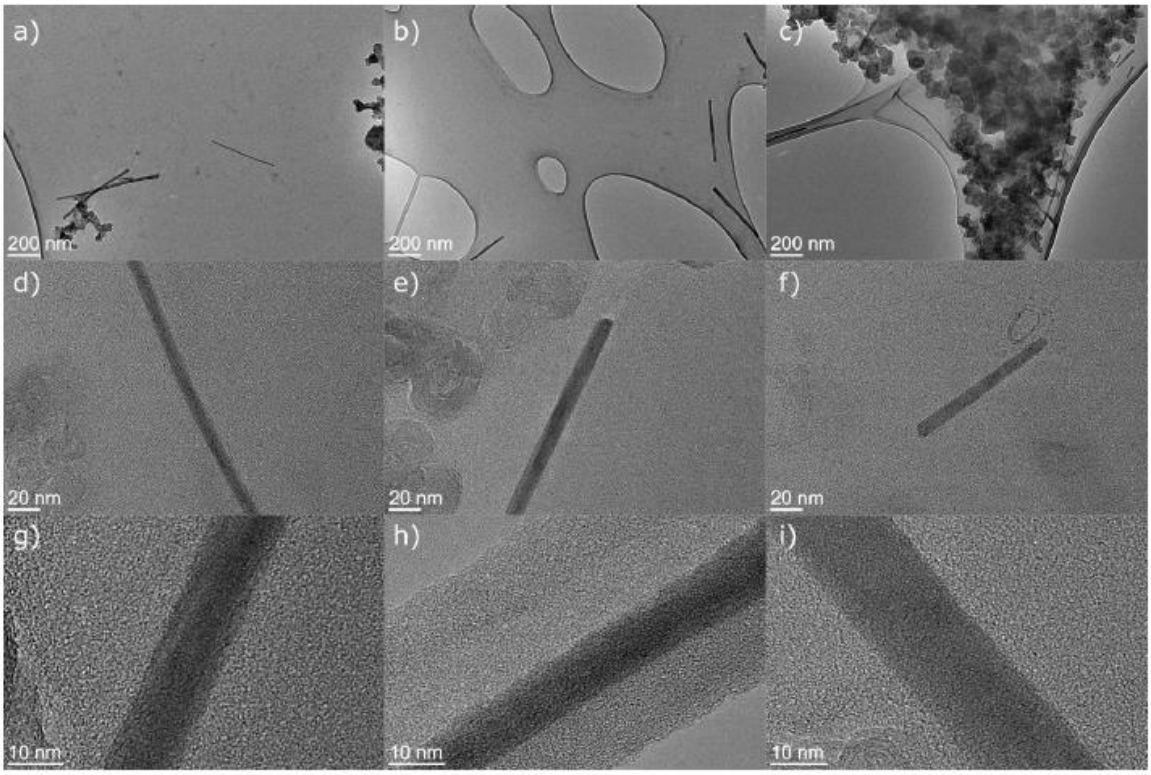

FIG. S2. (a-i) TEM micrographs of CuO NWs grown at 255±5 °C.

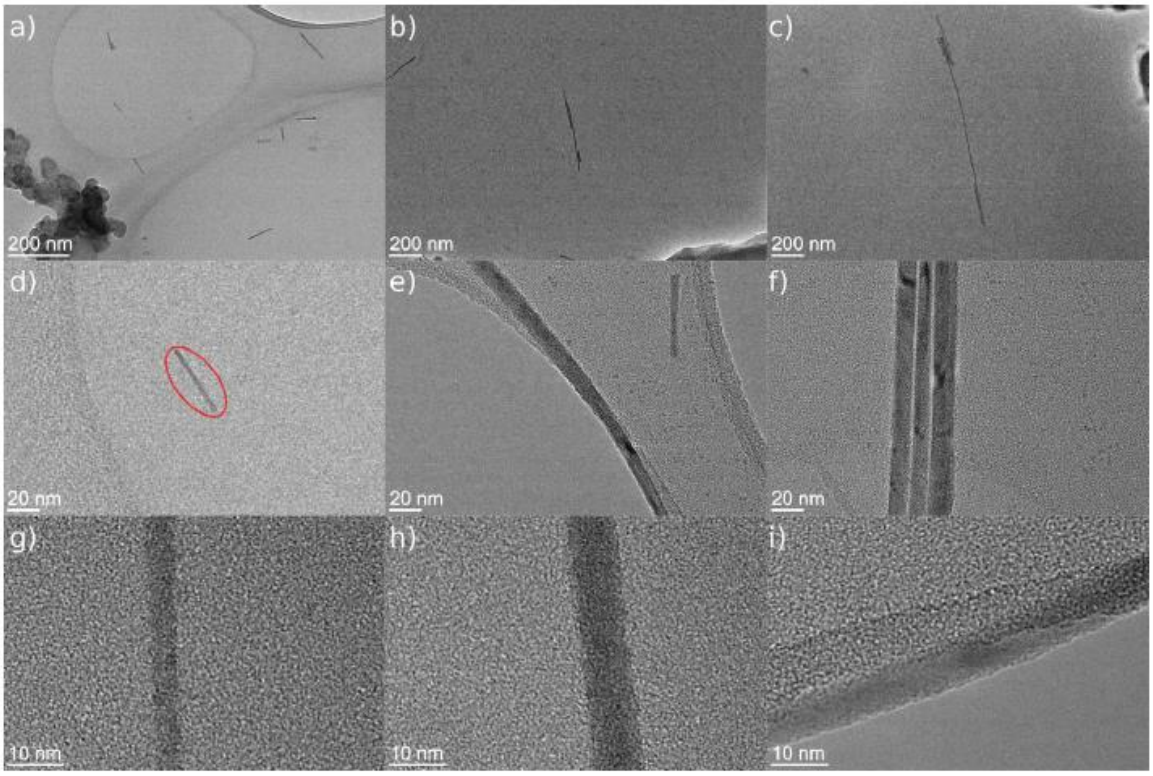

FIG. S3. (a-i) TEM micrographs of CuO NWs grown at 214±5 °C. In figure S3(d) circled with a red ellipse is an example of NW with a diameter below 4 nm. This diameter is close to the limit for the lowest NW diameter which can be achieved at this temperature.

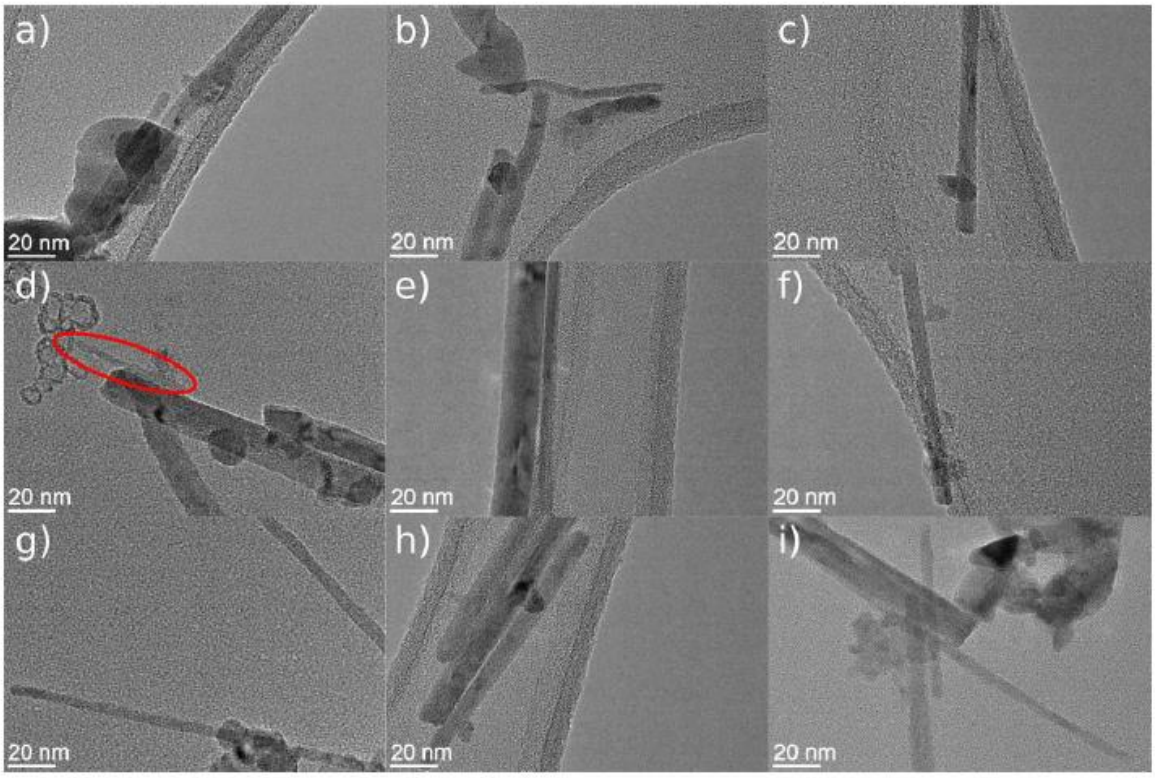

FIG. S4. (a-i) TEM micrographs of CuO NWs grown at 207±5 °C. In figure S4(d) circled with a red ellipse is a NW with diameter below 4 nm. This diameter is close to the limit for the lowest NW diameter which can be achieved at this temperature.

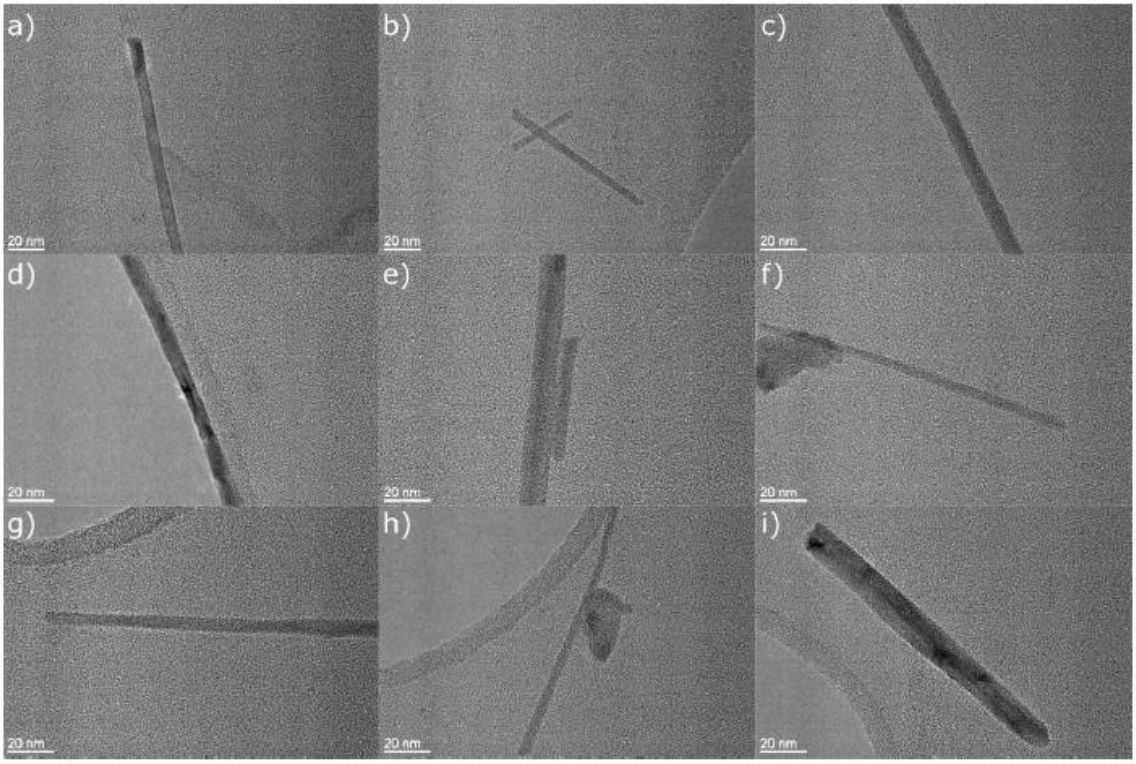

FIG. S5. (a-i) TEM micrographs of CuO NWs grown at 197±5 °C.

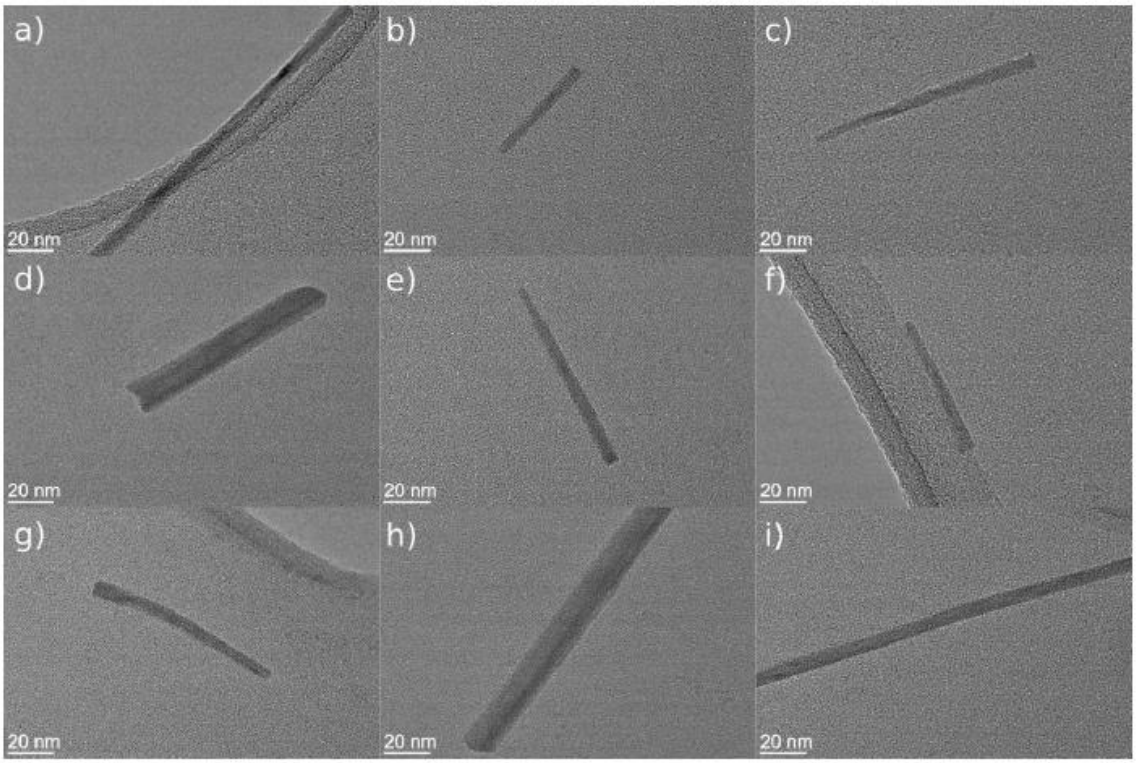

FIG. S6. (a-i) TEM micrographs of CuO NWs grown at 187±5 °C.

Theoretical modelling

The obtained data, coupled with reported results [1], allows estimation of values of the energies that are very important in the theoretical description of a NW nucleation process, namely, surface energy σ_s and volume energy ΔG_V of formation of nuclei of a certain radius r at a specified temperature T_s. This estimation, in turn, makes it possible to predict a radius of a critical nuclei r_{cr} and calculate the smallest radius of NWs for various growth temperatures.

To do that, the following deduction is used. Generation of spherical nuclei of a new phase is accompanied by a change in free energy ΔG_i that is conditioned by generation of new surface S and volume V. In the absence of fields and charges, the relation between the values is described as

$$\Delta G_i = 4\pi r^2 \alpha \frac{\partial G_i}{\partial S} + \frac{4}{3}\pi r^3 \alpha \frac{\partial G_i}{\partial V} = 4\pi r^2 \alpha \sigma_S - \frac{4}{3}\pi r^3 \alpha \Delta G_V \quad \text{(S1)}$$

where σ_s and ΔG_V are energies per unit surface and volume (eV), respectively; r is the radius of spherical nuclei; α is a part of CuO spherical grain surface and volume, which undergo the transformation of CuO grain into CuO nanowire nuclei and contains the defect, which is likely to be a twin boundary, that is necessary to grow a nanowire.

The critical radius can be found in the condition $\partial \Delta G_i / \partial r = 0$:

$$r_{cr} = \frac{2\sigma_S}{\Delta G_V} \quad \text{(S2)}$$

By relating the energies σ_s and ΔG_V to the energy ε_{c2s} of formation of a surface a_0^2 (where a_0 is a lattice constant), and energy ε_V of formation of a volume a_0^3: $\sigma_S = \frac{\varepsilon_{c2s}}{a_0^2}$, $\Delta G_V = \frac{\varepsilon_V}{a_0^3}$, the following relation is deduced:

$$r_{cr} = 2a_0 \frac{\varepsilon_{c2s}}{\varepsilon_V} \quad \text{(S3)}$$

To develop a dependence of a critical nuclei on temperature, the following assumptions are used:

$$\sigma_S = \frac{1}{a_0^2}\left(\varepsilon_{c2s0} - \frac{k_B T_s}{e}\right) \quad (4)$$

$$\Delta G_V = \frac{1}{a_0^3}\left(\varepsilon_{V0} - \frac{k_B T_s}{e}\right) \quad \text{(S5)}$$

where ε_{c2s0} and ε_{V0} are the minimal values of the energies ε_{c2s} and ε_V, which describe the depth of the corresponding potential well at the formation of a critical nuclei.

Then one may obtain from (S3):

$$r_{cr} = 2a_0 \frac{e\varepsilon_{c2s0} - k_B T_s}{e\varepsilon_{V0} - k_B T_s} \quad \text{(S6)}$$

If a lowest temperature T_{smin} of NW formation exists, the smallest critical radius can be expressed as

$$r_{min}(T_{smin}) = 2a_0 \frac{e\varepsilon_{c2s0} - k_B T_{smin}}{e\varepsilon_{V0} - k_B T_{smin}} \quad \text{(S7)}$$

For the highest temperature T_{smax}, where NW formation is still possible, the relation for the critical radius is:

$$r_{min}(T_{smax}) = 2a_0 \frac{e\varepsilon_{c2s0} - k_B T_{smax}}{e\varepsilon_{V0} - k_B T_{smax}} \quad \text{(S8)}$$

After evaluating ε_{c2s0} from the last two expressions, and equating the parts, one obtains an expression for ε_{V0}:

$$\varepsilon_{V0} = \frac{k_B T_{smax}}{e} \frac{\left(1 - \frac{T_{smin}\, r_{min}(T_{smin})}{T_{smax} r_{min}(T_{smax})}\right) - \frac{2a_0}{r_{min}(T_{smax})}\left(1 - \frac{T_{smin}}{T_{smax}}\right)}{1 - \frac{r_{min}(T_{smin})}{r_{min}(T_{smax})}} \quad \text{(S9)}$$

Then, ε_{c2s0} is

$$\varepsilon_{c2s0} = \varepsilon_{V0} \frac{r_{min}(T_{smax})}{2a_0} - \frac{k_B T_{smax}}{e}\left(\frac{r_{min}(T_{smax})}{2a_0} - 1\right) \quad \text{(S10)}$$

As can be seen, dependence (S6) suggests that lower temperature results in the formation of smaller critical nuclei. Obviously, $r_{cr} \to \infty$ at the limit $k_B T_s \to \varepsilon_{V0}$.

In the experiments, the value of $r_{min}(T_{smin})$ is 1.5 nm for T_{smin} = 214 °C, and $r_{min}(T_{smax})$ is about 25 nm for T_{smax} = 700 °C [1]. Thus, the depth of a potential well ε_{V0} = 0.086 eV, and the depth of a potential well ε_{c2s0} = 0.15 eV, as calculated from (S9) and (S10). These values can be used in modelling the nucleation process of CuO NWs. In turn, the value ε_{V0} allows us to calculate the maximal temperature when the nucleation still can occur: $T_{smax} = e\varepsilon_{V0}/k_B - 273$ = 719 °C.

Figure 1(a) in the main text shows results of calculations of critical nuclei radius depending on growth temperature, where a fast transition from nano- to microstructure formation can be observed at the limit $T_s \to T_{max}$, which is conditioned by the tendency of the denominator to zero in (S6). Figure S7(a) illustrates the accuracy of the proposed approach, when $n \times r_{min}(T_{smax})$ is used instead of $r_{min}(T_{smax})$ in the above expressions, which is related to a possible error by n times in measurements of the smallest value of the nuclei [1]. As can be seen, for the higher values (n = 2, 3, 4) of the minimal nuclei grown at the limit 700 °C, the process converges, while for values lower than deduced from the measurements (n = 0.5), the error in the description of the nucleation process can be rather high.

The absence of critical nuclei at $T_s > T_{max}$ = 719 °C is explained in Figure S7(b). As can be seen, the energy ΔG_V that is spent on the formation of unit volume is negative above the critical temperature; thus, the formation of nuclei is energetically unfavorable.

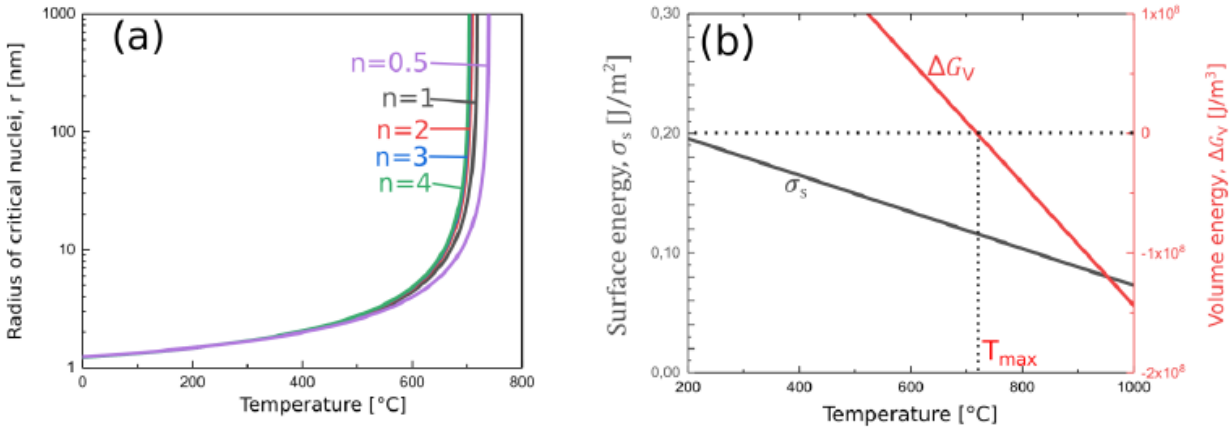

FIG. S7. (a) Radius of critical nuclei depending on temperature when the minimal radius of the NW at the highest temperature is varied (n is the parameter). (b) Surface energy and volume energy of nuclei formation depending on temperature.

Moreover, the developed approach allows for estimating the nuclei's density as a temperature function. In order to do that, the value of the energy of a critical nuclei formation (S1) is used with the substitution of expression (S2) into it, which yields

$$\Delta G_{cr}(T_s, \alpha) = \frac{16\pi}{3}\alpha\frac{{\sigma_S}^3(T_s)}{{\Delta G_V}^2(T_s)} \tag{S11}$$

The rate of the nuclei formation, or rate of nucleation, per unit area, nuclei/(m^{2}s), can be estimated by use of the following expression[1]:

$$\delta n_{nw}(T_s, \alpha) = \frac{\nu_0(T_s)}{a_0^2} exp\left(-\frac{\Delta G_{cr}(T_s,\alpha)}{k_B T_s}\right) = \frac{2k_B T_s}{a_0^2 h} exp\left(-\frac{\Delta G_{cr}(T_s,\alpha)}{k_B T_s}\right) \tag{S12}$$

Figure S8 shows the dependence of the rate of the nuclei formation as a function of the substrate temperature, and α is considered as a parameter. To obtain the number density of nanowires grown after t seconds of the thermal growth, a product $\delta n_{nw}(T_s, \alpha)t$ should be found. In the experiments, the maximal number density of nanowires obtained after 720 minutes of growth was approximately 25·μm^{-2}, so the corresponding rate of nucleation should be about 5.8·10^8 s^{-1}m^{-2}. To fit the parameter, α=0.22 is the best choice, which means that only approximately one-fifth of CuO grain surface and volume undergo the transformation to be a nucleus for the following nanowire growth. The dependencies $\Delta G_{cr}(T_s, \alpha)$ also shown in Figure S8 reveal the reason for the weak nucleation at the extended temperatures found in experiments[1], namely too large energy necessary for the nuclei formation. Certainly, the dependence does not cover the whole temperature range of about 200 °C to approximately 700 °C observed in the experiments, which can be attributed to the simplicity of the developed model of nucleation that can be used as the first approach only.

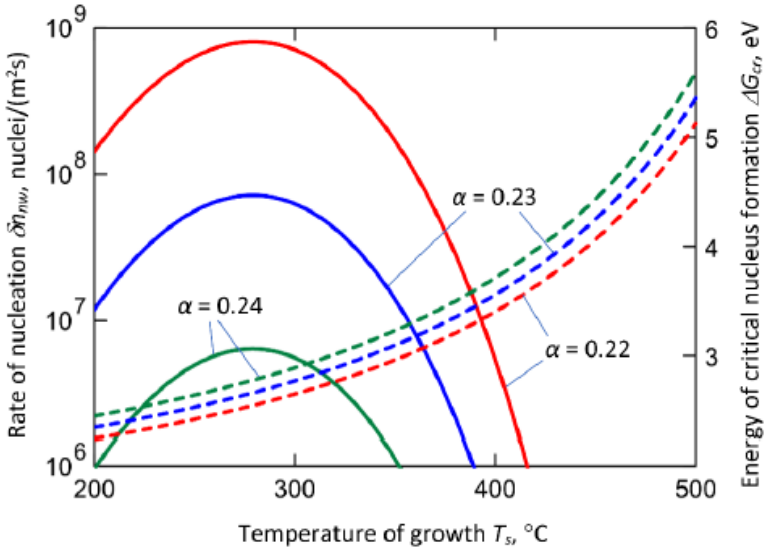

FIG. S8. Dependence of the rate of nucleation $\delta n_{nw}(T_s, \alpha)$ and energy of a critical nucleus $\Delta G_{cr}(T_s, \alpha)$ formation as functions of the substrate temperature; α is considered as a parameter.

References:

[1] O. Baranov, M. Košiček, G. Filipič, and U. Cvelbar, Appl. Surf. Sci. **566**, 150619 (2021).

2.3 Plasma-Assisted Synthesis of Metal Oxide Nanostructures

In Section 2.3, the growth of metal oxide NWs is expanded to plasma-assisted methods and other metals besides copper. In this research, it was demonstrated that a combination of plasma and thermal oxidation is a universal tool for the synthesis of metal oxide nanostructures, particularly nanostructures with low dimensionality, such as NWs and nanorods. To show the versatility of the methods, nanostructures made of different metal oxides (iron, copper, and zinc) were synthesized by exposing metal foils to glow discharge of the argon-oxygen mixture at a controlled temperature. In this way, predominantly NWs, along with nanobelts were obtained. The growth mechanism for the obtained nanostructures was proposed. Plasma can aid the nanostructure growth process through ion bombardment of the initial metal foil, which can result in the formation of "microhillocks" on the metal surface. The tops of these "hillocks" have higher energy than the other areas, resulting in preferential adsorption of the oxygen species followed by oxidation and formation of low-dimensional nanostructures. In summary, this demonstrates the generalization of metal oxidation as a method to grow the metal oxide NWs.

This section addresses Objective 1. The results of this subsection were published in a peer-reviewed scientific article in the journal *Nanomaterials*.

Regarding my contribution, I contributed to the analysis of the experimental results and the writing of the manuscript with the other co-authors.

nanomaterials

MDPI

Article

Single-Crystalline Metal Oxide Nanostructures Synthesized by Plasma-Enhanced Thermal Oxidation

Bin Guo [1,2], Martin Košiček [3,4], Junchi Fu [1,2], Yazhou Qu [1], Guanhua Lin [1,2], Oleg Baranov [3,5], Janez Zavašnik [3], Qijin Cheng [1,2,*], Kostya (Ken) Ostrikov [6,7] and Uroš Cvelbar [3,4,*]

1 School of Electronic Science and Engineering, College of Energy, Xiamen University, Xiamen 361005, China; guobin19920917@163.com (B.G.); fjc@ronbaymat.com (J.F.); qyz1991@live.com (Y.Q.); guanhualin1992@gmail.com (G.L.)
2 Shenzhen Research Institute of Xiamen University, Shenzhen 518000, China
3 Jožef Stefan Institute, Jamova Cesta 39, SI-1000 Ljubljana, Slovenia; martin.kosicek@ijs.si (M.K.); oleg.baranov@ijs.si (O.B.); janez.zavasnik@ijs.si (J.Z.)
4 Jožef Stefan Postgraduate School, Jamova Cesta 39, SI-1000 Ljubljana, Slovenia
5 National Aerospace University, Kharkov 61070, Ukraine
6 School of Chemistry, Physics and Mechanical Engineering, Queensland University of Technology, Brisbane QLD 4000, Australia; kostya.ostrikov@qut.edu.au
7 Joint CSIRO-QUT Sustainable Processes and Devices Laboratory, Lindfield NSW 2070, Australia
* Correspondence: qijin.cheng@xmu.edu.cn (Q.C.); uros.cvelbar@ijs.si or uros.cvelbar@guest.arnes.si (U.C.)

Received: 4 September 2019; Accepted: 29 September 2019; Published: 2 October 2019

Abstract: To unravel the influence of the temperature and plasma species on the growth of single-crystalline metal oxide nanostructures, zinc, iron, and copper foils were used as substrates for the study of nanostructure synthesis in the glow discharge of the mixture of oxygen and argon gases by a custom-made plasma-enhanced horizontal tube furnace deposition system. The morphology and microstructure of the resulting metal oxide nanomaterials were controlled by changing the reaction temperature from 300 to 600 °C. Experimentally, we confirmed that single-crystalline zinc oxide, copper oxide, and iron oxide nanostructures with tunable morphologies (including nanowires, nanobelts, etc.) can be successfully synthesized via such procedure. A plausible growth mechanism for the synthesis of metal oxide nanostructures under the plasma-based process is proposed and supported by the nanostructure growth modelling. The results of this work are generic, confirmed on three different types of materials, and can be applied for the synthesis of a broader range of metal oxide nanostructures.

Keywords: metal oxide nanostructures; plasma-enhanced thermal oxidation; growth mechanism; material characterization; nanostructure growth modelling

1. Introduction

One-dimensional nanostructures have unique mechanical, optical, and electronic properties and represent an important platform for a wide range of applications [1–3]. Especially, one-dimensional metal oxide nanomaterials show great potential for nano-electronic applications due to their magnetic and redox characteristics [4,5].

For our experiment, three different and most reported metal oxide systems were investigated, based on their unique characteristics, properties, and applications, as well as easy comparison with the existing results. In particular, ZnO is a metal-oxide (MO) semiconductor with a wide band gap of 3.37 eV and a large exciton binding energy of 60 meV [2,6]. Due to its unique properties, it is exploited in a wide range of applications, such as ultraviolet lasers, detectors, optical waveguides, laser diodes, surface acoustic wave devices, transparent electrode coatings, acousto-optic devices, thin

film transistors, piezoelectric sensors, solar cells, etc. [7–10]. Fe_2O_3 is a transition metal oxide with a band gap of 2.2 eV, which has been used for centuries in the food industry, medicine, pigments, and ceramics [11–13]. Especially nanosized Fe_2O_3 exhibits catalytic, magnetic, and gas-sensitive properties that can be further exploited [14,15]. CuO is a *p*-type narrow bandgap semiconducting material with a band gap of 1.2 eV [16]. In particular, CuO nanomaterials have optical, electrical, magnetic, and catalytic properties, which have great application potential as catalytic, photothermal photoconductive materials, field emitters, gas sensors, etc. [17–19].

Currently, the most commonly used synthesis routes for the above-mentioned metal oxide nanomaterials include template method [20], hydro- or solvothermal synthesis [21], laser ablation method [22], thermal oxidation method [23], etc. Important criteria for large-scale synthesis of MO nanomaterials are their production cost, quality and uniformity of such obtained nanomaterials, and controllable morphology of nanostructures. The template method can assure good control over the morphology of nanostructures, but it is expensive and time-consuming [24]. Hydrothermal synthesis is fast, efficient and relatively cheap, but the morphology of the product is only poorly controllable by, for example, using surfactants [24]. Laser ablation synthesis can provide more control over the morphology and quality of the nanomaterials, but the process itself is expensive and unsuitable for mass production [25]. Thermal oxidation method can provide good control over the morphology of the nanomaterials, but the reproducibility of the preparation process is insufficient [26–29].

Recently, plasma-assisted synthesis of various nanostructures has been extensively studied [30,31]. For the synthesis of MO nanostructures, metal substrates were treated with oxygen or other gases under plasmas [32]. One of the most significant advantages of such an approach is the short synthesis time, which is reduced by an order of magnitude compared to thermal methods. To form an oxide via thermal oxidation synthesis process, an oxygen molecule has to adsorb on the heated substrate, where it dissociates to form atomic oxygen, and subsequently, the atomic oxygen reacts with metal [33]. On the contrary, plasma already contains atomic oxygen species; therefore, by using oxygen plasmas as a treating agent, one can skip the oxygen dissociation step [34]. Methods utilizing plasmas are cheap, easy to scale-up, and are environmentally friendly, which makes them perfect for the large-scale or even industrial synthesis of nanostructures. Up to now, multiple routes of the plasma synthesis have been described, utilizing different mechanisms of nanostructure growth and control [31].

For the Zn–Fe–Cu oxide model system investigated in this paper, a few different plasma-assisted synthesis approaches have been proposed [30]. Namely, a promising route to obtain ZnO nanostructures in bulk quantities within a very short time is the so-called flight through method [30], where Zn particles enter plasma on one side, fly through (usually by free fall), and exit as oxide nanowires. Through the plasma synthesis method on the Zn or Zn/Cu surface, ultra-thin zinc oxide nanowires (NWs) can be obtained as well [35]. Similarly, plasma methods have been used for the synthesis of Cu oxide [36–40] and Fe oxide nanostructures [30,31,41]. Since copper and iron have a relatively high melting point (1085 and 1538 °C, respectively) compared to Zn (420 °C), the growth mechanism of metal oxide nanostructures, although following the same concept, slightly differs from that of zinc oxide nanostructures [31].

Two basic growth mechanisms of MO nanostructures are proposed as methods of direct exposure of a metal substrate to the plasma [30,37], namely solid–liquid–solid (SLS) and solid–solid (SS) growth mechanisms. In the SLS growth mechanism, tiny droplets of liquid metal form on the solid metal surface when the metal is exposed to temperatures close to its melting point. Oxygen atoms from the plasma first diffuse in the liquid phase of the metal and form solid oxides, which then act as nucleation sites for further nanowire growth. This mechanism is common in metals with low melting points [37]. On the other hand, in the SS growth mechanism, oxygen atoms pass directly into solid metal phase [37]. Oxygen atoms are incorporated inside the metal phase on hotter sites and metal oxide phases are formed, at which point an oxide layer is grown and nuclei act as sites for further nanowire growth [31].

In this work, a custom-made plasma-enhanced horizontal tube furnace deposition system, i.e., plasma-enhanced thermal oxidation (PETO), has been developed and described in an attempt to

synthesize a broad range of metal oxide nanostructures, including ZnO, Fe_2O_3, CuO, etc. Using the PETO method, we were able to produce stable and high-quality metal oxide nanomaterials at a low processing temperature and within a short growth time. Moreover, we have systematically investigated the structural and morphological properties of the synthesized low-dimensional MO nanostructures. Finally, a viable growth mechanism supported by the nanostructure growth modeling has been proposed to interpret the obtained experimental results.

2. Materials and Methods

Zinc, iron, and copper foils were used as substrates for the preparation of corresponding metal oxides nanostructures by custom-made plasma-enhanced horizontal tube furnace deposition system. The system is composed of a horizontal quartz-glass one-temperature zone tube furnace, an RF power generator, a vacuum system, a heating device, and a gas input system, as shown in Figure 1. Two cylindrical metal electrodes with sharp tips were placed at both ends of the quartz tube to produce plasmas. The size of the metal foils used in the experiment was 10 mm × 10 mm × 0.25 mm. At first, metal foils were ultrasonically cleaned with deionized water, acetone, and absolute ethanol for 20 min, respectively, and then placed into the reactor. The entire system was evacuated to a base pressure of 10 Pa or less. The quartz tube was first heated up to working temperature (300–600 °C) within 20 min, and then a gas mixture of argon and oxygen was introduced. Flow rates of Ar and O_2 gases were set as 45 and 5 sccm, respectively. Thereafter, we turned on the plasma power and adjusted the current to 1.3 A. For all the samples, plasma was discharged for 30 min. Finally, the plasma power was turned off, the gas inlets were cut off, and the system was allowed to cool down to room temperature.

Figure 1. Schematic diagram of a custom-made plasma-enhanced horizontal tube furnace deposition system. The vacuum-sealed glass cylinder reactor has two electrodes with pointed ends from each side, and these two electrodes are used to ignite plasma.

The crystal structure of the synthesized metal oxide nanostructures was determined by X-ray diffraction (XRD, Ultima IV, Rigaku, Tokyo, Japan) operating in a locked couple mode, wherein the incident X-ray wavelength was 1.54 Å (Cu K_α line) at 40 kV and 40 mA. The microstructure of the synthesized metal oxide nanostructures was characterized by field emission scanning electron microscope (SEM, Supra 55, Carl Zeiss, Oberkochen, Germany) operated at 5 kV and high-resolution transmission electron microscope (TEM, JEM 2100, Jeol, Tokyo, Japan) operated at 200 kV. Raman measurements were conducted via Raman spectrometer (Xplora Plus, Horiba, Kyoto, Japan) using a 638 nm semiconductor laser for excitation. Before the measurement, Raman spectrometer was calibrated with single crystal silicon. The Raman spectra were recorded with a power of 1 mW and an integration time of 30 s.

3. Results and Discussion

3.1. XRD Analysis

The phase composition of the synthesized MO nanostructures on Zn, Cu, and Fe foils was first identified by XRD. The results are summarized in Figure 2a–c, presenting the XRD spectra of the synthesized zinc oxide, copper oxide, and iron oxide nanostructures at different growth temperatures,

respectively. As shown in Figure 2a, at a growth temperature of 500 °C, diffraction peaks corresponding to ZnO (JCDPS card no. 65-3411) can be observed; these peaks are characteristic for a hexagonal wurtzite-type polymorph. In Figure 2b, characteristic diffraction peaks for CuO (JCDPS card no. 45-0937) can be observed at a growth temperature of 500 °C, while in Figure 2c, diffraction peaks, which can be identified for Fe_2O_3 (JCDPS card no. 36-1451), are observed at a high growth temperature of 600 °C. Also, the peaks of Zn (JCDPS card no. 65-3358), Cu (JCDPS card no. 04-0836) plus Cu_2O (JCDPS card no. 05-0667), and Fe (JCDPS card no. 52-0513) plus Fe_3O_4 (JCDPS card no. 65-3107) appear in Figure 2a–c, respectively. With the increase of the growth temperature, the diffraction peaks of Zn, Cu, and Fe_3O_4 gradually become weaker and disappear almost completely, indicating the decomposition of the oxide nanostructures at elevated temperatures. Based on the XRD experiments, the optimum growth temperature window for each oxide phase has been determined.

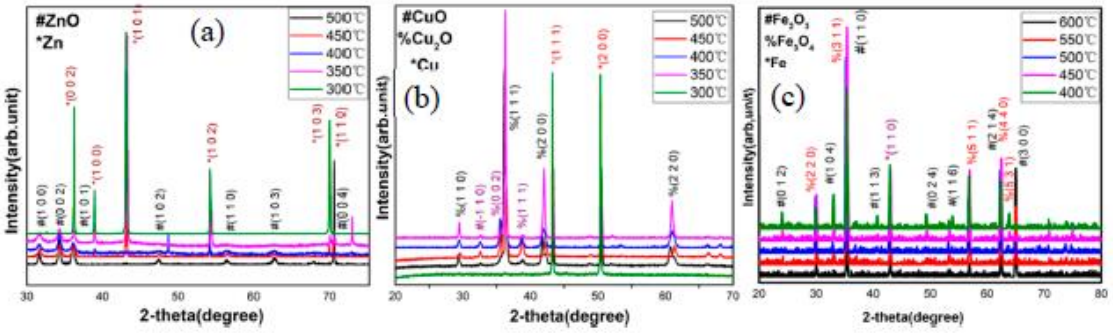

Figure 2. XRD patterns of the metal oxide nanostructures grown at various temperatures: (**a**) ZnO nanostructures were grown at 300–500 °C; (**b**) CuO nanostructures grown at 300–500 °C; (**c**) Fe_2O_3 nanostructures grown at 400–600 °C.

The results of XRD analysis confirm the successful synthesis of ZnO, CuO, and Fe_2O_3 by exposing zinc, copper, and iron foils to the glow discharge of the mixture of oxygen and argon gases by our custom-made plasma-enhanced horizontal tube furnace deposition system.

3.2. Electron Microscopy Characterization

The influence of the growth temperature on the surface morphology of the Zn, Cu, and Fe oxide nanostructures are presented in Figures 3–5, respectively. In the case of ZnO nanostructures (Figure 3), the NWs grown at 400 °C had a sturdy base with a sharp tip. The average diameter and length of these nanostructures were approximately 396 nm and 0.4 µm, respectively. With an increase of the growth temperature to 450 °C, a mixture of finer and longer NWs and nanobelts were obtained, with an average diameter and length about 110 nm and 1.4 µm, respectively. With further increase in the growth temperature to 500 °C, the average diameter and length of the nanostructures were about 130 nm and 1.8 µm, respectively. From these observations, we can derive the basic trend: with the increase of the growth temperature, ZnO nanostructures preferentially grow in c-axis (NWs become longer), while nanobelts eventually entirely disappear. From the TEM micrographs of ZnO NWs grown at a processing temperature of 450 °C and a deposition time of 0.5 h (Figure 3d,e), we could see well-defined single-crystal ZnO with a uniform diameter of 110 nm and a sharp tip. It is noteworthy that the length of the nanowire could not be precisely measured, possibly because of the effect of sonication during the sample preparation. Selected-area electron diffraction pattern (SAEDP) corresponds to the hexagonal wurtzite-type ZnO structure (Figure 3d-inset) and indicates that the ZnO NWs grow in the <0001> direction.

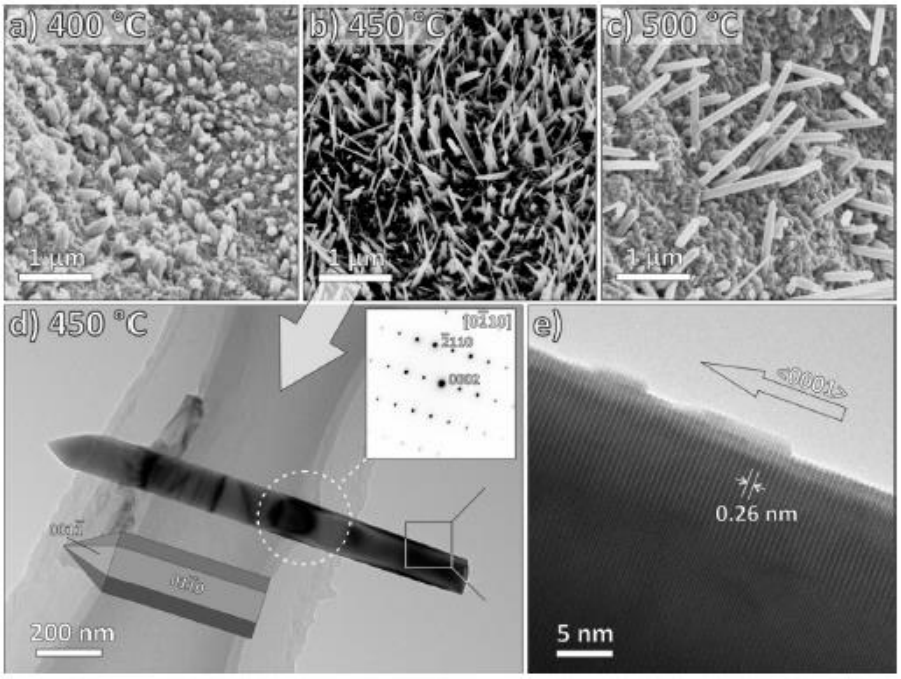

Figure 3. (**a**–**c**): SEM images of ZnO nanostructures synthesized at different growth temperatures: (**a**) 400 °C, (**b**) 450 °C, and (**c**) 500 °C, respectively; time period of growth was 30 min. (**d**) TEM micrograph of a single-crystalline ZnO NW grown at 450 °C with the corresponding SAED pattern (inset) and a model of crystal in the corresponding orientation. (**e**) High-resolution TEM micrograph of a ZnO nanowire, with the marked interplanar spacing of 0.26 nm. The NW is elongated in the <0001> direction.

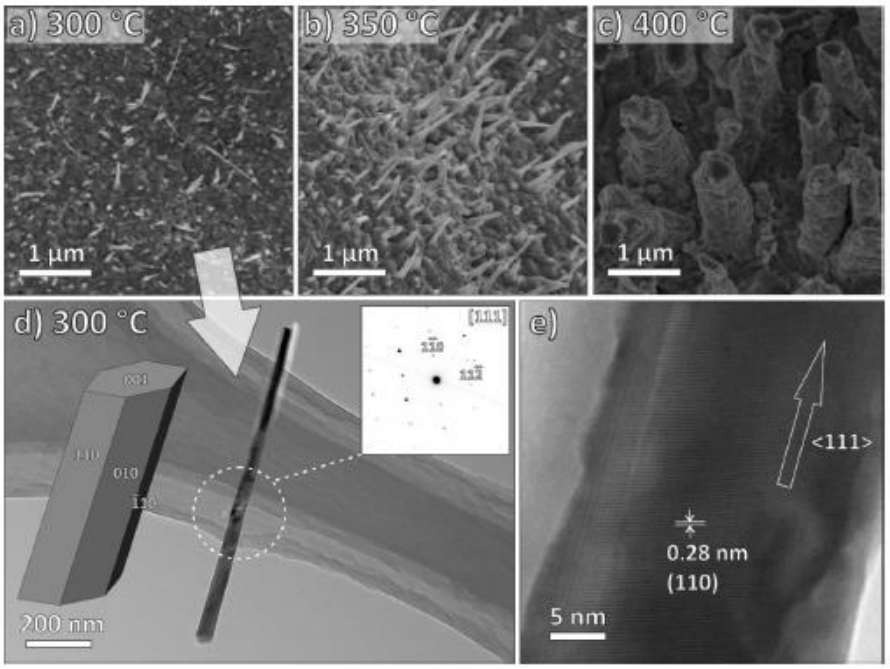

Figure 4. SEM images of copper oxide nanostructures synthesized at different growth temperatures: (**a**) 300 °C, (**b**) 350 °C, and (**c**) 400 °C, respectively; time period of growth was 30 min. (**d**) Top-view TEM image of a single copper oxide nanostructure grown at a processing temperature of 300 °C viewed along [111] zone axis (corresponding SAEDP in inset) and an NW model in the same orientation. (**e**) High-resolution TEM image of the copper oxide nanostructure with the marked interplanar spacing of 0.28 nm. From the SAEDP, we can obtain that the growth direction of the CuO NW is <111>.

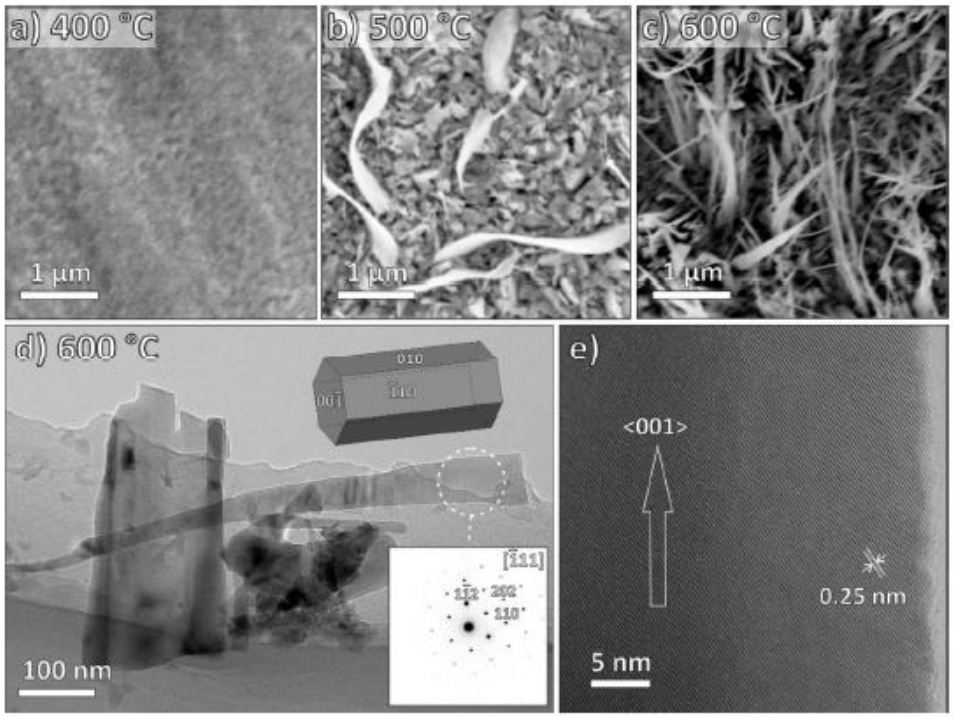

Figure 5. (**a**–**c**): SEM images of iron oxide nanostructures synthesized at different growth temperatures: (**a**) 400 °C, (**b**) 500 °C, and (**c**) 600 °C, respectively; time period of growth was 30 min. (**d**) TEM micrograph of a single-crystallineα-Fe_2O_3 nanostructure grown at 600 °C with the corresponding SAED pattern (inset) and a model of crystal in the corresponding orientation. (**e**) High-resolution TEM micrograph of anα-Fe_2O_3 nanostructure, with the marked interplanar spacing of 0.25 nm. The nanostructure is elongated in the <001> direction.

Plasma treatment of the copper foil at 300 °C (Figure 4a) resulted in sporadic Cu-oxide NWs grown on the surface of the copper foil. The average diameter and length were approximately 70 nm and 0.8 µm, respectively. With the increase of the growth temperature to 350 °C (Figure 4b), we were able to observe the increased density of the Cu-oxide NWs, although the average diameter and length (about 75 nm and 0.9 µm, respectively) did not increase significantly. With a further increase of the growth temperature to 400 °C (Figure 4c), the obtained copper oxide nanostructures became sturdy, and their average diameter and length were about 600 nm and 1.4 µm, respectively. TEM observations of Cu oxide NWs grown at a processing temperature of 300 °C and a deposition time of 30 min (Figure 4d,e) revealed a single-crystalline uniform elongated NW with a diameter of 70 nm and a length of 800 nm. The SAEDP (Figure 4d-inset) corresponds to monoclinic single-crystalline CuO and indicates that the CuO NW is elongated in the <111> direction.

During the plasma experiments with the Fe foil (Figure 5a–c), we observed no surface nanostructures at a growth temperature below 400 °C. When the growth temperature increased to 500 °C, some sparse iron oxide nanobelts could be observed (Figure 5b). Moreover, when the growth temperature was further increased to 600 °C, the whole surface of the Fe foil was covered with dense iron oxide nanobelts (Figure 5c). Some of them were scraped for further TEM analysis (Figure 5d–e), and initial observation (Figure 5d) revealed partially broken, but otherwise well-developed crystalline flattened NWs. SAEDP corresponds to hexagonal α-Fe_2O_3 (hematite). From the high-resolution TEM image (Figure 5e) and the corresponding SAEDP, we concluded that the preferred growth direction of the Fe_2O_3 NWs is along the [001] axis.

SEM and TEM analysis revealed that ZnO, CuO, and Fe_2O_3 nanostructures with the morphology of nanowire and nanobelt can be obtained in our process. Moreover, the diameter and length of the synthesized ZnO, CuO, and Fe_2O_3 nanostructures can be tailored via the change of growth temperature.

Table 1 summarizes the characteristics of zinc oxide, copper oxide, and iron oxide nanostructures obtained in this work.

Table 1. Characteristics of the zinc oxide, copper oxide, and iron oxide nanostructures produced in this work.

MO	ZnO	CuO	Fe_2O_3
Growth time	30 min	30 min	30 min
Growth temperature	300–500 °C	300–500 °C	400–600 °C
Diameter	110–396 nm	70–600 nm	/
Length	0.4–1.8 μm	0.8–1.4 μm	/
Growth direction	<0001>	<111>	<001>

3.3. Raman Analysis

The synthesized ZnO nanostructures had a hexagonal (wurtzite-type) structure (SG C_{6v}). In this structure, there are 12 normal vibration modes of ZnO (three of 12 modes are acoustic phonon vibrations, while nine of 12 modes are optical phonon vibrations). The normal lattice vibrations in the cluster basis theory satisfy $\Gamma_{opt} = A_1(z) + 2B_1 + E_1(x,y) + 2E_2$, where A_1 contains A_1(LO) and A_1(TO), while E_1 contains E_1(LO) and E_1(TO). These A_1 and E1 optical phonons are frequently observed in the Raman and infrared spectroscopy. In addition, two B_1 modes are inactive for Raman and infrared spectroscopy, and they are usually called silent mode. Also, two E_2 modes are nonpolar optical phonon and are Raman active [42,43].

A typical Raman spectrum of ZnO nanostructures produced at a processing temperature of 450 °C is presented in Figure 6a; there is a strong Raman scattering peak located at 437 cm^{-1}. This peak is the nonpolar E_2 mode of the ZnO phase. A weak peak located at 559 cm^{-1} is the A_1 (LO) vibration mode of the ZnO crystal [27]. This peak is specific for ZnO nanostructures, which is consistent with the SEM result. The peak of the E_1 (LO) vibration mode of the ZnO crystal located at approximately 583 cm^{-1} was not found in the Raman spectrum, and this peak is related to the oxygen deficiency of zinc oxide. Therefore, it is reasonable to conclude that the synthesized ZnO nanomaterials contained few oxygen-related defects.

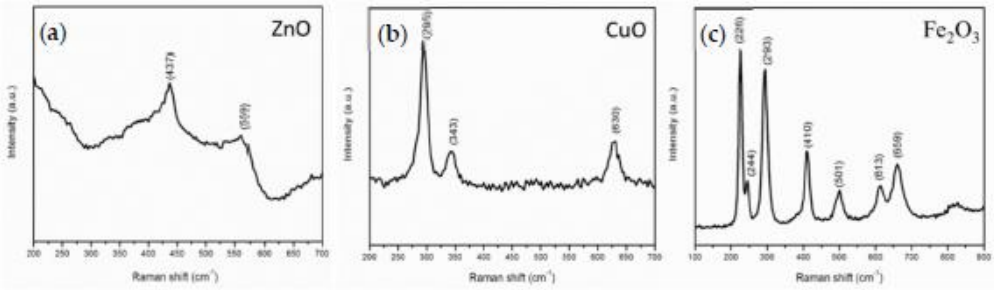

Figure 6. Characteristic Raman spectra of the ZnO nanostructures (**a**), CuO nanostructures (**b**), Fe_2O_3 nanostructures (**c**), produced at a processing temperature of 450 °C, 300 °C, 600 °C, respectively.

The space group of copper oxide is C^6_{2h}. There are 12 optical phonon active modes, and these vibration modes satisfy $\Gamma_{opt} = 4A_u + 5B_u + A_g + 2B_g$. Among these vibration modes, A_g and $2B_g$ are Raman active. According to the Raman spectrum of copper oxide nanostructures produced at a processing temperature of 300 °C shown in Figure 6b, there are three Raman scattering peaks located at 295, 343, and 630 cm^{-1} in the range of 200–700 cm^{-1}, which represent vibration modes for A_g, B_{1g} and B_{2g}, respectively. These three peaks are red-shifted compared to the corresponding Raman peaks of the copper oxide crystals located at 303, 350, and 636 cm^{-1}, respectively, which is attributed to the tensile stress [43].

The Raman spectrum of the iron oxide nanostructures produced at a processing temperature of 600 °C is presented in Figure 6c. Fe_2O_3 belongs to the D^6_{3d} space group. Six Raman peaks located at 226, 244, 293, 410, 501, and 613 cm^{-1} in the range of 100–700 cm^{-1} are attributed to the iron oxide nanostructures. The Raman peaks located at 226 and 244 cm^{-1} originate from A_{1g} Raman vibration modes while the other four peaks located at 293, 410, 501, and 613 cm^{-1} originate from E_g Raman vibration modes. In addition, the peak located at 659 cm^{-1} belongs to Fe_3O_4 [15].

Raman analysis further substantiated that ZnO, CuO, and Fe_2O_3 nanostructures can be obtained in our custom-made plasma-enhanced horizontal tube furnace deposition system.

3.4. Growth Mechanism

The present work is a catalyst-free plasma-assisted processing route for the production of single-crystalline metal oxide nanostructures. However, in the presence of the plasma species, classical growth mechanisms from thermal oxidation have to be modified. In the described synthesis, not only the surface temperature but also the plasma plays an essential role by exciting the gas reactants and thus promoting the chemical reaction. As shown in Figure 7, under the optimum processing temperature, small metal particles are formed on the surface of the metal foil. Then, in the O_2-Ar gas atmosphere, oxygen gas is ionized into O^+ and O^{2+} ions while argon gas assists oxygen gas to be ionized effectively under the plasma discharge. After that, oxygen molecules are also converted to metastable oxygen atoms, neutral oxygen atoms, excited oxygen molecules, molecular oxygen ions, etc. Finally, these oxygen species react with metal atoms on the surface, and subsequently, metal oxide nanostructures are formed. Some of the chemical reactions occurring during the growth process for our system are described below:

$$O^+ + Ar \rightarrow O^* + Ar^+ \quad (1)$$

$$O^+ + O_2 \rightarrow O^* + O_2^+ \quad (2)$$

$$O^* + Zn \rightarrow ZnO$$

$$O^* + Cu \rightarrow CuO$$

$$O^* + Fe \rightarrow Fe_2O_3. \quad (3)$$

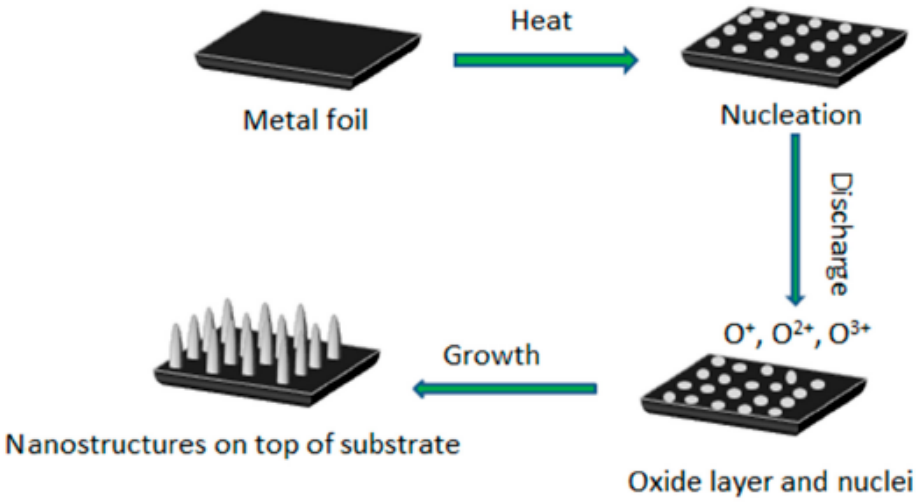

Figure 7. Schematic illustration of the initial stages of the growth process for the metal oxide nanostructures produced under plasma. These stages lead to the nucleation, nanowire growth, and formation of a thin oxide layer.

In the above Equations (1)–(3), O* represents an activated or metastable oxygen atom [31,44].

It is worthwhile to mention that the surface of the metal particles can form micro-hillocks due to the surface roughness of the metal foils during Ar ion bombardment. The surface energy of these micro-hillocks is high so that the activated oxygen atoms can adsorb on these micro-hillocks and then the metal particles will gradually transform to low-dimensional metal oxide nanostructures. This is an entropy reduction process, i.e., $\Delta S < 0$. Owing to the spontaneous process, Gibbs free energy (ΔG) is also less than zero. According to the equation $\Delta G = \Delta H - T\Delta S$, it can be concluded that the enthalpy is reduced, so this is an exothermic process [43,44]. Notably, the adsorption of metal oxide species on the substrate is an exothermal process. Also, the recombination of activated oxygen atoms in the gas environment, the adsorption of argon and oxygen ions on the substrate, and the reaction of oxygen ions with metal particles release some extra energy on the metal micro-hillocks [31,44,45].

When the experimentally measured length and diameter of CuO and ZnO nanowires are considered at different growth temperatures, the difference in the aspect ratios becomes apparent. Specifically, CuO nanowires, grown in the temperature range from 300 °C to 400 °C, were initially long and thin at 300 °C (aspect ratio is about 11.4), and gradually changed to the bulk shape with the aspect ratio of about 2.3 at 400 °C. At the same time, ZnO nanowires started to grow at 400 °C and they also had the bulk shape (aspect ratio of about 1.0), which then turned to an elongated structure with the aspect ratio of about 13.8 when the growth temperature rose to 500 °C.

To explain the difference in the growth behavior, a theoretical model described elsewhere [38] was applied. For the modelling we selected CuO and ZnO nanostructures due to similarity of their chemical formula and similarity of the observed geometry of the growing nanostructures (as Fe_2O_3 nanostructures exhibit a more ribbon-like structure with pronounced anisotropy perpendicular to the vertical growth direction).

Table 2 lists the experimental and theoretical values for the ZnO and CuO nanostructures synthesized at different growth temperatures and a growth time of 30 min. One can notice the values L_{nw} (30 min) and D_{nw} (30 min) of ZnO and CuO nanostructures are very close to the corresponding experimentally measured values.

Table 2. Comparison of the experimental and theoretical values for the ZnO and CuO nanostructures synthesized at different growth temperatures and a growth time of 30 min.

Metal Oxide	Growth Temperature, °C	Experimental Value		Theoretical Value	
		Length, μm	Diameter, μm	Length, μm	Diameter, μm
ZnO	400	0.4	0.396	0.374	0.377
	450	1.4	0.110	1.267	0.106
	500	1.8	0.130	1.823	0.106
CuO	300	0.8	0.070	0.763	0.075
	350	0.9	0.075	0.873	0.075
	400	1.4	0.6	1.486	0.558

The experimental results are plotted in Figure 8, where the difference in growth behavior is clearly seen. The growth temperature for ZnO shifted to the higher temperature, and the length of the nanowires exhibited monotonic growth at the temperature increase. Qualitatively, this behavior can be explained by the increased diffusion of the species at the elevated temperature, yet the adsorption of oxygen on the surface is still significant. However, the diameter of the CuO nanostructures also increased with the temperature, while ZnO nanostructures showed the opposite trend. Our numerical simulations reveal the nature of the process.

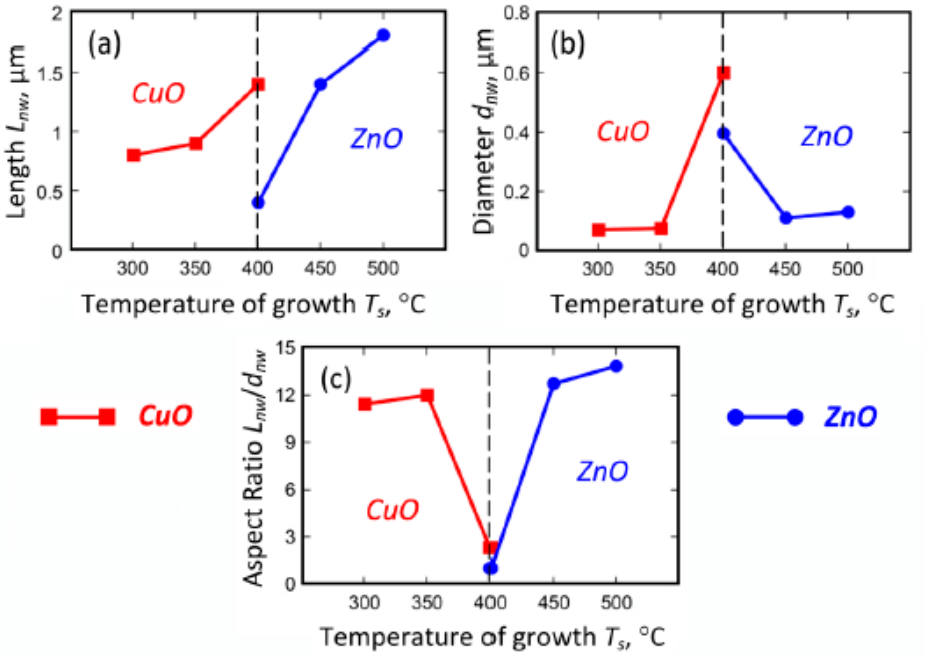

Figure 8. Experimental results on measurement of CuO and ZnO nanostructures: (**a**) length; (**b**) diameter; (**c**) aspect ratio.

When trying to fit the simulation with the experimental data, we found that two parameters were responsible for the difference in the growth behavior, namely, the activation energy ε_d of the copper (or zinc) diffusion and the density of the oxygen molecules adsorbed on the substrate surface.

In the model, the copper (or zinc) diffusion is described with the expression:

$$D_a = D_0 exp\left(-\frac{e\varepsilon_d}{k_B T_s}\right), \tag{4}$$

where ε_d is the activation energy, eV; D_0 is a constant; T_s is the growth temperature (K). The adsorption of oxygen molecules is expressed as a ratio of the surface density n_{O2} of the molecules (m^{-2}) to the density n_0 of the adsorption nodes (m^{-2}) on the substrate surface, and is described by the Langmuir adsorption isotherm [46]:

$$\frac{n_{O2}}{n_0} = \frac{P_{O2}}{P_0 + P_{O2}}, \tag{5}$$

where P_{O2} is the partial pressure of oxygen, Pa; P_0 is a constant that does not depend on the pressure P_{O2}, but depends on the temperature; n_0 is a surface density of the oxide adsorption nodes. The value of the constant P_0 is expressed as [46]

$$P_0 = \left(\frac{M_{O2}}{2\pi h^2}\right)^{3/2} (k_B T_s)^{5/2} exp\left(-\frac{e\varepsilon_{aO2}}{k_B T_s}\right), \tag{6}$$

where M_{O2} is the mass of the oxygen molecule, kg; ε_{aO2} is the oxygen adsorption energy, eV; h is Planck's constant.

The partial pressure of oxygen is expressed as

$$P_{O2} = \frac{\phi_{O2}}{\phi_{Add} + \phi_{O2}} P, \tag{7}$$

where ϕ_{O2} and ϕ_{Add} are the flow rates of the oxygen and additional gas (argon, in our case) sccm and P is the total gas pressure in the chamber, Pa.

We applied the different values of the diffusion activation energy ε_d and oxygen adsorption energies ε_{aO2} to fit the experiment and obtained the growth dependencies of the nanowire length (L_{nw}) and diameter (D_{nw}), shown in Figure 9a for CuO and in Figure 9b for ZnO.

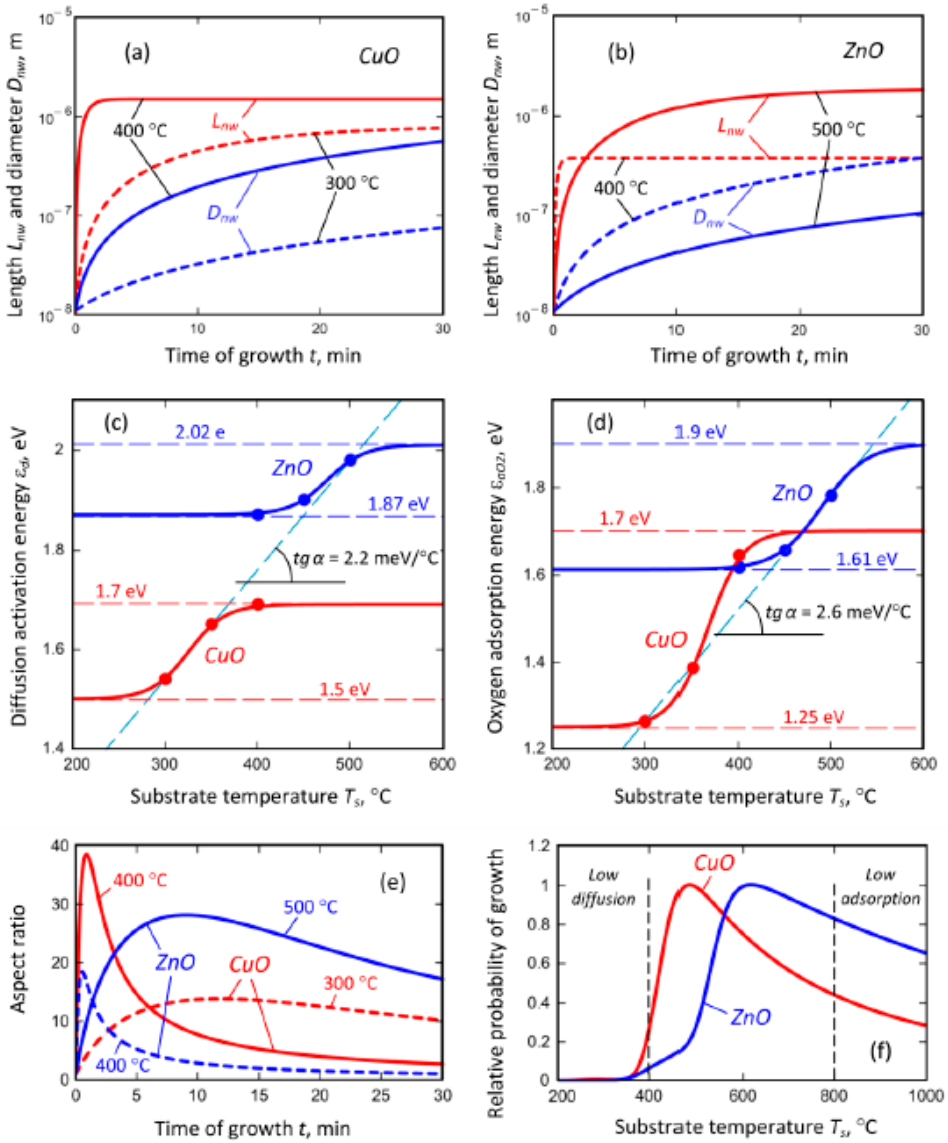

Figure 9. Results of calculations of the oxide dynamics: (**a**,**b**) dependencies of the nanowire length and diameter on the growth time; (**c**,**d**) dependencies of the copper diffusion activation energy and oxygen adsorption energy on the growth temperature; (**e**) nanowire aspect ratio at dependence on the time of growth; (**f**) relative probability of the nanowire growth at dependence on the substrate temperature.

Generally, we calculated the growth dynamics for three values of the growth temperature for both oxides: 300, 350, and 400 °C for CuO; 400, 450, and 500 °C for ZnO. However, the dependencies for the intermediate temperatures (350 °C for CuO and 450 °C for ZnO) almost superimposed with the characteristics for 300 °C for CuO and 500 °C for ZnO; and thus they are not shown in Figure 9 a–b. However, the diffusion activation energy ε_d and oxygen adsorption energies ε_{aO2} used in the calculations were quite different, and they are present as dots in Figure 9c (ε_d) and Figure 9d (ε_{aO2}). While considering the energies, one can notice that the diffusion activation energy ε_d for CuO seemed to saturate on the upper limit (1.7 eV), while the diffusion activation energy ε_d for ZnO seemed to saturate on the lower limit (1.87 eV). It should be stressed that the energies were calculated for the plasma-enhanced growth and these adsorption and diffusion energies can differ significantly from

the values predicted for the thermal growth on ideal crystal lattice due to the ion bombardment of the surface. Then, we speculated that the dependencies should have a similar behavior at the dependence on the temperature, which means that both energies should have saturated values. As a result, the analytical expressions were obtained as follows:

$$\varepsilon_{d(CuO)} = \left(1 - \xi_{d(CuO)}\right)\varepsilon^{low}_{d(CuO)} + \xi_{d(CuO)}\varepsilon^{high}_{d(CuO)} \quad (8)$$

$$\varepsilon_{d(ZnO)} = \left(1 - \xi_{d(ZnO)}\right)\varepsilon^{low}_{d(ZnO)} + \xi_{d(ZnO)}\varepsilon^{high}_{d(ZnO)} \quad (9)$$

where $\varepsilon^{low}_{d(CuO)} = 1.5$ eV; $\varepsilon^{high}_{d(CuO)} = 1.7$ eV; $\varepsilon^{low}_{d(ZnO)} = 1.87$ eV; $\varepsilon^{high}_{d(ZnO)} = 2.02$ eV.

Similar arguments led us to the conclusion that the oxygen adsorption energies ε_{aO2} can be fit with the following equations

$$\varepsilon_{aO2(CuO)} = \left(1 - \xi_{aO2(CuO)}\right)\varepsilon^{low}_{aO2(CuO)} + \xi_{aO2(CuO)}\varepsilon^{high}_{aO2(CuO)} \quad (10)$$

$$\varepsilon_{aO2(ZnO)} = \left(1 - \xi_{aO2(ZnO)}\right)\varepsilon^{low}_{aO2(ZnO)} + \xi_{aO2(ZnO)}\varepsilon^{high}_{aO2(ZnO)} \quad (11)$$

where $\varepsilon^{low}_{aO2(CuO)} = 1.2$ eV; $\varepsilon^{high}_{aO2(CuO)} = 1.7$ eV; $\varepsilon^{low}_{aO2(ZnO)} = 1.61$ eV; $\varepsilon^{high}_{aO2(ZnO)} = 1.9$ eV.

In the above expressions, the functions $\xi_{i(j)}$ are described by the equation

$$\xi_{i(j)} = \frac{exp\left[\frac{T_s - \left(L_{i(j)} - \delta L_{i(j)}\right)}{\delta L_{i(j)}}\right]}{1 + exp\left[\frac{T_s - \left(L_{i(j)} - \delta L_{i(j)}\right)}{\delta L_{i(j)}}\right]} \quad (12)$$

with parameters $L_{d(CuO)} = 345$ K, $\delta L_{d(CuO)} = 20$ K; $L_{d(ZnO)} = 495$ K, $\delta L_{d(ZnO)} = 20$ K; $L_{aO2(CuO)} = 385$ K, $\delta L_{aO2(CuO)} = 19$ K; $L_{aO2(ZnO)} = 514$ K, $\delta L_{aO2(ZnO)} = 24.5$ K; and the function $1 - \xi_{i(j)}$ has the shape of the Fermi–Dirac distribution [46].

The results of the approximation are shown in Figure 9c,d. From the analysis of the graphical dependencies, it can be seen that the slopes of the curves on both Figure 9c,d are almost the same, i.e., 2.2 meV/°C for diffusion (ε_d), and 2.6 meV/°C for adsorption (ε_{aO2}). This result allows us to assume that the nature of the change for the adsorption and diffusion energies on the growth temperature is the same and does not depend on the oxide chemical composition.

In addition, we calculated the dependence of the aspect ratio of the nanowires for CuO and ZnO, shown for different growth temperatures in Figure 9e. In spite of the fact that the experimentally measured values exhibited short and bulk nanowires for the growth temperature of 400 °C for both oxides, the calculations show the possibility to obtain the structure with a rather high aspect ratio of about 20 to 40 for the short plasma exposure time of about 1–2 min, yet the length of the nanowires were quite small. It should be noted that the possibility of growing the high-aspect nanowires over the short exposure time was confirmed by the experimental results obtained for the plasma-enhanced growth of CuO nanowires described in our previous paper [38].

Then, the calculated energies were used to estimate the relative probability of the nanowire growth described by the expression [47]:

$$P_{rel-growth} = \frac{\frac{P_{O2}}{P_0(T_s) + P_{O2}} exp\left(-\frac{e\varepsilon_d}{k_B T_s}\right)}{\frac{P_{O2}}{P_{0(T_{s(max)})} + P_{O2}} exp\left(-\frac{e\varepsilon_d}{k_B T_{s(max)}}\right)} \quad (13)$$

where $T_{s(max)}$ is the temperature where the maximum of the function $\frac{P_{O2}}{P_0(T_s) + P_{O2}} exp\left(-\frac{e\varepsilon_d}{k_B T_s}\right)$ is obtained, i.e., we related the whole distribution to its maximum value. The calculated result is shown in

Figure 9f. We can see that both curves exhibit a maximum that separates the region where the growth is suppressed by the low diffusion due to the low temperature, from the region where the growth is suppressed by the small adsorption caused by the high substrate temperature. These results seem to be generic and could be further applied for the explanation of similar growth patterns of single-crystal metal oxide nanostructures.

Now, we can conclude the reason for the different behavior of the nanostructure growth; when at the temperature increase, CuO NWs become thick, while ZnO exhibits a large aspect ratio. According to the calculations, the oxygen adsorption energy increases with the temperature in the measured temperature range. However, for CuO the increase was more significant (Figure 9d)—from 1.25 to 1.7 eV (+0.45 eV or 36% from the initial value), while for ZnO the change was from 1.61 to 1.9 eV (+0.29 eV or 18% from the initial value). This results in the increased adsorption rates of oxygen on the side surface of the growing CuO nanostructure, and hence, the oxidation reaction is more intensive, and the nanostructure becomes thicker. On the contrary, the adsorption of oxygen on ZnO nanostructures decreases due to the increase of the temperature and not-so-strong increase of the adsorption energy, hence the nanostructure grows in height but not in diameter.

Another important point revealed by the modelling is a possible dependence of the adsorption energies on the ion flux extracted from plasma to the growth surface. Generally, the ion bombardment damages the surface and results in the generation of a large number of the surface defects, activation of chemical bonds, surface fictionalization etc. [48]. This effect can promote the formation of the nanostructures and tailor their parameters; however, the calculation of the adsorption energies is rather complicated since the methods based on a thermal equilibrium approach fail. Therefore, our calculation results may be useful concerning similar systems, where a plasma-enhanced approach is applied.

In this subsection, chemical reactions occurring for the growth of ZnO, CuO, and Fe_2O_3 nanostructures under the plasma-based process have been proposed. Moreover, a growth model has been developed for the interpretation of different growth behaviors of ZnO and CuO nanostructures by considering the activation energy ε_d of the copper (or zinc) diffusion, and the density of the oxygen molecules adsorbed on the substrate surface.

3.5. Advantages of Plasma-Based Process and Outlook of This Work

In comparison with neutral gas-based (thermal CVD) processes, the plasma-based approach has several advantages: (i) The plasma generates reactive oxygen radicals in the gas phase. This eliminates the need to heat the surface to high temperatures when dissociation of oxygen on the surface becomes effective. (ii) The plasma also creates an electric field through the formation of the plasma sheath. This electric field can effectively guide the nanowire growth and enable the growth of vertically aligned nanostructures. (iii) The plasma provides localized surface heating through recombination of as-created oxygen atoms and also through ion bombardment and neutralization, which can further increase the surface temperature. (iv) Plasma can also create localized nucleation spots via the ion bombardment as well as some other plasma-related effects, which makes the use of metal catalysts unnecessary. (v) The morphology, diameter, faceting, crystallinity, and composition of the metal oxide nanostructures can be effectively tailored by the process parameters.

Future work should involve in situ plasma diagnostic tools such as Langmuir probe and optical emission spectroscopy, to investigate the chemical reactions during the growth of metal oxide nanostructures in our custom-made plasma-enhanced horizontal tube furnace deposition system. Further comparisons of our process with other plasma-based processes, such as inductively coupled plasma process, and in-depth studies of the difference between our process and other plasma-based processes for the growth of metal oxide nanostructures are envisaged.

4. Conclusions

Several metal oxide nanostructures were grown on the metal foils by the customized plasma-enhanced thermal oxidation process. The morphology and microstructure of the synthesized metal oxide nanostructures can be effectively controlled by the process temperatures. Under catalyst-free conditions, plasma-treated metal foils were activated to grow metal oxide nanostructures. The synthesized single-crystal metal oxide nanostructures were investigated and characterized by XRD, SEM, TEM, and Raman spectroscopy. Moreover, a viable growth mechanism supported by nanostructure growth modelling was proposed to interpret the obtained experimental results. This work is relevant to the development of advanced processes for the synthesis of metal oxide nanostructures.

Author Contributions: Q.C. designed the experiment; B.G. and J.F. carried out the experiment and wrote the paper draft; M.K. contributed to writing and the oxide dynamics; Y.Q., G.L., and J.Z. characterized the synthesized metal oxide nanostructures and analyzed the characterization result; O.B., U.C., and K.O. contributed to the analysis of the experimental results, numerical modelling, results interpretation, and paper writing. All authors discussed the results and contributed to the manuscript preparation.

Funding: This research was funded by Shenzhen Science and Technology Innovation Committee (Grant No. JCYJ20170306141238532), China, and Slovenian Research Agency (ARRS) (Grant No. L2-7667 and P2-0082).

Acknowledgments: K.O. thanks the Australian Research Council for partial support.

Conflicts of Interest: The authors declare no conflict of interest.

References

1. Su, B.; Wu, Y.; Jiang, L. The art of aligning One-Dimensional (1D) nanostructures. *Chem. Soc. Rev.* **2012**, *41*, 7832–7856. [CrossRef] [PubMed]
2. Cheng, Q.J.; Ostrikov, K. Temperature-Dependent growth mechanisms of Low-Dimensional ZnO nanostructures. *Crystengcomm* **2011**, *13*, 3455–3461. [CrossRef]
3. Garino, N.; Limongi, T.; Dumontel, B.; Canta, M.; Racca, L.; Laurenti, M.; Castellino, M.; Casu, A.; Falqui, A.; Cauda, V.A. Microwave-Assisted synthesis of zinc oxide nanocrystals finely tuned forbiological applications. *Nanomaterials* **2019**, *9*, 212. [CrossRef] [PubMed]
4. Zhang, A.Q.; Zhang, L.; Sui, L.; Qian, D.J.; Chen, M. Morphology-Controllable synthesis of ZnO Nano-Microstructures by a solvothermal process in ethanol solution. *Cryst. Res. Technol.* **2013**, *48*, 947–955. [CrossRef]
5. Choopun, S.; Tubtimtae, A.; Santhaveesuk, T.; Nilphai, S.; Wongrat, E.; Hongsith, N. Zinc oxide nanostructures for applications as ethanol sensors and Dye-Sensitized solar cells. *Appl. Surf. Sci.* **2009**, *256*, 998–1002. [CrossRef]
6. Guo, K.W. Property of zinc oxide (ZnO) nanostructures potential for biomedical system and its common growth mechanism. *J. Appl. Biotechnol. Bioeng.* **2017**, *2*, 197–202. [CrossRef]
7. Cha, S.N.; Song, B.G.; Jang, J.E.; Jung, J.E.; Han, I.T.; Ha, J.H.; Hong, J.P.; Kang, D.J.; Kim, J.M. Controlled growth of vertically aligned ZnO nanowires with different crystal orientation of the ZnO seed layer. *Nanotechnology* **2008**, *19*, 235601. [CrossRef]
8. Cheng, Q.J.; Ostrikov, K. Property-Performance control of multidimensional, hierarchical, Single-Crystalline ZnO nanoarchitectures. *Chemphyschem* **2012**, *13*, 1535–1541. [CrossRef]
9. Yu, L.B.; Li, Z. Synthesis of $Zn_xCd_{1-x}Se$@ZnO hollow spheres indifferent sizes for quantum dots sensitized solarcells application. *Nanomaterials* **2019**, *9*, 132. [CrossRef]
10. Elhag, S.; Ibupoto, Z.H.; Khranovskyy, V.; Willander, M.; Nur, O. Habit-Modifying additives and their morphological consequences on photoluminescence and glucose sensing properties of ZnO nanostructures, grown via aqueous chemical synthesis. *Vacuum* **2015**, *116*, 21–26. [CrossRef]
11. Cao, M.; Li, Z.; Wang, J.; Ge, W.P.; Yue, T.L.; Li, R.H.; Colvin, V.L. Food related applications of magnetic iron oxide nanoparticles: Enzyme immobilization, protein purification, and food analysis. *Trends Food Sci. Tech.* **2012**, *27*, 47–56. [CrossRef]
12. Mahmoudi, M.; Hosseinkhani, H.; Hosseinkhani, M.; Boutry, B.; Simchi, A.; Journeay, W.S.; Subramani, K.; Laurent, S. Magnetic resonance imaging tracking of stem cells in vivo using iron oxide nanoparticles as a tool for the advancement of clinical regenerative medicine. *Chem. Rev.* **2011**, *111*, 253–280. [CrossRef] [PubMed]

13. Kostopoulou, A.; Brintakis, K.; Fragogeorgi, E.; Anthousi, A.; Manna, L.; Colin, S.B.; Billotey, C.; Ranella, A.; Loudos, G.; Athanassakis, I.; et al. Iron oxide colloidal nanoclusters as theranosticvehicles and their Interactions at the cellular level. *Nanomaterials* **2018**, *8*, 315. [CrossRef] [PubMed]
14. Zhao, Y.M.; Li, Y.H.; Ma, R.Z.; Roe, M.J.; McCartney, D.G.; Zhu, Y.Q. Two-Dimensional tungsten oxide nanowire networks. *Appl. Phys. Lett.* **2006**, *89*, 133116. [CrossRef]
15. Fu, Y.Y.; Wang, R.M.; Xu, J.; Chen, J.; Yan, Y.; Narlikar, A.; Zhang, H. Synthesis of large arrays of aligned alpha-Fe_2O_3 nanowires. *Chem. Phys. Lett.* **2003**, *379*, 373–379. [CrossRef]
16. Fortunato, E.; Figueiredo, V.; Barquinha, P.; Elamurugu, E.; Barros, R.; Goncalves, G.; Park, S.H.K.; Hwang, C.S.; Martins, R. Thin-Film transistors based on P-Type Cu_2O thin films produced at room temperature. *Appl. Phys. Lett.* **2010**, *96*, 191101. [CrossRef]
17. Jiang, X.C.; Herricks, T.; Xia, Y.N. CuO nanowires can be synthesized by heating copper substrates in air. *Nano Lett.* **2002**, *2*, 1333–1338. [CrossRef]
18. Tan, J.; Dun, M.; Li, L.; Zhao, J.; Li, X.; Hu, Y.; Huang, G.; Tan, W.; Huang, X. Self-template derived CuO nanowires assembled microspheres and its gas sensing properties. *Sens. Actuators B: Chem.* **2017**, *252*, 1–8. [CrossRef]
19. Zhang, P.; Wu, J.; Zhang, T.; Wang, Y.; Liu, D.; Chen, H.; Ji, L.; Liu, C.; Ahmad, W.; Chen, Z.D.; et al. Perovskite solar cells with ZnO Electron-Transporting materials. *Adv. Mater.* **2018**, *30*, 1703737. [CrossRef]
20. Sun, X.M.; Liu, J.F.; Li, Y.D. Use of carbonaceous polysaccharide microspheres astemplates for fabricating metal oxide hollow spheres. *Chem.-Eur. J.* **2006**, *12*, 2039–2047. [CrossRef]
21. Wu, W.P.; Wang, Y.Y.; Wu, Y.P.; Liu, J.Q.; Zeng, X.R.; Shi, Q.Z.; Peng, S.M. Hydro(solvo) thermal synthesis, structures, luminescence of 2-D zinc(II) and 1-D copper(II) complexes constructed from pyridine-2,6-Dicarboxylic acid N-Oxide and decarboxylation of the ligand. *Crystengcomm* **2007**, *9*, 753–757. [CrossRef]
22. Zhang, D.H.; Li, C.; Han, S.; Liu, X.L.; Tang, T.; Jin, W.; Zhou, C.W. Electronic transport studies of Single-Crystalline In_2O_3 nanowires. *Appl. Phys. Lett.* **2003**, *82*, 112–114. [CrossRef]
23. Shen, G.; Chen, P.C.; Ryu, K.; Zhou, C. Devices and chemical sensing applications of metal oxide nanowires. *J. Mater. Chem.* **2009**, *19*, 828–839. [CrossRef]
24. Sun, Z.; Liao, T.; Kou, L. Strategies for designing metal oxide nanostructures. *Sci. China Mater.* **2017**, *60*, 1–24. [CrossRef]
25. Devan, R.S.; Patil, R.A.; Lin, J.H.; Ma, Y.R. One-Dimensional Metal-Oxide nanostructures: Recentdevelopments in synthesis, characterization, andapplications. *Adv. Funct. Mater.* **2012**, *22*, 3326–3370. [CrossRef]
26. Lee, S.H.; Lee, S.W.; Oh, T.; Petrosko, S.H.; Mirkin, C.A.; Jang, J.-W. Direct observation of Plasmon-Induced interfacial charge separation in metal/semiconductor hybrid nanostructures by measuring surface potentials. *Nano Lett.* **2018**, *18*, 109–116. [CrossRef]
27. Bao, Y.; Wang, C.; Ma, J.Z. A Two-Step hydrothermal route for synthesis hollow Urchin-Like ZnO microspheres. *Ceram. Int.* **2016**, *42*, 10289–10296. [CrossRef]
28. Zhong, M.; Guo, W.M.; Li, C.L.; Chai, L. Morphology-Controllable growth of vertical ZnO nanorod arrays by a polymer soft template method: Growth mechanism and optical properties. *J. Alloy. Compd.* **2017**, *725*, 1018–1026. [CrossRef]
29. Mao, C.; Xiang, Y.; Liu, X.; Cui, Z.; Yang, X.; Yeung, K.W.K.; Pan, H.; Wang, X.; Chu, P.K.; Wu, S. Photo-Inspired antibacterial activity and wound healing acceleration by hydrogel embedded with Ag/Ag@AgCl/ZnO nanostructures. *ACS Nano* **2017**, *11*, 9010–9021. [CrossRef]
30. Kumar, V.; Kim, J.H.; Pendyala, C.; Chernomordik, B.; Sunkara, M.K. Gas-Phase, bulk production of metal oxide nanowires and nanoparticles using a microwave plasma jet reactor. *Phys. Chem. C* **2008**, *112*, 17750–17754. [CrossRef]
31. Ostrikov, K.; Levchenko, I.; Cvelbar, U.; Sunkara, M.; Mozetic, M. From nucleation to nanowires: A Single-Step process in reactive plasmas. *Nanoscale* **2010**, *2*, 2012–2027. [CrossRef] [PubMed]
32. Morrish, R.; Silverstein, R.; Wolden, C.A. Synthesis of stoichiometric FeS_2 through Plasma-Assisted sulfurization of Fe_2O_3 nanorods. *J. Am. Chem. Soc.* **2012**, *134*, 17854–17857. [CrossRef] [PubMed]
33. Yuan, L.; Zhou, G. The growth of One-Dimensional oxide nanostructures by thermal oxidation of metals. *Int. J. Nano Sci. Nao Eng. Nanotechnol.* **2012**, *4*, 1–22.

34. Cheng, Q.J.; Yan, W.; Randeniya, L.; Zhang, F.; Ostrikov, K. Plasma-Produced Phase-Pure cuprous oxide nanowires for methane gas sensing. *J. Appl. Phys.* **2014**, *115*, 124310. [CrossRef]
35. Altaweel, A.; Imam, A.; Ghanbaja, J.; Mangin, D.; Miska, P.; Gries, T.; Belmonte, T. Fast synthesis of ultrathin ZnO nanowires by oxidation of Cu/Zn stacks in low-pressure afterglow. *Nanotechnology* **2017**, *28*, 085602. [CrossRef]
36. Altaweel, A.; Filipic, G.; Gries, T.; Belmonte, T. Controlled growth of copper oxide nanostructures by atmospheric pressure micro-afterglow. *J. Cryst. Growth* **2014**, *407*, 17–24. [CrossRef]
37. Filipic, G.; Cvelbar, U. Copper oxide nanowires: A review of growth. *Nanotechnology* **2012**, *23*, 194001. [CrossRef]
38. Filipic, G.; Baranov, O.; Mozetic, M.; Cvelbar, U. Growth dynamics of copper oxide nanowires in plasma at low pressures. *J. Appl. Phys.* **2015**, *117*, 043304. [CrossRef]
39. Baranov, O.; Filipič, G.; Cvelbar, U. Towards a Highly-Controllable synthesis of copper oxide nanowires in Radio-Frequency reactive plasma: Fast saturation at the targeted size. *Plasma Sources Sci. Technol.* **2019**, *28*, 084002. [CrossRef]
40. Filipic, G.; Baranov, O.; Mozetic, M.; Ostrikov, K.; Cvelbar, U. Uniform surface growth of copper oxide nanowires in radiofrequency plasma discharge and limiting factors. *Phys. Plasmas* **2014**, *21*, 113506. [CrossRef]
41. Cvelbar, U.; Chen, Z.; Sunkara, M.K.; Mozetic, M. Spontaneous growth of superstructure alpha-Fe_2O_3 nanowire and nanobelt arrays in reactive oxygen plasma. *Small* **2008**, *4*, 1610–1614. [CrossRef] [PubMed]
42. Wu, J.J.; Liu, S.C. Catalyst-Free growth and characterization of ZnO nanorods. *J. Phys. Chem. B* **2002**, *106*, 9546–9551. [CrossRef]
43. Choopun, S.; Hongsith, N.; Wongrat, E.; Kamwanna, T.; Singkarat, S.; Mangkorntong, P.; Mangkorntong, N.; Chairuangsri, T. Growth kinetic and characterization of RF-Sputtered ZnO: Al nanostructures. *J. Am. Ceram. Soc.* **2008**, *91*, 174–177. [CrossRef]
44. Chen, W.Z.; Wang, B.B.; Qu, Y.Z.; Huang, X.; Ostrikov, K.; Levchenko, I.; Xu, S.; Cheng, Q.J. Catalyst-Free growth and tailoring morphology of zinc oxide nanostructures by Plasma-Enhanced deposition at low temperature. *J. Nanopart. Res.* **2017**, *19*, 95. [CrossRef]
45. Mozetic, M.; Cvelbar, U.; Sunkara, M.K.; Vaddiraju, S. A method for the rapid synthesis of large quantities of metal oxide nanowires at low temperatures. *Adv. Mater.* **2005**, *17*, 2138–2142. [CrossRef]
46. Kittel, C.; Kroemer, H. *Thermal Physics*; W. H. Freeman and Co.: New York, NY, USA, 1980.
47. Baranov, O.; Levchenko, I.; Xu, S.; Lim, J.W.M.; Cvelbar, U.; Bazaka, K. Formation of vertically oriented graphenes: What are the key drivers of growth? *2D Mater.* **2018**, *5*, 044002. [CrossRef]
48. Baranov, O.; Fang, J.; Ostrikov, K.; Cvelbar, U. TiN deposition and morphology control by scalable Plasma-Assisted surface treatments. *Mater. Chem. Phys.* **2017**, *188*, 143–153. [CrossRef]

Chapter 3

Exploration of Phase Transformations in CuO NWs

In Chapter 3, the previously synthesized CuO NWs were used as a model material to study phase transformations. The CuO–CuS system was chosen as copper oxides and copper sulfides are materials with a wide range of possible applications. The proposed phase transformation belongs to the class of anion-exchange reactions, where oxygen anions are replaced with sulfur anions. Even though CuO has a different crystal structure from copper sulfides, the sulfurization of CuO via a reaction with H_2S proceeds easily under mild conditions. While only two copper oxide phases are stable in ambient conditions (tenorite – CuO and cuprite – Cu_2O), there are numerous stable copper sulfide phases, such as villamaninite (CuS_2), covellite (CuS), yarrowite($Cu_{1.12}S$), spionkopite ($Cu_{1.39}S$), geerite ($Cu_{1.6}S$), anilite ($Cu_{1.75}S$), digenite ($Cu_{1.8}S$), roxbyite ($Cu_{1.8}S$), djurleite ($Cu_{1.96}S$) and chalcocite (Cu_2S).

Chapter 3 is divided into two sections. The main focus of Section 3.1 lies in studying the mechanism of thermal transformations with a particular emphasis on the effect of the amount of cations that can participate in the reaction.

The focus of Section 3.2 is the introduction of metastable species as anion-exchanging agents to influence the outcome of the transformation. In addition, the effects of size and their influence on the morphology of the transformed NWs are discussed as well.

3.1 Exploration of the Influence of Metal Supply on Phase Transformation in CuO Nanowires

In the research described in Section 3.1, anion-exchange reactions were performed on CuO NWs by exposing them to gaseous H_2S. The emphasis of the study was on the mechanism of the transformation. This research reports an interesting observation that was not highlighted in the literature yet. It was found that the mechanism and the outcome of the transformation differ if the NWs have a limited or unlimited supply of cations during the transformations. This was studied by sulfurizing the NWs with the roots still embedded in copper oxide layers acting as an additional source of copper cations and the sulfurization of NWs that were detached from the substrate and thus had a limited copper supply. The mechanisms of both types of transformations are discussed and supported by theoretical modeling.

The results of this subsection were summarized in a manuscript submitted to the journal *Nature Communications*.

Regarding my contribution, I performed the experiments, analyzed the results, and wrote the initial manuscript.

Driving the phase transformation in single crystals by diffusion

Authors and affiliations

Department of Gaseous Electronics, Jožef Stefan Institute, 1000 Ljubljana, Slovenia

Martin Košiček, Janez Zavašnik, Oleg Baranov, Uroš Puc, Uroš Cvelbar

Jožef Stefan International Postgraduate School, 1000 Ljubljana, Slovenia

Martin Košiček, Janez Zavašnik, Uroš Cvelbar, Uroš Puc

Department of Theoretical Mechanics, Engineering and Robomechanical Systems, National Aerospace University, 61070 Kharkiv, Ukraine

Oleg Baranov

Institute of Computational Physics, Zurich University of Applied Sciences (ZHAW), 8401 Winterthur, Switzerland

Uroš Puc

Abstract

Anion-exchange reactions provide a unique insight into the reaction processes that occur during the phase transformations in ionic nanomaterials and offer a promising method for synthesizing new nanomaterials. In this research we demonstrate that the outcome of the anion-exchange transformation in nanomaterials can vary depending on whether the treated nanomaterial has a limited or unlimited supply of cations. This was demonstrated by sulfurizing isolated CuO nanowires and CuO nanowires attached to copper-rich substrates. In the former case, the sulfurization proceeds via an anion-exchange mechanism with the outward diffusion of copper and oxygen species and the inward diffusion of sulfur species, resulting in polycrystalline covellite nanowires. On the other hand, an additional mechanism, resulting in copper diffusion from the copper-rich substrate into the nanowire, is present in the latter case, leading to the further growth of nanowires and the formation of larger chalcocite nanostructures. The reported difference between the two mechanisms is important from the fundamental and applicative perspectives.

Introduction

Solid-state ion-exchange reactions represent a promising route for the synthesis of ionic nanomaterials and show great potential, particularly for the synthesis of metastable nanoparticle morphologies and phases that are difficult to fabricate using bottom-up techniques [1–5]. Additionally, ion-exchange reactions provide a unique opportunity to observe different, yet unexplored, phenomena and mechanisms occurring at the nanoscale during phase-transformation reactions

In general, cation-exchange reactions are easier to achieve and more commonly lead to the preservation of the morphology and single crystallinity of the synthesized material compared to anion-exchange reactions. This is attributed to the larger size and lower mobility of the anions,

resulting in the greater rigidity and resilience of the anion sublattice during the transformations[1,6]. On the other hand, anion-exchange reactions are often accompanied by a structural breakdown, reorganization, and hollowing due to the large rearrangements accompanying the anion-exchange transformation. Commonly, anion-exchange reactions result in the formation of hollow structures due to the Kirkendall effect[1,6–8], which can be either a desirable or undesirable side effect and results from the more rapid outward diffusion of cations compared to a slower inward diffusion. This phenomenon is challenging to overcome and could present a problem when it is not wanted. Strategies to avoid it remain in development. One such strategy effectively utilized for this purpose is to use an anion-extracting agent to form anion vacancies, which aid the anion lattice diffusion and increase the anion mobility. This method was utilized on single-crystalline Fe_3O_4 nanoparticles to transform them into single-crystalline Fe_3S_4 nanoparticles[9]. Another research where hollowing and breakdown of the structure were avoided was the transformation of CdNCN nanoparticles to CdSe nanoparticles[10]. In this case, the anion diffusion was facilitated due to the anisotropic arrangement of the NCN^{2-} anions, resulting in the formation of 2D channels that facilitated the outward anion diffusion, while minimally impacting the cation sublattice. Nevertheless, improvements to the suppression of the Kirkendall effect in anion-exchange reactions are rare, and further research is required on this topic.

Metal oxides and sulfides are frequently studied template nanomaterials in anion-exchange reactions due to their facile synthesis and wide range of applications, including gas sensing[11–14], photocatalysis[15–26], catalysis[27–33], energy storage[34–50] and biomedical[51–54].

When performing an anion-exchange reaction, several factors can influence the outcome and must be considered. Apart from the experimental conditions, such as temperature, pressure, and anion-exchanging reagents, the morphology and phase of the initial nanomaterial also play a role[2]. Furthermore, structural rearrangements and ion migrations indicate that it might not be

trivial as to whether the anion exchange is performed on isolated nanoparticles or if the nanoparticles are in contact with an additional source of ions that could participate in the reaction. An example of such a system is nanoparticles grown on top of bulk material. This factor is commonly neglected in the literature; however, it may play a major role in the synthesis procedures and applications of nanomaterials.

The dependence of the phase-transformation mechanism on the metal cation supply has been confirmed in our research, where we used thermally grown CuO nanowires (NWs) as a template material for an anion-exchange reaction of oxygen with sulfur. We report an interesting finding that the mechanism of sulfurization differs depending on whether the NW roots are embedded in the copper-rich substrate, enabling them access to an unlimited supply of cations, or whether they are isolated with a limited cation supply. The difference is reflected in the phase and morphology of the sulfurized NWs. It is a consequence of the interaction between the substrate and the NWs that enables the transport of additional cations in the NW during the sulfurization of NWs with roots embedded in the substrate. We also observed that an additional supply of copper in the NWs during the transformation prevents the hollowing of the NWs during the anion-exchange reaction.

Results

CuO NWs used as template material for sulfurization were grown via the thermal oxidation of copper foil. The process of copper oxidation includes the formation of a Cu_2O layer directly on top of the copper substrate, upon which the CuO layer is formed and serves as the starting point for the growth of the NWs[55–58], as depicted in Fig. 1a, which shows a cross-sectional view of the CuO NWs grown at 490 °C. The NW roots are embedded in the upper CuO layer[55]. The presence of both phases was also confirmed by Raman spectroscopy, as shown in Supplementary Fig. 4b. The temperature used to prepare our template NWs was 265 °C, resulting in the highest NW

number density, with sufficiently thin NWs. As depicted in Fig. 1b, the surface of the oxidized copper foil is uniformly covered with CuO NWs growing from the formed CuO film. Most NWs are thin, with diameters below 20 nm (examples can be seen in Supplementary Fig. 3). However, thicker NWs with diameters up to 50 nm have also been observed (Fig. 1c,d). The NWs appear to be single crystalline with a central twin boundary, which was previously reported (marked with the red dashed line in Fig. 1c, and Supplementary Fig. 3) and is likely the reason for the one-dimensional growth of the CuO NWs[59]. Different twinning planes have been observed thus far[60]. NWs preferentially grow along the [1-10] direction. The CuO NWs grow at their tips, indicating that copper species are supplied from the underlying copper substrate to the top of the NW, where the reaction with oxygen can proceed to form CuO and elongate the NW[59,61]. The central twin boundaries are believed to play a major role in this process as they can serve as a pathway for the copper's transport from the underlying copper oxide layers to the tops of the NWs[61].

Oxide-to-sulfide phase transformations were conducted in two regimes (Fig. 1e): (1) First, the whole oxidized copper substrate with the grown CuO NWs was exposed to H_2S. In this case, the substrate represents an additional source of copper cations that could potentially participate in the sulfurization of the NWs. (2) In the second case, the NWs were detached from the substrate before the H_2S treatment. Here, only material present in the NW can participate in the sulfurization, and the amount of copper cations is limited.

The first sulfurization was performed on NWs still attached to the copper-rich substrate at room temperature (24 °C) at an H_2S pressure of 100 kPa for 2 hours. The substrate with the attached NWs appeared to corrode; it developed pronounced dents, pores and changed color from blackish to a more brownish hue (Supplementary Fig. 4a). The appearance of an additional peak at a wavenumber of approximately 470 cm^{-1} in the Raman spectrum indicates the presence of the sulfide phase (Supplementary Fig. 4b). SEM (Fig. 1f) and TEM (Fig. 1g) analyses indicate that upon sulfurization, the NWs became thicker, longer and polycrystalline. Most NWs experienced

thickening during the transformation. However, we also found some that underwent only a small increase in volume, indicating that they were still in the early stages of the transformation, allowing us to observe different levels of transformation (Fig. 1g and additional examples in Supplementary Fig. 5).

From the electron microscopy it is evident that a volume increase occurred during the sulfurization of the NWs. In the later stages of sulfurization, the volume of the NWs can increase by more than ten times. The sulfurized nanostructures exhibit a structure composed of a bulky head and trunk, which progressively narrows towards the bottom of the structure (Fig. 1f). This indicates that the reaction proceeds at a faster rate at the top of the NW and gradually decreases towards the base. The ratio between copper and sulfur was determined in both the NWs and the thin layer serving as the base for the NW growth using energy-dispersive X-ray spectroscopy (EDS) (Fig. 1h and Supplementary Fig. 12a, respectively). Both measurements yield the same Cu:S ratio of approximately 70:30, which is understandable since they exhibited the same chemical composition (CuO) prior to sulfurization. The sulfide formed was determined to be low chalcocite (Cu_2S) based on a polycrystalline selected-area-electron-diffraction (SAED) pattern analysis (Supplementary Fig. 12b).

Due to the volume increase of the NWs during sulfurization, it is clear that when sulfurization is performed on NWs with an unlimited supply of copper, additional copper species will diffuse inside the NW, contributing to the NW growth.

In the second experiment, the NWs were detached from the substrate and deposited on a TEM grid before sulfurization. The sulfurization was conducted under the same conditions as in the experiment with the NWs attached to the substrate (24 °C, H_2S pressure 100 kPa, 2 hours). By disconnecting the contact between the NWs and the underlying layers, the additional diffusion of copper species in the NW during sulfurization is prevented. The amount of cations potentially involved in the reaction is limited to the copper present in the initial CuO NW.

In this case the morphology of the NWs does not change significantly during the reaction. However, they become encapsulated with a predominantly amorphous sulfur-containing layer, approximately 3 nm thick (Fig. 1i-k and Supplementary Fig. 7). On the other hand, no sulfur was found on other parts of the TEM grid by EDS analysis (Fig. 1j), indicating that the layer is most likely a result of the chemical reaction between the CuO and H_2S on the NW surface. However, the tendency of CuO NWs to react with H_2S was not nearly as high as when the NWs were still in contact with the underlying substrate from which they grew.

Therefore, from the initial results it is clear that there are two possible reaction pathways to form the copper sulfide phase from the CuO NWs, both potentially contributing to the reaction: (i) Mechanism 1 involves an anion-exchange reaction of the oxygen anions in the CuO material present in the NWs with sulfur anions, and (ii) Mechanism 2 involves the reaction of H_2S with the copper species diffusing from the underlying substrate on which the NWs grow, into the NW during the reaction, contributing to additional NW growth. Mechanism 1 can in theory be isolated by disconnecting the NW from the source of the additional cations. On the other hand, since the reaction by Mechanism 1 barely proceeds under the conditions we used, Mechanism 2 was isolated in the sulfurization of NWs attached to the substrate. In fact, the remnants of CuO NWs can still be visible in the sulfurized attached NWs, as seen in Fig. 1f and examples in Supplementary Fig. 6.

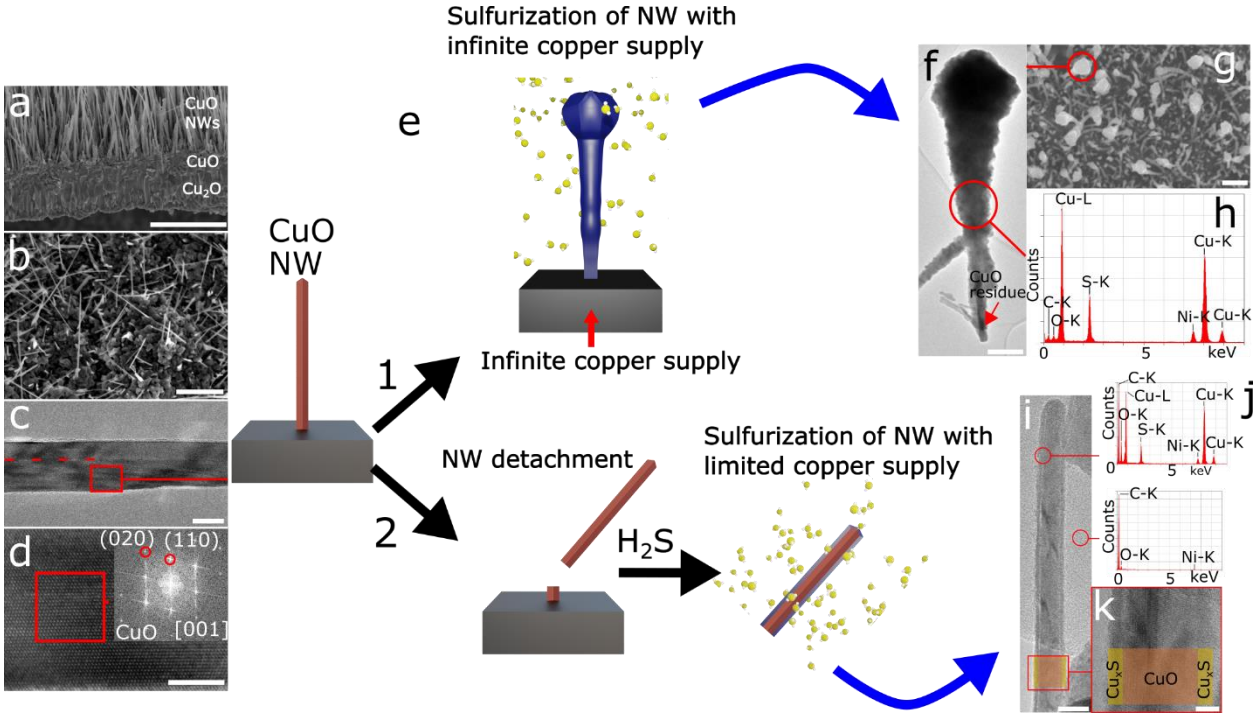

Fig. 1: Sulfurization of CuO NWs with a limited and unlimited supply of copper at 24°C, H_2S pressure 100 kPa for 2 hours. a Cross-sectional view of NWs synthesized at 490 °C, growing on top of oxide layers. **b** Top view of CuO NW array synthesized at 265 °C, used as a template material for sulfurization. **c** TEM micrograph of CuO NW. **d** Enlarged TEM micrograph with FFT pattern indicating NW growth perpendicular to 110 and 001 (zone axis) direction. **e** Schematics of the sulfurization: 1 Sulfurization of NWs with unlimited copper supply, 2 Sulfurization of NWs with limited copper supply. **f** TEM micrograph of nanostructure obtained by sulfurizing CuO NWs with an unlimited copper supply **g** SEM micrograph of the sulfurized substrate with CuO NWs **h** EDS spectrum indicating the ratio between Cu and S in the formed nanostructure is approximately 70:30. **i** TEM micrograph of the CuO NW after being detached from the substrate and sulfurized. **j** EDS spectra of NW and TEM carbon-grid support indicating that the sulfur is present in the NW, but not on the other parts of the TEM grid (nickel and carbon signals come from the components of the TEM grid). **k** TEM micrograph of the NW part, marked with a red square in **i** with visible amorphous copper sulfide layer encapsulating the NW. Scale bars correspond to **a** – 10 µm **b** – 500 nm, **c, i** – 20 nm, **d, k** – 5 nm, **f** – 200 nm, **g** – 1 µm.

After the experiments at room temperature, it became clear that the sulfurization process of CuO NWs differs depending on whether the NWs have limited or unlimited access to a supply of cations. However, when the NWs were isolated with a limited supply of cations, the reaction proceeded poorly at room temperature. We could not confirm whether the anion exchange

actually occurred in the isolated NWs, as only a thin amorphous sulfur-containing layer was present on the NW surface. Therefore, additional experiments with both regimes were conducted with a variety of experimental conditions. The sulfurization temperature was increased to 110 °C to enhance the rate of sulfurization and overcome the energy barrier for Mechanism 1. As observed in the room-temperature experiment, the NWs attached to the substrate exhibited a high reactivity with H_2S and could become completely overgrown by the sulfide phase. To prevent this, the sulfurization time was reduced to 30 minutes, including a 20-minute heating period from room temperature. Additionally, the H_2S pressure was lowered, and two different pressures were used: 10 kPa and 1 kPa.

A schematic of the process for NWs with unlimited copper supply is shown in Fig. 2a. The morphology and phase of the sulfurized NWs did not seem to be influenced by the pressure variation under the conditions used, as observed in Fig. 2b-h. Under these conditions (temperature: 110 °C, duration of sulfurization: 30 min, and H_2S pressures: 1 kPa and 10 kPa), the attached NWs again exhibited thickening, as seen in Fig. 2b,e,f. Some NWs showed nearly uniform diameters along their entire length, such as the one in Fig. 2e. However, there were still NWs where the top part was considerably thicker (examples can be seen in Supplementary Fig. 8), indicating a similar reaction dynamic to that observed in the room-temperature experiments on NWs with an unlimited copper supply. Most of the transformed NWs exhibited a segmented structure, with individual single-crystalline grains arranged in one dimension along the length of the NW and connected by grain boundaries (marked with a red dashed line in Fig. 2d,h). Some grains showed a degree of preferential orientation. For example, in the neighboring grains shown in Supplementary Fig. 9, only a slight tilt was observed, and both grains exhibited a parallel orientation in the [2-10] direction with respect to the NW. On the other hand, the grain in Fig. 2d exhibited an orientation where the [010] direction was parallel to the NW, indicating

that not all the grains were oriented in the same way. Again, the predominant copper phase observed was low chalcocite (as confirmed by the SAED pattern in Fig. 2c,g).

Isolated NWs with a limited supply of copper were also treated under the same conditions as schematically shown in Fig. 2i. This time, the copper oxide from the NWs clearly reacted with H_2S to form copper sulfides (Fig. 2j-r). When the NWs are isolated, they do not experience significant thickening during the reaction, as no additional material can be supplied. The newly transformed NWs are polycrystalline, with smaller sulfide grains than the NWs with an infinite copper supply. The NW surface also appears rougher, as some individual grains protrude from the surface. Voids within the structure are visible (Fig. 2o and Supplementary Fig. 10). SAED and HRTEM analyses indicate that, unlike the NWs with an unlimited copper supply, in this case the NWs predominantly consist of covellite (CuS). The electron-diffraction analysis in Supplementary Fig. 11 indicates that the grain orientation is random.

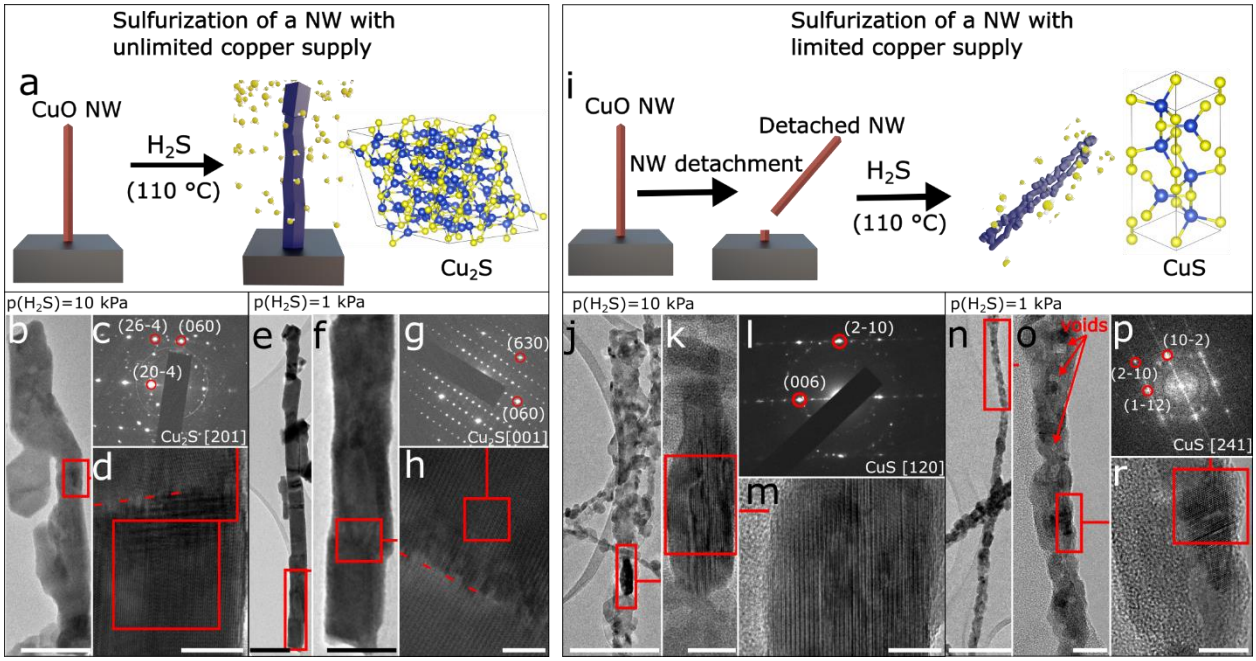

Fig. 2 Sulfurization of NWs with an unlimited and limited supply of copper at 110 °C, H_2S pressure 10 and 1 kPa for 30 min (of which 20 min included heating from room temperature) a Schematic representation of the sulfurization of Cuo NWs with an unlimited supply of copper **b,e,f** TEM micrographs of the NW with an unlimited supply of copper, sulfurized in a H_2S pressure of 10 kPa (**b**) and 1 kPa (**e,f**). **c, g** SAED patterns indicating the formation of the low

chalcocite phase in the transformed NWs in a H_2S pressure of 10 kPa (**c**) and 1 kPa (**g**). **d, h** TEM micrographs of enlarged parts of the areas marked in red in **b** and **f,** respectively, with marked grain boundaries (red dashed line). **i** Schematic representation of CuO NWs with limited copper supply. **j, n** TEM micrographs of NWs with limited copper supply sulfurized in a H_2S pressure of 10 kPa (**j**) and 1 kPa (**n**). **k, o** TEM micrographs of enlarged parts marked with a red rectangle in **j** and **n,** respectively. Voids in the NW structure can be visible in **o**. **l, p** SAED (**l**) and FFT (**p**) patterns taken from grains marked with red rectangles in **k** and **o,** respectively, indicating the presence of the covellite phase. **m, r** enlarged parts of the areas marked with red rectangles in **k** and **o,** respectively. Scale bars correspond to **b, f** – 100 nm, **d, h, m, r** – 10 nm, **e, j, n** – 200 nm, **k, o** – 20 nm.

Discussion

The experimental results could be explained by the theoretical modeling of the sulfurization processes (full description of the model can be found in Supplementary Information)

The results show that the mechanism of CuO NW sulfurization depends on the NW's supply of cations participating in the reaction. When the template CuO NWs are isolated with a limited cation supply, their sulfurization proceeds through the exchange of oxygen anions with sulfur Fig. 3a (Mechanism 1). As CuO and H_2S come into contact, H_2S dissociates to atomic S and two H atoms are adsorbed on the surface[62]. The H atoms can then reduce the CuO to Cu and extract the O anion, forming water molecules. The oxygen vacancy is then filled when a sulfur atom reacts with the copper, forming the CuS phase, while preserving the cation-to-anion atomic ratio in the overall reaction:

$$CuO + H_2S \rightarrow CuS + H_2O$$

In this way a CuS layer forms around the NW. The reaction induces further diffusion processes: sulfur species can diffuse inward through the formed sulfide layer, while copper and oxygen species diffuse outward toward the NW surface, where they become involved in the reaction with H_2S, increasing the thickness of the CuS layer. Since the outward diffusion is much faster, the anion-exchange transformation is accompanied by the formation of Kirkendall voids. A

similar reaction outcome is observed when isolated copper NWs are sulfurized with thiourea, resulting in the formation of hollow sulfide NWs[63]. Anion exchange occurs at the same rate along the entire NW, preserving the overall shape of the NW with a uniform diameter along its length. However, the single crystallinity is lost due to large rearrangements in the crystal structure caused by ion migrations, as seen in the transformed NW in Fig. 2o.

The described processes were also treated theoretically, considering the Langmuir H_2S adsorption on the NW surface and a calculation of the CuO outward flux (see Supplementary Material). The results were in good agreement with the experimental data.

According to the calculation predictions (Fig. 3b,c), the high pressure of 10^5 Pa and the low temperature of 24 °C result in a thin sulfide layer of about 2 nm after 2 hours of sulfurization, and a void with a radius of about 3 nm is formed in the central part of the NW. The real voids are not necessarily axisymmetric, and the difference can be explained by the assumptions used in the model. When the pressure is decreased by an order of a magnitude to 10^4 Pa, and the temperature is increased to 110 °C, significant changes in the shape of the NW are observed even after 30 min of the treatment (Fig. 3d,e). The whole volume of the CuO layer is consumed and converted to a CuS layer on the outer surface of the NW after just several minutes of the treatment. Thus, the NW is converted into a nanotube with CuS walls, while a mixed composite structure of CuO+CuS walls can also be obtained at shorter sulfurization times. A further decrease in the H_2S pressure to a value of 10^3 Pa does not significantly change the outcome. However, the time for complete transformation is prolonged (Fig. 3f,g). This demonstrates the possibility of flexible composition control of the resulting nanostructures by changing the experimental conditions. The most significant factor influencing the outcome of the transformation is temperature, which can be explained by the exponential dependence of the outward CuO flux on the temperature (Supplementary information).

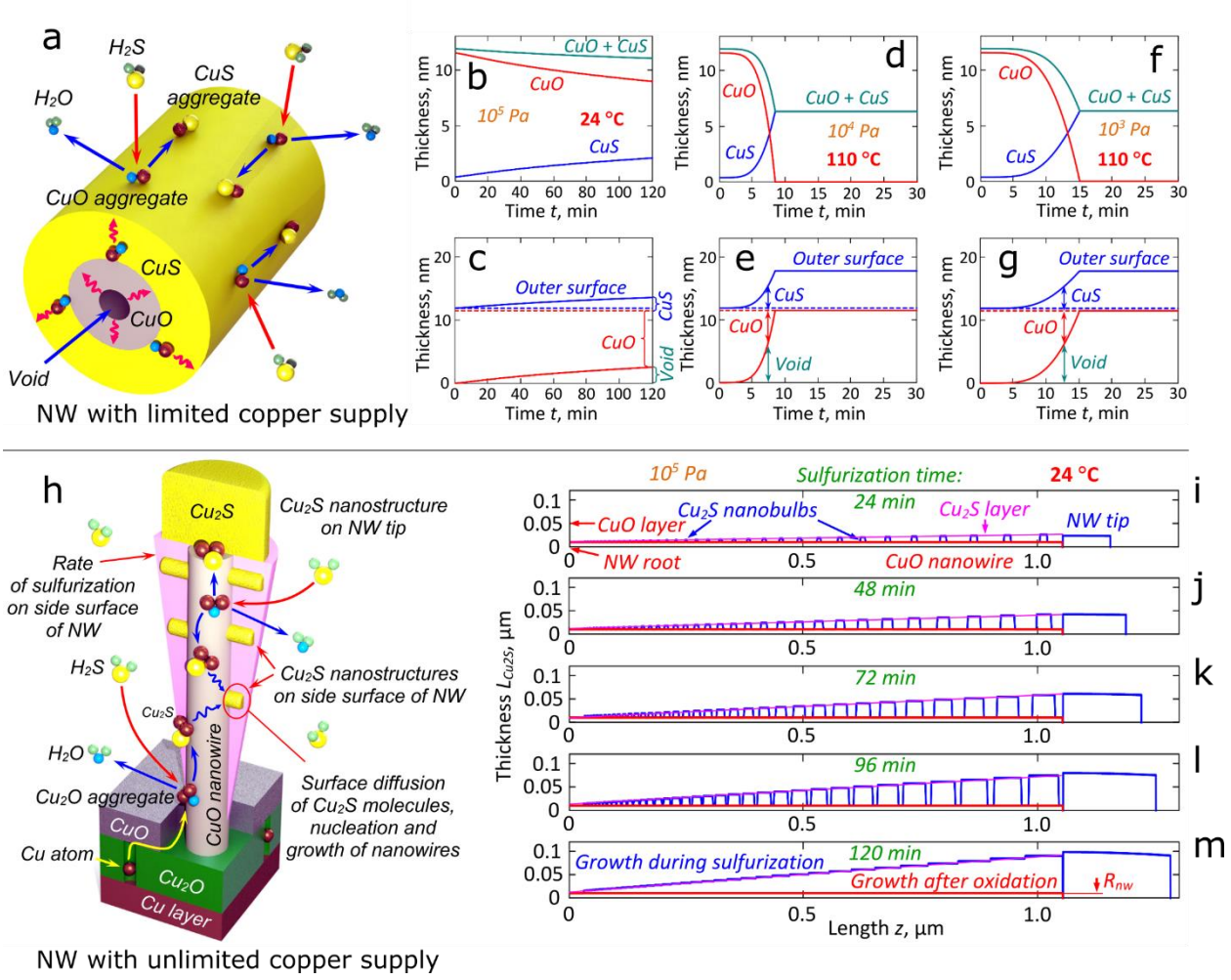

Fig. 3. Schematics of the processes during sulfurization of the CuO NWs with limited and unlimited supplies of copper with the results of theoretical modeling. **a** Schematic of the processes occurring during sulfurization of NW with limited copper supply with **b,d,f** time dependencies of the thicknesses of the formed CuS (blue line), CuO (red line) phase and their sum (teal line) at (**b**) 10^5 Pa and 24 °C, **(d)** 10^4 pa and 110 °C and **(f)** 10^3 pa and 110 °C. **c,e,g** changes of the NW shape with an indicated thickness of CuS (blue line), CuO (red line), and void (teal arrows) for sulfurization of NW with a limited copper supply at (**c**) 10^5 Pa and 24 °C, **(e)** 10^4 pa and 110 °C and **(g)** 10^3 pa and 110 °C. **h** Schematic of the processes during sulfurization of CuO NWs with unlimited supply of copper at 24 °C and 10^5 Pa with **b-f** Calculated evolution of Cu_2S layer (pink line), spherical Cu_2S structures (blue line) and CuO phase (red line) along the length of the NW for different sulfurization times: **b** 24 min, **c** 48 min, **d** 72 min, **e** 96 min, **f** 120 min.

On the other hand, when the template CuO NW roots are embedded in the substrate on which they grew, they have access to an unlimited supply of copper cations, which also participate in the reaction (Mechanism 2). Mechanism 2 alone can be observed during room-temperature

sulfurization, as the contribution of Mechanism 1 to the reaction is insignificant. This process is analogous to the thermal growth of CuO NWs, where oxygen reacts with copper at the top of the NW to elongate the NW. However, in this case, H_2S reacts with copper to form Cu_2S, and the sulfide does not continue to grow in one dimension, but instead in all three, completely overgrowing the NW and forming the bulky upper part of the newly formed nanostructure. The formation of the copper-rich Cu_2S phase results from the surplus copper supplied to the NW. From the phase diagrams of the copper-sulfur system, it is evident that a higher copper content favors the formation of copper-rich sulfides and vice versa[64]. In reference[63] it was observed that the CuS phase formed when sulfurizing the CuO phase with thiourea, while the Cu_2S phase was formed when sulfurizing the copper-rich Cu_2O phase, indicating that an excess of copper in the initial structure indeed preferentially results in copper-rich sulfides.

In contrast to Mechanism 1, Mechanism 2 can be observed even at room temperature. The most likely explanation for this difference is the copper-diffusion pathway. In Mechanism 2, the most probable diffusion pathway is surface diffusion on the sides of the NW, as the crystalline sulfide phase was observed on the sides of the NW in the initial stages of sulfurization (Supplementary Fig. 6), likely formed in the reaction between the copper species and the H_2S. On the other hand, in Mechanism 1, the outward diffusion of copper and oxygen species occurs through the crystal lattice of single-crystalline NWs with a higher activation energy compared to the other diffusion types in solid systems[65].

To describe the processes leading to the transformation, a mechanism supported by theoretical modeling was proposed. The processes occurring in the discussed system are illustrated in Fig. 3h and can be described on the atomic level in the following way. As the diffusing Cu species come into contact with the CuO phase, they enrich the CuO phase with copper. On the atomic level, this can be described by the local formation of Cu_2O aggregates in the CuO phase. In this way, the migration of copper species is associated with a set of events when a copper atom

leaves from the Cu_2O aggregate, converting it to back the CuO aggregate, and moves to the next CuO aggregate, which results in the formation of a new Cu_2O aggregate at a new position. This type of diffusion was considered when modeling the surface diffusion of copper species on the NW surface. When reaching an adsorbed H_2S molecule, the Cu_2O aggregate undergoes the following reaction, which is accompanied by the formation of the Cu_2S aggregate.

$$Cu_2O + H_2S \rightarrow Cu_2S + H_2O$$

After its nucleation, the Cu_2S phase grows, forming a layer, as well as spherical nanostructures ("nanobulbs"), observed in intermediate sulfurization stages (Supplementary Fig. 5c and d) of the Cu_2S phase. The probability of forming such structures is likely higher on parts with imperfections in the initial CuO crystal structure, representing areas with increased catalytic activity and sulfurization rate.

The dependence of Cu_2O aggregates, which will transform to Cu_2S, along the NW's length can be described using Bessel and modified Bessel functions[66] (Supplementary Information). During the sulfurization process, the H_2S concentration is most likely the highest at the top of the NW, which was also assumed in theoretical modeling (Supplementary Information), where the linear dependence of the H_2S concentration on the length of the NW was assumed. This dependence explains the formation of the conically shaped structures in Fig. 1f, as seen from the results in Fig. 3i-m, demonstrating the results of a calculation for a 1-µm-long and 10-nm-thick NW. The Cu_2S layer and "nanobulbs" grow over time, and their rate is higher in the upper parts of the NW (the parts with an increased H_2S concentration). The highest reaction rate at the top of the NW also suggests that this spot has the highest adsorption energies for the H_2S molecules. A similar observation can be observed in the growth of CuO NWs via thermal oxidation, where the top region also represents the most active spot for a reaction between copper and oxygen molecules[58,59,61]. The most likely reason for that is the presence of defects, such as the twin boundary, making the top part of the NW catalytically more active than the other parts. In this

way, the NW tips collect large concentrations of hydrogen sulfide molecules, which resembles the distribution of water drops along the top under the cover of a dense forest during rainfall.

When the temperature is elevated (110 °C), a combination of both mechanisms contributes to the reaction outcome, as schematically shown in Fig. 4a. Thus, sulfurization of the surface CuO material induces the outward diffusion of copper and oxygen ions according to Mechanism 1, as well as the upward diffusion of copper species from the underlying substrate according to Mechanism 2. Soon after the reaction's onset, the NW undergoes a breakdown of the single crystallinity due to rearrangements of the structure according to mechanism 1. Copper can now diffuse inside the NW through the newly formed grain boundaries that are present. Larger sulfide grains, compared to the isolated sulfurized NWs, indicate that the additional copper supplied inside the NW preferentially reacts on the already-existing grains, contributing to their growth rather than nucleating new grains. As the sulfide grains grow, their size eventually exceeds the diameter of the NW, and they become arranged in one dimension, forming a segmented structure (Fig. 4b). Simultaneously, the additional copper supply to the NW prevents the formation of Kirkendall voids. The outward diffusion of copper and oxygen, according to Mechanism 1, is accompanied by copper diffusion inside the NW, according to Mechanism 2, filling the space that, in the absence of the substrate, would become hollow due to the Kirkendall effect. Due to the higher concentration of H_2S molecules at the tops of the NW, most transformed NWs are still thicker at the top (Supplementary Fig. 8). Due to the excessive copper available, a copper-richer Cu_2S phase is formed.

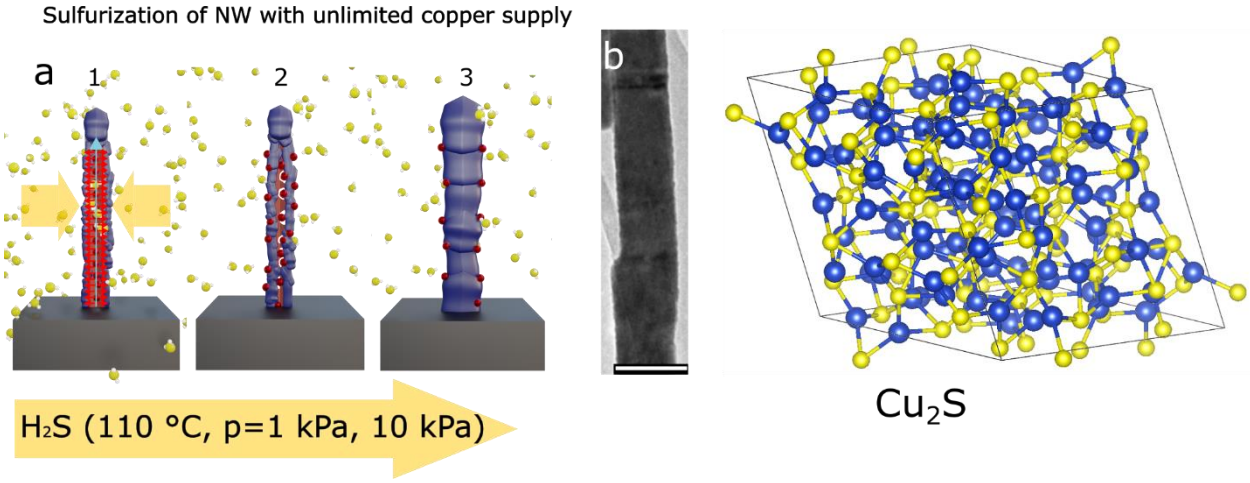

Fig. 4: Representation of mechanisms contributing to the sulfurization of CuO NWs with an unlimited supply of copper at elevated temperatures. a Stages of the NW sulfurization in NWs with an unlimited supply of copper. In addition to the anion-exchange mechanism, an additional mechanism contributes to the reaction with copper species (marked as red spheres) diffusing from the substrate towards the top of the NW. The diffusing copper predominantly attaches to existing grains, increasing their size and resulting in a segmented structure. **b** TEM micrograph of completely transformed NW attached to the copper-rich substrate with a model of the chalcocite structure. The scale bar corresponds to 100 nm.

In summary, this report demonstrates that the cation supply, whether limited or unlimited, plays a crucial role in the anion-exchange reaction of ionic nanomaterials. This was illustrated by the sulfurization of isolated CuO NWs and CuO NWs attached to a copper-rich substrate, representing a limited and unlimited supply of copper cations. The difference in the reaction outcome between these two scenarios is evident in the morphology and the phase of the sulfurized NWs. In the case of a limited copper supply, the sole mechanism involved is the conventional anion-exchange mechanism. This leads to the formation of polycrystalline covellite NWs, exhibiting Kirkendall voids and uniform diameters along their length. On the other hand, when NWs have unlimited access to copper cations due to their attachment to a copper-rich substrate, an additional mechanism comes into play. The copper cations diffuse inside the NWs, resulting in continued NW growth and the formation of considerably thicker chalcocite nanostructures. At higher temperatures, a combination of the anion-exchange mechanism and

the mechanism delivering copper cations inside the NWs can be observed in the NWs with an unlimited supply of copper, resulting in segmentally structured chalcocite NWs. In this case, the outward diffusion of copper and oxygen species is accompanied by the upward diffusion of additional copper species, filling the void space and preventing the formation of Kirkendall voids in the structure.

To the best of our knowledge, this dependence of the sulfurization mechanism on the metal oxide NWs has not been emphasized in the literature, despite its significance, not only in terms of fundamental science and the description of new reaction mechanisms in the solid-state but also for the practical applications of NWs in areas such as catalysis and sensing. In our case, the response of the CuO NWs in applications could vary depending on whether they are isolated or attached to a copper-rich substrate.

Methods

Synthesis of CuO NWs. CuO NWs were synthesized via thermal oxidation. Circular copper discs of 14-mm diameter (supplier: Alfa Aesar, purity 99.95%, thickness 0.25 mm, annealed and oxygen-free) were placed inside a quartz tube in a tube furnace (OTF-1200X, MTI Corporation). The process is schematically shown in Supplementary Fig. 1. The tube was partially opened to the atmosphere on one side using the KF 16 port. Oxygen was continuously supplied to the copper discs at a flow rate of 140 sccm to ensure oxygen-rich conditions. The oxidation temperature was set to 300 °C. However, since the furnace was not completely closed and oxygen was flowing through the quartz tube, we also measured the exact temperature using a thermocouple. It was found that the actual temperature in the furnace was 265 °C ± 5 °C. Oxidation was also conducted at higher temperatures (400 °C to 700 °C). However, higher temperatures resulted in thicker NWs. Our goal was to observe the sulfurization of thin NWs due to their increased surface-to-volume ratio and potentially higher reactivity. Therefore, the

NWs used for sulfurization were those synthesized at 265 °C. This temperature yielded NWs with a small diameter and a high number density. At lower temperatures, the NW number density dropped. The set temperature was reached after 30 minutes of heating, and the final temperature was maintained for an additional 6 hours. Afterwards, the oxygen supply was terminated, and the samples were left to cool to room temperature inside the furnace.

Preparation of the NWs for the sulfurization. An anion-exchange reaction was conducted by exposing the synthesized CuO NWs to H_2S gas. Two sets of experiments were performed. The first set of experiments involved the CuO NWs still attached to the oxidized copper substrate from which they grew. No further processing was required for this set before sulfurization. The second set of experiments was conducted on isolated NWs, where the NWs were detached from the substrate prior to oxidation. To detach the NWs, the substrate with the grown NWs was immersed in absolute ethanol and placed in an ultrasonic bath for 5 minutes. Subsequently, the ethanol, now containing the detached NWs, was drop-cast onto a nickel-supported lacey carbon TEM grid, which was then subjected to further treatment with H_2S, as described in the following paragraph.

Sulfurization. The CuO NW sulfurization was performed by placing the synthesized CuO NWs in the quartz tube inside a tube furnace. The experimental setup is shown in Supplementary Fig. 2. The tube furnace was closed and connected to a rotary pump. After placing the CuO NWs in the furnace, the air was evacuated from the tube to a base pressure of 1 Pa. Subsequently, hydrogen sulfide gas (H_2S) was introduced into the furnace. The experiments were performed on the NWs that were still attached to the oxidized copper substrate, as well as on isolated NWs that had been previously detached from the substrate using sonication and deposited on nickel-supported lacey carbon TEM grids. In the case of the isolated NWs, the entire TEM grid with the NWs was exposed to H_2S. Three different conditions were used for the sulfurization process, varying the pressure of H_2S, the temperature, and the sulfurization time. Firstly, the NWs were

exposed to H_2S at room temperature (24 °C) and a pressure of 100 kPa for 2 hours. In the subsequent experiment, the H_2S pressure was reduced to 1 kPa, and the temperature was increased to 110 °C. The temperature was reached after 20 minutes of heating from room temperature and maintained for an additional 10 minutes. H_2S was present inside the furnace from the beginning of the heating process. In the third experiment, all the conditions remained the same as in the second experiment, except for the H_2S pressure, which was increased to 10 kPa.

Electron microscopy. NWs were analyzed using a scanning electron microscope (SEM, JSM-7600F, JEOL Inc. and Prisma E, Thermo Fisher Scientific Inc.) and transmission electron microscope (TEM, JEM-2100, JEOL Inc).

Preparation for the TEM analysis was required for the NWs that were not detached prior to sulfurization. Preparation was the same as for the detachment to prepare isolated NWs for sulfurization. It included immersing the sulfurized NWs, attached to the substrate in the absolute ethanol, placing them in an ultrasonic bath for 5 minutes, and drop casting them on the nickel-supported lacey carbon TEM grid.

Raman Spectroscopy. Raman spectroscopic analysis was conducted on the oxidized copper foil before and after sulfurization at 100 kPa H_2S at room temperature for 2 hours. The measurements were conducted with a Raman spectrometer (NT-MDT, NTegra Spectra II) using a 633-nm laser.

Data availability

The data supporting this study's findings are available from the corresponding author upon reasonable request.

References

1. Saruyama, M., Sato, R. & Teranishi, T. Transformations of Ionic Nanocrystals via Full and

Partial Ion Exchange Reactions. *Acc. Chem. Res.* **54**, 765–775 (2021).
2. Wu, H. L. *et al.* Formation of pseudomorphic nanocages from Cu2O nanocrystals through anion exchange reactions. *Science (80-.).* **351**, 1306–1310 (2016).
3. Li, H. *et al.* Sequential cation exchange in nanocrystals: Preservation of crystal phase and formation of metastable phases. *Nano Lett.* **11**, 4964–4970 (2011).
4. Powell, A. E., Hodges, J. M. & Schaak, R. E. Preserving Both Anion and Cation Sublattice Features during a Nanocrystal Cation-Exchange Reaction: Synthesis of Metastable Wurtzite-Type CoS and MnS. *J. Am. Chem. Soc.* **138**, 471–474 (2016).
5. Kim, S. *et al.* Phase segregated Cu2−xSe/Ni3Se4 bimetallic selenide nanocrystals formed through the cation exchange reaction for active water oxidation precatalysts. *Chem. Sci.* **11**, 1523–1530 (2020).
6. Rivest, J. B. & Jain, P. K. Cation exchange on the nanoscale: An emerging technique for new material synthesis, device fabrication, and chemical sensing. *Chem. Soc. Rev.* **42**, 89–96 (2013).
7. Cho, G., Park, Y., Hong, Y. K. & Ha, D. H. Ion exchange: an advanced synthetic method for complex nanoparticles. *Nano Convergence* vol. 6 1–17 (2019).
8. Anderson, B. D. & Tracy, J. B. Nanoparticle conversion chemistry: Kirkendall effect, galvanic exchange, and anion exchange. *Nanoscale* **6**, 12195–12216 (2014).
9. Lim, Y., Lee, C. H., Jun, C. H., Kim, K. & Cheon, J. Morphology-Conserving Non-Kirkendall Anion Exchange of Metal Oxide Nanocrystals. *J. Am. Chem. Soc.* **142**, 9130–9134 (2020).
10. Jia, B. *et al.* Robust Anion Exchange Realized in Crystalline Metal Cyanamide Nanoparticles. *Chem. Mater.* **31**, 9532–9539 (2019).
11. Dey, A. Semiconductor metal oxide gas sensors: A review. *Mater. Sci. Eng. B* **229**, 206–217 (2018).
12. Miller, D. R., Akbar, S. A. & Morris, P. A. Nanoscale metal oxide-based heterojunctions for gas sensing: A review. *Sensors Actuators B Chem.* **204**, 250–272 (2014).
13. Sun, Y. F. *et al.* Metal Oxide Nanostructures and Their Gas Sensing Properties: A Review. *Sensors 2012, Vol. 12, Pages 2610-2631* **12**, 2610–2631 (2012).
14. Tang, H. *et al.* Recent advances in 2D/nanostructured metal sulfide-based gas sensors: mechanisms, applications, and perspectives. *J. Mater. Chem. A* **8**, 24943–24976 (2020).
15. Wang, L. *et al.* Inorganic Metal-Oxide Photocatalyst for H2O2 Production. *Small* **18**, 2104561 (2022).
16. Karthikeyan, C., Arunachalam, P., Ramachandran, K., Al-Mayouf, A. M. & Karuppuchamy, S. Recent advances in semiconductor metal oxides with enhanced methods for solar photocatalytic applications. *J. Alloys Compd.* **828**, 154281 (2020).
17. Mamiyev, Z. & Balayeva, N. O. Metal Sulfide Photocatalysts for Hydrogen Generation: A Review of Recent Advances. *Catal. 2022, Vol. 12, Page 1316* **12**, 1316 (2022).
18. Adhikari, S., Sarkar, D. & Madras, G. Hierarchical Design of CuS Architectures for Visible Light Photocatalysis of 4-Chlorophenol. *ACS Omega* **2**, 4009–4021 (2017).
19. Gusain, R., Gupta, K., Joshi, P. & Khatri, O. P. Adsorptive removal and photocatalytic degradation of organic pollutants using metal oxides and their composites: A comprehensive review. *Adv. Colloid Interface Sci.* **272**, 102009 (2019).
20. Ikram, M. *et al.* A review of photocatalytic characterization, and environmental cleaning, of metal oxide nanostructured materials. *Sustain. Mater. Technol.* **30**, e00343 (2021).
21. Xu, W. *et al.* Nanoporous CuS with excellent photocatalytic property. *Sci. Reports 2015 51* **5**, 1–11 (2015).
22. Wan, M. *et al.* One-Step Transformation from Cu2S Nanocrystal to CuS Nanocrystal with Photocatalytic Properties. *ChemistrySelect* **4**, 7512–7522 (2019).
23. Sun, S., Li, P., Liang, S. & Yang, Z. Diversified copper sulfide (Cu2−xS) micro-/nanostructures: a comprehensive review on synthesis, modifications and applications.

Nanoscale **9**, 11357–11404 (2017).
24. Sudhaik, A. *et al.* Copper sulfides based photocatalysts for degradation of environmental pollution hazards: A review on the recent catalyst design concepts and future perspectives. *Surfaces and Interfaces* **33**, 102182 (2022).
25. Tomboc, G. M., Gadisa, B. T., Joo, J., Kim, H. & Lee, K. Hollow Structured Metal Sulfides for Photocatalytic Hydrogen Generation. *ChemNanoMat* **6**, 850–869 (2020).
26. Zhang, S. *et al.* Research progress in metal sulfides for photocatalysis: From activity to stability. *Chemosphere* **303**, 135085 (2022).
27. Védrine, J. C. Heterogeneous Catalysis on Metal Oxides. *Catal. 2017, Vol. 7, Page 341* **7**, 341 (2017).
28. Liu, Y., Wang, W., Xu, X., Marcel Veder, J. P. & Shao, Z. Recent advances in anion-doped metal oxides for catalytic applications. *J. Mater. Chem. A* **7**, 7280–7300 (2019).
29. Védrine, J. C. Importance, features and uses of metal oxide catalysts in heterogeneous catalysis. *Chinese J. Catal.* **40**, 1627–1636 (2019).
30. Védrine, J. C. Metal Oxides in Heterogeneous Oxidation Catalysis: State of the Art and Challenges for a More Sustainable World. *ChemSusChem* **12**, 577–588 (2019).
31. Dai, Y. *et al.* Recent progress in heterogeneous metal and metal oxide catalysts for direct dehydrogenation of ethane and propane. *Chem. Soc. Rev.* **50**, 5590–5630 (2021).
32. Chen, S. *et al.* Defect and interface engineering in metal sulfide catalysts for the electrocatalytic nitrogen reduction reaction: a review. *J. Mater. Chem. A* **10**, 6927–6949 (2022).
33. Tang, T. *et al.* Design and synthesis of metal sulfide catalysts supported on zeolite nanofiber bundles with unprecedented hydrodesulfurization activities. *J. Am. Chem. Soc.* **135**, 11437–11440 (2013).
34. Barik, R. & Ingole, P. P. Challenges and prospects of metal sulfide materials for supercapacitors. *Curr. Opin. Electrochem.* **21**, 327–334 (2020).
35. Gao, Y. & Zhao, L. Review on recent advances in nanostructured transition-metal-sulfide-based electrode materials for cathode materials of asymmetric supercapacitors. *Chem. Eng. J.* **430**, 132745 (2022).
36. Liu, X., Huang, J. Q., Zhang, Q. & Mai, L. Nanostructured Metal Oxides and Sulfides for Lithium–Sulfur Batteries. *Adv. Mater.* **29**, 1601759 (2017).
37. Zhao, Y. *et al.* Recent Developments and Understanding of Novel Mixed Transition-Metal Oxides as Anodes in Lithium Ion Batteries. *Adv. Energy Mater.* **6**, 1502175 (2016).
38. Xiao, Y., Lee, S. H. & Sun, Y. K. The Application of Metal Sulfides in Sodium Ion Batteries. *Adv. Energy Mater.* **7**, 1601329 (2017).
39. Xu, X., Liu, W., Kim, Y. & Cho, J. Nanostructured transition metal sulfides for lithium ion batteries: Progress and challenges. *Nano Today* **9**, 604–630 (2014).
40. Fang, Y., Luan, D. & Lou, X. W. Recent Advances on Mixed Metal Sulfides for Advanced Sodium-Ion Batteries. *Adv. Mater.* **32**, 2002976 (2020).
41. Zhao, J., Zhang, Y., Wang, Y., Li, H. & Peng, Y. The application of nanostructured transition metal sulfides as anodes for lithium ion batteries. *J. Energy Chem.* **27**, 1536–1554 (2018).
42. Yan, B. *et al.* Design, synthesis, and application of metal sulfides for Li–S batteries: progress and prospects. *J. Mater. Chem. A* **8**, 17848–17882 (2020).
43. Kajana, T. *et al.* Potential transition and post-transition metal sulfides as efficient electrodes for energy storage applications: review. *RSC Adv.* **12**, 18041–18062 (2022).
44. Theerthagiri, J. *et al.* Recent progress and emerging challenges of transition metal sulfides based composite electrodes for electrochemical supercapacitive energy storage. *Ceram. Int.* **46**, 14317–14345 (2020).
45. Das, A., Raj, B., Mohapatra, M., Andersen, S. M. & Basu, S. Performance and future directions of transition metal sulfide-based electrode materials towards

supercapacitor/supercapattery. *Wiley Interdiscip. Rev. Energy Environ.* **11**, e414 (2022).
46. Wang, Y. *et al.* Mesoporous Transition Metal Oxides for Supercapacitors. *Nanomater. 2015, Vol. 5, Pages 1667-1689* **5**, 1667–1689 (2015).
47. Ma, Y. *et al.* Recent advances in transition metal oxides with different dimensions as electrodes for high-performance supercapacitors. *Adv. Compos. Hybrid Mater. 2021 44* **4**, 906–924 (2021).
48. Zhang, Y., Li, L., Su, H., Huang, W. & Dong, X. Binary metal oxide: advanced energy storage materials in supercapacitors. *J. Mater. Chem. A* **3**, 43–59 (2014).
49. Su, H., Jaffer, S. & Yu, H. Transition metal oxides for sodium-ion batteries. *Energy Storage Mater.* **5**, 116–131 (2016).
50. Reddy, M. V., Subba Rao, G. V. & Chowdari, B. V. R. Metal oxides and oxysalts as anode materials for Li ion batteries. *Chem. Rev.* **113**, 5364–5457 (2013).
51. Kannan, K., Radhika, D., Sadasivuni, K. K., Reddy, K. R. & Raghu, A. V. Nanostructured metal oxides and its hybrids for photocatalytic and biomedical applications. *Adv. Colloid Interface Sci.* **281**, 102178 (2020).
52. Argueta-Figueroa, L. *et al.* Nanomaterials made of non-toxic metallic sulfides: A systematic review of their potential biomedical applications. *Mater. Sci. Eng. C* **76**, 1305–1315 (2017).
53. Mujahid, M. H. *et al.* Metallic and metal oxide-derived nanohybrid as a tool for biomedical applications. *Biomed. Pharmacother.* **155**, 113791 (2022).
54. Goel, S., Chen, F. & Cai, W. Synthesis and Biomedical Applications of Copper Sulfide Nanoparticles: From Sensors to Theranostics. *Small* **10**, 631–645 (2014).
55. Košiček, M., Zavašnik, J., Baranov, O., Šetina Batič, B. & Cvelbar, U. Understanding the Growth of Copper Oxide Nanowires and Layers by Thermal Oxidation over a Broad Temperature Range at Atmospheric Pressure. *Cryst. Growth Des.* **22**, 6656–6666 (2022).
56. Yuan, L., Wang, Y., Mema, R. & Zhou, G. Driving force and growth mechanism for spontaneous oxide nanowire formation during the thermal oxidation of metals. *Acta Mater.* **59**, 2491–2500 (2011).
57. Xiang, L. *et al.* A brief review on the growth mechanism of CuO nanowires via thermal oxidation. *J. Mater. Res.* **33**, 2264–2280 (2018).
58. Baranov, O., Košiček, M., Filipič, G. & Cvelbar, U. A deterministic approach to the thermal synthesis and growth of 1D metal oxide nanostructures. *Appl. Surf. Sci.* **566**, 150619 (2021).
59. Rackauskas, S. *et al.* In situ study of noncatalytic metal oxide nanowire growth. *Nano Lett.* **14**, 5810–5813 (2014).
60. Sheng, H. *et al.* Twin structures in CuO nanowires. *J. Appl. Crystallogr.* **49**, 462–467 (2016).
61. Sun, X. *et al.* Atomic-Scale Mechanism of Unidirectional Oxide Growth. *Adv. Funct. Mater.* **30**, 1906504 (2020).
62. Sun, S., Zhang, D., Li, C. & Wang, Y. DFT study on the adsorption and dissociation of H2S on CuO(111) surface. *RSC Adv.* **5**, 21806–21811 (2015).
63. Lee, Y. I. Selective transformation of Cu nanowires to Cu2S or CuS nanostructures and the roles of the Kirkendall effect and anion exchange reaction. *Mater. Chem. Phys.* **180**, 104–113 (2016).
64. Waldner, P. Gibbs Energy Modeling of the Cu-S Liquid Phase: Completion of the Thermodynamic Calculation of the Cu-S System. *Metall. Mater. Trans. B Process Metall. Mater. Process. Sci.* **51**, 805–817 (2020).
65. Zhu, Y., Mimura, K., Lim, J. W., Isshiki, M. & Jiang, Q. Brief review of oxidation kinetics of copper at 350 °C to 1050 °C. *Metall. Mater. Trans. A 2006 374* **37**, 1231–1237 (2006).
66. Polyanin, A. D. & Zaitsev, V. F. *Handbook of Exact Solutions for Ordinary Differential Equations*. (Chapman & Hall/CRC, 2003).

Acknowledgments:

This work acknowledges the support from the Slovenian Research Agency ARRS, program P1-0417, project N2-0107. O.B. acknowledges the support from the project funded by the National Research Foundation of Ukraine under grant agreement no. 2020.02/0119 and the NATO Science for Peace and Security Programme under grant id. G5814 project NOOSE.

Author contributions:

All authors contributed to writing the paper. M. K., J. Z., U. P. and U. C. formulated the idea. M. K. performed the synthesis and sulfurization of the CuO nanowires, contributed to SEM and TEM analysis, analyzed the data, and wrote the original draft. J. Z. contributed to the TEM analysis and editing of the manuscript draft. U. P. contributed to the data analysis and manuscript editing. O. B. designed a theoretical model and performed simulations. U. C. supervised the research and prepared the final version of the manuscript.

Competing interest:

The authors have no competing interests to declare.

Materials and Correspondence:

Correspondence to: Uroš Cvelbar

Supporting information file for manuscript:

Driving the phase transformation in single crystals by diffusion

Martin Košiček[a,b], Janez Zavašnik[a,b], Oleg Baranov[a,c], Uroš Puc[b,d], Uroš Cvelbar[a,b]

[a]Department of Gaseous Electronics, Jožef Stefan Institute, 1000 Ljubljana, Slovenia

[b]Jožef Stefan International Postgraduate School, 1000 Ljubljana, Slovenia

[c]Department of Theoretical Mechanics, Engineering and Robomechanical Systems, National Aerospace University, 61070 Kharkiv, Ukraine

[d]Institute of Computational Physics, Zurich University of Applied Sciences (ZHAW), 8401 Winterthur, Switzerland

Additional experimental details

CuO NWs were synthesized via the thermal oxidation of copper foils. The experimental setup is shown in Supplementary Fig. 1. Copper foil was placed on an alumina holder in the tube furnace, heated, and oxidized in a stream of oxygen.

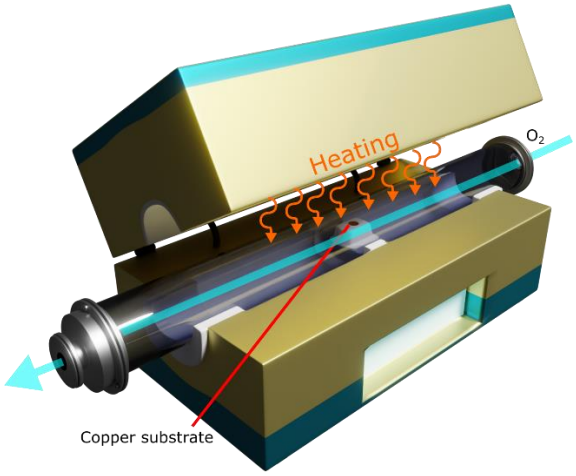

Supplementary Fig. 1: Schematic of thermal oxidation process.

The exact temperature in the furnace was determined by measurements with a thermocouple. The exact temperature differed significantly from the one set (when the temperature was set to 300 °C, the thermocouple showed 265 °C). The temperature measurement error was estimated based on the observed hysteresis, as the temperature achieved by heating the furnace from room temperature was slightly different from the temperature achieved by first overheating the furnace to a higher temperature followed by cooling to the set temperature.

Sulfurization of NWs was conducted in the same experimental setup, except the oxygen was replaced with hydrogen sulfide (H_2S). In this case, H_2S was not flowing through the quartz tube. Instead, quartz tube was filled with H_2S to the desired pressure and sealed (Supplementary Fig. 2).

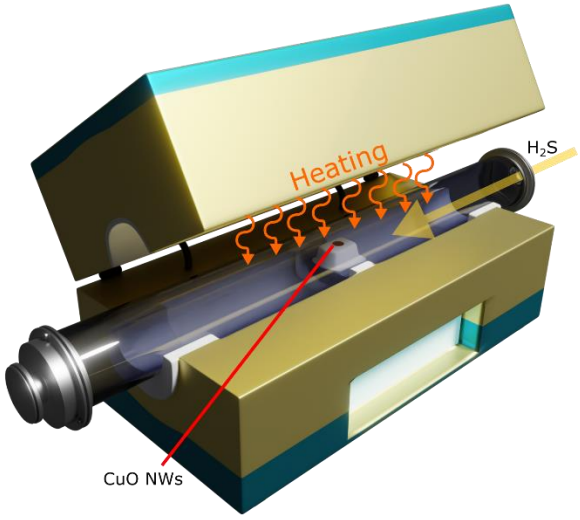

Supplementary Fig. 2: Schematic representation of CuO NWs sulfurization process

TEM micrographs of copper oxide nanowires

CuO nanowires (NWs) synthesized by the thermal oxidation of copper foils exhibit a central twin boundary. Examples of such NWs are seen in Supplementary Fig. 3

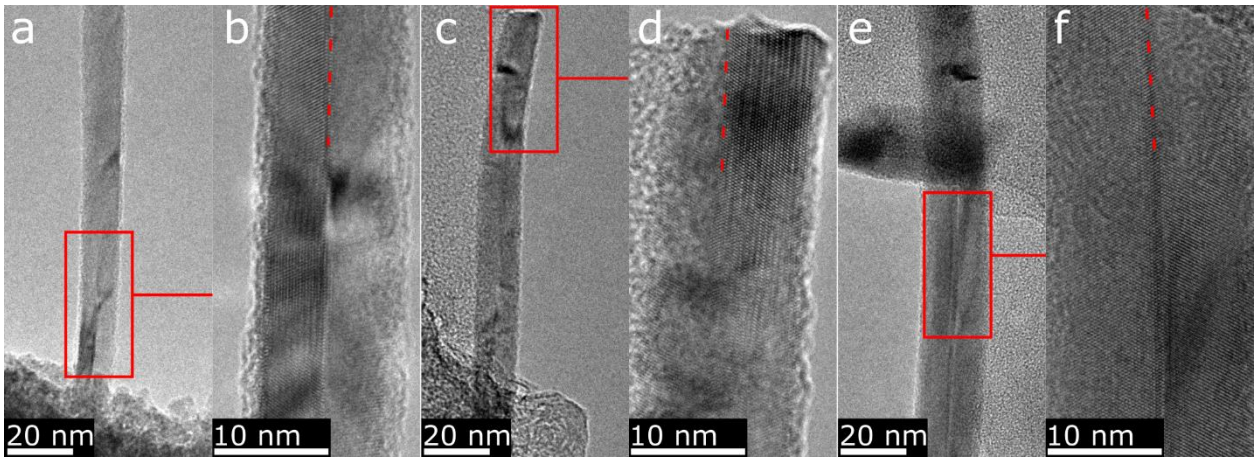

Supplementary Fig. 3: Examples of CuO nanowires synthesized via thermal oxidation of copper foils. a, c, e low magnification micrographs with corresponding high magnification micrographs (**b, d, f**). Central twin boundaries are marked with red dashed lines.

Raman spectra

Raman spectra of the oxidized copper foil with grown NWs were taken at room temperature for two hours before and after sulfurization. Supplementary Fig. 4a shows photographs of photographs of oxidized copper oxide foil with NWs before and after the oxidation, and Supplementary Fig. 4b shows corresponding Raman spectra. An additional peak at around 470 cm^{-1} is observed, corresponding to the S-S bond in copper sulfides, indicating the formation of the copper sulfide phase.

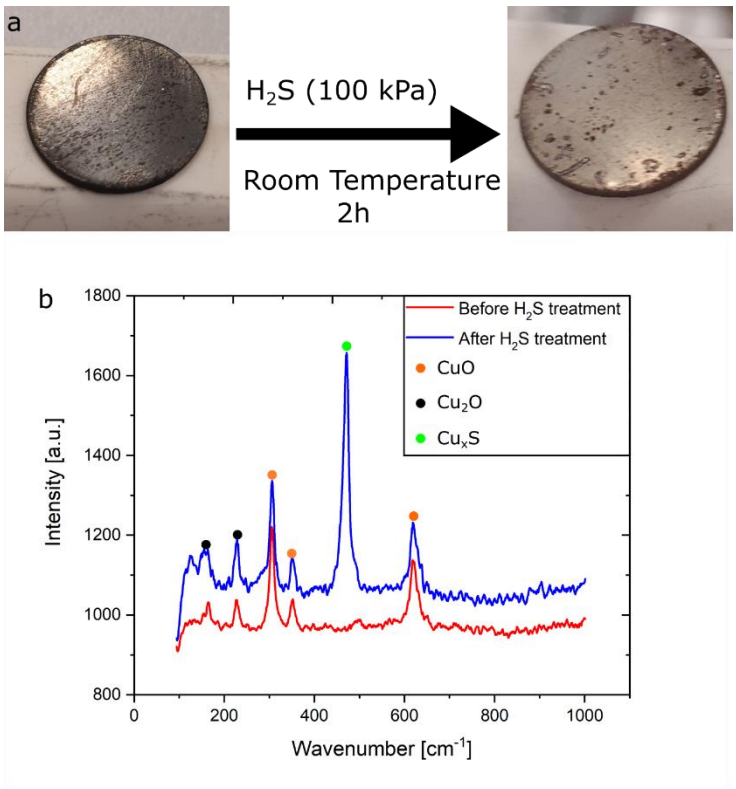

Supplementary Fig. 4: Raman analysis of substrate with embedded NWs before and after oxidation. **a** Photographs of the oxidized copper foil with CuO NWs before and after oxidation. **b** Corresponding Raman spectra.

TEM analysis of the sulfurized NWs

- **TEM analysis of the attached NWs sulfurized for two hours at H_2S pressure 100 kPa and room temperature**

TEM analysis of the sample sulfurized for two hours at H_2S pressure 100 kPa and room temperature indicated that some of the transformed NWs were thin and still in the initial stages of the transformation, as seen in Supplementary Fig. 5, while others considerably grew and thickened. This allowed us to observe different stages of the transformation, as seen in Supplementary Fig. 5a-e. The diffraction pattern of the structure in Supplementary Fig. 5e is also shown. As can be seen, there are too few grains in the structure to produce ring patterns. It is virtually impossible to deduce the phase from the pattern as numerous copper sulfides exhibit similar diffraction patterns, and we would need the complete ring of the electron-diffraction pattern to figure out the phase.

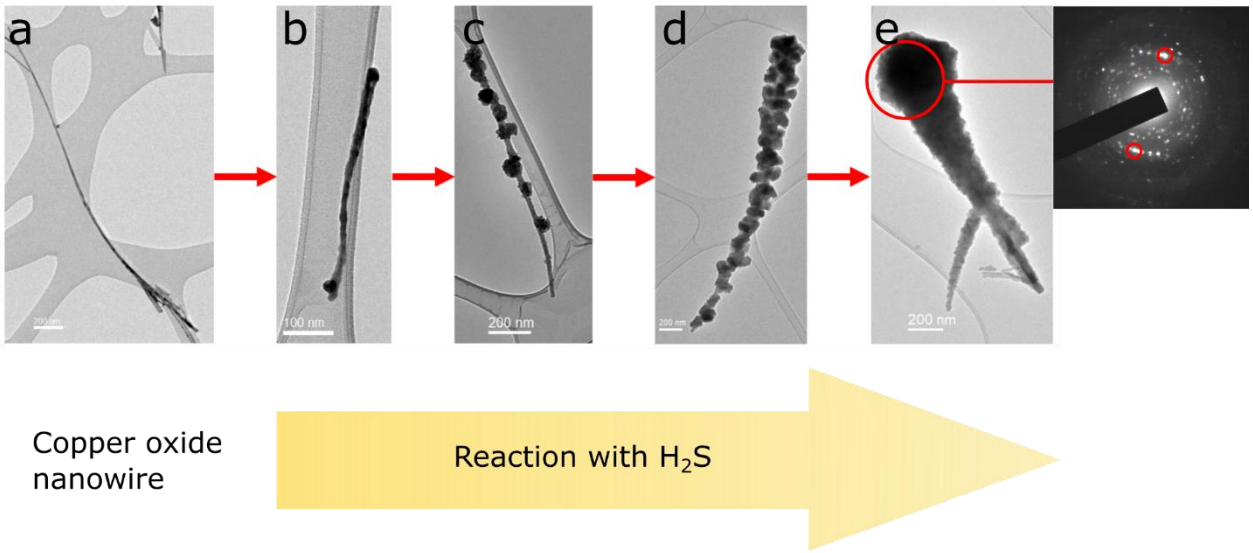

Supplementary Fig. 5: Sulfurized NWs from the oxidized copper foil exposed to H_2S at 100 kPa for 2 hours at room temperature. NWs at different stages of the sulfurization were found. **a** CuO NW prior to sulfurization. **b** Thin sulfurized NW at the beginning stages of sulfurization. **c** NW with visible nucleated copper sulfide grains along its surface. **d** NW overgrown by the sulfide crystals, showing a higher rate of sulfurization on top of the NW. **e** NW completely overgrown by copper sulfide phase. The top part undergoes the highest sulfurization rate. Polycrystalline diffraction pattern from the nanostructure is also shown. However, there are not enough grains in the sample to produce a ring pattern. The strong peak marked with a red circle corresponds to a lattice d-spacing of approximately 1.95 Å and could correspond to the (630) or (060) plane of chalcocite. However, other phases, such as djurleite, anilite, and roxbyite, exhibit strong diffraction peaks at the same d-value.

Even though the sulfurized NWs appear polycrystalline, the single-crystalline remnants of CuO NWs were still found in the center of the NW, encapsulated by the sulfide phase. Examples of NWs where such a center is visible can be seen in Supplementary Fig. 6a-d.

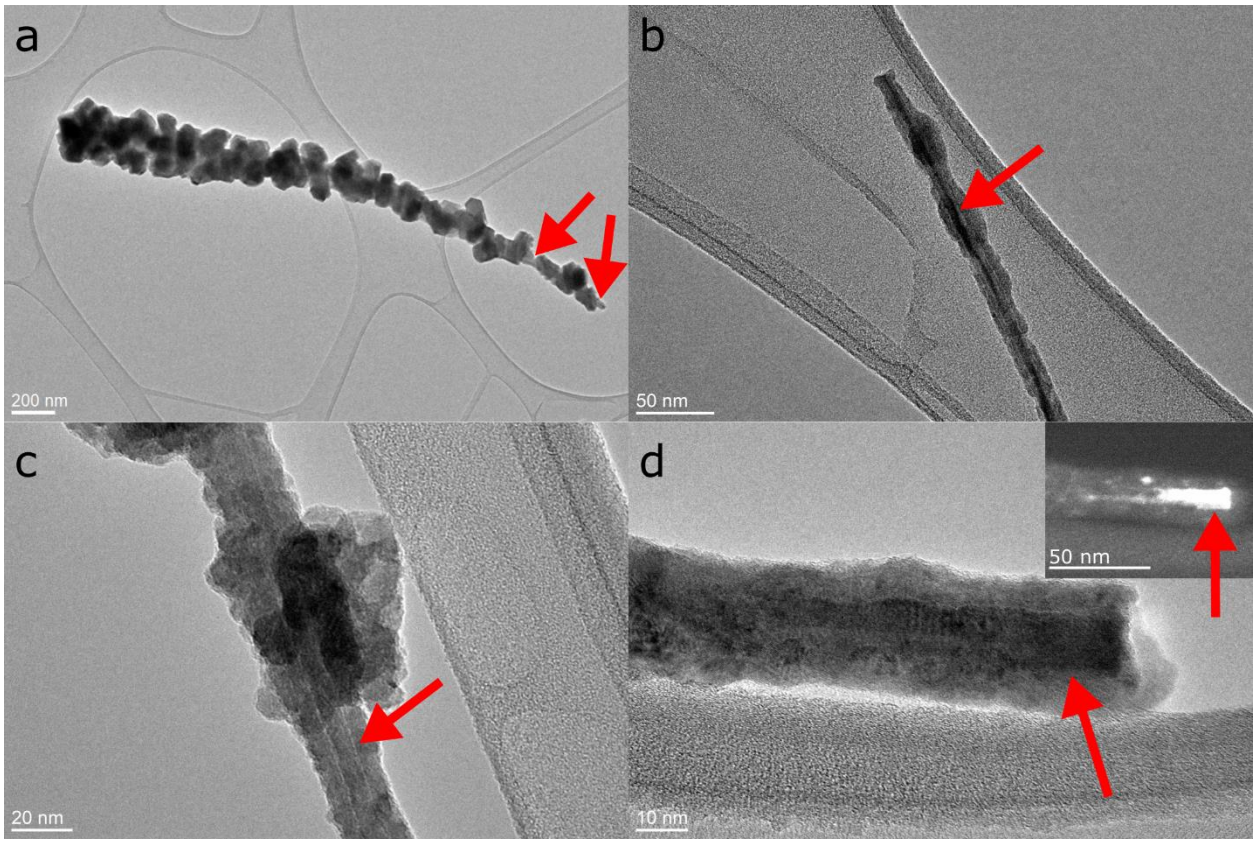

Supplementary Fig. 6: TEM micrographs of the sulfurized isolated CuO NWs with visible residues of the original CuO NW in the center of the newly formed nanostructures. a-d The residues are marked with red arrows. The CuO residue is clearly visible in the dark-field micrograph in the inset of **d**.

- **TEM analysis of the isolated NWs sulfurized for 2 hours at a H_2S pressure of 100 kPa and room temperature**

TEM analysis of the isolated NWs for 2 hours at a H_2S pressure of 100 kPa and room temperature resulted in the formation of an amorphous sulfur-containing layer around the NWs, as seen in examples in Fig 1i,k in the main text and Supplementary Fig. 7a-d

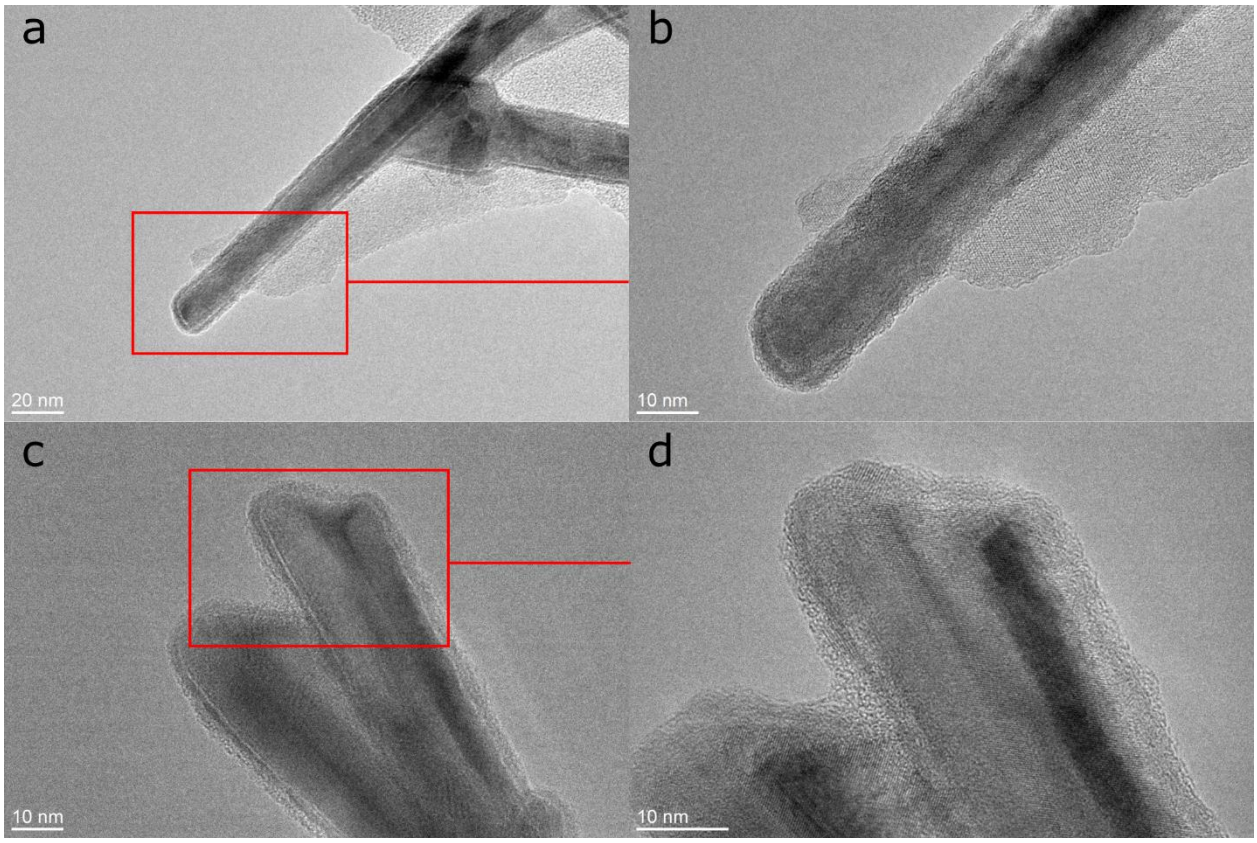

Supplementary Fig. 7: TEM micrographs of NWs encapsulated in thin, amorphous, sulfur-containing layer. a-d Additional examples of CuO NWs that were detached from the oxidized copper substrate on which they were grown and treated with H_2S for 2 hours, at room temperature and a H_2S pressure of 100 kPa.

- **TEM analysis of the attached NWs sulfurized at a H_2S pressures of 10 kPa and 1 kPa at 110 °C for 30 min (of which 20 min included heating from room temperature to 110 °C).**

When exposed to H_2S at increased temperature, CuO NWs transformed into the copper sulfide NWs composed of individual single-crystalline segments arranged along the NW length. Some transformed NWs exhibited uniform diameters along their length (example in Fig. 2e,f in the main text), while most were still thicker at the top (examples in Supplementary Fig. 8a-d).

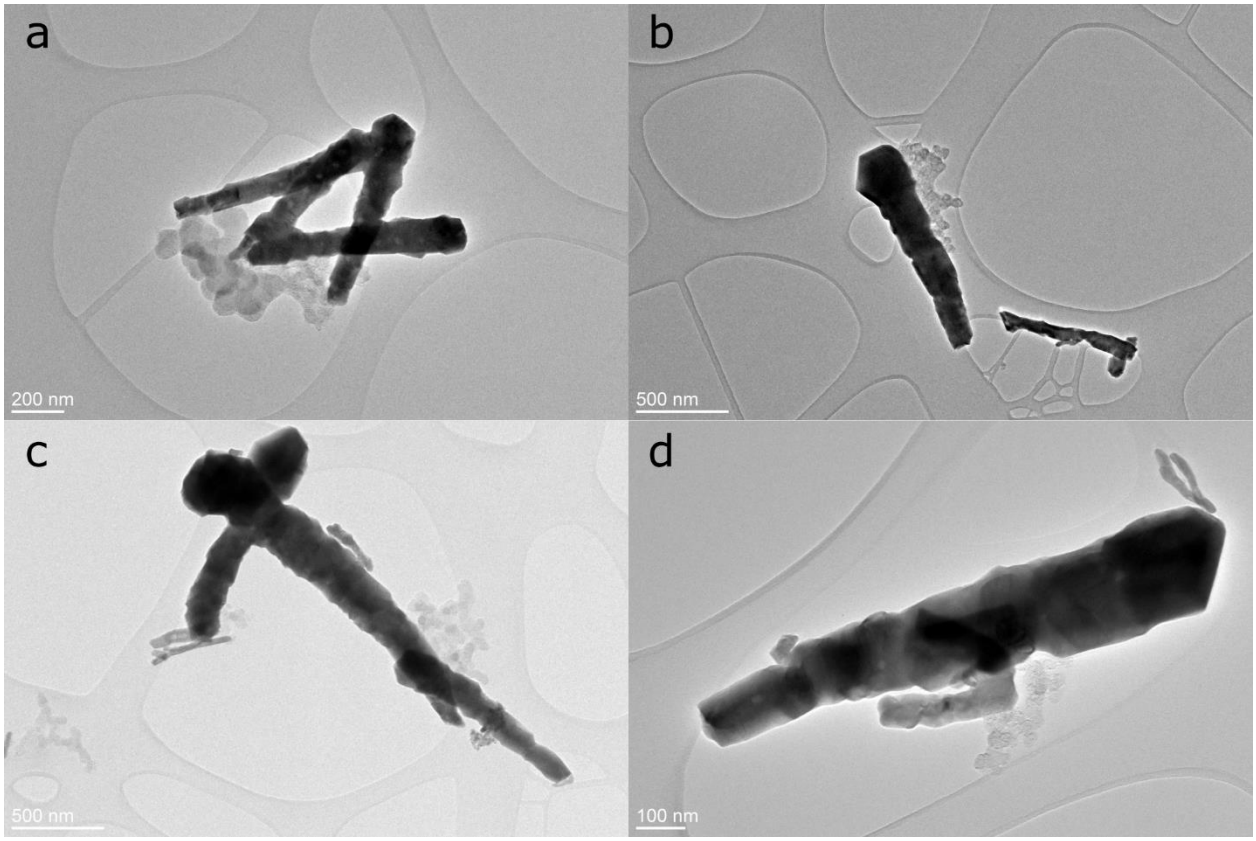

Supplementary Fig. 8: TEM micrographs of nanostructures with thicker top parts. a-d Examples of nanostructures obtained with sulfurization of attached NWs with H_2S at 110 °C, H_2S pressure of 1 kPa for 30 min (of which 20 min included heating from the room temperature to 110 °C).

Some grains that comprise the segmented structure have similar orientations, indicating the epitaxial growth of copper sulfide on the copper oxide. Example of such segments can be seen in Supplementary Fig. 9:

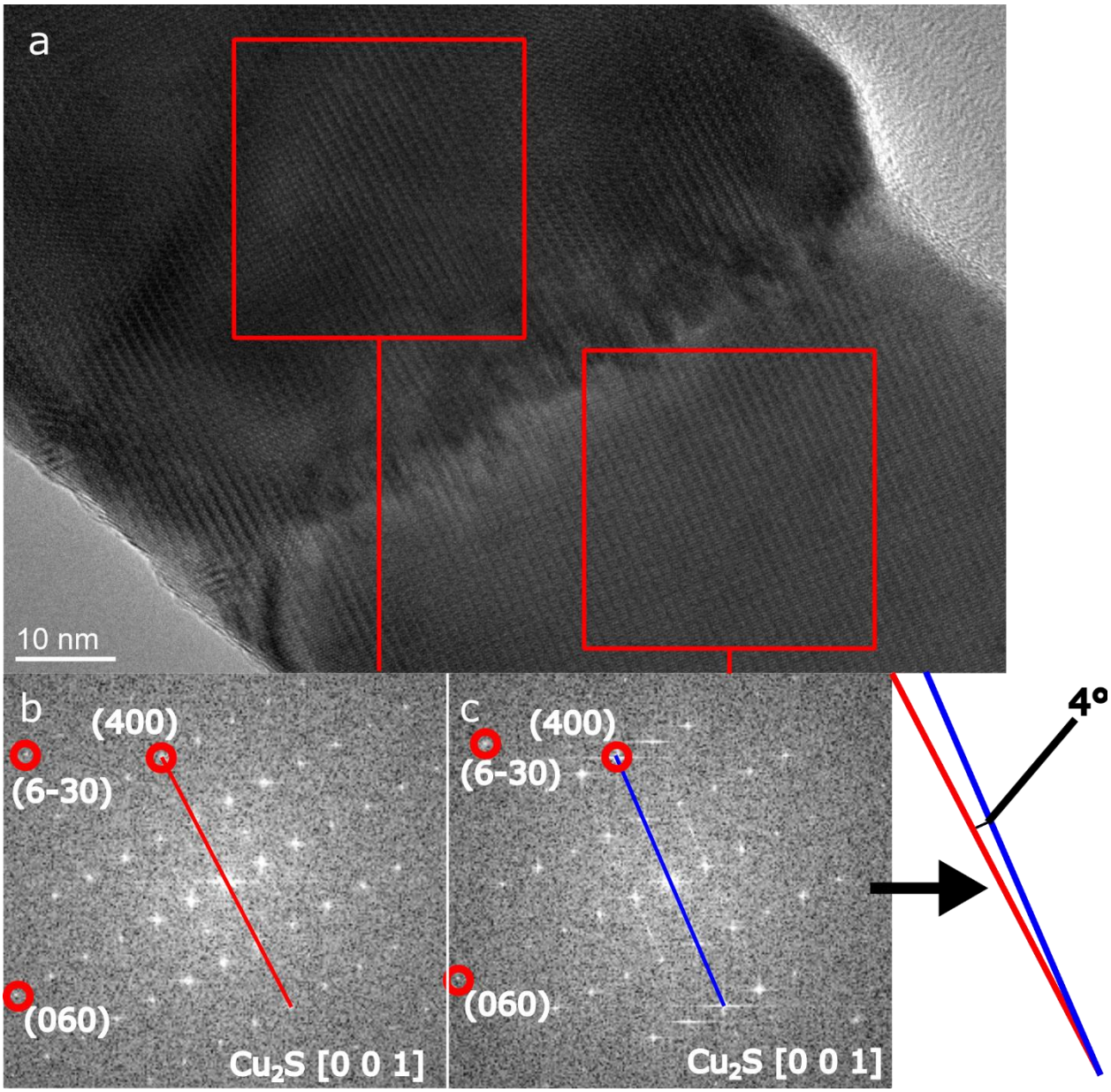

Supplementary Fig. 9: Grain boundary between two segments in the segmented structure of the copper sulfide NW. **a** TEM micrograph of the grain boundary in the NW obtained by sulfurizing CuO NWs embedded in the copper-rich substrate with H_2S at 110 °C, H2S pressure of 10 kPa for 30 min (of which 20 min included heating from room temperature to 110 °C). **b, c** FFTs of neighboring segments indicate that the segments are slightly tilted towards one another. Nevertheless, they exhibit similar orientations.

- **TEM analysis of the isolated NWs sulfurized at H_2S pressures of 10 kPa and 1 kPa at 110 °C for 30 min (of which 20 min included heating from room temperature to 110 °C).**

When isolated NWs were exposed to H_2S at increased temperature, polycrystalline sulfide NWs were observed exhibiting Kirkendall voids. Examples of NWs with such a structure are shown in Supplementary Fig. 10a-f.

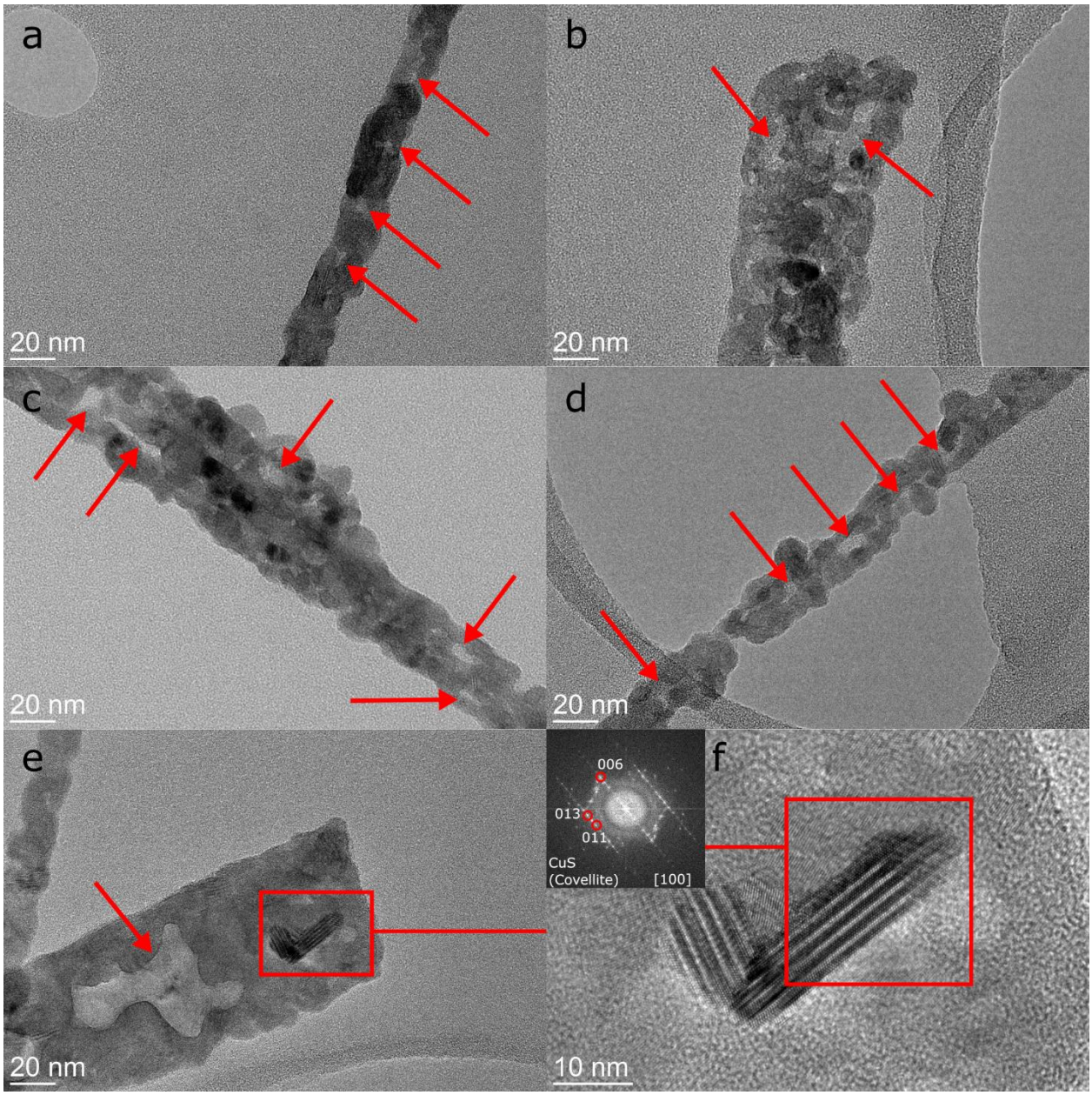

Supplementary Fig. 10: Examples of isolated copper sulfide NWs after copper oxide NWs were isolated and treated with H_2S. Examples include NWs treated at H_2S pressures of 10 kPa (a-c) and 1 kPa. (d, e) at 110 °C for 30 min (of which 20 min included heating from room temperature to 110 °C). Voids in the newly formed structures are indicated with red arrows. f enlarged part, from which grain with covellite CuS phase is observed as determined from the inset FFT.

Grains in isolated transformed NWs were randomly oriented and predominantly composed of covellite phase, as demonstrated in Supplementary Fig. 11.

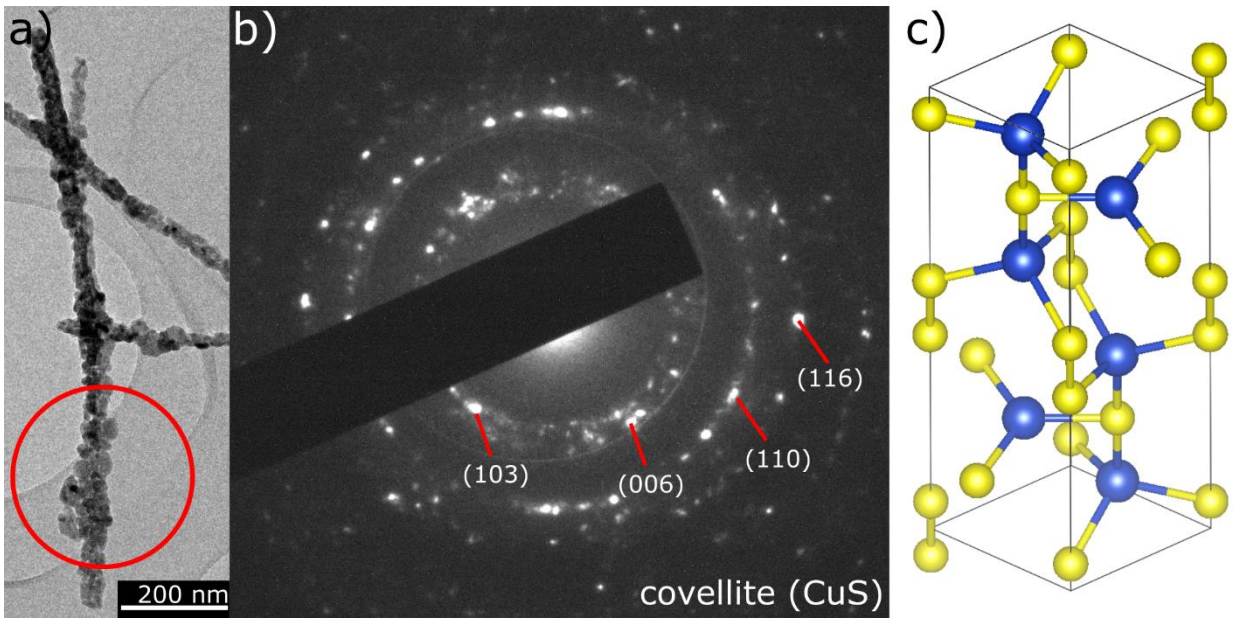

Supplementary Fig. 11: Electron-diffraction analysis of sulfurized isolated NWs. a TEM micrograph of the isolated NW sulfurized at at 110 °C, H_2S pressure of 1 kPa for 30 min (of which 20 min included heating from room temperature to 110 °C). **b** SAED pattern of the area marked with a red circle in **a**. **c** Model of covellite crystal structure.

TEM analysis of the copper sulfide layer below sulfurized NWs

Energy-dispersive x-ray spectroscopy EDS measurements performed on the CuO sample sulfurized for 2 hours at a H_2S pressure of 100 kPa and room temperature indicate that apart from the NWs, the copper oxide layers below NWs also sulfurize (Supplementary Fig. 12a). This is confirmed by the polycrystalline electron-diffraction pattern in Supplementary Fig. 12b.

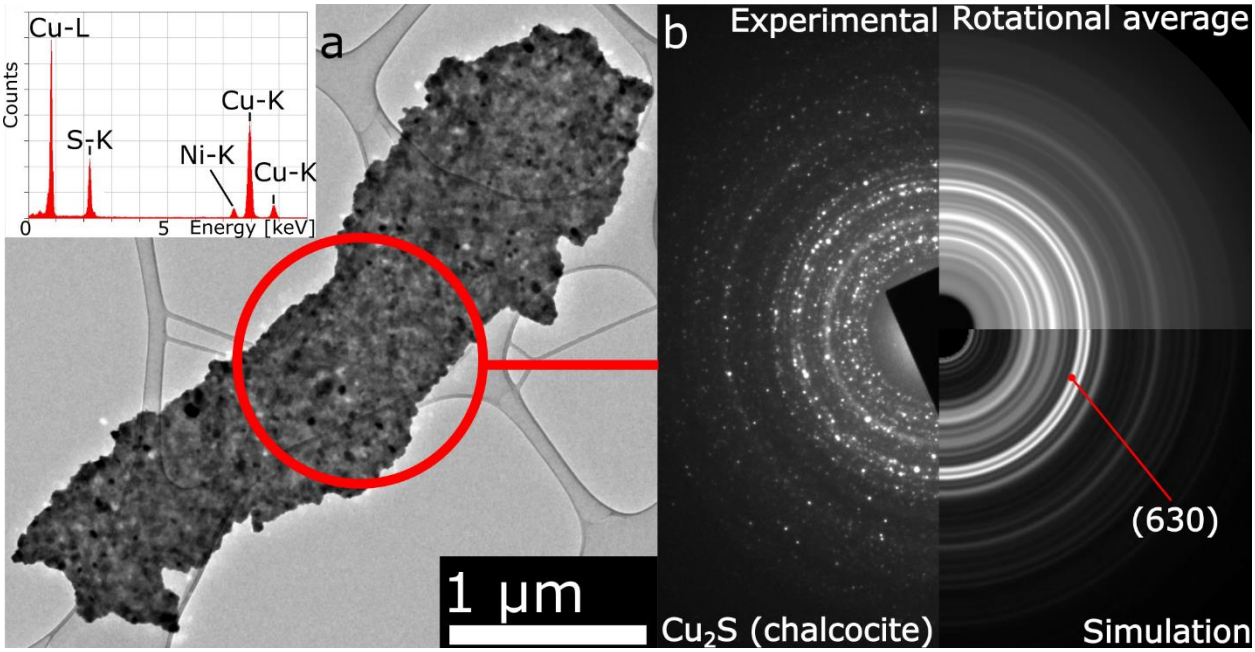

Supplementary Fig. 12: Analysis of the sulfurized layer serving as the base for NW growth for 2 hours at a H_2S pressure of 100 kPa and room temperature. a TEM micrograph with EDS. b Corresponding polycrystalline electron-diffraction pattern confirming the presence of low chalcocite phase in the layer

Theoretical model

A theoretical model was proposed to describe the results of the experiments.

When a nanowire of copper oxide is removed from the ground oxide layer, the delivery of copper atoms from the external source (i.e., the copper layer) is terminated. That is why the sulfurization is provided by the CuO stem of the nanowire, according to the equation:

$$CuO + H_2S \rightarrow CuS + H_2O. \quad \text{(S1)}$$

It is assumed that after the reaction, a layer of copper sulfide is formed on the surface of the nanowire; for that, the bonding energy is high, so copper and sulfur do not diffuse into the depth of the nanowire. In contrast, CuO aggregates from the nanowire body diffuse towards the surface of the copper sulfide that is exposed to the action of hydrogen sulfide. On the surface, the sulfurization reaction occurs, thus increasing the thickness of the CuS layer. Due to the low diffusivity, the lower boundary of the CuS layer does not shift from its initial position, which is located at a distance R_{nw} from the nanowire center. At the same time, the diffusion of species from the CuO layer to the surface of the CuS layer results in a decrease in the thickness of the CuO layer. Since the initial coordinate of the lower boundary of the CuS layer is not changed, and both the layers are considered continuous, the decrease in thickness of the CuO layer means the generation of an internal void . The schematic of the processes is shown in Fig. 3a.

Hydrogen sulfide molecules are adsorbed on the surface of a detached nanowire, and the density n_{H2S} of the adsorbed molecules with respect to the density n_{CuS} of the adsorption nodes is[1]

$$\frac{n_{H2S}}{n_{CuS}} = \frac{P_{H2S}}{P_0 + P_{H2S}}, \quad \text{(S2)}$$

where P_{H2S} is the pressure of hydrogen sulfide, Pa; $n_{CuS} = a_{CuS}^{-2}$ (a_{CuS} is a lattice period of CuS); P_0 is the constant that depends on the temperature:

$$P_0 = \left(\frac{M_{H2S}}{2\pi\hbar^2}\right)^{3/2} (k_B T_s)^{5/2} exp\left[-\frac{e(\varepsilon_{aH2S} - \varepsilon_{i-H2S})}{k_B T_s}\right], \quad \text{(S3)}$$

where M_{H2S} is the mass of the hydrogen sulfide molecule, kg; ε_{aH2S} is the adsorption energy (eV) of the molecule on the surface; and $\varepsilon_{i\text{-}H2S}$ is the internal energy (eV) of the molecule.

The flux of CuO aggregates that diffuse through the CuS layer describes the diffusion along a layer with a thickness L_{CuS}, while the reaction (S1) takes place on the surface of the CuS layer only. Thus, the density $n_{CuO}(z)$ of the CuO aggregates on the CuS surface is described by the equation with D_{CuO} as a diffusion coefficient:

$$D_{CuO} \frac{d^2 n_{CuO}}{dz^2} = 0, \quad \text{(S4)}$$

$$n_{CuO} - n_{CuO0} = -\frac{\varphi_{CuO}}{D_{CuO}} a_{CuS} L_{CuS}, \quad \text{(S5)}$$

$$D_{CuO} = D_{0c1} exp\left[-\frac{e\varepsilon_{c1}}{k_B T_s}\right] = \alpha_{Dc1} \frac{\nu_0 a_{CuS}^2}{2} exp\left[-\frac{e\varepsilon_{c1}}{k_B T_s}\right] = \alpha_{Dc1} \frac{k_B T_s}{h} a_{CuS}^2 exp\left[-\frac{e\varepsilon_{c1}}{k_B T_s}\right], \quad \text{(S6)}$$

where ε_{c1} is the diffusion activation energy; L_{CuS} is the thickness of the CuS layer; ν_0 is the frequency of the lattice oscillations; and h is Plank's constant.

The flux of CuO aggregates φ_{CuO} at the surface is determined by the rate of reaction (S1), that is:

$$\varphi_{CuO}(L_{CuS}) = \frac{1}{2} n_{CuO} \frac{n_{H2S}}{n_{CuS}} \nu_0 exp\left[-\frac{e(\varepsilon_{c1}+\varepsilon_{x-dis})}{k_B T_s}\right], \quad \text{(S7)}$$

where $\varepsilon_{x\text{-}dis}$ is the energy of CuO dissociation in the presence of an H_2S molecule.

After combining equations (S5) and (S7), the flux φ_{CuO} can be found:

$$\varphi_{CuO} = \frac{n_{H2S}}{1+\frac{a_{CuS}\nu_0}{2D_{0c1}} L_{CuS} \frac{n_{H2S}}{n_{CuS}} exp\left[-\frac{e\varepsilon_{x-dis}}{k_B T_s}\right]} \frac{\nu_0}{2} \frac{n_{CuO0}}{n_{CuS}} \nu_0 exp\left[-\frac{e(\varepsilon_{c1}+\varepsilon_{x-dis})}{k_B T_s}\right]. \quad \text{(S8)}$$

Then, the rate of increase of the thickness of the CuS layer and the corresponding rate of the decrease of the thickness of the CuO layer are

$$\frac{dL_{CuS}}{dt}(L_{CuS}) = \varphi_{CuO} a_{CuS}^3 = \frac{1}{1+\frac{a_{CuS}\nu_0}{2D_{0c1}} L_{CuS} \frac{n_{H2S}}{n_{CuS}} exp\left[-\frac{e\varepsilon_{x-dis}}{k_B T_s}\right]} \frac{n_{H2S}}{n_{CuS}} \frac{\nu_0}{2} \frac{R_{nw}}{R_{nw}+L_{CuS}} n_{CuO0} a_{CuS}^3 exp\left[-\frac{e(\varepsilon_{c1}+\varepsilon_{x-dis})}{k_B T_s}\right], \quad \text{(S9)}$$

$$\frac{dL_{CuO}}{dt}(L_{CuS}) = -\varphi_{CuO} a_{CuO}^3 = -\frac{1}{1+\frac{a_{CuS}\nu_0}{2D_{0c1}} L_{CuS} \frac{n_{H2S}}{n_{CuS}} exp\left[-\frac{e\varepsilon_{x-dis}}{k_B T_s}\right]} \frac{n_{H2S}}{n_{CuS}} \frac{\nu_0}{2} \frac{R_{nw}-L_{CuO}}{R_{nw}} n_{CuO0} a_{CuO}^3 exp\left[-\frac{e(\varepsilon_{c1}+\varepsilon_{x-dis})}{k_B T_s}\right], \quad \text{(S10)}$$

with the initial conditions $L_{CuS}(0) = L_{CuS0}$, $L_{CuO}(0) = R_{nw}$.

When a nanowire of copper oxide is attached to the ground oxide layer in the presence of gaseous hydrogen sulfite, the diffusion of Cu_2O aggregates along the CuO surface is defined by the sulfurization process as on a side surface as on the tip of the nanowire. The processes occurring in the discussed system are illustrated in Fig. 3h.

Migration of the Cu_2O aggregate along the CuO layer is described with a set of events when one copper atom is released from the aggregate, thus converting it to the CuO aggregate, and moves to the next position, which results in the formation of Cu_2O aggregate at the position.

When reaching an adsorbed H_2S molecule, the Cu_2O aggregate undergoes the following reaction, accompanied by the formation of the Cu_2S aggregate.

$$Cu_2O + H_2S \rightarrow Cu_2S + H_2O. \quad \text{(S11)}$$

The initial concentration n_{Cu20nw} of Cu_2O aggregates at the nanowire root is determined by the processes of copper diffusion along the oxide layers, and the copper flux is not affected by H_2S molecules at that:

$$n_{Cu20nw} = n_{Cu2O} - \frac{\varphi_{Cu2nw}}{D_{Cu2}} a_{CuO} L_{CuO} = n_{Cu2O} - \frac{\varphi_{Cu2nw}}{D_{0c2}} a_{CuO} L_{CuO} exp\left(\frac{e\varepsilon_{c2}}{k_B T_s}\right), \quad \text{(S12)}$$

where the initial density n_{Cu2O} is the density of Cu_2O in the Cu_2O/CuO boundary; $n_{Cu2O} = a_{Cu2O}^{-2}$; a_{Cu2O} and a_{CuO} are the lattice periods of Cu_2O and CuO, respectively.

Under the condition of the sulfurization reaction on the side surface of a nanowire, the distribution of the copper atoms along the nanowire surface is:

$$D_{Cus} \frac{\partial^2 n_{cu}(z)}{\partial z^2} = -n_{Cu}(z) \frac{n_{H2S}(z)}{n_{CuO}} \nu_0 exp\left(-\frac{e\varepsilon_{x-dis}}{k_B T_s}\right), \quad \text{(S13)}$$

where $n_{H2S}(z)$ is the density of H_2S molecules adsorbed on the side surface of the nanowire; $\varepsilon_{x\text{-}dis}$ is the energy of dissociation of adsorbed H_2S molecule at the proximity of Cu_2O aggregate.

The diffusion coefficient D_{Cus} is expressed as

$$D_{Cus} = D_{Cus0} exp\left(-\frac{e\varepsilon_{c2s}}{k_B T_s}\right), \tag{S14}$$

$$\frac{\partial^2 n_{cu}(z)}{\partial z^2} = -n_{Cu}(z)\frac{n_{H2S}(z)}{n_{CuO}}\frac{\nu_0}{D_{Cus0}} exp\left(-\frac{e(\varepsilon_{x-dis}-\varepsilon_{c2s})}{k_B T_s}\right), \tag{S15}$$

where ε_{c2s} is the energy of the release of the Cu atom from Cu_2O aggregate, which should be spent to allow migrating of the Cu_2O aggregate along the CuO layer; $n_{CuO} = a_{CuO}^{-2}$.

To describe the results of the experiment, the density of H_2S molecules is assumed to be changed linearly along the length of the nanowire:

$$n_{xS}(z) = \alpha_{xs0} z. \tag{S16}$$

Thus, the resulting equation to find the density of Cu_2O aggregates along the nanowire in the presence of an H_2S molecule is

$$\frac{\partial^2 n_{cu}(z)}{\partial z^2} = -\frac{n_{Cu}(z)}{n_{CuO}}\alpha_{xs0} z\frac{\nu_0}{D_{Cus0}} exp\left(-\frac{e(\varepsilon_{x-dis}-\varepsilon_{c2s})}{k_B T_s}\right) = -a_n z n_{Cu}(z) \tag{S17}$$

where $a_n = \frac{\alpha_{xs0}}{n_{CuO}}\frac{\nu_0}{D_{Cus0}} exp\left(-\frac{e(\varepsilon_{x-dis}-\varepsilon_{c2s})}{k_B T_s}\right)$.

The solution is expressed in terms of the Bessel functions and modified Bessel functions[2]

$$n_{Cu}(z) = C_1\sqrt{z}J_{\frac{1}{3}}\left(\frac{2}{3}\sqrt{a_n}z^{\frac{3}{2}}\right) + C_2\sqrt{z}Y_{\frac{1}{3}}\left(\frac{2}{3}\sqrt{a_n}z^{\frac{3}{2}}\right) \tag{S18}$$

To find the constants C_1 and C_2, the boundary conditions are implied

$$n_{Cu}(0) = n_{Cu20nw}; \qquad \frac{d}{dz}n_{Cu}(z) = 0. \tag{S19}$$

Since the following relations take place

$$\lim_{z\to 0^+} n_{Cu}(z) = -\frac{2C_2}{3^{\frac{1}{6}}\cdot a_n^{\frac{1}{6}}\cdot\Gamma\left(\frac{2}{3}\right)} = -\frac{1.23}{a_n^{\frac{1}{6}}}C_2; \quad \lim_{z\to 0^+}\left[\frac{d}{dz}n_{Cu}(z)\right] = \frac{3^{\frac{2}{3}}\cdot a_n^{\frac{1}{6}}\cdot\Gamma\left(\frac{2}{3}\right)\cdot(\sqrt{3}C_1+C_2)}{2\pi} = 0.448a_n^{\frac{1}{6}}(\sqrt{3}C_1 + C_2), \tag{S20}$$

the constants are:

$$C_1 = 0.469a_n^{\frac{1}{6}}n_{Cu20nw}; \qquad C_2 = -0.813a_n^{\frac{1}{6}}n_{Cu20nw}, \tag{S21}$$

The solution of the above equation allows us to obtain $n_{cu}(z)$, under condition of $n_{Cu}(0) = n_{Cu20nw}$

$$n_{Cu}(z) = 0.813a_n^{\frac{1}{6}}n_{Cu20nw}\left[\sqrt{\frac{z}{3}}J_{\frac{1}{3}}\left(\frac{2}{3}\sqrt{a_n}z^{\frac{3}{2}}\right) - \sqrt{z}Y_{\frac{1}{3}}\left(\frac{2}{3}\sqrt{a_n}z^{\frac{3}{2}}\right)\right] = n_{Cu20nw}F_B(z), \tag{S22}$$

$$F_B(z) = 0.813a_n^{\frac{1}{6}}\left[\sqrt{\frac{z}{3}}J_{\frac{1}{3}}\left(\frac{2}{3}\sqrt{a_n}z^{\frac{3}{2}}\right) - \sqrt{z}Y_{\frac{1}{3}}\left(\frac{2}{3}\sqrt{a_n}z^{\frac{3}{2}}\right)\right]. \tag{S23}$$

The number of copper atoms converted per one second from Cu_2O to Cu_2S by a side surface of one nanowire with length L_{nw} is:

$$N_{Cus}(L_{nw}) = \int_0^{L_{nw}} n_{Cu}(z)\frac{\alpha_{xs0}}{n_{CuO}}\nu_0 exp\left(-\frac{e\varepsilon_{x-dis}}{k_B T_s}\right)2\pi R_{nw}(z)zdz. \tag{S24}$$

However, by considering the experimentally observed constant distribution of the nanowire radius R_{nw} along the length, the expression is simplified:

$$N_{Cus}(L_{nw}) = \frac{\alpha_{xs0}}{n_{CuO}} \nu_0 exp\left(-\frac{e\varepsilon_{x-dis}}{k_B T_s}\right) 2\pi R_{nw} \int_0^{L_{nw}} n_{Cu}(z) z dz. \quad \text{(S25)}$$

It should be stressed that during the sulfurization process, the length of the nanowire L_{nw}, which is the length of the CuO structure, stays constant. However, the flux of Cu_2O aggregates that are delivered to the nanowire tip forms a 'head' on the nanowire. The parameters of growth for the head can be calculated using the reported model, which considers a similar two-stage growth of a nanowire under the condition that the characteristics of the adsorption of the 'main' part of the nanowire and the 'head' are different[3].

The number of copper atoms converted per second from Cu_2O to Cu_2S by the top surface of the nanowire with length L_{nw} is:

$$N_{Cut}(L_{nw}) = n_{Cu}(L_{nw}) \frac{n_{H2St}}{n_{CuO}} \nu_0 exp\left(-\frac{e\varepsilon_{x-dis}}{k_B T_s}\right) \pi R_{nw}^2, \quad \text{(S26)}$$

where n_{H2St} is the density of H_2S molecules adsorbed on the tip of the nanowire.

Hence, the flux of copper atoms consumed by one nanowire is

$$\varphi_{Cu2nw}(L_{nw}) = \frac{1}{\pi R_{nw}^2(0)} [N_{Cus}(L_{nw}) + N_{Cut}(L_{nw})] =$$

$$= \frac{n_{Cu20nw}}{R_{nw}^2(0)} \frac{\nu_0}{n_{CuO}} exp\left(-\frac{e\varepsilon_{x-dis}}{k_B T_s}\right) \begin{bmatrix} \int_0^{L_{nw}} F_B(z) \alpha_{xs0} 2R_{nw} z dz + \\ + F_B(L_{nw}) n_{xt} R_{nw}^2 \end{bmatrix} = \frac{n_{Cu20nw}}{R_{nw}^2(0)} \frac{\nu_0}{n_{CuO}} exp\left(-\frac{e\varepsilon_{x-dis}}{k_B T_s}\right) F(L_{nw}), \quad \text{(S27)}$$

$$F_c(L_{nw}) = \begin{bmatrix} \int_0^{L_{nw}} F_B(z) \alpha_{xs0} 2R_{nw} z dz + \\ + F_B(L_{nw}) n_{xt} R_{nw}^2 \end{bmatrix}. \quad \text{(S28)}$$

After substituting (S27) into (S12), the density of the copper atoms at the nanowire root is:

$$n_{Cu20nw}(L_{CuO}, L_{nw}) = \frac{n_{Cu2O}}{1 + \frac{a_{CuO}\nu_0}{D_{0c2}} L_{CuO} \gamma_L F_c(L_{nw})}, \quad \text{(S29)}$$

$$\gamma_L = \frac{1}{n_{CuO} R_{nw}^2} exp\left[-\frac{e(\varepsilon_{x-dis} - \varepsilon_{c2})}{k_B T_s}\right]. \quad \text{(S30)}$$

The rate of the nanowire growth due to the formation of the Cu_2S head is

$$\frac{dL_{nw}}{dt}(L_{CuO}, L_{nw}) = N_{Cut}(L_{nw}) \frac{a_{Cu2S}^3}{\pi R_{nw}^2} =$$
$$n_{Cu20nw}(L_{CuO}, L_{nw}) F_B(L_{nw}) \frac{n_{xt}}{n_{CuO}} a_{Cu2S}^3 \nu_0 exp\left(-\frac{e\varepsilon_{x-dis}}{k_B T_s}\right), \quad \text{(S31)}$$

where a_{Cu2S} is a lattice period of Cu_2S.

The rate of growth of the Cu_2S layer on the side surface of the nanowire is:

$$\frac{dL_{Cu2S}}{dt}(z, L_{CuO}, L_{nw}) = n_{Cu}(z) \frac{n_{xs}(z)}{n_{CuO}} \nu_0 exp\left(-\frac{e\varepsilon_{x-dis}}{k_B T_s}\right) a_{Cu2S}^3 =$$

$$= n_{Cu20nw}(L_{CuO}, L_{nw}) F_B(z) \frac{\alpha_{xs0}}{n_{CuO}} z a_{Cu2S}^3 \nu_0 exp\left(-\frac{e\varepsilon_{x-dis}}{k_B T_s}\right). \quad \text{(S32)}$$

$$L_{Cu2S}(z, L_{CuO}, L_{nw}, t) = n_{Cu20nw}(L_{CuO}) F_B(z) \frac{\alpha_{xs0}}{n_{CuO}} z a_{Cu2S}^3 \nu_0 exp\left(-\frac{e\varepsilon_{x-dis}}{k_B T_s}\right) t =$$

$$= \frac{n_{Cu2O}}{1+\frac{a_{CuO}\nu_0}{D_{0c2}}L_{CuO}\gamma_L F_c(L_{nw})} F_B(z)\frac{\alpha_{xs0}}{n_{CuO}} z a_{Cu2S}^3 \nu_0 exp\left(-\frac{e\varepsilon_{x-dis}}{k_B T_s}\right) t. \quad \text{(S33)}$$

The time dependencies of the thicknesses $L_{Cu2O}(t)$ and $L_{CuO}(t)$, the length $L_{nw}(t)$ of the nanowires, and the thickness $L_{Cu2S}(z, L_{CuO}, L_{nw}, t)$ can be found by solving the system[4].

The results of the experiments were simulated with the developed model. The experimental dependence of the temperature was defined by the expression: $T_s(t) = (T_{max} - T_0)(1 - exp[-t/\tau]) + 293$ (K), where T_0 = 20 °C, τ = 450 s. Two different temperatures T_{max} (24 °C and 110 °C) were used in combination with three hydrogen sulfide gas pressures: 10^5, 10^4, and 10^3 Pa.

The following dependencies of energies on temperature were used to fit the results of the experiments for the detached nanowires: $\varepsilon_{aH2S}(T_s) - \varepsilon_{i-H2S}(T_s) = 0.255\left(\frac{T_{s0}}{T_s}\right)^{\upsilon}$ for the difference between the adsorption and internal energies of the H_2S molecule on the CuS layer; $\varepsilon_{c1}(T_s) = 0.51\left(\frac{T_{s0}}{T_s}\right)^{\upsilon}$ for the diffusion of the CuO aggregate through the CuS layer; $\varepsilon_{x-dis}(T_s) = 0.273\left(\frac{T_{s0}}{T_s}\right)^{\upsilon}$ for the transformation of the CuO aggregate into the CuS aggregate, where υ = 1.85 and T_{s0} = 297 K.

According to the developed model, there is a uniform distribution of adsorbed H_2S molecules along the surface of the detached nanowire. The reaction of CuO molecules that compose the initial surface of the nanowire, acts as a driving force to pump copper oxide from the volume of the nanowire, since the diffusion of CuS molecules that form a crust on the surface of the nanowire as a result of reaction (S1) into the CuO layer is implied as being much lower (to the point of being negligible) than the diffusion of the CuO molecules through the CuO layer to the surface to react with H_2S molecules. The latter assumption is necessary to explain the formation of the voids in the volume of the nanowire during the sulfurization. The dependencies of the thicknesses of the CuS and CuO layers, as well as their sum over time are shown in Figures 3 b, d, f, while the changes to the nanowire shape, including the formation of the axisymmetric void, are shown in Fig. 4 c, e, g. At the high pressure of 10^5 Pa and low temperature of 24 °C only a thin layer of about 2 nm is formed after 2 h of sulfurization and a slightly bigger void with a radius of about 3 nm is formed in the central part of the nanowire. The void formation was not observed in the experiment; however, the real voids are not necessary, and should be axisymmetric, and the difference can be explained by the assumptions used in the model. It should also be noted that the volume for one CuS molecule is larger than the volume for the CuO molecule, and the volume of a certain radius, which is consumed in the central part of the nanowire, occupies the volume with the lesser radius on the outer part of the nanowire, which is considered in the model. When the pressure is decreased by an order of a magnitude to 10^4 Pa, but the temperature is increased to 110 °C, the significant changes in the shape of the nanowire are observed even after 30 min of the treatment. The whole volume of the CuO layer is consumed and converted to a CuS layer on the outer surface of the nanowire after just 8 minutes. Thus, the nanowire is converted into a nanotube with CuS walls, while mixed composite structure of CuO+CuS walls can also be obtained, if the treatment time is shorter than some critical time. A further decrease of the H_2S pressure to 10^3 Pa does not change the picture significantly, while it changes the critical time to about 15 minutes, thus showing a possibility for flexible control of the composition of the resulting nanostructure. In reality, multiple void

formations are observed instead of the simulated void formation, and the real structure is changed from a solid nanowire to a shell nanostructure.

- ✓ *The treatment of CuO nanowires with hydrogen sulfide allows flexible shaping of the nanowires when nanostructures with voids are grown, which can be used for various storage applications. The temperature of the process is a much more effective control parameter than the gas pressure, which is explained by the exponential dependence of the processes on the temperature.*

The same temperature dependence on time was used to simulate the results of the experiments conducted for the attached nanowires that underwent sulfurization. During the first stage, the sulfurization of the attached nanowires according to the schematic in Figure 1 was considered for a hydrogen sulfide gas pressure of 10^5 Pa for times of 24, 48, 72, 96 and 120 minutes. Equations (S24)–(S28) describe the formation of a Cu_2S layer along the surface of a nanowire with a constant radius R_{nw} and length L_{nw}, which were set to 50 nm and 1 μm in the simulation, respectively. The equations allowed calculating the dependence $L_{Cu2S}(z, t)$ along the nanowire, which is shown in Fig. 3 i-m by the magenta line. Then, the obtained by equation (S18) dependence $n_{cu}(z)$ was used to calculate the growth of 1D nanostructures; for that the reported model was utilized [3]. The nanostructures ('nanobulbs') are indicated with a blue line, and special initial conditions were implied with respect to the initial coordinates of the nanobulbs and their initial radii:

$$z_i = z_{i-1} - \frac{4}{2+\alpha} R_{i-1}; \qquad \alpha = \frac{2R_0}{L_{nw}}; \qquad R_0 = 0.04\ \mu m; \qquad i = 1..35. \tag{S39}$$

The parameters were conditioned to illustrate the growth of the nanobulbs and the dependence of the concentration of Cu_2O molecules along the nanowire and to form a continuous conical Cu_2S structure. It should be noted that the reported model [3] was used separately for each nanobulb; the nucleation stage is not considered and is replaced by a fixed set of initial radii and lengths of the nanobulbs in the applied system of equations.

To calculate the growth of a 'head' of Cu_2S on the tip of the nanowire, another model [2] was used under the condition that a concentration $n_{cu}(L_{nw})$ is calculated with the present model.

The assumption about non-uniform (i.e., linearly dependent) distribution of the adsorbed H_2S molecules along the nanowire makes it possible to explain the experimental results. The nature of this distribution is a discussion issue, and can be conditioned by the interaction of gaseous hydrogen sulfide with a dense array of CuO nanowires.

The following energies were used to fit the results of the experiments: energy $\varepsilon_{aH2S} - \varepsilon_{i-H2S}$ = 0.47 eV and $\varepsilon_{aH2S} - \varepsilon_{i-H2S}$ = 1.2 eV for the difference between the adsorption and internal energies of the H_2S molecule on the side of the nanowire and its tip, respectively, and energy ε_{c2s} = 0.435 eV for the activation of diffusion for the Cu_2O aggregate along the surface of the nanowire; energy $\varepsilon_{x\text{-}dis}$ = 0.835 eV for the transformation of the Cu_2O aggregate into the Cu_2S aggregate.

- ✓ *At the relatively high adsorption and diffusion activation energies, which disable the effective diffusion of H_2S molecules and their re-distribution along the surface of the attached nanowire (unlike the distribution of oxygen along CuO nanowire), the molecules are stuck at the place where they adsorb. The tips of the nanowires collect a large concentration of hydrogen sulfide molecules, which resembles the*

distribution of water drops along the top under the cover of a dense forest during rainfall.

References

1. Kittel, C. & Kroemer, H. *Thermal Physics*. (W. H. Freeman and Company, 1980).

2. Polyanin, A. D. & Zaitsev, V. F. *Handbook of Exact Solutions for Ordinary Differential Equations*. (Chapman & Hall/CRC, 2003).

3. Baranov, O. *et al.* Hierarchical Nanomaterials by Selective Deposition of Noble Metal Nanoparticles: Insight into Control and Growth Processes. *Adv. Theory Simulations* 2300288 (2023) doi:10.1002/ADTS.202300288.

4. Baranov, O., Košiček, M., Filipič, G. & Cvelbar, U. A deterministic approach to the thermal synthesis and growth of 1D metal oxide nanostructures. *Appl. Surf. Sci.* **566**, 150619 (2021).

3.2 Plasma-Facilitated 1D-to-2D Phase Transformation from CuO to CuS

In the research described in Section 3.2, the anion-exchange reactions were again performed on CuO NWs. However, instead of gaseous H_2S, the sulfurization was performed with microwave H_2S plasma as a sulfurizing agent. In this way, metastable reactive species were introduced in the reaction. This was done with the intention to study the effect of a non-equilibrium environment on the anion-exchange reaction. The outcome of the transformation was compared to thermal sulfurization. The differences in mechanisms were discussed and supported by theoretical modeling. Furthermore, we also studied how the diameter of the NWs affects the transformation outcome. While the single crystallinity was not completely preserved, the thinnest NWs resulted in single-crystalline grains entirely in one dimension.

The results of this subsection were summarized in a manuscript submitted to the journal *ACS Nano*.

Regarding my contribution, I performed the experiments, analyzed the results, and wrote the initial manuscript.

Plasma-facilitated 1D-to-2D phase transformation from CuO to CuS

Martin Košiček[a,b], Oleg Baranov[a,c], Janez Zavašnik[a,b], and Uroš Cvelbar[a,b].*

[a]Jožef Stefan Institute, Jamova cesta 39, 1000 Ljubljana, Slovenia

[b]Jožef Stefan International Postgraduate School, Jamova cesta 39, 1000 Ljubljana, Slovenia

[c]Department of Theoretical Mechanics, Engineering and Robomechanical Systems, National Aerospace University, Chkalova Str 17, 61070 Kharkiv, Ukraine

KEYWORDS: Copper Oxide Nanowires, Copper Sulfide, Phase transformation, 2D nanostructures, Anion exchange, Plasma

ABSTRACT

The increasing demand for novel nanomaterials necessitates innovative techniques to tailor their properties and morphologies. In this context, the development of strategies to control conversions between distinct material morphologies is important. This research unveils an intriguing observation of a plasma-assisted, anion-exchange, phase transformation that facilitates the conversion from 1D copper oxide nanowires to 2D copper sulfide nanoplates. The process of anion exchange was performed by sulfurizing copper oxide nanowires using both thermal and microwave plasma-assisted methods. Our investigation reveals that plasma-assisted sulfurization triggers the initiation of 2D-

structure growth from the initial nanowire, followed by complete conversion of the original 1D copper oxide into 2D copper sulfide structures. This transformation in dimensionality is likely propelled by the accumulation of surface charges within the plasma environment, particularly in regions of heightened curvature in the emerging copper sulfide phase. The intensified electric field in these zones directs the flow of charged plasma species towards these specific areas. Furthermore, the preferred adsorption of the sulfur species on the nanoplate edges drives the outward diffusion of copper ions from the nanowire core to the edges of the forming nanoplates, where the sulfurization predominantly occurs. These suggestions were supported with theoretical modelling of the sulfurization processes. The morphology of the transformed nanowires depends on the initial nanowire diameter and the duration of the treatment. This study thus underscores the potential of plasma-assisted techniques, showcasing their efficacy in the advanced processing of nanomaterials by enabling controlled and distinctive nano-modifications.

Nanofabrication often requires the capacity to produce materials with unconventional phases and structured morphologies encompassing different dimensionalities. In this regard, the recent focus is on 0D, 1D and 2D nanomaterials [1–4]. These types of materials are particularly interesting due to their increased surface-to-volume ratio and distinct size-dependent transport properties linked to quantum confinement [5].

Beyond the conventional routes of bottom-up nanostructure growth through bulk, solution, or deposition techniques, a strategy for crafting nanomaterials of distinct morphology is also feasible via the phase transformations of pre-existing nanomaterials. In this context, a method enabling a controlled dimensionality conversion between 1D and 2D materials would be very significant. However, thus far, reports on

interdimensional transformations, particularly between 1D and 2D nanomaterials, are scarce. An example of such a transformation was exhibited by Lu et al., who induced a conversion from 1D to 2D in $CrCl_3$ nanowires (NWs) using a scanning-tunneling microscope [6]. Nevertheless, a straightforward technique that facilitates both dimensionality alteration and chemical modification remains elusive.

This is where plasma-assisted techniques, rapidly emerging as potent methods for nanomaterial synthesis and modifications [7–12], could be exploited. The use of plasma could pave the way for interdimensional transformations in nanomaterials. Plasma-assisted processes, due to their generation of reactive species like ions and radicals in a non-equilibrium environment, often diverge significantly from standard thermal methods in terms of rates and mechanisms. This renders them ideal for the rapid production and modification of nanomaterials with 1D and 2D morphologies [13,14]. The dimensionality of plasma-produced nanostructures can be adjusted by manipulating the plasma parameters. For instance, the oxidation of metallic copper substrates in a microwave plasma afterglow, with plasma species supplied through a 400-µm-wide hole, yields CuO nanostructures of varying morphologies. Their dimensionality depends on their distance from the plasma-treatment center, with greater distances leading to lower dimensionality [15]. In addition to tailoring the structure dimensionality, plasma can serve as a tool for chemical modification during a dimensionality transformation. For instance, in ionic materials like metal oxides, plasma could facilitate ion exchange, which is an effective transformation strategy for producing diverse structured nanomaterial morphologies [16,17]. In such reactions, existing nanomaterials are treated with specific precursors that induce ion exchange, reshaping the material into metastable morphologies and phases that are often unattainable with standard bottom-up methods. Cation-exchange reactions more commonly lead to the preservation of the initial nanomaterial morphology, while anion-

exchange reactions are particularly useful for the synthesis of core-shell or hollow nanomaterials [16,17]. Ion-exchange reactions are most commonly performed in solutions; however, the utilization of gaseous ion-exchanging precursors has also been reported [18–22].

On the other hand, the potential of plasma-based methods to achieve ion-exchange transformations in nanomaterials is, to a large extent, still unexplored in spite of the numerous advantages that plasma-based methods possess. Therefore, coupling the ion-exchange strategy with plasma-based methods could open new possibilities for the modification and synthesis of ionic nanomaterials.

In our ongoing research we investigate plasma-assisted ion exchange involving oxygen and sulfur using a model system of metal oxide NWs. Plasma-assisted sulfurization has previously proved effective in the synthesis of metal sulfide materials such as MoS_2 thin films prepared by the plasma-assisted sulfurization of metallic Mo film [23] as well as MoO_3 via anion exchange [24]. Plasma-assisted sulfurization was also used to transform MoO_3 nanoplates into MoS_2 nanoplates [25]. Here, it was found that the MoO_3 is first reduced to MoO_2, followed by an oxide-to-sulfide anion-exchange transformation. Furthermore, plasma-assisted anion exchange via sulfurization was used to obtain FeS_2 films from Fe_2O_3 nanorods [26] and MoS_2–WS_2 vertical heterostructures from a Mo-W film[27].

Our focus here lies in demonstrating the plasma's capacity to enable a 1D-to-2D phase transformation in CuO NWs, transforming them into (CuS) nanoplates. These CuS structures exhibit promising properties for numerous applications such as photocatalysis [28–30], electrocatalysis [31], photothermal therapy [32–36], supercapacitors [37–41], and lithium-ion batteries [42–44].

Remarkably, this 1D-to-2D transformation is absent from thermal sulfurization, where it is predominantly equiaxed grains that are formed. This transition holds not only

scientific interest, but also a practical value, as the structured CuS plates enhance the effective surface area of the transformed NWs, expanding their potential for catalytic, sensing, and other applications.

RESULTS AND DISCUSSION

Our model 1D material, CuO nanowires (NWs), was synthesized through the thermal oxidation of copper foil. In this process, a grainy copper oxide layer covered with thin CuO NWs forms on the copper surface, as shown in Figure S1a. The diameters of the NWs range from approximately 6 nm to around 40 nm, with an average diameter of 13±5 nm (see Figure S1b). The NWs exhibit a single-crystalline structure and grow along the [110] direction (Figure 1a, b). Before sulfurization, the CuO NWs were detached from their growth substrate and transferred onto TEM grids. Subsequently, the NWs underwent sulfurization within the afterglow region of a H_2S/Ar microwave plasma (the experimental setup is shown in the Figure S2b) for 30 minutes, without the application of external heating.

As depicted in Figures 1c-e, this treatment enabled the conversion from 1D-to-2D structures, leading to the complete transformation of the 1D CuO NWs into 2D nanostructures that form along the length of the original NWs. The altered phase was identified as covellite (CuS) (Figure S8b), signifying the replacement of oxygen anions with sulfur during the process. To comprehensively investigate this remarkable dimensionality conversion resulting from anion exchange, we initially assessed whether it was an outcome of plasma-specific factors or if it could also be achieved through a thermal sulfurization in the absence of plasma. Therefore, we conducted thermal sulfurization experiments on CuO NWs at room temperature and elevated temperature, maintaining the other experimental parameters identical to those in the plasma-based experiment. The room-temperature experiment exhibited no discernible reaction after 30

minutes (Figure S10). As a result, in the subsequent experiment, the temperature was elevated to mimic the temperature to which our NWs were exposed in the plasma. The temperature that is achieved by the plasma treatment was estimated using a thermocouple positioned in the plasma afterglow, in the same region where the TEM grid with CuO NWs was treated (Figure S3a). The measured temperature was sensitive to the thermocouple's position and fluctuated between 60 °C and 90 °C (Figure S3b,c). However, due to potential variations in the plasma species' recombination and the heating effect between the sample and the thermocouple, the measured temperature is an approximate value. Given our intention to assess whether thermal sulfurization could replicate the plasma's effects, the thermal treatment temperature should not fall below that in the plasma. Hence, to account for the potential differences, the temperature was slightly elevated to 100°C. This approach ensured that the plasma temperature did not exceed that of the thermal treatment, while still maintaining a comparable temperature range. Following a 30-minute thermal treatment, the nanostructures exhibited a CuO NW core enveloped by small, equiaxed, copper sulfide grains (Figure 1f-h).

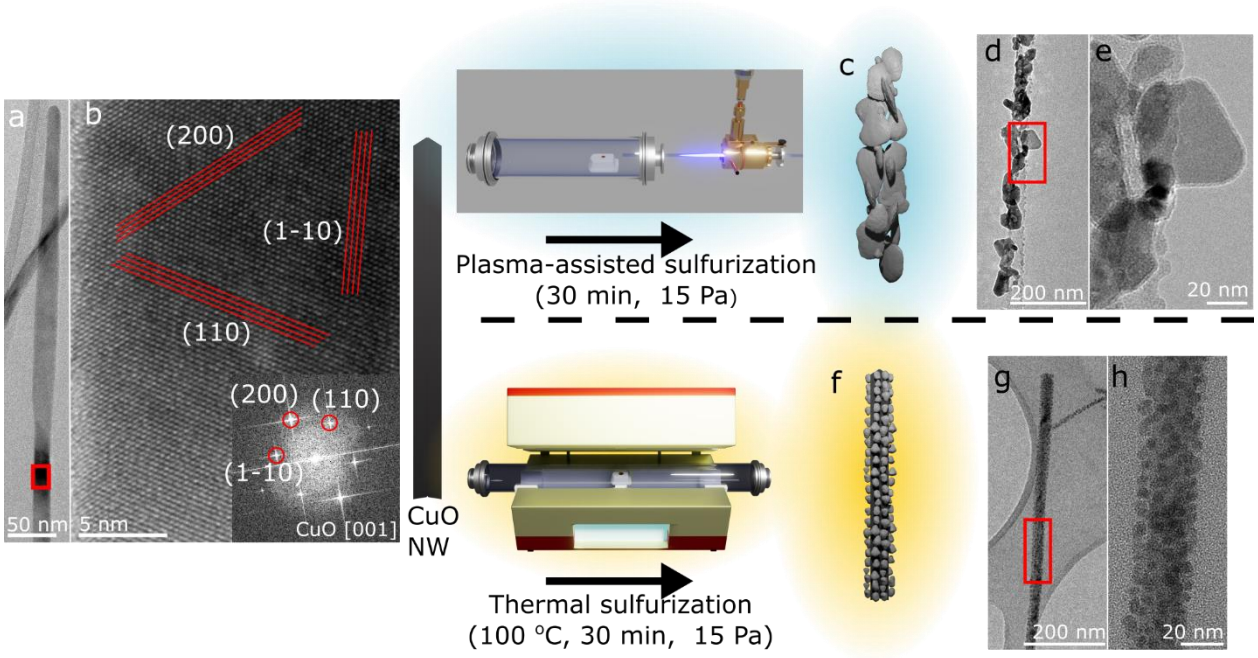

Figure 1. CuO NWs and resulting morphologies of their thermal and plasma-assisted sulfurization: **a** TEM micrograph of a CuO NW. **b** HRTEM micrograph of a CuO NW from area marked with red square in **a**. **c** Schematic representation of 2D structures formed after plasma-assisted sulfurization of CuO NW. **d,e** TEM micrograph of 2D structures formed after plasma-assisted sulfurization of CuO NW at lower (**d**) and higher (**e**) magnification. **f** Schematic representation of nanostructure formed after thermal sulfurization of NW at 100 °C with small, eqiuaxed grains formed on CuO NW surface. **g,h** TEM micrograph of nanostructures formed after thermal sulfurization of CuO NW at 100 °C at lower (**g**) and higher (**h**) magnifications.

While the growth of 2D structures remained absent in the case of thermally treated samples, it remained unclear whether the thermal reactions indeed occur through different mechanisms than their plasma-assisted counterparts, or if the thermal transformation simply progresses at a slower pace, with 2D structures emerging at subsequent stages of the process. To fully examine the evolution of the copper sulfide grains over time—from their inception to the comprehensive conversion of the initial CuO NWs into the sulfide

phase—we conducted a full array of experiments, varying the treatment duration for both the plasma-assisted and thermally treated specimens. The outcomes of these investigations are outlined in Figure 2.

In the domain of plasma-assisted sulfurization (Figure 2a-e), the nucleation of the sulfide phase on the NW surface becomes apparent after just 1 minute of treatment (Figure 2a). This stage involves the emergence of small, CuS grains on the NW surface, followed by their subsequent growth, resulting in core-shell configurations after 5 minutes of treatment (Figure 2b). The CuO NW core retains its single-crystalline structure, while the growing CuS shell is polycrystalline, characterized by randomly oriented, equiaxed CuS grains surrounding the CuO core (Figure S4i). A progressive thickening of the sulfide shell occurs after 10 minutes (Figure 2c). However, the true onset of the 2D structure's formation starts only after 15 minutes (Figure 2d). At this point some NWs exhibit both equiaxed and planar grains. The diameters of the equiaxed CuS grains closely resemble the thickness of the CuS nanoplates (Figure S6). This suggests that the initiation of the 1D-to-2D transformation likely originates in the equiaxed grains within the CuS layer, which eventually assume a preferential 2D growth. By the 30-minute mark, the CuO NWs are entirely transformed into CuS nanoplates (Figure 2e). This shift in the nanostructure's growth trajectory is further evident in the temporal dependence of grain size (Figure 2f), where the continuous upward trend in grain size experiences an abrupt leap in the CuS grain diameter after 15 minutes of plasma treatment.

In contrast, substituting the plasma treatment with a thermal treatment at 100 °C, without altering the other experimental conditions, results in a more gradual transformation. There were no observable changes to the surfaces within the initial treatment periods of 1 to 10 minutes (Figure 2g-i). The emergence of minute sulfide grains

becomes evident solely after 15 minutes of treatment (Figure 2j). Similar to the dynamics of the plasma-assisted transformation, the grains grow with the treatment time (Figure 2j-n), with the identified sulfide phase being covellite (Figure S11a). However, in this instance, growth does not coincide with the formation of 2D grains. Instead, equiaxed, sulfide grains persist even after 90 minutes of treatment, when the CuO NWs are entirely converted into sulfide NWs. This further confirms that the reasons behind the shift from 1D to 2D upon transformation should be attributed to the processes induced by plasma.

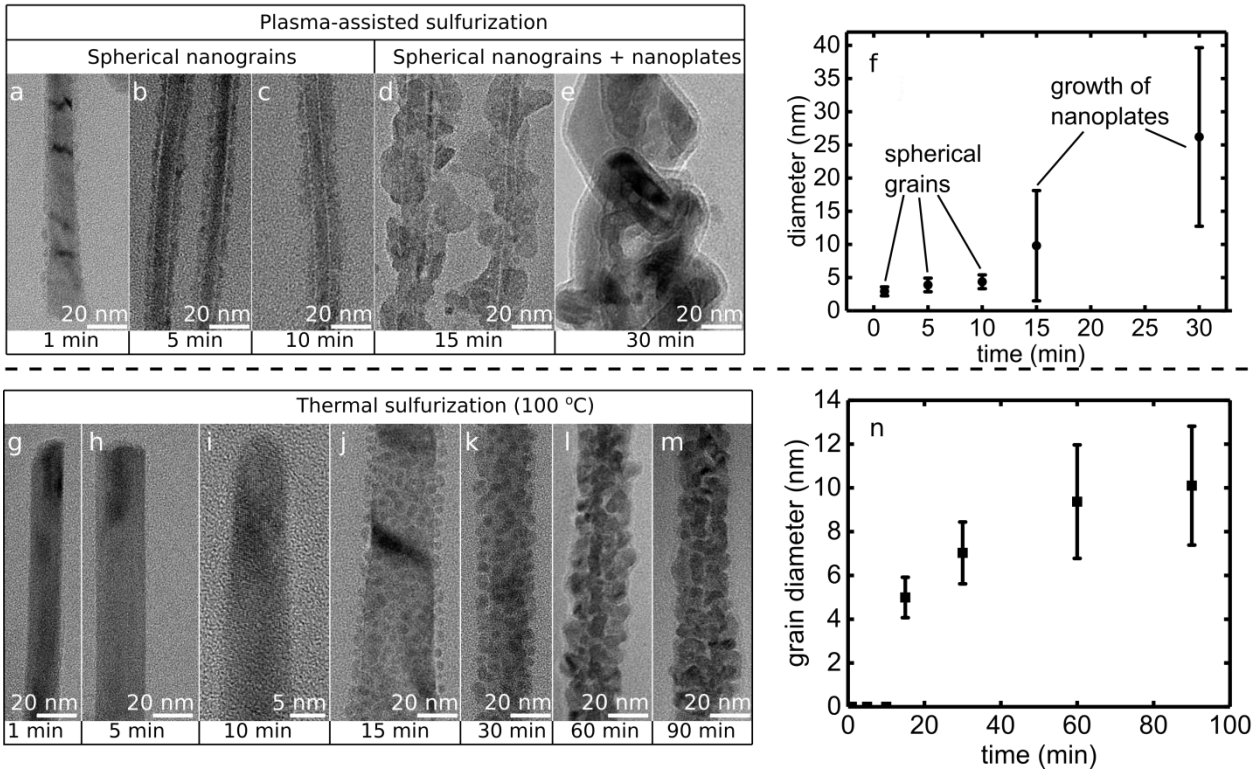

Figure 2. Time evolution of CuS grains upon plasma-assisted and thermal sulfurization of CuO NWs. **a-e** TEM micrographs of CuO NWs sulfurized with plasma for **a** 1 min, **b** 5 min, **c** 10 min, **d** 15 min and **e** 30 min. **f** time dependence of CuS grains formed upon plasma-assisted sulfurization of CuO NWs. **g-m** TEM micrographs of CuO NWs sulfurized by thermal sulfurization at 100 °C for **g** 1 min, **h** 5 min, **i** 10 min, **j** 15 min, **k**

30 min, **l** 60 min and **m** 90 min. **n** time dependence of CuS grains formed upon thermal sulfurization of CuO NWs.

The nanoplates formed on the CuO NW surface are visualized in the TEM micrograph of Figure 3a, where an example of a CuO NW subjected to 15 minutes of plasma-assisted sulfurization is presented. The CuS nanoplates, viewed perpendicularly to their normal, are indicated by yellow arrows, while other nanoplates are denoted by red arrows. As can be seen in Figure 3a, CuS nanoplates originate in the outer region of the CuS shell and grow tangentially to the NW surface. The orientation of the nanoplates in Figures 3b and c suggests that the expansion of the nanoplates occurs perpendicular to the [001] direction, as demonstrated in Figure 3d (more examples indicating such orientation can be found in Figure S5a-f).

The experimental findings in Figures 3a-c suggest a mechanism for CuS nanoplate formation, schematically depicted in Figures 3e-h. This mechanism was also supported with theoretical modelling of the adsorption of sulfur species and processes describing CuO diffusion during nanoplate formation with the results presented in figure 3i-k (a detailed description of the model can be found in the Supporting Information).

During sulfurization, reactive sulfur species (RSS) generated in the plasma come into contact with the CuO NW surface (figure 3e), instigating the exchange of oxygen anions with sulfur. In addition, the plasma contains excited species of argon and hydrogen, as indicated in the optical emission spectrum (Figure S3d). Surface reactions encompass the formation of the CuS phase through the interaction between the copper ions and the RSS, while oxygen ions participate in reactions with excited hydrogen species to generate water molecules. In the initial stages, the morphological development of the structure follows the typical anion-exchange mechanism—the formation of CuS nuclei is followed by the rapid formation of a CuS layer (figure 3f) yielding a core/shell structure of CuO/CuS [17].

This is true for both the thermal and plasma-assisted sulfurization, with the thermal type being slower. Subsequent reactions induce the outward diffusion of copper and oxygen ions toward the NW surface through the CuS layer. Further progression of the reaction most commonly results in the formation of voids in the crystal structure as the outward diffusion of copper and oxygen ions proceeds faster than the inward diffusion of sulfur species. The coalescence of the voids in the later stages could result in the formation of hollow parts of the structure, which can be visible in completely transformed, thermally sulfurized NWs (figure 2m).

As the grains in the CuS shell expand, the layer can cleave or fracture to release the stress that is accumulated due to rapid growth, as illustrated in Figure 3g. The cleaved portion might partially detach from the layer and orient upward, aligning tangentially with the NW surface to minimize the strain. This serves as the foundation for the tangential growth of the 2D structures. Covellite is known for exhibiting perfect cleavage along the (001) crystal planes [45–47]. Furthermore, the (001) face is the most stable [48]. However, even though the CuS is naturally prone to maximize the surface area of the (001) face, our results indicate that the growth of 2D CuS structures is greatly facilitated by plasma-specific effects. Hence, plasma-surface interactions should be a pivotal consideration in describing the mechanism. Similarly, in reference [49] it was found that when growing 2D $Cu_{(2-x)}S$ structures via chemical vapor deposition, the utilization of plasma can enhance the aspect ratio of the structures that are formed, indicating the plasma's favorability towards the preferred growth direction of nanostructures.

In our case, the key distinction between plasma and thermal sulfurization resides in the nature of the sulfurizing species—H_2S molecules in the thermal treatment and RSS in plasma. The excited species in plasma can be classified into two categories that potentially contribute to the reaction: electrically charged ions along with free electrons

on one side, and excited metastable neutral species on the other. Generally, in the afterglow region, the concentration of neutral species surpasses that of the charged species by several orders of magnitude [50,51], thus positioning them as the predominant sulfurizing agents in our scenario. However, in our case the positioning of the NWs was close to the glow region known as the "early afterglow" (Figure S2b), where the density of the charged particles cannot be disregarded. Charged species like ions and electrons might play an important role in the formation of 2D nanostructures. The principal impact of the charged species within a plasma environment is the generation of a surface charge on the exposed areas. When CuO NWs come into contact with plasma, a "plasma sheath" forms around them due to their interaction with charged particles. In non-equilibrium plasmas, electrons exhibit higher temperatures than other charged species, leading to an elevated flux of electrons towards the NW surface, causing the NW to acquire a negative charge. The accumulated charge in turn, attracts positive ions from the plasma, thereby increasing their concentration within the sheath. This process screens the negative surface charge from the plasma surroundings. The electric field encompassing the NW acquires a greater intensity around the sharp regions with high curvatures. Consequently, the flow of positively charged species from the plasma becomes preferentially directed towards these sharp points on the surface [52], particularly along the exposed edges of the cleaved parts in the CuS layer. This phenomenon aids their further growth and promotes the tangential expansion of the resulting 2D nanostructures. Furthermore, the defects that might form due to the bombardment of the sharp edges with positive argon ions increase the surface-adsorption ability also for neutral plasma species, which are otherwise unaffected by the electric field. This preferential adsorption of sulfur species in turn attracts the CuO units, directing their diffusion towards the cracked edges and in this way facilitating the preferential progression of the CuS phase’s formation on these parts.

A theoretical model (Supporting Information) was developed to reveal the main features of the 1D-to-2D transformation found in the experiment. The model is based on the assumptions of rapid growth of the CuS layer on the surface of the CuO NW, which is accompanied by stress that leads to the formation of cracks along the surface of a thin CuS layer, as well as partial flaking of the layer. The flaked part serves as a nucleus for the future growth of the 2D nanostructure, when copper oxide aggregates diffuse through the CuS layer and are accumulated at the nucleus, which is characterized by anisotropic of properties with respect to the adsorption of sulfurizing species from the gas phase. The side surfaces of the nucleus adsorb fewer molecules due to the smaller number of surface defects, in comparison with the defected surface of sharp edges of the flaked thin film. The edges also create local electric fields, which enhances the ion bombardment, and the generation of more defects, thus enhancing the molecules' adsorption on the edges. The increased concentration of the sulfurizing reagent promotes the diffusion of CuO aggregates towards these parts of the nanostructure, which results in a preferential growth. The process is limited by the quantity of the material contained in the NW parts under the nucleus of the 2D nanostructure, so the number density of the nanoplates along the NW determines their sizes.

As experimentally observed and confirmed with a theoretical analysis (figure 3i), the onset of the CuS nanoplate growth impedes the further growth of the CuS layer encapsulating the CuO core, as most of the CuO phase is consumed in the CuS nanoplate formation instead of the CuS layer. On the other hand, the consumption rate of the CuO phase is increased due to the increased adsorption of sulfur species on the surface of the nanoplate. In this way the nanoplates act as pumps for the CuO phase. The pumping flux increases with the progress of the nanoplate's development, as calculated in the model (figure 3j). Therefore, the mechanism based on the different adsorption tendencies of the

different nanoplate faces can explain the nanoplate-formation mechanism and the growth of the nanoplates. The results also correlate well with the experimental observations for the nanoplate's width and thickness, as observed in figure 3k.

- ✓ *According to the results of a numerical analysis, the difference between the adsorption energies for the various parts of a nanostructure and the internal energy of the gas molecules plays a vital role in determining the morphological shape, like for the 2D nanoplates and for 1D nanowires* [53]. *When the internal energy exceeds the adsorption energy, the molecular adsorption becomes extremely low, and the corresponding dimension does not change, so the difference between the adsorption energies affected by the internal energy of the molecules defines the aspect ratio.*

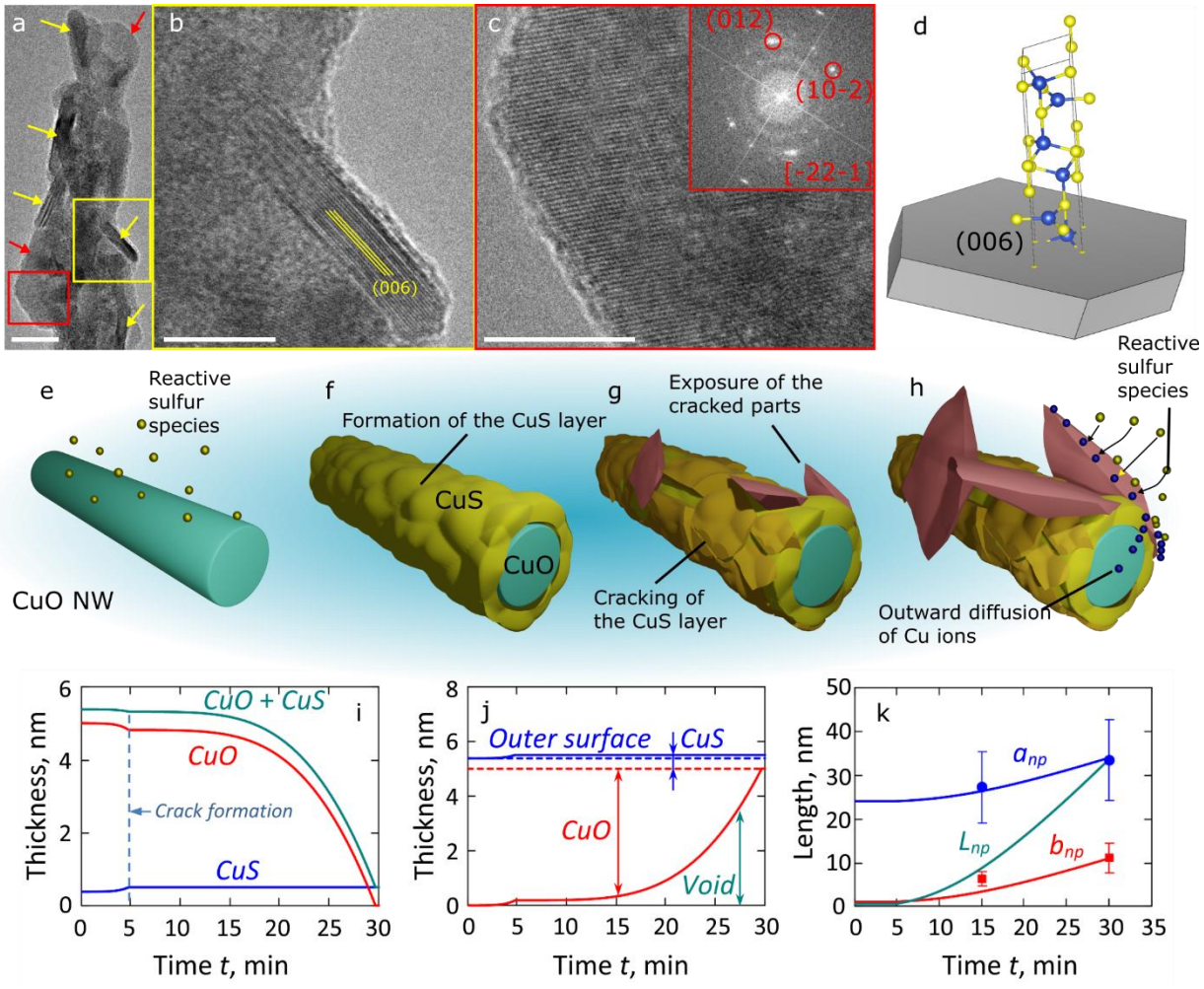

Figure 3. Formation of CuS nanoplates on the CuO NW surface. **a -** TEM micrograph of a NW sulfurized with plasma for 15 min with the visible formation of CuS nanoplates. Nanoplates viewed perpendicular to their normal are marked with yellow arrows, whereas the other nanoplates are marked with red arrows. **b -** Enlarged part of the area marked with yellow square in **a**, with visible (006) crystal planes, indicating the preferential growth direction of the nanoplate. **c -** Enlarged part of the area marked with red square in **a -** with FFT indicating the orientation of a nanoplate. **d -** Model of a CuS nanoplate. **e-h -** Schematic representation of the mechanism leading to the growth of 2D CuS nanostructures on a NW surface. **e -** Initial interaction between RSS and CuO NW surface. **f -** Formation of polycrystalline CuS shell around the NW as a result of reaction between CuO and RSS. **g -** formation of cleavages and fractures in the CuS layer and exposure of the edges to plasma environment. **h -** growth of 2D structures from the grains on the exposed edges due to preferential diffusion of the copper ions to these areas. **i-k -** Results of the experiments and calculations of CuS nanoplate growth over time in plasma at 100 °C: **i -** thickness of CuO and CuS layers, and total diameter of nanowire; **j -** sectional view of CuO nanowire at its sulfurization **k -** growth of CuS nanoplate with a height L_{np}, width a_{np}, and thickness b_{np}. The scale bars correspond to **a** 20 nm, **b**,**c** 10 nm.

The transformed NWs consistently adopt a polycrystalline nature, primarily consisting of 2D structures. However, their morphologies vary, as depicted in the examples in Figure 4, showcasing the different NWs resulting from 15 minutes of plasma-assisted sulfurization. Some NWs, such as the one illustrated in Figure 4a, still retain a CuO core enveloped by a CuS shell composed of both smaller equiaxed and larger planar grains. Such a structural type is commonly observed in the transformation of thicker NWs. The presence of the CuO core is discernible in the TEM image of Figure 4a and is confirmed by the EDS mapping, which reveals the concurrent existence of copper, oxygen, and

sulfur within the NW (Figures 4b-e). Further examples with a clearly visible CuO core can be found in the Figure S4g-i.

A second morphological type emerges from the complete transformation of CuO NWs into multiple 2D CuS nanoplates oriented radially and axially, as seen in Figure 4f. The complete transformation is affirmed through HRTEM imaging, which exclusively identifies CuS grains (as exemplified in Figure 4g, alongside its corresponding FFT pattern in Figure 4h). The third morphology is once again an outcome of the complete conversion of CuO NWs into CuS nanoplates. In this case, the nanoplates align exclusively along a single dimension, along the axial direction of the initial CuO NW (Figure 4i). The 1D alignment and single-crystalline nature of the CuS plates are confirmed with higher-magnification images (Figure 4j) and their corresponding FFT (Figure 4k). Hence, in these structures, the single crystallinity is preserved in the radial direction during the transformation.

These variations in the morphologies of transformed NWs can be attributed to differences in the NW diameter and the duration of the treatment. Rough estimations of the required conditions (diameter and treatment time) for each morphology are depicted in Figure 4l. As described above, the CuS shell develops around the CuO NW, becoming apparent after 5–10 minutes of plasma treatment (Figure 2b,c). By the 15-minute mark, certain NWs have already initiated the transition to 2D nanoplates, while others retain a CuO/CuS core/shell, some of which are still predominantly composed of equiaxed grains forming a CuS layer (Figure S4g-i). As a result, the initiation of the 2D plate growth is not synchronized across all the NWs. The starting point for this initiation is estimated to be between 12 and 18 minutes (indicated by the time error bars on point 1 in Figure 4l). The thinnest NWs, which begin their transformation from 1D CuO to 2D CuS at an earlier stage (e.g., after 12 minutes of treatment), can achieve a full transformation within 15

minutes. The maximum diameter that preserves the radial single crystallinity is estimated by calculating the diameter of a cylindrical CuO NW that contains the same number of CuO units as there are CuS units in the average CuS plate (further details in Supporting Information with figures S12 and S13). This estimation, for a treatment time of 15 minutes, is on average approximately 10 nm (point 1 in Figure 4l), and for 30 minutes, it is around 15 nm (point 3 in Figure 4). The values are different, as after 15 minute, most of the nanoplates are still growing, whereas after 30 minutes, they attain their final dimensions.

In simple terms, an average 10-nm CuO NW will undergo a complete transformation into CuS nanoplates, while preserving the single crystallinity in the radial direction after 15 minutes of plasma treatment. Conversely, an average 15-nm CuO NW will undergo the same transformation under an extended treatment and will still contain a CuO phase after 15 minutes.

For NWs thicker than 15 nm, their transformed morphology depends on their diameter, the moment at which the transformation began, and the overall treatment duration. Larger diameters, later initiation of the 2D growth and a shorter treatment time make the preservation of the CuO core more likely. This is because thicker NWs have a greater volume of CuO material and a longer outward diffusion path of copper and oxygen ions. Prolonged plasma exposure of the thick NWs increases the likelihood of complete transformation, coupled with a breakdown of single crystallinity in all directions. After 30 minutes, even the thickest CuO NWs (approximately 40 nm thick) are wholly converted into CuS nanoplates, indicating that the threshold diameter value for complete transformation extends beyond 40 nm. This value, in conjunction with point 1 in Figure 4l, was used to estimate the slope of the boundary between fully and partially transformed NWs in Figure 4l. In addition, for more precise estimations, additional plasma

sulfurization for 25 min was performed and the formed CuS nanoplates measured (point 2 in figure 4l). An example of the nanoplates formed after 25 min of plasma treatment can be seen in Figure S7.

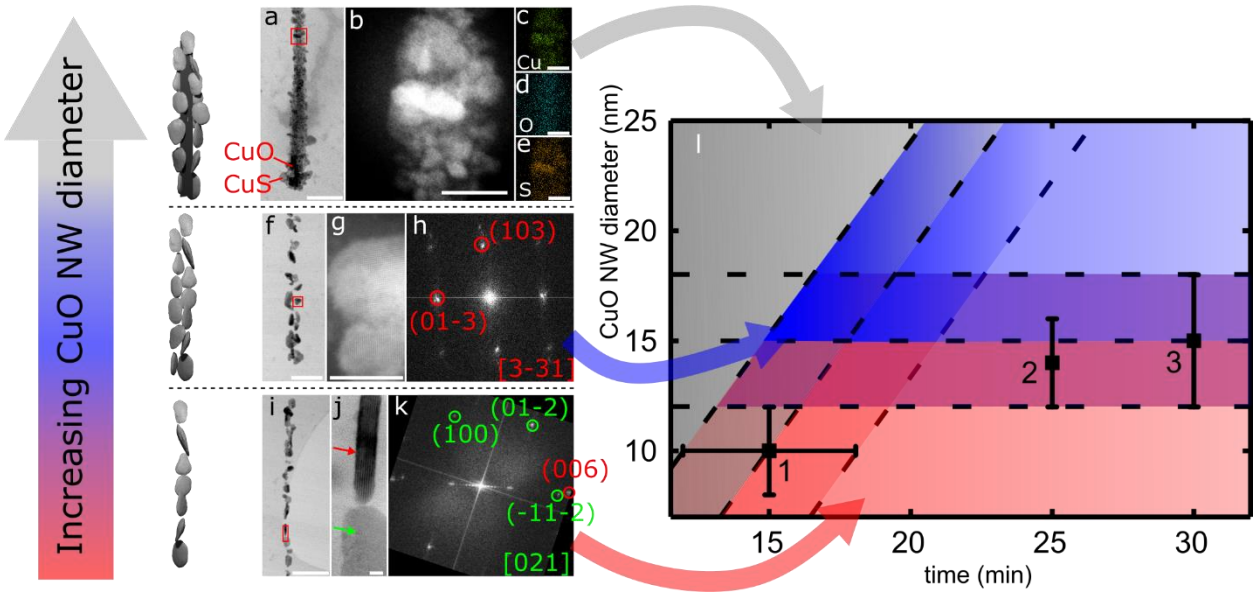

Figure 4. Different morphologies of transformed NWs with an estimation of the conditions needed for their formation. **a** TEM micrograph of the structure type which exhibits a CuO core, with a CuS shell, from which the 2D CuS structures grow. **b** dark-field TEM micrograph of the part marked with a red square in **a**. **c-e** EDS elemental maps of the part in **b**. **c** copper map, **d** oxygen map and **e** sulfur map. **f** TEM micrograph of the structure type where CuO NW completely transformed to CuS nanoplates, with multiple CuS plates in radial and axial directions. **g** dark-field TEM micrograph of the grain marked with a red square in **f**. and **h** its corresponding FFT indicating the CuS single crystal viewed form [3-31] direction. **i** TEM micrograph of the structure type with completely transformed CuO NW to CuS nanoplates, with CuS nanoplates arranged along the length of the NW with the preservation of single crystallinity in the radial direction. **j** TEM micrograph of the part marked with a red rectangle in **i** with **k**, the corresponding FFT pattern. Peaks circled in red and green correspond to grains marked with red and

green arrows in **j** respectively. **l** Estimated morphology diagram, indicating the influence of CuO NW diameter and treatment time on the morphology of the resulting NW. Scale bars correspond to 100 nm (**a**, **f**, **i**), 20 nm (**b-e**) and 5 nm (**g, j**).

In summary, we undertook both thermal and microwave plasma-assisted sulfurization processes on CuO NWs to examine the exchange of oxygen anions with sulfur. Our findings reveal that beyond the ion-exchange phase transformation, plasma-assisted sulfurization instigates a remarkable dimensionality shift from 1D CuO NWs to 2D CuS nanoplates. This unique transition was absent in the context of thermal sulfurization, strongly suggesting that it stems from plasma-specific influences.

The plasma-assisted sulfurization of CuO NWs starts with the rapid growth of a CuS layer that envelopes the initial CuO NW. The growth rate is a key factor that defines the development of surface stress in the layer, which can be enough to cause the partial flaking of the envelope. Further development of the nanoplates is characterized by anisotropic growth due to the adsorption properties, with sharp edges adsorbing more plasma species than the flat side surface. Thus, plasma makes it possible to transform 1D nanostructures into 2D nanostructures by growing 2D envelopes on the surface of the 1D nanowires, and then exfoliating the envelopes by use of the stress generated during the action of the intensive plasma fluxes. The possibilities for plasma chemistry can also be beneficial for the process by providing the combinations of the materials with the best inclination to form the large stresses in the surface layers.

- ✓ *Fast growth of surface layers in plasma results in a large surface stress which, in turn, is a key factor determining the formation of nuclei based on the flaked parts of the surface layer. Moreover, local electric fields generated at the interaction of the plasma with the nuclei affect the redistribution of charged plasma species, thus promoting the anisotropic growth of the nanostructures* [54].

The configuration of the resulting structures and the arrangement of the 2D plates primarily depend on the thickness of the NWs and the duration of the treatment. NWs with diameters below 15 nm can maintain their single-crystalline character in the radial direction when completely transformed.

METHODS

Synthesis of copper oxide nanowires

The initial CuO NWs were synthesized by the thermal oxidation of copper foils in a tube furnace (OTF-1200X, MTI Corporation). 1-cm-wide copper discs (supplier Alfa Aesar, purity 99.95%, thickness 0.25 mm, annealed and oxygen-free) were positioned on alumina holders, which were placed in the quartz tube (80 mm in diameter) inside the furnace (schematic representation of experimental setup is shown in figure S1a). One side of the quartz tube served as an oxygen inlet and the other side was opened to the atmosphere with a KF 16 port. During the oxidation, oxygen was introduced to the quartz tube with a flow of 180 sccm. The temperature program was set as follows. Heating from room temperature (20 °C) to 265 °C in 30 min, followed by 12 h annealing at 265 °C. The temperature was also measured with a thermocouple positioned in the same position as the sample. After the heating stopped, the oxygen supply was terminated, and the samples were left to cool to room temperature in the furnace.

Sulfurization of NWs

Preparation of CuO NWs for sulfurization

Oxidized copper substrates with CuO NWs were put inside a beaker and immersed in 1 ml of absolute ethanol. Beakers with samples were then put on an ultrasonic bath for 5 min to detach the NWs from the copper substrates and disperse them in ethanol. A couple

of drops of ethanol with dispersed NWs were then drop-cast on nickel-supported lacey carbon TEM grids.

Thermal sulfurization

TEM grids with CuO NWs were subjected to treatment with H_2S gas at room temperature (24°C) and 100 °C on alumina holders placed inside the quartz tube (diameter 80 mm) in the same tube furnace where copper oxidation was conducted. A schematic of the setup can be seen in figure S2a. The treatment at room temperature was performed for 30 min. The treatment at 100 °C was performed for 1 min, 5 min, 10 min, 15 min, 30 min, 60 min and 90 min. One side of the quartz tube served as the inlet for argon and H_2S gas. The other side was connected to a rotary pump. When heating the furnace from 0 to 100 °C, the quartz tube with the sample was filled with argon gas to 1 bar. When 100 °C was reached, the tube was evacuated to the base pressure of 1–2 bar and the flow of gaseous mixture 2% H_2S in Ar was introduced to the quartz tube at a total pressure of 15 Pa.

Plasma-assisted sulfurization

The CuO NWs were also sulfurized with the use of microwave plasma. The TEM grids with deposited CuO NWs were placed inside the quartz tube (80 mm in diameter). One side of the tube was connected to the rotary pump and the other served as an inlet for an 8-mm-wide quartz tube, which served as the entry for plasma species, generated by surfatron connected to the microwave generator via coaxial cable. The experimental setup can be seen in figure S2b The distance between surfatron and sample was 11 cm. The sample was placed directly in front of the exit of the 8-mm tube (position 2 in figure S3b). The gaseous mixture used for plasma sulfurization was 2% H_2S in argon. The gas was constantly supplied in the tube furnace with the sample. The pressure was maintained at

15 Pa. The sulfurization was conducted for 1, 5, 10, 15 and 30 min. The power used was 150 W; the reflected power was 0 W.

In both thermal and plasma-assisted procedures, toxic H_2S gas was used. Even though the concentration in the gas mixture was relatively small (2% H_2S, 98% Ar) and small quantities were used (pressure of the mixture was maintained at 15 Pa), caution still needed to be taken when performing the experiments. The reaction chamber must be well sealed to prevent leakage of the gas in the laboratory.

Electron microscopy analysis

CuO NWs and sulfurized NWs were analyzed with scanning electron microscopy (SEM, Prisma E, Thermo Fisher Scientific Inc.) operating at 10 kV and a transmission electron microscope (TEM, JEM-2100, JEOL Inc.) operating at 200 kV.

ASSOCIATED CONTENT

Supporting Information.

The following files are available free of charge.

Theoretical model for formation of CuS 2D structures, schematics of the experimental set-up for the synthesis of CuO NWs and their sulfurization, plasma characterization (temperature measurements and OES spectrum), additional TEM analysis of CuO and CuS structures formed after sulfurization of CuO NWs, calculation of CuO NW diameter that transforms to CuS nanoplate (PDF)

AUTHOR INFORMATION

Corresponding Author

*Uroš Cvelbar, e-mail: uros.cvelbar@ijs.si

Author Contributions

M. K., U.C. and J.Z. conceptualized the research. M.K. performed the experiments, contributed to the TEM analysis, analyzed the data and wrote the initial manuscript. O. B. performed the theoretical modelling, J.Z. contributed to the TEM analysis and co-supervised the research, U.C. supervised the research and prepared the final version of the manuscript. All the authors contributed to writing and editing of the manuscript and gave approval to the manuscript in its final form.

Notes

The authors declare no competing interest

ACKNOWLEDGMENT

This work was supported by the Slovenian Research Agency ARRS, program P1-0417, project N2-0107. O. B. acknowledges support from the project funded by the National Research Foundation of Ukraine, under grant agreement no. 2020.02/0119 and the NATO Science for Peace and Security Program under grant id. G5814 project NOOSE.

ABBREVIATIONS
FFT fast Fourier transform
HRTEM high-resolution transmission electron microscopy
NWs nanowires
RSS reactive sulfur species
SEM scanning electron microscopy
OES optical emission spectroscopy
TEM transmission electron microscopy

REFERENCES

(1) Yoo, S. C.; Lee, D.; Ryu, S. W.; Kang, B.; Ryu, H. J.; Hong, S. H. Recent Progress in Low-Dimensional Nanomaterials Filled Multifunctional Metal Matrix Nanocomposites. *Prog. Mater. Sci.* **2023**, *132*, 101034. https://doi.org/10.1016/J.PMATSCI.2022.101034.

(2) Hu, X. Le; Shang, Y.; Yan, K. C.; Sedgwick, A. C.; Gan, H. Q.; Chen, G. R.; He, X. P.; James,

T. D.; Chen, D. Low-Dimensional Nanomaterials for Antibacterial Applications. *J. Mater. Chem. B* **2021**, *9* (17), 3640–3661. https://doi.org/10.1039/D1TB00033K.

(3) Zhao, X.; Xuan, J.; Li, Q.; Gao, F.; Xun, X.; Liao, Q.; Zhang, Y.; Zhao, X.; Xuan, J.; Li, Q.; Gao, F.; Xun, X.; Liao, Q.; Zhang, Y. Roles of Low-Dimensional Nanomaterials in Pursuing Human–Machine–Thing Natural Interaction. *Adv. Mater.* **2023**, 2207437. https://doi.org/10.1002/ADMA.202207437.

(4) Kim, J.; Lee, J.; Lee, J. M.; Facchetti, A.; Marks, T. J.; Park, S. K. Recent Advances in Low-Dimensional Nanomaterials for Photodetectors. *Small Methods* **2023**, 2300246. https://doi.org/10.1002/SMTD.202300246.

(5) Zhang, Z.; Ouyang, Y.; Cheng, Y.; Chen, J.; Li, N.; Zhang, G. Size-Dependent Phononic Thermal Transport in Low-Dimensional Nanomaterials. *Phys. Rep.* **2020**, *860*, 1–26. https://doi.org/10.1016/J.PHYSREP.2020.03.001.

(6) Lu, S.; Guo, D.; Cheng, Z.; Guo, Y.; Wang, C.; Deng, J.; Bai, Y.; Tian, C.; Zhou, L.; Shi, Y.; He, J.; Ji, W.; Zhang, C. Controllable Dimensionality Conversion between 1D and 2D CrCl3 Magnetic Nanostructures. *Nat. Commun. 2023 141* **2023**, *14* (1), 1–8. https://doi.org/10.1038/s41467-023-38175-4.

(7) Zheng, J.; Yang, R.; Xie, L.; Jianglan, Q.; Yang, L.; Xingguo, L. Plasma-Assisted Approaches in Inorganic Nanostructure Fabrication. *Adv. Mater.* **2010**, *22* (13), 1451–1473. https://doi.org/10.1002/ADMA.200903147.

(8) Zhianmanesh, M.; Gilmour, A.; Bilek, M. M. M.; Akhavan, B. Plasma Surface Functionalization: A Comprehensive Review of Advances in the Quest for Bioinstructive Materials and Interfaces. *Appl. Phys. Rev.* **2023**, *10* (2), 21301. https://doi.org/10.1063/5.0130829/2882604.

(9) Mariotti, D.; Sankaran, R. M. Perspectives on Atmospheric-Pressure Plasmas for Nanofabrication. *J. Phys. D. Appl. Phys.* **2011**, *44* (17), 174023. https://doi.org/10.1088/0022-3727/44/17/174023.

(10) Cvelbar, U. Towards Large-Scale Plasma-Assisted Synthesis of Nanowires. *J. Phys. D. Appl. Phys.* **2011**, *44* (17). https://doi.org/10.1088/0022-3727/44/17/174014.

(11) Li, S.; Lu, Z.; Yuan, B.; Hu, R.; Zhu, M. Applications of Plasma-Assisted Systems for Advanced Electrode Material Synthesis and Modification. *ACS Appl. Mater. Interfaces* **2021**, *13* (12), 13909–13919. https://doi.org/10.1021/ACSAMI.0C22907.

(12) Chiappim, W.; Neto, B. B.; Shiotani, M.; Karnopp, J.; Gonçalves, L.; Chaves, J. P.; Sobrinho, A. da S.; Leitão, J. P.; Fraga, M.; Pessoa, R. Plasma-Assisted Nanofabrication: The Potential and Challenges in Atomic Layer Deposition and Etching. *Nanomater. 2022, Vol. 12, Page 3497* **2022**, *12* (19), 3497. https://doi.org/10.3390/NANO12193497.

(13) Ostrikov, K.; Neyts, E. C.; Meyyappan, M. Plasma Nanoscience: From Nano-Solids in Plasmas to Nano-Plasmas in Solids. *http://dx.doi.org/10.1080/00018732.2013.808047* **2013**, *62* (2), 113–224. https://doi.org/10.1080/00018732.2013.808047.

(14) Levchenko, I.; Ostrikov, K. Nanostructures of Various Dimensionalities from Plasma and Neutral Fluxes. *J. Phys. D. Appl. Phys.* **2007**, *40* (8), 2308. https://doi.org/10.1088/0022-3727/40/8/S11.

(15) Altaweel, A.; Filipič, G.; Gries, T.; Belmonte, T. Controlled Growth of Copper Oxide Nanostructures by Atmospheric Pressure Micro-Afterglow. *J. Cryst. Growth* **2014**, *407*, 17–24. https://doi.org/10.1016/j.jcrysgro.2014.08.029.

(16) Cho, G.; Park, Y.; Hong, Y. K.; Ha, D. H. Ion Exchange: An Advanced Synthetic Method for Complex Nanoparticles. *Nano Convergence*. Korea Nano Technology Research Society December 1, 2019, pp 1–17. https://doi.org/10.1186/s40580-019-0187-0.

(17) Saruyama, M.; Sato, R.; Teranishi, T. Transformations of Ionic Nanocrystals via Full and Partial Ion Exchange Reactions. *Acc. Chem. Res.* **2021**, *54* (4), 765–775. https://doi.org/10.1021/ACS.ACCOUNTS.0C00701.

(18) Cummins, D. R.; Russell, H. B.; Jasinski, J. B.; Menon, M.; Sunkara, M. K. Iron Sulfide (FeS) Nanotubes Using Sulfurization of Hematite Nanowires. *Nano Lett.* **2013**, *13* (6), 2423–2430. https://doi.org/10.1021/nl400325s.

(19) Jiang, S.; Huang, R.; Li, W.; Huang, X.; Sheng, H.; Wu, F.; Lv, Y.; Fu, Y.; Zhao, C.; Mai, W. Low-Temperature Vapor-Phase Anion-Exchange Strategy for Wide-Bandgap Double-Perovskite Cs2AgBiCl6Films toward Weak Ultraviolet Light Imaging. *ACS Appl. Mater. Interfaces* **2022**, *14* (22), 26279–26286. https://doi.org/10.1021/ACSAMI.2C06008.

(20) Lim, Y.; Lee, C. H.; Jun, C. H.; Kim, K.; Cheon, J. Morphology-Conserving Non-Kirkendall Anion Exchange of Metal Oxide Nanocrystals. *J. Am. Chem. Soc.* **2020**, *142* (20), 9130–9134. https://doi.org/10.1021/jacs.0c03230.

(21) Thangala, J.; Chen, Z.; Chin, A.; Ning, C. Z.; Sunkara, M. K. Phase Transformation Studies of Metal Oxide Nanowires. *Cryst. Growth Des.* **2009**, *9* (7), 3177–3182. https://doi.org/10.1021/cg801198p.

(22) Zhang, B.; Jung, Y.; Chung, H. S.; Van Vugt, L.; Agarwar, R. Nanowire Transformation by Size-Dependent Cation Exchange Reactions. *Nano Lett.* **2010**, *10* (1), 149–155. https://doi.org/10.1021/NL903059C.

(23) Yoon, H. W.; Aydin, K.; Park, H. J.; Kim, S.; Kwak, D.; Kim, T.; Ahn, C. Friction Characteristics of Molybdenum Disulfide Thin Films Synthesized via Plasma Sulfurization. *Adv. Eng. Mater.* **2021**, *23* (12), 2100971. https://doi.org/10.1002/ADEM.202100971.

(24) Choi, J. H.; Lee, S. W.; Kim, H. B.; Ahn, J. H. Effects of Plasma Conditions on Sulfurization of MoO3 Thin Films and Surface Evolution for Formation of MoS2 at Low Temperatures. *Appl. Surf. Sci.* **2020**, *532*, 147462. https://doi.org/10.1016/J.APSUSC.2020.147462.

(25) Kumar, P.; Singh, M.; Sharma, R. K.; Reddy, G. B. Reaction Mechanism of Core–Shell MoO2/MoS2 Nanoflakes via Plasma-Assisted Sulfurization of MoO3. *Mater. Res. Express* **2016**, *3* (5), 055021. https://doi.org/10.1088/2053-1591/3/5/055021.

(26) Morrish, R.; Silverstein, R.; Wolden, C. A. Synthesis of Stoichiometric FeS 2 through Plasma-Assisted Sulfurization of Fe 2O 3 Nanorods. *J. Am. Chem. Soc.* **2012**, *134* (43), 17854–17857. https://doi.org/10.1021/JA307412E.

(27) Seok, H.; Megra, Y. T.; Kanade, C. K.; Cho, J.; Kanade, V. K.; Kim, M.; Lee, I.; Yoo, P. J.; Kim, H. U.; Suk, J. W.; Kim, T. Low-Temperature Synthesis of Wafer-Scale MoS2-WS2Vertical Heterostructures by Single-Step Penetrative Plasma Sulfurization. *ACS Nano* **2021**, *15* (1), 707–718. https://doi.org/10.1021/ACSNANO.0C06989.

(28) Borah, D.; Saikia, P.; Sarmah, P.; Gogoi, D.; Rout, J.; Ghosh, N. N.; Bhattacharjee, C. R. Composition Controllable Alga-Mediated Green Synthesis of Covellite CuS Nanostructure: An Efficient Photocatalyst for Degradation of Toxic Dye. *Inorg. Chem. Commun.* **2022**, *142*, 109608. https://doi.org/10.1016/J.INOCHE.2022.109608.

(29) Iqbal, S.; Bahadur, A.; Anwer, S.; Shoaib, M.; Liu, G.; Li, H.; Raheel, M.; Javed, M.; Khalid, B. Designing Novel Morphologies of L-Cysteine Surface Capped 2D Covellite (CuS)

Nanoplates to Study the Effect of CuS Morphologies on Dye Degradation Rate under Visible Light. *CrystEngComm* **2020**, *22* (24), 4162–4173. https://doi.org/10.1039/D0CE00421A.

(30) Nancucheo, I.; Segura, A.; Hernández, P.; Hernández-Montelongo, J.; Pesenti, H.; Arranz, A.; Benito, N.; Romero-Sáez, M.; Contreras, B.; Díaz, V.; Recio-Sánchez, G. Covellite Nanoparticles with High Photocatalytic Activity Bioproduced by Using H2S Generated from a Sulfidogenic Bioreactor. *J. Environ. Chem. Eng.* **2022**, *10* (3), 107409. https://doi.org/10.1016/J.JECE.2022.107409.

(31) Liu, Y.; Zhang, H.; Behara, P. K.; Wang, X.; Zhu, D.; Ding, S.; Ganesh, S. P.; Dupuis, M.; Wu, G.; Swihart, M. T. Synthesis and Anisotropic Electrocatalytic Activity of Covellite Nanoplatelets with Fixed Thickness and Tunable Diameter. *ACS Appl. Mater. Interfaces* **2018**, *10* (49), 42417–42426. https://doi.org/10.1021/ACSAMI.8B15895.

(32) Pal, K.; Mahato, P.; Singh, S.; Roy, P. NIR-Responsive 5-Fluorouracil Delivery Using Polydopamine Coated Polygonal CuS Nanoplates for Synergistic Chemo-Photothermal Therapy on Breast Cancer. *J. Drug Deliv. Sci. Technol.* **2023**, *80*, 104092. https://doi.org/10.1016/J.JDDST.2022.104092.

(33) Shi, H.; Yan, R.; Wu, L.; Sun, Y.; Liu, S.; Zhou, Z.; He, J.; Ye, D. Tumor-Targeting CuS Nanoparticles for Multimodal Imaging and Guided Photothermal Therapy of Lymph Node Metastasis. *Acta Biomater.* **2018**, *72*, 256–265. https://doi.org/10.1016/J.ACTBIO.2018.03.035.

(34) Wu, X.; Liu, K.; Huang, Q.; Zhang, Q.; Yang, X.; Liu, X.; Wang, R. Photothermal Therapy Based on CuS Nanoparticles for Alleviating Arterial Restenosis Induced by Mechanical Injury of Endovascular Treatment. *Front. Mater.* **2021**, *7*, 591281. https://doi.org/10.3389/FMATS.2020.591281.

(35) Zhang, C.; Fu, Y. Y.; Zhang, X.; Yu, C.; Zhao, Y.; Sun, S. K. BSA-Directed Synthesis of CuS Nanoparticles as a Biocompatible Photothermal Agent for Tumor Ablation in Vivo. *Dalt. Trans.* **2015**, *44* (29), 13112–13118. https://doi.org/10.1039/C5DT01467K.

(36) Zhao, Y.; Cai, Q.; Qi, W.; Jia, Y.; Xiong, T.; Fan, Z.; Liu, S.; Yang, J.; Li, N.; Chang, B. BSA-CuS Nanoparticles for Photothermal Therapy of Diabetic Wound Infection In Vivo. *ChemistrySelect* **2018**, *3* (32), 9510–9516. https://doi.org/10.1002/SLCT.201802069.

(37) El-Hout, S. I.; Mohamed, S. G.; Gaber, A.; Attia, S. Y.; Shawky, A.; El-Sheikh, S. M. High Electrochemical Performance of RGO Anchored CuS Nanospheres for Supercapacitor Applications. *J. Energy Storage* **2021**, *34*, 102001. https://doi.org/10.1016/J.EST.2020.102001.

(38) Fu, W.; Han, W.; Zha, H.; Mei, J.; Li, Y.; Zhang, Z.; Xie, E. Nanostructured CuS Networks Composed of Interconnected Nanoparticles for Asymmetric Supercapacitors. *Phys. Chem. Chem. Phys.* **2016**, *18* (35), 24471–24476. https://doi.org/10.1039/C6CP02228F.

(39) Ghosh, K.; Srivastava, S. K. Enhanced Supercapacitor Performance and Electromagnetic Interference Shielding Effectiveness of CuS Quantum Dots Grown on Reduced Graphene Oxide Sheets. *ACS Omega* **2021**, *6* (7), 4582–4596. https://doi.org/10.1021/ACSOMEGA.0C05034.

(40) Huang, K. J.; Zhang, J. Z.; Fan, Y. One-Step Solvothermal Synthesis of Different Morphologies CuS Nanosheets Compared as Supercapacitor Electrode Materials. *J. Alloys Compd.* **2015**, *625*, 158–163. https://doi.org/10.1016/J.JALLCOM.2014.11.137.

(41) Lu, Y.; Liu, X.; Wang, W.; Cheng, J.; Yan, H.; Tang, C.; Kim, J. K.; Luo, Y. Hierarchical,

Porous CuS Microspheres Integrated with Carbon Nanotubes for High-Performance Supercapacitors. *Sci. Reports 2015 51* **2015**, *5* (1), 1–11. https://doi.org/10.1038/srep16584.

(42) Dutta, D. P.; Pathak, D. D.; Abraham, S.; Ravuri, B. R. An Insight into the Sodium-Ion and Lithium-Ion Storage Properties of CuS/Graphitic Carbon Nitride Nanocomposite. *RSC Adv.* **2022**, *12* (20), 12383–12395. https://doi.org/10.1039/D2RA02014A.

(43) Jiang, K.; Chen, Z.; Meng, X. CuS and Cu2S as Cathode Materials for Lithium Batteries: A Review. *ChemElectroChem* **2019**, *6* (11), 2825–2840. https://doi.org/10.1002/CELC.201900066.

(44) Kalimuldina, G.; Nurpeissova, A.; Adylkhanova, A.; Adair, D.; Taniguchi, I.; Bakenov, Z. Morphology and Dimension Variations of Copper Sulfide for High-Performance Electrode in Rechargeable Batteries: A Review. *ACS Appl. Energy Mater.* **2020**, *3* (12), 11480–11499. https://doi.org/10.1021/ACSAEM.0C01686.

(45) Cook, R. B. Covellite: Summitville, Rio Grande County, Colorado. *Rocks Miner.* **2010**, *81* (4), 296–300. https://doi.org/10.3200/RMIN.81.4.296-300.

(46) Gaspari, R.; Manna, L.; Cavalli, A. A Theoretical Investigation of the (0001) Covellite Surfaces. *J. Chem. Phys.* **2014**, *141* (4). https://doi.org/10.1063/1.4890374/528683.

(47) Soares, A. L.; Dos Santos, E. C.; Morales-García, Á.; Duarte, H. A.; De Abreu, H. A. The Stability and Structural, Electronic and Topological Properties of Covellite (001) Surfaces. *ChemistrySelect* **2016**, *1* (11), 2730–2741. https://doi.org/10.1002/SLCT.201600422.

(48) Morales-García, Á.; He, J.; Soares, A. L.; Duarte, H. A. Surfaces and Morphologies of Covellite (CuS) Nanoparticles by Means of Ab Initio Atomistic Thermodynamics.

CrystEngComm **2017**, *19* (22), 3078–3084. https://doi.org/10.1039/C7CE00203C.

(49) Taplick, M.; Ruhmlieb, C.; Kipp, T.; Mews, A. Two-Dimensional Superstructures from the Gas Phase: Directed Assembly of Copper-Sulfide Nanoplatelets. *Nano Lett.* **2023**, *23* (4), 1313–1319. https://doi.org/10.1021/ACS.NANOLETT.2C04531.

(50) Brockhaus, A.; Korzec, D.; Werner, F.; Yuan, Y.; Engemann, J. Characterization of a Microwave Plasma by in Situ Diagnostics. *Surf. Coatings Technol.* **1995**, *74–75* (PART 1), 431–442. https://doi.org/10.1016/0257-8972(95)08217-4.

(51) Moreno, S. H.; Stankiewicz, A. I.; Stefanidis, G. D. A Two-Step Modelling Approach for Plasma Reactors – Experimental Validation for CO2 Dissociation in Surface Wave Microwave Plasma. *React. Chem. Eng.* **2019**, *4* (7), 1253–1269. https://doi.org/10.1039/C9RE00022D.

(52) Filipič, G.; Baranov, O.; Mozetič, M.; Cvelbar, U. Growth Dynamics of Copper Oxide Nanowires in Plasma at Low Pressures. *J. Appl. Phys.* **2015**, *117* (4), 043304. https://doi.org/10.1063/1.4906501.

(53) Baranov, O.; Košiček, M.; Filipič, G.; Cvelbar, U. A Deterministic Approach to the Thermal Synthesis and Growth of 1D Metal Oxide Nanostructures. *Appl. Surf. Sci.* **2021**, *566*, 150619. https://doi.org/10.1016/J.APSUSC.2021.150619.

(54) Filipič, G.; Baranov, O.; Mozetič, M.; Ostrikov, K.; Cvelbar, U. Uniform Surface Growth of Copper Oxide Nanowires in Radiofrequency Plasma Discharge and Limiting Factors. *Phys. Plasmas* **2014**, *21* (11), 0–7. https://doi.org/10.1063/1.4901813.

For table of contents only

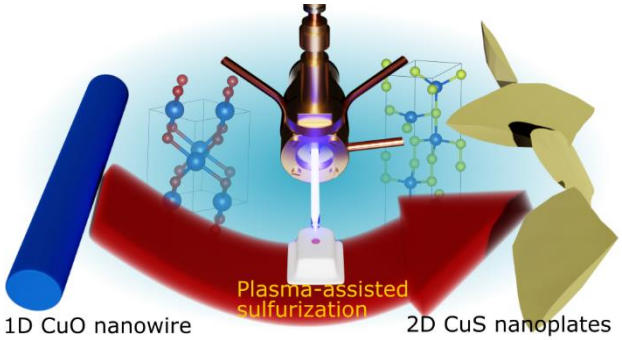
Plasma-assisted
sulfurization
1D CuO nanowire
2D CuS nanoplates

Supporting Information File for manuscript:

Plasma-facilitated 1D-to-2D phase transformation from CuO to CuS

Martin Košiček[a,b], Oleg Baranov[a,c], Janez Zavašnik[a,b], and Uroš Cvelbar[a,b].*

[a]Jožef Stefan Institute, Jamova cesta 39, 1000 Ljubljana, Slovenia

[b]Jožef Stefan International Postgraduate School, Jamova cesta 39, 1000 Ljubljana, Slovenia

[c]National Aerospace University, Chkalova Street 17, 61070 Kharkiv, Ukraine

Additional data on synthesis and analysis of CuO NWs:

Copper (II) oxide nanowires (CuO NWs) were prepared via the thermal oxidation of copper foils in a horizontal tube furnace, as schematically shown in figure S1a. From the literature [1] it is known that upon copper oxidation, a Cu_2O layer is formed first, followed by a CuO layer on top. The surface of the CuO layer exhibits a grainy structure and serves as a base for the growth of the CuO NWs (figure S1b). The NW parameters (length, diameter and number density) depend on the conditions used. In our case, we used a temperature of 265 °C, as in our previous research we found that around this temperature the NWs are thin and still exhibit high density[2]. The NW diameters synthesized at this temperature range between 6 and 40 nm, with an average value of 13 nm. Their distribution is shown in figure S1c. An increase in the oxidation temperature results in thicker NWs. Their density also decreases at temperatures above 500 °C[1]. On the other hand, when the temperature is decreased below 250 °C, the NWs become even thinner; however, their density also drastically decreases, because temperatures around 200 °C already represent a limiting value for the growth of CuO NWs [2].

Experimental details can be found in Methods Section in the main text.

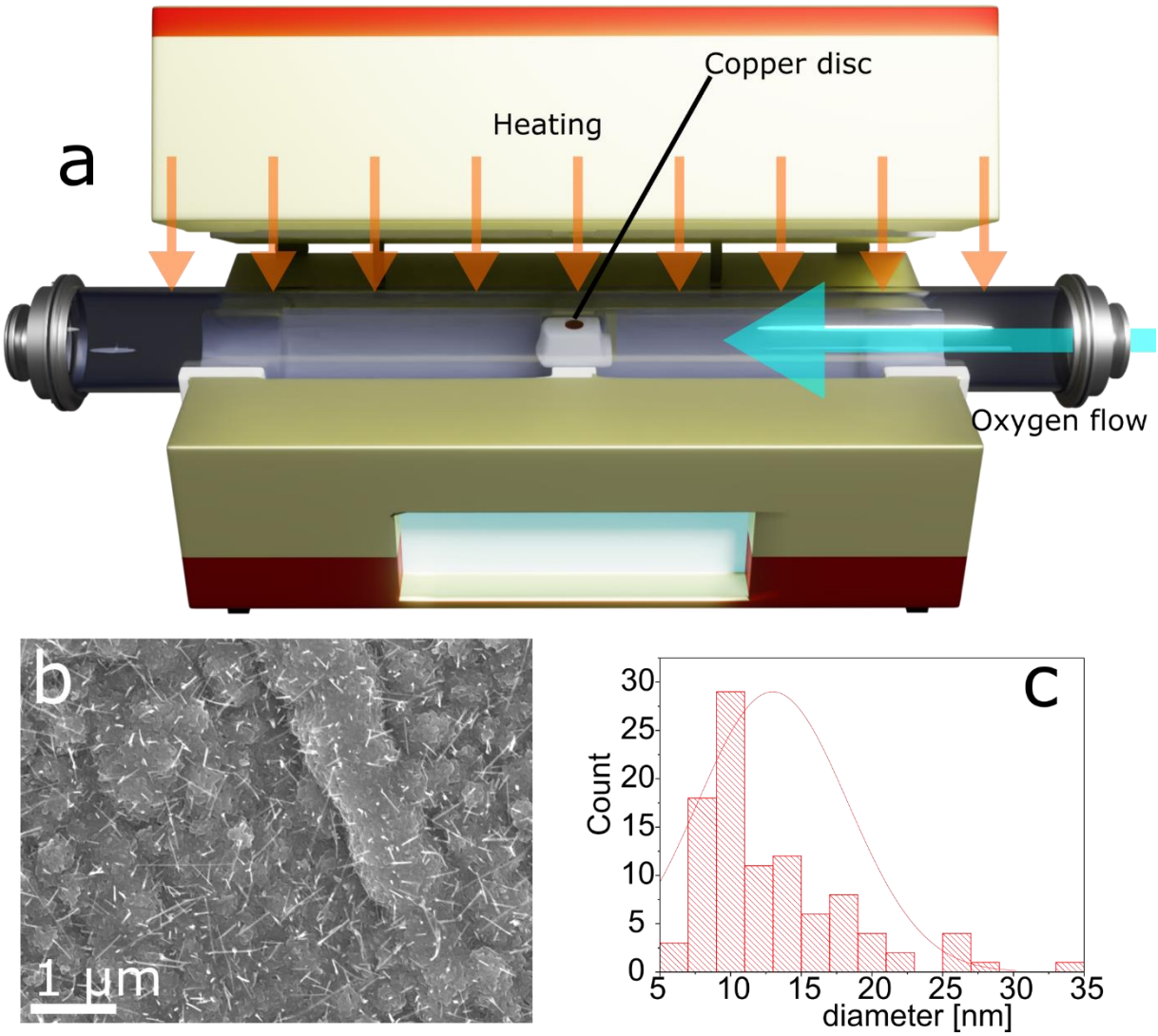

Figure S1. Synthesis and additional analysis of CuO NWs. **a** Schematic of experimental setup. Copper discs were placed in the tube furnace and oxidized at 265 °C in oxygen flow. b SEM micrograph of the surface of oxidized copper discs demonstrating the grainy CuO structure and CuO NWs grown from the surface. c Distribution of NW diameters with normal distribution curve

Experimental setup of plasma-assisted and thermal sulfurization of CuO NWs

Thermal sulfurization was conducted with the same tube furnace, where the copper oxidation was conducted. For sulfurization, separate quartz tube was used. The experimental setup is schematically shown in figure S2a.

Plasma-assisted sulfurization was performed with the use of surfatron-induced microwave plasma. The sample was placed in the early afterglow region of the plasma, as shown in the experimental setup in figure S2b.

Experimental details can be found in the Methods section in the main text.

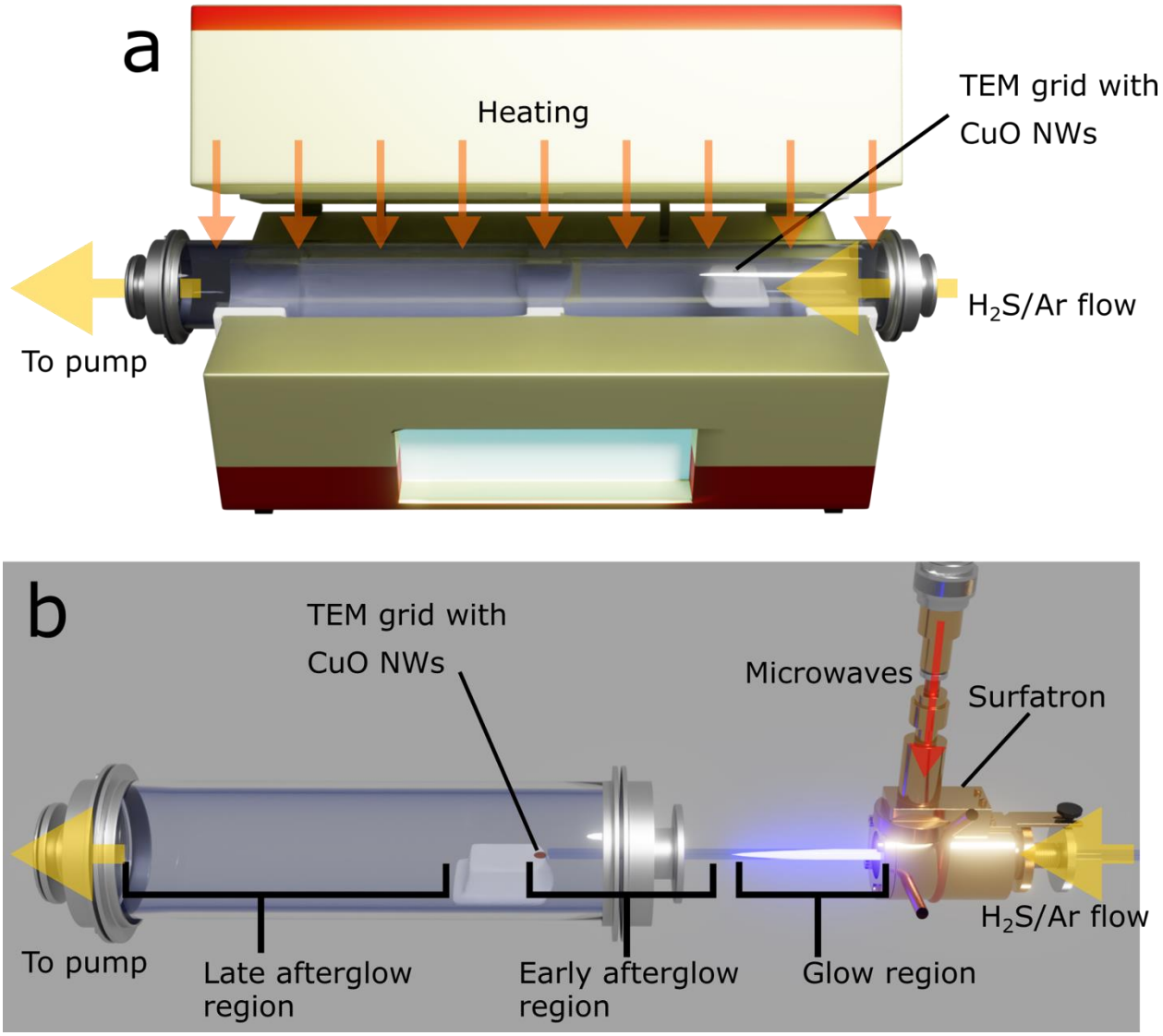

Figure S2. Schematic representation of experimental set-ups for thermal and plasma-assisted sulfurization of CuO NWs. **a** Tube furnace used for thermal sulfurization. **b** Set up used for plasma-assisted sulfurization.

Plasma characterization and temperature measurements

To measure the temperature that the treated sample reached when exposed to plasma we measured the temperature around the area where the sample was positioned with a thermocouple (see figure S3a). We found that the temperature greatly depends on the positioning, with the smallest movement affecting the temperature. The plasma temperature was measured in three positions on the ceramic holder (figure S3b). As expected, the temperature was the highest, directly in front of the quartz tube, serving as inlet for the reactive plasma species into the larger tube with the sample (figure S3c) (position 3), which is where the sample was placed. In all cases, the temperature rises for around 10 min when plateau is reached (figure S3c).

The glow region of the plasma was also characterized with optical emission spectroscopy (OES), which reveals atomic peaks of argon and hydrogen as well as molecular peaks associated with the S_2 molecules [3] (figure S3d).

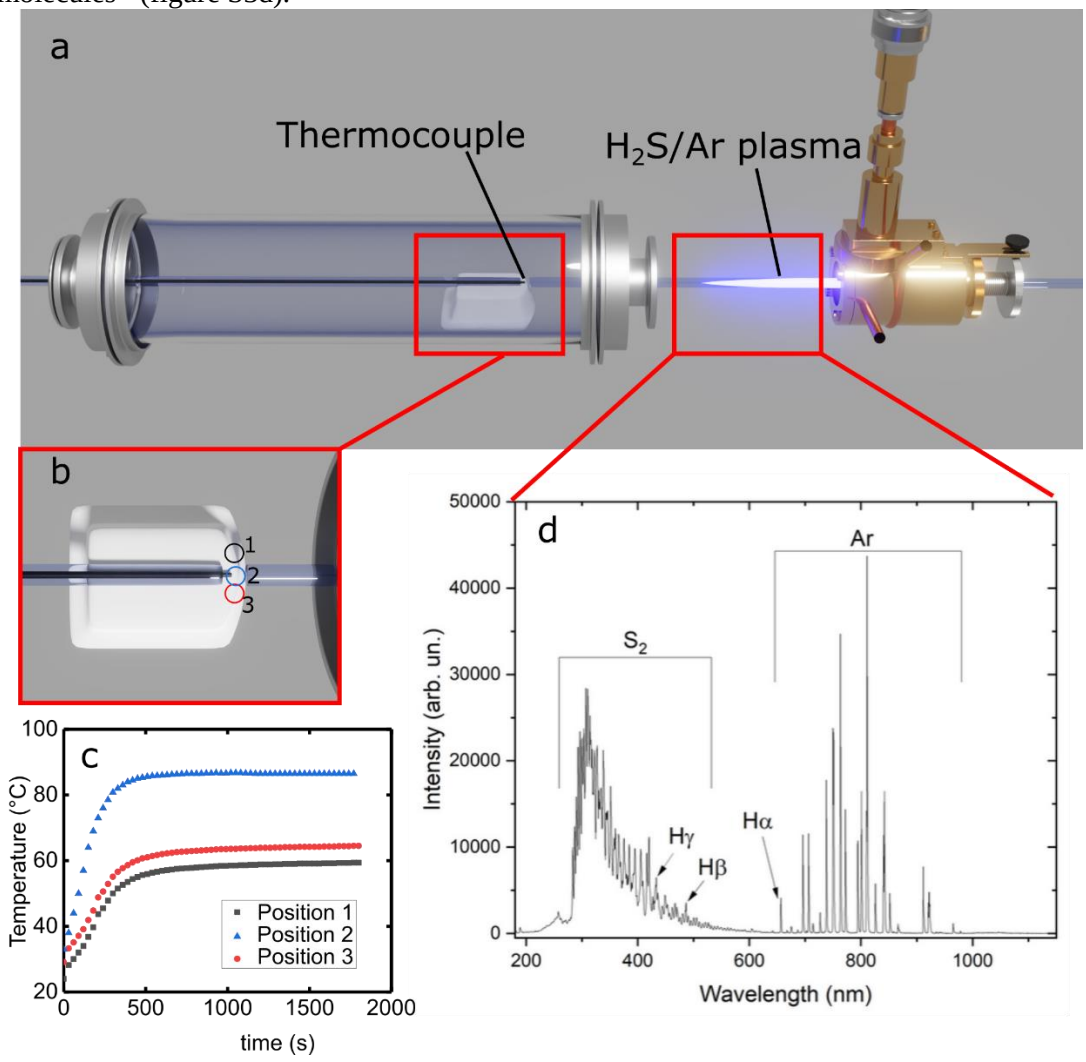

Figure S3. Temperature and optical emission measurements for plasma characterization. **a** Experimental setup for measuring temperature by positioning thermocouple where CuO NWs were treated. **b** Different positions on the alumina holder where temperature was measured. **c** Time dependence of the temperature during plasma treatment on the positions in plasma afterglow marked in figure **b**. **d** Optical emission spectrum of the glow area with indicated peaks corresponding to argon, hydrogen and S_2 molecule.

TEM analysis of transformed NWs

Plasma-assisted sulfurization for 15 min

After 15 min of plasma-assisted sulfurization the transformed NWs can possess three different morphologies. The first two morphologies are present in CuO NWs that are already completely transformed to CuS nanoplates. In such cases, the single crystallinity can be preserved in the radial NW direction by the formation of isolated nanoplates arranged in the axial direction of the initial NW (figures S4a-c). In the second case, the transformation from oxide to sulfide is also complete; however, multiple CuS nanoplates in the radial direction are formed, indicating that NWs exhibit polycrystalline character in all three directions (figures S4d-f). The third morphology type can be observed in NWs where the transformation from CuO phase to CuS phase is still not complete yet, and the CuO core is still visible (figures S4g-i). From the ring pattern in selected-area electron-diffraction (SAED) pattern (figure S4i) it can be seen that the orientation of the CuS grains around the CuO is random.

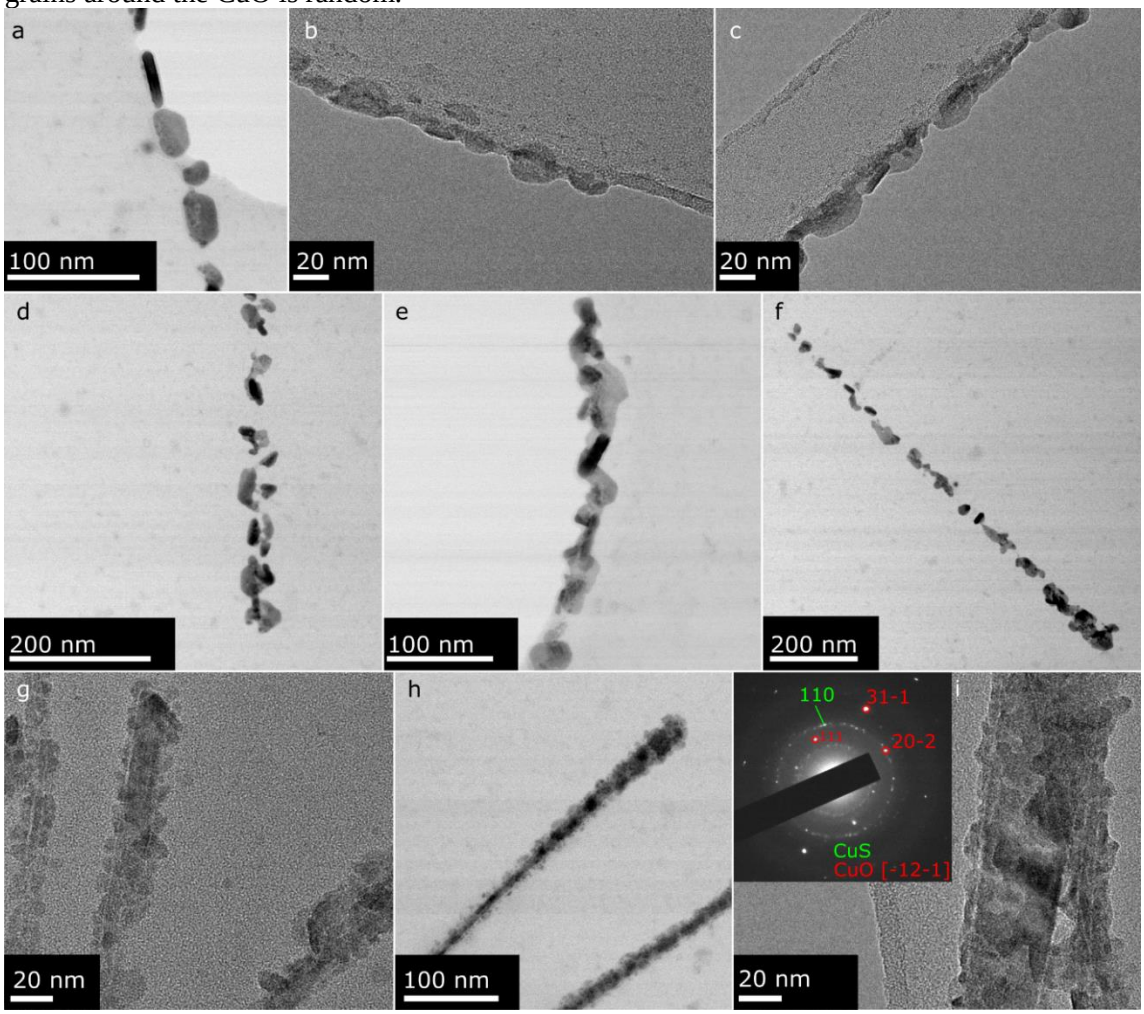

Figure S4. Morphologies of CuO NWs that were sulfurized with plasma for 15 min: **a-c** Structure formed by complete transformation of CuO NW to CuS nanoplates, which become arranged axially along the length of the original NW **d-e** Structure formed by complete transformation with multiple CuS plates in axial and radial directions. **g-i** Structures where CuO core is retained and 2D growth of CuS structures has not yet begun. SAED pattern inset in **i** indicates the presence of single-crystalline CuO core thar is encapsulated with randomly oriented CuS grains.

The nanoplates grow tangentially to the NW surface and the normal of the 2D plates corresponds to the 001 direction. Examples of additional nanoplates that start growing on the NW surface after 15 minutes of plasma treatment viewed perpendicular to their normal, with visible normal directions, are shown in figures S5a-f.

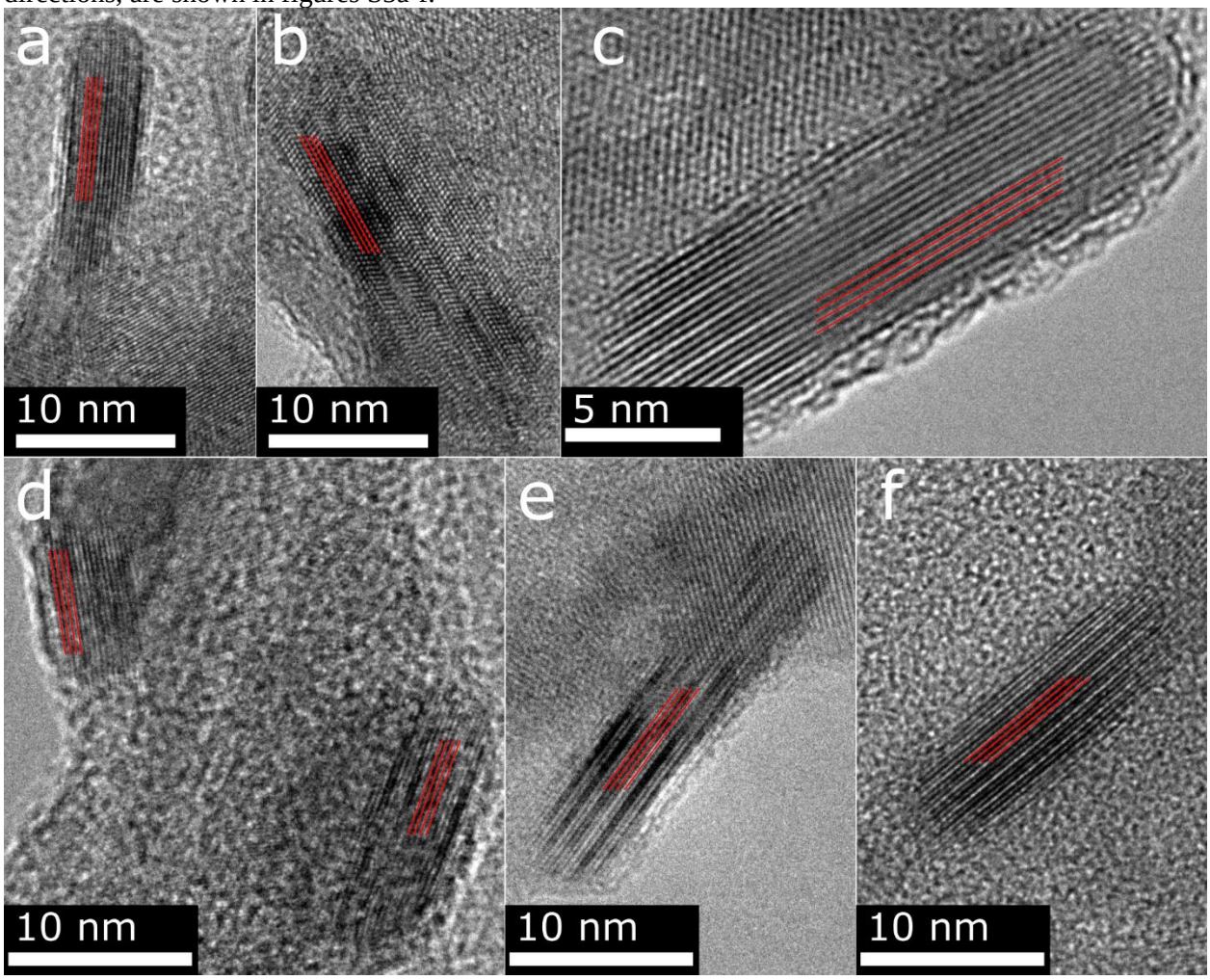

Figure S5. a-f Additional examples of CuS nanoplates. In all figures the (006) planes are marked with red lines.

In some NWs, treated for 15 min, equiaxed grains were still present. The diameter of the equiaxed grains closely corresponds to the thickness of the CuS plates (see Figure S6), suggesting that the growth of the nanoplates is initiated on individual equiaxed grains, which at some point grow by expansion in 2D.

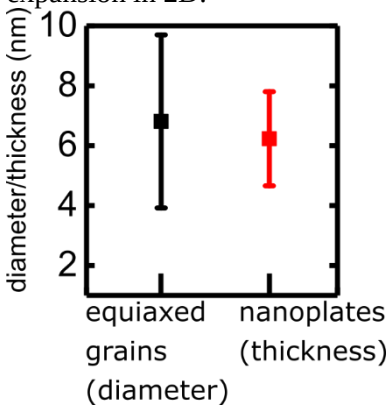

Figure S6. Comparison between diameter of formed CuS equiaxed grains and thickness of CuS nanoplates formed after 15 min of plasma sulfurization. Similar values between the two suggest that the growth of CuS nanoplates originates in the equiaxed grains.

Plasma-assisted sulfurization for 25 min

Plasma-assisted sulfurization was also performed for 25 min for a further evaluation of the CuS nanoplates, and for a better experimental assessment of which initial CuO diameter and plasma treatment time result in which morphology (main text figure 4l). Examples of structures formed after 25 min in plasma can be seen in figure S7.

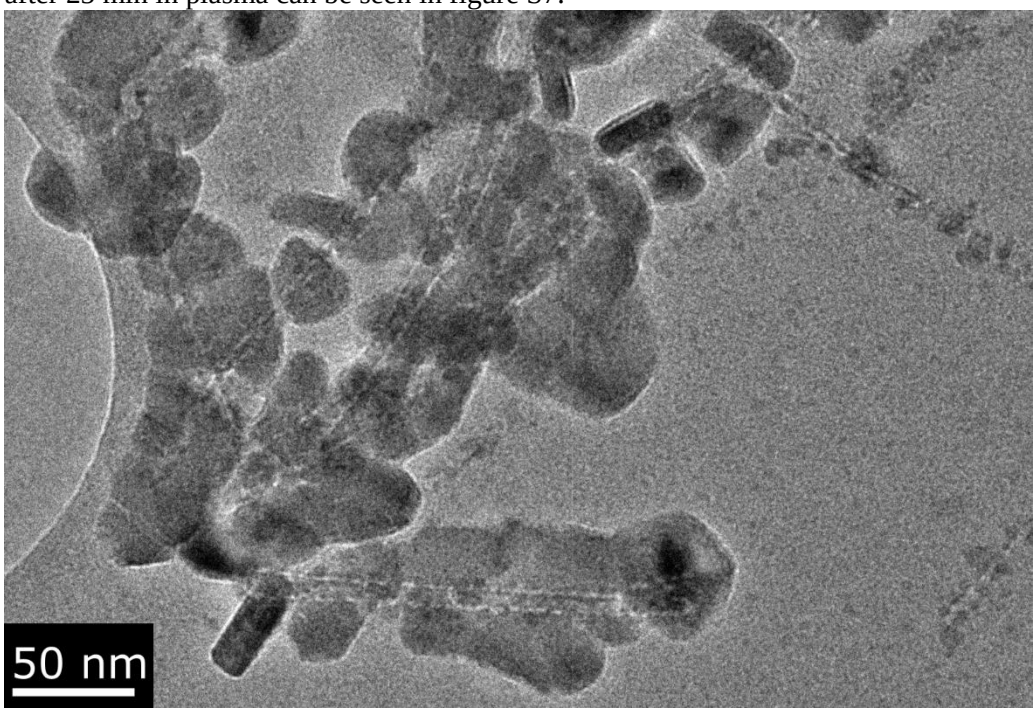

Figure S7. Example of CuS nanoplates formed after Cuo NWs were sulfurized for 25 min.

Plasma-assisted sulfurization for 30 min

After 30 min of plasma-assisted sulfurization, the CuO phase is completely transformed to CuS. The polycrystalline SAED pattern of a transformed NW bundle (figure S8a) for CuS-phase identification is shown in figure S8b. The diffraction pattern confirms the covellite phase (covellite structure is shown in figure S8c).

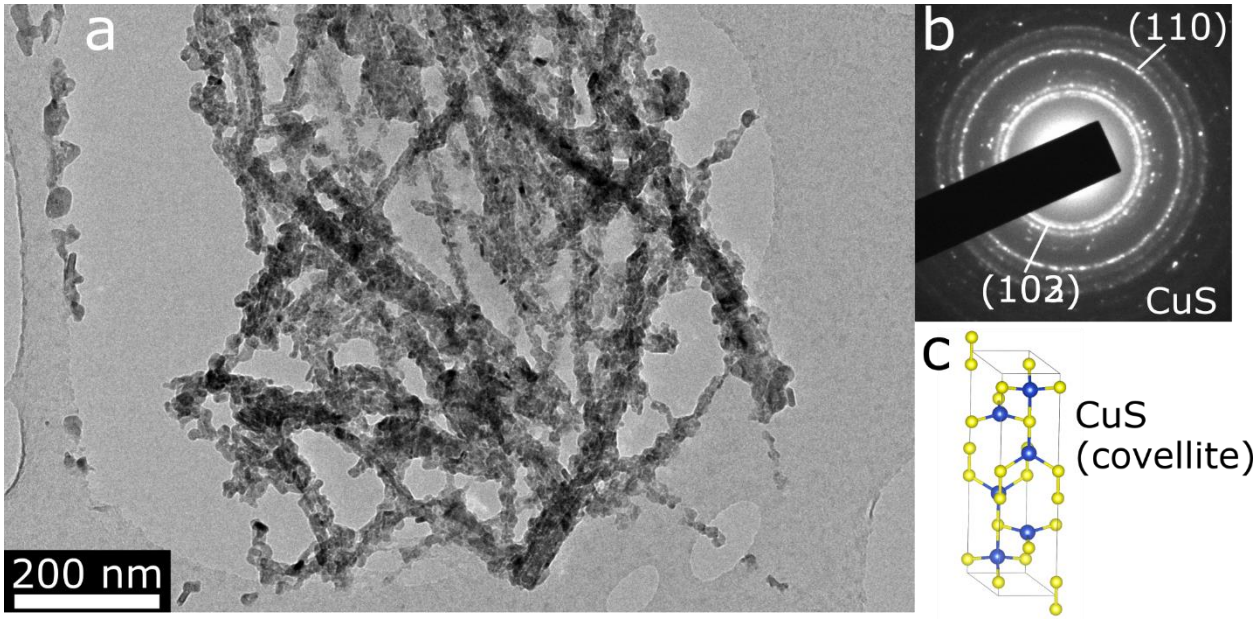

Figure S8. TEM analysis of the NWs for confirmation of the covelite (CuS) phase. **a** TEM micrograph of the NW bundle, sulfurized with plasma for 30 min. **b** Polycrystalline SAED pattern of the NWs in **a**, corresponding to the covellite phase. **c** Model of a covellite unit cell.

Different structures of completely transformed NWs can also be visible in samples sulfurized for 30 min. In contrast to the 15-min treatment, all NWs are completely transformed to CuS, hence the transformed NWs attain either a morphology where the individual CuS plates are arranged in an axial NW, or the morphology that exhibits several CuS nanoplates in a radial direction. Examples of such morphologies are shown in figures S9a,b respectively.

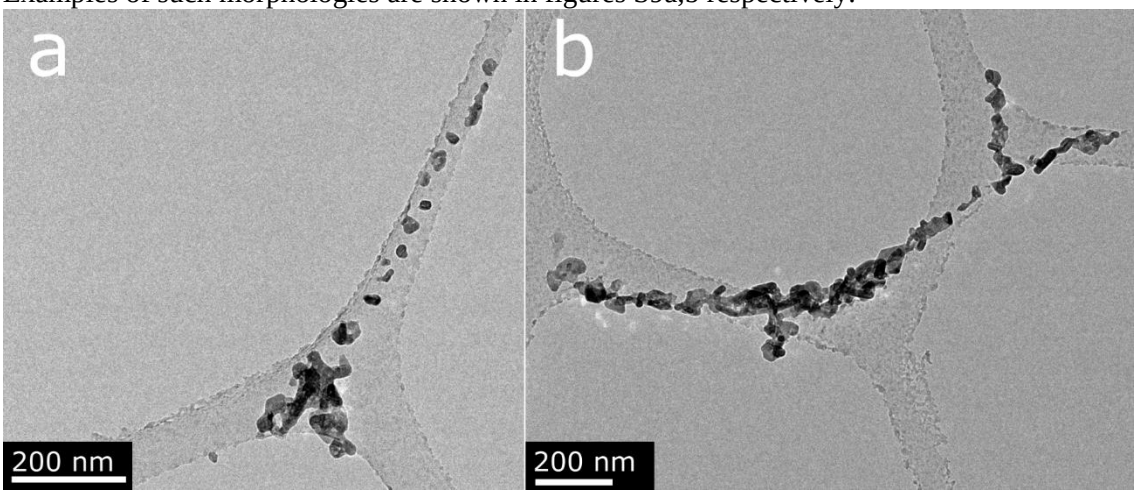

Figure S9. Examples of different morphologies obtained after plasma-assisted sulfurization of CuO NWs for 30 min. **a** Structure, where individual CuS plates are arranged one by one in axial direction of initial NW. Here the single-crystalline character was preserved in the radial direction during transformation. This type of morphology is only visible in the middle and upper parts of the NW. Lower part was most likely thicker in initial CuO. NW transforms to structure with multiple CuS plates in radial direction. **b** Structure where CuS plates are again arranged in axial direction of initial NW; however, the structure also exhibits several CuS plates in radial direction. In this case, the single-crystalline character was not preserved in any direction.

Thermal sulfurization of NWs at room temperature

Thermal sulfurization was first performed at room temperature, by exposing the sample to an Ar/H_2S flow, using exactly the same experimental setup as in plasma without plasma ignition. After 30 min of such treatment, no change was observed in the CuO NWs (figure S10a-f)

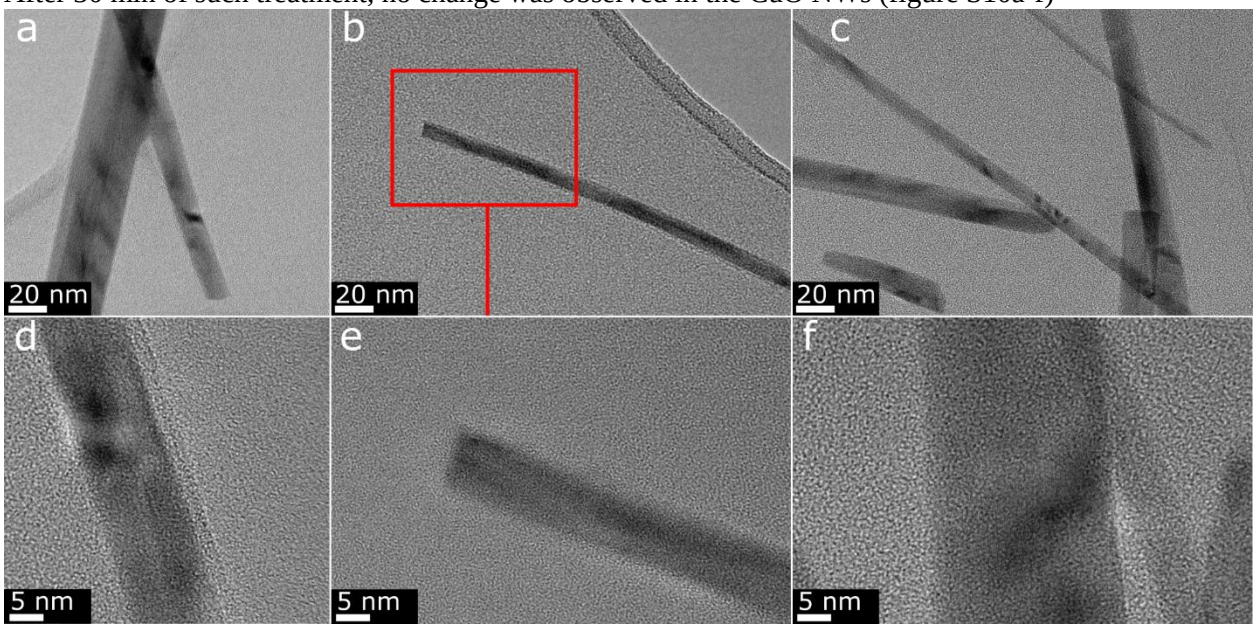

Figure S10. a-f Examples of NWs, treated for 30 min at room temperature in a flow of H_2S in argon. No visible changes in the NW structure are found.

Thermal sulfurization of NWs at 100 °C for 90 min

The longest time used for the thermal sulfurization of CuO NWs was 90 min, to achieve complete CuO-to-CuS transformation. Additional examples of NWs treated in this way can be seen in figure S11a-c. The SAED pattern inset in figure S11a confirms that the transformed NWs are composed of covellite CuS grains.

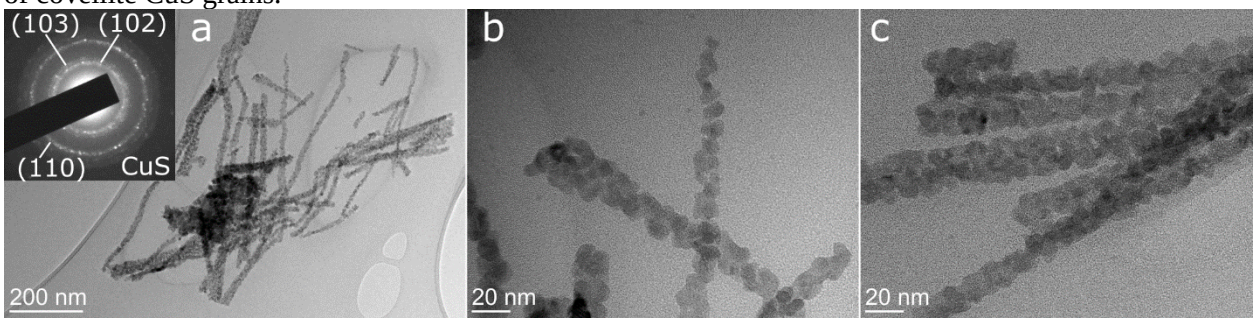

Figure S11. a-c examples of structures formed upon thermal sulfurization of CuO NWs. Inset SAED pattern in **a** confirms the presence of CuS phase.

Calculations of maximum initial CuO NW diameters for the preservation of single crystallinity in radial NW direction during plasma-assisted sulfurization

To determine the lowest CuO NW diameter that will, when sulfurized, result in only one CuS plate in a radial direction (i.e., where the resulting CuS structure will exhibit individual CuS nanoplates arranged in a row along the axial direction of the initial CuO NW), we calculated the radius of a CuO NW that would, upon transformation, give an average nanoplate, as seen in the drawing in figure S12. We did this by measuring the surface areas of several nanoplates. We did this by assuming the cylindrical shape of the CuO NW, which would result in the planar CuS, where the amount of CuO units is the same as the amount of CuS units.

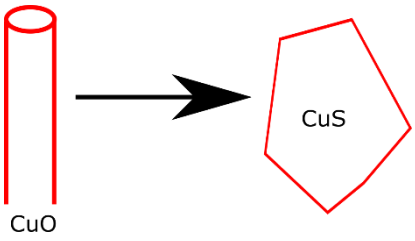

Figure S12. Scheme of transformation from a cylindrical NW segment to planar nanoplate segment.

Therefore, amount n of CuO and CuS are equal:

$$n(CuO) = n(CuS) \tag{S1}$$

By expressing the amount with mass (m) and molar mass (M) we get:

$$\frac{m(CuO)}{M(CuO)} = \frac{m(CuS)}{M(CuS)} \tag{S2}$$

Mass can be then substituted with density (ρ) and volume (V). Volume can then be further substituted with $\pi r^2 h$ for a cylindrical NW, where r is its radius and h is the length of a NW segment that will transform to nanoplate. For a nanoplate, the volume can be expressed as the product of the surface of the main face (S) and its thickness (t). When measuring the surface of a nanoplate in the TEM, we need to consider that the image of a plate represents a 2D projection. Therefore, we also need to determine the orientation of the plate and consider the angle θ between the normal of the plate and the direction of view.

By considering these substitutions and expressing the NW radius, we obtain:

$$r(CuO) = \sqrt{\frac{\rho(CuS)\cdot S(CuS)\cdot d(CuS)\cdot M(CuO)}{cos\theta\cdot\rho(CuO)\cdot M(CuS)\cdot\pi\cdot h}} \tag{S3}$$

An example for the calculations of the CuO NW radius can be seen in figure S13. The surface area of the main face (S) and length along the NW axial direction (h) of a nanoplate marked in a red square in figure S13a were measured. For the h value we can take the dimension of a nanoplate, or we can also consider the empty space between two neighboring grains. The measured values are 38 and 44 nm, respectively (figure S13b). For the thickness of the nanoplate, the average measured value of 6.23 nm was used (figure S6), for the densities of CuS and CuO, 4.76 and 6.31 g/cm^3 were used, respectively. For the θ value, the angle between the direction of view [021], determined by FFT (figure S13c), and the normal to planar CuS structure, [001], was used, which corresponds to 24.9 °C. By also considering the CuO and CuS molar masses of 75.545 g/mol and 95.611 g/mol, respectively, the value of the CuO NW diameter that resulted in the formation of this nanoplate is 4.9 nm for an h value of 44 nm and 5.3 nm for an h value of 38 nm. Both values are around 5 nm (diameter 10 nm). By performing the same calculations on other nanoplates obtained by plasma-assisted sulfurization for 15 and 30 min, the obtained results suggest that for 15 minutes, the value of CuO NW diameter that would result in complete transformation to a single nanoplate is approximately 10 nm and 15 nm for sulfurization times of 15 min and 30 min, respectively.

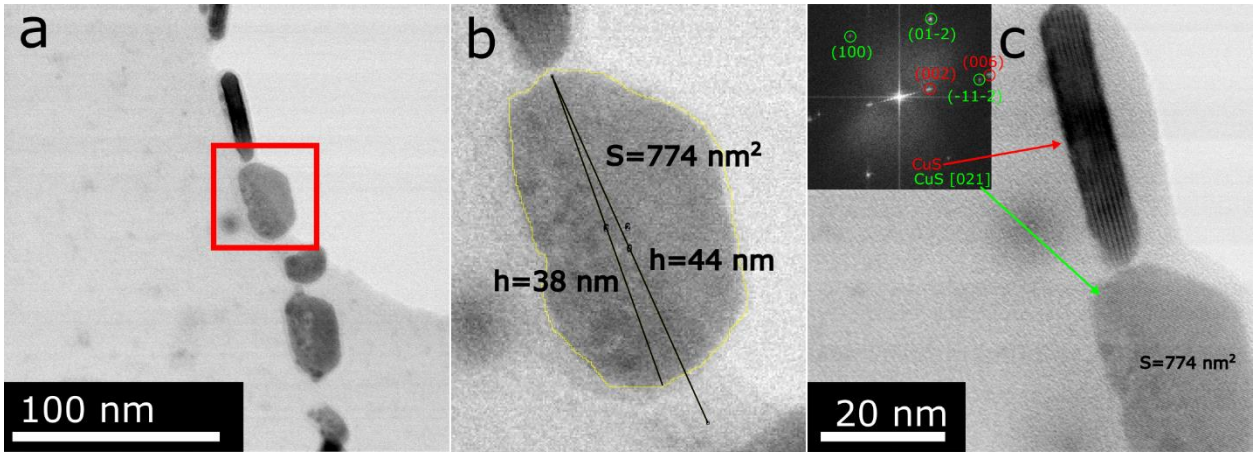

Figure S13. Example of measurements of a nanoplate for further calculations of the CuO NW diameter from which the nanoplate was formed. a nanoplate marked with a red square, on which the calculations were performed. b Measurements of nanoplate surface and length along the initial CuO NW axial direction. c determination of orientation of CuS nanoplate from FFT. Spots marked with red and green correspond to grains marked with red and green arrows, respectively.

Theoretical model

To describe the mechanism of CuS nanoplate growth, the theoretical model describing the processes during plasma-assisted sulfurization was employed.

In the model, the following conversion of a copper oxide (CuO) aggregate in the presence of a hydrogen sulfide (H_2S) molecule is considered, which results in the formation of a copper sulfide (CuS) aggregate and a molecule of water (H_2O):

$$CuO + H_2S \rightarrow CuS + H_2O. \quad \text{(S4)}$$

When a detached NW is exposed to the reaction, a layer of copper sulfide is formed on the NW surface, so CuO aggregates should cross the CuS layer to be involved in reaction (S4). Hydrogen sulfide molecules are adsorbed on the surface of a detached NW, and the density n_{H2S} of the adsorbed molecules with respect to the density n_{CuS} of the adsorption nodes is:

$$\frac{n_{H2S}}{n_{CuS}} = \frac{P_{H2S}}{P_0 + P_{H2S}}, \quad \text{(S5)}$$

where P_{H2S} is the pressure of hydrogen sulfide, Pa; $n_{CuS} = a_{CuS}^{-2}$ (a_{CuS} is a lattice period of CuS); P_0 is a constant that depends on the temperature:

$$P_0 = \left(\frac{M_{H2S}}{2\pi\hbar^2}\right)^{3/2} (k_B T_s)^{5/2} exp\left[-\frac{e(\varepsilon_{aH2S} - \varepsilon_{i-H2S})}{k_B T_s}\right], \quad \text{(S6)}$$

where M_{H2S} is the mass of the hydrogen sulfide molecule, kg; ε_{aH2S} is the adsorption energy (eV) of the molecule on the surface; $\varepsilon_{i\text{-}H2S}$ is the internal energy (eV) of the molecule.

During this rhw diffusion of CuS aggregates into the CuO layer is considered to be much slower, which leads to the generation of a void in the body of the NW.

The schematic of the processes is shown in figure S14.

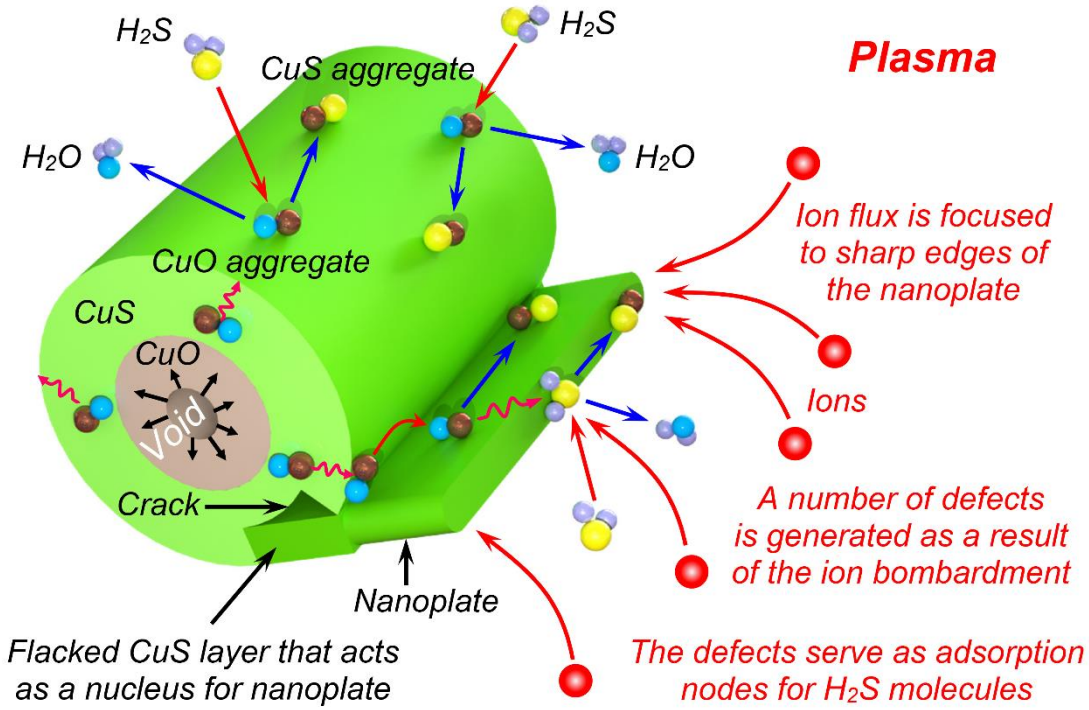

Figure S14. Formation of CuS nanoplate on surface of CuS layer formed as a result of sulfurization of CuO NW exposed to plasma-enhanced process in atmosphere of hydrogen sulfide gas. Diffusion of CuO aggregates to the outer surface of the CuS layer is accompanied with the generation of a void in the body of the CuO NW due to the difference of the diffusion fluxes. The rapid growth of the CuS layer in the plasma led to the generation of stress in the surface layer, which, in turn, results in cracking of the latter. The crack absorbs the CuO aggregates; moreover, the flaked part of CuS layer straightens and becomes a protrusion from the CuS layer, which attracts species from the plasma due to the local electric field. As a result, the flaked protrusion becomes a nucleus for the future nanoplate.

The flux of CuO aggregates through the CuS layer of thickness L_{CuS} is not involved in the reaction (S4) while diffusing through the surface, and CuO is converted into CuS aggregates only on the surface that is exposed to the direct action of the H_2S molecules. So, the density $n_{CuO}(z)$ of the CuO aggregates on the CuS layer is:

$$D_{CuO}\frac{d^2 n_{CuO}}{dz^2} = 0, \tag{S7}$$

$$n_{CuO} - n_{CuO0} = -\frac{\varphi_{CuO}}{D_{CuO}} a_{CuS} L_{CuS}, \tag{S8}$$

$$D_{CuO} = D_{0c} exp\left[-\frac{e\varepsilon_c}{k_B T_s}\right] = \frac{\nu_0 a_{CuS}^2}{2} exp\left[-\frac{e\varepsilon_c}{k_B T_s}\right] = \frac{k_B T_s}{h} a_{CuS}^2 exp\left[-\frac{e\varepsilon_c}{k_B T_s}\right], \tag{S9}$$

where D_{CuO} as a diffusion coefficient; ε_c is the energy of activation of the CuO diffusion through the CuS layer; L_{CuS} is the thickness of the CuS layer; ν_0 is the frequency of the lattice oscillations; and h is Plank's constant.

Thus, the flux φ_{CuO} of CuO aggregates at the surface of CuS is:

$$\varphi_{CuO}(L_{CuS}) = \frac{1}{2} n_{CuO} \frac{n_{H2S}}{n_{CuS}} \nu_0 exp\left[-\frac{e(\varepsilon_c + \varepsilon_{x-dis})}{k_B T_s}\right], \tag{S10}$$

where $\varepsilon_{x\text{-}dis}$ is the energy of dissociation of the CuO aggregate in the presence of a molecule of water.

After combining the equations, the flux φ_{CuO} is:

$$\varphi_{CuO} = \frac{n_{H2S}}{1+\frac{a_{CuS}\nu_0}{2D_{0c1}}L_{CuS}\frac{n_{H2S}}{n_{CuS}}exp\left[-\frac{e\varepsilon_{x-dis}}{k_BT_s}\right]}\frac{\nu_0}{2}\frac{n_{CuO0}}{n_{CuS}}\nu_0 exp\left[-\frac{e(\varepsilon_{c1}+\varepsilon_{x-dis})}{k_BT_s}\right], \quad \text{(S11)}$$

which makes it possible to determine the rate of growth of the CuS layer:

$$\frac{dL_{CuS}}{dt}(L_{CuS}) = \varphi_{CuO}a_{CuS}^3 =$$

$$= \frac{1}{1+\frac{a_{CuS}\nu_0}{2D_{0c1}}L_{CuS}\frac{n_{H2S}}{n_{CuS}}exp\left[-\frac{e\varepsilon_{x-dis}}{k_BT_s}\right]}\frac{n_{H2S}}{n_{CuS}}\frac{\nu_0}{2}\frac{R_{nw}}{R_{nw}+L_{CuS}}n_{CuO0}a_{CuS}^3 exp\left[-\frac{e(\varepsilon_{c1}+\varepsilon_{x-dis})}{k_BT_s}\right], \quad \text{(S12)}$$

with the initial condition $L_{CuS}(0) = L_{CuS0}$.

After reaching a certain thickness, the CuS layer undergoes cracking due the rapid growth, when the internal stress cannot be released by rebuilding the structure. The crack formation on the surface of the CuS layer re-distributes the fluxes of the CuO aggregates that reached the surface of the CuS layer, since the crack is considered as a place with enhanced adsorption properties, so the CuO aggregates tend to group around the crack, which becomes a nucleus for the future nanoplate. At that point, the cracked layer unrolls and starts protruding from the rest of the CuS layer. The protrusion generates a local electric field that attracts the positively charged species from the plasma, thus focusing the flux of the building material towards the protrusion, and especially its edges. The ions bombard the surface and generate a number of defects, which functionalize the surface and increase its adsorption ability. In this way the redistribution of the treating flux stimulates the growth of the protrusion, which is transformed into a nanoplate. At that point, the adsorption on the top and side surfaces of the nanoplate and its side is characterized by the energies ε_{aH2St} and ε_{aH2Ss}, respectively:

$$\frac{n_{H2St}}{n_{CuS}} = \frac{P_{H2S}}{\left(\frac{M_{H2S}}{2\pi\hbar^2}\right)^{3/2}(k_BT_s)^{5/2}exp\left[-\frac{e(\varepsilon_{aH2St}-\varepsilon_{i-H2S})}{k_BT_s}\right]+P_{H2S}},$$

$$\frac{n_{H2Ss}}{n_{CuS}} = \frac{P_{H2S}}{\left(\frac{M_{H2S}}{2\pi\hbar^2}\right)^{3/2}(k_BT_s)^{5/2}exp\left[-\frac{e(\varepsilon_{aH2Ss}-\varepsilon_{i-H2S})}{k_BT_s}\right]+P_{H2S}}. \quad \text{(S13)}$$

It is assumed for simplicity that after the crack formation all the CuO aggregates are supplied to the nucleus of the nanoplate, so the growth of the CuS layer is terminated, and further the flux of CuO aggregates feeds the formation of the CuS nanoplate only. Thus, as the rate of the decrease of the CuO layer is:

$$\frac{dL_{CuO}}{dt}(L_{CuS}) = \begin{cases} -\frac{1}{1+\frac{a_{CuS}\nu_0}{2D_{0c}}L_{CuS}}\frac{P_{H2S}}{P_0+P_{H2S}}\frac{R_{nw}-L_{CuO}}{R_{nw}}\frac{\nu_0}{2}\left(\frac{a_{CuO}}{a_{CuS}}\right)^3 exp\left[-\frac{e(\varepsilon_c+\varepsilon_{x-dis})}{k_BT_s}\right], & L_{CuS} < L_{CuScr}; \\ -\frac{1}{1+\frac{a_{CuS}\nu_0}{2D_{0c1}}L_{CuS}\frac{n_{H2S}}{n_{CuS}}exp\left[-\frac{e\varepsilon_{x-dis}}{k_BT_s}\right]}\frac{n_{H2S}}{n_{CuS}}\frac{\nu_0}{2}\frac{\pi a_n b_n}{\pi R_{nw}h_{max}}n_{CuO0}a_{CuO}^3 exp\left[-\frac{e(\varepsilon_c+\varepsilon_{x-dis})}{k_BT_s}\right], & L_{CuS} \geq L_{CuScr} \end{cases}, \quad \text{(S14)}$$

with the initial condition $L_{CuO}(0) = R_{nw}$; L_{CuScr} is a critical thickness of the CuS layer during the plasma treatment, when the crack formation is initiated; a_n and b_n are half-width and half-thickness of a nanoplate cross-section at the nanoplate root (nucleus); the parameters are also semi-major and semi-minor axes of the nanoplate cross-section that is considered to be elliptical. It should be emphasized that the crack generation depends greatly on the rate of growth of the corresponding layer structure, and the rate is much higher during the plasma treatment, in comparison with the processes of thermal treatment. However, stress generation is not considered in the model, and L_{CuScr} is considered as a parameter.

For further nanoplate growth, the transport of CuO aggregates into the CuS is determined by the sulfurization process on the side and top surfaces of the nanoplate.

The diffusion of the CuO aggregate along the part of CuS nanoplate surface that is located in the CuS layer (in the crack) is not accompanied by the conversion into CuS aggregates:

$$n_{CuOnp} = n_{CuO} - \frac{\varphi_{Cunp}}{D_{CuO}}a_{CuS}L_{CuS}, \quad \text{(S15)}$$

where n_{Cu0np} is the density of CuO aggregates at the root of the nanoplate, and the initial density n_{Cu0} of copper aggregates equals the density of bulk CuO.

Under the conditions of the oxidation reaction on the side surface of nanoplate, the distribution of the copper aggregates along the nanoplate surface is determined by the equation:

$$D_{Cus}\frac{\partial^2 n_{cu}(z)}{\partial z^2} = -n_{Cu}(z)\frac{n_{H2Ss}}{n_{CuS}}\nu_0 exp\left(-\frac{e\varepsilon_{x-dis}}{k_B T_s}\right), \quad \text{(S16)}$$

where n_{H2Ss} is the number density of hydrogen sulfide molecules adsorbed on the side surface of the nanoplate.

The diffusion coefficient D_{Cus} is expressed as

$$D_{Cus} = D_{0c}exp\left(-\frac{e\varepsilon_{cs}}{k_B T_s}\right) = \frac{\nu_0 a_{CuS}^2}{2}exp\left[-\frac{e\varepsilon_{cs}}{k_B T_s}\right] = \frac{k_B T_s}{h}a_{CuS}^2 exp\left[-\frac{e\varepsilon_{cs}}{k_B T_s}\right], \quad \text{(S17)}$$

$$\frac{\partial^2 n_{cu}(z)}{\partial z^2} = n_{Cu}(z)\frac{n_{H2Ss}}{n_{CuS}}\frac{\nu_0}{D_{Cus0}}exp\left(-\frac{e(\varepsilon_{x-dis}-\varepsilon_{cs})}{k_B T_s}\right), \quad \text{(S18)}$$

where ε_{cs} is the energy of diffusion of the CuO aggregate along the side surface of the CuS nanoplate.

The solution of the equation for $n_{Cu}(0) = n_{Cu0np}$ is

$$n_{Cu}(z) = n_{Cu0np}cos\left[\left(\frac{n_{H2Ss}}{n_{CuS}}\frac{\nu_0}{D_{Cus0}}exp\left[-\frac{e(\varepsilon_{x-dis}-\varepsilon_{cs})}{k_B T_s}\right]\right)^{1/2} z\right]. \quad \text{(S19)}$$

The number of CuO aggregates converted to CuS per unit time by the side surface of a nanoplate with the length L_{np} is:

$$N_{Cus}(L_{np}) = \int_0^{L_{np}} n_{Cu}(z)\frac{n_{H2Ss}}{n_{CuS}}\nu_0 exp\left(-\frac{e\varepsilon_{x-dis}}{k_B T_s}\right)\sqrt{2}\pi\sqrt{a_n^2(z)+b_n^2(z)}dz =$$

$$= n_{Cu0np}\frac{n_{H2Ss}}{n_{CuS}}\nu_0 exp\left(-\frac{e\varepsilon_{x-dis}}{k_B T_s}\right)\sqrt{2}\pi\int_0^{L_{np}}\sqrt{a_{np}^2(z)+b_{np}^2(z)}cos\left[\left(\frac{n_{H2Ss}}{n_{CuS}}\frac{\nu_0}{D_{Cus0}}exp\left[-\frac{e(\varepsilon_{x-dis}-\varepsilon_{cs})}{k_B T_s}\right]\right)^{1/2} z\right]dz, \quad \text{(S20)}$$

By assuming that the radius of a nanoplate is weakly changing from the root to the top, the expression is simplified:

$$N_{Cus}(L_{np}) = \sqrt{2}\pi\sqrt{a_n^2(0)+b_n^2(0)}\,\frac{\frac{n_{H2Ss}}{n_{CuS}}\nu_0 exp\left(-\frac{e\varepsilon_{x-dis}}{k_B T_s}\right)}{\left(\frac{n_{H2Ss}}{n_{CuS}}\frac{\nu_0}{D_{Cus0}}exp\left[-\frac{e(\varepsilon_{x-dis}-\varepsilon_{cs})}{k_B T_s}\right]\right)^{1/2}}\times$$

$$\times\, n_{Cu0np}sin\left[\left(\frac{n_{H2Ss}}{n_{CuS}}\frac{\nu_0}{D_{Cus0}}exp\left[-\frac{e(\varepsilon_{x-dis}-\varepsilon_{cs})}{k_B T_s}\right]\right)^{1/2} L_{np}\right]. \quad \text{(S21)}$$

The rate of conversion of CuO aggregates by the top surface of the nanoplate is:

$$N_{Cut}(L_{np}) = n_{Cu}(L_{nw})\frac{n_{H2St}}{n_{CuS}}\nu_0 exp\left(-\frac{e\varepsilon_{x-dis}}{k_B T_s}\right)\pi a_n(L_{np})b_n(L_{np}) =$$

$$= \pi a_n(L_{np})b_n(L_{np})\frac{n_{H2St}}{n_{CuS}}\nu_0 exp\left(-\frac{e\varepsilon_{x-dis}}{k_B T_s}\right)n_{CuOnp}cos\left[\left(\frac{n_{H2Ss}}{n_{CuS}}\frac{\nu_0}{D_{Cus0}}exp\left[-\frac{e(\varepsilon_{x-dis}-\varepsilon_{cs})}{k_B T_s}\right]\right)^{1/2} L_{np}\right], \quad \text{(S22)}$$

where n_{H2St} is the concentration of hydrogen sulfide molecules adsorbed on the top surface of the nanoplate.

The total consumption of CuO aggregates by the nanoplate is

$$\varphi_{Cunp}(L_{np}) = \frac{1}{\pi a_n(0)b_n(0)}\left[N_{Cus}(L_{np}) + N_{Cut}(L_{np})\right]. \quad \text{(S23)}$$

By assuming that the cross-section of a nanoplate is weakly changing from the nanoplate bottom to the top, the expression is simplified:

$$\varphi_{Cunp}(L_{np}) = n_{CuOnp}\frac{n_{H2Ss}}{n_{CuS}}\nu_0 exp\left(-\frac{e\varepsilon_{x-dis}}{k_B T_s}\right)F(L_{np}), \quad \text{(S24)}$$

$$F(L_{np}) = \left[\begin{array}{c} \frac{\sqrt{2}\sqrt{a_n^2(0)+b_n^2(0)}}{a_n(0)b_{np}(0)} \left(\frac{n_{H2Ss}}{n_{CuS}} \frac{\nu_0}{D_{Cus0}} exp\left[-\frac{e(\varepsilon_{x-dis}-\varepsilon_{cs})}{k_B T_s} \right] \right)^{-1/2} sin\left[\left(\frac{n_{H2Ss}}{n_{CuS}} \frac{\nu_0}{D_{Cus0}} exp\left[-\frac{e(\varepsilon_{x-dis}-\varepsilon_{cs})}{k_B T_s} \right] \right)^{1/2} L_{np} \right] + \\ + \frac{n_{H2St}}{n_{H2Ss}} cos\left[\left(\frac{n_{H2Ss}}{n_{CuS}} \frac{\nu_0}{D_{Cus0}} exp\left[-\frac{e(\varepsilon_{x-dis}-\varepsilon_{cs})}{k_B T_s} \right] \right)^{1/2} L_{np} \right] \end{array} \right] \quad \text{(S25)}$$

After substitution the flux can be found:

$$\varphi_{Cunp}(L_{np}) = \frac{n_{H2Ss}\nu_0 exp\left(-\frac{e\varepsilon_{x-dis}}{k_B T_s}\right) F(L_{np})}{1+\frac{a_{CuS}\nu_0}{D_{0c1}} L_{CuS} \frac{n_{H2Ss}}{n_{CuS}} exp\left[-\frac{e(\varepsilon_{x-dis}-\varepsilon_c)}{k_B T_s}\right] F(L_{np})}. \quad \text{(S26)}$$

Thus, the density of the copper oxide aggregates at the nanoplate root can be found:

$$n_{CuOnp}(L_{CuS}) = n_{CuOnp} = \frac{n_{CuO}}{1+\frac{a_{CuS}\nu_0}{D_{0c2}} L_{CuS} \gamma_L F(L_{np})}, \quad \text{(S27)}$$

$$\gamma_L = \frac{n_{H2Ss}}{n_{CuS}} exp\left[-\frac{e(\varepsilon_{x-dis}-\varepsilon_c)}{k_B T_s}\right], \quad \text{(S28)}$$

The rate of the nanoplate's height L_{np} increasing is

$$\frac{dL_{np}}{dt}(L_{np}) = N_{Cut}(L_{np}) \frac{a_{CuS}^3}{\pi a_{np}(L_{np}) b_{np}(L_{np})} =$$

$$= n_{CuOnp}(L_{np}) \frac{n_{H2St}}{n_{CuS}} \nu_0 exp\left(-\frac{e\varepsilon_{x-dis}}{k_B T_s}\right) a_{CuS}^3 cos\left[\left(\frac{n_{H2Ss}}{n_{CuS}} \frac{\nu_0}{D_{Cus0}} exp\left[-\frac{e(\varepsilon_{x-dis}-\varepsilon_{cs})}{k_B T_s} \right] \right)^{1/2} L_{np} \right]. \quad \text{(S29)}$$

The rate of growth of the nanoplate's width $a_{np} = 2a_n$ and thickness $b_{np} = 2b_n$ are, respectively:

$$\frac{da_{np}}{dt}(z,t,L_{np}) = \frac{db_{np}}{dt}(z,t,L_{np}) = 2n_{Cu}(z) \frac{n_{H2Ss}}{n_{CuS}} \nu_0 exp\left(-\frac{e\varepsilon_{x-dis}}{k_B T_s}\right) a_{CuS}^3 =$$

$$= 2n_{CuOnp}(L_{nw}) \frac{n_{H2Ss}}{n_{CuS}} \nu_0 exp\left(-\frac{e\varepsilon_{x-dis}}{k_B T_s}\right) a_{CuS}^3 cos\left[\left(\frac{n_{H2Ss}}{n_{CuS}} \frac{\nu_0}{D_{Cus0}} exp\left[-\frac{e(\varepsilon_{x-dis}-\varepsilon_{cs})}{k_B T_s} \right] \right)^{1/2} z \right]. \quad \text{(S30)}$$

The model was applied to clarify the processes that guide the transformation of a 1D CuO NW into a 2D CuS nanoplate. The dependence of the sample temperature was described by the expression: $T_s(t) = (T_{max} - T_0)(1 - exp[-t/\tau]) + 293$ (K), where T_{max} = 100 °C; T_0 = 20 °C, τ = 450 s.

The following dependencies of energies on temperature were used to fit the results of the experiments: energy: $\varepsilon_{aH2S}(T_s) - \varepsilon_{i-H2S}(T_s) = 0.154\left(\frac{T_{s0}}{T_s}\right)^{\upsilon}$ for the difference between the adsorption and internal energies of the H_2S molecule on the CuS layer; $\varepsilon_{c1}(T_s) = 0.51\left(\frac{T_{s0}}{T_s}\right)^{\upsilon}$ for the diffusion of the CuO aggregate through the CuS layer; $\varepsilon_{x-dis}(T_s) = 0.273\left(\frac{T_{s0}}{T_s}\right)^{\upsilon}$ for the transformation of the CuO aggregate into the CuS aggregate, $\varepsilon_{aH2Ss}(T_s) = 0.009\left(\frac{T_{s0}}{T_s}\right)^{\upsilon}$ for the energy of adsorption of the H_2S molecule on the CuS nanoplate side surface; $\varepsilon_{aH2St}(T_s) = 0.098\left(\frac{T_{s0}}{T_s}\right)^{\upsilon}$ for the energy of adsorption of the H_2S molecule on the CuS nanoplate's top surface; $\varepsilon_{i-H2S}(T_s) = 0.59\left(\frac{T_{s0}}{T_s}\right)^{\upsilon}$ for the internal energy of the H_2S molecule; where υ = 1.85 and T_{s0} = 297 K.

The result of the calculation shows that crack formation can change the conditions of growth of the main component, since the rate of transformation of the CuO layer into the CuS layer becomes much slower (Figure 3i). At the same time, the void formation is intensified as the nanoplate increases its size, since the surfaces of the nanoplate adsorb a larger number of H_2S molecules. Thus, the 2D nanostructure acts like a pump for the underneath layer of CuO oxide, and the more the surface of the nanostructure is developed, the more powerful is the flux of the pumped-out CuO aggregates (Figure 3j). It should be noted that the anisotropy of the growth of the 2D nanoplate originates from the shape of the flake of the external layer of the 1D nanostructure, which acts as pattern for the deposition by providing the area with different

energies of adsorption. At that point, the top surface of the nanoplate preserves the defectiveness of the crack, from which the whole nanoplate was created, while the side surfaces have fewer defects (Figure 3k).

The simulation of a nanoplate shape (figure S15a-d) confirm the necessity of feeding the nanoplates from the neighboring regions of the NW, which are not located directly under the nucleus; the length of these regions limits the nanoplate growth – the denser are the concentrations of the nanoplate nuclei along the surface of the NW, the less the nanoplates will grow. According to the model assumption, the number of nuclei depends on the crack generation, which, in turn, is controlled by the rate of growth of the layer on the surface of a 1D NW, and the fastest growth is provided by plasma.

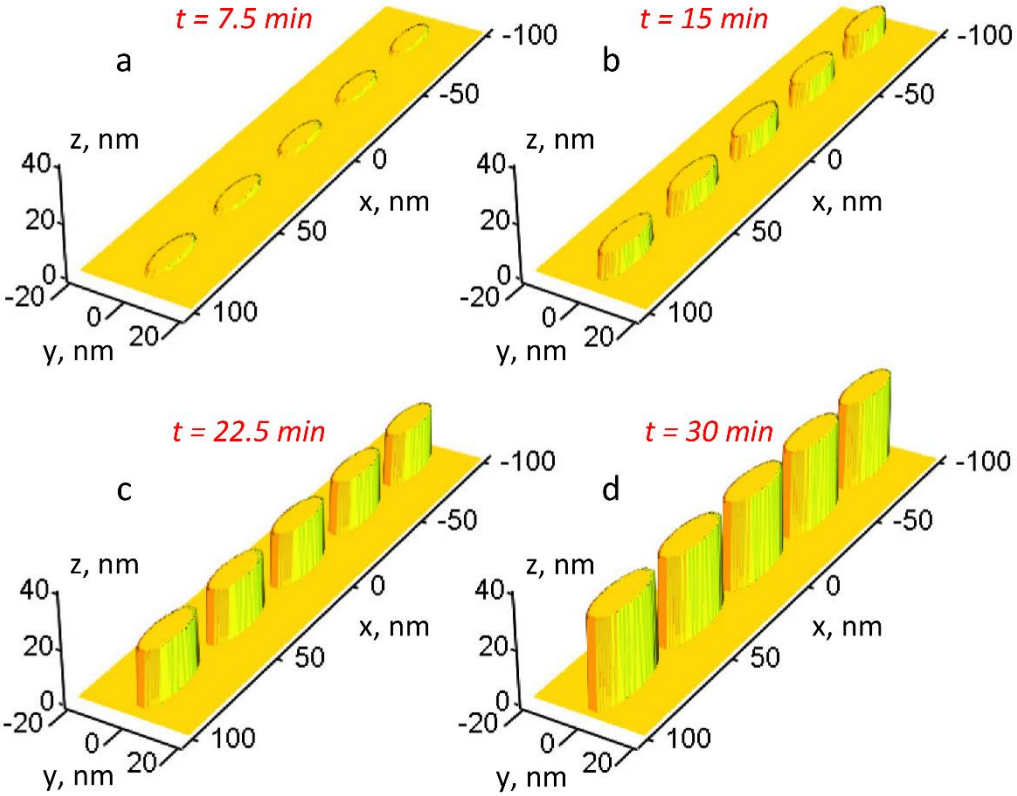

Figure S15. Results of simulation of a shape of CuS nanoplates grown on the surface of a fragment of CuO NW during the NW plasma sulfurization for different times: **a** – 7.5 min; **b** – 15 min; **c** – 22.5 min; **d** – 30 min. The NW is directed towards the x-axis.

References

(1) Košiček, M.; Zavašnik, J.; Baranov, O.; Šetina Batič, B.; Cvelbar, U. Understanding the Growth of Copper Oxide Nanowires and Layers by Thermal Oxidation over a Broad Temperature Range at Atmospheric Pressure. *Cryst. Growth Des.* **2022**, *22* (11), 6656–6666. https://doi.org/10.1021/ACS.CGD.2C00863.

(2) Košiček, M.; Baranov, O.; Zavašnik, J.; Cvelbar, U. In Search of the Limits of CuO Thermal Oxidation Nanowire Growth by Combining Experiment and Theory. *Appl. Phys. Lett.* **2023**, *123* (4), 41601. https://doi.org/10.1063/5.0151293/2904213.

(3) Basuvalingam, S. B.; Zhang, Y.; Bloodgood, M. A.; Godiksen, R. H.; Curto, A. G.; Hofmann, J. P.; Verheijen, M. A.; Kessels, W. M. M.; Bol, A. A. Low-Temperature Phase-Controlled Synthesis of Titanium Di- And Tri-Sulfide by Atomic Layer Deposition. *Chem. Mater.* **2019**, *31* (22), 9354–9362. https://doi.org/10.1021/ACS.CHEMMATER.9B02895.

Chapter 4

Beyond the Growth and Phase Transformation of CuO Nanowires

In Chapter 4, the growth of CuO NWs is further expanded by developing strategies to enhance the NW growth. Furthermore, copper oxidation was studied for the practical example of electronic components. This involved two studies. First, the strategy to enhance the NW growth by delaying the growth saturation is presented. The second study looked at copper oxidation in a 3D integrated circuit using broadband dielectric spectroscopy (BDS).

4.1 Development of the Strategy to Overcome the Saturation Point in the CuO NW Growth

In Subsection 4.1, the topic of CuO NW growth by copper oxidation is revisited with a search for a strategy that will reach beyond the growth saturation point. The saturation during NW growth occurs when the NW length increases to a point where efficient copper delivery to the NW top becomes insufficient. This phenomenon is particularly emphasized when copper delivery occurs on the NW surface, where it can potentially be involved in the reaction with oxygen before reaching the top of the NW. The proposed strategy to avoid these limitations involves multiple stages. In the first stage, the conventional growth of CuO NWs via copper oxidation is carried out. This is then followed by the deposition of metallic gold NPs on the NW sides. In this way, oxygen adsorption on the NW sides is prevented, and copper diffusion towards the NW top is not disrupted. After the gold deposition, the oxidation procedure is repeated to further elongate the NW beyond the length that would result in growth saturation in the absence of gold.

This section addresses Objective 1. The results of this subsection were published in a peer-reviewed scientific article in the journal *Advanced Theory and Simulations*.

Regarding my contribution, I contributed to the analysis of the results and jointly wrote the paper with the other co-authors.

RESEARCH ARTICLE

ADVANCED THEORY AND SIMULATIONS
www.advtheorysimul.com

Hierarchical Nanomaterials by Selective Deposition of Noble Metal Nanoparticles: Insight into Control and Growth Processes

Oleg Baranov, Thierry Belmonte, Igor Levchenko, Kateryna Bazaka, Martin Košiček, and Uroš Cvelbar**

Complex hierarchical metamaterials are currently the focus of many cutting-edge studies due to their potential to advance such critically important areas of technology as energy storage and transformation, sensing, photovoltaics, nano-medicine, antibacterial and self-regenerating materials. However, the deterministic design of novel hierarchical metamaterials remains problematic due to the lack of efficient, highly reliable methods for controlling the internal structure and architecture of materials. A comprehensive advanced model is proposed to simulate the formation of complex hierarchical metamaterials with a controllable structure. The control is achieved via selective deposition of noble metal nanoparticles (Au, Au, Pd, Pt). Moreover, the novel method for the nanofabrication is theoretically examined and experimentally verified. This approach allows for the sophisticated spatiotemporal control of growth conditions and, as a result, achieving the targeted internal structure of metamaterials. This opens a way to the deterministic design and formation of complex multi-material metamaterials on the basis of metal oxides and noble metal nanoparticles. Moreover, a fundamental insight related to the longstanding question about the prevalence of bottom-up versus top-down growth for various materials and systemswhich is challenging to directly verify experimentally is presented.

1. Introduction

Complex hierarchical nanomaterials and metamaterials are currently in the focus of research efforts worldwide.[1–3] Multicomponent architectures at nanoscale feature many unique properties and functions, which enable various applications including biological,[4] gas and mechanical sensors,[5,6] devices for energy collection and storage,[7–9] nanoscale therapeutic systems,[10,11] platforms for light-driven[12] and chemical catalytic reactions,[13,14] biotechnological applications,[15,16] hydrogen fuel production,[17] wastewater decontamination,[18] and technologies for space exploration and space economy.[19–22] However, the use of the trial and error approach which is often applied for designing the hierarchical metamaterials is limited by its high cost. Besides, it is slow and does not guarantee the desired results. Here we propose, theoretically examine via advanced simulations, and then experimentally verify a new approach for the deterministic assembly of complex nanomaterials. In this approach, selective deposition of metal nanoparticles is used to sophisticatedly control the formation of the desired internal structure.

As a model system we have selected the hierarchical metamaterial primarily consisting of long metal oxide (CuO) nanowires loaded with noble metal (gold) nanoparticles. Such systems are promising due to their outstanding morphology-conditioned properties.[23] Among other metal oxide nanowires, arrays of

O. Baranov
Department of Theoretical Mechanics
Engineering and Robomechanical Systems
National Aerospace University
Kharkiv 61070, Ukraine
E-mail: oleg.baranov@post.com

O. Baranov, M. Košiček, U. Cvelbar
Department of Gaseous Electronics
Jozef Stefan Institute
Ljubljana 1000, Slovenia
E-mail: uros.cvelbar@ijs.si

The ORCID identification number(s) for the author(s) of this article can be found under https://doi.org/10.1002/adts.202300288

DOI: 10.1002/adts.202300288

T. Belmonte
IJL
Université de Lorraine, CNRS
Nancy F-54000, France

I. Levchenko, K. Bazaka
School of Engineering, College of Engineering, Computing and Cybernetics
The Australian National University
Canberra ACT 2600, Australia

I. Levchenko
Plasma Sources and Application Center
NIE
Nanyang Technological University
Singapore 639798, Singapore

M. Košiček, U. Cvelbar
Jožef Stefan International Postgraduate School
Ljubljana Slovenia

ADVANCED SCIENCE NEWS
www.advancedsciencenews.com

ADVANCED THEORY AND SIMULATIONS
www.advtheorysimul.com

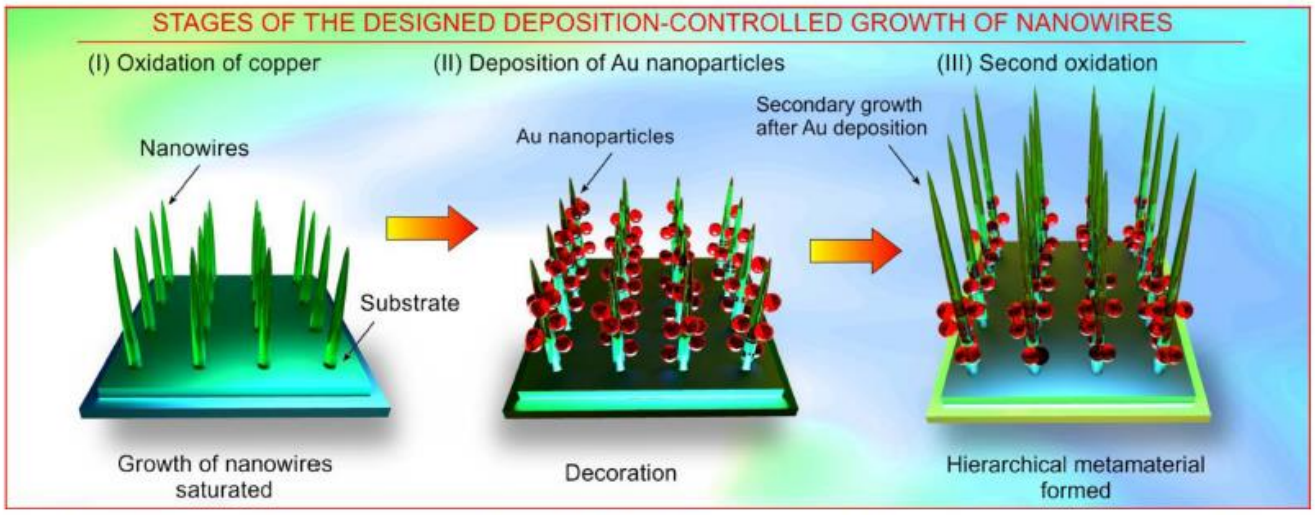

Figure 1. General scheme of the proposed process and simplified scheme of the processes during the decoration-controlled nanowire growth. Stages of the designed deposition-controlled growth of nanowires: I) afterglow oxidation of copper; II) deposition of Au nanoparticles; III) second oxidation.

copper oxide nanowires exhibit excellent properties required for advanced batteries,[24] field emission devices,[25] and supercapacitor applications.[26,27] However, copper oxide-based metamaterials suffer from such shortcomings as, for example, high rates of agglomeration, low conductivity, and insufficial electrochemical stability. These could be overcome by synergistically combining CuO with, for example, conducting polymers, carbon nanotubes or graphene-based materials[28,29] using in situ modification of copper foam,[30] room temperature chemical synthesis,[31] high temperature annealing,[32] thermal oxidation of pre-synthesized copper nanowires,[33] facile solution-phase technique,[34] anodization in sodium bicarbonate solution,[35] thermal oxidation of copper foil in oxygen[36] and many other methods.[37]

Such a plethora of available technologies naturally gave rise to many studies aimed to reveal the parameters that control the growth, with the central question: Is it possible to efficiently control the architecture, structure, and morphology of the growing material through the simple adjustment of the synthesis conditions? Experiments that varied temperature,[38] heating rate,[39] oxygen flow,[40] humidity and external electric field,[41] initial roughness of copper substrates[42] and others have demonstrated these parameters cannot definitively control the growth. Besides, nearly all of the above-mentioned parameters are interdependent and not always could be directly controlled—for example, substrate roughness affects surface growth via diffusion, yet itself can change during the process due to sputtering; strong electric fields could be generated at long nanowires due to charging,[43] and so on. Based on this, we can state:

It is unlikely that complex hierarchical metamaterials could be deterministically assembled using a relatively simple control sequence of direct controls such as temperature, time, gas pressure, and similar.

This means that some specialized control tools are needed for the selective, deterministic control of the architecture, structure, and morphology of the growing hierarchical metamaterial. In this article we demonstrate that i) the method of selective deposition of nanoparticles is effective in controlling the morphology of the growing copper oxide nanoarrays, and ii) this method is deterministic, that is, the targeted structure can be predicted, modeled, and then synthesized. For this, we first modeled the whole growth under the selective deposition control that aimed to significantly enlarge the nanowires by re-distribution of diffusional fluxes using deposited nanoparticles, and then performed the direct experiment which demonstrated the formation of targeted structures. Similar methods could be designed for material architectures that target specific applications, thus avoiding the trialanderror method.

The discussed technological process includes three separate stages (**Figure 1**). i) At the first stage, an array of copper oxide nanowires on the substrate was formed by use of a microwave atmospheric plasma discharge (until the nanowires could not grow anymore). ii) Then, the deposition of gold nanoparticles on the array to cover the side surfaces of the nanowires by the noble metal was made. iii) Finally, re-exposure of the modified array in the microwave plasma was used to increase the length of the nanowires. This process was examined by simulation and then by real physical synthesis. In this process, plasma is necessary to significantly accelerate the growth process, while the stage of the intermediate deposition of gold allows overcoming the limit of the maximal length of the nanowires conditioned by the limited diffusion path of copper from the nanowire root to the tip. Hence, the combination of the plasma-enhanced growth and the deposition of noble metals is utilized as a promising tool to synthesize the metal oxide nanowires in a productive and cost-effective way.

2. General Description of the Model

The fast saturation of the dependence of nanowire length on time was experimentally observed in the process that utilizes low-pressure plasma.[44] In contrast, atmospheric plasma used

ADVANCED SCIENCE NEWS
www.advancedsciencenews.com

ADVANCED THEORY AND SIMULATIONS
www.advtheorysimul.com

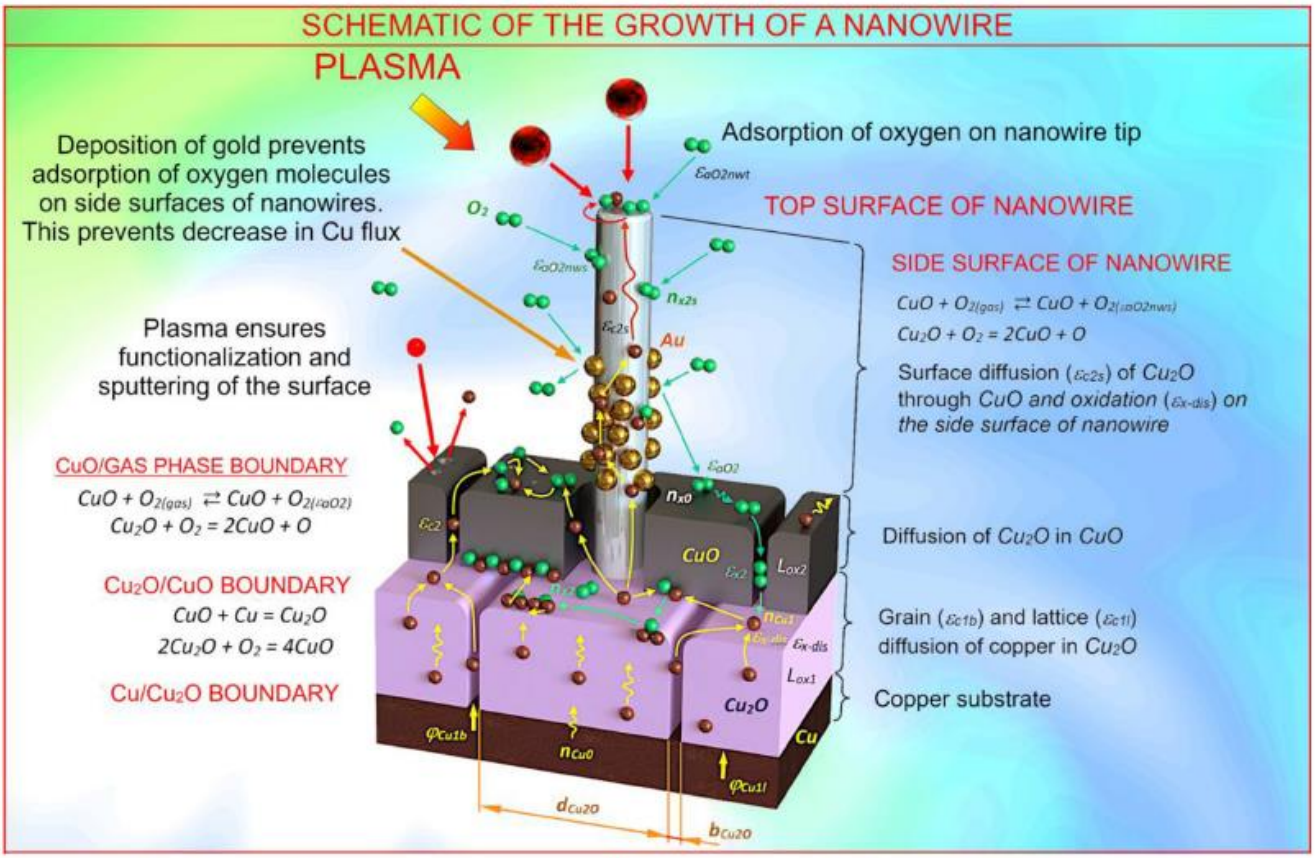

Figure 2. Schematic of the growth of nanowire partially decorated with noble metal nanoparticles. The oxide layer usually consists of two sub-layers, namely copper (II) oxide (or cupric oxide CuO), and copper (I) oxide (or cuprous oxide Cu_2O). Both oxides are formed because of the diffusion of the species, which can be lattice, boundary, or surface diffusion. In this case, the copper atoms moving from the copper layer are involved into the oxidation process on a side surface of the growing nanowire. A large number of elementary processes is involved in the growth, and all of them should be properly addressed in the advanced model (see details in the Supporting Information).

in this work is not associated with the ballistic effects caused by the ion bombardment, which results in less damaged surfaces of the growing nanowires. Moreover, a large number of radicals ensures the high chemical activity of oxygen plasma at atmospheric pressure, as well as its ability to conduct the fast oxidation of copper substrates. The substrates exhibit the formation of a layered structure of Cu_2O and CuO oxides, which are also denoted as copper (I) (or cuprous), and copper (II) (or cupric) oxides, respectively. Formation of the layers is conditioned by the interaction of oxygen molecules adsorbed on the substrate surface from the gas phase, and copper atoms diffusing toward the surface from the bulk copper. It is believed that nucleation of nanowires occurs in CuO layer, which is evidenced by a typical morphology of the nanowires protruding from this layer. Further growth of these one–dimensional (1D) nanostructures is described by the processes of the delivery of copper atoms through the oxide layers, and diffusion of these atoms along the nanowire surface. Since oxygen is adsorbed by the side surface of the nanowires, the flux of copper atoms is decreased with the distance from the nanowire root due to the reaction of oxidation. After some time, the nanowire ceases to grow, because all copper atoms are consumed on their diffusion path to the tip. However, deposition of noble metals, like gold, protects the side surfaces from the oxygen adsorption, thus forming a shield for the copper atoms, and allowing the nanowire growth to be resumed (**Figure 2**).

To provide a theoretical description with a purpose of establishing the possible control means when applying the stage of noble metal deposition in the process of copper oxide nanowire growth, a multifactor model was developed. The central point of the proposed strategy of intermediate deposition is to combat a growth saturation, when the nanowires stop growing at some point. Instead, after the intermediate deposition, continued growth was expected and then confirmed by simulations and direct experiment. Figure 1 illustrates the proposed strategy (left panel) and the simplified set of the physical and chemical processes taken into account (see the full schematics of the processes in Figure 2). The oxide layer usually consists of two sub-layers, namely copper (II) oxide (or cupric oxide CuO), and copper (I) oxide (or cuprous oxide Cu_2O).[44,45] Both oxides are formed via lattice, boundary, and surface diffusion. The copper atoms moving from the copper layer are oxidated at the side surface of the growing nanowire, so the copper flow from the nanowire (NW) base to the NW top decreases, and the longer the NW, the lower the flow of copper atoms.[46] At some stage, the growth is terminated because all

ADVANCED SCIENCE NEWS
www.advancedsciencenews.com

ADVANCED THEORY AND SIMULATIONS
www.advtheorysimul.com

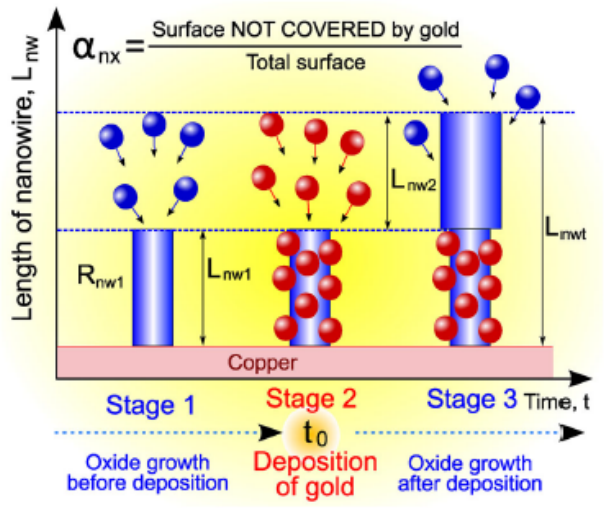

Figure 3. Scheme of controlling the nanowire array morphology by the intermediate deposition of gold. Here, t_0 is a time when gold nanoparticles are deposited on nanowire, L_{nw2} is a gold-free length of a part of the nanowire grown after gold deposition on the part L_{nw1}, L_{nwt} is a total length of the nanowire after the treatment. Intermediate deposition of noble metals (e.g., gold in the case of study) allows efficient control over the morphology of a complex nanomaterial directly during the formation process.

diffusing copper is oxidized on the NW sides. The intermediate deposition of noble metal allows to resume the growth since the noble metals do not interact with the oxygen and prevents O_2 adsorption, and the surface is relatively free from the adsorbed oxygen (**Figure 3**). The copper atoms now can reach the top, copper is delivered to the NW top where it is involved into the reaction with the oxygen adsorbed on the NW top, and the NW continues to grow.

This mechanism was proposed, simulated with a multifactor model (see the detailed description of the model in the Supporting Information), and experimentally verified. In the model, the following scenario was used: first (see the detailed description of the model in the Supporting Information), oxygen molecules are adsorbed on the surface of the sample and react with copper atoms which diffuse through a layer of copper oxide to the surface exposed to the oxygen. Oxygen molecules are dissociated with the actions, but the key factor of the actual oxide layer growth is the diffusion of copper atoms from the top of the Cu_2O oxide surface to the top surface of CuO oxide, where the generation of a new CuO oxide layer occurs (Figure 2).[47,48] This key process was modeled in three stages: i) dissociation of the cuprous oxide, ii) jump of the released copper atom into the neighboring node occupied by the cupric oxide, and iii) the generation of the cuprous oxide in the new location of the copper atom (see details in the Supporting Information).

One principal problem in modeling such systems is the difference in the characteristic energies of the adsorbed particles on various surfaces on NW, thus all processes were modeled separately. For example, three different expressions for the Langmuir adsorption isotherm were used via three different Langmuir constants P_i:

$$P_{0i}\,|_{i=1,2,3} = \left(\frac{M_{O2}}{2\pi h^2}\right)^{3/2} (k_B T_s)^{5/2} \exp\left[-\frac{e(\varepsilon_{ai}-\varepsilon_i)}{k_B T_s}\right] \quad (1)$$

where M_{O2} is the mass of O_2 molecule, ϵ_{ai} are the adsorption energies of O_2 molecule on CuO surface ($i = 1$), side surface of CuO nanowire ($i = 2$), and tip of CuO nanowire ($i = 3$), respectively; ϵ_i is the internal energy of O_2 molecule; h is the Planck's constant (kg × m^2 s^{-1}); e is the elementary electric charge (C); k_B is the Boltzmann constant (kg × m^2 s^{-2} K^{-1}); and pressure P_{0i} has the standard dimension $N \times m^{-2}$ (kg × m^{-1} s^{-2}).[49] The diffusion of copper atoms through the Cu_2O layer occurs in two different ways: either through the boundaries between the oxide grains or directly through the body of the grains. On the other hand, when considering a diffusion of molecular oxygen adsorbed on the upper surface of CuO oxide to the boundary between CuO and Cu_2O, only the mechanism of the diffusion along the boundaries of CuO grains (short-circuit diffusion) was considered. The stage of the intermediate deposition results in changing the number of adsorption nodes (Figure 2), which could be occupied by oxygen molecules, because the deposited atoms of noble metal occupy a part of them.

The key factors of growth were calculated as follows (see the full model in the Supporting Information provided). In particular, the key growth parameters such as the rate of increase of the nanowire length dL_{nw}/dt and radius dR_{nw}/dt are described by the expressions:

$$\frac{dL_{nw}}{dt}(L_{nw}) = n_{Cu2Onw}(L_{nw}) \cos\left[\left(\frac{n_{x2s}}{n_0}\frac{\nu_0}{D_{Cus0}} exp\left[-\frac{e(\varepsilon_{x-dis}-\varepsilon_{c2s})}{k_B T_s}\right]\right)^{1/2} L_{nw}\right] \frac{n_{x2t}}{n_0}\nu_0 \exp\left(-\frac{e\varepsilon_{x-dis}}{k_B T_s}\right) a_0^3 \quad (2)$$

$$\frac{dR_{nw}}{dt}(z,t,L_{nw}) = n_{Cu2Onw}(L_{nw}) \frac{n_{x2s}}{n_0}\nu_0 \exp\left(-\frac{e\varepsilon_{x-dis}}{k_B T_s}\right) a_0^3 \cos\left[\left(\frac{n_{x2s}}{n_0}\frac{\nu_0}{D_{Cus0}} \exp\left[-\frac{e(\varepsilon_{x-dis}-\varepsilon_{c2s})}{k_B T_s}\right]\right)^{1/2} z\right] \quad (3)$$

two main reactions: $Cu_2O + O \rightarrow 2CuO$ and $CuO + Cu \rightarrow Cu_2O$. Importantly, the oxide boundary can be shifted because of the re- which show strong dependence on the density of oxygen molecules adsorbed on side surface of the nanowire n_{x2s} and on

ADVANCED SCIENCE NEWS
www.advancedsciencenews.com

ADVANCED THEORY AND SIMULATIONS
www.advtheorysimul.com

the nanowire tip n_{x2t}, as well as on the current nanowire length L_{nw}. In turn, both of the parameters are exponentially dependent on the energies of adsorption ϵ_{aO2s} and ϵ_{aO2t} on the corresponding area:

$$\frac{n_{x2s}(t)}{n_0} = \alpha_{nx} \frac{P_{O2}}{\left(\frac{M_{O2}}{2\pi\hbar^2}\right)^{3/2}(k_B T_s)^{5/2}\exp\left[-\frac{e(\epsilon_{aO2s}-\epsilon_{i-O2})}{k_B T_s}\right] + P_{O2}} \quad (4)$$

$$\frac{n_{x2t}(t)}{n_0} = \alpha_{nxt} \frac{P_{O2}}{\left(\frac{M_{O2}}{2\pi\hbar^2}\right)^{3/2}(k_B T_s)^{5/2}\exp\left[-\frac{e(\epsilon_{aO2t}-\epsilon_{i-O2})}{k_B T_s}\right] + P_{O2}} \quad (5)$$

parts of the side surface and tip area, which are non-covered by the noble metal. The above expressions state that the concentration of the adsorbed oxygen is linearly dependent on these factors.

Much more complicated is the dependence of the concentration of copper atoms at the roots of the nanowires n_{Cu20nw} on the factors of growth including the current parameters of the system:

$$n_{Cu20nw}(L_{ox2}) = \frac{n_0}{1 + 2\frac{a_0\nu_0}{2D_{0c2}}L_{ox2}\frac{n_{x2s}(t)}{n_{0s}}\exp[-\varphi_{c2}]\left[\frac{2(\alpha_{c2s}\exp[-\varphi_{c2s}])^{-1/2}}{R_{nw}(0)}\sin\left[(\alpha_{c2s}\exp[-\varphi_{c2s}])^{1/2}L_{nw}\right] + \frac{n_{x2t}}{n_{x2s}}\cos\left[(\alpha_{c2s}\exp[-\varphi_{c2s}])^{1/2}L_{nw}\right]\right]} \quad (6)$$

This fact explains the characteristic morphology of 1D objects that grow like nanowires. The difference of the adsorption energies, when $\epsilon_{aO2s} < \epsilon_{aO2t}$, results in much lower concentration of oxygen molecules on the side surface. It allows the atoms of copper to migrate from the nanowire root toward its tip without being involved into the reaction of oxidation on the side surface, which is accompanied by thickening of the nanowire, and to be oxidized only on the tip, where the concentration of the adsorbed oxygen is large enough. Moreover, the shape of the nanowires is affected greatly by the internal energy of oxygen molecule ϵ_{i-O2}, which can reverse the sign of the exponent at $\epsilon_{aO2s} < \epsilon_{i-O2}$, thus changing the growth conditions. The mechanism of this effect can be described by analogy of interaction of over-pressurized balloon that interacts with a surface and bursts thus releasing the internal energy stored in the balloon and transferring it to the translational energy of the motion of the balloon remnants relative to the surface. Thus, the adsorption energy of oxygen molecule is decreased when the crystalline structure of the side surface of nanowire is close to the ideal structure. Besides, the transition of energy to the internal states of the molecules additionally decreases the probability of the molecule attachment to the surface. In contrast, the defected surface of the nanowire tips is beneficial for the oxygen adsorption, oxidation of copper, and non-anisotropic growth of the nanowires. In particular, the dependence of the growth process on the adsorption energy explains why the thermally-grown nanowires possess higher aspect ratio than those obtained in plasma-driven processes, where the nanowire surface is intensively bombarded by the plasma ions, which results in generation of defects, increase of the oxygen adsorption energy, and decrease of the aspect ratio. Moreover, as it follows from the above equations, high excitation of oxygen molecules caused by the plasma environment, can suppress the nanowire growth at all. However, there is a way to overcome the limitations caused by the oxygen adsorption by covering the side surface of the nanowires with nanoparticles of noble metals, which is described by factors α_{nx} and α_{nxt} that equal to the

where $\varphi_{c2} = \frac{e(\epsilon_{x-dis}-\epsilon_{c2})}{k_B T_s}$, $\varphi_{c2s} = -\frac{e(\epsilon_{x-dis}-\epsilon_{c2s})}{k_B T_s}$, $\alpha_{c2s} = \frac{n_{x2s}}{n_0}\frac{\nu_0}{D_{Cus0}}$, L_{ox2} is the current thickness of CuO oxide layer. The concentration depends on the energy $\epsilon_{x\text{-dis}}$ of oxygen molecule dissociation in the presence of Cu_2O composite, energy ϵ_{c2} of Cu diffusion in CuO layer, and energy ϵ_{c2s} of Cu diffusion along the side surface of CuO nanowire toward its tip.

The complete model comprising 50 equations was then solved numerically according to the following algorithm that enabled calculation of all essential energies, states, and growth parameters (**Figure 4**). First, the initial conditions have been assigned as a typical value set for the similar experiments. Next, all essential mechanical and chemical processes were simulated. The results were presented as the growth rates described in detail in the next section.

3. Results and Discussions

A final system of the equations describing the growth was assembled (see Supporting Information, Equations S1–S50, Supporting Information) and then used for the modeling at the conditions used in the experiment. These data allowed calculating the thicknesses of both oxides, length $L_{nw}(t)$, and diameter $2R_{nw}(t)$ of nanowires on time t. **Figure 5** shows the calculated dependences of the length and diameter on growth time, moment of deposition of noble metal (gold), diffusion energy of copper along the nanowire surface ϵ_{c2s}, and fraction α_{nx} of the side surface of nanowires not covered with the noble metal. Figure 5 also shows markers that correspond to the experiments by Altaweel et al.[50] used as benchmarks to realistically calibrate the growth rates. At later stages the growth saturates.[51] Apparently, intermediate deposition onto the saturated nanowires allows obtaining the maximum length after secondary oxidation.

The model predicts that the maximum length is significantly affected by the energy ϵ_{c2s} of copper diffusion on nanowire, so we used two values of this parameter for the calculations. Impor-

ADVANCED SCIENCE NEWS
www.advancedsciencenews.com

ADVANCED THEORY AND SIMULATIONS
www.advtheorysimul.com

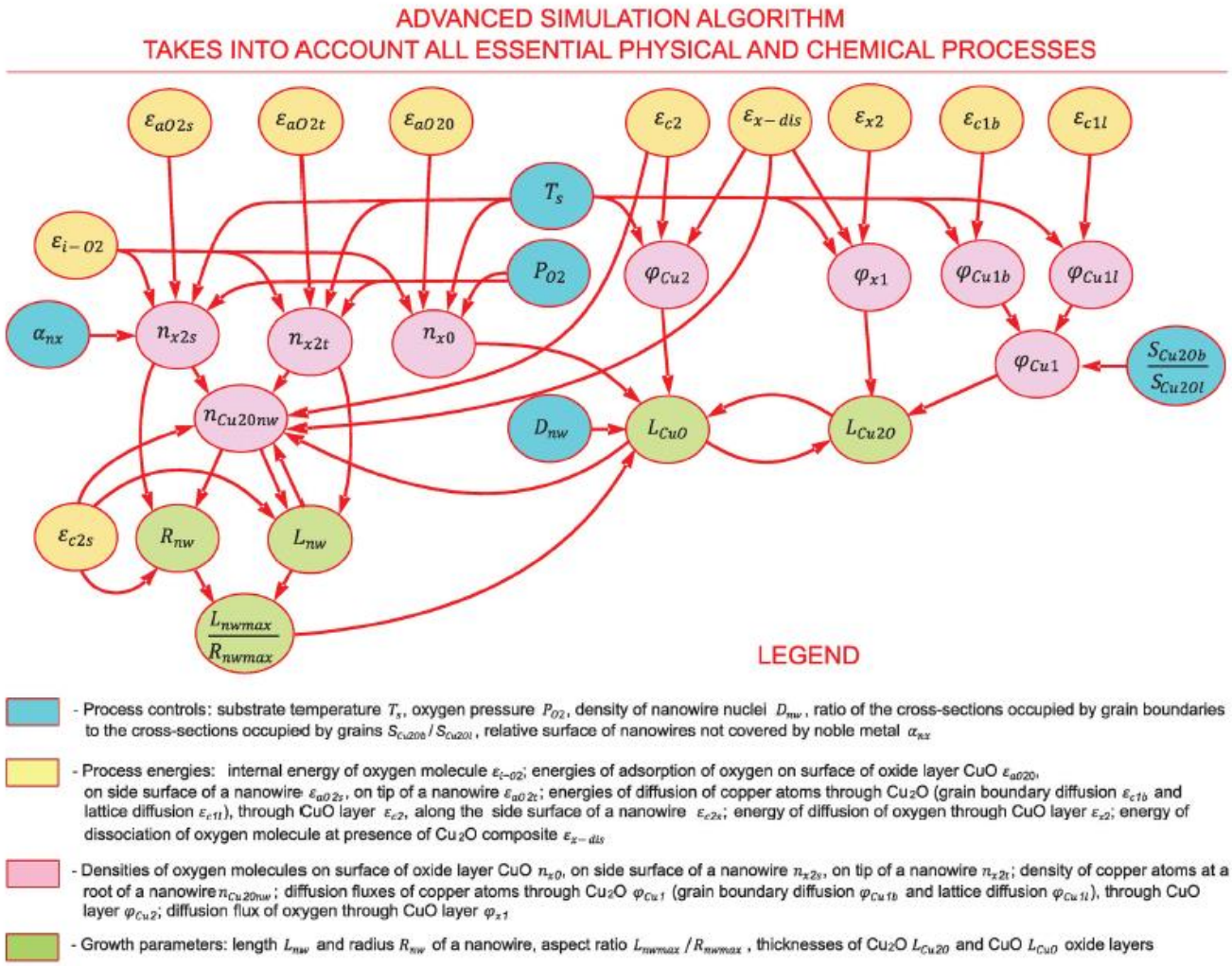

Figure 4. General scheme of the simulation for modeling the noble metal decoration-mediated growth of nanowires. Starting from setting the initial parameters typical for the experiments, the simulation route followed all essential chemical and physical processes to simulate the growth in detail (see the abbreviations for energies and other parameters in the Supporting Information provided).

tantly, the values of energies can be changed by varying concentrations of defects on the surface via ion bombardment. The lower value of the diffusion energy leads to the formation of longer nanowires—about 6.5 μm (Figure 5b), instead of 2.8 μm for an energy of 0.56 eV (Figure 5a). The dotted lines predict the growth process after gold deposition at a certain time t_i (after 4, 8, or 12 h of nanowire growth). Figure 5d,e shows the results for different values of ratio α_{nx}. When reducing $\alpha_{nxs} = 1.0$ (absence of gold on the side surface of the nanowire) to $\alpha_{nxs} = 0.15$ (gold covers 85% of the side surface), almost twofold increase in the length of the nanowire is predicted, that is, the formation of long and thin nanowires is available. Importantly, the diffusion activation energy ϵ_{c2s} does not affect the diameter of the nanowire, while the ratio α_{nx} allows adjusting the nanowire diameter.

Thus, under the condition of ion bombardment ($\epsilon_{c2s} = 0.56$ eV) and significant coverage of the side surface with noble metal ($\alpha_{nx} = 0.15$), the nanowires with a length of 9 μm and a diameter of 0.1 μm (aspect ratio 90) were produced instead of the nanowires with 3 and 0.13 μm, respectively (aspect ratio 23). When the intensity of ion bombardment is decreased ($\epsilon_{c2s} = 0.46$ eV), even longer (12 μm at the maximum) nanowires with almost constant diameter along the length can be achieved. The results of three–dimensional modeling are shown in Figure S1, Supporting Information, which clearly indicates the effectiveness of the proposed approach.

Importantly, the state of the oxygen adsorbed on the nanowire surface should not be neglected, according to the simulation. The concentration of oxygen on the surface should be controlled independently by choosing the appropriate growth conditions, when the crystalline structure is not damaged by the treating fluxes, to avoid formation of large number of surface defects followed by the increase of the activation energy ϵ_{c2s}. It can be achieved by use of atmospheric plasma post glow, when the surface is treated by oxygen radicals and exited states, but not the oxygen ions as in the case of implementation of low-pressure plasma discharges. The "mild" atmospheric plasma conditions are associated with lower

ADVANCED SCIENCE NEWS
www.advancedsciencenews.com

ADVANCED THEORY AND SIMULATIONS
www.advtheorysimul.com

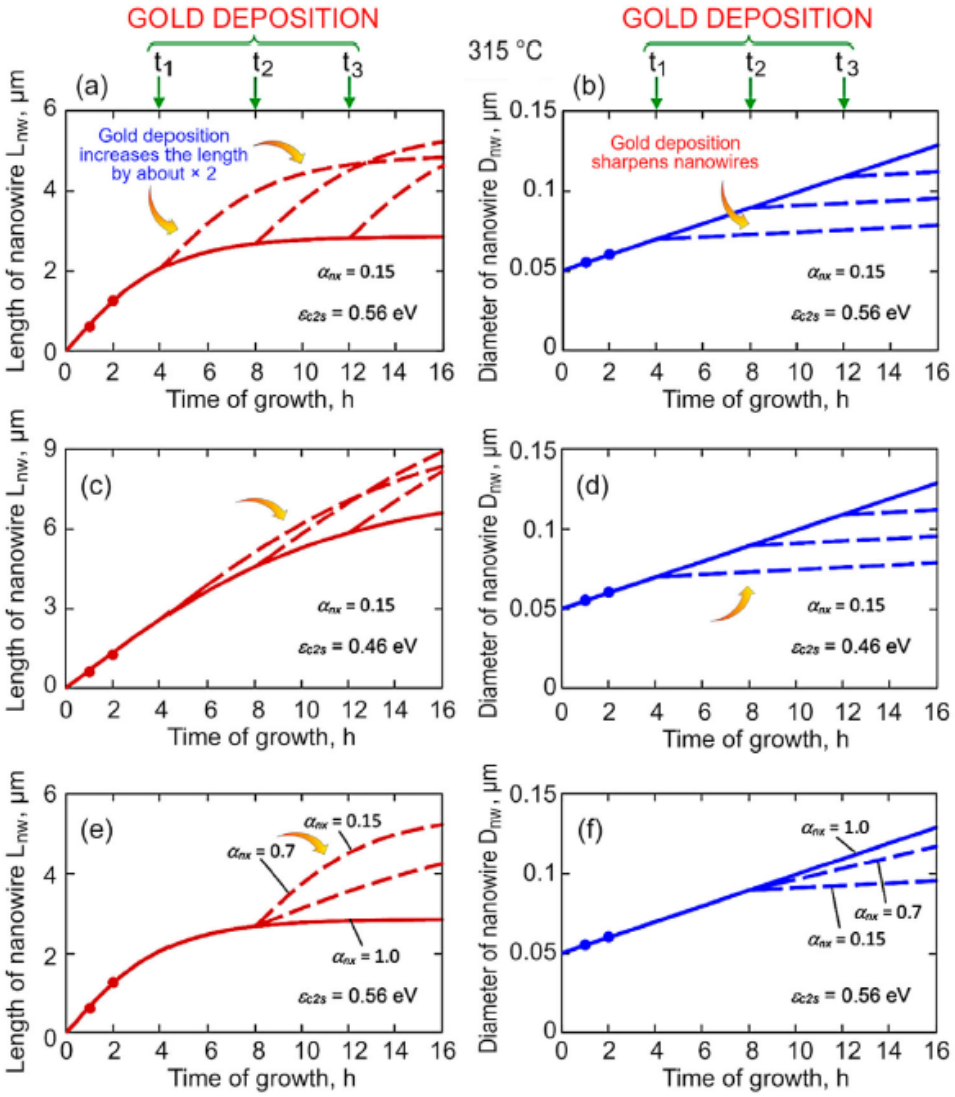

Figure 5. Results of simulations. The calculated dependences of a,c,e) length $L_{nw}(t)$ and b,d,e) diameter $D_{nw}(t)$ of nanowires on growth time t, moment of gold nanoparticle deposition t_i, activation energy ϵ_{c2s} of copper diffusion along the nanowire, and ratio α_{nxs} of the side surface not covered with gold. Solid lines describe the growth without intermediate deposition, while the golden arrows and dashed lines highlight the growth for the trends obtained for the gold-mediated growth process. Specifically, the dashed lines in (a–d) denote the growth for various moments of gold nanoparticle deposition t_i, while the dashed lines in (e,f) show the growth for different coverages (α_{nx}) of the side surface of nanowires with gold. Dots mark the experimental results.[50] a,b) Combination of the correct time moment, when the dependence of the length on time reaches the saturation, that is, a nanowire cannot grow anymore, and a sufficient dose of deposition [e,f) when the nanoparticles of noble metal protect the already-grown surface from further oxidation], allows obtaining the best results, when twofold increase of the nanowire length is achieved. The procedure of the gold deposition can be repeated again for the part of the nanowire grown after the previous stage of the gold deposition to lengthen the nanowire further.

energy ϵ_{c2s} and, correspondingly, longer and thinner nanowires (c,d) as compared to the case of low-pressure RF plasma, where the energy ϵ_{c2s} is increased due to the ion bombardment (a,b), and the nanowires becomes shorter and thicker at the saturation point.

Moreover, the radius of the upper part of the nanowire after the gold deposition exceeds the radius of the lower part (half-covered by the gold particles). This was explained by the different oxidation activity of these parts due to the gold deposit that prevents the adsorption of oxygen on the lower part, and not affects the adsorption of the side surface grown after the gold deposition. When the gold covers almost all side surface of the nanowire ($\alpha_{nxs} = 0.01$), the maximal increment in the nanowire length can be obtained, as it is shown in Figure 5e.

To demonstrate the possible efficiency of the intermediated deposition, a faster plasma-enhanced process was used for the simulation. As was demonstrated by Filipič et al.,[46] when applying RF discharge to the growth of oxide structures, the dependence of a nanowire length on time reaches the saturation mode just 20 min after the process started. The results of the simulation using this model are also shown in **Figure 6**, where the length and diameter of the nanowires are calculated as a function of time t,

ADVANCED SCIENCE NEWS
www.advancedsciencenews.com

ADVANCED THEORY AND SIMULATIONS
www.advtheorysimul.com

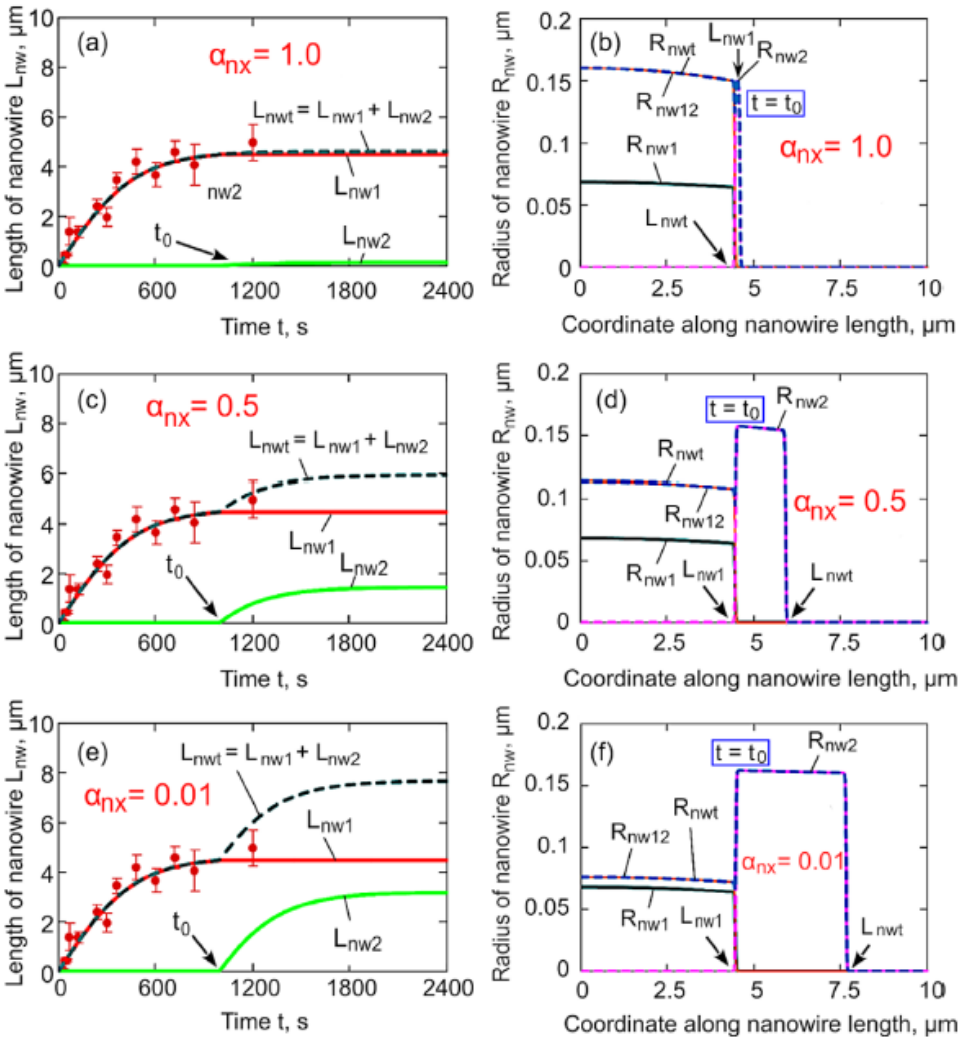

Figure 6. Results of simulations. Dependence of the nanowire a,c,e) length on time t, and b,d,f) shape of nanowires for t = 1000 s and t = 2400 s for different coverage (α_{nx}) of side surface with gold nanoparticles. a,b) Growth of nanowire without gold deposition (α_{nx} = 1.0); gold was deposited at t_0 = 1000 s, when the saturation mode was reached so the length of the nanowires reached its maximum, and the gold nanoparticles covered c,d) a half of the side surface (α_{nx} = 0.5) or e,f) almost all side surface of the nanowire (α_{nxs} = 0.01). The nanowire length and radius are L_{nw1} and R_{nw1} b,d,f) at the moment $t = t_0$, and b) stay almost the same if the deposition is not conducted. d,f) With gold, the radius of the covered part is increased at t = 2400 s to the radius R_{nw12}, and additional substructure with a radius R_{nw2} and length L_{nw2} is formed on the tip of the nanowire, thus increasing the total length to L_{nwt} (dashed line R_{nwt} presents the final shape of the nanowires). Dots mark the experimental results.[51]

moment of deposition of gold nanoparticles t_0, and ratio α_{nx}. The points shown in Figure 6 present the experimental data reported in the cited paper. Figure 6a,b describes the growth of a nanowire without gold deposition (α_{nx} = 1.0). The implementation of the gold deposition in the amount to cover a half of the side surface of a nanowire (α_{nx} = 0.5) changes the nanowire morphology as shown in Figure 6c,d. The nanowire length increased up to about 40% (Figure 6c), while the change in the nanowire radius is not so significant (Figure 6d) as it was demonstrated in Figure 6f.

In Figure 6a–e the continuous red lines present the results of simulations made by use of the developed model to explain the experimental data shown by the red dots. The experiments were conducted until the saturation of the dependence of a nanowire length on time was achieved, and it was expected that further measurements will follow the red line. The black dashed lines represent the cases with deposition of gold that occurs at t_0. Thus, the red and black lines coincide up to the moment t_0. After this time moment, the dashed lines indicate the growth of the nanowires that are promoted by the deposition of gold (dotted lines). Without the deposition, the growth is terminated due to the saturation (red line after t_0). So, the deposition protects the side surface of the nanowires from the oxidation and increases the diffusion path of copper atoms, thus ensuring the increase of the nanowire length. When deposition is very small (a), the length only slightly increases and the intermediate coverage of the side surface with gold (c) results in the significant prolongation. The nanowire length is doubled when almost the entire side surface is covered (e).

Figure 6a,b clearly illustrates the presence of the saturation mode in the nanowire growth observed in the experiments with

low-pressure RF plasma; here a highly-defected nanowire surface formed under the condition of significant ion bombardment is suggested within a frame of the developed model. The theoretical calculations explain the saturation by the existence of a maximal path that a flux of copper atoms, which diffuse from the nanowire root toward the tip, can overcome under a condition of the flux losses caused by the reaction of oxidation on the side surface of the nanowire. In this case, the higher concentration of adsorbed oxygen molecules on the side surface results in shortening of the diffusion path, and the ion bombardment promotes the adsorption by increasing the number of surface defects and the value of the adsorption energy. Deposition of noble metal (gold) decreases the adsorption energy thus hindering the oxygen adsorption; thus, the copper flux can overcome the longer path as is shown in Figure 6c. At the same time, long exposition of the nanowire that was "armored" by the gold nanowire at the lower part, can result in decrease of oxygen adsorption on the gold layer, or even termination (Figure 6e) while the tip of the nanowire that was formed after the deposition can increase its diameter with time, as it is shown in Figure 6d). If the gold nanoparticles cover almost the whole surface of a nanowire after the deposition stage, the mushroom-like nanostructure can be developed as is shown in Figure 6f.

4. Control Experiment

A direct control experiment was performed to check the simulations-derived growth behavior and thus to confirm the key principles of growth control via selective noble material deposition.

eA schematic of the experimental setup and the description of the process are presented in Figure S2, Supporting Information. Microwave generator operating at 2.45 GHz and 100 W of applied power was used for growing CuO oxide nanowires in Ar with 10 vol% of O_2 plasma at atmospheric pressure (see the detailed description in the Supporting Information). After reaching a 600 nm length in 1 h of the process, the nanowires were covered by gold nanoparticles in a metallizer and then were oxidized for one more hour. The produced materials were characterized by scanning electron microscopy, transmission electron microscopy, and energy–dispersive X–ray spectroscopy methods (Figures S3 and S4, Supporting Information). The lengths of the nanowires are between 1 and 1.5 μm, with a large number of nanoparticles with diameters between 2 and 5 nm observed at the base of the nanowires. On the other hand, no nanoparticle was visible at the top of the wires (Figure S3c, Supporting Information). To confirm these observations, high resolution images were taken respectively at the top (Figure S3d, Supporting Information) and at the base of the nanowires (Figure S3e,f, Supporting Information). The crystal structure of the upper part of the nanowire is comparable to observations made on the nanowires without gold deposits. In particular, in the upper part of the image, the spacing between two consecutive planes is 0.25 nm, which is compatible with the lattice parameter of the (-111) plane of the monoclinic phase of CuO. To fully verify the nature of the nanoparticles, energy dispersion spectra (EDS) were acquired respectively in the middle (Figure S4a, Supporting Information) and at the base of the nanowires (Figure S4b, Supporting Information). These spectra clearly show the presence of gold at the base of the nanowires. No trace of gold is visible at the top of the nanowires. In addition, a random analysis of the nanowires in the sample confirmed that the nanoparticles are only present in the lower part, approximately between the base (at the interfacial zone between the film and the wires) and the middle of the nanowire.

5. Conclusions

A method to control the nanowire growth by the intermediate deposition of nanoparticles of noble metals on a side surface of the nanowires is proposed, analyzed numerically, and verified experimentally. The intermediate deposition and the nanoparticle-induced re-mapping of surface processes can drastically change the morphology of the nanowires due to the reduction of the oxidation reactions on a side surface of the nanowires, shielded by noble nanoparticles. This makes it possible for the copper atoms to diffuse along the nanowire surface from the nanowire bottom to the tip to reach higher altitude above the level of copper oxide, and finally to increase to nanowire length. According to the simulations and the verification experiment, the intermediate deposition can be a promising tool in the development of new technologies of copper oxide nanostructures.

Moreover, the experiment has presented a fundamental insight related to the longstanding question about the bottom-up and top-down growth types that vary for various materials and systems, and is quite difficult for the direct experimental verification.[52,53] In this experiment the metal nanoparticles could be considered as markers of the nanoparticle growth zone and they did not change their location on the nanowire during the second round of oxidation, this directly indicates that copper oxide nanowires do not grow from the bottom like human hair. This experiment provides a strong verification in favor of the assumption about the growth of copper oxide nanowires on their tips, so the nanowires increase their lengths when a new layer of material is added as a result of oxidation on the nanowire tip.

Supporting Information

Supporting Information is available from the Wiley Online Library or from the author.

Acknowledgements

O.B. acknowledges the support from the project funded by the National Research Foundation of Ukraine, under grant agreement no. 2020.02/0119 and the NATO Science for Peace and Security Programme under grant id. G5814 project NOOSE. U.C. and M.K. acknowledge the support from Slovenian Research Agency grant N2-0107 and program P1–0417. K.B. acknowledges funding from the Australian Research Council (FT190100819 and DP180101254) and the Australian National University Futures Scheme. I.L. acknowledges the support from the Nanyang Technological University, NIE, and the Australian National University.

Conflict of Interest

The authors declare no conflict of interest.

ADVANCED SCIENCE NEWS
www.advancedsciencenews.com

ADVANCED THEORY AND SIMULATIONS
www.advtheorysimul.com

Data Availability Statement

The data that support the findings of this study are available in the Supporting Information of this article.

Keywords

deposition, fundamental insight, hierarchical nanomaterials

Published online:

[1] I. Levchenko, K. Bazaka, M. Keidar, S. Xu, J. Fang, *Adv. Mater.* **2018**, *30*, 1702226.
[2] C. Carra, A. Medvids, D. Litvinas, P. Ščajev, T. Malinauskas, A. Selskis, H. E. Roman, K. Bazaka, I. Levchenko, C. Riccardi, *ACS Appl. Nano Mater.* **2022**, *5*, 4787.
[3] C.-H. Yu, B.-Y. Tseng, Z. Yang, C.-C. Tung, E. Zhao, Z.-F. Ren, S.-S. Yu, P.-Y. Chen, C.-S. Chen, M. J. Buehler, *Adv. Theory Simul.* **2022**, *5*, 2200459.
[4] C. Zhang, N. Wang, Y. Xu, H.-Y. Tan, Y. Feng, *Adv. Theory Simul.* **2021**, *4*, 2000279.
[5] O. Baranov, K. Bazaka, T. Belmonte, C. Riccardi, E. Roman, M. Mandhakini, S. Xu, U. Cvelbar, I. Levchenko, *Nanoscale Horiz.* **2023**, *8*, 568.
[6] M. A. Fadardi, T. Movlarooy, *Adv. Theory Simul.* **2023**, *6*, 2200875.
[7] S.-J. Yang, Y.-K. Lin, Y.-C. Pu, Y.-J. Hsu, *J. Phys. Chem. Lett.* **2022**, *13*, 6298.
[8] C. Zhang, Z. Peng, C. Huang, B. Zhang, C. Xing, H. Chen, H. Cheng, J. Wang, S. Tang, *Nano Energy* **2021**, *81*, 105609.
[9] I. Levchenko, O. Baranov, C. Riccardi, H. E. Roman, U. Cvelbar, E. P. Ivanova, M. Mohandas, P. Ščajev, T. Malinauskas, S. Xu, K. Bazaka, *Adv. Mater. Interfaces* **2023**, *10*, 2201739.
[10] Z. Chen, S. Zhang, I. Levchenko, I. I. Beilis, M. Keidar, *Sci. Rep.* **2017**, *7*, 12163.
[11] P. Liu, G. Wang, Q. Ruan, K. Tang, P. K. Chu, *Bioact. Mater.* **2021**, *6*, 2134.
[12] K. Li, Y. de Rancourt de Mimérand, X. Jin, J. Yi, J. Guo, *ACS Appl. Nano Mater.* **2020**, *3*, 2830.
[13] Q. Xiang, X. Ma, D. Zhang, H. Zhou, Y. Liao, H. Zhang, S. Xu, I. Levchenko, K. Bazaka, *J. Colloid Interface Sci.* **2019**, *556*, 376.
[14] R. Réocreux, E. C. H. Sykes, A. Michaelides, M. Stamatakis, *J. Phys. Chem. Lett.* **2022**, *13*, 7314.
[15] S. Sasi, K. Prasad, J. Weerasinghe, O. Bazaka, E. P. Ivanova, I. Levchenko, K. Bazaka, *Trends Biotechnol.* **2023**, *41*, 46.
[16] A. Kumar, A. Aljumaili, O. Bazaka, E. P. Ivanova, I. Levchenko, K. Bazaka, *Mater. Horiz.* **2021**, *8*, 3201.
[17] Y. Xu, M. Fan, W. Yang, Y. Xiao, L. Zeng, X. Wu, Q. Xu, C. Su, Q. He, *Adv. Mater.* **2021**, *33*, 2101455.
[18] X. Zhang, Y. Liu, *Environ. Sci.: Nano* **2020**, *7*, 1008.
[19] I. Levchenko, K. Bazaka, T. Belmonte, M. Keidar, S. Xu, *Adv. Mater.* **2018**, *30*, 1802201.
[20] I. Levchenko, M. Keidar, J. Cantrell, Y.-L. Wu, H. Kuninaka, K. Bazaka, S. Xu, *Nature* **2018**, *562*, 185.
[21] N. Singhal, I. Levchenko, S. Huang, L. Xu, G.-C. Potrivitu, O. Cherkun, J. Fang, K. Bazaka, S. Xu, *Adv. Eng. Mater.* **2019**, *21*, 1900401.
[22] I. Levchenko, S. Xu, G. Teel, D. Mariotti, M. L. R. Walker, M. Keidar, *Nat. Commun.* **2018**, *9*, 879.
[23] B. Guo, M. Košiček, J. Fu, Y. Qu, G. Lin, O. Baranov, J. Zavašnik, Q. Cheng, K. Ostrikov, U. Cvelbar, *Nanomaterials* **2019**, *9*, 1405.
[24] Y. Su, T. Liu, P. Zhang, P. Zheng, *Thin Solid Films* **2019**, *690*, 137522.
[25] C. Tang, X. Liao, W. Zhong, H. Yu, Z. Liu, *RSC Adv.* **2017**, *7*, 6439.
[26] C. S. Lee, J. Bae, *J. Mater. Sci.: Mater. Electron.* **2018**, *29*, 15097.
[27] D. Majumdar, S. Ghosh, *J. Energy Storage* **2021**, *34*, 101995,
[28] S. Steinhauer, *Chemosensors* **2021**, *9*, 51.
[29] V. H. Luan, J. H. Han, H. W. Kang, W. Lee, *Composites, Part B* **2019**, *178*, 107464.
[30] T. Ma, L. Gao, Y. Liu, L. Zhang, X. Yang, *Ionics* **2021**, *27*, 1995.
[31] A. Ghosh, M. Miah, A. Bera, S. K. Saha, B. Ghosh, *J. Alloys Compd.* **2021**, *862*, 158549.
[32] A. Shariffar, H. Salman, T. A. Siddique, M. O. Manasreh, *Appl. Phys. A* **2021**, *127*, 750.
[33] R. Kottappara, S. Palantavida, S. C. Pillai, B. K. Vijayan, *Surf. Interfaces* **2021**, *22*, 100876.
[34] S. Kulkarni, R. Ghosh, *Sens. Actuators, B* **2021**, *335*, 129701,
[35] D. Gizinski, A. Brudzisz, M. R. Alzahrani, K.-K. Wang, W. Z. Misiołek, W. J. Stepniowski, *Crystals* **2021**, *11*, 624.
[36] S. H. Mohamed, K. M. Al-Mokhtar, *Appl. Phys. A* **2018**, *124*, 493.
[37] I. Levchenko, M. Mandhakini, K. Prasad, O. Bazaka, E. P. Ivanova, M. V. Jacob, O. Baranov, C. Riccardi, H. E. Roman, S. Xu, K. Bazaka, *Adv. Mater. Technol.* **2022**, *7*, 2101471.
[38] L. Feng, H. Yan, H. Li, R. Zhang, Z. Li, R. Chi, S. Yang, Y. Ma, B. Fu, J. Liu, *AIP Adv.* **2018**, *8*, 045109.
[39] L. Nkhaili, A. Narjis, A. Agdad, A. Tchenka, A. El Kissani, A. Outzourhit, A. Oueriagli, *Adv. Condens. Matter Phys.* **2020**, *2020*, 5470817.
[40] F. Cao, S. Jia, H. Zheng, L. Zhao, H. Liu, L. Li, L. Zhao, Y. Hu, H. Gu, J. Wang, *Phys. Rev. Mater.* **2017**, *1*, 053401.
[41] R. Sondors, J. Kosmaca, G. Kunakova, L. Jasulaneca, M. M. Ramma, R. Meija, E. Kauranens, M. Antsov, D. Erts, *Nanomaterials* **2020**, *10*, 1051.
[42] G. Fritz-Popovski, F. Sosada-ludwikowska, A. Köck, J. Keckes, G. A. Maier, *Sci. Rep.* **2019**, *9*, 807.
[43] I. Levchenko, S. Xu, O. Baranov, O. Bazaka, E. P. Ivanova, K. Bazaka, *Molecules* **2021**, *26*, 4091.
[44] O. Baranov, G. Filipič, U. Cvelbar, *Plasma Sources Sci. Technol.* **2019**, *28*, 084002.
[45] O. Baranov, M. Košiček, G. Filipič, U. Cvelbar, *Appl. Surf. Sci.* **2021**, *566*, 150619.
[46] G. Filipič, O. Baranov, M. Mozetic, K. Ostrikov, U. Cvelbar, *Phys. Plasmas* **2014**, *21*, 113506.
[47] A. Brady-Boyd, E. Chery, S. Armini, *J. Phys. Chem. Lett.* **2022**, *13*, 8130.
[48] L. N. Walters, E. L. Wang, J. M. Rondinelli, *J. Phys. Chem. Lett.* **2022**, *13*, 6236.
[49] C. Kittel, H. Kroemer, *Thermal Physics*, W. H. Freeman and Co., New York **1980**.
[50] A. Altaweel, G. Filipič, T. Gries, T. Belmonte, *Nippon Kessho Seicho Gakkaishi* **2014**, *407*, 17.
[51] G. Filipič, O. Baranov, M. Mozetic, U. Cvelbar, *J. Appl. Phys.* **2015**, *117*, 043304.
[52] B. P. Isaacoff, K. A. Brown, *Nano Lett.* **2017**, *17*, 6508.
[53] H. Sun, F. Liu, L. Zhang, K. Ko, B. McLean, H. An, S. Kim, M. Huang, M.-G. Willinger, R. S. Ruoff, J. Suh, Z.-J. Wang, F. Ding, *Adv. Funct. Mater.* **2022**, *32*, 2206961.

ADVANCED THEORY AND SIMULATIONS

Supporting Information

for *Adv. Theory Simul.*, DOI 10.1002/adts.202300288

Hierarchical Nanomaterials by Selective Deposition of Noble Metal Nanoparticles: Insight into Control and Growth Processes

Oleg Baranov, Thierry Belmonte, Igor Levchenko, Kateryna Bazaka, Martin Košiček and Uroš Cvelbar**

Supporting Information

Hierarchical nanomaterials by selective deposition of noble metal nanoparticles: Insight into control and growth processes

Oleg Baranov[1,2], Thierry Belmonte[3], Igor Levchenko[4,5], Kateryna Bazaka[4], Martin Košiček[2,6] and Uroš Cvelbar[2,6*]*

[1] *Plasma Laboratory, National Aerospace University, Kharkiv, Ukraine*
[2] *Department of Gaseous Electronics, Jozef Stefan Institute, Ljubljana 1000, Slovenia (EU).*
[3] *Université de Lorraine, CNRS, IJL, F-54000 Nancy, France (EU)*
[4] *School of Engineering, College of Engineering, Computing and Cybernetics, The Australian National University, Canberra, ACT 2600*
[5] *Plasma Sources and Application Center, NIE, Nanyang Technological University, Singapore 639798*
[6] *Jožef Stefan International Postgraduate School, Ljubljana, Slovenia (EU)*

*Corresponding author email: O.Baranov@khai.edu and uros.cvelbar@ijs.si

Table of Contents

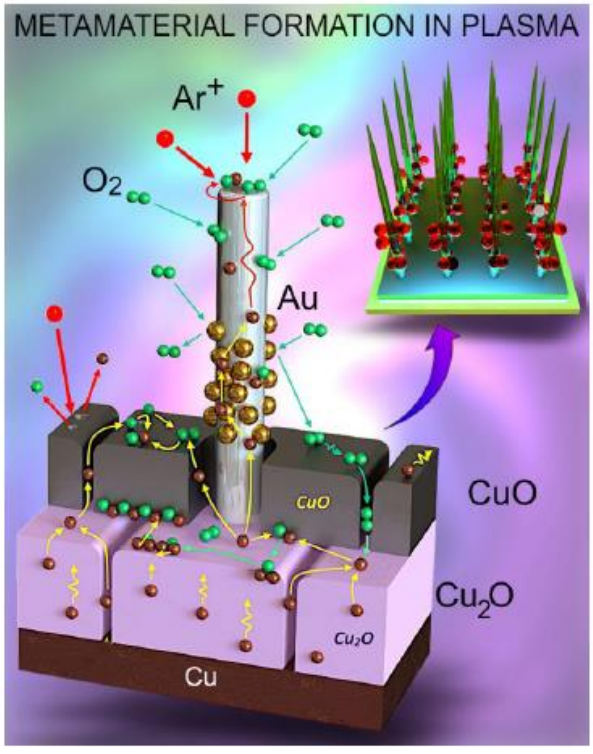

1. Description of the model

To provide a theoretical description with a purpose of establishing the possible control means when applying the stage of noble metal deposition in the process of copper oxide nanowire growth, a multifactor model was developed. A schematic of the nanowire growth at the presence of noble metal of the side surface of a nanowire is shown in **Figure 2** in the paper.

In the model, the following reactions on a copper sample and oxide layers that are formed on the sample as a result of its oxidation after exposure to oxygen environment are discussed. First of all, oxygen molecules adsorb on the surface of the sample where they meet copper atoms that diffuse from a layer of copper through a layer of copper oxide to the surface of the oxide exposed to the oxygen atmosphere.

Oxygen molecules are dissociated at the oxidation of Cu_2O. The released oxygen and by-diffusion-delivered copper atoms are subject to the following reactions:

$$Cu_2O + O \rightarrow 2CuO, \tag{S1}$$

$$CuO + Cu \rightarrow Cu_2O. \tag{S2}$$

The oxide boundary can be shifted because of the reactions, but the key factor of the actual oxide layer growth is the diffusion of copper atoms from the top of the Cu_2O oxide surface to the top surface of CuO oxide, where the generation of a new CuO oxide layer occurs.

To describe the copper diffusion to the surface of the oxide we considered a three-stage process: dissociation of the cuprous oxide, "jump" of the released copper atom into the neighbouring node occupied by the cupric oxide, and the generation of the cuprous oxide in the new location of the copper atom; the following reactions take place:

$$Cu_2O \rightarrow CuO + Cu \rightarrow Cu_2O \tag{S3}$$

This last process can be considered as diffusion of Cu_2O oxide into CuO oxide: the copper atom reacts with the CuO oxide at each "jump" in that case. When the generated Cu_2O composition reaches the upper layer of the CuO oxide, it can be involved into reaction (S1) where the new CuO adsorption node is generated, which results in growing of the CuO oxide layer.

The adsorption of oxygen molecules can occur on a surface of oxide (CuO) layer (n_{x0}, m^{-2}), on a side surface of a nanowire (n_{x2s}, m^{-2}), as well as on a tip (n_{x2t}, m^{-2}) of the nanowires. The densities are related to a density of the adsorption nodes, which is a surface density of atoms of CuO oxide n_0. Due to the difference in the energies of the adsorption, three different expressions of the same form of Langmuir adsorption isotherm are used [1]:

$$\begin{aligned} \frac{n_{x0}}{n_0} &= \frac{P_{O2}}{P_{00}+P_{O2}}, \\ \frac{n_{x2s}}{n_0} &= \frac{P_{O2}}{P_{0s}+P_{O2}}, \\ \frac{n_{x2t}}{n_0} &= \frac{P_{O2}}{P_{0t}+P_{O2}}. \end{aligned} \tag{S4}$$

where P_{00}, P_{0s}, P_{ot} are the constants that depend on surface temperature, and P_{O2} is the partial pressure of oxygen, Pa; the constants are expressed as

$$P_{0i} = \left(\frac{M_{O2}}{2\pi h^2}\right)^{3/2} (k_B T_s)^{5/2} exp\left[-\frac{e(\varepsilon_{aO2i}-\varepsilon_{i-O2})}{k_B T_s}\right], \tag{S5}$$

where M_{O2} is the mass of O_2 molecule, kg; ε_{aO2i} are the adsorption energies (eV) of O_2 molecule on CuO surface ($i \rightarrow 0$), side surface of CuO nanowire ($i \rightarrow s$), and tip of CuO nanowire ($i \rightarrow t$), respectively; $\varepsilon_{i\text{-}O2}$ is the internal energy (eV) of O_2 molecule; h is the Planck's constant ($kg \times m^2 s^{-1}$); e is the elementary electric charge (C); k_B is the Boltzmann constant ($kg \times m^2 s^{-2} K^{-1}$); and pressure P0i has the standard dimension $N \times m^{-2}$ ($kg \times m^{-1} s^{-2}$).

According to the literature [2], copper atoms can diffuse through Cu_2O layer in two different ways: either through the boundaries between the oxide grains (this flux is designated as φ_{Cu1b}) or directly through the body of the grains

(this flux is designated as φ_{Cu1l}). The total flux of the copper atoms diffusing from the copper part of the sample to the boundary between Cu_2O and CuO oxides considers the relative cross-sections occupied by the inter-grain boundaries or grains:

$$\varphi_{Cu1} = P_{Cu1b}\varphi_{Cu1b} + P_{Cu1l}\varphi_{Cu1l}, \tag{S6}$$

where P_{Cu1b} and P_{Cu1l} are the ratio of the cross-sections associated with two mechanisms, respectively, to the total cross-section:

$$P_{Cu1b} = \frac{S_{Cu2Ob}}{S_{Cu2Ob}+S_{Cu2Ol}}, \qquad P_{Cu1l} = \frac{S_{Cu2Ol}}{S_{Cu2Ob}+S_{Cu2Ol}}. \tag{S7}$$

where S_{Cu2Ob} and S_{Cu2Ol} are the cross-sections occupied by the grain boundaries and grains, respectively.

In turn, they are expressed as:

$$S_{Cu2Ob} = \frac{\pi\left(d_{Cu2O}+\frac{b_{Cu2O}}{2}\right)^2}{4} - \frac{\pi d_{Cu2O}^2}{4} = \frac{\pi d_{Cu2O}^2}{4}\left(\left(1+\frac{b_{Cu2O}}{2d_{Cu2O}}\right)^2 - 1\right), \qquad S_{Cu2Ol} = \frac{\pi d_{Cu2O}^2}{4}, \tag{S8}$$

where d_{Cu2O} and b_{Cu2O} are a diameter of Cu_2O grain a thickness of the grain boundary, respectively.

After substitution, one may obtain:

$$P_{Cu1b} = \left(\left[1+\frac{b_{Cu2O}}{2d_{Cu2O}}\right]^2 - 1\right)\left(1+\frac{b_{Cu2O}}{2d_{Cu2O}}\right)^{-2}, \qquad P_{Cu1l} = \left(1+\frac{b_{Cu2O}}{2d_{Cu2O}}\right)^{-2}. \tag{S9}$$

It is assumed that copper atoms delivered to the boundary between the oxides, are consumed at their interaction with CuO layer according to reaction (2), and this reaction is a driving force of the diffusion; any reactions in the volume of Cu_2O layer of a thickness L_{ox1} are not considered. Then a density $n_{cu}(z)$ of the copper atoms is:

$$D_{Cu1i}\frac{d^2 n_{Cui}}{dz^2} = 0, \tag{S10}$$

$$n_{Cu} - n_{Cu0} = -\frac{\varphi_{Cu1i}}{D_{Cu1i}}a_0 L_{ox1}, \tag{S11}$$

where D_{Cu1i} is a diffusion coefficient, which is dependent on the temperature T_s, potential well ε_{c1i}, numerical coefficient α_{Dc1}, and lattice vibration frequency ν_0:

$$D_{Cu1i} = D_{0c1i}exp\left[-\frac{e\varepsilon_{c1i}}{k_B T_s}\right] = \alpha_{Dc1i}\frac{\nu_0 a_0^2}{2}exp\left[-\frac{e\varepsilon_{c1i}}{k_B T_s}\right], \tag{S12}$$

In turn, the latter depends on the temperature [3]:

$$\nu_0 = \frac{2k_B T_S}{h}, \tag{S13}$$

where h is the Plank's constant.

To describe the fluxes through the boundaries between Cu_2O grains and the volume of Cu_2O grain, indexes "b" or "l" should be substituted.

The fluxes delivered to the boundary between the oxides ($z = L_1$), are

$$\varphi_{Cu1i} = \frac{1}{2}n_{Cu}\nu_0 exp\left[-\frac{e\varepsilon_{c1i}}{k_B T_s}\right]. \tag{S14}$$

A dependence of the fluxes on thickness of Cu2O layer can be found by combining the equations (S11) and (S14):

$$\varphi_{Cu1i} = \frac{1}{1+\frac{a_0\nu_0}{2D_{0c1i}}L_{ox1}}\frac{n_{Cu0}\nu_0}{2}exp\left[-\frac{e\varepsilon_{c1i}}{k_B T_s}\right]. \tag{15}$$

Then, the total flux of copper atoms supplied to the CuO/Cu_2O boundary can be found:

$$\varphi_{Cu1} = \left(\frac{1}{\left(1+\frac{d_{Cu2O}}{2b_{Cu2O}}\right)\left(1+\frac{a_0\nu_0}{2D_{0c1b}}L_{ox1}\right)}exp\left[-\frac{e\varepsilon_{c1b}}{k_B T_s}\right] + \frac{1}{\left(1+\frac{2b_{Cu2O}}{d_{Cu2O}}\right)\left(1+\frac{a_0\nu_0}{2D_{0c1l}}L_{ox1}\right)}exp\left[-\frac{e\varepsilon_{c1l}}{k_B T_s}\right]\right)\frac{n_{Cu0}\nu_0}{2}, \tag{S16}$$

where a_0 is Cu_2O lattice parameter; n_{cu0} is the surface density of atoms of the copper sample, m^{-2}.

When considering a diffusion of molecular oxygen adsorbed on the upper surface of CuO oxide to the boundary between CuO and Cu_2O, only the mechanism of the diffusion along the boundaries of CuO grains (short-circuit diffusion) is taken into account. When the molecule reaches the boundary between the oxides, thermal dissociation of O_2 at presence of Cu_2O oxide occurs. At that, the flux of oxygen molecules does not react on the way to the inter-oxide boundary. Thus, the flow φ_{x2} of the oxygen molecules can be found similarly to the flows of copper atoms through Cu_2O layer:

$$n_{x2} - n_{x0} = -\frac{\varphi_{x2} a_0}{D_{0x2}} L_{ox2}, \tag{S17}$$

where D_{0x2} is a constant; n_{x0} is the surface density of adsorbed oxygen molecules on the top surface of CuO oxide, m^{-2}; L_{ox2} is a current length of CuO layer.

Under a condition that one molecule of oxygen can decay to two atoms when contacting with Cu_2O, the flux of oxygen atoms to the boundary between the oxide is:

$$\varphi_{x1} = n_{x1} v_{x-dec} = 2n_{x2} v_{x-dec} = 2n_{x2} \frac{\nu_0}{2} exp\left(-\frac{e\varepsilon_{x2}}{k_B T_s}\right) exp\left(-\frac{e\varepsilon_{x-dis}}{k_B T_s}\right) = n_{x2} \nu_0 exp\left(-\frac{e(\varepsilon_{x2}+\varepsilon_{x-dis})}{k_B T_s}\right), \tag{S18}$$

where ε_{x2} is a potential well for physisorption on the CuO grain, eV; n_{x2} is a surface density of the oxygen molecules at the boundary between the CuO and Cu_2O oxides, while n_{x1} is a surface density of oxygen atoms after the dissociation; $\nu_0/2\, exp(-e(\varepsilon_{x2} + \varepsilon_{x-dis})/k_B T_s)$ is a frequency of the jumps of O_2 toward Cu_2O oxide from CuO oxide and dissociation at the jump, $\varepsilon_{x\text{-}dis}$ is the energy of the dissociation at the presence of Cu_2O.

By combining equations (S17) and (S18), the flux of oxygen atoms to the boundary between CuO and Cu_2O is:

$$\varphi_{x1} = \frac{n_{x0}}{1+\frac{a_0 \nu_0}{2D_{0x2}} L_{ox2}} \frac{\nu_0}{2} exp\left(-\frac{e(\varepsilon_{x2}+\varepsilon_{x-dis})}{k_B T_s}\right). \tag{S19}$$

A counter flux of copper atoms from the Cu_2O/CuO boundary to the top of the CuO oxide is found by use of the speculations like the above:

$$\varphi_{Cu2} = \frac{1}{2} n_{Cu2} \frac{n_{x0}}{n_0} \nu_{c2} = \frac{n_{x0}}{1+\frac{a_0 \nu_0}{2D_{0c2}} L_{ox2}} \frac{\nu_0}{2} exp\left(-\frac{e(\varepsilon_{c2}+\varepsilon_{x-dis})}{k_B T_s}\right), \tag{S20}$$

where D_{0c2} is a constant; n_{Cu2} is a surface density of the copper atoms present in the form of Cu_2O oxide at the top of CuO oxide; n_{x0}/n_0 is a probability to find an adsorbed oxygen molecule on the surface of the CuO oxide; ν_{c2} is a frequency of the jumps of the copper atom toward O_2 molecule from Cu_2O oxide and dissociation of the oxide at the jump, ε_{c2} is the energy of dissociation at the reaction (S3).

Unlike the growth of CuO and Cu_2O layers, the diffusion of copper from the bottom part of a nanowire to its tip is accompanied with loss of copper flux due to reaction of oxidation (S1) oxidation on the side surface and top of the nanowire. However, by considering the fact that the nanowire roots are submerged into the layer of CuO oxide, a part of the flux of copper is not oxidised while diffusing along the nanowire root. At that the density n_{Cu20nw} of copper atoms at the bottom of a nanowire is connected with the initial density n_{Cu20} of copper atoms by the equation:

$$n_{Cu20nw} = n_{Cu20} - \frac{\varphi_{Cu2nw}}{D_{Cu2}} a_0 L_{ox2} = n_0 - \frac{\varphi_{Cu2nw}}{D_{0c2} exp\left(\frac{e\varepsilon_{c2}}{k_B T_s}\right)} a_0 L_{ox2}. \tag{S21}$$

where the density n_{Cu20} is considered to be equal to n_0, since this is the density of Cu_2O in the Cu_2O/CuO boundary.

As for the side surface, where the oxidation takes place, the distribution of the copper atoms along the nanowire surface is:

$$D_{Cus0} exp\left(-\frac{e\varepsilon_{c2s}}{k_B T_s}\right) \frac{\partial^2 n_{cu}(z)}{\partial z^2} = -n_{Cu}(z) \frac{n_{x2s}}{n_0} \nu_0 exp\left(-\frac{e\varepsilon_{x-dis}}{k_B T_s}\right), \tag{S22}$$

$$\frac{\partial^2 n_{cu}(z)}{\partial z^2} = -n_{Cu}(z) \frac{n_{x2s}}{n_0} \frac{\nu_0}{D_{Cus0}} exp\left(-\frac{e(\varepsilon_{x-dis}-\varepsilon_{c2s})}{k_B T_s}\right), \tag{S23}$$

where n_{x2s} is the number density of oxygen molecules adsorbed on the side surface of a nanowire, and ε_{c2s} is the energy of dissociation in reaction (S3).

For $n_{Cu}(0) = n_{Cu20nw}$ the solution is

$$n_{Cu}(z) = n_{Cu20nw} cos\left[\left(\frac{n_{x2s}}{n_0}\frac{v_0}{D_{Cus0}} exp\left[-\frac{e(\varepsilon_{x-dis}-\varepsilon_{c2s})}{k_B T_s}\right]\right)^{1/2} z\right]. \quad (S24)$$

A rate of conversion (s^{-1}) of Cu atoms from Cu_2O to CuO on the side surface of a nanowire is:

$$N_{Cus}(L_{nw}) = \int_0^{L_{nw}} n_{Cu}(z)\frac{n_{x2s}}{n_0} v_0 exp\left(-\frac{e\varepsilon_{x-dis}}{k_B T_s}\right) 2\pi R_{nw}(z) dz =$$

$$= n_{Cu20nw}\frac{n_{x2s}}{n_0} v_0 exp\left(-\frac{e\varepsilon_{x-dis}}{k_B T_s}\right) 2\pi \int_0^{L_{nw}} R_{nw}(z) cos\left[\left(\frac{n_{x2s}}{n_0}\frac{v_0}{D_{Cus0}} exp\left[-\frac{e(\varepsilon_{x-dis}-\varepsilon_{c2s})}{k_B T_s}\right]\right)^{1/2} z\right] dz. \quad (S25)$$

Since a nanowire radius usually changes weakly along the nanowire, the following assumption $R_{nw}(0) \approx R_{nw}(L_{nw})$ can be used to simplify the expression:

$$N_{Cus}(L_{nw}) = 2\pi R_{nw}(0) \frac{\frac{n_{x2s}}{n_0} v_0 exp\left(-\frac{e\varepsilon_{x-dis}}{k_B T_s}\right)}{\left(\frac{n_{x2s}}{n_0}\frac{v_0}{D_{Cus0}} exp\left[-\frac{e(\varepsilon_{x-dis}-\varepsilon_{c2s})}{k_B T_s}\right]\right)^{1/2}} \times$$

$$\times n_{Cu20nw} sin\left[\left(\frac{n_{x2s}}{n_0}\frac{v_0}{D_{Cus0}} exp\left[-\frac{e(\varepsilon_{x-dis}-\varepsilon_{c2s})}{k_B T_s}\right]\right)^{1/2} L_{nw}\right]. \quad (S26)$$

As for the reactions on the nanowire tip, the rate of the conversion by the tip of a nanowire with the length L_{nw} is:

$$N_{Cut}(L_{nw}) = n_{Cu}(L_{nw})\frac{n_{x2t}}{n_0} v_0 exp\left(-\frac{e\varepsilon_{x-dis}}{k_B T_s}\right) \pi R_{nw}^2(L_{nw}) =$$

$$= \pi R_{nw}^2(L_{nw})\frac{n_{x2t}}{n_0} v_0 exp\left(-\frac{e\varepsilon_{x-dis}}{k_B T_s}\right) n_{Cu20nw} cos\left[\left(\frac{n_{x2s}}{n_0}\frac{v_0}{D_{Cus0}} exp\left[-\frac{e(\varepsilon_{x-dis}-\varepsilon_{c2s})}{k_B T_s}\right]\right)^{1/2} L_{nw}\right], \quad (S27)$$

where n_{x2t} is the density of O_2 molecules adsorbed on the tip.

The flux of Cu atoms consumed by a nanowire is

$$\varphi_{Cu2nw}(L_{nw}) = \frac{1}{\pi R_{nw}^2(0)}[N_{Cus}(L_{nw}) + N_{Cut}(L_{nw})]. \quad (S28)$$

By use of the assumption $R_{nw}(0) \approx R_{nw}(L_{nw})$ the expression is simplified:

$$\varphi_{Cu2nw}(L_{nw}) = n_{Cu20nw}\frac{n_{x2s}}{n_0} v_0 exp\left(-\frac{e\varepsilon_{x-dis}}{k_B T_s}\right) F(L_{nw}), \quad (S29)$$

$$F(L_{nw}) = \left[\frac{2\left(\frac{n_{x2s}}{n_0}\frac{v_0}{D_{Cus0}} exp\left[\frac{e(\varepsilon_{x-dis}-\varepsilon_{c2s})}{k_B T_s}\right]\right)^{-1/2}}{R_{nw}(0)} sin\left[\left(\frac{n_{x2s}}{n_0}\frac{v_0}{D_{Cus0}} exp\left[-\frac{e(\varepsilon_{x-dis}-\varepsilon_{c2s})}{k_B T_s}\right]\right)^{1/2} L_{nw}\right] + \right.$$

$$\left. + \frac{n_{x2t}}{n_{x2s}} cos\left[\left(\frac{n_{x2s}}{n_0}\frac{v_0}{D_{Cus0}} exp\left[-\frac{e(\varepsilon_{x-dis}-\varepsilon_{c2s})}{k_B T_s}\right]\right)^{1/2} L_{nw}\right]\right] \quad (S30)$$

Combination of (S21) and (S29) results in:

$$\varphi_{Cu2nw}(L_{nw}) = \frac{n_{x2s} v_0 exp\left(\frac{e\varepsilon_{x-dis}}{k_B T_s}\right) F(L_{nw})}{1+\frac{a_0 v_0}{D_{0c2}} L_{ox2}\frac{n_{x2s}}{n_0} exp\left[\frac{e(\varepsilon_{x-dis}-\varepsilon_{c2})}{k_B T_s}\right] F(L_{nw})}, \quad (S31)$$

and after substitution (S31) to (S21):

$$n_{Cu20nw}(L_{ox2}) = \frac{n_0}{1+2\frac{a_0 v_0}{2D_{0c2}} L_{ox2}\gamma_L F(L_{nw})}, \quad (S32)$$

At a time t the nanowires grown per unit of area consume the flux:

$$\varphi_{Cu2n}(t) = \int_0^{L_{nw-m}} \rho_D(L)\varphi_{Cu2nw}(L)dL = \int_0^{L_{nw-m}} \rho_D(L) \frac{n_{x2s}v_0 exp\left(-\frac{e\varepsilon_{x-dis}}{k_B T_s}\right)F(L)}{1+\frac{a_0 v_0}{D_{0c2}}L_{ox2}\frac{n_{x2s}}{n_0}exp\left[-\frac{e(\varepsilon_{x-dis}-\varepsilon_{c2})}{k_B T_s}\right]F(L)} dL, \quad \text{(S33)}$$

where $\rho_D(L)$ is the density of distribution of the nanowires on length.

Finally, two expressions can be obtained for the rate of the nanowire growth in length

$$\frac{dL_{nw}}{dt}(L_{nw}) = N_{Cut}(L_{nw})\frac{a_0^3}{\pi R_{nw}^2(L_{nw})} =$$

$$= n_{Cu20nw}(L_{nw})cos\left[\left(\frac{n_{x2s}}{n_0}\frac{v_0}{D_{Cus0}}exp\left[-\frac{e(\varepsilon_{x-dis}-\varepsilon_{c2s})}{k_B T_s}\right]\right)^{1/2} L_{nw}\right]\frac{n_{x2t}}{n_0}v_0 exp\left(-\frac{e\varepsilon_{x-dis}}{k_B T_s}\right)a_0^3, \quad \text{(S34)}$$

and the rate of growth of nanowire radius

$$\frac{dR_{nw}}{dt}(z,t,L_{nw}) = n_{Cu}(z)\frac{n_{x2s}}{n_0}v_0 exp\left(-\frac{e\varepsilon_{x-dis}}{k_B T_s}\right)a_0^3 =$$

$$= n_{Cu20nw}(L_{nw})\frac{n_{x2s}}{n_0}v_0 exp\left(-\frac{e\varepsilon_{x-dis}}{k_B T_s}\right)a_0^3 cos\left[\left(\frac{n_{x2s}}{n_0}\frac{v_0}{D_{Cus0}}exp\left[-\frac{e(\varepsilon_{x-dis}-\varepsilon_{c2s})}{k_B T_s}\right]\right)^{1/2} z\right]. \quad \text{(S35)}$$

In the case of application of the stage of intermediate deposition the schematic of the nanowire growth is shown in **Scheme S1**.

The stage of the intermediate deposition results in changing the number of adsorption nodes, which could be occupied by oxygen molecules, because the deposited atoms of noble metal occupy a part of the nanowire surface yet do not serve as adsorption nodes for oxygen. This fact is reflected by introducing the additional conditions:

$$\frac{n_{x2s}(t)}{n_0} = \begin{cases} \frac{P_{O2}}{P_{0s}+P_{O2}}, & t < t_{dep} \\ \alpha_{nx}\frac{P_{O2}}{P_{0s}+P_{O2}}, & t \geq t_{dep} \end{cases}, \quad \text{(S36)}$$

$$\frac{n_{x2t}(t)}{n_0} = \begin{cases} \frac{P_{O2}}{P_{0s}+P_{O2}}, & t < t_{dep} \\ \alpha_{nxt}\frac{P_{O2}}{P_{0s}+P_{O2}}, & t \geq t_{dep} \end{cases} \quad \text{(S37)}$$

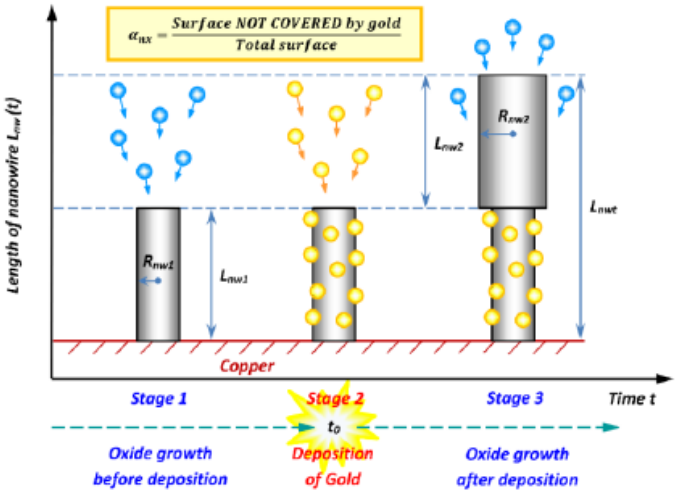

Scheme S1. A schematic of changing a morphology of a nanowire in a case when the maximum length of the nanowire is achieved before the stage of the intermediate deposition of gold: t_0 is a time when the discharge is powered off, and gold nanoparticles are deposited on a surface of a nanowire (time of the deposition of gold is not considered); L_{nw1} is a length of the nanowire at the moment t_0; R_{nw1} is a radius of the nanowire at the moment t_0; L_{nw2} is a length of a part of the nanowire grown after at the moment t_0 (gold is deposited on the part L_{nw1}, while the part L_{nw2} is considered as gold-free); R_{nw12} is a radius of the part L_{nw1} of the nanowire grown after t_0; R_{nw2} is a radius of the part L_{nw2} of the nanowire grown after t_0; L_{nwt} is a total length of the nanowire after the treatment

where t_{dep} is the time when the deposited metal is considered as acting on the side and top surfaces of a nanowire; α_{nx} and α_{nxt} are the coefficient less than unity, which describe the parts of the side and top NW surfaces that are non-covered by the noble metal, respectively.

Finally, a system of the equations is set:

$$\frac{dL_{ox1}}{dt}=\begin{cases}\left(\frac{P_{b1}}{1+a_{b1}L_{ox1min}}+\frac{P_{l1}}{1+a_{l1}L_{ox1min}}\right)A_c, & (L_{ox1}(t)\le L_{ox1min})\wedge(L_{ox2}(t)\le L_{ox2min})\\ \left(\frac{P_{b1}}{1+a_{b1}L_{ox1}}+\frac{P_{l1}}{1+a_{l1}L_{ox1}}\right)A_c-\left(\frac{2B_c}{1+bL_{ox2min}}+\frac{2C_c}{1+cL_{ox2min}}\right)-D_{nw}\frac{a_{ox1}^3}{a_{ox2}^3}D_c(L_{ox2min}), & (L_{ox1}(t)>L_{ox1min})\wedge(L_{ox2}(t)\le L_{ox2min})\\ \left(\frac{P_{b1}}{1+a_{b1}L_{ox1}}+\frac{P_{l1}}{1+a_{l1}L_{ox1}}\right)2A_c-\left(\frac{2B_c}{1+bL_{ox2}}+\frac{2C_c}{1+cL_{ox2}}\right)-D_{nw}\frac{a_{ox1}^3}{a_{ox2}^3}D_c(L_{ox2}), & (L_{ox1}(t)>L_{ox1min})\wedge(L_{ox2}(t)>L_{ox2min})\\ \left(\frac{P_{b1}}{1+a_{b1}L_{ox1min}}+\frac{P_{l1}}{1+a_{l1}L_{ox1min}}\right)2A_c, & (L_{ox1}(t)\le L_{ox1min})\wedge(L_{ox2}(t)>L_{ox2min})\\ 0, & \text{otherwise}\end{cases} \tag{S38}$$

$$\frac{dL_{ox2}}{dt}=\begin{cases}\left(\frac{2B_c}{1+bL_{ox2min}}+\frac{2C_c}{1+cL_{ox2min}}\right), & (L_{ox1}(t)>L_{ox1min})\wedge(L_{ox2}(t)\le L_{ox2min})\\ -\left(\frac{P_{b1}}{1+a_{b1}L_{ox1}}+\frac{P_{l1}}{1+a_{l1}L_{ox1}}\right)A_c+\left(\frac{2B_c}{1+bL_{ox2}}+\frac{2C_c}{1+cL_{ox2}}\right), & (L_{ox1}(t)>L_{ox1min})\wedge(L_{ox2}(t)>L_{ox2min})\\ -\left(\frac{P_{b1}}{1+a_{b1}L_{ox1min}}+\frac{P_{l1}}{1+a_{l1}L_{ox1min}}\right)A_c, & (L_{ox1}(t)\le L_{ox1min})\wedge(L_{ox2}(t)>L_{ox2min})\\ 0, & \text{otherwise}\end{cases} \tag{S39}$$

$$\frac{dL_{ox}}{dt}=\begin{cases}\left(\frac{P_{b1}}{1+a_{b1}L_{ox1min}}+\frac{P_{l1}}{1+a_{l1}L_{ox1min}}\right)A_c, & (L_{ox1}(t)\le L_{ox1min})\wedge(L_{ox2}(t)\le L_{ox2min})\\ \left(\frac{P_{b1}}{1+a_{b1}L_{ox1}}+\frac{P_{l1}}{1+a_{l1}L_{ox1}}\right)A_c-D_{nw}\frac{a_{ox1}^3}{a_{ox2}^3}D_c(L_{ox2min}), & (L_{ox1}(t)>L_{ox1min})\wedge(L_{ox2}(t)\le L_{ox2min})\\ \left(\frac{P_{b1}}{1+a_{b1}L_{ox1}}+\frac{P_{l1}}{1+a_{l1}L_{ox1}}\right)A_c-D_{nw}\frac{a_{ox1}^3}{a_{ox2}^3}D_c(L_{ox2}), & (L_{ox1}(t)>L_{ox1min})\wedge(L_{ox2}(t)>L_{ox2min})\\ \left(\frac{P_{b1}}{1+a_{b1}L_{ox1min}}+\frac{P_{l1}}{1+a_{l1}L_{ox1min}}\right)A_c, & (L_{ox1}(t)\le L_{ox1min})\wedge(L_{ox2}(t)>L_{ox2min})\\ 0, & \text{otherwise}\end{cases} \tag{S40}$$

$$\frac{dR_{nw}}{dt}=\begin{cases}\alpha_L(t)\frac{n_{x2s}(t)}{n_{x2t}(t)}n_{Cu20nw}(L_{ox2min}), & (L_{ox1}(t)>L_{ox1min})\wedge(L_{ox2}(t)\le L_{ox2min})\\ \alpha_L(t)\frac{n_{x2s}(t)}{n_{x2t}(t)}n_{Cu20nw}(L_{ox2}), & (L_{ox1}(t)>L_{ox1min})\wedge(L_{ox2}(t)>L_{ox2min})\\ 0, & \text{otherwise}\end{cases} \tag{S41}$$

$$\frac{dL_{nw}}{dt}=\begin{cases}\alpha_L(t)n_{Cu20nw}(L_{ox2min})cos(\beta_L L_{nw}), & (L_{ox1}(t)>L_{ox1min})\wedge(L_{ox2}(t)\le L_{ox2min})\\ \alpha_L(t)n_{Cu20nw}(L_{ox2})cos(\beta_L L_{nw}), & (L_{ox1}(t)>L_{ox1min})\wedge(L_{ox2}(t)>L_{ox2min})\\ 0, & \text{otherwise}\end{cases} \tag{S42}$$

with the following initial conditions: $L_{ox1}(0) = L_{10}$, $L_{ox2}(0) = L_{20}$, $L_{ox}(0) = L_{10} + L_{20}$.

The parameters used in the system are:

$$A_c=n_{CuO}a_0^3\frac{\nu_0}{2};\qquad B_c=2n_{x0}a_0^3\frac{\nu_0}{2}exp\left(-\frac{e(\varepsilon_{x2}+\varepsilon_{x-dec})}{k_BT_s}\right);\qquad C_c=n_{x0}a_0^3\frac{\nu_0}{2}exp\left(-\frac{e(\varepsilon_{c2}+\varepsilon_{x-dec})}{k_BT_s}\right); \tag{s43}$$

$$D_c(L_i)=n_{Cu20nw}(L_i)\pi R_{nw}^2(L_{nw})\alpha_L(t)cos(\beta_L(t)L_{nw})+2\pi R_{nw}(0)\frac{n_{x2s}(t)}{n_{x2t}(t)}\frac{\alpha_L(t)}{\beta_L(t)}sin(\beta_L(t)L_{nw}); \tag{s44}$$

$$P_{b1}=\frac{1}{\left(1+\frac{d_{Cu20}}{2b_{Cu20}}\right)}exp\left[-\frac{e\varepsilon_{c1b}}{k_BT_s}\right];\qquad P_{l1}=\frac{1}{\left(1+\frac{2b_{Cu20}}{d_{Cu20}}\right)}exp\left[-\frac{e\varepsilon_{c1l}}{k_BT_s}\right]; \tag{s45}$$

$$a_{b1}=\frac{a_0\nu_0}{2D_{0c1b}};\qquad a_{l1}=\frac{a_0\nu_0}{2D_{0c1l}};\qquad b=\frac{a_0\nu_0}{2D_{0x2}};\qquad c=\frac{a_0\nu_0}{2D_{0c2}}; \tag{s46}$$

$$\frac{n_{x2s}(t)}{n_0}=\begin{cases}\frac{P_{O2}}{P_{0s}+P_{O2}}, & t<t_{dep}\\ \alpha_{nx}\frac{P_{O2}}{P_{0s}+P_{O2}}, & t\ge t_{dep}\end{cases};\qquad \frac{n_{x2t}(t)}{n_0}=\begin{cases}\frac{P_{O2}}{P_{0s}+P_{O2}}, & t<t_{dep}\\ \alpha_{nxt}\frac{P_{O2}}{P_{0s}+P_{O2}}, & t\ge t_{dep}\end{cases}; \tag{s47}$$

$$\alpha_L(t)=\frac{n_{x2t}(t)}{n_0}a_{0s}^3\nu_0exp\left(-\frac{e\varepsilon_{x-dis}}{k_BT_s}\right);\qquad \beta_L(t)=\left(\frac{n_{x2s}(t)}{n_0}\frac{\nu_0}{D_{Cus0}}exp\left[-\frac{e(\varepsilon_{x-dis}-\varepsilon_{c2s})}{k_BT_s}\right]\right)^{1/2}; \tag{s48}$$

$$\gamma_L(t)=\frac{n_{x2s}(t)}{n_{0s}}exp\left[-\frac{e(\varepsilon_{x-dis}-\varepsilon_{c2})}{k_BT_s}\right];\qquad n_{Cu20nw}(L_i)=\frac{n_0}{1+2cL_i\gamma_L F(L_{nw})}; \tag{s49}$$

$$F(L_{nw})=\frac{2}{\beta_L R_{nw}(0)}sin(\beta_L(t)L_{nw})+\frac{n_{x2t}}{n_{x2s}}cos(\beta_L(t)L_{nw}). \tag{s50}$$

2. Details of simulation

The model simulated the growth of CuO nanowires at the fixed conditions described in the experimental section. Thus, the oxygen partial pressure was set to $2.1 \cdot 10^4$ Pa, and the experimental dependence of the sample temperature is approximated by the expression: $T_s(t) = (T_{max} - T_0)(1 - exp[-t/\tau]) + 293$ (K), where T_{max} = 315 °C; T_0 = 20 °C, τ = 40 s.

The adsorption energy ε_{aO2} = 1.46 eV on a surface of CuO oxide was set to fit the experimental data and is higher than the value of 1.35 eV perfect calculated by Sun *et al.* [4] for the adsorption of O_2 on the perfect and oxygen-deficient CuO surface with vacancies. This difference can be explained by the higher disorder in crystallinity of the real oxide. The energy ε_{aO2nws} = 0.1 eV of oxygen adsorption of side surface of a nanowire corresponds to the lowest energy of O_2 adsorbed on the perfect and oxygen-deficient CuO (111) surface [4], where the adsorption energies of the modes O_2 being perpendicular to the I, III, IV, V, VI, VII and VIII sites are between 0.1–0.18 eV. At the same time, the energy ε_{aO2nwt} = 0.385 eV is located in the range between the energy of 0.32 eV that is calculated for the O_2 adsorbed on the II site ($O_{2(a)}$ mode), and the energy of 0.45 eV that fits to $O_{2(b)}$ mode [4]; both of the modes correspond to the adsorption of O_2 on the perfect CuO (111) surface. It should be mentioned that Hu *et al.* also pointed that the attraction between O_2 and CuO (111) is weak; according to their data the binding energy is 0.27 eV per O_2 molecule [5].

3. Additional simulation results

The value of the dissociation energy of O_2 on the Cu_2O surface $\varepsilon_{x\text{-}dis}$ = 0.65 eV is close to the value of 0.85 eV for O_2 dissociation on the Cu_2O (111) surface (M(d)→P3 reaction) and is higher that the energy of 0.18 eV (M(e)→P4 reaction) that were calculated by Zhang *et al.* for O_2 dissociation on the Cu_2O oxygen-deficient surface [6].

The energies ε_{c1b} = 0.98 eV and ε_{c1l} = 1.5 eV of the boundary and lattice diffusion of copper atoms through Cu_2O layer were set to correspond the reported data [2,7] and to fit the results on the measured thicknesses of Cu_2O and CuO oxides.

The energy ε_{x2} = 0.8 eV of O_2 diffusion through CuO layer is engaged to describe the growth of CuO layer not only in this experiment, but also the results obtained by Zhu *et al.* and Yuan *et al.* in their experiments [8,9]. The energies ε_{c2} = 0.66 eV and ε_{c2s} = 0.46 eV (or 0.56 eV) of Cu diffusion in the CuO layer and along the side surface of CuO nanowire toward its tip were set to fit the ratio of thicknesses of both oxides to the data from the experiments. The internal energy ε_{iO2} = 0.31 eV of oxygen molecules adsorbed on surfaces of oxide layer and nanowires, is used to fit the experimental data within the frame of the developed model.

The results of 3D modelling are shown in **Figure S1**, which clearly indicates the effectiveness of the proposed approach.

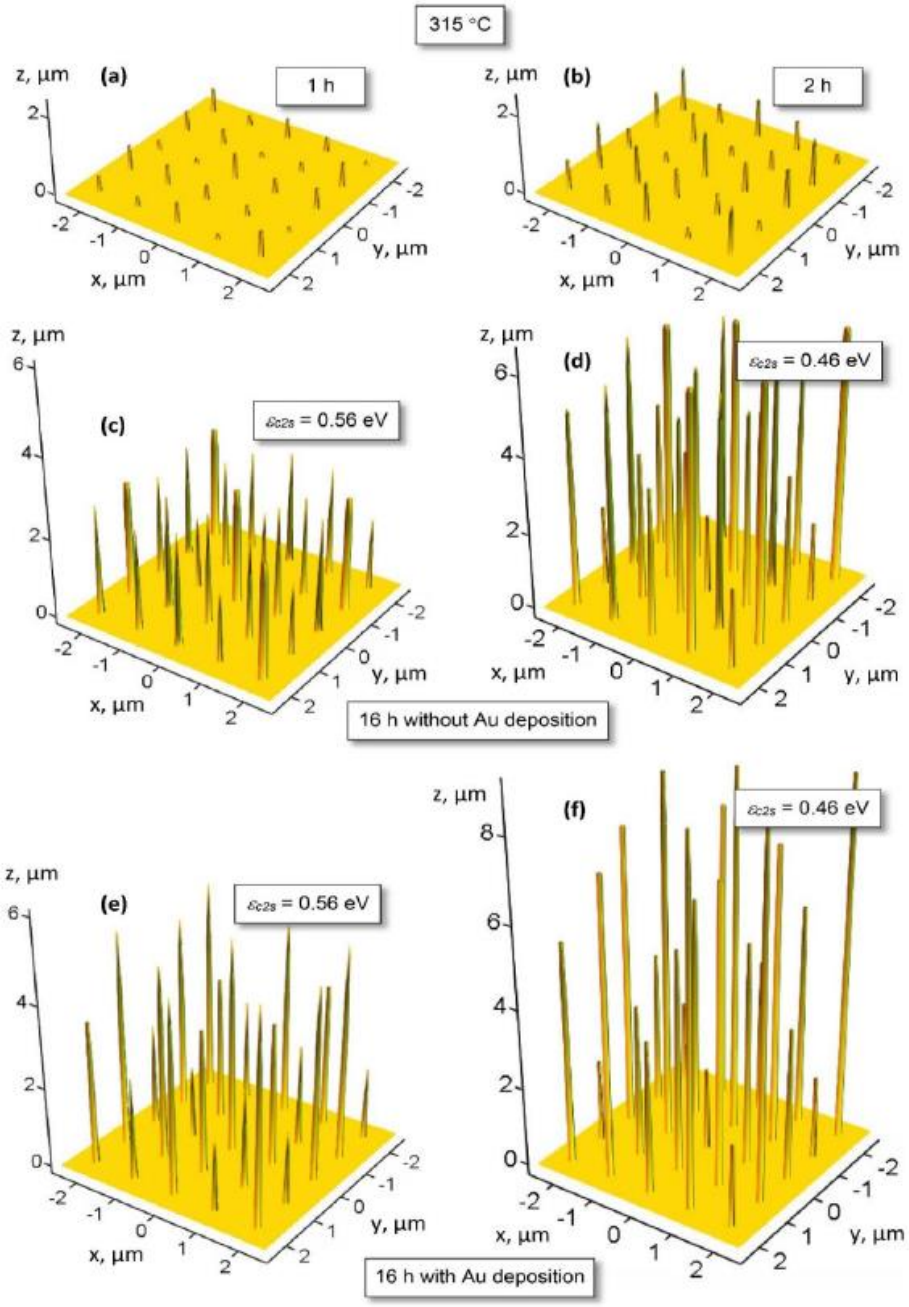

Figure S1. Growth of copper oxide nanowires at the dependence on the activation energy ε_{c2s} of copper diffusion along the surface of the nanowire; gold deposition was realized after 8 hours of nanowire growth (Fig. 6): a – one hour of growth, b – two hours; c, d – 16 hours without gold deposition: c – ε_{c2s} = 0.56 eV; d – ε_{c2s} = 0.46 eV; d, e – 16 hours of growth under condition of the deposition of gold at the eighth hour of growth: e – ε_{c2s} = 0.56 eV; f – ε_{c2s} = 0.46 eV.

4. Description of the experiment

The reactor was made of a fused silica tube passing through a resonant cavity connected to a microwave generator operating at 2.45 GHz and 100 W of applied power. During the plasma source operation, Ar - 10 vol.% O_2 plasma at atmospheric pressure is forced to stay on the tube axis by a rotating fan. Neutral species that are not subjected to the influence of the electric field exit the reactor through an orifice of 400 µm in diameter. A total flow rate of 275 sccm (standard cubic centimetre per minute) is injected in

the plasma, which produces a laminar post-discharge, containing atomic oxygen and various neutral excited species of oxygen like the singlet state of O_2. The beam diameter is nearly twice the diameter of the hole (~ 800 µm). Under these experimental conditions, the gas temperature is ~1200 K and high thermal gradients exist. The evolution of the surface temperature of the substrate was determined by heat transfer simulation from time-resolved infrared measurements on the sample backside. The surface temperature reaches a steady state after about 3 minutes and the maximum temperature lies in the range [280 – 350 °C], depending on the experimental conditions. The hole-substrate distance is 2 mm and the treatment is performed in a confined environment to prevent air contamination. Coloured rings appear on the substrate area hit by the afterglow over a diameter comprised between 1 and 2 centimetres.

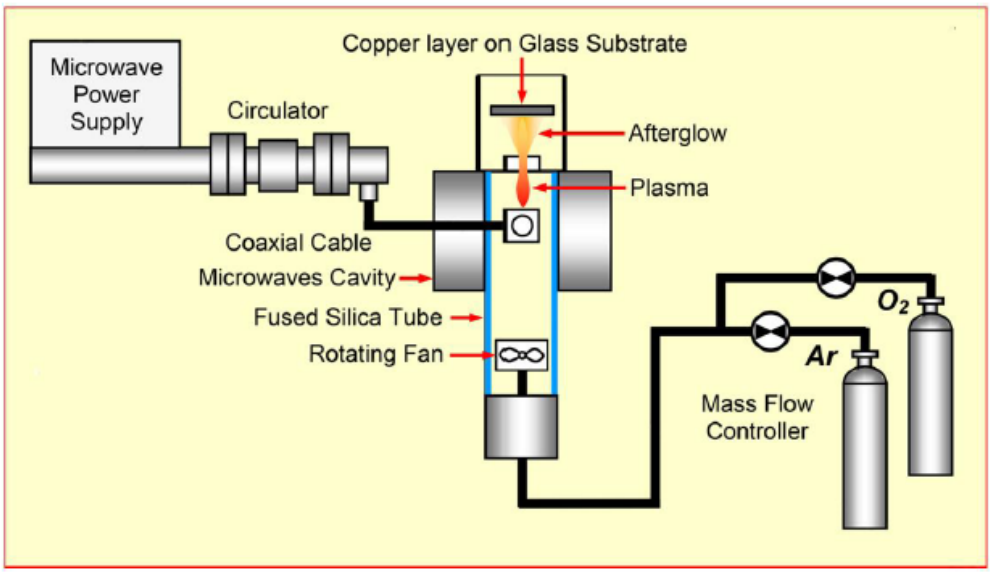

Figure S2. Schematic of the experimental setup. The hole-substrate distance is two millimetres, and the treatment is performed in a confined environment to prevent air contamination.

5. Experimental results

To follow the growth of nanowires during synthesis, gold particles were used. The synthesis process was divided into 2 steps of one hour each, under the conditions described previously (Ar - 10 vol.% O_2, 275 Nccm, 100 W). Under these conditions, a one hour-long treatment led to the formation of relatively long nanowires: around 600 nm in the optimal growth zone. After this first step, the sample was covered by gold in a metallizer (Denton Vacuum Desk IV). The duration of the deposit was short enough for the gold to form separated nanoparticles on the surface of the sample.

Gold was chosen because of its non-oxidizable nature. After gold deposit, the sample underwent a second oxidation treatment for one hour under the same conditions. The obtained nanowires were characterized by transmission electron microscopy (TEM). It can be seen in the general view (Figure S3) that the lengths of the nanowires are between 1 and 1.5 µm. A large number of nanoparticles with diameters between 2 and 5 nm are observed at the base of the nanowires (Figure S3b).

On the other hand, no nanoparticle was visible at the top of the wires (Figure S3c). To confirm these observations, high resolution images were taken respectively at the top (Figure S3d) and at the base of the nanowires (Figure S3e,f). The crystal structure of the upper part of the nanowire is comparable to observations made on the nanowires without gold deposits. In particular, in the upper part of the image, the spacing between two consecutive planes is 0.25 nm, which is compatible with the lattice parameter

of the (-111) plane of the monoclinic phase of CuO. Other interplanar spacings of approximately 0.23 and 0.20 nm are measured observed at the base of the nanowires, especially in the nanoparticles. These spacings correspond respectively to the (111) and (200) planes of the face centered cubic phase of gold (JCPDS 03-065-2870) but also to the (111) and (11-2) planes of CuO.

To fully determine the nature of the nanoparticles, energy dispersion spectra (EDS) were acquired respectively in the middle (Figure S4a) and at the base of the nanowires (Figure S4b). These spectra clearly show the presence of gold at the base of the nanowires. No trace of gold is visible at the top of the nanowires. In addition, a random analysis of the nanowires in the sample confirmed that the nanoparticles are only present in the lower part, approximately between the base (at the interfacial zone between the film and the wires) and the middle of the nanowire.

These observations show that nanowires continued growing during the second oxidation stage without affecting the position of the gold nanoparticles. These results confirm that the growth of nanowires is not affected by the base of the wire but by diffusion of copper ions towards the top. In addition, nanoparticles seem to be present on the surface of nanowires. However, the diameters of the nanowires increase weakly between 1 and 2 hours of treatment under these experimental conditions: on average between 55 and 60 nm. These experiments therefore do not allow a decision to be made between surface and volume diffusion mechanisms.

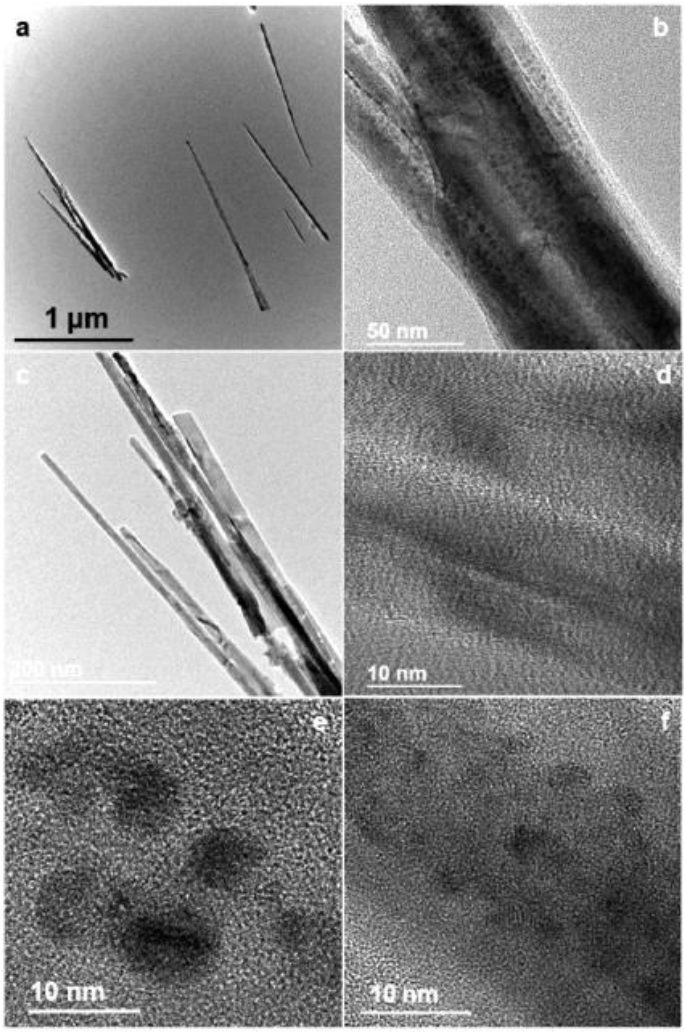

Figure S3. Electron microscopy of CuO nanowire: (a) General overview of CuO nanowires after the deposition of Au nanoparticles and two-step oxidation process; (b) Base and (c) top of the nanowires; High resolution of top (d) and base (e and f) of the nanowires.

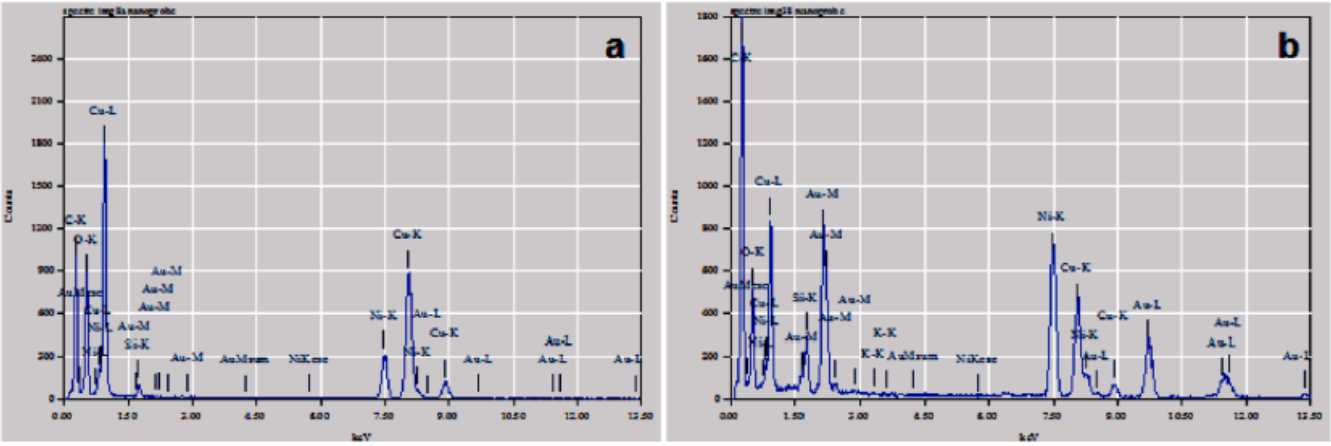

Figure S4. EDX measurements at the top (a) ant base (b) of a nanowire.

References

[1] C. Kittel, and H. Kroemer, Thermal Physics, W. H. Freeman and Co, New York, 1980.

[2] Y. Zhu, K. Mimura, J.-W. Lim, M. Isshiki, Q. Jiang, Brief Review of Oxidation Kinetics of Copper at 350 °C to 1050 °C. *Metall. and Mat. Trans. A* **2006**, *37*, 1231–1237.

[3] I. Levchenko, U. Cvelbar, M. Keidar, Graphene Flakes in Arc Plasma: Conditions for the Fast Single-Layer Growth, Graphene 5 (2016), 81–89, http://dx.doi.org/10.4236/graphene.2016.52009

[4] S. Sun, C. Li, D. Zhang, Y. Wang, Density functional theory study of the adsorption and dissociation ofO2on CuO(1 1 1) surface, Applied Surface Science 333 (2015) 229–234, https://doi.org/10.1016/j.apsusc.2015.02.018

[5] J. Hu, D. Li,| J. G. Lu, R. Wu, Effects on Electronic Properties of Molecule Adsorption on CuO Surfaces and Nanowires, The Journal of Physical Chemistry C 114 (2010) 17120–17126, https://pubs.acs.org/doi/pdf/10.1021/jp1039089

[6] R. Zhang, H. Liu, H. Zheng, L. Ling, Z. Li, B. Wang, Adsorption and dissociation of O2 on the Cu2O(1 1 1) surface: Thermochemistry, reaction barrier, Applied Surface Science 257 (2011) 4787–4794, https://doi.org/10.1016/j.apsusc.2010.12.040

[7] N. L. Peterson, C. L. Wiley, Diffusion and Point Defects in Cu2O. *J. Phys. Chem. Solids* **1984**, *45 (3)*, 281–294.

[8] L. Yuan, Y. Wang, R. Mema, G. Zhou, Driving force and growth mechanism for spontaneous oxide nanowire formation during the thermal oxidation of metals, Acta Mater. 59 (2011) 2491–2500. https://doi.org/10.1016/j.actamat.2010.12.052

[9] Y. Zhu, K. Mimura, M. Isshiki, Oxidation Mechanism of Copper at 623–1073 K, Materials Transactions 43 (9) (2002) 2173–2176, https://doi.org/10.2320/matertrans.43.2173

4.2 Exploration of Copper Oxidation in Integrated Electronic Circuits with Broadband Dielectric Spectroscopy

In Section 4.2, copper oxidation was studied using the practical example of an integrated electronic circuit via broadband dielectric spectroscopy (BDS). The oxidation was studied by cycling the temperature between low and high temperatures. With this method, the formation of roughened CuO layers during the cycles is clearly demonstrated, indicating that copper oxidation might play a role in the material ageing of electronic components.

This objective addresses Objective 1. The results of this subsection were published in a peer-reviewed scientific article in the journal *Electroanalysis.*

Regarding my contribution, I analyzed the results and jointly wrote the paper with the other co-authors.

Full Paper Wiley Online Library ELECTROANALYSIS

DOI: 10.1002/elan.202060246

Broadband Microwave Signal Dissipation in Nanostructured Copper Oxide at Air-film Interface**

Papa K. Amoah,[a] Martin Košiček,[c, d] Jesus Perez,[a] Christopher E. Sunday,[a, e] Stéphane Moreau,[b] Uroš Cvelbar,[c] and Yaw S. Obeng[a]

Celebrating the 65th Birthday of Prof Emmanuel I. Iwuoha: Electrochemistry in Africa

Abstract: Contactless broadband microwave spectroscopy (a.k.a., broadband dielectric spectroscopy (BDS)) enables the accurate *operando* analysis of the electrical and magnetic properties without compromising the kinetic conditions of the experiment. The BDS method is sensitive to the actual electronic structure of species, and it is most relevant to redox reactions involving charge-transfer. In this paper, using BDS, we have studied and characterized the oxidation of a copper layer in a purposely built prototypical 3-D integrated circuit (3D-IC) during cycled high-temperature storage. We show that the microwave signal loss in these devices is attributable to the energy dissipation through the signal's interactions with the copper oxidation product. The results demonstrate that contactless BDS could be leveraged into an excellent metrology for applications that use metal oxide as sensing elements.

Keywords: Contactless broadband microwave spectroscopy · copper oxidation · high-temperature storage · microwave signal loss · energy dissipation · metal oxide · sensing elements · numerical modeling · interfacial roughness

1 Introduction

Metal oxide nanostructures (MO) have been intensively studied due to their applications in multiple fields, such as in optoelectronics, gas sensing, photovoltaics, field-effect transistors, UV lasers, and field emission sources, etc. [1]. However, the intrinsic properties of these materials are not well understood because the electrical techniques used in characterizing them invariably introduce parasitic artefacts that distort the measurands. Thus, non-contact metrology will enable an unbiased understanding of how these metal oxides actually work at the atomic level [2,3]. Contactless broadband dielectric spectroscopy (BDS) is a sensitive probe to the actual electronic structure of species. It enables the accurate operando evaluation of the electrical and magnetic properties of materials without compromising the kinetic conditions of the experiment. The BDS method is most relevant to redox reactions which involves charge transfer regardless of the nature of the charge carriers, i.e., electrons and holes [4]. Microwave signals distort when inserted into materials due to the interactions with the intrinsic electrical and magnetic properties of the material. In general, electromagnetic wave signal-material interactions result in changes in the signal's characteristics such as attenuation constant, phase constant, and propagation constant. As such, these material state-sensitive parameters can be used to monitor changes in the mechanical and chemical nature of the analyte.

Distributed element models are used to describe such signal-material interactions, because of the speeds and the frequencies involved. With these models, it is possible to describe the time-dependent variability in current along with the various circuit elements. We take advantage of these variations to extract information about the intrinsic properties of the materials under study. For example, as the materials change under external stimuli, the voltage and phase of the probing microwave signal change in response. These changes provide information about the material properties and the context of its application, e.g.,

[a] P. K. Amoah, J. Perez, C. E. Sunday, Y. S. Obeng
Physical Measurement Laboratory
National Institute of Standards and Technology
100 Bureau Drive, Gaithersburg, MD 20899
[b] S. Moreau
Univ. Grenoble Alpes, CEA, LETI, 38000 Grenoble, France.
[c] M. Košiček, U. Cvelbar
Jožef Stefan Institute, Ljubljana, Slovenia
[d] M. Košiček
Jožef Stefan International Postgraduate School, Ljubljana, Slovenia
[e] C. E. Sunday
Functional Material Group, Department of Chemical Engineering
Cape Peninsula University of Technology
Symphony Way, Bellville, 7535, Cape Town, South Africa.

[**] Certain commercial equipment, instruments, or materials are identified in this paper in order to specify the experimental procedure adequately. Such identification is not intended to imply recommendation or endorsement by the National Institute of Standards and Technology, nor is it intended to imply that the materials or equipment identified are necessarily the best available for the purpose. Contribution of the National Institute of Standards and Technology, not subject to copyright.

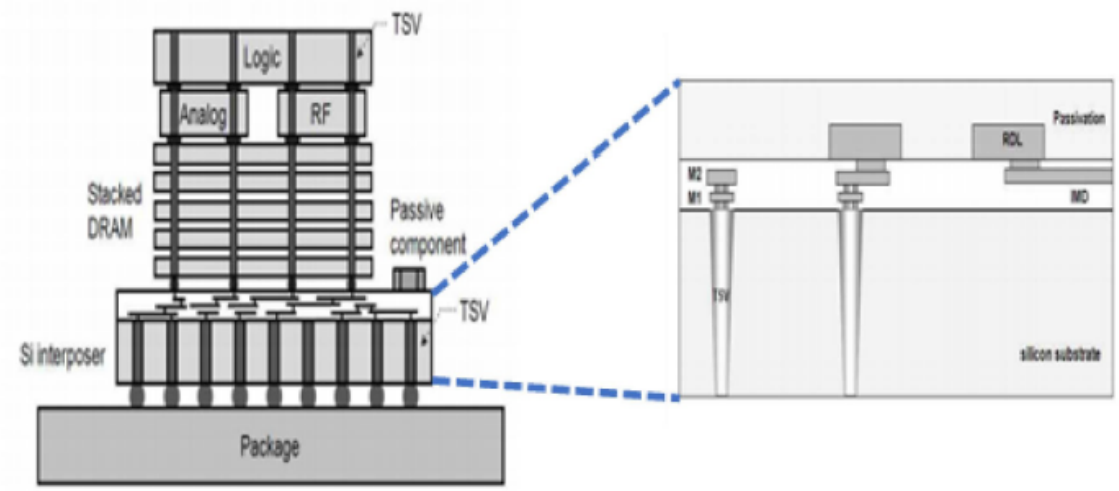

Fig. 1. A schematic cross-section of the test structure used in this work, presenting the essential components of 3D stacked IC using through-silicon via (TSV) and a silicon interposer, with a callout that shows the copper RDL layer of interest in this work (adapted from reference [7]). The called out figure is deliberately exaggerated to reveal the RDL.

construction and function in an integrated circuit packaging. In this paper, using BDS (typically in the range of 10 MHz to 40 GHz), we have studied the oxidation of a copper layer in a purposely built through-silicon via (TSV) enabled 3-D integrated circuit (3D-IC) during cycled high-temperature storage. The devices under test (DUT) were comprised of two-level stacked dies, with a Cu damascene redistribution level (RDL) that allows for circuitry fan-out and lateral communication between the chips, as shown in Figure 1 [5,6]. In this work, we specifically focused on the RDL features.

2 Experimental

The controlled oxidation of the copper layer was accomplished with modified highly accelerated temperature and humidity stress test (i.e., unbiased HAST, JEDEC Standard JESD22-A118B). The temperature was cycled between −65 °C and temperatures of 25, 75, 100 and 125 °C, respectively.

A dedicated ground-signal-ground (GSG) test structure built into the devices was used to monitor the microwave scattering data (S-parameters) in these experiments. The S-parameters were obtained with a two-port measurement configuration on a vector network analyzer (PNA–L N5230 C, 10 MHz- 40 GHz, Keysight, Inc., Santa Rosa, CA) at room temperature in an open laboratory ambient. We used the microwave signal loss between ports 1 and 2 of the vector network analyzer (i.e., RF insertion loss, S21 amplitude) to monitor the oxidation of the RDL copper interconnects. We extracted the electrical characteristics from the S-parameters of the device under test (DUT) by numerical RLCG modeling with a custom MATLAB (MathWorks, Natick, MA) code.

The direct current resistance (R_{DC}) of the oxidized RDL was obtained at room temperature by linear voltammetry (i.e., current-voltage (I–V) curves) after storing the devices overnight at room temperature in the air after thermal cycling. The overnight storing was to eliminate uncertainties in the calculated resistance due to device temperature variability.

3 Results and Discussion

3.1 Microwave Monitoring of Material Changes

Figure 2 shows the room temperature electrical resistance (R_{DC}) of the test structure as a function of peak thermal cycling temperature. The data suggest that the R_{DC} of the test structure increased with increasing thermal cycling peak temperature. This contrasts with the expected decrease in electrical resistance of copper films with thermal exposure due to secondary recrystallization of the copper [8]. The increase in R_{DC} of the Cu could be due to grain boundary "stuffing" formed by copper oxidation or segregation of impurities at the grain boundaries. The R_{DC} increase due to the grain boundary stuffing should have an upper limit due to the decreasing availability of copper grain boundaries. The secondary grain growth with thermal exposure reduces the grain boundary density. The oxidation of copper at our experimental temperatures is controlled by grain boundary diffusion [9]. Thus, the 'stuffing' phenomenon will be limited by the decreasing availability of grain boundaries, and the R_{DC} was expected to plateau with increasing thermal exposure.

Figure 3 compares the micrographs of the Copper RDL in (A) "as-received" and (B) after 4 days at 200 °C showing the development of a thick film of copper oxide film around copper trace feature. Figure 4 compares the

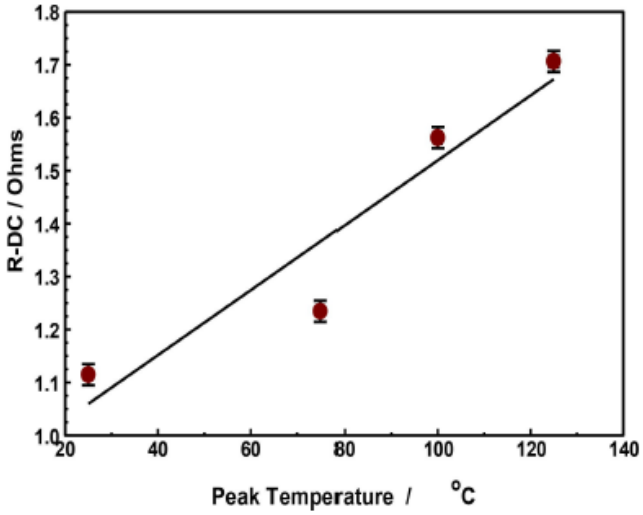

Fig. 2. Calculated room temperature direct-current resistance (R_{DC}, from direct current voltammograms) after 500 thermal cycles between −65 °C and various peak temperatures. The black line connecting the data points is a visual guide only. The error bars represent the standard deviation of the measured R_{DC} of at least four different samples.

microwave insertion loss profile of the DUTs after fixed numbers of thermal cycles, for a peak temperature of 125 °C, in the 0 to 40 GHz range. The figure shows a monotonic increase in signal loss with increasing number of thermal cycles, which suggests that the overall resistance of devices increases with increasing thermal treatment. The data is more consistent with the increased resistance of Cu RDL due to cross-section reduction from oxidation, as shown in Figure 3, than copper grain boundary stuffing. Furthermore, the formation of an oxide layer also depends on the nature of the strain at the metal-air interface. The changes in the thermo-mechanical properties of the copper interconnects with thermal cycling are of significance since local stress is known to affect the thermodynamics of copper metal oxidation [10]. We have also demonstrated elsewhere that thermal cycling results in significant increases in the mean hydrostatic stresses in the copper of TSV interconnects due to increased strain-hardening [11]. However, we note that the RDLs features studied in this work are unconstrained on three sides and can relax from the thermo-mechanical perspectives. Based on these observations, we attribute the increasing resistance to reduction of the copper film cross-section due to metal consumption during thermal oxidation of the metal.

The final oxidation product layer is composed of three regions Cu_2O, CuO, and air-filled CuO-nanofibers layer [9]. The growth of the oxidation layer is via the diffusion of either Cu ions or O ions along the boundaries of the Cu_2O grains. The driving force for copper ions diffusion from the metallic copper towards the surface-air interface can be ascribed to the net result of two synergistic chemical potential gradients, viz., (i) due to difference in oxygen partial pressure in atmospheric and in metal oxide environment, and (ii) due to stress gradient induced by the unit cell size difference between the Cu_2O and CuO [12]. The local stress and diffusion can be further increased by using plasma-assisted oxidation of copper [13]. The conductive polycrystalline copper oxide nanostructure mixtures are paramagnetic [14], and are known to absorb microwaves, mostly through dielectric loss [15]. The copper oxide layer is also redox-active. These intrinsic properties of copper oxide products could be leveraged into nanoelectronic applications [16].

As presented in Figure 5, the insertion loss (S21) increases with increasing thickness of the copper oxide film around the copper trace. Furthermore, Figure 6 displays the monotonic change in the phase angle at a discrete frequency (arbitrarily taken at 61 MHz for this work) as a function of the copper oxide thickness (i.e., number of thermal cycles at 125 °C). The changes in the phase angle are attributable to changes in the complex permittivity and permeability of the evolving copper oxide film [16]. It is obvious from the foregoing that the microwave signal loss observed in the oxidized copper

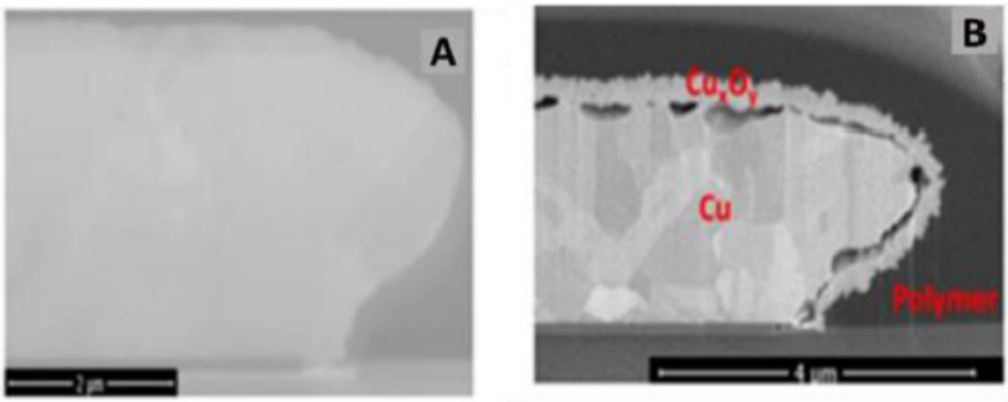

Fig. 3. Micrographs showing the development of copper oxide films around RDL feature: (A) "as-received" and (B) after 4 days at 200 °C. (Adapted from reference [17].)

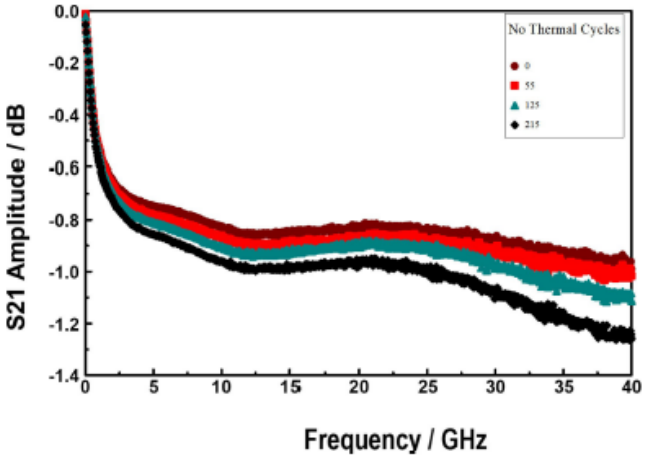

Fig. 4. Microwave Insertion loss (S21) as a function of the number of thermal cycles between −65 and 125 °C in 85 % Relative Humidity, exhibiting increasing loss with increasing cycling.

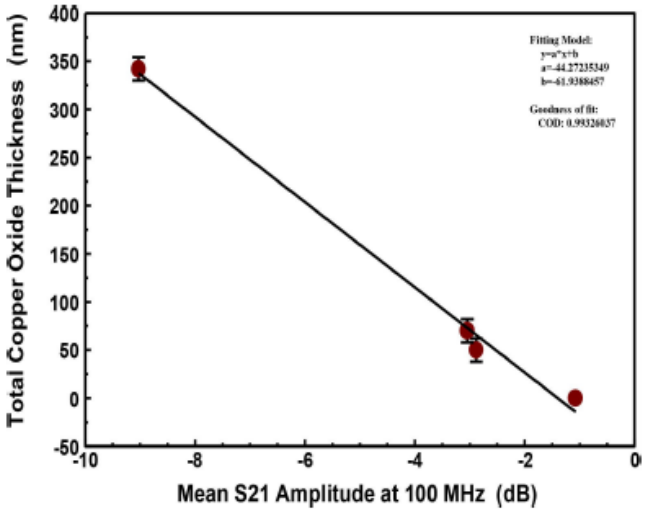

Fig. 5. Correlation between the total copper oxide film thickness and the microwave insertion loss (S21) at 100 MHz attributable to copper oxide growth around copper RDL features. The error bars represent the standard deviation of the copper oxide thickness measurements of at least six sections of SEM micrographs, such as in Figure 3.

samples in this work is due to energy dissipation in the copper oxide film formed around the Cu traces. We have previously shown that in such test structures, under extreme experimental conditions, the insertion loss may also result from significant thermo-mechanical damage [18] or accelerated materials aging [17].

Figure 7 represents a composite transverse section micrograph of an oxidized copper substrate. Raman spectroscopy reveals grading in the material composition in the copper oxide film; comprised of a Cu/ Cu_2O/CuO stack, with a filamentous quasi-one-dimensional nanostructured CuO layer at the air/film interface. In the process of thermal oxidation of copper, Copper (I) oxide

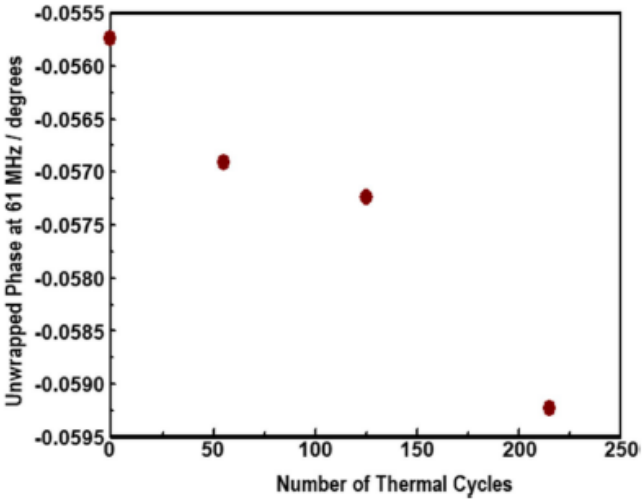

Fig. 6. Correlation between the microwave signal phase angle attributable to copper oxide growth around copper RDL features. Note: The error bars for the unwrapped phase angle are much smaller than the data symbols.

(Cu_2O) layer is first formed, followed by an intermediate compact copper (II) oxide (CuO) layer, and finally, various nanostructures potentially grow at the air-metal-oxide interface. We have demonstrated through finite element electrodynamic modeling (COMSOL Multiphysics Burlington, MA, USA) that the analytical partitioning of the microwave signal loss in such stressed DUTs required explicit accounting for the roughness of the copper oxide film formed around the copper members of the DUT, as shown in Figure 4B [19].

Figure 8 shows simulated signal attenuation as a function of the oxidized copper surface/air interface roughness (expressed as the root-mean-square (RMS) roughness); the signal attenuation increases with increasing surface roughness. At high frequencies, the microwave signal propagates mostly along the outer skin of the RDL copper. As the copper oxidizes the microwave energy is dissipated through at least three mechanisms: ohmic loss including skin effect, dielectric loss due to dipoles in the copper oxide film absorption of the microwave energy to generate heat, and radiative losses with the RDL features acting as antennae. In the skin effect, the microwave signal is absorbed at conductor surface bumps (assuming that the bumps are much smaller than the wavelength of the propagative wave [20]). The skin effect losses increase as the projected area of the coper-copper oxide interface increases due to increasing roughness. In addition, the dielectrics surrounding the RDL feature (i.e., copper oxide products) also alter the current density in the interconnects through energy storage. The relative dielectric constant, (ε_r) of copper oxidation product depends on its effective composition, thus, on the thermal history of the DUT. Based on the sensitivity analysis of the simulation results presented in Figure 8, we postulate that the dielectric loss dominates above 2 GHz. We note that

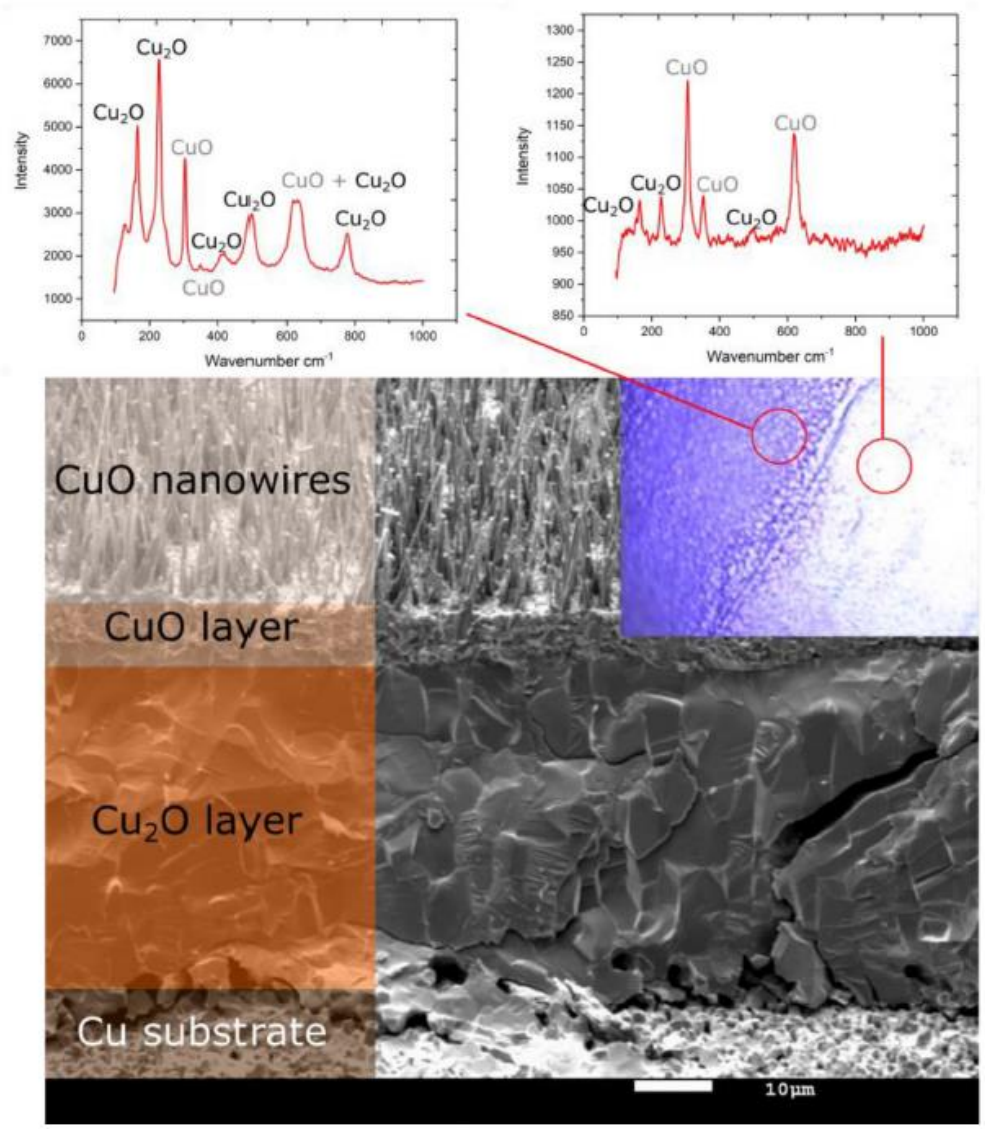

Fig. 7. A composite transverse micrograph and Raman spectra showing two types of oxides form on the surface of the copper during oxidation: CuO and Cu_2O.

our simulation results may not be accurate, since the finite element solvers we used were not optimized for broadband microwave applications. However, the skin effect simulations are reasonably accurate

4 Perspective: Microwave Monitoring of Metal Oxide in Sensing Applications

Having characterized microwave signal propagation in copper-oxide films, we now discuss some potential electroanalytical applications of microwave spectroscopy in metal-oxides. Specifically, in this section, we discuss microwave monitoring of reactions of metal-oxides, with a focus on copper-oxide, in gas and bioanalytical sensing applications. The premise of this section is the microwave energy dissipation in metal-oxide films change due to changes in their dielectric, magnetic, electromagnetic impedance, and the microstructure in response to charge transfer reactions with other redox-active species in the environment [21].

4.1 Metal Oxides in Gas Sensing

Metal-oxides (e.g., ZnO, CuO, NiO, CuO, Cr_2O_3, Co_3O_4, and Mn_3O_4) are highly sensitive to gaseous compounds such as volatile organic compounds (VOCs) and inorganic materials such as H_2S, water, etc. Their sensory responses and abilities depend on active material characteristics such as semiconductor type and morphology. Under ambient conditions, in p-type semiconductors, such as CuO, adsorbed oxygen molecules extract electrons to

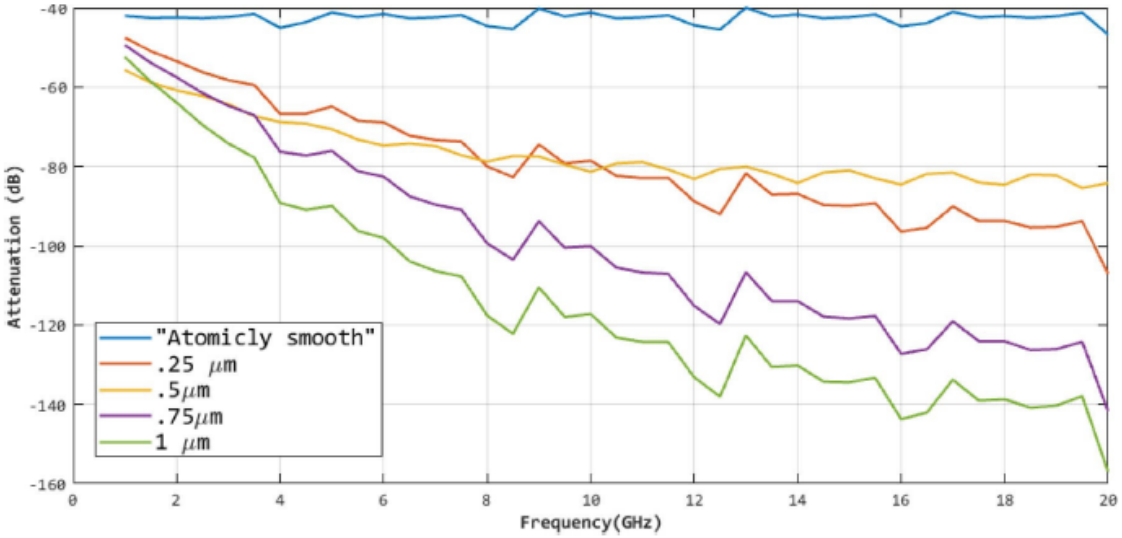

Fig. 8. Graphical summary of COMSOL simulations comparing the impact of Roughness of Cu_2O/CuO/ Air Interface on Microwave Signal Attenuation.

cause further hole formation on the surface of active sensing material, resulting in increased electrical resistance (R_{DC}) of the sensing element [22]. When oxidizing gasses, such as NO_2 or O_2, are introduced, they will withdraw even more electrons from active sites in the sensor and further decrease its resistivity. On the other hand, when reducing gasses, such as H_2S, are introduced, they donate electrons into the holes on the surface of the sensing material and thus increase its resistivity. These electron transfer processes set up dipoles on the surface of the MO [23], which induce microwave signal loss through dielectric heating [24]. The signal loss is characteristic of the electronic structure of the interfaces involved. For sensors based on CuO, the nanofilaments (1-D nanomaterials) at the film /air interface represent the optimal morphology, as they exhibit large surface to volume ratio. Indeed, nanowires (NWs) (as shown in Figure 7) have demonstrated very low detection limit for H_2S; 10 ppb H_2S detection has been achieved [25].

The sensing abilities of metal oxides can be tuned by mixing them with other oxides, as was demonstrated by [22,26]. These electron transfer processes create dipoles that are responsive to microwave probing. The sensing capabilities of these p-type semiconductors can be further improved either by controlling the carrier concentration through aliovalent doping, doping/loading the sensor material with oxide or noble metal catalysts or forming a junction between p- and n-type oxide semiconductors [27]. For example, the sensing abilities of CuO for oxidizing gasses can be further improved by decorating the CuO nanowires with TiO_2 nanoparticles (NPs), while the sensing capability for reducing gases is reduced [22]. Addition of n-type TiO_2 nanoparticles results in the formation of p-n junctions on TiO_2–CuO contact, which creates a flux of electrons from TiO_2 to CuO, and flux of holes in the opposite direction. Due to the reduction of the hole accumulation layer in CuO, resistivity of the sensing material increases. Presence of electron-withdrawing oxidizing gasses increases the hole accumulation layer back to the level of CuO NWs without the TiO_2 NPs and thus drastically decrease the resistivity. On the other hand, reducing gasses further decrease the hole accumulation layer, which was already drastically suppressed by TiO_2 NPs and thus increase in resistivity is not so pronounced, therefore, sensing activity was lowered when compared to CuO NWs without TiO_2 NPs. When it comes to H_2S sensing with p-type CuO, two mechanisms were described in the literature. The first one is described above, where H_2S is reduced by oxygen species adsorbed on CuO and electrons are released in CuO to fill holes, and thus increasing CuO resistivity. However, it was found that at higher levels of H_2S, the resistivity of sensing material decreases [28]. This is the result of sulfurization of CuO in higher H_2S levels (above 5 ppm). Higher conductivity of sensing material was ascribed to the higher contact area between adjacent nanowires induced by copper sulfide formation. However, the higher conductivity of copper sulfide may also be the reason. All these charge transfer processes alter the physico-chemical properties of the CuO, including changes in the magnetic properties, and hence its interaction with microwaves [29].

Such media supported metal oxides are advantageous in affording larger surface to volume ratios, thus presenting larger reactive surfaces for gas interaction [15,30]. A nanostructured CuO supported on semiconducting polymer membrane, such as cellulose, for gas sensing, has been demonstrated. However, these sensing applications depend on monitoring changes in electrical resistance with a circuit containing the MO-sensor, and are limited by the parasitic artefacts in the circuit such as erratic contact resistances between MO-electrode and the other electrical elements in the measurement circuit. Such

connections hamper the accurate determination of absolute resistance and relative changes that are needed for a rigorous and quantitative correlation of charge transport and catalytic properties. We suggest that non-contact BDS may be a better metrology for such a sensing application [31]. We have independently investigated and characterized cellulosic paper [32,33], which, when combined with metal oxides, could be suitable for cost-effective microwave monitored gas sensing applications. From our experience, the paper substrate for metal oxide support must be carefully chosen for BDS monitoring.

4.2 BDS Monitoring of Metal-oxide Nanostructures in Bio-applications

4.2.1 Metal-oxide Nanostructures in Disinfection

In the era of the viral pandemic, there is a heightened need for technology that improves the efficacy of personal protective equipment (PPE), such as respiratory face masks, etc. Metal oxides (MO) are known to have antiviral and other biocidal properties, copper oxide impregnated polymeric materials for PPE applications have been introduced. CuO impregnated face masks have been demonstrated to have significantly higher direct contact inactivation of both the human influenza A virus and avian influenza virus in comparison to control masks [34]. The antibacterial activity of CuO nanoparticles is generally attributed to the released Cu (II) ions, but uncertainties remain about their mechanism of toxic action. Cu-based nanoparticles may undergo profound charge-transfer transformations, under different biological and environmental conditions, which can induce significant changes in their structural and physicochemical properties and in turn, affect their toxicity. For example, depending on the amino-acidic side chain, ligands attach to the surface of CuO nanoparticles and/or alter their properties [35]. In principle, like the paper-supported MO for sensing application discussed above, non-contact BDS has the potential for monitoring the quality and capacity of such MO-impregnated PPE, as well as identify the pathogens the wearer of the PPE has been exposed to. This is possible due to the changes in the physicochemical properties of the metal oxide when exposed to biomolecules [36].

4.2.2 Metal Oxides in Electrogenerated Chemiluminescence (ECL)

Electrogenerated chemiluminescence (ECL) involves the reaction of electrogenerated species to form excited luminophores, usually via an energetic redox reaction. ECL, when combined with other bioanalytical techniques, affords stupendous increases in sensitivity, by several logs of dynamic range, and provide advantages over other assays based on radio-isotopic labels, fluorescence, enzymatic activity, etc. [37]. The detection of emission in monolayer films on metallic and degenerate semiconductor surfaces showed that emission from the excited states generated by electron transfer could compete with quenching by the electrode. Potential applications of such films include active displays and means of trace analysis [38]. By adsorption of the ECL-active molecule on the surface of the electrode, significant increases in sensitivity should be possible [39]. An ECL sensor fabricated by immobilizing $Ru(bpy)_3^{2+}$-modified CuO nanoparticles (NPs) on a TiO_2 nanotube array (TN) electrode has displayed a 30% enhanced ECL signal, and a detection limit of 9.6×10^{-10} M of tripropylamine (TPA [40]). The addition of the CuO to the n-type TiO_2 nanotubes results in the formation of p-n junctions on TiO_2–CuO contact, which creates a flux of electrons from TiO_2 to CuO, and flux of holes in the opposite direction. This changes the energetics of the redox reactions with the $Ru(bpy)_3^{2+}$ moiety. The charge transfer processes are readily monitored with non-contact microwave spectroscopy. Microwaves could be used to probe the electrode solution interface to acquire further mechanistic insights and potentially enhance the efficiency of the redox processes. Such non-contact sensing will enable remote monitoring in many areas of science including, but not limited to, environmental microbiology, virology, neurobiology, molecular biology, immunology, study, and treatment of infectious diseases [37].

5 Conclusions

Using non-contact microwave spectroscopy, we have studied the oxidation in copper-based interconnects at relatively low temperatures, around 150 °C, and showed that the roughness at the air interface is due to a composite film comprised of $Cu/Cu_2O/CuO/CuO$-nanofibers. The copper-oxide oxidation product is very redox-active and effectively dissipates microwave energy. The charge transfer reactions change the electrical properties of the copper oxide films and their microwave propagation characteristics; the extent of microwave signal loss; and loss characteristics depend on the exact physicochemical properties of the copper oxide film. We propose to leverage the changes in the microwave signal to extract analytical information about a variety of systems, such as study of material aging, gas sensing and, biomedical sensing.

Data Availability Statement

The datasets generated during and/or analysed during the current study are available from the corresponding author on reasonable request.

References

[1] *Metal Oxide Nanostructures and their Applications*, ed. Y.-B. H. Ahmad Umar. American Scientific Publishers, CA, USA, (http://www.aspbs.com/mona/).

[2] N. G. Orji, et al., *Nature Electronics* **2018**, *1*, 532–547.
[3] Y. S. Obeng, *ECS Journal of Solid State Science and Technology* **2015**, *5*, P3025-P3030.
[4] A. M. Wernbacher, et al., *J. Phys. Chem. C* **2019**, *123*, 8005–8017.
[5] R. Mahajan, B. Sankman, *3D Packaging Architectures and Assembly Process Design.* In: Li Y., Goyal D. (eds) 3D Microelectronic Packaging. Springer Series in Advanced Microelectronics, vol 57. Springer, Cham. https://doi.org/10.1007/978-3-319-44586-1_2.
[6] T. Frank, et al., *Microelectronics Reliability* **2013**, *53*, 17–29.
[7] K. Yoon et al., "Modeling and analysis of coupling between TSVs, metal, and RDL interconnects in TSV-based 3D IC with silicon interposer," 2009 11th Electronics Packaging Technology Conference, Singapore, 2009, pp. 702–706, doi: 10.1109/EPTC.2009.5416458..
[8] S. Kang, et al., *J. Electron. Mater.* **2001**, *30*, 1506–1512.
[9] S.-K. Lee, H.-C. Hsu, W.-H. Tuan, *Materials Research* **2016**, *19*, 51–56.
[10] D. Kramer, Y. Wang, J. Wharton, *Faraday Discuss.* **2015**, *180*, 137–149.
[11] C. Okoro, et al., *J. Appl. Phys.* **2014**, *115*, 243509.
[12] L. Yuan, et al., *Acta Mater.* **2011**, *59*, 2491–2500.
[13] O. Baranov, G. Filipič, U. Cvelbar, *Plasma Sources Sci. Technol.* **2019**, *28*. 084002.
[14] A. A. Samokhvalov, et al., *Phys. Solid State* **1998**, *40*, 268–271.
[15] B. Guo, et al., *Nanomaterials* **2019**, *9*, 1405.
[16] M. Green, X. Chen, *Journal of Materiomics* **2019**, *5*, 503–541.
[17] P. K. Amoah, et al., *ECS Journal of Solid State Science and Technology*, **2018**, *7*, N143-N149.
[18] C. Okoro, et al., *Electron Devices IEEE Transactions on*, **2013**, *60*, 2015–2021.
[19] Papa K. Amoah, Jesus Perez, Yaw S. Oben, *Application of Broadband RF Metrology to Integrated Circuit Interconnect Reliability Analyses: Monitoring Copper Interconnect Corrosion in 3D-ICs,. in Proceedings of the 2020 International Conference on Microelectronic Test Structures, April 6–9,, Session 7.5.* **2020**, Edinburgh, United Kingdom: IEEE.
[20] Y. Shlepnev, *Unified approach to interconnect conductor surface roughness modelling. in 2017 IEEE 26th Conference on Electrical Performance of Electronic Packaging and Systems (EPEPS).* **2017**.
[21] X. F. Zhang, et al., *Appl. Phys. Lett.* **2006**, *89*, 053115.
[22] S.-W. Choi, et al., *J. Mater. Chem. C* **2014**, *2*, 8911–8917.
[23] T. I. Barry, F. S. Stone, *Proceedings of the Royal Society of London. Series A, Mathematical and Physical Sciences* **1960**, *255*, 124–144.
[24] D. Stuerga, *Microwave-Material Interactions and Dielectric Properties, Key Ingredients for Mastery of Chemical Microwave Processes*, in *Microwaves in Organic Synthesis.* A. Loupy (Ed.). p. 1–61 doi:10.1002/9783527619559.ch1.
[25] S. Steinhauer, et al., *Sens. Actuators B* **2013**, *186*, 550–556.
[26] Y. Wang, et al., *Sens. Actuators B* **2015**, *209*, 515–523.
[27] H.-J. Kim, J.-H. Lee, *Sens. Actuators B* **2014**, *192*, 607–627.
[28] J. Chen, et al., *J. Phys. Chem. C* **2008**, *112*, 16017–16021.
[29] A. Rydosz, A. Brudnik, K. Staszek, *Materials* **2019**, *12*, 13.
[30] W. Hittini, et al., *Sci. Rep.* **2020**, *10*, 2940.
[31] C. Heine, et al., *Applied Physics A* **2013**, *112*: 289–296.
[32] M. Kombolias, et al., *Anal. Lett.* **2020**, *53*, 424–435.
[33] M. Kombolias, et al., *Tappi journal* **2018**, *17*, 501–506.
[34] G. Borkow, et al., *PLoS One* **2010**, *5*, e11295.
[35] E. Badetti, et al., *Nanomaterials* **2019**, *9, 792*.
[36] M. J. Limo, et al., *Chem. Rev.* **2018**, *118*, 11118–11193.
[37] P. W. Rhyne, et al., *Bioanalysis* **2009**, *1*, 919–935.
[38] W. Miao, *Chem. Rev.* **2008**, *108*, 2506–2553.
[39] Y. S. Obeng, A. J. Bard, *Langmuir* **1991**, *7*, 195–201.
[40] Z. Yan, et al., *Electroanalysis* **2014**, *26*, 2017–2022.

Received: August 28, 2020
Accepted: August 31, 2020
Published online on September 21, 2020

Chapter 5

Conclusions and Perspectives

CuO NWs were fabricated via thermal oxidation and used as a model material for studying phase transformations. In the first part of the thesis, the mechanism of NW growth was unraveled, and optimization of the experimental parameters was performed to achieve the growth of the ultrathin NWs. These were then used as a model material to study the mechanisms of oxide-to-sulfide phase transformations and explore different phenomena and influencing factors, disclosing new phenomena not observed before. The main conclusions are summarized with respect to each thesis objective:

Objective 1: Understanding the mechanism driving the growth of metal oxide NWs formed during the oxidation of a metal foil.

The mechanism of nanowire metal oxide NW growth by plasma-assisted metal-foil oxidation was studied by oxidizing Zn, Cu and Fe foils. The oxygen plasma synthesis proved to be a universal tool for obtaining metal oxide nanostructures, such as NWs and nanobelts. The plasma assists with oxidation via ion bombardment of the metal surface, forming microstructured "hillocks" or nucleated sites that serve as a starting point for the nanostructure's growth. In addition, due to the presence of reactive species in the plasma, the oxidation proceeds faster than in conventional thermal oxidation.

Nevertheless, despite all the advantages of plasma utilization, thermal oxidation without plasma is more straightforward as it requires no special equipment and allows better control over the final NW parameters. Thermal oxidation proved particularly useful for the production of dense CuO NW arrays. Therefore, as the model material to study phase transformations, we selected CuO NWs obtained via copper thermal oxidation, and in the subsequent research, this material was employed in the experiments.

The mechanism of the CuO NW thermal growth was studied experimentally with electron microscopy, as well as theoretical modeling. According to the results, the overall process and mechanism of NW formation can be described in the following way. Copper thermal oxidation starts with the formation of smaller equiaxed Cu_2O grains, which extend to randomly oriented columnar grains forming a Cu_2O layer, serving as a pathway for the diffusion of copper species towards the surface. On the top of the Cu_2O layer, the CuO layer is formed, consisting of preferentially oriented grains. The position of the Cu_2O–CuO interface is mainly governed by the concentration gradient of oxygen molecules diffusing inside the layers. We found that oxygen pressure does not significantly affect the growth of the Cu_2O layer, which grows through the decomposition of the CuO layer.

In contrast, it greatly affects the growth of the CuO layer, which grows on top via a reaction between copper and oxygen. CuO NWs originate in the CuO layer, most likely in equiaxed grains, which exhibit defects in the form of a twin boundary. This defect acts as a site with increased catalytic activity, where oxidation proceeds much faster, elongating the NW in one dimension. Copper supply to the NW top occurs through surface and twin-boundary diffusion. Depending on which type of diffusion is dominant, NWs can exhibit different morphologies. NWs, where the twin boundary is the prevailing diffusion, are longer and thinner than NWs, where surface diffusion is the prevailing type. This is because, during surface diffusion, copper species can react on the NW side, contributing to its thickening, and, therefore, fewer copper atoms reach the top of the NW, contributing to NW elongation. The reason why these NWs still attain an elongated shape is the redistribution of internal energy of the oxygen molecules during the adsorption on the NW surface. This energy can be partially used to desorb the oxygen molecule. Due to the catalytic

characteristics of the NW tops with more imperfections than the NW sides, the energy for oxygen adsorption is higher on the NW tops. Therefore, fewer oxygen molecules are desorbed on the NW top, which in this way collects more oxygen molecules, contributing to the oxidation reaction. Since oxygen adsorption and copper diffusion, the main processes driving the oxidation, strongly depend on the temperature, the temperature is the main factor influencing the NW growth and morphology.

Objective 2: Finding the conditions for the synthesis of ultra-thin CuO NWs and determining the lower NW diameter limit that can be achieved using thermal oxidation

The second objective focused on finding the thinnest NWs that can be achieved by thermal oxidation to optimize the synthesis parameters for obtaining ultra-thin NWs.

The time and oxygen pressure did not significantly influence the NW diameters. However, they do influence the NW density. The conditions were selected for obtaining the maximum NW density to facilitate the evaluation of the NW growth. The main parameter that influences the NW diameters is the oxidation temperature. Therefore, by gradually decreasing the oxidation temperature, we found that the lowest temperature where NWs were still observed was 187 ± 5 °C. Since the average diameter of the NWs directly correlates with the temperature, with lower oxidation temperatures resulting in thinner NWs, this temperature was where the thinnest NWs were obtained. The average diameter of such NWs was found to correspond to approximately 8 nm. However, the thinnest NWs found to grow at this temperature exhibited thicknesses between 3 and 4 nm. The correlation between NW diameters and the temperature was explained with the theoretical modeling of the thermodynamics of NW nucleation and evaluation of the temperature dependence of the critical NW nucleus. After initiation of their growth, NWs grow only in one dimension, without considerable thickening. Therefore, the size of the critical CuO nucleus was assumed to correspond to the smallest value of the NW diameter. Small changes in the oxidation temperature (up to 50 °C) have a small impact on the critical diameter of CuO NWs. Hence, very thin NWs can also be observed at slightly higher oxidation temperatures than the determined limiting temperature. This is useful as the NW density at the limiting temperature is very low. We can obtain denser NW arrays that are still sufficiently thin by moderately increasing the temperature. Satisfactory agreement between the experiments and the simple modeling approach indicated that the thermodynamics of NW nucleation indeed plays a role in determining the NW diameters. The reasons why NWs do not grow below the determined temperature can be connected to the ceased formation of the CuO phase at lower temperatures and insufficient grain-boundary diffusion of copper through the oxide layers.

Objective 3: Exploration of the anion-exchange phase-transformation mechanism and factors influencing the mechanism, using copper oxide and copper sulfide as a model system

Objective 3 focused on using the produced NWs as a model system to study the mechanism of oxide-to-sulfide phase transformations. This was done by sulfurization of the NWs with H_2S gas under different conditions and in different environments.

In the first part of the study, NWs were treated with H_2S in two regimes. In the first regime, isolated NWs were sulfurized, while in the other regime, NWs that were still attached to the underlying substrate from which they grew, were treated. In this way, the amount of copper that is accessible to the NWs and can participate in sulfurization reactions differs between the two regimes. In the case of the isolated NWs, the amount of copper is limited to the copper present in the NW. On the other hand, when the NWs are attached to a macro-scaled copper foil, they have access to a practically infinite amount of copper, which could diffuse inside the NW and contribute to the reaction. It was found that the result of the transformation differs depending on the regime used. Sulfurization of the isolated NWs results in the anion exchange of oxygen anions with sulfur. Due to the faster outward diffusion of copper and oxygen species compared to the inward diffusion of sulfur species, the resulting nanowires are polycrystalline and exhibit Kirkendall voids. On the contrary, if the NWs are still attached to the underlying substrate, an additional mechanism comes into play, which includes the reaction of copper species from the underlying layers, diffusing in the NW during the reaction with H_2S. Due to the additional supply of material in the NW, the resulting structures are considerably thicker. This process is analogous to the growth of CuO NWs. However, instead of growing in 1D, the nanostructures grow in all directions.

Nevertheless, the topmost part of the NW is still the most active site for the reaction and thickens the most. The copper sulfide phase was also dependent on the regime used. When

isolated NWs were used, the NW transformed upon sulfurization to the covellite (CuS) phase. On the other hand, when the NWs had access to an additional copper supply, the resulting phase was Cu_2S.

To further explore the mechanism of anion exchange, the CuO NWs were sulfurized in the post-glow region of a microwave Ar/H_2S plasma. It was found that apart from the phase transformation, plasma induces a dimensionality change by transforming the 1D CuO NW to 2D CuS nanoplates that are arranged along the NW length. The nanoplates originate in equiaxed grains that are formed on the NW surface in the initial sulfurization stages. If the NW diameter is sufficiently small, the transformed NW attains a shape with single-crystalline nanoplates arranged one-dimensionally along the NW length. Hence, the single crystallinity is preserved along the two dimensions of the NW. The critical NW diameter for this to happen depends on the reaction time, and it amounts to approximately 10 nm for the time when the thinnest NWs are completely converted.

Further outlook

The analysis of CuO NW thermal growth with developed theoretical approaches explaining the processes occurring during oxidation represents a contribution towards the controlled synthesis of CuO NWs, which will facilitate their utilization in applications. However, exploring the NW growth mechanisms and factors influencing the morphology should be continued in the future as there are countless factors, such as humidity, use of an external electric field, composition of oxidized metal, etc., which still require further analysis for a complete assessment of the influences on NW growth. Therefore, even though the thermal growth of CuO NWs has been reported in numerous studies for more than 20 years, we can expect further research on their growth for many years to come.

Concerning phase transformations in nanomaterials, the ion-exchange transformation for the synthesis of advanced materials is still new and, to a large extent, unexplored. For example, in this thesis, two phenomena related to such transformations, i.e., dependence of the transformation mechanism on the cation supply and dimensionality transition, have been reported, which have not been emphasized in the literature yet. This indicates that there are many more interesting phenomena waiting to be discovered, which will further contribute to the understanding of the dynamic processes in the solid state occurring on the nanoscale, enabling further advances in the design and synthesis of new nanomaterials.

In addition, relating to the research done in this thesis, expanding the results obtained on other ionic materials models is necessary to confirm the universality of the studied phenomena. Furthermore, the transformation of NWs indicated that the preservation of single crystallinity of the transformed NWs is possible in two dimensions as a single-crystalline NW transformed into multiple single crystals arranged in 1D. However, the conditions required to successfully execute an anion exchange on a nanowire while completely retaining its single crystallinity pose a challenge and should be the subject of further research.

References

[1] M. Meyyappan and M. K. Sunkara, *Inorganic Nanowires Applications, Properties and Characterization*, 1st ed. Boca Raton: CRC Press, 2009.

[2] A. L. Briseno, S. C. B. Mannsfeld, S. A. Jenekhe, Z. Bao, and Y. Xia, "Introducing organic nanowire transistors," *Mater. Today*, vol. 11, no. 4, pp. 38–47, Apr. 2008, doi: 10.1016/S1369-7021(08)70055-5.

[3] L. N. Quan *et al.*, "Introduction: 1D Nanomaterials/Nanowires," *Chem. Rev.*, vol. 119, no. 15, pp. 8955–8957, Aug. 2019, doi: 10.1021/ACS.CHEMREV.9B00423.

[4] L. Dai, C. H. Sow, C. T. Lim, and V. B. C. T, "Metal Oxide Nanowires – Structural and Mechanical Properties," in *Nanowires - Fundamental Research*, 2012. doi: 10.5772/16349.

[5] R. S. Devan, R. A. Patil, J. H. Lin, and Y. R. Ma, "One-dimensional metal-oxide nanostructures: Recent developments in synthesis, characterization, and applications," *Adv. Funct. Mater.*, vol. 22, no. 16, pp. 3326–3370, 2012, doi: 10.1002/adfm.201201008.

[6] E. Comini and G. Sberveglieri, "Metal oxide nanowires as chemical sensors," *Mater. Today*, vol. 13, no. 7–8, pp. 36–44, Jul. 2010, doi: 10.1016/S1369-7021(10)70126-7.

[7] T. Q. Nguyen, "Scalable production and applications of metal oxide," 2016.

[8] Gregor Filipič and Uroš Cvelbar, "Copper oxide nanowires: a review of growth," *Nanotechnology*, vol. 23, no. 19, p. 194001, Apr. 2012, doi: 10.1088/0957-4484/23/19/194001.

[9] E. Comini, G. Faglia, M. Ferroni, A. Ponzoni, A. Vomiero, and G. Sberveglieri, "Metal oxide nanowires: Preparation and application in gas sensing," *J. Mol. Catal. A Chem.*, vol. 305, no. 1–2, pp. 170–177, 2009, doi: 10.1016/j.molcata.2009.01.009.

[10] J. B. Rivest and P. K. Jain, "Cation exchange on the nanoscale: An emerging technique for new material synthesis, device fabrication, and chemical sensing," *Chem. Soc. Rev.*, vol. 42, no. 1, pp. 89–96, Dec. 2013, doi: 10.1039/c2cs35241a.

[11] M. Lu, M. K. Li, L. B. Kong, X. Y. Guo, and H. L. Li, "Silicon quantum-wires arrays synthesized by chemical vapor deposition and its micro-structural properties," *Chem. Phys. Lett.*, vol. 374, no. 5–6, pp. 542–547, Jun. 2003, doi: 10.1016/S0009-2614(03)00747-4.

[12] T. Dlugosch, A. Chnani, P. Muralidhar, A. Schirmer, J. Biskupek, and S. Strehle, "Thermal oxidation synthesis of crystalline iron-oxide nanowires on low-cost steel substrates for solar water splitting," *Semicond. Sci. Technol.*, vol. 32, no. 8, p. 084001, Jul. 2017, doi: 10.1088/1361-6641/aa7593.

[13] S. Grigorescu *et al.*, "Thermal air oxidation of Fe: Rapid hematite nanowire growth and photoelectrochemical water splitting performance," *Electrochem. commun.*, vol. 23, no. 1, pp. 59–62, Sep. 2012, doi: 10.1016/j.elecom.2012.06.038.

[14] L. Yuan *et al.*, "The origin of hematite nanowire growth during the thermal oxidation of iron," *Mater. Sci. Eng. B*, vol. 177, no. 3, pp. 327–336, Feb. 2012, doi: 10.1016/J.MSEB.2011.12.034.

[15] M. R. Khanlary, V. Vahedi, and A. Reyhani, "Synthesis and characterization of ZnO nanowires by thermal oxidation of zn thin films at various temperatures," *Molecules*, vol. 17, no. 5, pp. 5021–5029, May 2012, doi: 10.3390/molecules17055021.

[16] C. X. Zhao *et al.*, "Large-scale synthesis of bicrystalline ZnO nanowire arrays by thermal oxidation of zinc film: Growth mechanism and high-performance field emission," *Cryst. Growth Des.*, vol. 13, no. 7, pp. 2897–2905, Jul. 2013, doi: 10.1021/cg400318f.

[17] B. J. Hansen, G. Lu, and J. Chen, "Direct oxidation growth of CuO nanowires from copper-containing substrates," *J. Nanomater.*, vol. 2008, no. 1, 2008, doi: 10.1155/2008/830474.

[18] B. J. Hansen, N. Kouklin, G. Lu, I. K. Lin, J. Chen, and X. Zhang, "Transport, analyte detection, and opto-electronic response of p-type CuO nanowires," *J. Phys. Chem. C*, vol. 114, no. 6, pp. 2440–2447, Feb. 2010, doi: 10.1021/JP908850J/ASSET/IMAGES/LARGE/JP-2009-08850J_0005.JPEG.

[19] M. Kaur *et al.*, "Growth and branching of CuO nanowires by thermal oxidation of copper," *J. Cryst. Growth*, vol. 289, no. 2, pp. 670–675, Apr. 2006, doi: 10.1016/J.JCRYSGRO.2005.11.111.

[20] X. Liu, Z. Li, Q. Zhang, F. Li, and T. Kong, "CuO nanowires prepared via a facile solution route and their photocatalytic property," *Mater. Lett.*, vol. 72, pp. 49–52, Apr. 2012, doi: 10.1016/J.MATLET.2011.12.077.

[21] H. H. Lin, C. Y. Wang, H. C. Shih, J. M. Chen, and C. Te Hsieh, "Characterizing well-ordered CuO nanofibrils synthesized through gas-solid reactions," *J. Appl. Phys.*, vol. 95, no. 10, pp. 5889–5895, May 2004, doi: 10.1063/1.1690114.

[22] C. Ma, L. Zhu, S. Chen, and Y. Zhao, "Simple and rapid preparation of CuO nanowires and their optical properties," *Mater. Lett.*, vol. 108, pp. 114–117, Oct. 2013, doi: 10.1016/J.MATLET.2013.06.101.

[23] M. Vila, C. Díaz-Guerra, and J. Piqueras, "Optical and magnetic properties of CuO nanowires grown by thermal oxidation," *J. Phys. D. Appl. Phys.*, vol. 43, no. 13, p. 135403, Mar. 2010, doi: 10.1088/0022-3727/43/13/135403.

[24] X. Zhao, P. Wang, Z. Yan, and N. Ren, "Room temperature photoluminescence properties of CuO nanowire arrays," *Opt. Mater. (Amst).*, vol. 42, pp. 544–547, Apr. 2015, doi: 10.1016/J.OPTMAT.2014.12.032.

[25] S. Steinhauer, "Gas Sensors Based on Copper Oxide Nanomaterials: A Review," *Chemosens. 2021, Vol. 9, Page 51*, vol. 9, no. 3, p. 51, Mar. 2021, doi: 10.3390/CHEMOSENSORS9030051.

[26] J. Chen, K. Wang, L. Hartman, and W. Zhou, "H2S detection by vertically aligned CuO nanowire array sensors," *J. Phys. Chem. C*, vol. 112, no. 41, pp. 16017–16021, Oct. 2008.

[27] J. H. Kim, A. Katoch, S. W. Choi, and S. S. Kim, "Growth and sensing properties of networked p-CuO nanowires," *Sensors Actuators B Chem.*, vol. 212, pp. 190–195, Jun. 2015, doi: 10.1016/J.SNB.2014.12.081.

[28] J. Y. Kim, J. H. Lee, J. H. Kim, A. Mirzaei, H. Woo Kim, and S. S. Kim, "Realization of H2S sensing by Pd-functionalized networked CuO nanowires in self-heating mode," *Sensors Actuators B Chem.*, vol. 299, p. 126965, Nov. 2019, doi: 10.1016/J.SNB.2019.126965.

[29] D. Li, J. Hu, R. Wu, and J. G. Lu, "Conductometric chemical sensor based on individual CuO nanowires," *Nanotechnology*, vol. 21, no. 48, p. 485502, Nov. 2010, doi: 10.1088/0957-4484/21/48/485502.

[30] X. Li, Y. Wang, Y. Lei, and Z. Gu, "Highly sensitive H2S sensor based on template-synthesized CuO nanowires," *RSC Adv.*, vol. 2, no. 6, pp. 2302–2307, Feb. 2012, doi: 10.1039/C2RA00718E.

[31] S. Steinhauer, E. Brunet, T. Maier, G. C. Mutinati, and A. Köck, "Suspended CuO nanowires for ppb level H2S sensing in dry and humid atmosphere," *Sensors Actuators B Chem.*, vol. 186, pp. 550–556, Sep. 2013, doi: 10.1016/J.SNB.2013.06.044.

[32] O. Lupan *et al.*, "Single and networked CuO nanowires for highly sensitive p-type

semiconductor gas sensor applications," *Phys. status solidi – Rapid Res. Lett.*, vol. 10, no. 3, pp. 260–266, Mar. 2016, doi: 10.1002/PSSR.201510414.

[33] M. Mashock, K. Yu, S. Cui, S. Mao, G. Lu, and J. Chen, "Modulating gas sensing properties of CuO nanowires through creation of discrete nanosized p-n junctions on their surfaces," *ACS Appl. Mater. Interfaces*, vol. 4, no. 8, pp. 4192–4199, Aug. 2012, doi: 10.1021/am300911z.

[34] J. Tan *et al.*, "Self-template derived CuO nanowires assembled microspheres and its gas sensing properties," *Sensors Actuators B Chem.*, vol. 252, pp. 1–8, Nov. 2017, doi: 10.1016/J.SNB.2017.05.107.

[35] Q. Zhang *et al.*, "CuO/Cu2O nanowire arrays grafted by reduced graphene oxide: synthesis, characterization, and application in photocatalytic reduction of CO2," *RSC Adv.*, vol. 7, no. 69, pp. 43642–43647, Sep. 2017, doi: 10.1039/C7RA07310K.

[36] V. Scuderi *et al.*, "Photocatalytic activity of CuO and Cu2O nanowires," *Mater. Sci. Semicond. Process.*, vol. 42, pp. 89–93, Feb. 2016, doi: 10.1016/j.mssp.2015.08.008.

[37] B. K. Deka, A. Hazarika, J. Kim, Y. Bin Park, and H. W. Park, "Multifunctional CuO nanowire embodied structural supercapacitor based on woven carbon fiber/ionic liquid–polyester resin," *Compos. Part A Appl. Sci. Manuf.*, vol. 87, pp. 256–262, Aug. 2016, doi: 10.1016/J.COMPOSITESA.2016.05.007.

[38] V. H. Luan, J. H. Han, H. W. Kang, and W. Lee, "Highly porous and capacitive copper oxide nanowire/graphene hybrid carbon nanostructure for high-performance supercapacitor electrodes," *Compos. Part B Eng.*, vol. 178, p. 107464, Dec. 2019, doi: 10.1016/J.COMPOSITESB.2019.107464.

[39] Q. Liu *et al.*, "In Situ Imaging the Oxygen Reduction Reactions of Solid State Na-O2 Batteries with CuO Nanowires as the Air Cathode," *Nano Lett.*, vol. 18, no. 6, pp. 3723–3730, Jun. 2018, doi: 10.1021/acs.nanolett.8b00894.

[40] F. Wang *et al.*, "Controlled synthesis of uniform ultrafine CuO nanowires as anode material for lithium-ion batteries," *J. Alloys Compd.*, vol. 509, no. 41, pp. 9798–9803, Oct. 2011, doi: 10.1016/J.JALLCOM.2011.07.109.

[41] L. Wang, K. Zhang, Z. Hu, W. Duan, F. Cheng, and J. Chen, "Porous CuO nanowires as the anode of rechargeable Na-ion batteries," *Nano Res.*, vol. 7, no. 2, pp. 199–208, Dec. 2013, doi: 10.1007/s12274-013-0387-6.

[42] Z. Wang, Y. Zhang, H. Xiong, C. Qin, W. Zhao, and X. Liu, "Yucca fern shaped CuO nanowires on Cu foam for remitting capacity fading of Li-ion battery anodes," *Sci. Reports 2018 81*, vol. 8, no. 1, pp. 1–10, Apr. 2018, doi: 10.1038/s41598-018-24963-2.

[43] X. Zhang *et al.*, "Ag nanoparticles enhanced vertically-aligned CuO nanowire arrays grown on Cu foam for stable hybrid supercapacitors with high energy density," *Electrochim. Acta*, vol. 296, pp. 535–544, Feb. 2019, doi: 10.1016/J.ELECTACTA.2018.11.046.

[44] A. Waris *et al.*, "A comprehensive review of green synthesis of copper oxide nanoparticles and their diverse biomedical applications," *Inorg. Chem. Commun.*, vol. 123, p. 108369, Jan. 2021, doi: 10.1016/J.INOCHE.2020.108369.

[45] M.-S. Jo *et al.*, "Aligned CuO nanowire array for a high performance visible light photodetector," *Sci. Reports 2022 121*, vol. 12, no. 1, pp. 1–11, Feb. 2022, doi: 10.1038/s41598-022-06031-y.

[46] Y. H. Ko, G. Nagaraju, S. H. Lee, and J. S. Yu, "Facile preparation and optoelectronic properties of CuO nanowires for violet light sensing," *Mater. Lett.*, vol. 117, pp. 217–220, Feb. 2014, doi: 10.1016/J.MATLET.2013.11.119.

[47] L. B. Luo *et al.*, "One-dimensional CuO nanowire: synthesis, electrical, and optoelectronic devices application," *Nanoscale Res. Lett.*, vol. 9, no. 1, p. 637, Dec. 2014, doi: 10.1186/1556-276X-9-637.

[48] L. Yuan, Y. Wang, R. Mema, and G. Zhou, "Driving force and growth mechanism for spontaneous oxide nanowire formation during the thermal oxidation of metals," *Acta*

Mater., vol. 59, no. 6, pp. 2491–2500, Apr. 2011, doi: 10.1016/j.actamat.2010.12.052.
[49] L. Xiang, J. Guo, C. Wu, M. Cai, X. Zhou, and N. Zhang, "A brief review on the growth mechanism of CuO nanowires via thermal oxidation," *J. Mater. Res.*, vol. 33, no. 16, pp. 2264–2280, Aug. 2018, doi: 10.1557/JMR.2018.215/FIGURES/6.
[50] J. Shi *et al.*, "Synergistic effects on thermal growth of CuO nanowires," *J. Alloys Compd.*, vol. 815, p. 152355, Jan. 2020, doi: 10.1016/j.jallcom.2019.152355.
[51] M. Chen, Y. Yue, and Y. Ju, "Growth of metal and metal oxide nanowires driven by the stress-induced migration," in *Journal of Applied Physics*, May 2012, vol. 111, no. 10, p. 104305. doi: 10.1063/1.4718436.
[52] R. Mema, L. Yuan, Q. Du, Y. Wang, and G. Zhou, "Effect of surface stresses on CuO nanowire growth in the thermal oxidation of copper," *Chem. Phys. Lett.*, vol. 512, no. 1–3, pp. 87–91, 2011, doi: 10.1016/j.cplett.2011.07.012.
[53] S. Rackauskas *et al.*, "In situ study of noncatalytic metal oxide nanowire growth," *Nano Lett.*, vol. 14, no. 10, pp. 5810–5813, Oct. 2014, doi: 10.1021/nl502687s.
[54] X. Sun *et al.*, "Atomic-Scale Mechanism of Unidirectional Oxide Growth," *Adv. Funct. Mater.*, vol. 30, no. 4, p. 1906504, Jan. 2020, doi: 10.1002/adfm.201906504.
[55] F. Cao *et al.*, "Thermal-induced formation of domain structures in CuO nanomaterials," *Phys. Rev. Mater.*, no. 5, Oct. 2017, doi: 10.1103/PhysRevMaterials.1.053401.
[56] E. Fernandez-Bartolome, A. Martinez-Martinez, E. Resines-Urien, L. Piñeiro-Lopez, and J. S. Costa, "Reversible single-crystal-to-single-crystal transformations in coordination compounds induced by external stimuli," *Coord. Chem. Rev.*, vol. 452, p. 214281, Feb. 2022, doi: 10.1016/J.CCR.2021.214281.
[57] A. Chaudhary, A. Mohammad, and S. M. Mobin, "Recent Advances in Single-Crystal-to-Single-Crystal Transformation at the Discrete Molecular Level," *Crystal Growth and Design*, vol. 17, no. 5. American Chemical Society, pp. 2893–2910, May 03, 2017. doi: 10.1021/acs.cgd.7b00154.
[58] G. Cho, Y. Park, Y. K. Hong, and D. H. Ha, "Ion exchange: an advanced synthetic method for complex nanoparticles," *Nano Convergence*, vol. 6, no. 1. Korea Nano Technology Research Society, pp. 1–17, Dec. 01, 2019. doi: 10.1186/s40580-019-0187-0.
[59] M. Saruyama, R. Sato, and T. Teranishi, "Transformations of Ionic Nanocrystals via Full and Partial Ion Exchange Reactions," *Acc. Chem. Res.*, vol. 54, no. 4, pp. 765–775, Feb. 2021, doi: 10.1021/ACS.ACCOUNTS.0C00701.
[60] H. L. Wu *et al.*, "Formation of pseudomorphic nanocages from Cu2O nanocrystals through anion exchange reactions," *Science (80-.).*, vol. 351, no. 6279, pp. 1306–1310, Mar. 2016, doi: 10.1126/science.aad5520.
[61] Z. Fan, L. C. Lin, W. Buijs, T. J. H. Vlugt, and M. A. Van Huis, "Atomistic understanding of cation exchange in PbS nanocrystals using simulations with pseudoligands," *Nat. Commun. 2016 71*, vol. 7, no. 1, pp. 1–8, May 2016, doi: 10.1038/ncomms11503.
[62] U. Jeong, P. H. C. Camargo, Y. H. Lee, and Y. Xia, "Chemical transformation: a powerful route to metal chalcogenide nanowires," *J. Mater. Chem.*, vol. 16, no. 40, pp. 3893–3897, Oct. 2006, doi: 10.1039/B606682H.
[63] U. Jeong, Y. Xia, and Y. Yin, "Large-scale synthesis of single-crystal CdSe nanowires through a cation-exchange route," *Chem. Phys. Lett.*, vol. 416, no. 4–6, pp. 246–250, Dec. 2005, doi: 10.1016/j.cplett.2005.09.106.
[64] R. Ma, Y. Wang, and T. E. Mallouk, "Patterned Nanowires of Se and Corresponding Metal Chalcogenides from Patterned Amorphous Se Nanoparticles," *Small*, vol. 5, no. 3, pp. 356–360, Feb. 2009, doi: 10.1002/smll.200801190.
[65] A. Dorn, P. M. Allen, D. K. Harris, and M. G. Bawendi, "In situ electrical monitoring of cation exchange in nanowires," *Nano Lett.*, vol. 10, no. 10, pp. 3948–3951, Oct. 2010, doi: 10.1021/nl102560b.
[66] A. E. Powell, J. M. Hodges, and R. E. Schaak, "Preserving Both Anion and Cation Sublattice Features during a Nanocrystal Cation-Exchange Reaction: Synthesis of

Metastable Wurtzite-Type CoS and MnS," *J. Am. Chem. Soc.*, vol. 138, no. 2, pp. 471–474, Jan. 2016, doi: 10.1021/JACS.5B10624.

[67] H. Li *et al.*, "Sequential cation exchange in nanocrystals: Preservation of crystal phase and formation of metastable phases," *Nano Lett.*, vol. 11, no. 11, pp. 4964–4970, Nov. 2011, doi: 10.1021/NL202927A.

[68] S. Kim *et al.*, "Phase segregated Cu2−xSe/Ni3Se4 bimetallic selenide nanocrystals formed through the cation exchange reaction for active water oxidation precatalysts," *Chem. Sci.*, vol. 11, no. 6, pp. 1523–1530, Feb. 2020, doi: 10.1039/C9SC04371C.

[69] G. Gariano *et al.*, "Role of the Crystal Structure in Cation Exchange Reactions Involving Colloidal Cu2Se Nanocrystals," *J. Am. Chem. Soc.*, vol. 139, no. 28, pp. 9583–9590, Jul. 2017, doi: 10.1021/jacs.7b03706.

[70] H. S. Dong, S. M. Hughes, Y. Yin, and A. P. Alivisatos, "Cation exchange reactions in ionic nanocrystals," *Science (80-.).*, vol. 306, no. 5698, pp. 1009–1012, Nov. 2004, doi: 10.1126/science.1103755.

[71] Z. Li, M. Saruyama, T. Asaka, Y. Tatetsu, and T. Teranishi, "Determinants of crystal structure transformation of ionic nanocrystals in cation exchange reactions," *Science (80-.).*, vol. 373, no. 6552, pp. 332–337, Jul. 2021, doi: 10.1126/SCIENCE.ABH2741.

[72] J. Park, H. Zheng, Y. W. Jun, and A. P. Alivisatos, "Hetero-epitaxial anion exchange yields single-crystalline hollow nanoparticles," *J. Am. Chem. Soc.*, vol. 131, no. 39, pp. 13943–13945, Oct. 2009, doi: 10.1021/ja905732q.

[73] Y. K. Hong, Y. Park, H. Kang, H. Son, and D. H. Ha, "Nanoparticle transformation from ZnO to ZnS through anion exchange with di-tert-butyl disulphide," *Dalt. Trans.*, vol. 50, no. 6, pp. 2192–2199, Feb. 2021, doi: 10.1039/D0DT03940C.

[74] Y. Lim, C. H. Lee, C. H. Jun, K. Kim, and J. Cheon, "Morphology-Conserving Non-Kirkendall Anion Exchange of Metal Oxide Nanocrystals," *J. Am. Chem. Soc.*, vol. 142, no. 20, pp. 9130–9134, May 2020, doi: 10.1021/jacs.0c03230.

[75] B. Jia *et al.*, "Robust Anion Exchange Realized in Crystalline Metal Cyanamide Nanoparticles," *Chem. Mater.*, vol. 31, no. 22, pp. 9532–9539, Nov. 2019, doi: 10.1021/ACS.CHEMMATER.9B03934.

[76] J. Thangala, Z. Chen, A. Chin, C. Z. Ning, and M. K. Sunkara, "Phase transformation studies of metal oxide nanowires," *Cryst. Growth Des.*, vol. 9, no. 7, pp. 3177–3182, Jul. 2009, doi: 10.1021/cg801198p.

[77] X. Jiang, T. Herricks, and Y. Xia, "CuO Nanowires Can Be Synthesized by Heating Copper Substrates in Air," *Nano Lett.*, vol. 2, no. 12, pp. 1333–1338, 2002, doi: 10.1021/NL0257519.

[78] A. M. B. Gonçalves, L. C. Campos, A. S. Ferlauto, and R. G. Lacerda, "On the growth and electrical characterization of CuO nanowires by thermal oxidation," *J. Appl. Phys.*, vol. 106, no. 3, Aug. 2009, doi: 10.1063/1.3187833/370342.

[79] C. H. Xu, C. H. Woo, and S. Q. Shi, "Formation of CuO nanowires on Cu foil," *Chem. Phys. Lett.*, vol. 399, no. 1–3, pp. 62–66, Nov. 2004, doi: 10.1016/j.cplett.2004.10.005.

[80] K. Zhang, C. Rossi, C. Tenailleau, P. Alphonse, and J.-Y. Chane-Ching, "Synthesis of large-area and aligned copper oxide nanowires from copper thin film on silicon substrate," *Nanotechnology*, vol. 18, no. 27, p. 275607, Jun. 2007, doi: 10.1088/0957-4484/18/27/275607.

[81] C. C. Moise *et al.*, "On the growth of copper oxide nanowires by thermal oxidation near the threshold temperature at atmospheric pressure," *J. Alloys Compd.*, vol. 886, p. 161130, Dec. 2021, doi: 10.1016/J.JALLCOM.2021.161130.

[82] J. Hilman, A. J. Yost, J. Tang, B. Leonard, and T. Y. Chien, "Low temperature growth of CuO nanowires through direct oxidation," *Nano-Structures and Nano-Objects*, vol. 11, pp. 124–128, Jul. 2017, doi: 10.1016/j.nanoso.2017.08.004.

Bibliography

Publications Related to this PhD Thesis

Journal Articles

M. Košiček, J. Zavašnik, O. Baranov, B. Šetina Batič, and U. Cvelbar, "Understanding the growth of copper oxide nanowires and layers by thermal oxidation over a broad temperature range at atmospheric pressure," Crystal Growth & Design, vol. 22, no. 11, pp. 6656–6666, 2022. doi:10.1021/acs.cgd.2c00863

O. Baranov, M. Košiček, G. Filipič, and U. Cvelbar, "A deterministic approach to the thermal synthesis and growth of 1D metal oxide nanostructures," Applied Surface Science, vol. 566, p. 150619, 2021. doi:10.1016/j.apsusc.2021.150619

M. Košiček, O. Baranov, J. Zavašnik, and U. Cvelbar, "In search of the limits of CuO thermal oxidation nanowire growth by combining experiment and theory," Applied Physics Letters, vol. 123, no. 4, 2023. doi:10.1063/5.0151293

B. Guo et al., "Single-Crystalline Metal Oxide Nanostructures Synthesized by Plasma-Enhanced Thermal Oxidation," Nanomaterials, vol. 9, no. 10, pp. 1405–1405, 2019, doi: https://doi.org/10.3390/nano9101405.

O. Baranov et al. 'Hierarchical nanomaterials by selective deposition of noble metal nanoparticles: Insight into control and Growth Processes', Advanced Theory and Simulations, p. 230028, 2023 doi:10.1002/adts.202300288.

P.K. Amoah, et al. 'Broadband microwave signal dissipation in nanostructured copper oxide at Air-Film Interface, Electroanalysis, vol. 32, no. 12, pp. 2795–2802, 2020 doi:10.1002/elan.202060246.

Conference Paper

M. Košiček, G. Filipič, J. Zavašnik, U. Cvelbar. Manipulation of a single crystal nanowire on an atomic level, 236th ECS Meeting, 13-17. October, 2019, Atlanta, GA. ECS, 2019

M. Košiček, G. Filipič, J. Zavašnik, U. Cvelbar. Making nanowires of metal oxides at low-pressure. Međunarodni Znanstveni Sastanak Vakuumska Znanost i Tehnika, Njivice, 16-17. May 2019. Zagreb: Croatian Vacuum Society, 2019.

U. Cvelbar, G. Filipič, O. Baranov, M. Košiček, J. Zavašnik. On the quest for deterministic approach to plasma synthesis and conversion of nanowires, 24th International Symposium on Plasma Chemistry, 9-14 June, 2019, Naples (Italy).

M. Košiček, J. Zavašnik, G. Filipič, V. Shvalya, U. Cvelbar. Phase transformations in copper oxide nanowires, iPlasmaNano - X, September 15-20, 2019, Poreč, Croatia.

U. Cvelbar, M. Košiček, G. Filipič, J. Zavašnik. Plasma-assisted design of metastable nanomaterials with improved properties, Joint International Conferences and Exhibition, Smart Materials & Surfaces - SMS 2019, European Graphene Forum - EGF 2019, Nano Medicine - NanoMed 2019, 23 - 25 October. 2019, Lisbon, Portugal,

M. Košiček, J. Zavašnik, U. Cvelbar. Exploring plasma-induced phase transformations in one dimensional nanomaterials, iPlasmaNano-XI, The 11th International Symposium on Plasma Nanoscience, 4-8 September 2022, Seville, Spain

M. Košiček, J. Zavašnik, O. Baranov, B. Šetina Batič, U. Cvelbar. Fundamental insights into thermal growth of single-crystal copper-oxide nanowires: 22nd IEEE International Conference on Nanotechnology (IEEE-NANO 2022), 4-8 July, 2022, Palma de Mallorca, Spain

Other Publications

Journal Articles

R. Khobragade et al., “Exploring the effect of morphology and surface properties of nanoshaped Pd/CeO_2 catalysts on CO_2 hydrogenation to methanol,” Applied Catalysis A: General, vol. 627, p. 118394, 2021. doi:10.1016/j.apcata.2021.118394.

N. M. Santhosh et al., “Label-Free Mycotoxin Raman Identification by high-performing plasmonic vertical carbon nanostructures,” Small, vol. 17, no. 49, 2021. doi:10.1002/smll.202103677.

A. Vasudevan et al., “From faceted nanoparticles to nanostructured thin film by plasma-jet redox reaction of Ionic Gold,” Journal of Alloys and Compounds, vol. 928, p. 167155, 2022. doi:10.1016/j.jallcom.2022.167155

Biography

The author of this thesis completed his Bachelor's degree in Chemistry, entitled "Dissociation equilibria in water solutions of simple and polymeric carboxylic acids" at the Faculty for Chemistry and Chemical Technology, University of Ljubljana, Slovenia, in 2016 and completed his Master's degree entitled "Osmotic coefficients of poly(α-alkylcarboxylic acids) sodium salts" at the same faculty in 2018. Both bachelor's and master's degree were acquired under the supervision of Prof. Dr. Ksenija Kogej. In 2018, he started his work at the Jožef Stefan Institute (JSI), Ljubljana, Slovenia, at the Department of Gaseous Electronics (F6) as a young researcher and started his doctoral studies at Jožef Stefan post-graduate school (IPS), Ljubljana, Slovenia. His research topic was the study of metal oxide nanostructure growth with a particular focus on copper oxide nanowires and their phase transformations achieved by thermal and plasma-assisted methods. During his work, he was trained in various analytic methods, particularly in electron microscopy techniques (SEM and TEM). He presented his work at several international conferences. At 236th ECS meeting in Atlanta, Georgia, USA, he won the 1st DST division award for best presentation among young scientists.